UNIVERSITÀ
DEGLI STUDI
FIRENZE

DOTTORATO DI RICERCA IN
Scienze della Terra

CICLO XXXI

COORDINATORE Prof. Lorella Francalanci

The Brittle/Ductile Transition at Upper Crustal Level: Geometry, Strain Partitioning and Fluid Circulation. The Case Study of the Calamita Unit (Elba Island, Northern Apennines, Italy).

Settore Scientifico Disciplinare GEO/03

Dottorando
Dott. Samuele Papeschi

Tutore
Prof. Giovanni Musumeci

Co-Tutore
Dott. Francesco Mazzarini

Coordinatore
Prof. Lorella Francalanci

Anni 2015/2018

Abstract

This study focuses on the detailed investigation of the brittle/plastic transition in quartz-feldspathic rocks at upper-middle crustal conditions and aims to better understand the role of fluids and temperature during deformation. The Calamita Unit (Elba Island, Italy) is a high metamorphic grade unit (T ~ 650 °C) that has been intruded by a monzogranite body at shallow crustal level (P < 0.2 GPa) and coevally deformed during regional shortening for a limited time span (< 1 Ma). These conditions outline the Calamita Unit as an ideal case study to investigate the brittle/plastic transition at approximately constant pressure (i.e. depth) during temperature decrease, reproducing upper-middle crustal conditions.

The Calamita Schists are a metapsammitic complex exposed in the lower part of the Calamita Unit. Pseudosection modelling and Ti-in-biotite thermometry constrain the peak metamorphic assemblage, marked by andalusite + cordierite + biotite + K-feldspar, at upper amphibolite facies conditions (T ~ 600 – 700 °C; P ~ 0.2 GPa), with microstructures suggesting partial melting. The retrograde path is constrained by chlorite geothermometry in the 300 – 500 °C temperature range. Detailed field mapping and structural analysis have revealed at map-scale a pattern of heterogeneous deformation characterized by west-dipping high-strain domains localizing eastward-directed deformation interleaved with relatively low-strain domains. In high-strain domains, mylonitic fabrics are, in turn, overprinted in the brittle regime by non-Andersonian subhorizontal faults associated with Riedel shears networks, formed subparallel to C' shear bands. Microstructural analysis highlights that temperature decrease and fluid influx controlled the mechanical evolution of the investigated rocks, which are marked by the transition from a high-metamorphic grade foliation to shear bands and mylonites with widespread S-C and S-C' fabrics, characterized by retrograde, synkinematic white mica and chlorite.

Quartz microfabric displays an evolution from fast grain boundary migration, developed close to peak metamorphic conditions, to subgrain rotation and bulging recrystallization, tracking decreasing temperature during deformation. During decreasing temperature, deformation localized in mylonitic quartz ribbons at amphibolite facies conditions (450 °C < T < 600 °C), where recrystallization was accommodated by dislocation creep of quartz under dominant prism <a> slip, causing the development of strong Y-maximum crystallographic preferred orientations (CPO). Secondary rhomb and acute rhomb <a> slip assisted the recrystallization of grains unfavorably oriented for prism <a> slip, with the activation of slip systems whose misorientation axis lies close to the vorticity axis. At greenschist facies conditions (300 °C < T < 450 °C), deformation localized in phyllonitic domains, producing phase mixing of phyllosilicates and tiny quartz grains. Relic,

large quartz grains hardened and fractured along synthetic and conjugate shear bands. The propagation of shear bands occurred under fluid-rich conditions and was controlled by cyclic fracturing and precipitation of new quartz and phyllosilicate grains, deposited by circulating fluids. Precipitated new quartz grains developed a CPO parallel to shear bands controlled by the opening of dilatant sites. The nucleation of fine-grained quartz and 'soft' phyllosilicates enhanced strain softening and assisted strain partitioning into localized C' shear bands at the brittle/plastic transition.

In the brittle regime (T ~ 300 °C), deformation localized on previously formed C' shear bands, favorably oriented for reactivation, that acted as ductile precursors for misoriented non-Andersonian faults. Brittle deformation in fault zones was controlled by the cyclical interaction between fracturing, taking advantage of weak crystallographic planes in quartz such as the rhombs, and fluid infiltration, assisting the precipitation of new quartz and phyllosilicate grains, lacking a clear preferred orientation.

The data presented in this thesis highlight the role played by fluids during deformation of quartz-feldspathic rocks at the brittle/plastic transition, that efficiently control (1) strain softening of 'stiff' domains and (2) strain localization into shear bands that have the potential to act as precursors for non-Andersonian fault zones. The proposed model predicts the development of brittle structures discordantly overprinting ductile fabrics developed in the same kinematic regime, which bears implications for the tectonic evolution of rock volumes (i.e. tectonic units and/or metamorphic complexes) exhumed though the brittle/plastic transition.

Riassunto

Questo studio ha come obiettivo l'analisi dettagliata della transizione fragile/duttile in rocce quarzo-feldspatiche in condizioni alto-medio crostali e di vincolare il ruolo dei fluidi e della temperatura durante la deformazione. L'Unità del Calamita (Isola d'Elba, Italia) è un complesso metamorfico di alto grado (T ~ 650 °C), intruso da un corpo monzogranito a bassa profondità (P < 0.2 GPa) e nel contempo deformato dalla tettonica compressiva a scala regionale, per un intervallo di tempo inferiore a 1 Ma. Queste condizioni rendono l'unità del Calamita un caso studio ideale per studiare la transizione fragile/duttile a condizioni di pressione (profondità) approssimativamente costanti durante la diminuzione di temperatura, riproducendo condizioni tipiche di crosta medio-superiore.

Gli Scisti del Calamita sono un complesso di metapsammiti, esposto nella parte inferiore dell'Unità del Calamita e caratterizzato da un metamorfismo di contatto di medio-alto grado. Pseudozioni PT e geotermometria sulla biotite vincolano la paragenesi termometamorfica di picco (andalusite + cordierite + biotite + K-feldspato) in facies anfibolitica superiore (T ~ 600 – 700 °C; P ~ 0.2 GPa), con microstrutture che suggeriscono fusione parziale. Il percorso retrogrado è ben definito dalla geotermometria sulla clorite, che indica temperature di riequilibrazione comprese fra 300 e 500 °C.

La cartografia di terreno e l'analisi geologico-strutturale di dettaglio hanno rivelato la distribuzione, a scala cartografica, di domini di alto strain immergenti ad ovest che ripartiscono una deformazione con cinematica top-verso-Est all'interno di domini di relativo basso-strain. I domini di alto strain presentano tessiture milonitiche con strutture S-C' con una sovraimpronta fragile caratterizzata da faglie non-Andersoniane suborizzontali associate ad una rete di strutture tipo Riedel, orientate parallelamente a zone di taglio C'. L'analisi microstrutturale evidenzia come la diminuzione di temperatura e l'afflusso di fluidi hanno controllato l'evoluzione meccanica delle rocce investigate, caratterizzate dalla transizione da una foliazione metamorfica di alto grado a shear band e miloniti con diffusi fabric S-C ed S-C' e caratterizzati dalla crescita retrograda e sincinematica di mica bianca e clorite.

Il microfabric del quarzo mostra un evoluzione da una ricristallizzazione per grain boundary migration, sviluppato in condizioni prossime al picco termometamorfico, ad una ricristallizzazione per subgrain rotation e bulging. Durante la diminuzione della temperatura, la deformazione si è localizzata in bande di quarzo milonitiche in facies anfibolitica (450 °C < T < 600 °C), in cui la deformazione è stata accomodata dal dislocation creep del quarzo, dominato dal sistema di slip prisma <a>, causando lo sviluppo di orientazioni cristallografiche preferenziali con massimi

paralleli a Y. L'attività secondaria del rombo <a> e del rombo acuto <a>, controllata dalla vorticità del sistema, ha assistito la ricristallizzazione di grani con orientazione sfavorevole per l'attivazione del sistema di slip prisma <a>. In facies scisti verdi (300 °C < T < 450 °C), la deformazione si è localizzata in domini fillonitici, producendo misture di fillosilicati e grani di quarzo a grana fine. Domini relitti di quarzo a grana grossa diventarono più competenti durante la deformazione, fratturandosi lungo shear band sintetiche e coniugate. La propagazione delle shear band è avvenuta in condizioni ricche in fluidi, controllata dall'interazione ciclica fra una fratturazione localizzata e la deposizione di quarzo e fillosilicati da parte di fluidi circolanti. I grani di quarzo precipitati hanno sviluppato un'orientazione cristallografica preferenziale parallela alle shear band, controllata dall'apertura di siti dilatanti. La deposizione di quarzo a grana fine e fillosilicati ha facilitato la ripartizione dello strain e la localizzazione della deformazione in shear band C' alla transizione fragile/duttile.

In condizioni fragili (T ~ 300 °C), la deformazione si è localizzata su shear band C', orientate favorevolmente per una riattivazione fragile, che hanno agito come precursori duttili per faglie non-Andersoniane. La deformazione fragile in zone di faglia è stata controllata dall'interazione ciclica fra processi di fratturazione, che hanno sfruttato piani cristallografici di debolezza nel quarzo come il rombo, e l'interazione fluido-roccia, che ha assistito la deposizione di nuovi cristalli di quarzo e fillosilicati a grana fine, privi di un'orientazione cristallografica preferenziale.

Il dato presentato in questa tesi sottolinea l'importanza dei fluidi durante la deformazione di rocce quarzo-feldspatiche alla transizione fragile/duttile, che controllano efficientemente (1) i processi di indebolimento di domini più competenti e (2) la localizzazione della deformazione in shear band, che possono poi agire come precursori per sistemi di faglie non-Andersoniane. L'evoluzione così ricostruita risulta nello sviluppo di strutture fragili discordanti su strutture duttili, entrambe sviluppate nello stesso regime tettonico, con implicazioni per l'evoluzione tettonica di volumi crostali (unità tettoniche o complessi metamorfici) esumati attraverso la transizione fragile/duttile.

Acknowledgements

I would like to express my deep gratitude to my advisors, Giovanni Musumeci and Francesco Mazzarini, for all the time, effort and perseverance that dedicated to assist my development as a person and researcher. It is impossible to thank them here properly for all the effort, the encouragement, advice and financial support they have given me during this three short years. My heartfelt thanks goes to Giulio Viola and Paolo Garofalo for supporting me with fruitful discussion, unlimited support and for acting in more than one occasion as 'unofficial advisors' during this work. I believe them all to be inspirational scientists and I hope to follow their examples in my scientific career.

Danke schön to Hans-Joachim Massonne for providing me the opportunity to carry out electron microprobe analysis and pseudosection modelling in Stuttgart and for all the invaluable advice and support to my research, even well after the end of my period abroad. I would also like to thank Thomas Theye for all the support and help with the machine and for the wonderful gift (the volumes of Ramsay's Modern Structural Geology – beautiful!). *Grazie* to Federico Lucci for many fruitful discussion in the endless research nights at the institute. The members of the Institute fur Mineralogie und Kristallchemie were also tremendously helpful during my time there: many thanks in particular to Moritz Schmelz for the beautiful and nicely ultra-polished thin sections that he made for me for free and Matthias Leiss for the invaluable help with the XRF analysis. Thanks also to Peng-Lei Liu for the Sunday-time technical assistance on the microprobe. One very big 'thank you' goes also to Angela Siegel and Joachim Opitz for shipping my XRF dust back to Pisa and to Dirk Spengler for his careful English translation of the German literature on the Elba Island. Many thanks to Pierre Lanari, Franck Bourdelle and Pietro Armienti for all the help with chlorite classification and geothermometry and to Alicia Lopez-Carmona and Gisella Rebay for assisting my learning of pseudosection modelling. Thanks, Alicia, for gifting a copy of your thesis: it has been precious for the metamorphism chapter!

I would like to thank Luca Menegon for hosting me in Plymouth and for the opportunity to carry out EBSD analysis there. I am also into debt with Giulia degli Alessandrini, Lucy Campbell (in Plymouth) and Simone Papa (in Padua) for all the help with EBSD data processing: one beer is not enough to thank you properly! Many thanks to Camille Dusseaux and her husband to help me achieve my dream to visit Millok Haven, Devonshire. In Pisa, I would like to thank the INGV staff (in particular Massimo Pompilio) for the technical support with the SEM and Caterina Morigi and Michele Marroni for all the teaching, rock laboratory and field trips that we have had together, and of course all my Geology I students! Thanks to Eric Ryan, Espen Torgersen, Nathan Church and

Acknowledgements

Raffaele Gazzola for sharing many great moments in the harsh field work on the Elba Island. Big cheers to my past and present DST – Pisa mates and in particular to Maria Di Rosa for all the time spent together sharing the chaos of the office. I hope not to have forgotten anyone and apologies for that, in case!

The reviewers of the papers submitted during this short three years – Sven Morgan, Elena Druguet, Florian Fusseis and Paul Bons – are deeply thanked for the helpful discussions and comments that helped also to improve the quality of the research presented in this thesis. And how not to mention Espen Torgersen and Chiara Frassi for the unofficial review of the manuscripts? Last but not least, I cannot properly thank here Giulio Viola and Michael Stipp for all the time, effort, careful comments on my thesis: I have really felt that you were trying to help me grow as a scientist and not simply reviewing a thesis and I thank you all for this.

My wife, Carlotta Papeschi, is the best supporting crew ever! She sustained together with me all the highs and low of graduate research: the months spent abroad, the overnight work, changes of mood during paper review and thesis writing. She has been always there to help me, to support me, even to hear me repeat over and over again oral presentations! And she is still at my side after 6 months abroad and 3 months of thesis writing. I would have never been able to achieve such a result without her! I can't even remember how many times Loredana Salutini and Milo have assisted me for the travelling abroad to conferences, brought me to the airport at 3 a.m. and also listened to oral presentations at 4 a.m. in the morning. You are the best supporting crew ever!

I would finally to acknowledge financial support for research and travel to Stuttgart and Plymouth to the Erasmus+ traineeship program of the European Union and to the PEGASO PhD Program of the Tuscany Region. Additional funding was received from PRA – University of Pisa (responsible: Sergio Rocchi). Travel funding to conferences was granted by the Società Geologica Italian and by the TECTask commission, which I kindly thank.

This thesis is dedicated to the memory of my kitten, Dro. She was there with me, together in the same room, during the last months of my thesis writing but unfortunately, she was unable to witness the end with me. I miss her so much.

Acknowledgements

Early wake ups often reward with marvelous sceneries during field work on the Elba Island.

Contents

Contents

Contents

List of Figures

Contents

Contents

List of Tables

Chapter 1

Introduction

'Τὰ ὄντα ἰέναι τε πάντα καὶ μένειν οὐδέν' – 'All entities move and nothing remains still' –
ascribed to Heraclitus, from Plato's Cratylus (4th century BC)

The rheology of the Earth's crust controls how deformation is accommodated at major plate boundaries and partitioned in crustal fault and shear zones (Ramsay, 1980; Rutter et al., 2001). Many shear zones are rooted in the lower crust extending upward for tens of kilometers to the upper crust. Examples are found worldwide either in active crustal boundaries, such as the Himalayan Main Central Thrust (Gansser, 1964; Grujic et al., 1996; Hodges, 2000), the San Andreas Fault (Brune et al., 1969; Chester et al., 1993), the Alpine Fault (Wellman, 1955; Carter and Norris, 1976; Toy et al., 2008), the Periadriatic Fault (Ahrendt, 1980; Schmid et al., 1989) and the Red River Shear Zone (Huang, 1960, 1978; Leloup et al., 1995), and, in fossil orogenic systems, the Moine Thrust (Christie, 1963; McClay and Coward, 1981; Law et al., 1984; Law, 1987) or the South Armorican Shear Zone (Berthé et al., 1979; Berthé and Brun, 1980; Jégouzo, 1980). Crustal-scale shear zones are characterized by different deformation mechanisms acting at different depth that have been shown to depend in first order from temperature and pressure (e.g. Kohlstedt et al., 1995). Assuming a 'normal' geothermal gradient of 25 °C/Km, deformation in the upper crust is mainly controlled by brittle or pressure sensitive failure strength and frictional sliding ('brittle behavior'; Byerlee, 1978; Kohlstedt et al., 1995; Zoback and Harjes, 1997), whereas the lower crust is characterized by crystal-plastic deformation ('plastic -or viscous- behavior'; Sibson, 1983; Kohlstedt et al., 1995). The middle crust is the locus where the deformation style progressively switches from 'brittle' (frictional) to 'plastic' (crystal-plastic) between two broadly defined, major rheological interfaces known as 'the brittle/ductile transition' or BDT and the 'brittle/plastic transition' or BPT (Sibson, 1977, 1980, 1983; Rutter et al., 1986; Kohlstedt et al., 1995; Stipp and Kunze, 2008; Behr and Platt, 2014; see Chapter 2).

Many models (i.e. depth-strength profiles) suggest that the maximum crustal strength is reached in the ductile middle crust immediately below the BDT (Sibson, 1983; Kohlstedt et al., 1995; Behr and Platt, 2011), which is significantly stronger than the upper and lower crust or even the upper mantle (e.g. Jackson, 2002). According to Behr and Platt (2014), the middle crust represents the 'strongest load-bearing element of the upper 25 km of the crust' and hence controls strain

localization and slip rates of crustal shear zones rooting therein. Nevertheless, rock behavior at mid-crustal conditions remains incompletely understood, in particular regarding the role of: (1) strain partitioning in different lithologies, (2) the common cyclic interplay between plastic and brittle processes, (3) fluid-rock interaction and metamorphic/metasomatic reactions and (4) pre-existing ductile fabrics on the nucleation of brittle structures. The interaction of these processes is difficult to constrain based on laboratory experiments alone, which are generally performed at faster strain rates and higher temperature conditions to replicate microstructures and rheology of crustal rocks in reasonably short experimental times. One of the largest limitations is represented by the difficulty of carrying out experiments on polyphase rocks, because laboratory measurements are performed at higher temperature than in nature and partial melting reaction may occur (see Kohlstedt et al., 1995 for a review). The study of deformation processes and microstructures in natural rocks represents the link between experiments (e.g. Hirth and Tullis, 1992; Gleason and Tullis, 1995; Bons and den Brok, 2000; Stipp et al., 2006; Holyoke III and Tullis, 2006; Trepmann et al., 2007; Stipp and Kunze, 2008; Muto et al., 2011) and nature (Takeshita and Hara, 1998; Stöckhert et al., 1999; Stipp et al., 2002a, b; Kjøll et al., 2015; Ceccato et al., 2017; Trepmann et al., 2017). However, it is often difficult to find a 'natural laboratory' (e.g. Stipp et al., 2002a, b), i.e. a place where boundary conditions (e.g. temperature and pressure) are well known, few parameters controlled deformation and the effect of later deformation overprint can be considered absent or minimal. Such a 'natural laboratory' has been identified in the Calamita Unit, in the southeastern sector of the Elba Island, Italy, and represents the subject of this thesis.

1.1 Tectonic setting of the Calamita Unit

The Calamita Unit hosts a shallow depth Miocene intrusion (Porto Azzurro monzogranite; Musumeci et al., 2015). It consists of a metapsammitic formation, known as the Calamita Schists, overlain by tectonic slices of marbles and metasiliciclastics rocks (Barberi et al., 1967a, b). The thermal anomaly related to the intrusion determined high-grade contact metamorphism up to 650 °C in the Calamita Schists at very low-pressure conditions ($P < 0.18$-0.20 GPa; Duranti et al., 1992). Coeval regional shortening led to the development of compressive top-to-NE shear zones within the contact aureole (Musumeci et al., 2015). The cooling of the pluton and the contact aureole (Calamita Unit) caused the switch in deformation style from plastic to brittle, with the development of top-to-the-NE thrust faults (Musumeci and Vaselli, 2012). Geochronological data constrain ductile shearing between 6.8 – 6.3 Ma (Musumeci et al., 2015) and the brittle overprint

between 6.1 and 4.9 Ma (Viola et al., 2018), indicating that the switch from crystal-plastic to brittle deformation in this unit occurred in less than 1 Ma.

1.2 Why study deformation in the Calamita Unit?

The Calamita Unit represents a magnificent 'natural laboratory' to study deformation of shear zones at the brittle/ductile transition because:

- It is located in a well-known structural setting;
- P/T conditions of deformation are well-known;
- It allows to study the effect of varying deformation parameters (temperature, water content, strain rate…) in an environment where pressure (loading) is relatively constant (P ~ 0.18 – 0.20 GPa);
- Switch from ductile to brittle deformation occurred over a very short time span (less than ~ 1 Ma);
- The kinematic framework (sense of tectonic transport) was constant during deformation;
- The area is characterized by a wide field exposure and easily accessible outcrops documenting well the relationships between ductile and brittle structures.

These factors suggest that the Calamita Unit represents an upper crustal proxy of the deformation processes that normally occur at depth during exhumation of mid- to lower crustal metamorphic units along major crustal shear zones.

1.3 Research questions

This doctoral project has been undertaken with the aim to contribute to major research questions:

1. What are the deformation mechanisms controlling deformation at the brittle/ductile transition?
2. What is the role of fluids during deformation?
3. What is the effect of the transition from plastic to brittle behavior in strain localization?
4. What is the role of pre-existing anisotropies in strain localization?

1.4 Study area and methods

The contribution to the above research questions is based on the detailed study and interpretation of structures and lithologies exposed in the Calamita Schists, which constitute the main lithology of the Calamita Unit and the host rock of the Porto Azzurro pluton. The knowledge about the structural evolution of the Calamita Schists has been improved through a multidisciplinary

1. Introduction

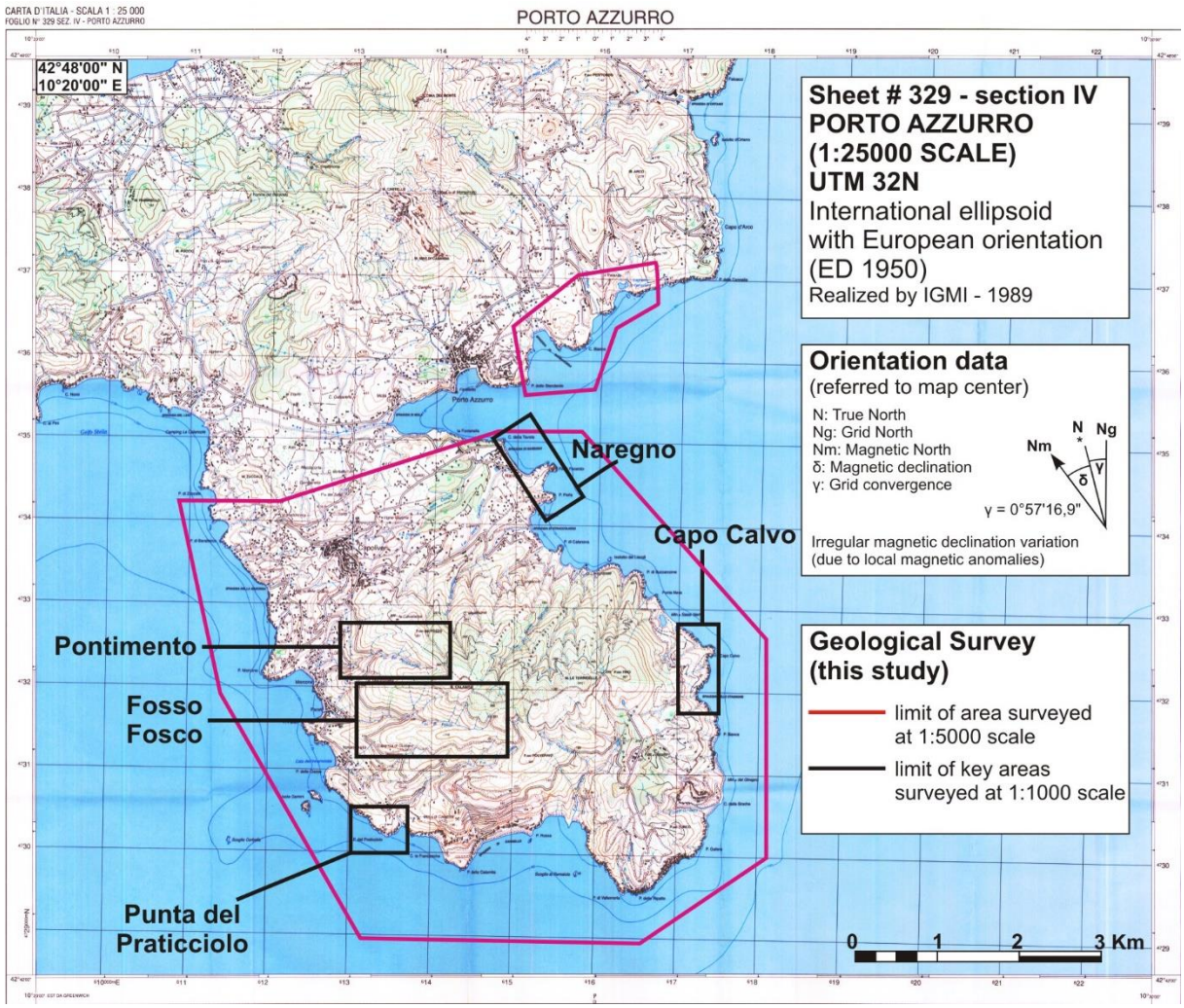

Figure 1.1 – 1:25000 scale topographic map of the study area, realized by the *Istituto Geografico Militare Italiano* (IGMI, 1989) indicating the position of the area surveyed at 1:5000 scale (purple line) and of the key areas surveyed at 1:1000 scale.

approach involving structural and microstructural analytical techniques and detailed analysis of the metamorphism through petrographic and petrological investigations.

Structural analysis, based on the measurement of structural elements (e.g. foliations, lineations, slickenlines…), has been performed on the entire, extensively outcropping Calamita Unit in the Calamita peninsula (SE Elba Island) from the Mola plain and the Porto Azzurro town in the North to Capo Calamita in the South (Fig. 1.1), over an area of about 21 Km^2 located between 42°46'20''N – 42°42'26''N and 10°22'00''E – 10°26'00''E (sheets 329010, 329020, 329050 and 329060 of the *Carta Tecnica Regionale* at 1:5000 scale of the Tuscan Region). Several key areas, where lithologies and deformation structures can be observed in great detail, have been mapped at 1:1000 scale, notably Capo Calvo, Punta del Praticciolo, Fosso di Fosco, Fosso del Pontimento and Naregno (see Fig. 1.1. and Appendix C). The detailed mesoscale analysis of those areas has been aimed to reconstruct the geometries and deformation features of shear zones and faults and their spatial and temporal relationships.

1. Introduction

Microscale fabrics were investigated through transmitted-light microscopy at the Microtectonics Lab of the University of Pisa on a suite of thin sections of samples collected by G. Musumeci and F. Mazzarini (labelled C, G, CS and CN in Appendix C, D) and derived from samples collected in the course of this thesis (labelled SP in Appendix C, D). Microstructural analysis was focused on understanding metamorphism/deformation relationships and deformation mechanisms, with a particular focus on quartz microstructures. Quartz microstructures and crystallographic preferred orientation were also investigated in detail by Electron BackScatter Diffraction (EBSD) on 3 samples (2 mylonites and 1 cataclasite) at the Plymouth Electron Microscopy Center (Plymouth University, U.K.). Metamorphic constraints were derived using the pseudosection approach combined with classical biotite and chlorite geothermometry. XRF analysis and Electron Micro Probe Analysis were performed at the *Institut für Mineralogie und Kristallchemie* (Universitat Stuttgart) on 3 selected samples, 2 of them corresponding to the mylonites selected for EBSD analysis. Additional spot analysis on metamorphic minerals and detailed microstructural images were acquired using the Scanning Electron Microscope (SEM) at the *Instituto Nazionale di Geofisica e Vulcanologia* (INGV, Pisa).

1.5 Structure of the thesis

The second Chapter of this thesis contains a discussion of general concepts and open problems regarding brittle and crystal-plastic processes and on how they interact during deformation, in order to establish establishing a conceptual framework for the discussion of the data presented in this thesis. The third Chapter contains a brief overview on the tectonic and structural framework of the Elba Island and the Calamita Unit and a re-definition of the lithostratigraphy of the Calamita Unit. Appendix A and B contain a list of abbreviations and a list of mineral abbreviations, respectively. Structural analysis of mesoscale features at the peninsula scale and in key outcrops is presented in Chapter 4. The petrographic and microstructural analysis of selected samples is discussed in Chapter 5. Chapters 4-5 include also a discussion of the thermal and structural evolution of the Calamita Unit. The location of investigated samples is shown both in the chapters themselves and in Appendix C at the end of the thesis, whereas a table with microstructural description and a summary of structural elements described at the microscale is available in Appendix D.

The EBSD data is presented and discussed in Chapter 6. Chapter 7 is devoted to the presentation of the metamorphic constraints: Appendix E1 contains a detailed description of the methodology of metamorphism analysis while the location of spots and recalculated point analyses are available in Appendix E2. The last chapter (Chapter 8) contains a summary of results and conclusions,

discussing the advancements towards the research questions postulated in the introduction, and directions for future research. Two articles were published based on the work presented in this PhD thesis: their abstracts are provided in Appendix F. The references, using American Psychological Association (APA) format, are listed at the end of the body of the manuscript, before the Appendix section.

Chapter 2

The Brittle/Ductile Transition

'Tiny mineral grains could drive plate tectonics' – J. Wendel, 2015

This chapter provides a brief overview of the rheology of crustal rocks and shear zones and deformation processes in the brittle and ductile regime. The discussion is focused on the interplay between plastic and brittle deformation mechanisms at the brittle-ductile transition (BDT) and how the interaction between these processes affects: (1) rheology, (2) strength and (3) development of brittle (or ductile) structures over pre-existing fabrics.

2.1 Rheology of crustal rocks

Our understanding of the rheology of the Earth's crust is derived from decades of laboratory experiments on rock mechanics and deep drilling direct observations (Sibson, 1977; Brace and Kohlstedt, 1980; Evans and Kohlstedt, 1995; Kohlstedt et al., 1995; Gleason and Tullis, 1995; Stipp et al., 2006). These studies predict a brittle behaviour for the upper crust, following a frictional criterion known as Byerlee's law (Byerlee, 1968, 1978), whereas the lower crust deforms by plastic (or viscous) mechanisms, described by a power law (e.g. Gleason and Tullis, 1995; Hirth et al., 2001). Quartz is the primary constituent of the crust and therefore 'pure quartzite' power laws are thought to approximate reasonably well the rheology of the crust (Kohlstedt et al., 1995; Ranalli, 2000; Handy and Brun, 2004). More elaborate models predict a different power law for the lower crust, where feldspar-dominated lithologies are more abundant and control the rheology (Ranalli and Murphy, 1987; Wilks and Carter, 1990; Burgmann and Dresen, 2008).

The variation of rheology with depth within the crust can be represented using strength-depth profiles (Sibson, 1977; Brace and Kohlstedt, 1980; Ranalli and Murphy, 1987; Gleason and Tullis, 1995; Kohlstedt et al., 1995; Burgmann and Dresen, 2008). In these profiles, the strength of the upper crust increases linearly with depth following Byerlee's law until the temperature becomes high enough for plastic deformation to take over frictional deformation. At greater depth, the strength of the lower crust decreases exponentially with depth as a function of temperature following the plastic flow power law. The zone of intersection between Byerlee's law and the power law occurs within a transitional zone, roughly located at 10-15 Km depth: the brittle-ductile transition (BDT). The BDT marks the transition from discontinuous frictional deformation (i.e.

localized cataclastic flow according to Kohlstedt et al., 1995) to distributed deformation. Beyond the BDT, deformation usually involves both plastic and brittle mechanisms (i.e. nonlocalized ductile or semibrittle flow, as defined by Kohlstedt et al., 1995). At greater depth (and higher temperature), plastic deformation takes over brittle deformation at the brittle-plastic transition (BPT). In other words, the BDT marks the change in deformation mode, whereas the BPT marks the change in dominant deformation mechanisms (Rutter et al., 1986; Kohlstedt et al., 1995). The crustal volume comprised between the BDT and the BPT corresponds (1) to the domain of maximum crustal strength (Sibson, 1983; Kohlstedt et al., 1995; Behr and Platt, 2011) and (2) the base of the seismogenic crust, i.e. the crustal layer where most of the seismicity occurs (Sibson, 1984; Scholz, 1988).

2.1.1 The crustal strength envelope

The behavior of the Earth's brittle upper crust is defined by a linear relation between normal stress and shear stress, known as Byerlee's law, governed by the coefficient of friction (μ; between 0.6 and 1.0) derived from laboratory experiments (Byerlee, 1978; Burgmann and Dresen, 2008). Frictional strength increases linearly with pressure (i.e. depth) reaching up to 60-300 MPa of peak strength at the BPT, where thermally-activated crystal plastic deformation becomes the dominant deformation mechanism (Brace and Kohlstedt, 1980; Kohlstedt et al., 1995). Differently from frictional strength, plastic strength is controlled by temperature and decreases exponentially with depth (Brace and Kohlstedt, 1980; Poirier, 1985). The flow law that describes the behavior of crystalline materials is a power law primarily dependent on composition. While the upper crust is generally assumed to be quartz dominated and characterized by a BPT occurring at ~ 250 – 300 °C (Voll, 1976; Stöckhert et al., 1999; van Daalen et al., 1999; Stipp et al., 2002a), the rheology of the lower crust is thought to be feldspar dominated and characterized by a BPT occurring at ~ 450 °C (Sibson, 1977; Tullis and Yund, 1987; Scholz, 1988). Finally, the rheology of the mantle is controlled by olivine, whose BPT occurs at ~ 700 °C (Carter and Avé Lallement, 1970; Nicolas and Christensen, 1987; Mainprice and Nicolas, 1989; Suhr, 1993). This lithological stratification results in a rheological stratification of the lithosphere, with superimposed layers characterized by different strength and rheology (Fig. 2.1; Brace and Kohlstedt, 1980; Ranalli and Murphy, 1987; Ranalli, 2000; Burgmann and Dresen, 2008).

Several factors influence lithospheric strength, as strain rate, geothermal gradient or presence of fluids. At high strain rate, plastic strength increases and the power law shifts to the right in Fig. 2.1; consequently, the intersection between brittle and plastic laws occurs at greater depth. On the

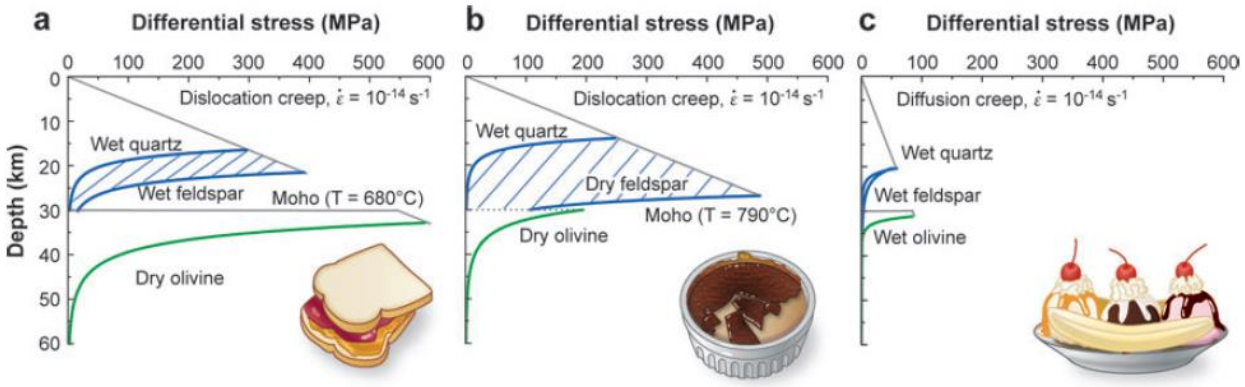

Figure 2.1 - Alternative models of lithospheric strength (after Burgmann and Dresen, 2008), constructed using **(a-b)** hydrostatic fluid pressure ($\lambda = 0.4$) and **(c)** low friction due to high pore fluid pressure ($\lambda = 0.9$) in strike-slip regime. λ is the pore fluid factor defined as the ratio between pore fluid pressure and normal stress (Cox, 2010). See Burgmann and Dresen (2008) for details about the power laws and geotherms used. The blue striped area corresponds to the domain where quartz has a plastic behavior and feldspar deforms by brittle mechanisms (i.e. semibrittle deformation of Kohlstedt et al., 1995). **(a)** Jelly-sandwich crustal strength envelope characterized by strong upper crust and mantle and a weak, wet lower crust; **(b)** Crème brûlée crustal strength envelope showing a strong crust (wet quartz and dry feldspar) underlain by a weak, dry mantle; **(c)** Banana-split crustal strength envelope considering the case of a lithosphere weakened by near lithostatic water pressure and deforming by linear diffusion creep.

other hand, water-saturated conditions (i.e. lithostatic water pressure) significantly reduce both frictional and plastic strength.

Alternative models of crustal rheology have been proposed through the years to explain the distribution of earthquakes in the crust and the structures observed in exhumed metamorphic rocks. Three examples are summarized in Fig. 2.1, using food analogies after Burgmann and Dresen (2008). The jelly sandwich model (Fig. 2.1a) is characterized by a weak lower crust sandwiched between a strong upper crust and an even stronger upper mantle, which therefore controls the rheology of the lithosphere. Alternative models are represented by the crème brûlée model (Fig. 2.1b), in which a strong upper crust overlays a weak upper mantle (e.g. Jackson, 2002) and the banana split model, which describes a generally weak lithosphere (Fig. 2.1c). In the examples shown, completely different behaviors are determined by slight changes in water content or geothermal gradient. Considering the case of the crème brûlée model (Fig. 2.1b), a minor increase of the geothermal gradient from 23 °C/Km (as in Fig. 2.1a) to 26 °C/Km (as in Fig. 2.1b) and the presence of a dry lower crust weakens the upper mantle enough that all significant strength is concentrated in the crust. In spite of the model considered, peak crustal strength resides at the BPT (of quartz and feldspar in Fig. 2.1a, of feldspar in Fig. 2.1b and of quartz in Fig. 2.1c). In the banana split model, due to near lithostatic water pressure conditions occurring in the entire crust, the lithosphere is characterized by a generally weak behavior, with minimum strength sustained by the middle crust and the upper mantle. Within the crust indeed, in spite of the model considered, peak strength resides at the BPT (of quartz and feldspar).

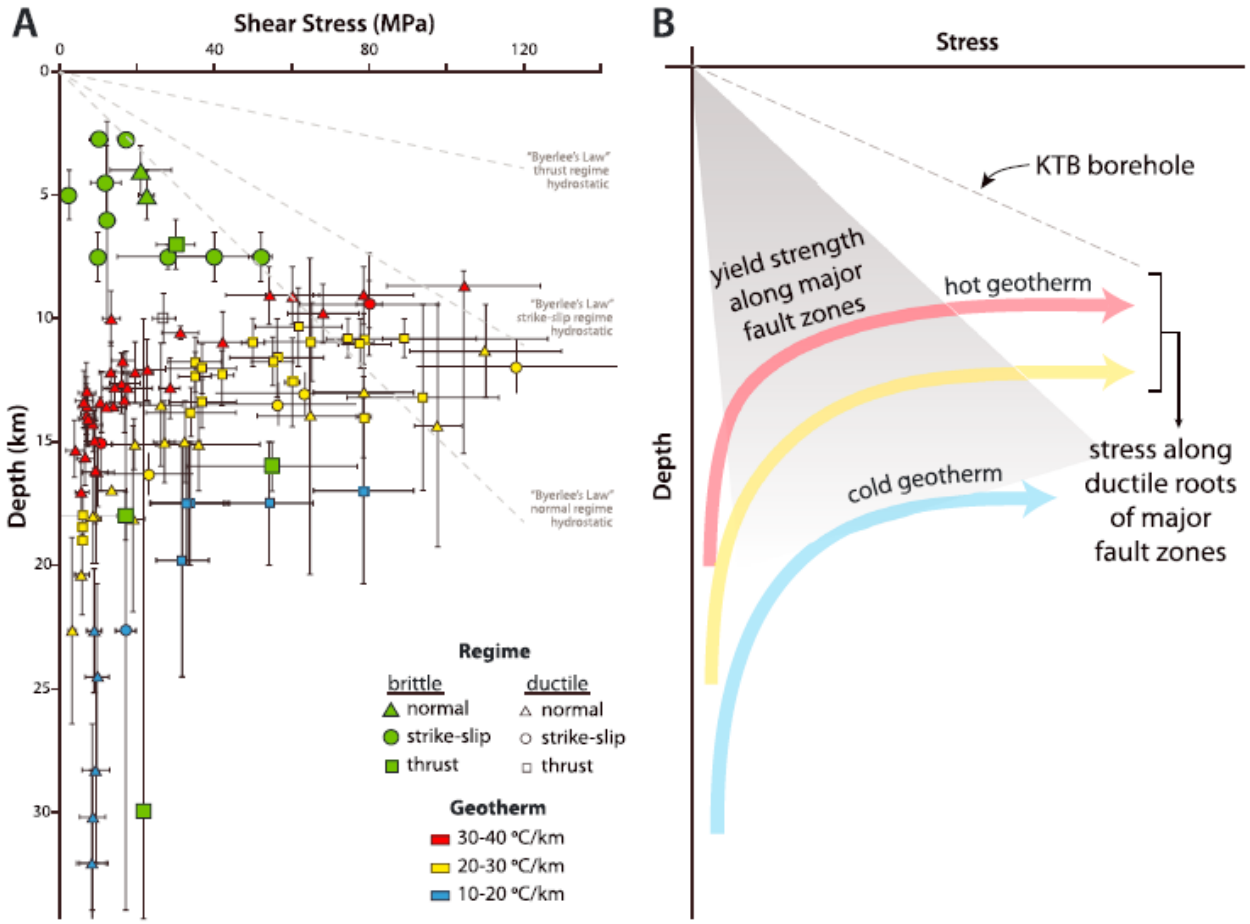

Figure 2.2 - (a) Global compilation of stress-depth data after Behr and Platt (2014) showing paleopiezometric data along major ductile shear zones colored as a function of the geothermal gradient and stress estimates from crustal faults (in green). Byerlee's laws for normal, strike-slip and thrust regimes for hydrostatic fluid pressure are shown; **(b)** Simplified sketch of **Fig. 2.2a** showing the yield strength of major fault zones (in grey) and the reconstructed geotherms along major shear zones (red, yellow and blue). Notice how the maximum differential stress measured at the BDT significantly exceeds the strength of the upper crust. See text for comments. Original image after Behr and Platt (2014).

Behr and Platt (2014) published a global compilation of stress-depth data with paleostress estimates obtained from paleopiezometry in the ductile crust and shear stress estimates on major crustal faults for the upper crust (Fig. 2.2a). This compilation reveals that the frictional strength of brittle faults is significantly lower than the plastic strength of mid-crustal shear zones, measured close to the BPT, due to weakening mechanisms that contribute to effectively reduce fault strength such as (1) the presence of 'soft' fault gouge (e.g. Byerlee, 1968, 1978; Morrow et al., 1984; Blanpied et al., 1991, 1995; Wintsch et al., 1995; Takahashi et al., 2007; Collettini et al., 2009; Ikari et al., 2009; Lockner et al., 2011), (2) mechanisms involving elevated fluid pressure (e.g. King Hubbert and Rubey, 1959; Lachenbruch, 1980; Sibson, 1981, 1985; Chester et al., 1993; Axen and Selverstone, 1994; Sleep and Blanpied, 1994; Beeler et al., 2000; Collettini et al., 2006) or (3) the reactivation of weak ductile precursors (e.g. Laubach and Marshak, 1987; Shea et al., 1993; Shail and Alexander, 1997; Duveau et al., 1998; Beacom et al., 2001; Butler et al., 2008; Ferreira et al., 2008; Massironi et al., 2011; Bistacchi et al., 2012; Ikari et al., 2015; Bolognesi and Bistacchi, 2016, 2018). On the other hand, paleopiezometric estimates close to the BPT reveal a

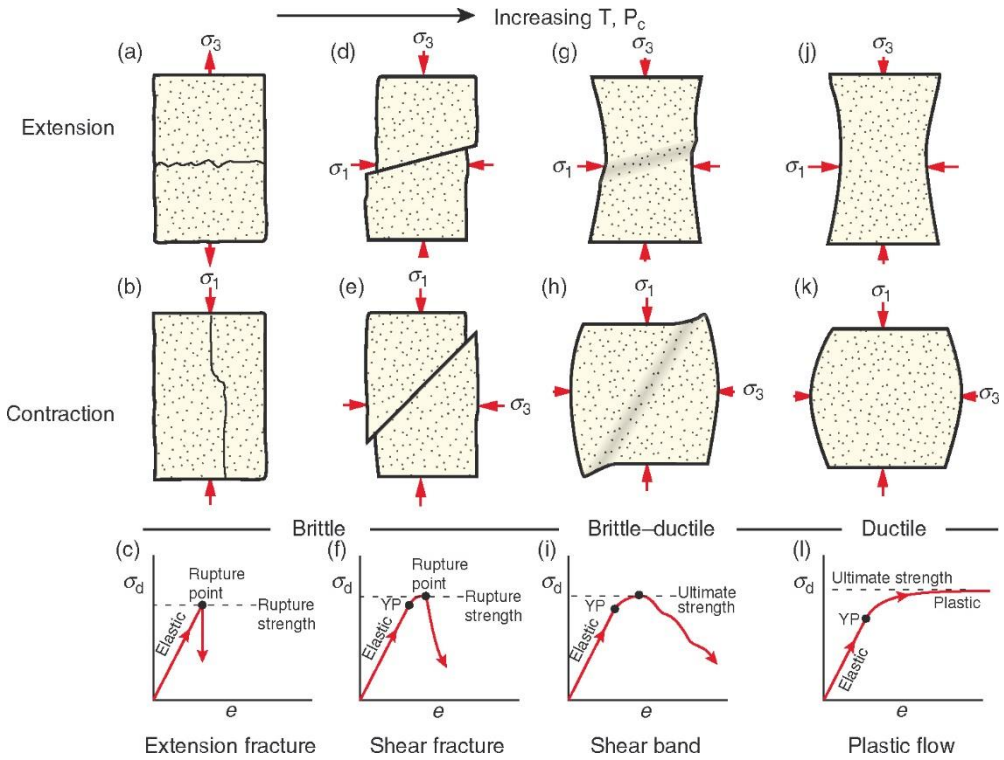

Figure 2.3 - (after Fossen, 2016) – Experimental deformation structures developing under **(a-d-g-j)** extension and **(b-e-h-k)** contraction and related **(c-f-i-l)** strain-stress diagrams. From left to right, temperature (T) and confining pressure (Pc) increase and deformation switches from the brittle to the ductile regime.

strong middle crust, sustaining very high shear stresses (Fig. 2.2b; Pennacchioni and Cesare, 1997; Stipp et al., 2002a; Fitz Gerald et al., 2006; Stipp and Kunze, 2008; Behr and Platt, 2011, 2013, 2014; Kidder et al., 2012). Understanding the complex interplay between plastic and frictional processes in the middle crust is, therefore, crucial to understand rheology, behavior and mechanics of strain localization of mid-crustal shear zones.

2.2 Deformation mechanisms

2.2.1 Brittle regime

In the brittle (or frictional) regime, deformation is accommodated by brittle failure of rocks (Fig. 2.3a, b) and frictional sliding along fractures (Fig 2.3d, e; Evans and Kohlstedt, 1995). Deformation of rocks starts when the rupture strength is reached and new fractures develop (Fig. 2.3c). Sliding on fractures is favored as they are significantly weaker (Fig. 2.3f) than the surrounding host rocks and, therefore, frictional sliding localizes on fractures (Fig. 2.3d, e, f). Alternatively, pre-existing planes of weakness such as foliation planes or fractures may be reactivated in the brittle regime (Sibson, 1985; Butler et al., 2008).

Models of fault development predict an earlier stage of fracture growth and propagation, weakening the host rock (Fig. 2.4a; i.e. process zone of Vermilye and Scholz, 1998), and a later stage of fracture linkage, in which deformation becomes progressively localized in fault zones

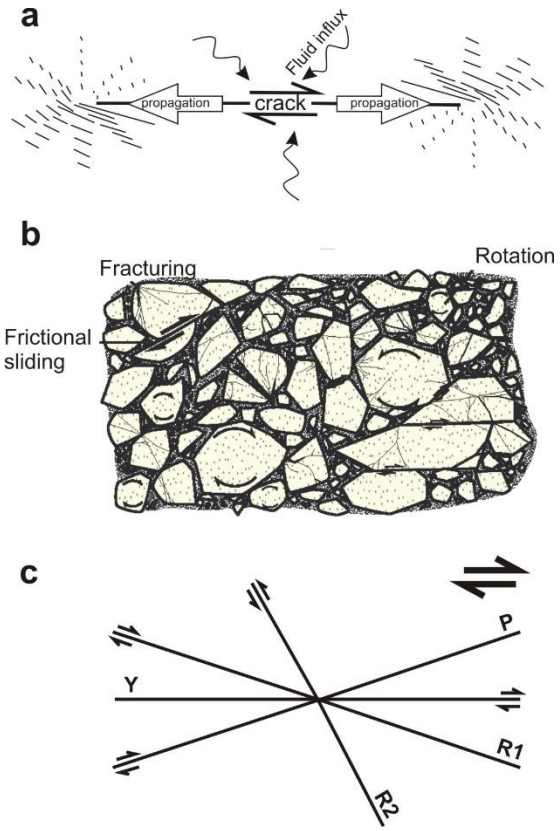

Figure 2.4 - (a) model of progressive fracture propagation with microfracturing concentrated at the tip and through-going fracture development occurs in the core zone (modified after Vermilye and Scholz, 1998). Opening of fractures may cause fluid influx and assist further weakening of the fracture core; **(b)** Scheme of cataclastic flow with coexistence of block rotation, fracturing, frictional sliding and development of a fine-grained cataclastic matrix (after Fossen, 2016); **(c)** Scheme showing geometry and orientation of Riedel shear structures (simplified after Logan et al., 1992).

(Fig. 2.4b; Sibson, 1977; Wise et al., 1984; Vermilye and Scholz, 1998). In the fault core, fragments of the wall rocks are progressively crushed and enveloped in a very fine-grained cataclastic matrix, which may form by milling of the host rock or fluid-rock interaction (i.e. Fig. 2.4a) with the precipitation of authigenic, synkinematic fine-grained matrix (e.g. phyllosilicates or clay minerals; Fig. 2.4b). Development of a fine-grained matrix may be associated with the formation of a cataclastic foliation and even S-C structures in cataclastic rocks (Chester et al., 1993; Evans and Chester, 1995; Lin, 1999; Wintsch et al., 2000). These processes are responsible for strain softening of the fault core and progressive strain localization in faults in the brittle regime, with wall rocks remaining relatively undeformed.

The nucleation, propagation and shearing of a fault zone may be associated with subsidiary Riedel shear fractures (after Riedel, 1929), localized in the fault core or associated with the main slip planes. According to Logan et al. (1992), Y shears, oriented parallel to the main fault plane and showing the same sense of shear, are commonly associated with conjugate, synthetic normal R1 and antithetic reverse R2 shears, respectively oriented at low and high angle with respect to Y shears. An additional set of synthetic Riedel shears is represented by P shears, characterized by opposite dips with respect to R1 shears.

2.2.2 Ductile regime

Ductile deformation is the accumulation of strain in geological materials without loss of internal cohesion, resulting from any deformation mechanism (brittle or plastic; Kohlstedt et al., 1995). In this regime, once the yield strength of the material is reached, deformation starts to be accumulated (Fig. 2.3i, l). Close to the BDT, brittle processes (but also fluid influx and metamorphic reactions) may weaken significantly the host rock and assist localization of ductile deformation at lower stresses beyond the yield strength (Fig. 2.3g, h), whereas at higher temperature conditions (i.e.

beyond the BPT) deformation is accumulated at steady stress (i.e. ultimate strength; Fig. 2.3j, k, l) and achieved by plastic flow (i.e. crystal plastic mechanisms). Crystal plasticity is primarily controlled by temperature and mineralogy (plastic deformation in quartz starts above ~250-300 °C: Voll, 1976; Stöckhert et al., 1999; van Daalen et al., 1999; Stipp et al., 2002b; in feldspars above ~450 °C: Sibson, 1977; Tullis and Yund, 1987; Scholz, 1988) and, secondarily, by strain rate, presence of fluids and grain size. During crystal-plasticity, dislocation creep determines the movement of dislocations within the crystal lattice. The activity of one (or more) slip systems is controlled by the conditions present during deformation, primarily temperature and strain rate (Poirier, 1985; Mainprice et al., 1986; Drury and Urai, 1990; Stipp et al., 2002b) or fluids (Blacic, 1975; Jaoul et al., 1984; Jung and Karato, 2001; Morgan and Law, 2004; Jung et al., 2006; Morgan et al., 2016). At the same time, recrystallization, either by subgrain rotation or migration of grain boundaries, determines the change in shape and size of the recrystallizing material (White, 1977; Poirier and Guillopé, 1979; Urai et al., 1986; Hirth and Tullis, 1992). It is generally acknowledged that the activity of dislocation creep is responsible for the development of lattice preferred orientations (Tullis et al., 1973; Schmid and Casey, 1986; Urai et al., 1986; Hirth and Tullis, 1992; Gleason et al., 1993; Zhang and Karato, 1995; Fliervoet et al., 1999; Muto et al., 2011; Ceccato et al., 2017).

Other deformation mechanisms in crystalline materials are collectively known as diffusion creep (Poirier, 1985; Wheeler, 1992) and commonly operate together with grain boundary sliding (Fliervoet et al., 1997). Sliding of grains past each other may also lead to the development of cavities (creep cavitation bands; Rybacki et al., 2008; Menegon et al., 2015) and promote fluid infiltration (solution transfer; Durney, 1972; Rutter, 1983; Bell and Cuff, 1989), causing precipitation of new phases and phase mixing (Kilian et al., 2011; Linckens et al., 2014; Viegas et al., 2016; Cross and Skemer, 2017; Gilgannon et al., 2017). These processes are activated at very fine grain size (i.e. grain size sensitive creep) and are thought to control extreme strain localization in shear zones, as shearing occurs at decreasing differential stress for finer grain size (Herwegh et al., 2011; Kilian et al., 2011; Menegon et al., 2015). Opposite to dislocation creep, diffusion creep and grain boundary sliding progressively obliterate any pre-existing CPO, developing a random crystal lattice orientation.

2.2.3 Semibrittle deformation

From a theoretical point of view, during deformation at constant strain rate, in an ideally monomineralic, equigranular and isotropic aggregate and in the presence of fluids of constant composition, the rheological behavior of a geologic material would transition from purely

cataclastic (at lower temperatures) to purely plastic (towards higher temperatures). However, natural rocks are far from being monomineralic, isotropic and equigranular and strain rate, fluid activity and composition can rarely be considered constant. Textural anisotropies, arising from compositional heterogeneities, presence of preferred orientation (of shape or crystallographic) and the shape and distribution of grain boundaries or lattice defects. As a consequence, beyond the BDT, the onset of crystal plasticity is accompanied by cataclastic mechanisms and deformation involves both components until the BPT and the switch to purely plastic flow is reached (Kohlstedt et al., 1995). Consider, for example, the case of a 2 phase mixture composed of feldspar and quartz: feldspar exhibit a brittle behavior below ~ 450 °C (Tullis and Yund, 1987, 1992) while quartz deforms plastically down to ~ 250-300 °C (Voll, 1976; van Daalen et al., 1999; Stöckhert et al., 1999; Stipp et al., 2002b). This difference in rheological behavior causes a microstructural dependence on the temperature of deformation and between ~ 300 – 450 °C quartz would deform by crystal-plastic mechanisms, whereas feldspar would develop porphyroclasts and fracture pervasively (Passchier, 1985; Jordan, 1988; Tullis et al., 1982, 1990; Passchier and Trouw, 2005; Handy et al., 2007; Viegas et al., 2016). Natural and experimental observation of deformed monomineralic aggregates have also shown the dependence of deformation mode on grain size, with fractured coarse grains surrounded by fine-grained recrystallized aggregates developed by dislocation creep (Gifkins, 1976; White, 1976; Shigematsu, 1999; van Daalen et al., 1999; Vernooij et al., 2006; Menegon et al., 2008). The orientation of the crystal lattice of a deforming material under semibrittle conditions controls how mineral grains react to deformation with grains in ‘soft’ orientation undergoing recrystallization and grains in ‘hard’ orientations, misoriented with respect to the favored slip systems, which may fracture during deformation (Takeshita and Wenk, 1988; Wenk et al., 1991; Lev and Hager, 2008; Muto et al., 2011; Kjøll et al., 2015; Ceccato et al., 2017). Furthermore, strain partitioning may cause localized fracturing in orientations where the shear stress has a higher magnitude, as it has been proposed to explain the development of brittle shear bands in ductile mylonites (Platt and Vissers, 1980; Simpson and De Paor, 1993; Blenkinsop and Treloar, 1995; Kurz and Northrup, 2008; Gillam et al., 2014; Bukovskà et al., 2016). Fluids may also flood fractures and enhance stress corrosion (Atkinson, 1984; Kerrich, 1986) or depose ‘soft’ (e.g. Goncalves et al., 2016) or fine-grained material by dissolution-precipitation creep (e.g. Takeshita and Hara, 1998; Bons and den Brok, 2000; Takeshita and El-Fakharani, 2013; Kjøll et al., 2015). Rocks deforming at semibrittle conditions may also register transient and episodic earthquake-related high-strain surges, developing brittle structures that are successively overprinted by low temperature plasticity (Trepmann and Stöckhert, 2003, 2013; Trepmann et al., 2007, 2017; Bestmann et al., 2012; Trepmann and Seybold, 2018). To summarize, in natural rocks

the transition from purely frictional to purely plastic mechanisms occurs over a wide range of temperature and pressure conditions and is characterized by a complex behavior with coexisting deformation mechanisms (Sibson, 1977; Kohlstedt et al., 1995) that may also interplay in a cyclical fashion (see below).

2.2.4 Brittle/ductile cyclicity

The coexistence of frictional and plastic deformation mechanisms, commonly referred to as semibrittle deformation (Kohlstedt et al., 1995), represents in practice a complex phenomenon. As shown above, the transition from purely brittle to purely plastic deformation can be achieved by increasing temperature, confining pressure or water content or decreasing the strain rate. Especially during exhumation of metamorphic rocks from deeper to shallow crustal levels, brittle structures are superimposed over previously formed ductile or plastic structures and a two-stage ductile-to-brittle deformation can be demonstrated. On the other hand, brittle and ductile structures are found associated in nature, sometimes overprinting each other in a cyclical fashion. Transient brittle events occurred during dominant ductile flow have been described at all crustal levels in: (1) Folded and dynamically recrystallized veins (e.g. Segall and Simpson, 1986; Kronenberg et al., 1990; Compton et al., 2017), (2) Mylonitized pseudotachylites (Sibson, 1980; Hobbs et al., 1986; McNulty, 1995; Menegon et al., 2017; Hawemann et al., 2018), (3) Shear bands (Bukovskà et al., 2016; Goncalves et al., 2016) and (4) Intracrystalline bands (van Daalen et al., 1999; Vernooij et al., 2006a,b; Kjøll et al., 2015). Several studies have documented the important role played by brittle precursors, i.e. brittle structures formed during a previous event or in the early stages of plastic deformation, in localizing ductile structures, in particular shear zones (Pennacchioni and Cesare, 1997; Guermani and Pennacchioni, 1998; Mancktelow and Pennacchioni, 2005, 2013; Fusseis et al., 2006; Pennacchioni and Mancktelow, 2007; Fusseis and Handy, 2008). Cyclically overprinting brittle and ductile structures have been described in rocks deformed at all crustal levels e.g. dry lower crustal rocks (Austrheim and Boundy, 1994; Camacho et al., 1995; Menegon et al., 2017; Hawemann et al., 2018), mid-crustal shear zones (Compton et al., 2017) and close to the BDT (Kjøll et al., 2015; Torgersen et al., 2015; Bukovskà et al., 2016; Molli et al., 2017; Trepmann and Seybold, 2018). These studies emphasized how transient and episodic embrittlement may cause the cyclical development of brittle structures acting as precursors for subsequent ductile deformation. Seismic events are thought to play a major role during brittle/ductile cyclicity as they correspond to major strain rate pulses which may affect the BDT zone (e.g. Molli et al., 2017; Trepmann et al., 2017) and propagate as far as the lower crust (e.g. Menegon et al., 2017; Hawemann et al., 2018). Pore fluid pressure fluctuations may also

trigger cyclical events of embrittlement, in particular in rocks deforming close to the BDT, promoting precipitation of new grains in cracks that in turn assist the localization of ductile deformation (Kjøll et al., 2015; Torgersen et al., 2015).

2.3 Quartz deformation mechanisms

Quartz is one of the most common rock forming minerals of the Earth's crust and one of the weakest during ductile deformation. It also represents one of the major constituents of the Calamita Schists and the primary subject of this thesis. In nature and experiments quartz shows a wide range of deformation microstructures (Hirth and Tullis, 1992; Stipp et al., 2002a, b; Stipp and Tullis, 2003) and a strong sensitivity to temperature, differential stress and to the presence of water in the crystal lattice (Griggs and Blacic, 1965; Hobbs, 1985; Luan and Paterson, 1992; Kronenberg, 1994; Post et al., 1996; Post and Tullis, 1998; Stipp et al., 2002b, 2006, 2010; Selverstone, 2005; Pennacchioni et al., 2010). Quartz microstructures are commonly used to constrain semi-quantitatively deformation temperature and kinematic regime in collisional belts (Srivastava and Mitra, 1996; Faghih & Sarkarinejad, 2011; Law, 2014; Frassi, 2015) and contact aureoles (e.g. Stipp et al., 2002b, Morgan and Law, 2004; Morgan et al., 2016), based on the comparison of quartz microstructures with those investigated by Stipp et al. (2002a, b) in the Tonale Fault or based on the application of the opening-angle thermometer (Kruhl, 1996, 1998), although this represents largely an oversimplification (see Law et al., 2014 for a review). Indeed, in spite of being one of the most extensively studied phase, quartz behavior is controlled by many other mechanisms rather than temperature, including stress and strain rate, and many factors, such as the complex role played by water during quartz deformation and the interplay between plastic and brittle mechanisms at the BDT, are still poorly understood.

In general, at temperature below ~250 - 300 °C (Voll, 1976; van Daalen et al., 1999; Stöckhert et al., 1999; Stipp et al., 2002a), quartz behaves predominantly brittle, fracturing and undergoing pressure solution and solution transfer with reprecipitation of siliceous material in veins or in healed fractures (e.g. Hirth and Tullis, 1994; Dunlap et al., 1997; van Daalen et al., 1999; Stipp et al., 2002a, b). Localized crystal-plastic deformation may occur along grain boundaries and produce patchy or undulose extinction within the crystals (Nishikawa and Takeshita, 1999, 2000; Derez et al., 2015). Above 300 °C, two are the competing processes during quartz recrystallization: (1) the migration of existing grain boundaries (grain boundary migration; Poirier and Guillopé, 1979; Means, 1983; Poirier, 1985; Drury and Humpreys, 1986) and (2) the formation of new grain boundaries after rotation of the crystal lattice of a subgrain (subgrain rotation; Poirier and Nicolas, 1975; White, 1977; Guillopé and Poirier, 1979). The interaction of these processes produce three

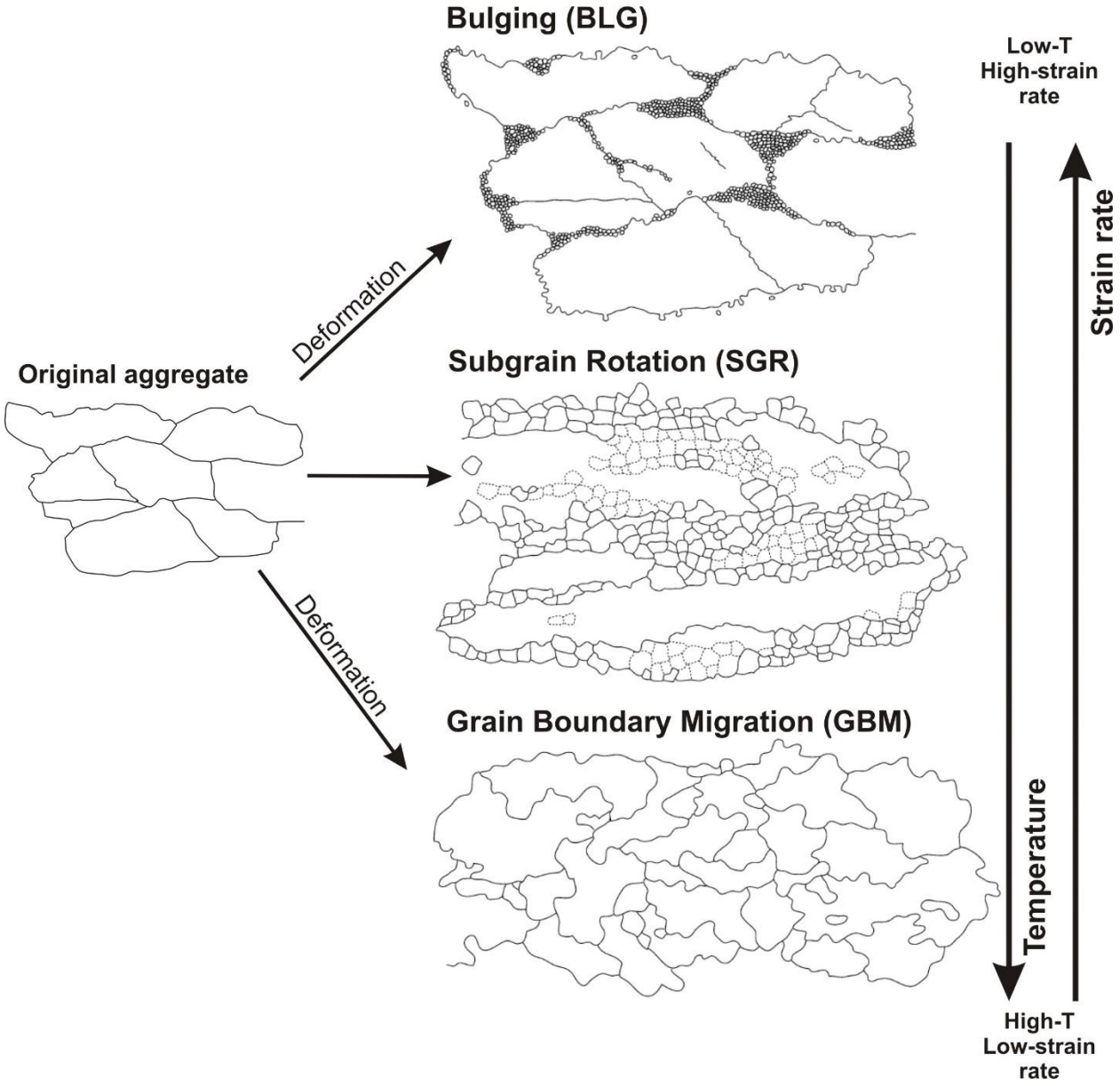

Figure 2.5 - The three main types of recrystallization mechanisms of an original crystalline aggregate. See text for explanations. Modified from Stipp et al. (2002b).

main deformation mechanisms in quartz, which, for increasing temperature, are (Stipp et al., 2002a,b): (1) Bulging (BLG; or slow grain boundary migration), (2) Subgrain rotation (SGR) and fast (3) Grain boundary migration (GBM) recrystallization. At low metamorphic grade (300 – 400 °C), BLG is the dominant recrystallization mechanism, causing the development of localized bulges with local recrystallized grains or extensive core-and-mantle structures (Bailey and Hirsch, 1962; Drury et al., 1985; Urai et al., 1986; Fig. 2.5). Recrystallization by BLG may coexist with brittle fracturing and dissolution-precipitation creep processes (Takeshita and Hara, 1998; Kjøll et al., 2015). At medium metamorphic grade conditions (e.g. 400 – 500 °C), the dominant recrystallization mechanism is represented by SGR recrystallization (Fig. 2.5; Lloyd and Freeman, 1994; Stipp et al., 2002a, b). The activity of SGR recrystallization causes the development of core-and-mantle structures, bimodal grain size distribution and extensive subgrain formation, partially

or totally overprinting relic quartz grains. At higher temperature (500 – 700 °C), fast GBM recrystallization becomes the dominant deformation mechanism, causing the development of strongly lobate grain boundaries with island grains (Fig. 2.5; Guillopé and Poirier, 1979; Lister and Dornsiepen, 1982; Mainprice et al., 1986; Urai et al., 1986; Jessell, 1987; Stipp et al., 2002b). The transition between the three main deformation mechanisms corresponds in general to an increase in grain size from 0-40 µm in the BLG-regime, to 40-120 µm in the SGR-regime and, finally, beyond 120 µm of average recrystallized grain size in the GBM-regime, based on a global compilation of data from nature by Stipp et al. (2010). It has been also shown that different slip systems are progressively activated in quartz with increasing temperature, with basal <a> and rhomb <a> slip being the dominant slip systems in the greenschist facies, prism <a> favored in amphibolite facies conditions and prism <c> occurring only at very high metamorphic grade conditions (Blumenfeld et al., 1986; Mainprice et al., 1986; Schmid and Casey, 1986; Toy et al., 2008 for a review).

Apart from this first order description of quartz microstructures and slip systems with respect to temperature, other parameters are equally important for the activation of different quartz deformation mechanisms. High strain rates, for instance, favor BLG and SGR recrystallization even at high temperature conditions whereas high differential stresses may cause the activation of more, coexisting, slip systems, since the critical resolved shear stress is reached for several slip systems (Hobbs, 1985). Water exerts a strong control over the rheology of quartz, which is extremely weak under wet conditions. On the other hand, under dry conditions quartz behaves as a strong phase even at very high metamorphic grade, as in the lower crustal study case described by Menegon et al. (2011a). The coexistence of large and tiny grains may cause strain partitioning, with strain hardening of larger grains, which may undergo fracturing while surrounding fine-grained grains are still deforming by dislocation or diffusion creep (e.g. van Daalen et al., 1999; Vernooij et al., 2006a,b; Menegon et al., 2008). Furthermore, the orientation of quartz grains in respect to the stress field may cause the coexistence of grains in ‘hard’ orientations, i.e. unfavorably oriented for slip in the favored slip system(s) and grains in ‘soft’ orientation, which causes strain partitioning between grains with different orientation (Stipp and Kunze, 2008; Muto et al., 2011; Kjøll et al., 2015; Ceccato et al., 2017) and between Dauphiné twins in single quartz grains (Stipp and Kunze, 2008; Menegon et al., 2011b). Finally, deformation processes in nature does not occur at constant strain rates and, especially at the BDT of large crustal shear zones, quartz may register surges of high-strain deformation followed by recrystallization at relaxing stresses (e.g. Trepmann and Stöckhert, 2003; Trepmann et al., 2017).

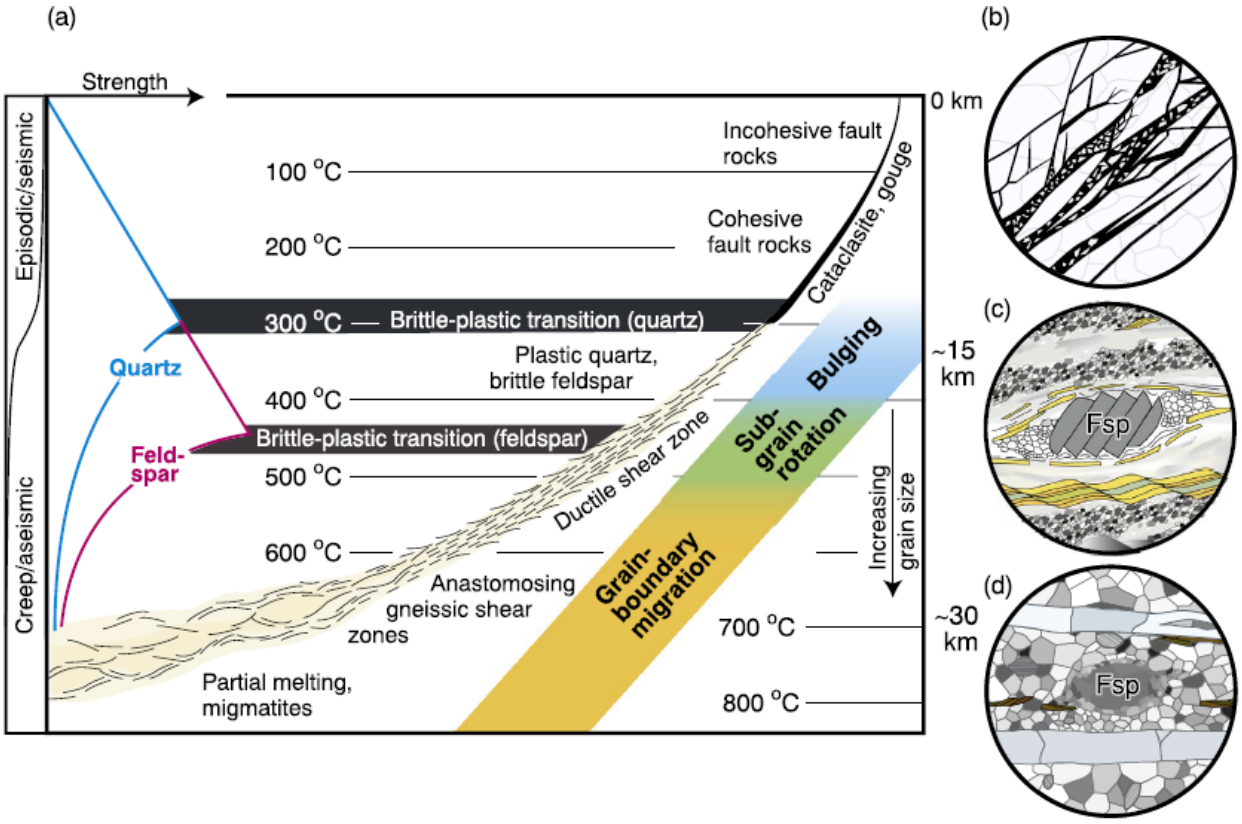

Figure 2.6 - Simplified model of crustal shear zone from Fossen and Cavalcante (2017): **(a)** diagram showing distribution of brittle and ductile deformation mechanisms for quartz and feldspar, the three types of dynamic recrystallization for quartz and (left) a depth-strength profile for quartz and feldspar; **(b)** brittle fracturing and cataclasis (fault); **(c)** dynamic recrystallization of quartz and fracturing of feldspar (brittle-ductile shear zone); **(d)** recrystallization of both quartz and K-feldspar (ductile shear zone). See text for further explanations.

2.4 Brittle and plastic processes in crustal shear zones

Deformation in the crust is commonly localized and accommodated into high-strain domains that bound rocks of relatively low-strain, referred to as shear zones or faults, when dominated by a plastic or frictional deformation mechanisms respectively (Fig. 2.6a; Ramsay and Graham, 1970; Sibson, 1977; Ramsay, 1980; Lister and Snoke, 1984; Pennacchioni, 2005; Fusseis et al., 2006; Carreras et al., 2010; Ponce et al., 2013). An alternative terminology (not used in this thesis) classifies shear zones as plastic (ductile or viscous) or brittle (i.e. faults), depending on the dominant deformation mechanisms and rheological behavior during deformation (Rutter et al., 2001; Fossen and Cavalcante, 2017). Shear zones containing both brittle and plastic deformation components are alternatively known as brittle-plastic (Rutter, 1986), frictional-plastic, brittle-viscous (Fusseis and Handy, 2008) or frictional-viscous shear zones (Stipp et al., 2002a, b) (see Fossen and Cavalcante, 2017 for a review). As a consequence, crustal shear zones i.e. shear zones transecting the entire crust, are characterized by a complete ‘rheological zonation’ with ductile roots, a semibrittle domain and an upper brittle zone (Fig. 2.6a; Ramsay and Graham, 1970; Sibson, 1977). In the example shown, the BPT for quartz and feldspar is shown (Sibson, 1983;

Hirth and Tullis, 1994; Gleason and Tullis, 1995), as well as the three main deformation mechanisms for quartz (BLG, SGR and GBM; Hirth and Tullis, 1992; Stipp et al., 2002a).

In the upper crust (T < 300 °C) deformation is controlled by frictional mechanisms, with development of cataclastic bands associated with brittle fracturing (Fig. 2.6b). If a component of vertical exhumation is involved, as it is typical for crustal shear zones, ductile structures are overprinted by brittle deformation. Many models predict the development of brittle faults or cataclastic bands that are oriented parallel to pre-existing ductile shear zones accommodating deformation from the ductile roots up to the brittle part of the crustal shear zone (e.g. Davis et al., 1986; Lister and Davis, 1989; Dinter et al., 1993; Ebert et al., 2007).

In the middle crust (300 °C < T < 450 °C), shear zones exhibit a more complex behavior, as feldspars still deform by brittle mechanisms while quartz behavior starts to be controlled by crystal-plastic mechanisms (Fig. 2.6c; Tullis et al., 1977, 1982; Simpson, 1985; Gapais, 1989; Gates and Glover III, 1989; Fitz Gerald and Stünitz, 1993; Stünitz and Fitz Gerald, 1993). In the example shown, competency contrast occurs between quartz and feldspar; however, in natural shear zones, strain partitioning may occur between different lithologies, leading to repartition of deformation between 'strong' and 'weak' domains (Jordan, 1988; Handy, 1989, 1994; Bons, 1993; Handy et al., 1999; Stünitz and Tullis, 2001; Passchier and Coelho, 2006; Jessell et al., 2009). An example is represented by anastomosing shear zones bounding relatively less deformed lozenges (e.g. Pennacchioni and Cesare, 1997; Pennacchioni, 2005; Fusseis et al., 2006; Carreras et al., 2010; Ponce et al., 2013). Strain is also internally partitioned within shear zones, as highlighted by shear bands that develop obliquely to the main foliation (Berthé et al., 1979; White, 1979; Lister and Snoke, 1984; Passchier, 1984; Law et al., 2004; Little et al., 2011; Gillam et al., 2014), alternatively known as extensional crenulation cleavage (Platt and Vissers, 1980). Many weakening processes (i.e. strain softening mechanisms) occur in mid-crustal shear zones, such as grain size reduction (White et al., 1980; Kilian et al., 2011; Platt, 2015), the formation of a lattice preferred orientation allowing slip on the 'softer' slip system (Rutter et al., 2001; Ji et al., 2004) or substitution of 'strong' phases with a mixture of 'soft' grains by metamorphic reaction (Steffen et al., 2001; Stünitz and Tullis, 2001), all contributing to keep deformation localized and enhancing competency contrast between the shear zone and low-strain domains (Fig. 2.3i). Widening of the shear zone occurs if strain hardening processes of the core (growth of 'strong' phases, accumulation of dislocations) or softening of the walls allows the shear zone to thicken at the expense of low-strain domains (Means, 1995; Fossen and Cavalcante, 2017).

2. The Brittle/Ductile Transition

At high-temperature conditions, shear zones are dominated by crystal plastic deformation, with silicates, like quartz and feldspars with coarse grained ribbons and porphyroblasts that define the foliation (Fig. 2.6d; White et al., 1980; Gapais, 1989; Hippertt et al., 2001; Rosenberg and Stünitz, 2003). The average grain size tends to be coarse, due to the dominant activity of GBM-recrystallization (Stipp et al., 2002b, 2010). Strain partitioning is quite uncommon, with large rock volumes deforming by low flow stress and therefore producing thicker high-grade shear zones characterized by a continuous mesoscale foliation (Passchier and Coelho, 2006).

This simple model appears to break down when shear zones and associated structures are analyzed in detail. As shown in par. 2.2.4, brittle structures have been reported at all structural levels related to dry conditions (Jackson et al., 2004; Gerald et al., 2006; Menegon et al., 2011a) or high strain rates (e.g. Gleason and Tullis, 1995) and many authors have shown the importance of brittle precursors in localizing ductile deformation (Segall and Simpson, 1986; Austrheim, 1987; Mancktelow and Pennacchioni, 2005; Fusseis et al., 2006; Pennacchioni and Mancktelow, 2007; Fusseis and Handy, 2008).

In a similar fashion, ductile structures have a profound influence over the geometries of brittle structures developing close or at the BDT. Efficient ductile precursors for brittle structures are represented not only by the metamorphic foliation but also by shear bands that may act as weak layers and facilitate fault nucleation in unlikely orientations in respect to those predicted by Anderson (1951)'s theory of faulting. Butler et al. (2008) documented for example the control of the basement foliation for the formation of brittle structures, with inclined foliations reactivated as thrust faults and steep foliations overprinted by complex fault arrays. More recently, Massironi et al. (2011) and Bistacchi et al. (2012) showed many natural study cases in the Alps, in which the orientation of pre-existing foliations and shear bands controls the geometry of brittle structures, suggesting that the presence of low-friction coefficient phyllosilicates aligned on ductile precursors (e.g. Zhang and He, 2016) allows deformation to be localized in misoriented, non-Andersonian, faults. This has been also shown experimentally by Ikari et al. (2015), who documented how brittle structures develop in foliated rock depending on how precursory foliations are oriented relatively to the imposed stress field.

Chapter 3

Geological Setting

The aim of this chapter is to provide a brief geological background and the 'state of the art' of the study area of this thesis. I hereby provide a brief summary of the tectonics of the northern Apennines, followed by a geological outline of the Elba Island. I also consider previous works on the study area with a focus on tectonics and interaction between large scale deformation and magmatic bodies. The lithostratigraphy of the study area is also defined here.

3.1 Geological outline

3.1.1 The northern Apennines

The northern Apennines (Fig. 3.1a) are a NW-SE striking Cenozoic collisional belt belonging to the Alpine system. They resulted from the Cretaceous-Eocene subduction of the Ligurian-Tethys Ocean and the following continental collision between the Adria microplate and Europe (Corsica margin; Boccaletti et al., 1971). The Oligocene to present evolution of the northern Apennines was characterized by the westward underthrusting of the Adriatic lithosphere (Adria plate) and the northeastward migration of the thrust front towards the Adriatic Sea–Po Plain foreland. The resulting structure (after Elter, 1975) is characterized, from top to bottom (Fig. 3.1a), by: 1) non metamorphic ocean-derived units (Ligurian Units *sensu latu*), 2) anchizone-grade cover nappes derived from Triassic-Oligocene Adria passive margin sequences (Tuscan Nappe, TN) and 3) low metamorphic grade continent-derived basement and cover nappes (Tuscan Metamorphic Units, TMUs). On the external (Adriatic) side, the northern Apennines are characterized by non-metamorphic units (Cervarola and Umbria-Marche units) stacked over east- and north-east verging thrust sheets.

The TMUs, at the base of the nappe stack (Fig. 3.1a), experienced greenschist to blueschists facies metamorphism with carpholite-bearing assemblages reported in southern Tuscany (Di Pisa et al., 1985; Franceschelli et al., 1986; Theye et al., 1997; Giorgetti et al., 1998; Molli et al., 2000). The pressure peak was constrained around 24-18 Ma and was followed by a Middle Miocene exhumation phase (Kligfield et al., 1986; Brunet et al., 2000; Fellin et al., 2007). In Late Miocene times, the northern Apennines belt was affected by magmatism related to the opening of the northern Tyrrhenian Sea as a back-arc basin (Boccaletti and Guazzone, 1972; Malinverno and

3. Geological Setting

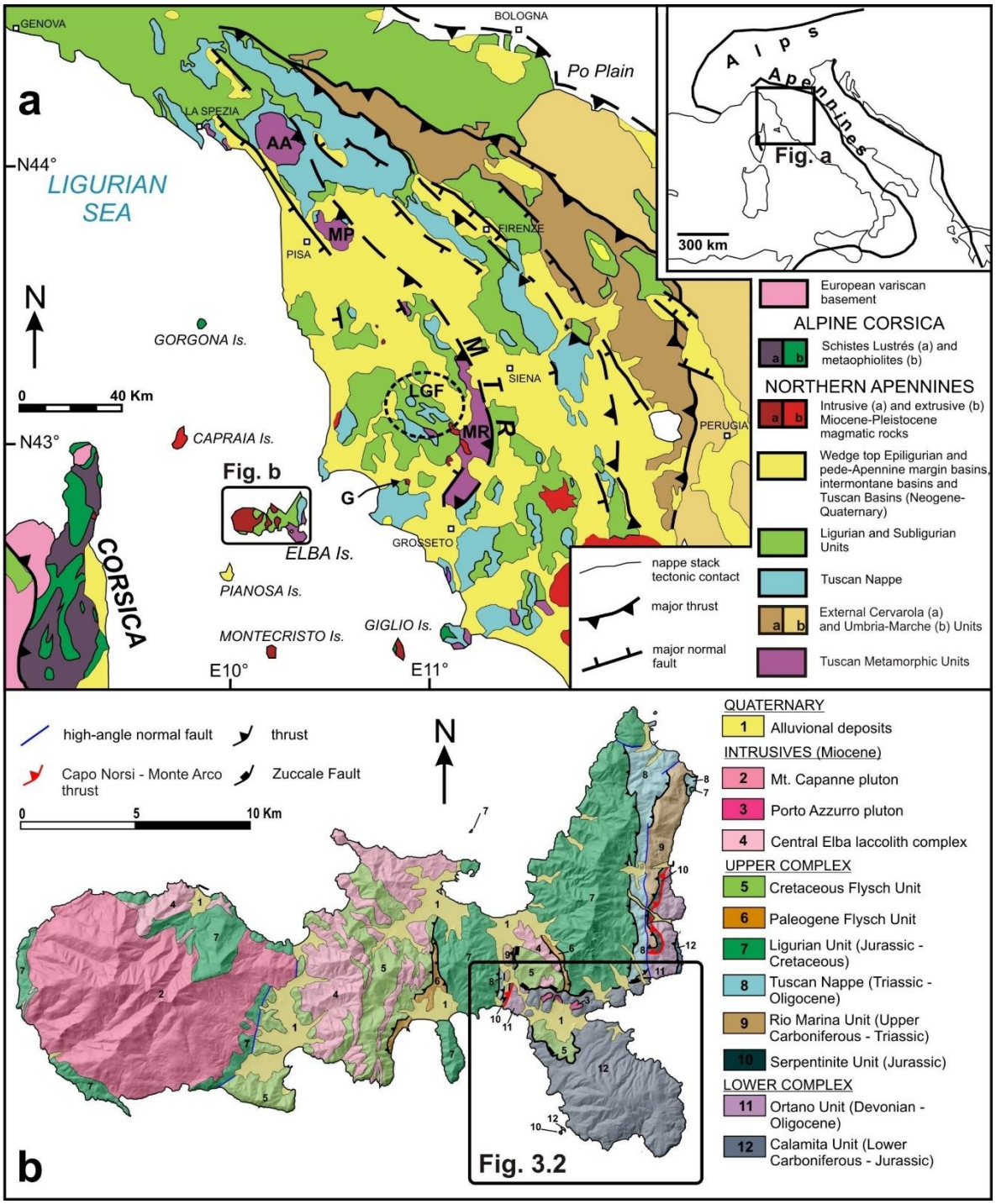

Figure 3.1 - (a) Tectonic sketch map of the northern Apennines and Alpine Corsica (modified after Bonini et al., 2014). MTR: Mid-Tuscan Ridge; AA: Alpi Apuane massif; MP: Monti Pisani massif; MR: Monticiano-Roccastrada massif; LGF: Larderello geothermal field; G: Gavorrano pluton; **(b)** Tectonic sketch map of the Elba Island (modified after Massa et al., 2017).

Ryan, 1986), with intrusives and extrusives rocks of mainly crustal derivation (Serri et al., 1993). The progressive younger age of the magmatic rocks from west to east supported a scenario of progressive eastward migration of the extensional front of the Apennines during the Miocene-Quaternary interval (Faccenna et al., 2001).

On the other hand, several seismic profiles image the Apennines hinterland as significantly shortened by thrust faults with poor evidence of extension (Ponziani et al., 1995; Cassano et al.,

1998; Finetti et al., 2001). Detailed structural investigations highlighted thrust faults controlling basement reactivation, growth of Miocene-Pliocene sedimentary basins (Boccaletti and Sani 1998; Bonini and Sani, 2002; Cerrina Feroni et al., 2006; Bonini et al., 2014) and emplacement of magmatic rocks (Musumeci et al., 2005, 2008). This has led some authors to infer the existence of a continuous or periodic compression in the northern Apennines until the Late Miocene or even Pliocene times (Boccaletti et al., 1999; Bonini and Sani, 2002; Musumeci et al., 2008; Bonini et al., 2014; Viola et al., 2018).

3.1.2 The Elba Island

Elba Island offers a complete structural section across the hinterland sector of the northern Apennines belt, consisting of a large monocline of continent- and ocean-derived nappes bound by north-south striking and west-dipping thrust faults (Barberi et al., 1967a; Pertusati et al., 1993; Keller and Coward, 1996; Massa et al., 2017). The nappe stack is subdivided into an Upper Complex and a Lower Complex, separated by a major thrust sheet (Fig. 3.1b), marked by strongly tectonized serpentinites (Rio Marina Thrust of Massa et al. 2017; referred to in this thesis as Capo Norsi – Monte Arco Thrust [CN-MAT] following Viola et al., 2018).

The Upper Complex consists of oceanic units (Fig. 3.1b; Cretaceous Flysch Unit, Paleogene Flysch Unit and Ligurian Unit) overlying continent-derived units (Fig. 3.1b; Triassic – Oligocene Tuscan Nappe and Upper Carboniferous - Triassic Rio Marina Unit, the latter with lower greenschist facies metamorphism). The Lower Complex (Fig. 3.1b) comprises the Ortano Unit, characterized by a Middle Ordovician basement (Musumeci et al., 2011) overlain by Jurassic – Oligocene metasediments, and the Calamita Unit, consisting of Lower Carboniferous basement rocks (Musumeci et al., 2011) overlain by slices of Triassic – Jurassic metasediments. Metamorphism of the Lower Complex ranges from greenschist to upper amphibolite facies (Duranti et al. 1992; Musumeci and Vaselli, 2012).

The west-dipping nappe stack of the Elba Island resulted from a first, Early Miocene phase of east-verging thrusting (Keller and Coward, 1996; Pertusati et al., 1993; Massa et al., 2017), dated around 19 Ma (Deino et al., 1992). During this stage, the Lower Complex and the Rio Marina Unit were underthrusted and attained greenschist (Pandeli et al., 2001) to blueschist facies metamorphism (Bianco et al., 2015). During the Middle Miocene, the entire nappe stack was refolded and reworked by out-of-sequence thrusting (CN-MAT; Fig. 3.1b), leading to major tectonic repetitions in the nappe stack (Massa et al., 2017). The metamorphic units were folded together with non-metamorphic units, suggesting that they were already exhumed in the upper crust at this stage.

3. Geological Setting

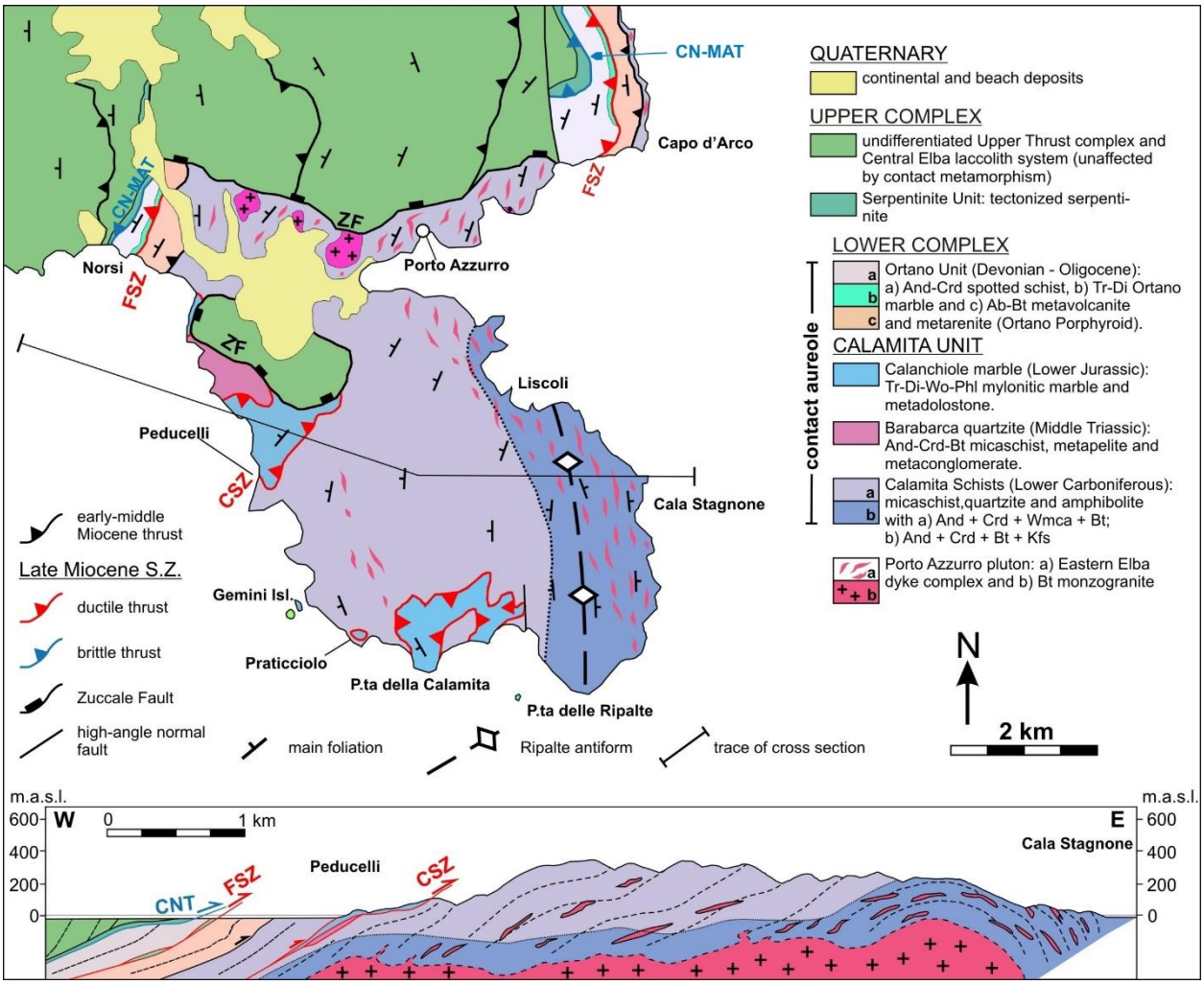

Figure 3.2 - Geological sketch map of the Calamita Promontory (modified after Musumeci et al., 2015). CN-MAT: Capo Norsi - Monte Arco Thrust; FSZ: Felciaio Shear Zone; CSZ: Calanchiole Shear Zone; ZF: Zuccale Fault.

The Late Miocene stage was characterized by the emplacement of large volumes of magma in the nappe stack (Fig. 3.1b), notably the Central Elba Sill Complex, the Monte Capanne Pluton in western Elba (8-7 Ma; Dini et al., 2002; Barboni and Shoene, 2014; Barboni et al., 2015) and the Porto Azzurro Pluton in eastern Elba (Fig. 3.2; 5.9 – 6.7 Ma; Musumeci et al., 2015). The emplacement of large intrusive bodies caused the development of medium to high grade contact aureoles at pressures not exceeding 0.15 – 0.20 GPa (Duranti et al., 1992). The previous greenschist to blueschist metamorphic assemblage was largely obliterated by low pressure contact metamorphism (Bouillin, 1983; Duranti et al., 1992; Rossetti et al., 2007). Similar low pressure facies metamorphism is reported also in mainland Tuscany, in the Larderello geothermal field (Fig. 3.1a), where buried, large Pliocene – Pleistocene plutons, were responsible for the development of contact aureoles with thickness ranging from 600 m up to 1700 m (Musumeci et al., 2002; Bertini et al., 2006). The Late Miocene high-temperature/low-pressure metamorphic event has been recorded only in Larderello and the Elba Island, whereas in the other Tuscan Units

the Early Miocene medium- to high-pressure metamorphism is preserved (Franceschelli et al., 1986).

Folds, shear zones and fault zones, documented in contact aureoles at the decimetric to metric scale, have been classically related either to (1) pluton ballooning causing gravitational collapse in the nappe stack (Pertusati et al., 1993; Westerman et al., 2004) or (2) extensional tectonics related to the opening of the northern Thyrrhenian Sea (Keller and Coward, 1996; Jolivet et al., 1998). More recently, Mazzarini et al. (2011) and Musumeci and Vaselli (2012) reported the occurrence in the Porto Azzurro Pluton aureole of a N-S striking regional antiform of foliation (Ripalte Antiform) and top to the-east decameter-thick shear zones (Calanchiole and Felciaio shear zones; CSZ and FSZ in Fig. 3.2), consistent with thrust kinematics. The Ripalte Antiform growth controlled the site of emplacement of leucogranite sheets and hydrothermal high temperature tourmaline veins (Mazzarini et al., 2011; Musumeci et al., 2015). The activity of shear zones was synkinematic with the growth of LP/HT mineral assemblages and produced tectonic slicing of high metamorphic grade rocks along the western side of contact aureole (Fig. 3.2; Musumeci and Vaselli, 2012).

The tectonic structures of the nappe stack and the late Miocene intrusive rocks in the Lower complex, were crosscut by the Zuccale fault, which cross cuts all tectonics structures with a total displacement of 6 km to the East and whose activity postdates pluton emplacement and cooling (ZF in Fig. 3.2; Collettini and Holdsworth, 2004; Smith et al., 2011; Musumeci et al., 2015). A still ongoing debate hinges on the interpretation of the ZF as a detachment or a thrust (see discussion in Musumeci et al., 2015). According to the original interpretation, the ZF would represent a regional extensional structure, while according to more recent views, the ZF would constitute the roof thrust of a large scale late Miocene duplex structure affecting the whole eastern Elba nappe stack (e.g. Musumeci and Vaselli, 2012; Papeschi et al., 2017). Recent geochronological constraints by Viola et al. (2018) bracketed the Zuccale Fault activity to the Lower Pliocene, demonstrating that its development occurred after the emplacement of the Porto Azzurro pluton and associated contact metamorphism and the activity of the FSZ, CSZ and CN-MAT.

3.2 The Calamita Unit

The Calamita Unit (Fig. 3.2) hosts the Porto Azzurro Pluton (Barberi et al., 1967b). It consists of three lithostratigraphic units:

- the Calamita Schists, a monotonous sequence of metapelites, metapsammites and quartzites (Barberi et al., 1967b) derived from the metamorphism of Early Carboniferous flysch deposits (Musumeci et al., 2011);
- the Barabarca quartzite, a thin slice of Middle Triassic metasandstones, schists and metaconglomerates (Garfagnoli et al., 2005);
- Calanchiole marble, a sequence of marbles, dolomitic marbles and calcschists of Lower Jurassic age (Garfagnoli et al., 2005);

The CSZ separates the Calamita Schists from the overlying metasedimentary units (Fig. 3.2; Musumeci and Vaselli, 2012). The Porto Azzurro is buried at 150-200 m below sea level, according to gravimetric data (Siniscalchi et al., 2008) and drill cores of granitic rocks in mining boreholes (Bortolotti et al., 2001). The kilometric size of this pluton is testified by the large extent of its contact aureole (~60 km^2) affecting the entire Calamita peninsula and part of eastern Elba (Duranti et al., 1992; Musumeci and Vaselli, 2012). Scattered exposures of biotite-monzogranite apophyses have been dated at 5.9 ± 0.2 ($^{40}Ar/^{39}Ar$ cooling age on Bt; Maineri et al. 2003), whereas leucogranite dykes intruding the Calamita Schists (Eastern Elba Dyke Complex; Mazzarini and Musumeci 2008; Fig. 3.2) yielded an age of ($^{40}Ar/^{39}Ar$ cooling age on magmatic muscovite; Musumeci et al., 2015) 6.3 ± 0.2 Ma. Lippolt et al. (1995) dated also iron bodies linked to the magmatic activity at 5.39 ± 0.46 (U-Th-He on adularia-specularite). The different cooling ages possibly suggest different generations or pulses of magma.

Contact metamorphism affects the Calamita Unit and part of the overlying Ortano Unit (Duranti et al., 1992). The upper limit of the aureole corresponds with the CN-MAT, thrusting the non-metamorphic rocks of the Upper Complex directly onto the Lower Complex (Fig. 3.2). According to Musumeci and Vaselli (2012), the Calamita Schists and the Barabarca quartzite equilibrated in the andalusite + cordierite + biotite + white mica zone, with high grade metamorphic rocks (andalusite + cordierite + K-feldspar + biotite) localized in the hinge zone of the Ripalte antiform, along the eastern coast of the Calamita peninsula (Fig. 3.2; Mazzarini et al., 2011). Peak metamorphic assemblages are variably affected by late sericitization and retrograde growth of static white mica. The Calanchiole marble is characterized by medium to high metamorphic grade calcite + dolomite + phlogopite + diopside + tremolite paragenesis (Musumeci and Vaselli, 2012). According to Duranti et al. (1992), the reported mineral assemblages suggest maximum metamorphic pressures lower than 0.2 GPa and temperatures exceeding 650 °C. $^{40}Ar/^{39}Ar$ ages on phlogopite in the Calanchiole marble and biotite in the Calamita Schists yielded 6.76 ± 0.08 Ma and 6.33 ± 0.07 Ma ages respectively, constraining contact metamorphism in this time interval

(Musumeci et al., 2015). An additional U/Pb age of 6.40 ± 0.15 Ma was obtained from the rim of a detrital zircon, consistent with $^{40}Ar/^{39}Ar$ ages (Musumeci et al., 2011).

Chapter 4

Structural Analysis

This chapter provides a description of the structures defining the geometry of the Calamita Unit at map- and meso-scale with a focus on the Calamita Schists, along with a detailed meso-scale structural analysis of the key outcrops investigated in this thesis. Planar elements are reported using the dip/dip direction notation while linear elements are expressed in trend/plunge. The data presented here are discussed at the end of the chapter, in order to define the structural evolution of the Calamita Unit. The map scale structures presented here have been published in Papeschi, S., Musumeci, G., & Mazzarini, F. (2017). "Heterogeneous brittle-ductile deformation at shallow crustal levels under high thermal conditions: The case of a synkinematic contact aureole in the inner northern Apennines, southeastern Elba Island, Italy". *Tectonophysics*, *717*, 547-564, while the detailed description of key outcrops has been published on Papeschi, S., Musumeci, G., & Mazzarini, F. (2018). Evolution of shear zones through the brittle-ductile transition: The Calamita Schists (Elba Island, Italy). *Journal of Structural Geology*, 113, 100-114 and integrated in this chapter with the structural analysis of other sections, named Fosso del Pontimento and Fosso di Fosco. Abbreviations used in the text are listed in Appendix A. Location of areas mentioned in the text is shown in Appendix C.

4.1 Map-scale structures

The Calamita Unit is characterized by a NNW-SSE striking metamorphic foliation, mesoscale folds, ductile and brittle shear zones. The main structural element of the Calamita Unit, at the macro- and mesoscopic scale, is the metamorphic foliation (therein after named Sp; see Appendix A), which is folded by the open, N-NW trending, upright Ripalte Antiform (Fig. 3.2, 4.1; Mazzarini et al., 2011). On the western limb of the antiform, the foliation dips gently to moderately toward the west, parallel to the CSZ (Fig. 3.2; Musumeci and Vaselli, 2012). The eastern limb of the antiform is characterized by moderately to steeply (up to vertical) east-dipping foliation (Fig. 4.1e).

In the Calamita Schists, the Sp is defined at the mesoscale by the parallel arrangement of metapelite and metapsammite layers and by the preferred orientation of mineral grains (andalusite, cordierite, biotite, white mica and K-feldspar), that also define the stretching lineation (Lp).

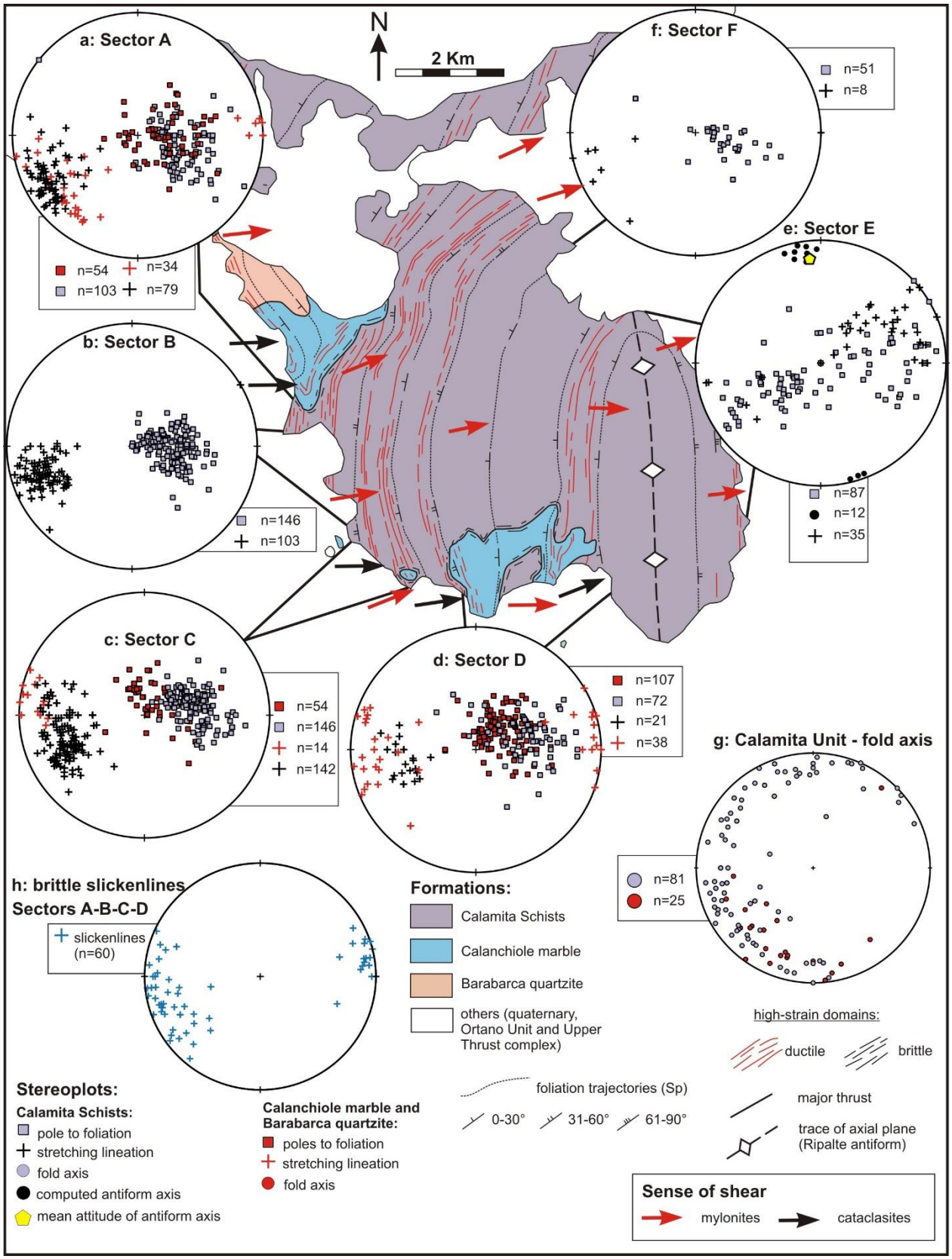

Figure 4.1 - Tectonic sketch map of the Calamita Unit showing the distribution of the main structural elements, low- and-high strain domains, ductile and brittle structures. Stereographic projections are equal area, lower hemispheres. Arrows mark hanging wall shear sense based on outcrop and micro-scale kinematic indicators (the direction is based on outcrop scale average stretching lineation)

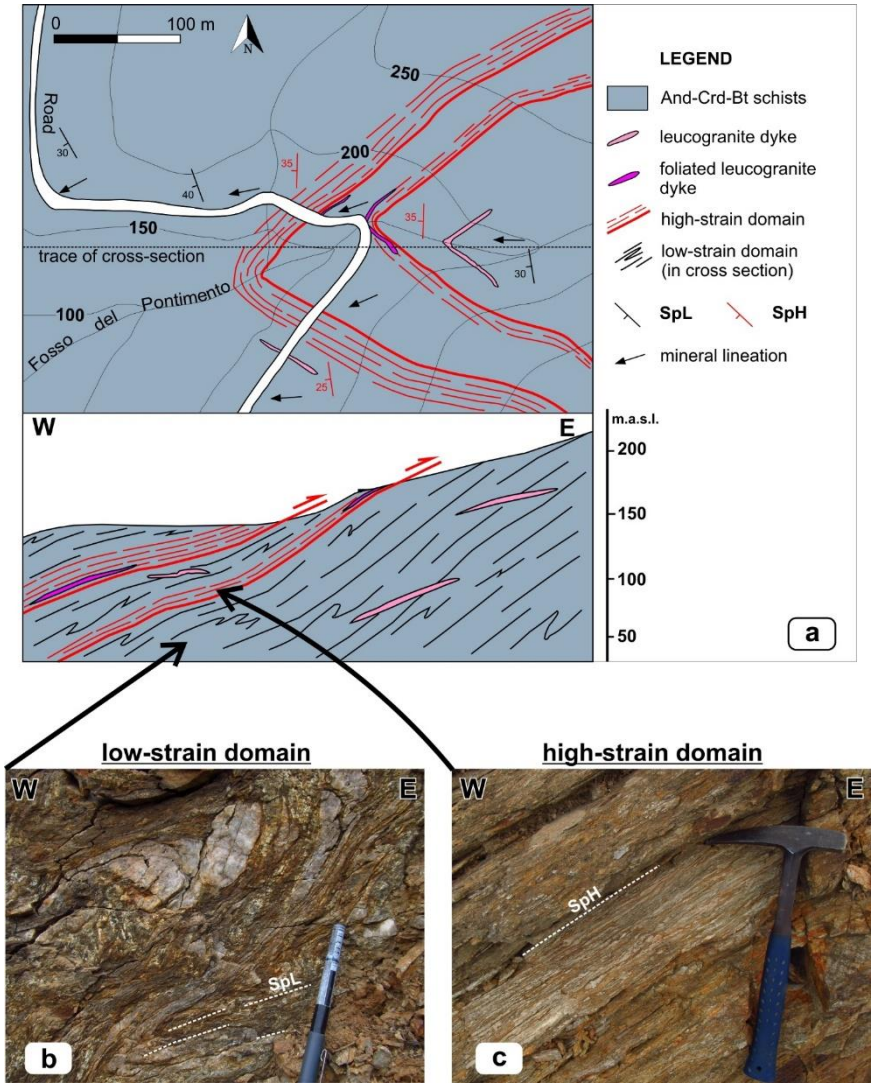

Figure 4.2 – Sketch map showing the distribution of high- and low-strain domains in sector B (Fosso del Pontimento; location in Fig. 4.1): **(a)** Geological map of the area, characterized by two decametric high-strain domains surrounded by domains of relatively low strain; **(b)** Low-strain domain with east-verging tight folds developed in quartz-rich layers and SpL axial plane foliation; **(c)** Mylonitic band with penetrative SpH foliation developed in a high-strain domain.

Detailed field structural mapping outlines the existence of low- and high-strain domains heterogeneously distributed in the Calamita Schists (Fig. 4.1, 4.2a). Low-strain domains constitute the majority of the Calamita Schists, whereas high-strain domains are meter- to decameter-thick zones of viscous deformation locally leading to proper mylonitic fabrics (Fig. 4.1). The orientation of structural elements (Sp, Lp) is the same in low- and high-strain domains. In figures and text, the labels SpL and LpL have been used to describe foliation and lineation in in low-strain domains and SpH and LpH in high-strain domains.

4.1.1 Low-strain domains

Low-strain domains (LSD) feature a millimeter-spaced SpL schistosity, which corresponds to the axial plane foliation of metric to decimetric east-verging, close to isoclinal asymmetric non-cylindrical folds with thickened hinges and variably thinned limbs (Fig. 4.2b). The intensity of foliation increases along the reverse limb of folds (Fig. 4.2b). Hinge zones locally preserve

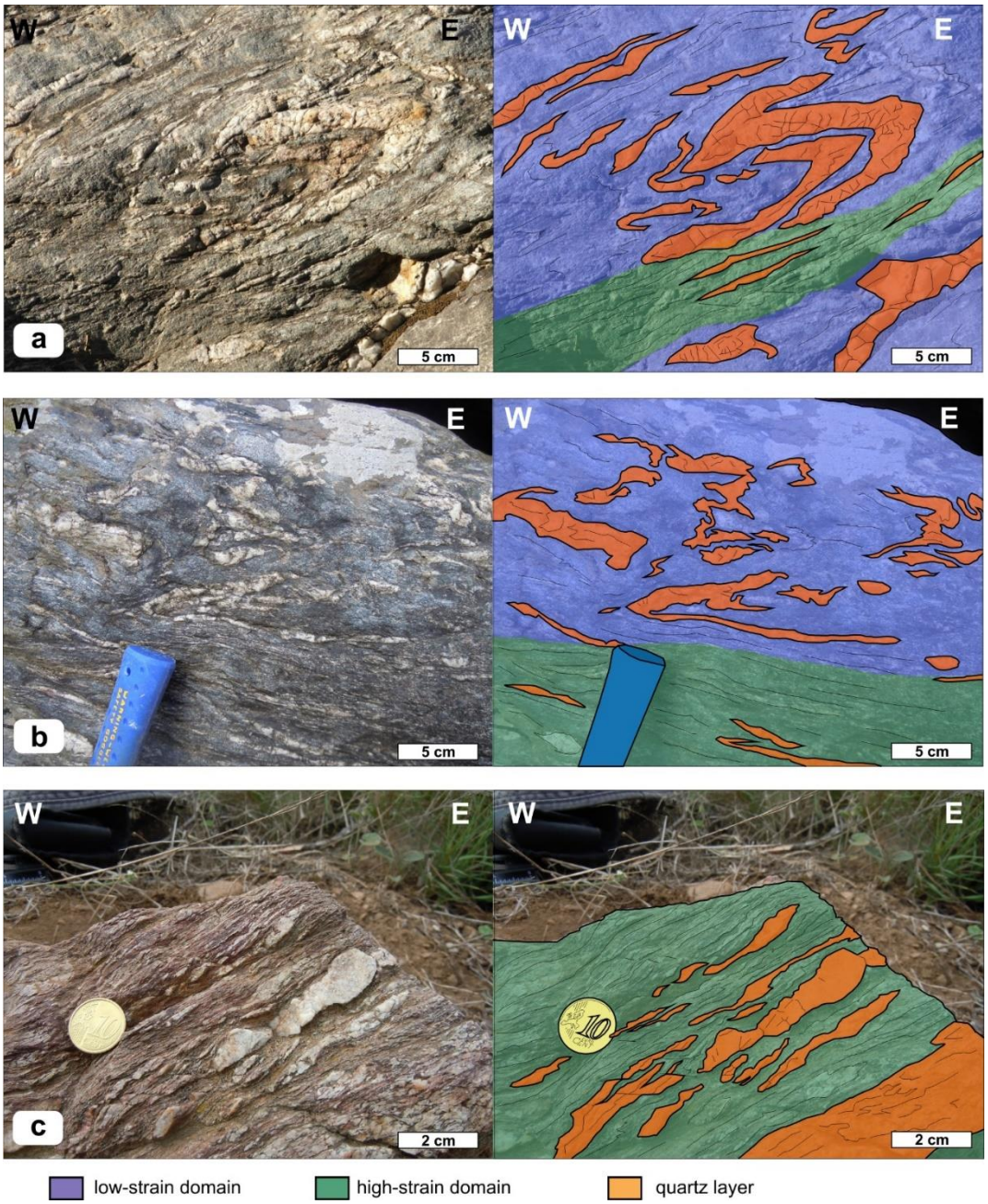

Figure 4.3 – Mesoscale examples of strain partitioning between high-strain domains and low-strain domains from the Pontimento area: **(a)** Localized well-foliated high-strain domain in the reverse limbs of folds highlighted by quartz layers in low-strain domains; **(b)** Abrupt transition from a coarse-grained low-strain domain with tight folds to a continuously foliated high strain domain with stretched quartz layers; **(c)** High-strain domain with strongly foliated alternations of metapelitic layers and quartz bands affected by asymmetric boudinage indicating top-to-the-east sense of shear. Note the contrast with the low-strain domain fabric shown in Fig. 4.3a.

evidence of an older foliation (in microlithons), defined by recrystallized quartz-rich and micaceous layers with partially preserved white mica and opaque grains. The SpL is defined by the preferred orientation of mineral grains (white mica, biotite, quartz, andalusite and cordierite), which locally wraps millimeter to centimeter-thick lenses with diablastic and radial aggregates of andalusite + cordierite + biotite (see Chapter 5 for a detailed description). The LpL stretching lineation, defined by quartz and biotite aggregates or elongated andalusite and cordierite grains,

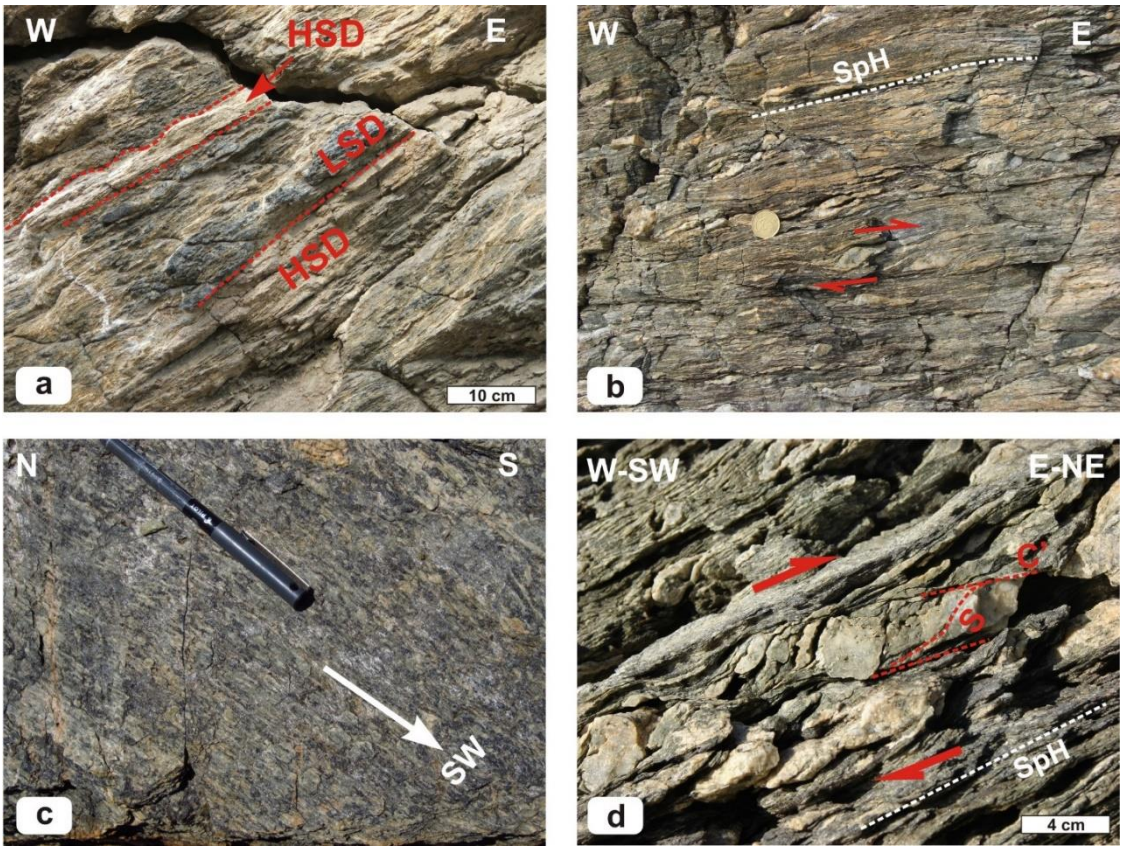

Figure 4.4 – Mesoscale structures (location of areas in Appendix C): **(a)** Strain partitioning with multiple, well-foliated high-strain domains (HSD) bounding coarse-grained low-strain domains (LSD) (Pontimento Area); **(b)** HSD: mylonitic schists characterized by asymmetric boudinage and sigmoidal quartz lenses indicating top-to-the-east sense of shear (Praticciolo area); **(c)** HSD: stretching lineations defined by quartz and biotite aggregates and andalusite-cordierite grains, trending E-W on a SpH foliation surface (Remaiolo area); **(d)** S-C' fabric developed in mylonitic quartz-rich schists indicating top-to-the-E sense of shear (Praticciolo area).

trends E to ENE with westward and eastward plunge on the opposite limbs of the Ripalte antiform (Fig. 4.1).

4.1.2 High-strain domains

High-strain domains (HSD) are defined by NS striking (Fig. 4.1) centimeter to meter-thick bands of intensely foliated andalusite-cordierite schist and quartzite (Fig. 4.2c). At map scale they can be traced throughout the Calamita Unit, dipping to the west in the western limb of the Ripalte Antiform (Fig. 4.1b, c, d) and to the east in its eastern limb (Fig. 4.1e).

In the field, the transition from LSD to HSD is marked by a sharp change in grain size and foliation intensity from medium- to coarse-grained and moderately foliated schist, often showing folds developed in quartzitic layers, to fine-grained schist with pervasively well-developed SpH foliation (Fig. 4.3a). HSD range from thin, localized domains of deformation in reverse limbs of folds (Fig. 4.3a) to thick and intensely foliated domains (Fig. 4.3b) with well-developed SpH foliation, defined by tight alternations of stretched quartz layers and continuous white mica + biotite layers with andalusite, cordierite and K-feldspar (Fig. 4.3c). In quartzites and

metapsammites, the SpH is defined by stretched quartz-feldspathic layers separated by thin, discontinuous mica-rich lenses (Fig. 4.2c). Strain partitioning is evident at the outcrop scale, outlined by the alternation of subparallel coarse-grained low-strain domains and fine-grained and well foliated high-strain domains (Fig. 4.4a). Within HSD, the SpH locally evolves into a mylonitic foliation mostly localized within quartz-feldspathic lithologies (Fig. 4.4b). Stretching lineations (LpH), associated with the SpH, are defined by (1) aggregates of white mica, biotite and quartz and (2) oriented andalusite, K-feldspar and tourmaline mineral grains (Fig. 4.4c). As shown in Fig. 4.1, the LpH has a constant trend of EW to SW-NE in the whole Calamita Unit and it is folded by the Ripalte Antiform. Kinematic indicators are well-visible in the field and include S-C and S-C' fabrics (Fig. 4.4d), deflection of veins and dykes, asymmetric boudins (Fig. 4.4b), consistent with overall top-to-the-east sense of shear. Boudinated layers correspond to quartz and/or calcsilicate lenses embedded in the schist, with boudinage style ranging from symmetric pinch-and-swell structures to asymmetric domino- or antithetic boudins. Centimeter- to decimeter-thick leucogranite dykes emplaced in the HSD locally display foliated to mylonitic fabric oriented parallel to the SpH of the host rocks (Fig. 4.2a).

4.1.3 Brittle structures

Brittle structures are mostly found localized in high-strain domains. In general, they range from small scale, localized Y shear fractures with centimetric eastward displacements (e.g. Fig. 4.5a) to larger Y-fault zones (e.g. Fig. 4.5b), also referred to as low-angle faults, characterized by metric to decametric top-to-the-E displacement, based on the position of corresponding markers in the footwall and hanging wall blocks. Y shears/faults are generally subhorizontal to gently E- and W-dipping and cross cut the main W-dipping metamorphic foliation (Sp) (Fig. 4.5a, b), often associated with subsidiary Riedel shear fractures, consistent with top-to-the-E sense of shear. Following the nomenclature by Logan et al. (1992), it is possible to distinguish conjugate sets of (1) moderately dipping (15 - 30°) synthetic top-to-the-east R1 shears (Fig. 4.5b) and (2) antithetic top-to-the-west steeply east-dipping (60-70°) R2-shears (Fig. 4.5b). R1 and R2 shears mutually cross cut, interacting also with Y faults and shears and isolating wedge-shaped fault cores. Small scale Y and Riedel shears contain millimeter-thick gouge or protocataclasite bands with little reorganization of rock fragments, whereas Y-faults with larger displacements locally show thick cohesive cataclasite bands (up to 20 cm in thickness) with bands of foliated ultracataclasite (thickness; 1-2 cm), localized at the top of the fault core (Fig. 4.5c). Slip planes are sometimes decorated with slickenlines and quartz slickenfibers (Fig. 4.5d) defining an E-W trending direction of tectonic transport (Fig. 4.1h). The distribution of Y-faults and associated Riedel shears is

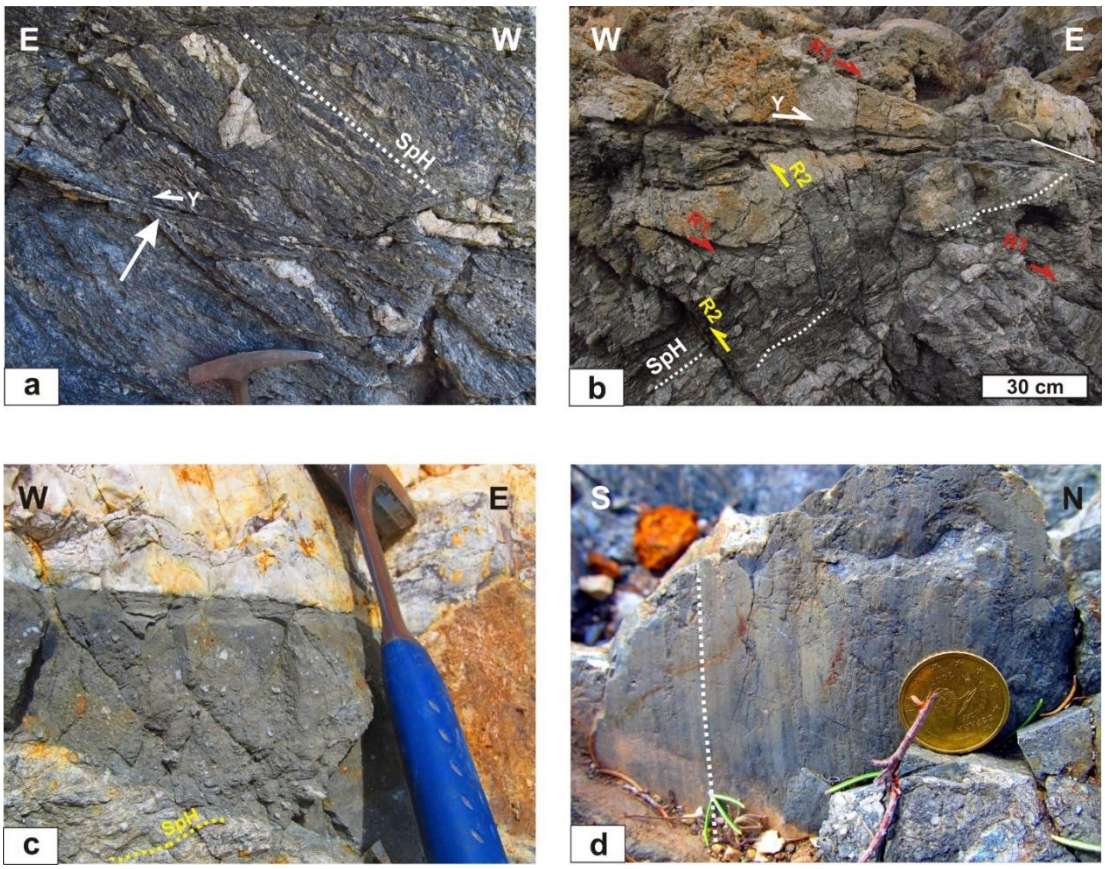

Figure 4.5 – Brittle deformation structures at the mesoscale: **(a)** Y shear fractures with small displacements cross cutting the W-dipping foliation of the Calamita Schists (Remaiolo area); **(b)** East-verging Y faults with thick cataclastic cores associated with arrays of Riedel shears (R1 and R2 shears) cross cutting former ductile structures (SpH) (Praticciolo area); **(c)** Cataclastic core zone of a Y-fault, discordantly cross cutting the SpH foliation (bottom of the image) and displaying a layered ultracataclasite band located at the contact with the hanging wall block (Praticciolo area); **(d)** Plane view of slickenlines developed on the polished surface of a subsidiary R1 shear fracture (Praticciolo area).

heterogeneous at the metric scale, with domains of micaschist pervasively cross cut by sets of shear fractures alternating with domains where the ductile fabric underwent little brittle overprint.

4.2 Mesoscale structural analysis of key outcrops

The following paragraphs are focused on the detailed investigation of meso- and microscale fabrics of HSDs, investigated in several sections, namely (1) the Capo Calvo HSD (Fig. 4.6a), (2) the Praticciolo HSD (Fig. 4.7a), (3) the Pontimento HSD (Fig. 4.9) and (4) the Fosco HSD (Fig. 4.10). These sections are characterized by different fabrics and relationships between ductile and brittle structures. Capo Calvo is located on the eastern limb of the Ripalte antiform, whereas Praticciolo, Pontimento and Fosco sections occur on the western limb of the Ripalte antiform (location in Appendix C). The insert maps provided for these sections show also the location of samples that have been investigated in detail in Chapter 5.

The attitude of structural elements (foliations, shear bands, lineations, shear fractures and slickenlines) has been measured at outcrop scale in the investigated sections. The Fisher vector

distribution has been calculated for every linear structural element and for poles to planar structural elements in each locality using Stereonet 10 (Allmendinger, 2005). Calculated mean vectors and statistical parameters are summarized in Tab. 4.1.

Table 4.1 – Fisher mean vectors (trend/plunge) to poles to planar and linear structural elements calculated for the investigated sections. For planar structural elements the mean plane in dip/dip direction notation is provided in brackets. N: number of measurements. a95: 95% confidence cone angle. a99: 99% confidence cone angle. K: Fisher constant. 1σ: circular standard deviation. Abbreviations of structural elements after Appendix A.

Locality: Capo Calvo							
Element	**N**	**Trend (°)**	**Plunge (°)**	**a95(°)**	**a99 (°)**	**K**	**1σ (°)**
Sp (33/061)	52	240.9	57.2	2.9	3.7	45.9	12.0
C' (53/062)	75	242.5	37.1	2.6	3.3	40.3	12.8
Lp	35	78.4	28.4	4.8	6	26.5	15.7
Locality: Praticciolo							
Sp/Sm (33/261)	135	79.2	56.9	2.3	2.9	28.6	15.1
C'1 (03/250)	108	70.5	87.1	1.5	1.9	78.5	9.1
C'2 (72/227)	17	47.3	18.2	19.8	25.3	4.2	39.5
Lp	129	254.6	32	2.5	3.1	25.9	15.9
Y (01/156)	56	336.0	89.1	2.5	3.1	60.0	10.5
R1 (22/080)	40	259.8	68.1	2.3	2.9	93.6	8.4
R2 (55/091)	36	270.7	35.2	9.5	11.9	7.4	29.7
Low angle fault (10/090)	20	269.8	79.4	5.4	6.9	37.0	13.3
slickenline	26	086.4	22.4	14.1	17.8	5.0	36.2
Locality: Fosso del Pontimento							
Sp/Sm (31/290)	60	109.9	59.4	4.0	4.9	22.5	17.1
Lp	46	245.4	21.8	4.3	5.3	25.2	16.1
Y (09/314)	28	134.5	80.6	4.3	5.4	41.4	13.7
slickenline	6	279.0	16.0	53.5	75.2	2.5	55.7
Locality: Fosso di Fosco							
Sp (24/273)	66	092.7	66.3	3.5	4.4	25.4	17.5
Lp	39	256.7	25.3	7.0	8.8	11.7	25.7
Y (04/112)	30	292.5	86.2	2.5	3.2	109.2	8.4
R1 (20/107)	16	286.6	69.9	4.3	5.4	75.9	10.1
slickenline	12	094.0	22.2	-	-	1.8	65.6

4.2.1 The Capo Calvo section

At Capo Calvo, the Calamita Schists are represented by high grade metapsammites (biotite + andalusite + cordierite + K-feldspar) intruded by leucogranite and pegmatite dykes (Fig. 4.6a).

The dominant mesoscale fabric is the high grade metamorphic foliation (Sp), characterized by 20-50° of dip and N050-070 of dip direction (Fig. 4.6a; Tab. 4.1). Mineral lineations are defined by aggregates of quartz and biotite and by the preferred orientation of andalusite, cordierite and K-feldspar: they trend about N050-N090 and plunge to the east-northeast (Fig. 4.6a; Tab. 4.1).

The Sp is defined by the subparallel disposition of biotite grains and elongated quartz-rich layers wrapping weakly foliated biotite-andalusite-cordierite-K-feldspar-plagioclase lozenges, whose asymmetric shape is consistent with top to the east sense of shear (Fig. 4.6b). The Sp is cross cut at low angle (20-30°) by top-to-the-east C and C' shear bands defining an S/C fabric in which the Sp corresponds to the oblique S foliation (Fig. 4.6b). C shear bands dip moderately (20 - 50°; Fig.

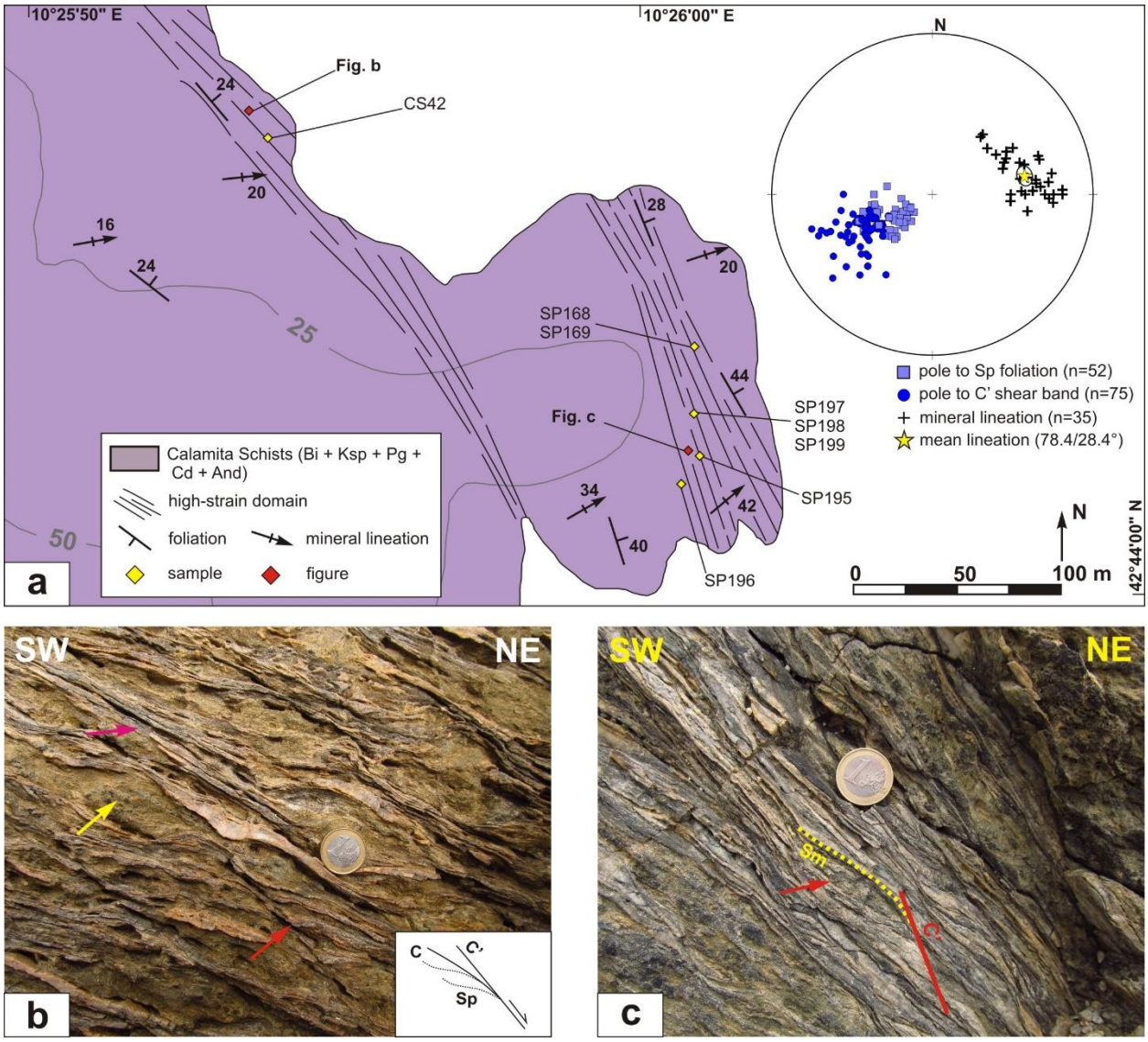

Figure 4.6 – (a) Simplified geological map of Capo Calvo with sample and figure location. Insert: stereographic projection (equal angle, lower hemisphere) showing poles to main foliation (Sp), C' shear bands and mineral lineation (Lp). The ellipse marks the trace of the 95% confidence cone and the yellow star the mean lineation vector. Sample details are available in Appendix D. **(b-c)** Mesoscale features of Capo Calvo: **(b)** Shear band cleavage characterized by moderately east dipping C shear bands (purple arrow) that cross cut the main metamorphic foliation (Sp). Lozenges of weakly foliated andalusite-cordierite-biotite aggregates (yellow arrow) are wrapped by the Sp. A single C' shear band (red arrow) is also visible. **(c)** Mylonitic shear zone characterized by stretched andalusite-cordierite-biotite pods (red arrow) parallel to the mylonitic foliation (Sm). Note the steeply east dipping C' shear bands that cross cut the Sm.

4.6a) towards the east with thickness ranging from few millimeters up to some centimeters and spacing ranging from several centimeters up to some decimeters. C' shear bands are characterized by steep eastward dip (between 40 and 80°; Fig. 4.6a) and make an angle of ~10-15° with C shear bands. They are discontinuous and characterized by millimetric thickness and a spacing of several centimeters.

C shear bands, defined by thin, stretched micaceous and quartzitic layers, form arrays of interconnected medium- to fine-grained shear planes with areas of linkage wrapping centimetric to millimetric lozenges with an oblique S foliation (Fig. 4.6b). Locally, in the most strained domains, such interconnected C shear band network evolve in mylonitic shear zones with well-

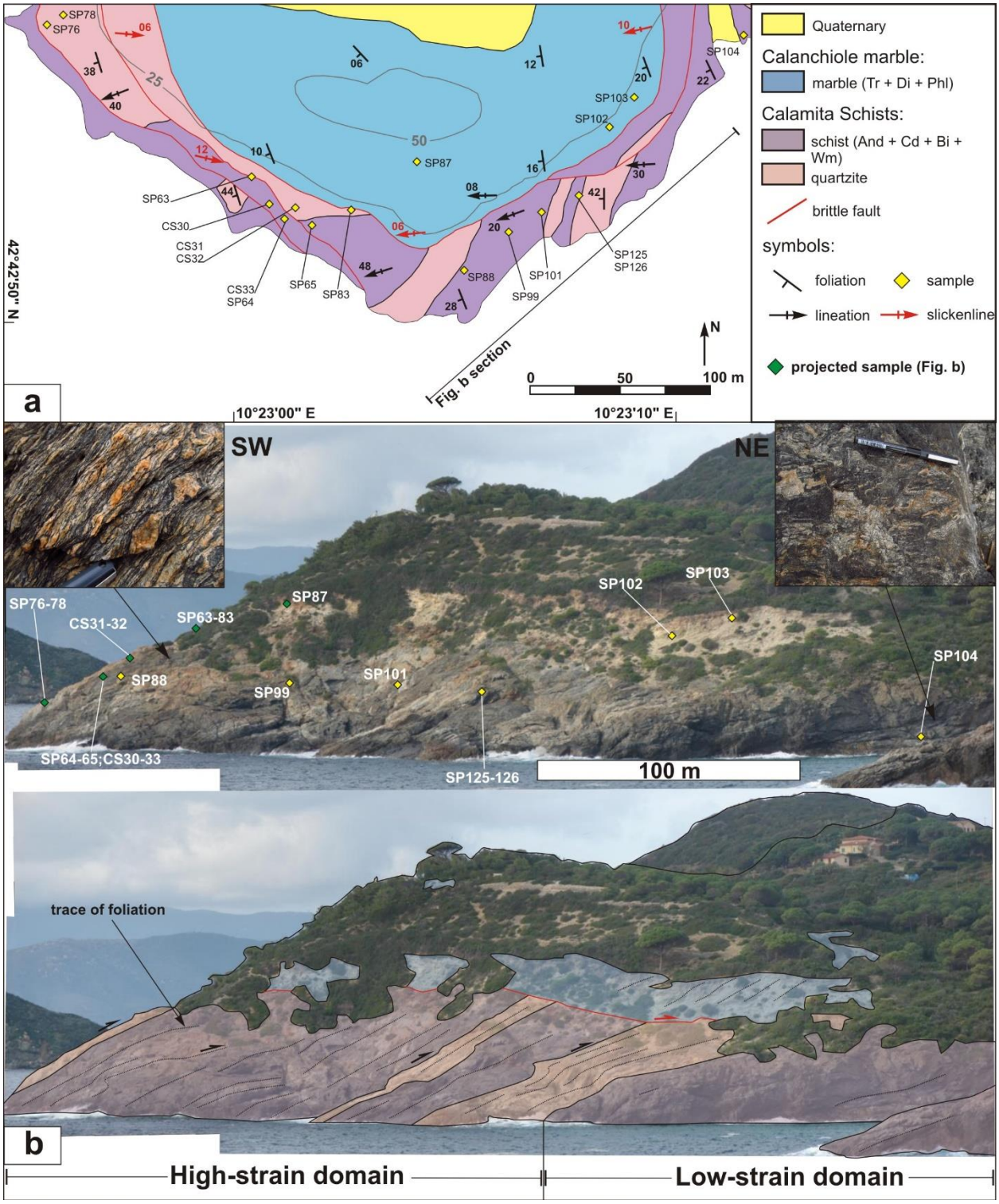

Figure 4.7 – Mesoscale features of the Praticciolo area. **(a)** Simplified geological map of the Praticciolo Cape with marked location of samples and figures. Sample details are available in Appendix D. **(b)** (above) Photo panorama along the section marked in Fig. 4.7a. See text for description. Samples projected on the section are marked by green dots. (below) Interpreted photo panorama with lithologies colored as in Fig. 4.7a.

developed mylonitic foliation (Sm), characterized by stretched quartz- and mica-rich layers enveloping boudinated andalusite-cordierite-biotite pods (Fig. 4.6c). The Sp foliation in the walls is dragged into parallelism with the Sm, consistently with top to the east sense of shear. Abundant

east dipping top-to-the-east C' shear bands, well-developed in mylonitic shear zones, cross cut the mylonitic foliation (Fig. 4.6c).

4.2.2 The Praticciolo section

The Praticciolo Cape, located at the southwestern tip of the Calamita Peninsula, (Fig. 3.2) exposes medium metamorphic grade rocks of the Calamita Schists and the Calanchiole marble (Fig. 4.7a). The Calanchiole marble discordantly overlies the Calamita Schists over a low-angle east-dipping fault zone (Fig. 4.7a, b). The Calamita Schists consists of white mica + biotite + andalusite + cordierite ± chlorite bearing schists and quartzites, while the Calanchiole marble is made up of impure and dolomitic marbles with diopside-tremolite-talc-phlogopite paragenesis interlayered with tremolite-talc phyllites.

The main foliation (Sp) in the Calamita Schists has a dip of ~30-40° and an average dip direction of 240-270° (Fig. 4.8a; Tab. 4.1). Mineral lineations, defined by trails of quartz and biotite aggregates and the preferred orientation of andalusite-cordierite grains, trend east-west and plunge to the west (Fig. 4.8a). A strain gradient from weakly foliated schist (low-strain domain) in the northeast to well foliated schists (high-strain domain) in the southwest characterize the Calamita Schists (Fig. 4.7b). The high strain domain is characterized by decimeter- to meter-thick bands of mylonites with S-C' structures and a west/southwest dipping mylonitic foliation (Sm; Fig. 4.8a), defined by alternations of stretched quartzite layers and mylonitic biotite-andalusite-bearing schists (Fig. 4.8c). The mylonitic fabric is displaced by gently east- to west-dipping millimetric C' shear bands that are characterized by top to the east sense of shear (Fig. 4.8a). Their spacing ranges from few millimeters in mylonitic schists, up to centimeters/decimeters in thick quartzite layers (Fig. 4.8c). Quartz-rich lenses and quartzites are affected by shear band boudinage and offset along C' shear bands with displacements from few millimeters up to several centimeters (Fig. 4.8c). A second set of steep, C' antithetic west-verging shear bands is sometimes present in thick and coarse quartz-rich lenses aligned on the Sm, intersecting synthetic east-verging C' shear bands at closely orthogonal angle (Fig. 4.8d).

A network of shear fractures and low-angle east dipping faults (0-15°; Fig. 4.8b) cross cuts the mylonitic fabric. Faults are characterized by decimetric to metric eastward displacements and feature cataclastic to ultracataclastic core zones, sometimes displaying foliated ultracataclasite bands (Fig. 4.5c). Quartz fibers define east-west trending slickelines (Fig. 4.8b). Shear fractures are organized in a Riedel shear pattern that, following the nomenclature by Logan et al. (1992), correspond to east-verging (1) gently east dipping (0-15°) Y shear fractures, (2) moderately east dipping (10-30°) synthetic R1 shear fractures and antithetic west-verging (3) steep (40-70°) R2

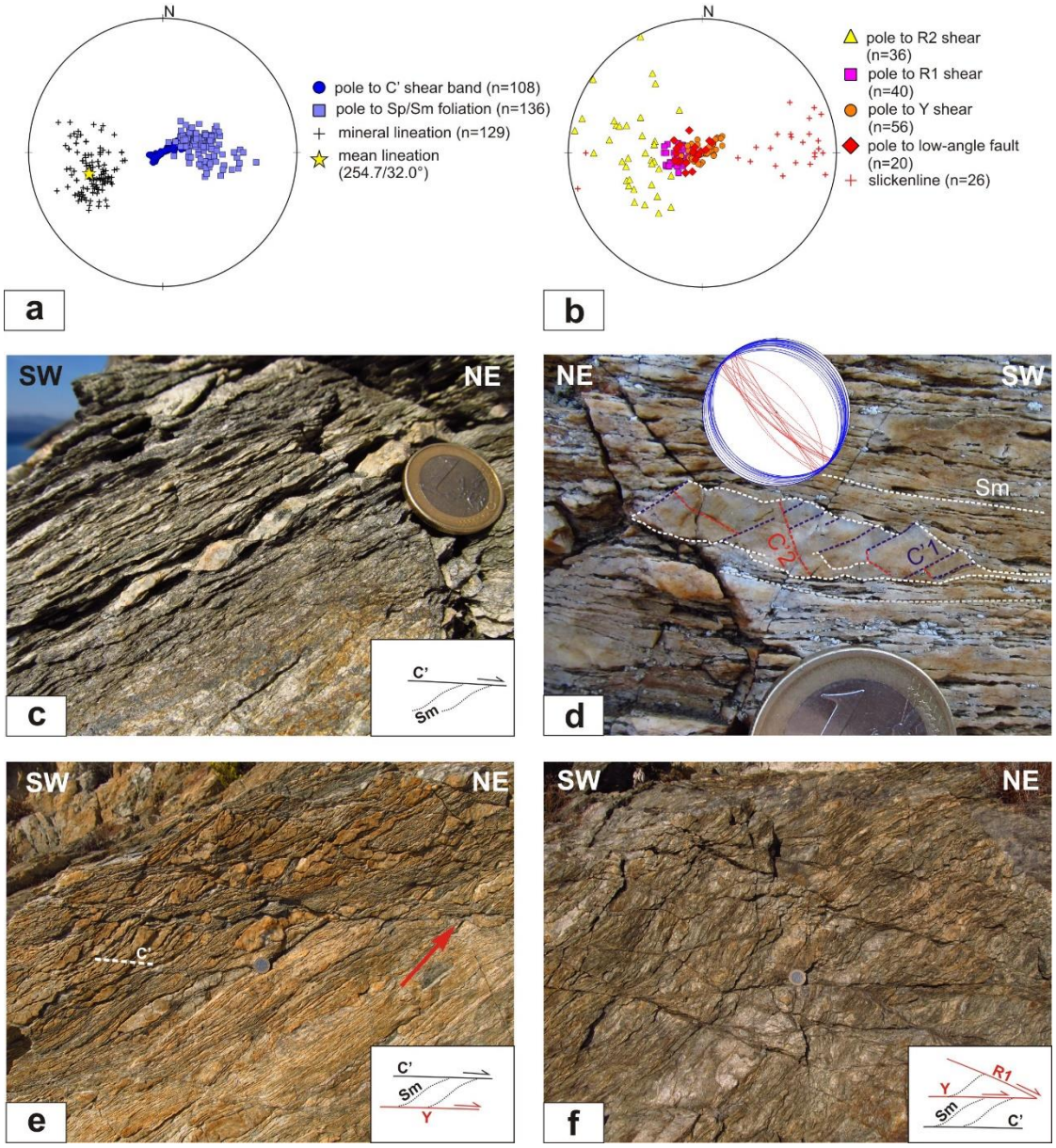

Figure 4.8 – Mesoscale features of the Calamita Schists at the Praticciolo: **(a-b)** Stereographic projections (equal angle, lower hemisphere) showing **(a)** poles to C' shear bands, foliation and lineation and **(b)** poles to low-angle brittle faults, Riedel Y, R1 and R2 shear fractures and brittle slickenlines. The trace of the 95% confidence cone around the mean lineation (yellow star) is marked by a black ellipse; **(c)** Mylonitic fabric characterized by west dipping foliation (Sm) with parallel quartzitic and foliated schistose bands, asymmetrically dragged along subhorizontal C' shear bands; **(d)** Conjugate synthetic (C'1) and antithetic (C'2) C' shear bands developed in a quartz-rich lens elongated on the Sm foliation. Insert: stereographic projection (equal angle, lower hemisphere) showing orientation of C'1 (in red) and C'2 (in blue) shear bands; **(e)** Mylonitic schist with top-to-the-E C' shear bands (white dotted line) overprinted by top-to-the-E Y shear fractures (red arrow); **(f)** Network of E-verging subhorizontal Y shear fractures bridged by moderately dipping R1 shear fractures affecting the W-dipping metamorphic foliation.

shear fractures (stereonets in Fig. 4.8b). Displacements measured on Riedel shears range from 1-2 millimeters to some centimeters. This Riedel shear geometry is overall consistent with eastward directed sense of shear. At outcrop scale, a parallelism exists between discrete C' shear bands (Fig. 4.8e) and Y shear fractures (Fig. 4.8e). Y shear fractures are often localized on C' shear bands separating boudins of quartz-rich layers (Fig. 4.8c). R1 shear fractures form *en-echelon* arrays that connect Y shear fracture segments in step over areas, allowing the linkage between parallel Y

shears segments (Fig. 4.8f). Intense damage zones, with a thickness of few centimeters up to decimeters, appear characterized by multiple Y, R1 and R2 shear fracture segments that dissect angular blocks of Calamita Schists. In damage zones, Riedel shears - in particular R2 shear fractures - locally exhibit decimetric displacements sometimes cross cutting low-angle fault zones.

4.2.3 The Pontimento section

Fosso del Pontimento is a narrow creek, located on the western flank of the Calamita Peninsula which is roughly oriented E-W and exposes a natural structural section across the Calamita Schists (Fig. 4.9a). The Calamita Schists in the area display biotite + white mica + andalusite + cordierite assemblage with K-felspar locally present. The main foliation (Sp) dips to the west (average dip/dip direction: 31/270°) and is associated with stretching lineations (Lp) directed 245/22° (Tab. 4.1; Fig. 4.9a). Stretching lineations are defined by aggregates of quartz and biotite or by the preferred orientation of porphyroclasts (andalusite, cordierite and K-feldspar).

The lower part of the creek corresponds to a low-strain domain (Fig. 4.9a), made up of weakly foliated schist and hornfels with alternations of metapelitic and quartzitic layers. The main foliation is folded by open- to tight east-verging folds with non cylindrical geometry and stretched reverse limbs (Fig. 4.9b). Moving upstream along the Pontimento section (i.e. to the west), the mesoscale fabric becomes progressively well-foliated (high-strain domain; Fig. 4.9c). The highest-strain domain is located between 150 and 200 meters of elevation along the stream and moving upstream high- and low-strain domains alternate through the section (Fig. 4.9a). In high strain domains, folds are rare and, when present, they are characterized by isoclinal to intrafoliar geometry. Stiff domains, such as thick quartz layers, form shear band or domino boudins indicating top-to-the-E sense of shear (Fig. 4.9c). The well-foliated schists are alternated with decimeter-thick mylonitic bands displaying strongly elongated quartz layers wrapped by fine-grained phyllosilicates (Fig. 4.9d) and S-C' fabric, constraining an eastward sense of shear. Foliated leucogranites are locally present, parallelized to the mesoscale foliation. S-C' structures and asymmetric boudins are largely reworked by shear fractures characterized by low-angle to moderately east dipping attitude associated with E-W trending slickenlines (stereographic projection in Fig. 4.9a). Locally, it is possible to recognize subhorizontal (0 - 10°) shear fractures, corresponding to Y-shears, and moderately east-dipping (up to 30°) shear fractures, representing R1 shears (Fig. 4.9e). Y shears are characterized by larger displacements than R1 shears and display mm- to cm-thick cataclastic core, which is not present in R1 shears (Fig. 4.9e). Measured displacements of shear fractures in this area never exceed few tens of centimeters.

4. Structural Analysis

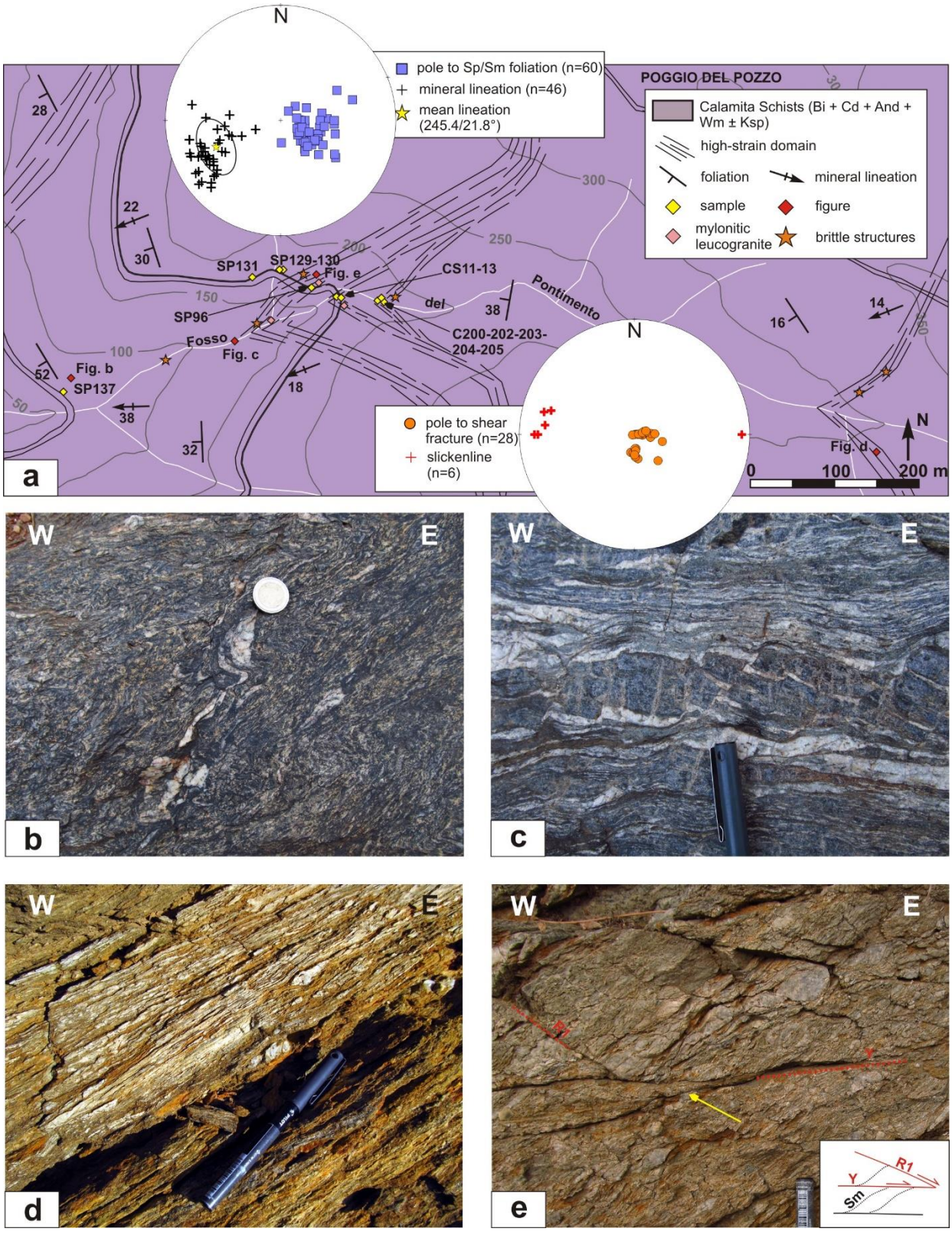

Figure 4.9 – Mesoscale features of the Pontimento section: **(a)** Schematic geological map with location of samples, figures and outcrops with brittle structures. The insert stereographic projections (equal angle, lower hemisphere) show orientation of ductile and brittle features in the area. The black ellipse marks the trace of the 95% confidence cone and the yellow star the mean lineation vector. Sample details are available in Appendix D; **(b)** Low-strain domain: tightly folded biotite schists and quartz lenses; **(c)** High-strain domain: well-foliated micaschist with boudinated calcsilicate layers. Top-to-the-E sense of shear; **(d)** High-strain domain: mylonitic band with sheared quartz-rich domains. Asymmetries indicating top-to-the-E sense of shear; **(e)** brittle shear fractures (R1: red dotted line; Y: yellow arrow) overprinting the mylonitic foliation (Sm) and characterized by top-to-the-E sense of shear.

4.2.4 The Fosco section

Fosso di Fosco is a creek running E-W and located 1 km south of Fosso del Pontimento. It is characterized by a scattered exposure of outcrops consisting of medium-grade rocks of the Calamita Schists (biotite + white mica + cordierite + andalusite) overprinted by brittle structures. This section has been described solely at the mesoscale.

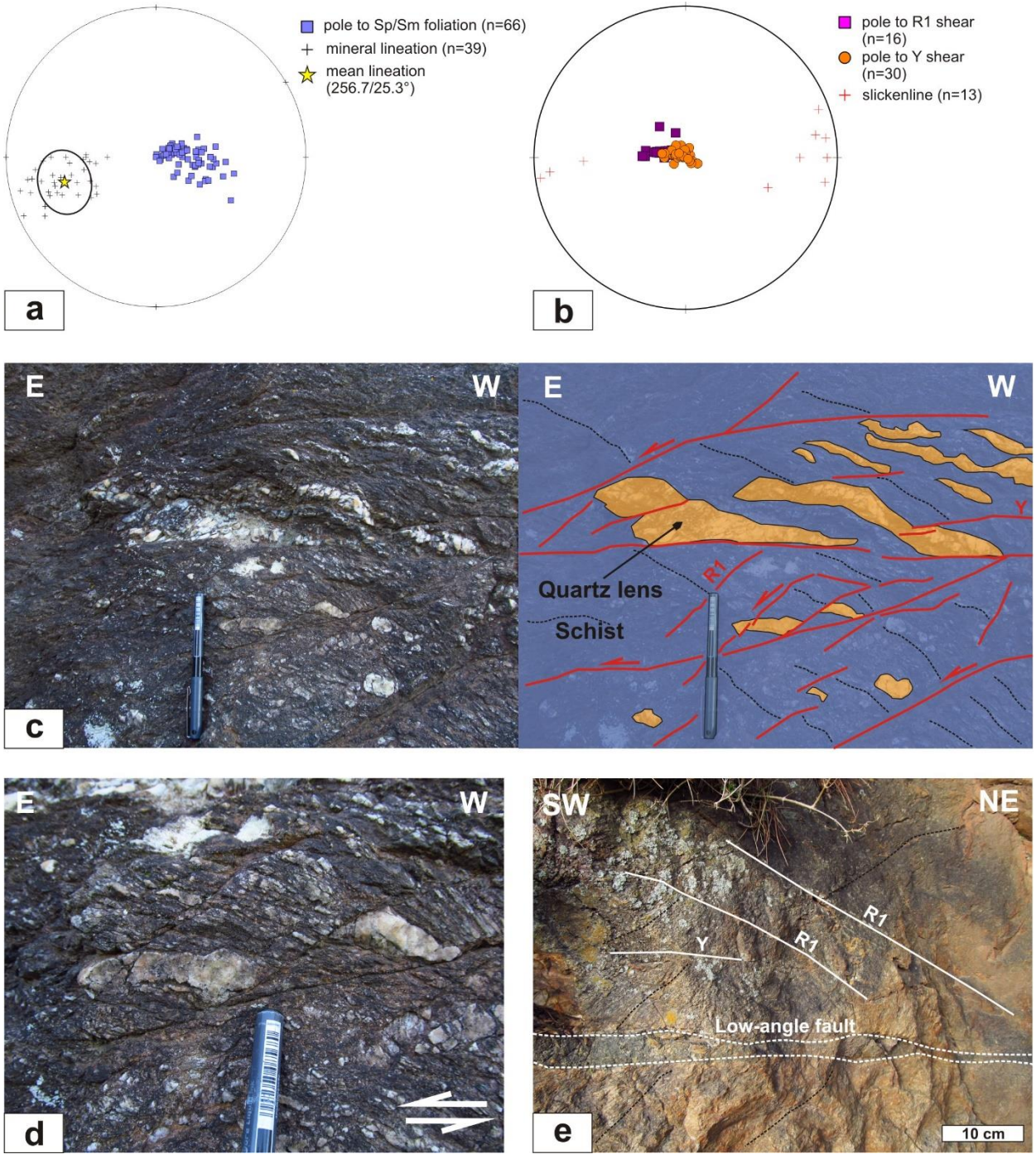

Figure 4.10 – Mesoscale features of the Fosco section: **(a-b)** Stereographic projections (equal angle, lower hemisphere) showing **(a)** pole to foliation and lineation and **(b)** poles to Y and R1 shears and brittle slickenlines. The trace of the 95% confidence cone around the mean lineation (yellow star) is marked by the black ellipse; **(c)** High-strain domain: well-foliated micaschist overprinted by E-dipping R1 shears and subhorizontal Y shears (sketched on the right). The black dotted line marks the Sp; **(d)** Detail of the eastward sense of shear defined by the displacement of quartz domains; **(e)** Low-angle brittle fault associated with R1 and Y shears in micaschist.

The main foliation (Sp) is oriented at 24/273° (dip/dip direction) and is associated with a mineral/aggregate lineation oriented 25/257° (Fig. 4.10a; Tab. 4.1). The mesoscale fabric is characterized by subparallel alternations of low-strain domains, containing hornfels and weakly-foliated schist cross cut by magmatic dykes, and high-strain domains, featuring well-foliated micaschist. Mesoscale folds are E-verging, display open to tight non cylindrical geometry and are localized predominantly in low-strain domains. Kinematic indicators are represented by asymmetric boudins and S-C' structures, defining top-to-the-E sense of shear.

The ductile fabric of high-strain domains is overprinted by brittle shear fractures and low-angle faults (Fig. 4.10c). Brittle structures can be distinguished in subhorizontal Y-shears and moderately E-dipping (10-20°) R1-shears, associated with E-W trending slickenlines (Fig. 4.10b). As shown in Fig. 4.10c, these structures cross cut the main W-dipping metamorphic foliation, defined by subparallel metapelite and quartz-rich layers, showing overall top-to-the-E sense of shear. Measured marker displacements range from some millimeters up to several centimeters (Fig. 4.10d). In addition, the metamorphic fabric is cross cut by subhorizontal low-angle fault zones with centimetric thickness, subparallel with Y shears and displaying eastward shear sense (Fig. 4.10e).

4.3 Discussion

4.3.1 Deformation in the Calamita Unit: geometries and fabrics

In the Calamita Unit deformation structures coeval with contact metamorphism were first recognized by Debenedetti (1953), who described the occurrence of cataclastic and mylonitic bands. Later, Pertusati et al. (1993) interpreted the dominant foliation in the Ortano Unit (referred to as S2) as evidence of local deformation related to the Porto Azzurro pluton emplacement. More recently, Mazzarini et al. (2011), Musumeci and Vaselli (2012) and Papeschi et al. (2017) provided evidence of regional-scale deformation in the south-eastern Elba Island coeval with pluton emplacement.

The reconstructed architecture of the Calamita Unit is shown in Fig. 4.1. Along the western side of the Calamita Unit, strain is partitioned in the east-verging CSZ, with high grade deformation fabrics and synkinematic mineral assemblages indicating the contemporaneity between deformation and thermal anomaly (Musumeci and Vaselli, 2012). In the Calamita Schists, below the CSZ, strain is partitioned between low-strain domains and localized, heterogeneously distributed west dipping top-to-the-E high-strain domains, parallel to the CSZ (Fig. 4.1). E-W trending lineations and kinematic indicators support a generally east-directed sense of tectonic transport (Fig. 4.1). The general attitude of foliations and lineations (see Fig. 4.1) reveals neither

deviations nor relevant rotations of structural elements throughout the whole Calamita Unit along both N-S and E-W directions. The occurrence of low- and high-strain domains (Fig. 4.2, 4.3) with similar geometry and constant eastward directed shear on the eastern and western limb of the Ripalte antiform but with opposite dips (e.g. Praticciolo: Fig. 4.7; Capo Calvo: Fig. 4.6) indicates that the foliated fabric, high-strain domains and lineations have been folded by the Ripalte antiform in a later stage (Mazzarini et al., 2011). The structural data presented here is consistent with the coexistence of regional-scale shear deformation coeval with contact metamorphism, the latter related to the emplacement of Late Miocene igneous bodies at shallow crustal level ($P \leq 0.2$ GPa) (Mazzarini et al., 2011; Musumeci and Vaselli, 2012; Musumeci et al., 2015; Papeschi et al., 2017, 2018). Furthermore, the documented brittle overprint, expressed by (1) fault zones and (2) Riedel shears reworking all previous fabrics and characterized by top-to-the-east shear sense indicators, indicates that in the Calamita Unit E-verging deformation outlasted the effects of contact metamorphism.

4.3.2 Brittle/ductile transition: shear fractures and role of precursory shear bands

The brittle stage of shear zone activity is evidenced by Y shear and subsidiary shear fractures that outline a network of R1 and R2 Riedel shears consistent with a top-to-the-east sense of shear parallel to the ductile direction of tectonic transport (Fig. 4.1, 4.8a,b). Brittle structures are predominantly developed within high-strain domains (Fig. 4.5, 4.8, 4.9, 4.10) parallel to C' shear bands.

The strict association of C' shear bands and Y shears, highlighted by their parallelism (Fig. 4.8a, b) and the observed localization of Y shears in relation to C' shear bands (Fig. 4.8e, f), suggests that C' shear bands acted as ductile precursors for Y shears. The brittle reactivation of C' shear bands could have been favored by the presence of low-friction coefficient phyllosilicates on C' shear bands (Zhang and He, 2016). On the other hand, the main mylonitic foliation (Sm), also defined by subparallel phyllosilicate layers (e.g. Fig. 4.8c), does not show evidence of brittle reactivation.

This feature could be related to the different orientation of shear bands and the Sm with respect to the maximum stress ($\sigma1$) in the brittle regime. Based on the structures observed at the Praticciolo, R1 and R2 shears are active simultaneously with Y shears and therefore the paleo-orientation of $\sigma1$ (i.e. the bisector plane of the mean conjugate R1 and R2 shears; Fig. 4.11a) can be estimated. The calculated mean $\sigma1$ direction is oriented 97.3/38.2 ± 19.1° and $\sigma3$ at 267.3/51.8 ± 19.1°. The $\sigma1$ orientation makes a ~30-40° angle with the average orientation of C' shear bands (dip/dipdir: 03/250) and is roughly orthogonal to the Sm foliation (33/261) (Fig. 4.11a). Slip tendency analyses

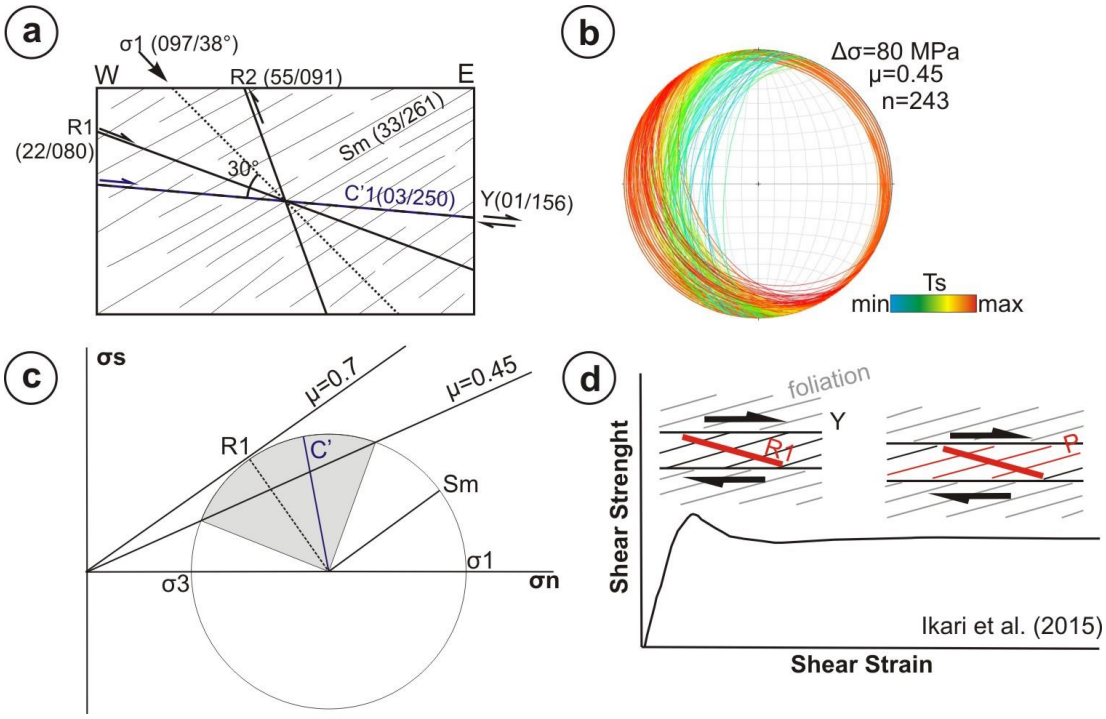

Figure 4.11 – (a) Block diagram illustrating the calculated mean orientation (expressed in dip/dip direction) of ductile and brittle structural elements and the calculated direction of σ1; **(b)** Slip tendency analysis for the Sm foliation and C' shear bands for μ = 0.45 and Δσ = 80 MPa. Foliations are colored in respect to the slip tendency Ts (Morris et al., 1996); **(c)** Sketched Mohr-Coulomb diagram with plotted failure envelopes for μ=0.7 and μ=0.45. The average orientation of C' shear bands, the Sm foliation and R1 shears in respect to σ1 is shown in the Mohr circle. The shaded area represents orientations of pre-existing foliations that are likely to be reactivated before failure across foliation takes place; **(d)** Failure experiment performed by Ikari et al. (2015) for a sample of Pennsylvania slate with foliation dipping in the opposite direction to the applied shearing. At low shear strain failure across foliation takes place with the nucleation of R1 shears. Then, at higher shear strain, the main foliation is reactivated by P shears.

were performed using the program FaultKin (Allmendinger et al., 1992), assuming zero pore fluid pressure and the same coefficient of static friction μ for the Sm foliation and shear bands. Several values of μ, between 0.2 and 0.7, have been used at varying conditions of differential stress (10 - 150 MPa) to evaluate the slip tendency Ts (Morris et al., 1996). As an example, in Fig. 4.11b the slip tendency analysis for C' shear bands and the Sm foliations is shown for a μ value of 0.45 and a differential stress of 80 MPa. Under these conditions, C' shear bands display the highest probability to reactivate (red circles in Fig. 4.11b) whereas the Sm foliation shows low slip tendency (cyan circles in Fig. 4.11b). The values reported in Fig. 11b represent just one of many combinations of differential stress - μ pairs under which C' shear bands are more likely to reactivate with respect to the foliation. Slip on the Sm foliation can be promoted by increasing the differential stress and/or the pore fluid pressure or by decreasing the μ coefficient. Thus, differential stress and the coefficient of static friction exert a strong control over the reactivation of ductile precursors and hence over the geometries of brittle structures. The favorable orientation for brittle reactivation of C' shear bands can be visualized by plotting the average orientation of C' shear bands and the Sm on the Mohr circle (Fig. 4.11c). In this example two cohesion-less

failure envelopes have been plotted, one for general failure (μ = 0.7) and the other for failure along shear bands/foliation (μ = 0.45). Although in this example both C' shear bands and the Sm are equally weak (μ=0.45), the Sm is so unfavorably oriented with respect to σ1 that failure takes place across the foliation (R1 shears) (Fig. 4.11c). The examples shown in Fig. 4.11b,c suggest that the foliation is not necessarily the only anisotropy that can be easily reactivated as less penetrative anisotropies, such as C' shear bands, may lie in a favorable orientation and therefore control the site of failure.

The situation described is similar to the experiments on sheared foliated rocks performed by Ikari et al. (2015) on a foliated black slate at various orientations in respect to the applied shear stress. In the experimental setting with foliation dipping in the opposite direction in respect to the shear sense (Fig. 4.11d), these authors observed the early nucleation of R1 shears across the foliation. Failure along the foliation occurs only at higher shear strain with the formation of foliation-parallel P shears (Fig. 4.11d). These authors concluded that under these conditions the main foliation is unfavorably oriented for slip and therefore R1 shears are forced to form from early stages of deformation (see also Sibson, 1985; Collettini and Sibson, 2001).

I suggest that the high strain domain in the Calamita Schists represent a natural analogue of the experiment of Ikari et al. (2015). Compared to the experiments of Ikari et al. (2015), the presence of a second set of weakness planes, represented by C' shear bands, might have caused the early localization of deformation onto precursory C' shear bands, producing networks of Y and R1 shears. This might have also inhibited the reactivation of the foliation, which on the other hand was observed to occur at higher shear strain in the experiments performed by Ikari et al. (2015). In all the investigated sections in the Calamita Schists, indeed, deformation appears concentrated in R1 and Y shears.

To summarize, I propose that at the brittle-ductile transition deformation switched progressively from the well-developed mylonitic foliation into discordant networks of shear fractures that formed as a consequence of the reactivation of precursory shear bands in the brittle regime, favoring strain localization into brittle fault networks that cross cut the metamorphic fabric. This hypothesis will be discussed in detail with the microstructural and EBSD data presented in Chapters 5-6.

4.3.3 Age of deformation

Among the available radiometric ages for the Calamita Unit, the 6.76 ± 0.08 Ma $^{40}Ar/^{39}Ar$ phlogopite age on diopside-phlogopite marble and 6.23 ± 0.06 Ma $^{40}Ar/^{39}Ar$ age on late white mica in andalusite-cordierite-biotite schists (Musumeci et al., 2011, 2015) are interpreted to provide

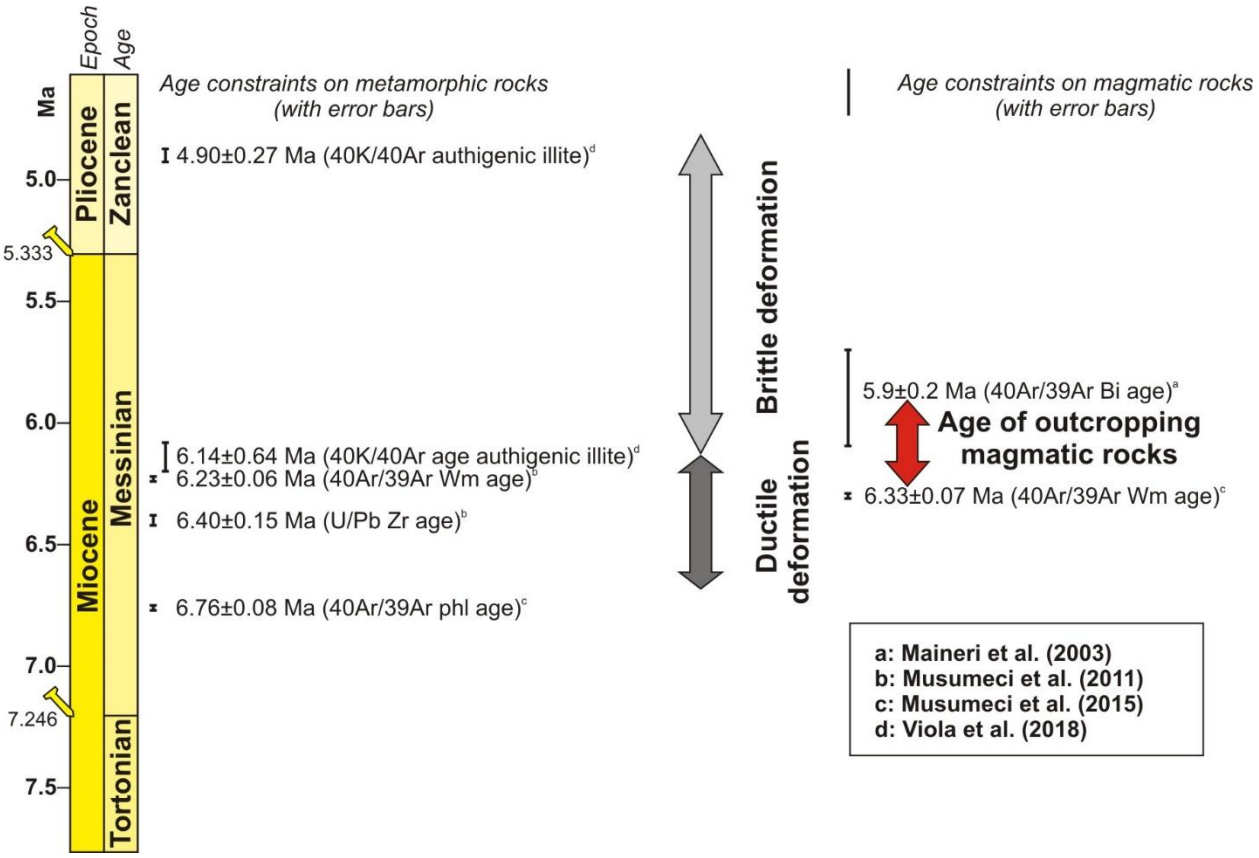

Figure 4.12 – Summary of the available age constraints on ductile and brittle deformation in the Calamita Unit and on the age of the outcropping magmatic products. The insert stratigraphic chart on the left is based on Cohen et al. (2013), updated 2018 version. See text for comments.

lower and upper limits for ductile deformation, as shown in Fig. 4.12. This age interval is corroborated by a 6.40 ± 0.15 Ma U/Pb age on zircon rims in andalusite-cordierite-biotite Calamita Schists (Fig. 4.12; Musumeci et al., 2011).

Interestingly, magmatic rocks emplaced in the Calamita Unit yielded younger age ranges (Fig. 4.12). A mylonitic leucogranitic dyke injected in a high-strain domain yielded a $^{40}Ar/^{39}Ar$ white mica age of 6.33 ± 0.07 Ma (Musumeci et al., 2015) and the exposed monzogranite was dated at 5.9 ± 0.2 Ma ($^{40}Ar/^{39}Ar$ on Bt; Maineri et al., 2003). Consequently, the leucogranitic dykes and monzogranite body, commonly referred to as the exposed part of the Porto Azzurro Pluton, *de facto* postdate the thermal peak (Fig. 4.12). This is also in line with the evolved compositions of the outcropping magmatic products (Peretti, 2007) and supports the hypothesis of Marinelli (1959) that the large areal extent of the aureole should be related to a less evolved (and hotter) magmatic intrusion than the exposed igneous rocks. From a structural point of view this is consistent with the cross-cutting relationships observed between the Dyke Complex, the monzogranite and their surrounding host rocks (Mazzarini and Musumeci, 2008). Only the age of mylonitic dykes (6.3 Ma), deformed in high-strain domains, overlaps with the white mica-age in the host metamorphic rocks and might be regarded as the lower limit for transition from ductile to brittle deformation.

Similar age constraints have been obtained from dated authigenic illite grains ($^{40}K/^{40}Ar$ method) on a cataclastic gouge collected on the Calanchiole Shear Zone (6.14 ± 0.64 Ma; Viola et al., 2018). A reasonable upper limit for semi-brittle deformation in the aureole is provided by the relative age of the brittle Capo Norsi – Monte Arco Thrust (west of the Calamita Peninsula; Fig. 3.2), which has been bracketed at 4.90 ± 0.27 Ma using the $^{40}K/^{40}Ar$ method on authigenic illite grains (see summary in Fig. 4.12; Viola et al., 2018).

4.3.4 Tectonic vs. pluton-related deformation

The structural features in the Calamita Unit and the available radiometric data provide clear evidence of long lasting deformation (at least 300-500 kyr) linked to overall top-to-the-E kinematic framework and characterized by earlier ductile fabrics overprinted by brittle structures. In order to discriminate between regional scale- and magma emplacement-related deformation, the following points should be considered:

1. constant N to NNE strike of foliation and trend of fold axes, as well as E-W trending stretching lineations;
2. nearly constant eastward sense of tectonic transport that characterizes ductile and brittle structures;
3. steep strain gradient defined by the occurrence of high-strain zones distributed throughout the Calamita Unit and their parallelism with the Calanchiole and Felciaio Shear Zones (Musumeci and Vaselli, 2012). The former is the main ductile-brittle structure away from the inferred contact with the intrusive body (see Fig. 3.2 and cross sections in Fig. 4.13), the latter is located in the outer portion of the contact aureole (Ortano Unit) and is responsible for tectonic doubling of the aureole (Musumeci and Vaselli, 2012);
4. upright geometry of the Ripalte Antiform and mesoscopic scale folds refolding ductile fabrics;
5. geometrical position of all deformation structures above the roof of the intrusion and their attitude, which is consistent with subhorizontal shortening instead of vertical flattening.

Considering the case of a pluton inflating upward, a centrifugal shear sense, showing opposite sense of shear on the opposite sides of the antiform would be expected. This is not consistent with the described study case, where the geometry of the structural elements in the aureole is independent from that of the buried Porto Azzurro Pluton, assuming the diameter of the pluton to be comparable to the areal extent of the contact aureole. A possible interpretation of the tectonic setting of the Calamita Unit is shown in Fig. 4.13. Based on the (1) presented data and (2) large-scale structural setting of the central-eastern Elba Island (Mazzarini et al., 2011; Musumeci and

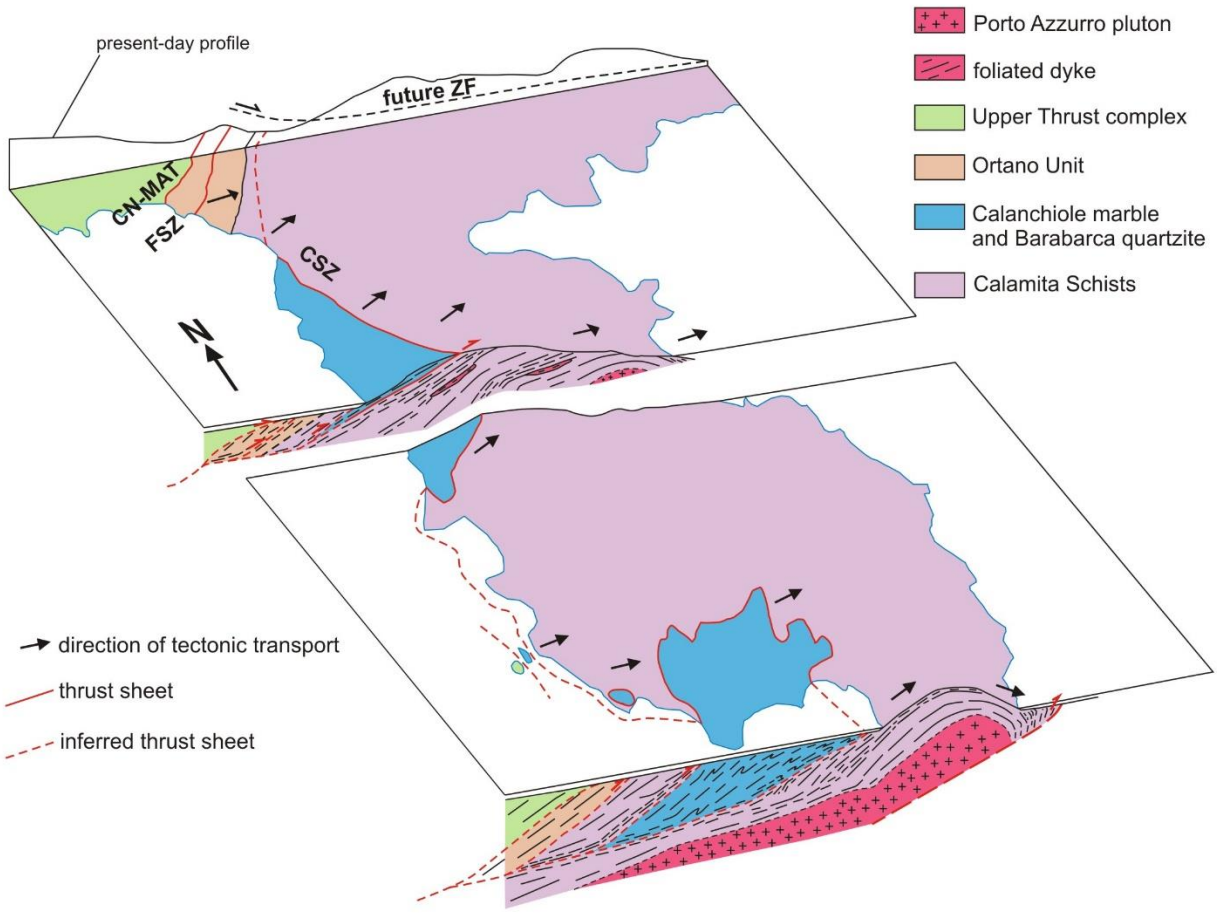

Figure 4.13 –Block diagram illustrating the reconstructed architecture of the metamorphic units (Calamita and Ortano) hosting the Porto Azzurro pluton. The Ripalte antiform in the eastern coast is interpreted as the hanging wall anticline of a thrust, inferred to be localized at the base of the pluton. See text for explanations.

Vaselli 2012; Musumeci et al. 2015), the Calamita Unit can be interpreted as bound by two major thrust zones. The upper thrust sheet corresponds to the Capo Norsi – Monte Arco Thrust at the base of the Upper Complex, which discordantly superimposes non-metamorphic rocks onto high metamorphic grade hornfels rocks belonging to the Calamita and Ortano Units (Musumeci and Vaselli, 2012) and whose activity outlasted contact metamorphism (Viola et al., 2018), although it might have been possibly active during the Early to Middle Miocene nappe stacking phase (Keller and Coward, 1996; Massa et al., 2017). The lower thrust structure is not exposed, but its occurrence can be inferred from the presence of the Ripalte Antiform (Mazzarini et al., 2011), which is characterized by long side up W-dipping limb and a short and narrow eastern subvertical limb. According to its geometry, the Ripalte antiform can be interpreted as a thrust ramp anticline (Fig. 4.13), which refolded high-strain domains and therefore was also active when ductile deformation related to thermal anomaly was already over. As shown in the cross sections in Fig. 4.13, the igneous intrusion is interpreted to underlie the whole antiform from the western to the eastern limb with intrusives and host rocks coupled on the hanging wall of the inferred thrust (Fig. 4.13). According to this reconstruction, the upper and lower thrusts represent the roof and floor

thrusts of a large scale duplex structure, where high-strain domains coincide with the smaller scale thrust sheets bounding single horses. The documented features support a model in which structures in the Calamita Unit resulted from the interaction between large-scale tectonics and a transient and localized thermal anomaly. Similar structures have been documented worldwide around plutons in several orogenic belts (Paterson et al., 1991a,b) as, for example, Archean-Proterozoic belts (Karlstrom and Williams, 1995; Collins and Sawyer, 1996; Benn et al., 1998), Paleozoic belts (Hannula et al., 1999) and Mesozoic magmatic arcs (Paterson et al., 1991b; Kalakay et al., 2001) but very few examples of deformation at shallow depth in relatively young orogenic belts have been documented so far.

The Eureka-Joshua Flat-Beer Creek pluton (Nabelek and Morgan, 2012; Morgan et al., 2013) is an example of shallow crustal level (P ~ 0.3 GPa) intrusion, whose emplacement led to host rock deformation concentrated in the inner aureole, where metasedimentary wall rocks were significantly shortened (60 - 70%). Evidence of pluton-related deformation is highlighted by the change of the attitude of the regional foliation from N-S to WNW-ESE in the southern side of the pluton, within the inner aureole. Rotation of the regional foliation was accompanied by a change in the dip angle from moderate to steep, associated with the development of a new cleavage parallel to the contact between the pluton and the aureole.

The Adamello Pluton -emplaced close to the Tonale Fault in the central Alps (Schmid et al., 1996)- is another example of contact metamorphism coeval with shearing along a regional fault zone at shallow crustal level (0.25 - 0.35 GPa; Stipp et al., 2002a; John and Blundy, 1993). Although the Adamello Pluton and the Tonale Fault are not genetically linked, the interaction of strike-slip deformation with the contact aureole produced a mylonitic belt made up of variably deformed contact metamorphic schist (Stipp et al., 2004). Within this belt, the metamorphic grade increases southward in direction of the pluton and away from the fault.

These two examples represent end-members of interaction between tectonics and magmatism. In the contact aureole of Eureka-Joshua Flat- Beer Creek pluton, structures have been interpreted as evidence of an expanding pluton with magma emplacement-related deformation leading to outward translation of wall rocks and stretching of the inner aureole (Morgan et al., 2013). On the other hand, in the contact aureole of the Adamello Pluton, the distribution of tectonic structures is independent from the geometry of the intrusive body and is steered by the regional background deformation (Stipp et al 2004). The new structural data illustrated here support the interpretation of the Calamita Unit as a contact aureole formed during ongoing regional scale E-W compressive deformation, with high-strain zones and a large antiform of foliation (see Fig. 4.13) without evident effects arising from the underlying pluton on the aureole geometry. Similar examples of

tectonically-assisted pluton emplacement within fault-bend folds in fold-and-thrust belts have been reported, for example, in the Sevier orogenic belt (Kalakay et al., 2001) and in the mainland Northern Apennines (e.g. in the Gavorrano area; Musumeci et al., 2005; Fig. 3.1). Among the many documented synkinematic plutons (e.g. Collins and Sawyer, 1996; Benn et al., 1998; Stipp et al., 2004; Nabelek and Morgan, 2012), this is, however, one of the few showing thrust-related deformation of a synkinematic buried intrusion, as revealed by deformation patterns in the contact aureole.

4.4 Summary and conclusions

The structural data presented in this chapter document an example of shallow crustal level ductile-brittle deformation heterogeneously distributed within high-strain domains. Deformation resulted from the interplay between regional-scale tectonics and a transient (< 1 Ma) and localized thermal anomaly, triggered by the emplacement of Late Miocene igneous rocks.

Deformation was characterized by the heterogeneous distribution of low- and high-strain domains, which has been documented at the map- and meso-scale. In high-strain domains, intensely foliated schist and bands of mylonites documented top-to-the-E ductile deformation coeval with contact metamorphism. Top-to-the-east cataclastic deformation invariably overprints earlier ductile fabrics and provides evidence that deformation outlasted the effects of the thermal anomaly and continued through to very low temperature conditions (T< 300 °C). Structural features recorded in the lowermost units of the Elba Island nappe stack highlight a Late Miocene regional-scale collisional tectonics that controlled upper crustal deformation and possibly the site of magma emplacement, similarly to other study cases with plutons emplaced in the core of growing antiforms (e.g. Kalakay et al., 2001).

The investigated study case represents a peculiar structural setting, i.e. ductile to brittle deformation in the upper crust at decreasing temperature conditions, offering an excellent natural laboratory where to study deformation processes occurring in crustal fault zones and related deformation mechanisms at the microscale.

Chapter 5

Microtectonics

In this chapter the microstructures of low- and high-strain domains are described with a focus on quartz microstructures and a detailed description of thin sections collected from key outcrops (see Chapter 4). The aim of this chapter is to (1) infer and discuss deformation mechanisms that were active in high-strain domains and to estimate (2) thermal conditions and (3) fluid circulation during deformation. The data presented here have been partly published on Papeschi, S., Musumeci, G., & Mazzarini, F. (2017). "Heterogeneous brittle-ductile deformation at shallow crustal levels under high thermal conditions: The case of a synkinematic contact aureole in the inner northern Apennines, southeastern Elba Island, Italy". *Tectonophysics, 717*, 547-564 and in Papeschi, S., Musumeci, G., & Mazzarini, F. (2018). Evolution of shear zones through the brittle-ductile transition: The Calamita Schists (Elba Island, Italy). *Journal of Structural Geology*, 113, 100-114. A detailed description of thin sections investigated listing sample label, locality, GPS coordinates, assemblage, lithology and fabric description is available in Appendix D.

5.1 Microstructural analysis

Method

Microstructural analysis has been carried out on 77 samples (Appendix D) collected from low- and high-strain domains in the Calamita Schists. Thin sections are oriented parallel to the lineation and perpendicular to the foliation (i.e. parallel to the XZ plane of the finite strain ellipsoid). Microstructural investigations were focused on: (1) the relationships between meso- and micro-scale structures, (2) blastesis/deformation relationships, (3) orientation of structural elements (foliations, shear bands…) and in particular (4) the detailed investigation of quartz microstructures. In the present thesis, the term 'microstructure' designates 'the arrangement of the parts of a rock at the microscale, including spatial relationships between the parts, their relative size and shape and the internal features of the parts' (Fettes and Desmons, 2007), while 'microfabric' is 'the complete spatial and geometrical configuration of all the components that make up a rock' (following Passchier and Trouw, 2005).

Most of the samples described here and in the next chapters have been collected in mesoscale structures (e.g. shear zones and folds) well exposed in natural coastal sections and creeks on the

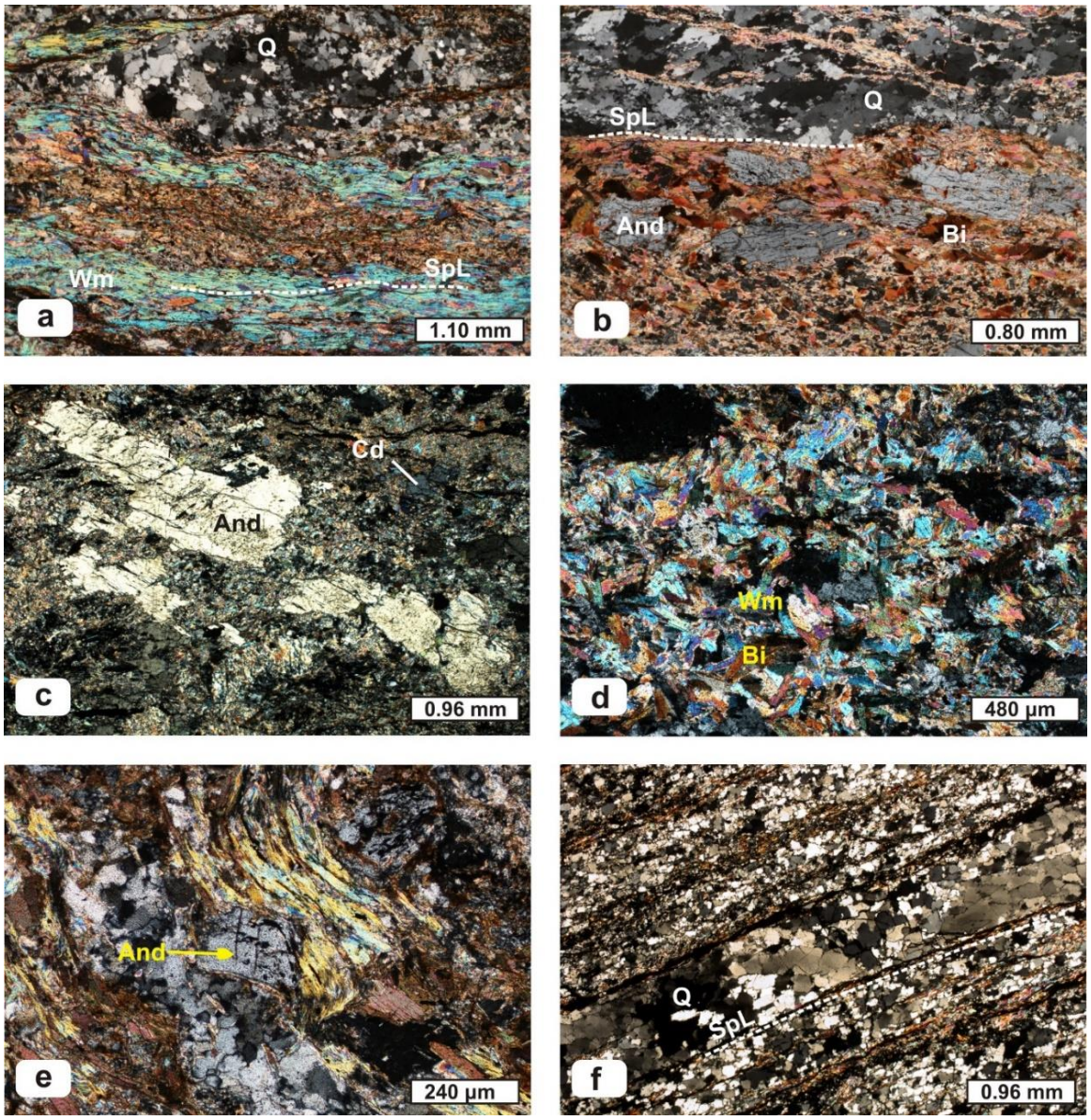

Figure 5.1 – Microphotographs of low strain domains collected at NX (mineral abbreviations in Appendix B): **(a)** Sub-parallel arrangement of mica- and quartz-rich domains defining the SpL foliation; **(b)** Layered coarse-grained quartz- and biotite-domains defining the SpL with associated subparallel andalusite grains with moderate preferred orientation; **(c)** Very coarse-grained andalusite-cordierite aggregates embedded in a fine-grained sericitic matrix with no preferred orientation; **(d)** Decussate aggregates consisting predominantly of white mica associated with biotite grains; **(e)** Euhedral synkinematic andalusite porphyroblast surrounded by white mica with internal foliation defined by elongate opaque inclusions; **(f)** Microstructure displaying subparallel quartz-domains with amoeboid shape bound by very thin biotite-white mica lepidoblastic layers. Note the larger grain size in the thicker layer at the center of the image.

Calamita Peninsula. A detailed description of microstructures of key outcrops (Capo Calvo, Praticciolo and Pontimento sections; see Chapter 4) follows the general description of the microfabric of low- and high-strain domains.

5.2 Microfabric of low-strain domains

The foliation in low-strain domains is generally defined by alternation of sub-parallel white mica and biotite domains and quartz-rich lenses, alternated to sericite-rich aggregates (Fig. 5.1a). The peak metamorphic assemblage is marked by andalusite, cordierite and K-feldspar, commonly with

poikiloblastic biotite inclusions, that occur either as porphyroblasts slightly parallel to the SpL and surrounded by white mica and biotite (Fig. 5.1b) or as large grains overgrowing the foliation. The peak metamorphic assemblage is largely overprinted by fine-grained sericite and pinite, enveloping large andalusite, K-feldspar and cordierite relics (Fig. 5.1c) and by white mica grains, showing generally a lepidoblastic microstructure, defining the SpL (Fig. 5.1a), and locally a decussate microstructure (Fig. 5.1d). White mica surrounds pre- to synkinematic andalusite and cordierite porphyroblasts with rotated internal foliation, mainly highlighted by opaque mineral grains inclusions (Fig. 5.1e). Microlithons, preserving crenulated older foliations are locally preserved in correspondence of fold hinges or preserved within coarse quartz-domains.

Quartz grains are medium to coarse grained (100 μm up to 1-2 mm) and show lobate grain boundaries (Fig. 5.1f). Dissection microstructures are common. In layered quartz domains, separated by lepidoblastic mica-domains, quartz grain size appears controlled by the spacing of mica-domains, with larger grains localized in thick and pure quartz layers (Fig. 5.1f). Intracrystalline deformation features are represented by undulose extinction patterns and subgrains associated with sparse, recrystallized new grains (10 – 100 μm grain size).

5.3 Microfabric of high-strain domains

General features

Within high-strain domains, the main foliation at the microscale is defined by alternations of lepidoblastic mica-domains and quartz layers and lenses. Quartz domains display a wide microstructural variability, ranging from equigranular coarse-grained aggregates (Fig. 5.2a) to disequigranular aggregates where large grains are enclosed within a fine- to very-fine grained recrystallized quartz matrix (Fig. 5.2b, c). The analyzed quartz domains range in thickness from some millimeters (3-4 mm) to few hundreds of microns (100 – 200 μm) with thicker domains corresponding to large boudins and fold hinges and thinner domains largely represented by layers/ribbons and/or stretched limbs.

In mica-rich domains, white mica and biotite grains show a strong preferred orientation, defining the foliation, and contain pre- to synkinematic andalusite, cordierite, K-feldspar and plagioclase porphyroblasts (Fig. 5.2d). Porphyroblasts sometimes contain internal foliations, defined by small opaque and quartz inclusions and display σ-type asymmetric shadows, largely defined by finely recrystallized sericite (e.g. pinitized cordierite in Fig. 5.2f). Additional kinematic indicators are represented by S-C and S-C' fabrics (e.g. Fig. 5.2e) and sheared mica-fish, mainly defined by white mica surrounded by quartz, all consistent with top-to-the-east sense of shear.

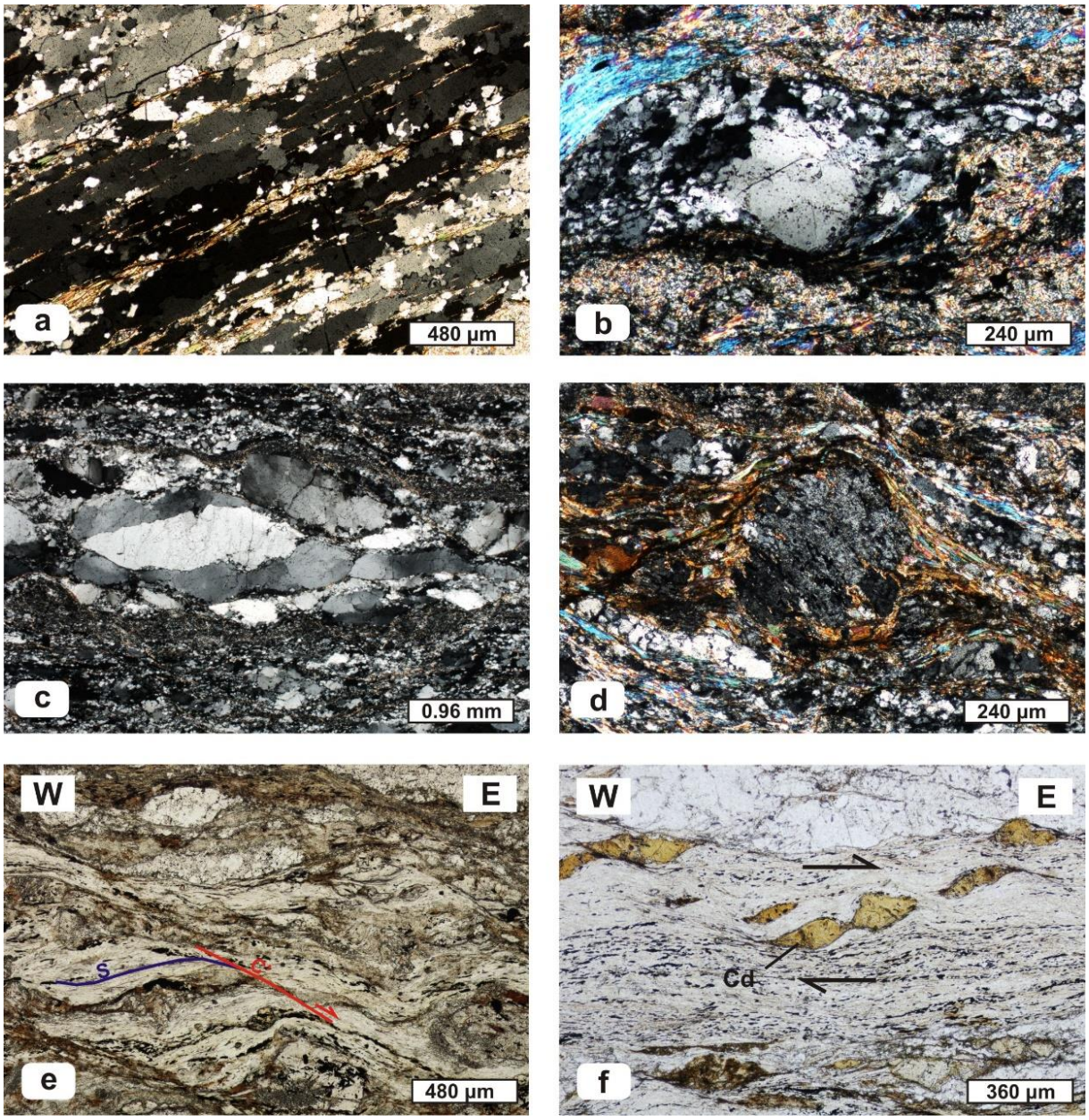

Figure 5.2 – Microstructures of high-strain domains. Mineral abbreviations are listed in Appendix B: **(a)** Coarse-grained quartz grains characterized by amoeboid quartz grains showing a well-developed lattice preferred orientation and small parallel biotite inclusions (NX); **(b)** Core-and-mantle structure defined by recrystallized quartz grains enveloping a larger old grain in a mylonitic micaschist (NX); **(c)** Large quartz grains surrounded by very fine recrystallized quartz grains and containing small quartz grains localized along grain boundaries (NX; detail in Fig. 5.9b, c); **(d)** Synkinematic cordierite porphyroblast in a biotite-cordierite-andalusite schist, with deflected internal foliations defined by opaque inclusions (NX); **(e)** S-C' fabric in a mylonitic schist with SpH (S) surfaces dragged along C' shear planes, defining top-to-the-east sense of shear (N//); **(f)** Pinitized cordierite porphyroblasts in a white mica-biotite-cordierite mylonitic schist with sigmoidal shape indicating top to east sense of shear (N//).

The transition from low- to high-strain domains is characterized by a progressive grain size reduction and increase in foliation intensity, which has been described in detail in the Pontimento section (par. 5.3.1, below). The microstructures of high-strain domains depend on the metamorphic grade and on the type of structures present at the mesoscale (anastomosing networks of shear bands to wider shear zones with mylonitic fabrics). Examples are described in detail in the Capo Calvo (par 5.3.2) and Praticciolo (par. 5.3.3) sections below.

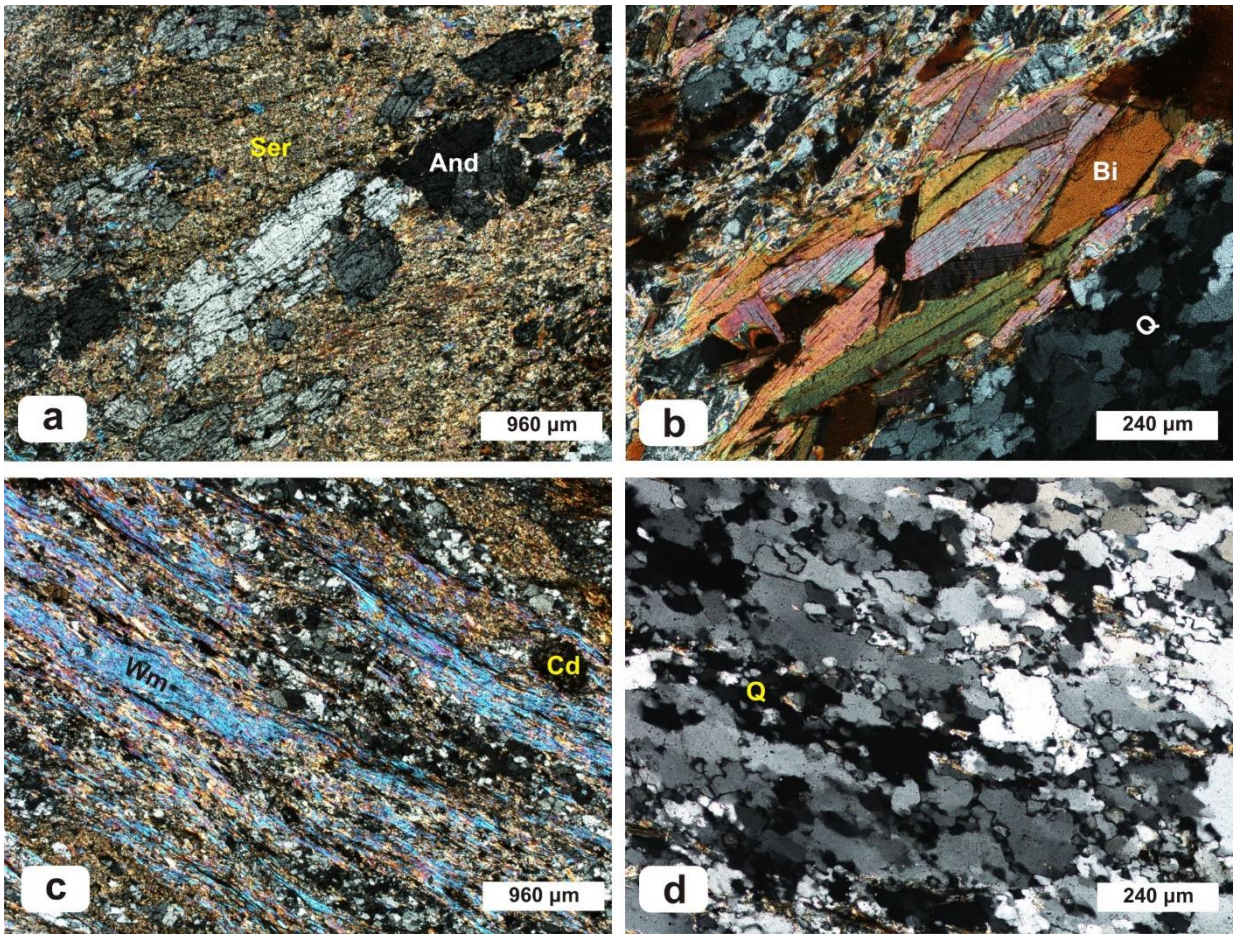

Figure 5.3 – Microstructures of the Pontimento section observed at NX: **(a-b)** Low-strain domains showing **(a)** large andalusite grains surrounded by misoriented sericite and white mica grains and **(b)** weak foliation defined by the preferred orientation of platy minerals (i.e. biotite in photo). Note also the lobate grain boundaries in quartz; **(c-d)** High-strain domains characterized by **(c)** well-developed fine-grained foliation, defined by subparallel mica-domains and quartz layers; **(d)** quartz with amoeboid grain boundaries and abundant subgrains associated with tiny, elongate, new grains. See Appendix B for mineral abbreviations.

5.3.1 Pontimento section: low- and high-strain domains

Low-strain domains at the Pontimento are characterized by alternations of quartz-layers and mica-rich domains defining the foliation. Large andalusite-cordierite grains (Fig. 5.3a) and aggregates of biotite with a weak preferred orientation (Fig. 5.3b) are surrounded by a matrix consisting of white mica grains (100 – 200 µm grain size) with decussate microstructure or fine-grained (< 10 µm) sericite aggregates (Fig. 5.3a). Quartz domains display lobate grain boundaries characterized by large grains (hundreds of µm) with dissection and pinning microstructures, locally affected by undulose extinction or formation of subgrain boundaries. Mesoscale folds (i.e. Fig. 4.9b) are defined at the microscale by alternations of folded quartz- and biotite-rich bands and, in the hinge zone, biotite and white mica grains are oriented parallel to the axial plane of the fold. Undulose extinction of quartz and kink bands in biotite are common.

High strain domains display a well-developed continuous foliation defined by alternations of recrystallized quartz layers surrounding relic cores and lepidoblastic white mica-rich domains (Fig. 5.3c). Andalusite and cordierite are largely replaced by fine-grained phyllosilicate aggregates and preserved as fractured porphyroclasts, mantled by fine-grained sericite. Quartz is characterized by aggregates of old and new quartz grains with a moderate shape preferred orientation and subgrains roughly the same size of recrystallized grains (Fig. 5.3d). Dissection microstructures are mainly concentrated in the core of thick quartz lenses.

Low- and high-strain domains are characterized by the same peak metamorphic assemblage (andalusite + cordierite + biotite + K-feldspar + plagioclase), overprinted by retrograde white mica, sericite and chlorite. However, in low-strain domains retrograde phases are largely static, whereas in high-strain domains they are synkinematic with respect to the mylonitic foliation. The different blastesis/deformation relationships reflect a strain gradient increasing from low- to high-strain domains.

5.3.2 Capo Calvo section

Microfabric

The main metamorphic foliation (Sp) is defined by alternations of millimetric quartz and thin biotite-rich layers and occur in pods and lozenges cut by an anastomosing network of C and C' shear bands and mylonitic shear zones (see Chapter 4).

In quartz domains, the Sp is outlined by the shape preferred orientation of biotite grains and quartz layers (Fig. 5.4a). The foliation contains aggregates of intergrown, coarse-grained (500 μm – 2 mm), euhedral andalusite, cordierite, K-feldspar and plagioclase porphyroclasts with poikiloblastic biotite inclusions (Fig. 5.4b), locally affected by sericitic alteration. The dominant quartz microstructure is marked by large grains (~500 μm) showing lobate grain boundaries and amoeboid shape (Fig. 5.4a), with dissection microstructures and patchy undulose extinction, and pinning microstructures, when platy biotite or mica inclusions are present.

The transition from the Sp to C shear bands is characterized by a strain gradient highlighted by mineralogical and grain size changes (Fig. 5.4c). Close to the transition between the Sp and C shear bands, coarse-grained quartz grains are mantled by recrystallized grains (10-100 μm) forming bulges and aggregates (Fig. 5.4d). Lepidoblastic biotite bands display undulose extinction and kink bands, roughly perpendicular to cleavage planes (Fig. 5.4d). Coarse-grained (up to 5 mm) K-feldspar, plagioclase, andalusite and cordierite porphyroclasts with strain caps are surrounded by sericite layers, stretched parallel to the Sp. The transition between the Sp and the C shear band (Fig. 5.4c) is marked by an abrupt decrease in grain size of both quartz and phyllosilicates from ~

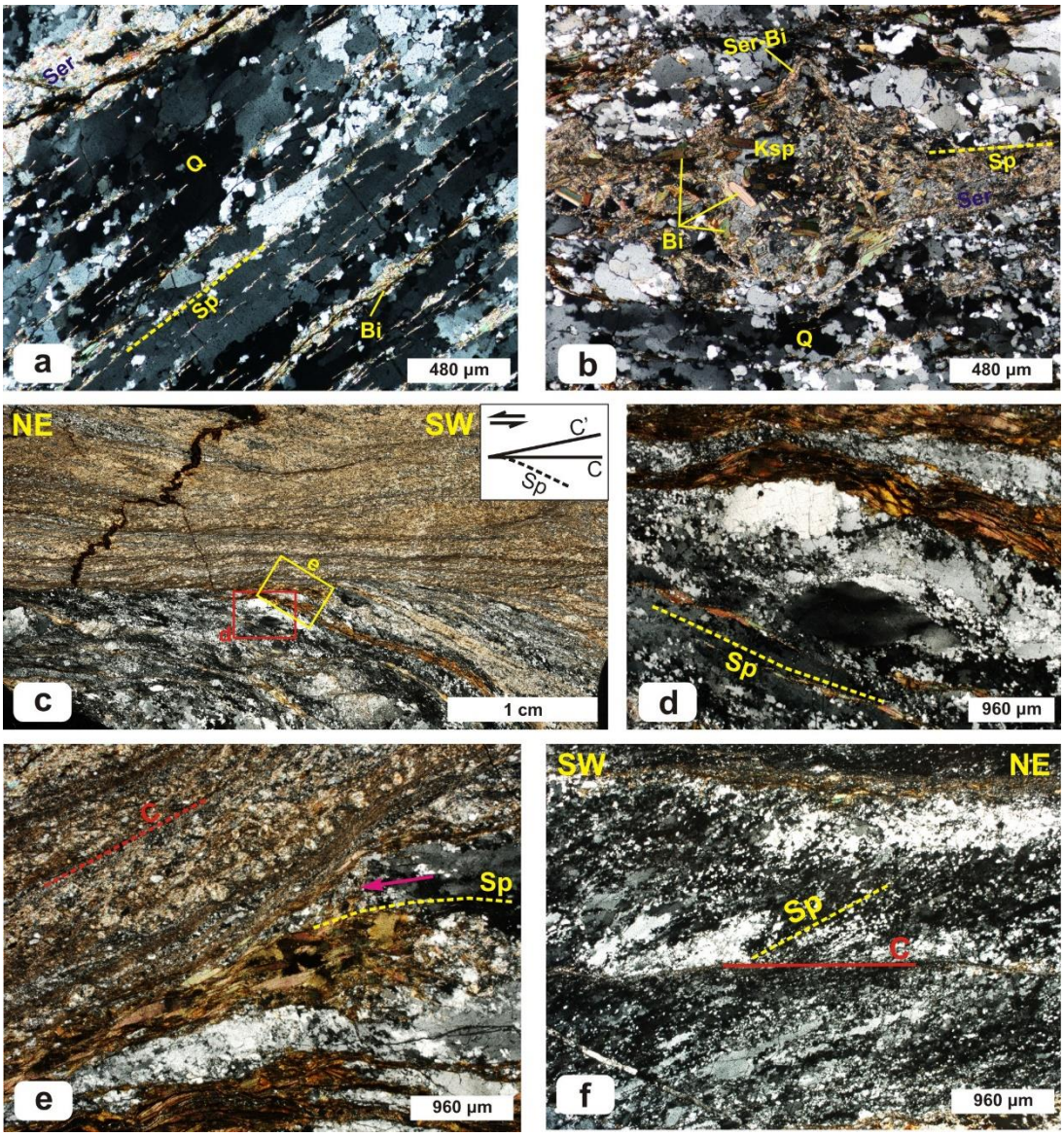

Figure 5.4 – Microstructures of Capo Calvo collected at NX: **(a)** Large amoeboid quartz grains with scattered parallel biotite inclusions defining the continuous Sp foliation (yellow dotted line); **(b)** Large K-feldspar porphyroblast with poikiloblastic biotite inclusions, surrounded by biotite, sericite and quartz; **(c)** Microphoto stitching showing the contact between the oblique Sp foliation (below) and a mylonitic C shear band (above). The squares mark the location of Fig. d and e; **(d)** Detail of the oblique Sp foliation marked by alternations of biotite layers and coarse quartz layers with core and mantle structures; **(e)** Contact between the Sp (lower right corner) and the C shear band (top left corner) marked by sharp grain size reduction and mineralogical change to fine-grained quartz, chlorite and sericite. Note the sinistral shear drag of the Sp (purple arrow); **(f)** Microstructures of a quartz-rich lozenge cross cut by C shear bands. Note the oblique Sp foliation marked by the preferred orientation of both old and new, recrystallized quartz grains. Mineral abbreviations after Appendix B.

500 µm on the Sp foliation to few tens of micrometers (Fig. 5.4e). Quartz and biotite bands are dragged in parallelism with C planes and dynamically recrystallized (Fig. 5.4e). C planes are characterized by a very fine-grained mylonitic foliation defined by thin, interlayered stretched quartz bands and very fine-grained (<10 µm) sericite-biotite-chlorite aggregates (Fig. 5.4e). Quartz consists of very tiny (<20 µm) equigranular grains with slightly sutured boundaries and undulose extinction. Ellipsoidal aggregates of sericite, 100-200 µm in size, contained in the C foliation, represent pseudomorphs over relic andalusite and cordierite grains. The mylonitic foliation is

dragged with top to the east sense of shear along micrometric C' shear bands, with a spacing of some hundreds of microns, marked by very fine-grained phyllosilicates.

In thick, quartz-rich layers, surrounded by C shear bands, the Sp foliation is defined by amoeboid aggregates of coarse old grains (100-500 μm) and finer (~50 μm) new grains (Fig. 5.4f). C shear bands are filled with mixtures of very fine grained chlorite and sericite that truncate the S foliation (Fig. 5.4f).

Table 5.1 – Calculated mean angles between foliation (Sp, Sm) and shear bands at the microscale. Errors at 1σ. Measurements obtained using the angle tool of ImageJ are listed in Appendix D. n = number of measurements.

sample • angle	n	Mean (1σ)	
SP196 • Sp/C'	43	41.9±4.6°	**Capo Calvo**
• Sp/C	30	21.1±4.6°	
• C/C'	43	15.2±1.9°	
SP196 (lozenge subset) • S/C	33	36.7±2.4°	
SP196 (contact subset) • S/C	27	21.1±3.5°	
CS30 • Sm/C'	201	38.4±3.7°	**Praticciolo**
SP65 • Sm/C'	221	34.8±3.4°	
• Sm/C' - antithetic	4	142.8±10.0°	
SP76 • Sm/C'	278	35.3±3.1°	
• Sm/C' - antithetic	14	144.0±9.2°	
SP78 • Sm/C'	120	31.2±3.1°	
• Sm/C' - antithetic	43	144.6±1.2°	

Shear bands: angular relations

The orientation of C and C' shear bands relative to the main foliation (Sp) has been measured in detail in sample SP196 (Fig. D1 in Appendix D) using the analyze particles routine of the software ImageJ (Schneider et al., 2012). Foliation orientation has been plotted in rose diagrams using OpenStereo (Grohmann and Campania, 2010), where the reference line (horizontal diameter) corresponds to the average orientation of C shear bands in the field. The S/C and C/C' angles have also been measured directly with the angle tool of ImageJ (measurements listed in Appendix D, mean reported in Tab. 5.1).

Sample SP196 displays the contact between high grade schists with Sp foliation and a mylonitic centimeter-thick C shear band (Fig. 5.5a). C shear bands define a strong maximum with 52% of the C planes measurements oriented close to the horizontal reference frame, while Sp foliation planes appear more scattered (Fig. 5.5b). A progressive decrease of the Sp/C angle within the lozenge, approaching the contact with the C shear band, has been observed (Fig. 5.5a). Therefore, three subdomains have been distinguished: (1) the wall rock, (2) the Sp/C contact, corresponding to the area within 1 centimeter from the contact with the C shear band (Fig. 5.5a) and (3) the C shear band itself, where the Sp foliation is not present. Within the wall rock subdomain, the mean Sp/C angle is 36.7 ± 2.4° (Fig. 5.5c) whereas in the Sp/C contact subdomain the mean Sp/C angle is just 21.1 ± 3.4° and Sp and C orientations locally overlap (Fig. 5.5d). Thus, a progressive decrease of the Sp/C angle approaching the C shear band subdomain is documented in sample

SP196. In the C shear band subdomain, the Sp is not present and C' shear bands, oriented at ~15° in respect to C shear bands (Fig. 5.5e) occur.

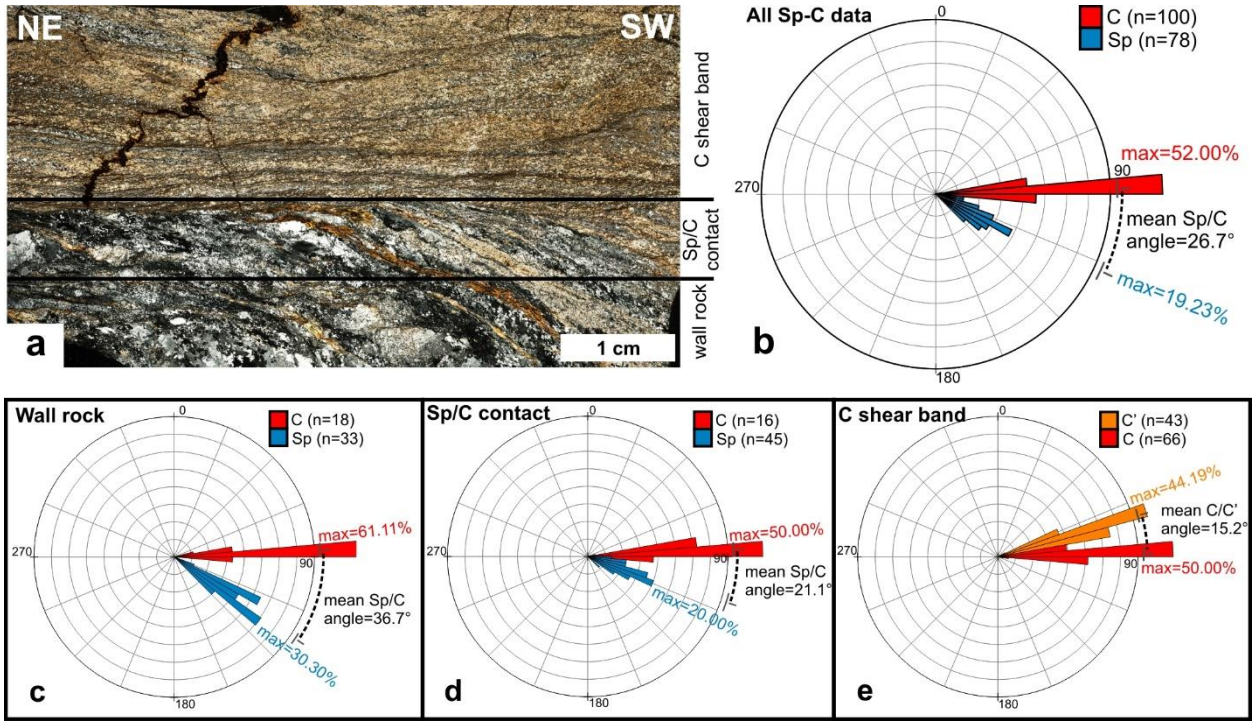

Figure 5.5 – Analysis of angles between the Sp foliation (lower half of Fig. a) and C-C' shear band planes (upper half of Fig. a) at the Capo Calvo section (sample SP196; details in Appendix D): **(a)** Photo stitching of thin section SP196 at NX. Three subdomains can be distinguished on a microstructural basis; the Sp domain (bottom), the Sp/C contact (center) and the C shear band (top); **(b-c-d-e)** Rose diagrams illustrating the distribution of the Sp foliation and C-C' shear band planes. Radius lines are every 22.5° and the histogram interval is set at 5°. Inner circle interval is set at 5% of total number of measurements. The cumulative maxima and the calculated angles are shown. See text for further details; **(b)** Sp and C orientations collected in the entire sample; **(c)** Sp and C orientations collected within the wall rock subdomain; **(d)** Sp and C orientations collected at the Sp/C contact subdomain; **(e)** C and C' orientations from the C shear band subdomain.

5.3.3 Praticciolo section

The mylonitic foliation (Sm) is defined by interlayered lepidoblastic mica domains (Fig. 5.6a) and quartz layers (Fig. 5.6b). Mica domains feature fine-grained (< 50 µm) white mica and chlorite characterized by a strong shape preferred orientation, that are locally dragged along east-verging C' shear bands (Fig. 5.6a). Micas surround andalusite and cordierite porphyroclasts (200 - 500 µm) and decussate aggregates of coarse-grained biotite, andalusite and cordierite elongated parallel to the mylonitic foliation. Fine-grained chlorite and sericite aggregates, stretched parallel to the mylonitic foliation, often form pseudomorphs over andalusite and cordierite grains (Fig. 5.6b) and biotite is commonly chloritized.

Quartz is characterized by a heterogeneous microfabric. Large, coarse-grained (>500 µm) quartz grains are characterized by linear to lobate grain boundaries with small bulges and constitute the core of large layers and boudins (Fig. 5.6b). Dissection microstructures are locally present, overprinted by patchy to undulose extinction patterns (Fig. 5.6d, e) with both fine and wide extinction bands (sensu Derez et al., 2015). Large quartz grains represent porphyroclasts

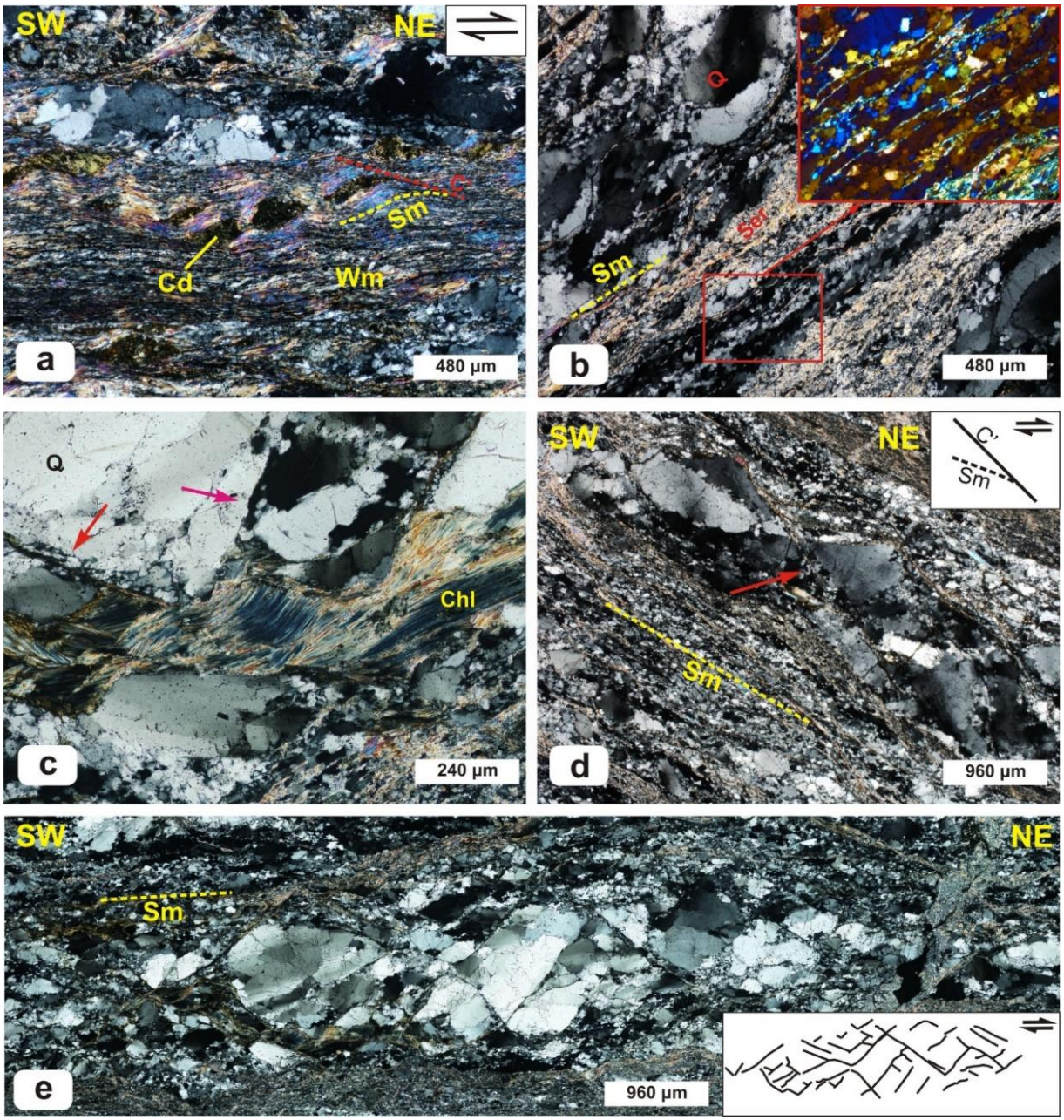

Figure 5.6 – Microphotographs of Praticciolo high-strain samples collected at NX: **(a)** Alternations of mylonitic mica-domains defining the mylonitic foliation (Sm; yellow dotted line) with sheared pinitized cordierite and quartz layers, affected by E-verging C' shear bands (red dotted line); **(b)** Mylonitic foliation (Sm) defined by sericite bands and recrystallized quartz bands. The gypsum plate insert outlines the c-axis orientation of recrystallized quartz grains; **(c)** Conjugate synthetic (red arrow) and antithetic (purple arrow) C' shear bands localized within quartz and associated with coarse chlorite grains. Note the tiny quartz grains localized in their cores; **(d)** Large quartz relics mantled by recrystallized quartz grains and cross cut by synthetic C' shear bands (red arrow); **(e)** Photo stitching of very coarse (500-900 µm) quartz porphyroclasts mantled by recrystallized quartz grains and chlorite-sericite aggregates defining the Sm. Note conjugate C' shear bands associated with fractures (sketched in the lower right corner) and the patchy undulose extinction of quartz. Mineral abbreviations after Appendix B.

embedded within finely recrystallized (~10-100 µm) new quartz grains organized in stretched bands with serrated grain boundaries and showing a moderate shape preferred orientation parallel to the mylonitic foliation and strong CPOs (Fig. 5.6b).

Networks of synthetic (Fig. 5.6d) and antithetic (Fig. 5.6e) C' shear bands pass through quartz porphyroclasts, defined by trails of very fine-grained (~10 µm) quartz and phyllosilicates (sericite

and chlorite; Fig. 5.6c). Synthetic C' shear bands show eastward sense of shear, making a moderate ~20-30° angle in respect to the mylonitic foliation (Fig. 5.6d). The antithetic set displays westward sense of shear and is predominantly developed in quartz porphyroclasts, where it is oriented roughly at orthogonal angle with synthetic C' shear bands and are associated with patterns of fractures with very limited or null (i.e. not observed) slip (Fig. 5.6e). Conjugate shear bands and fractures are commonly localized in coarse-grained quartz porphyroclasts, they are non-existent in fine-grained (recrystallized) quartz and mica-rich domains.

The angle between shear bands and the mylonitic foliation has been measured on thin section scans of 4 selected samples from the Praticciolo section (CS30, SP65, SP76 an SP78, scans available in Appendix D) using the angle tool of the software ImageJ (measurements listed in Appendix D; mean values in Tab. 5.1). The average acute angle between mylonitic foliation and synthetic C' shears (C'1) ranges between 31.2 ± 3.1° and 38.4 ± 3.7° while the average obtuse angle with the antithetic C' shears (C'2) is around 140°-145° (Tab. 5.1).

5.4 Quartz microfabric in high-strain domains

Representative samples from the above mentioned key outcrops with well-developed quartz microstructures (see Appendix C for location and Appendix D for description) were selected for quartz microstructural analysis. Based on grain size, grain shape and grain boundary microstructures, three types of quartz microstructures have been distinguished (Fig. 5.2a, b, c). They are referred to as stage 1, stage 2 and stage 3 microstructure, which implies also a time sequence of development.

Stage 1 microstructure

Stage 1 microstructure (Fig. 5.2a) is characterized by large, inequant to equant grains, ranging in size between 400 to 600 μm. Grain boundaries are moderately to strongly lobate (Fig. 5.7a, b), with local occurrence of straight boundaries (Fig. 5.7c). Large quartz grains tend to form boundaries characterized by ~90° angles of intersection (Fig. 5.7b). Tiny grains (20-100 μm) in optical continuity with larger grains (dissection microstructure) occur (Fig. 5.7d). When associated to micas, quartz is characterized by dragging, window, or pinning microstructures (Fig. 5.7e). Intracrystalline deformation features of stage 1 quartz grains range from straight to sweeping undulose extinction. Subgrain boundaries (size of subgrains: 50-100 μm; Fig. 5.7f) or bands of stage 2 and stage 3 grains (Fig. 5.2c) locally occur. A shape preferred orientation parallel to the SpH foliation is also locally present (e.g. Fig. 5.7f), as well as lattice preferred orientations, highlighted by quartz grains which appear extinct at the same polarizer orientation (Fig. 5.2a).

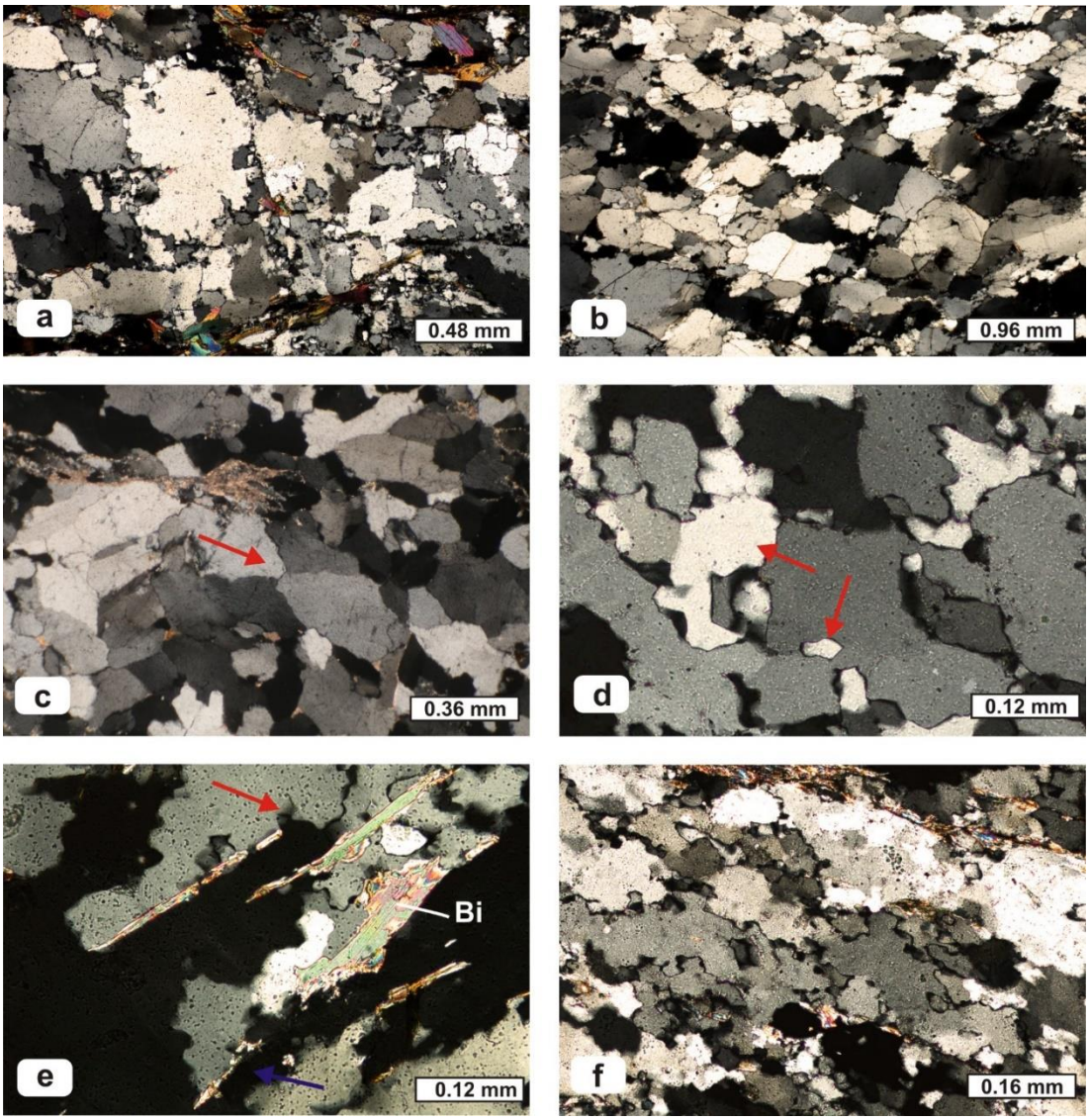

Figure 5.7 – Stage 1 microstructure images collected at NX: **(a)** Large quartz grains with lobate grain boundaries, reticular and dissection microstructures; **(b)** Large quartz grains with lobate boundaries showing undulose extinction; **(c)** Example of very-localized straight grain boundaries observed in a quartz layer within a biotite schist; **(d)** Amoeboid quartz microstructure with tiny grains in optical continuity with larger grains (dissection microstructure). Red arrows highlight two grains that appear extinct with the same polarizers orientation; **(e)** Detail of Fig. 5.2a showing the control exerted by biotite inclusions on quartz grain boundaries. A small window microstructure (red arrow) and a pinning microstructure (blue arrow) are visible; **(f)** Amoeboid quartz grains with optical subgrains.

Stage 2 microstructure

Stage 2 microstructure (Fig. 5.2b) is characterized by anhedral and fine grained (60 to 100 μm) equigranular quartz grains with serrated grain boundaries displaying weak undulose extinction. As shown in Fig. 5.8a, the transition between adjacent stage 1 and stage 2 microstructures corresponds to a sharp decrease in grain size. Stage 2 grains occur associated with subgrains (in neighboring grains) with comparable size and shape (Fig. 5.8b). Domains characterized by stage 2 grains usually show a wide grain size range from 10 to 100 μm with smaller grains (10 – 30 μm) overprinting larger grains (50 – 100 μm) and subgrains (e.g. Fig. 5.8b, c).

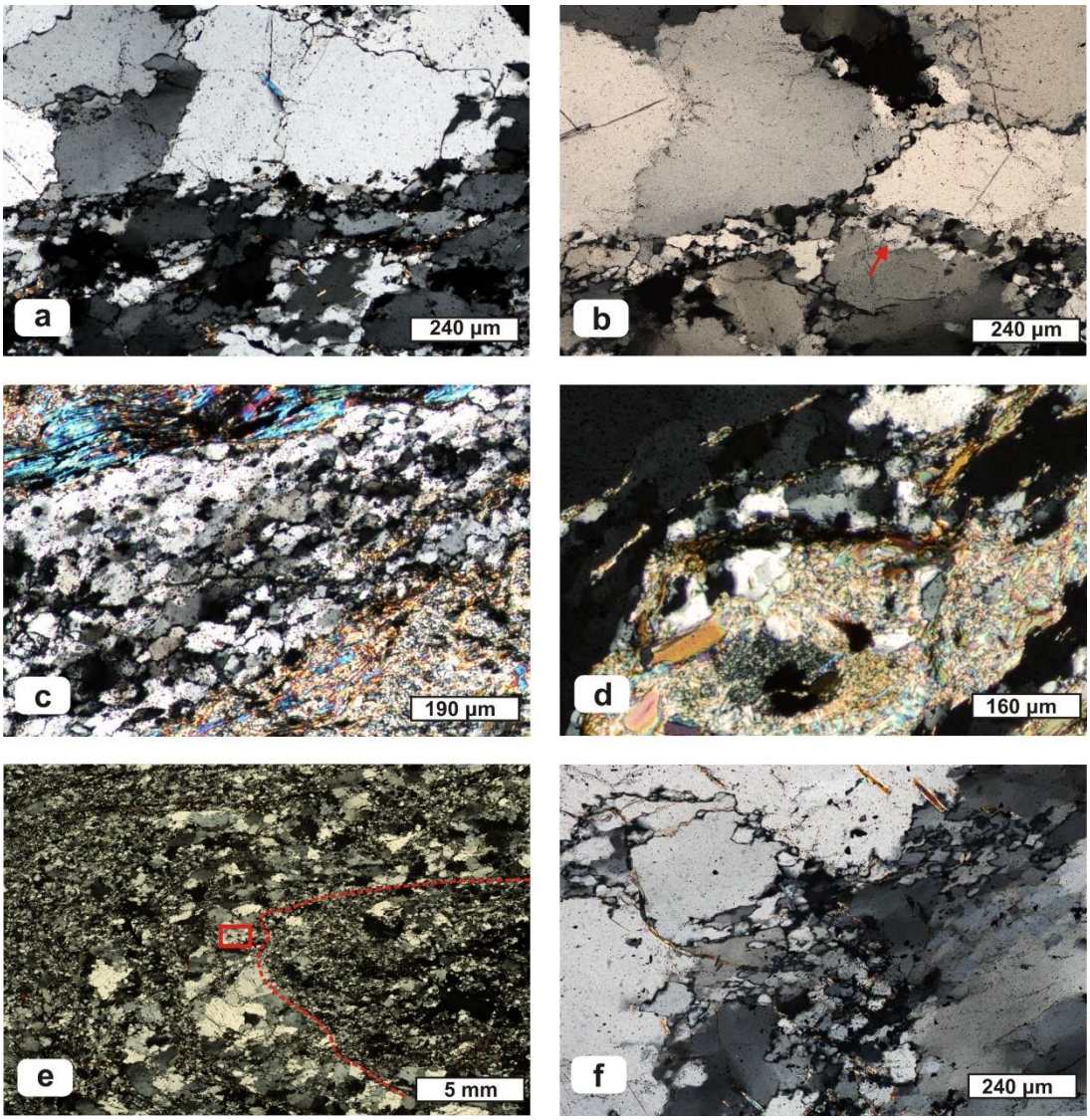

Figure 5.8 – Stage 2 microstructure images collected at NX: **(a)** Sharp decrease in grain size between stage 1 grains (above) and stage 2 grains (below). Note that relic stage 1 grains occur mixed with stage 2 grains in the lower half of the image; **(b)** Stage 2 grains localized along grain boundaries between stage 1 grains and showing serrated grain boundaries. The red arrow marks a small subgrain; **(c)** Recrystallized layer with coexisting grains and subgrains comparable in shape and size and displaying a shape preferred orientation subparallel to the SpH; **(d)** Detail of Fig. 5.2a with tiny, stage 2 grains localized on a strain cap around a sericitized andalusite porphyroclast; **(e)** Folded quartzitic layer characterized by alternating layers of coarse and fine-grained quartz and sparse, relic quartz grains surrounded by finely recrystallized quartz grains; **(f)** Detail of the hinge zone of the fold shown in Fig. 5.2e, where the preferred orientation of recrystallized stage 2 grains defines the axial plane foliation.

Domains with localized nucleation of stage 2 grains are represented by (1) grain boundaries and triple junctions of stage 1 grains (Fig. 5.8b), (2) recrystallized domains, where aggregates of grains (< 70 µm; Fig. 5.8c) mantle stage 1 grains, forming core-and-mantle structures (Fig. 5.2b), and (3) at the edge of quartz-domains, in contact with mica-domains. Strain caps around andalusite and cordierite porphyroclasts represent another site where the local nucleation of stage 2 grains occurs (Fig. 5.8d). The analysis of limbs and hinge zones of micro-folded quartz layers (Fig. 5.8e) reveals the presence of stage 2 grains with a slight shape preferred orientation which defines the axial plane foliation (Fig. 5.8f).

Stage 3 microstructure

Very fine-grained (less than 10 μm) quartz grains with anhedral shape and, generally, straight extinction (Fig. 5.9a) characterize stage 3 microstructure. Stage 3 grains occur as (1) bulges and aggregates localized on the grain boundaries of larger stage 2 and 3 grains, (2) very fine-grained recrystallized bands and mantling larger grains in mylonitic samples (e.g. Fig. 5.2c) and they define (3) conjugate and synthetic C' shear bands that cross cut relic grains (Fig. 5.9b). In particular, shear bands display stage 3 grains with a moderate shape and lattice preferred orientation defining a foliation, obliquely oriented with respect to the shear band and defining the local sense of shear (Fig. 5.9c). Stage 3 grains are also associated to cataclastic bands in brittle fault zones, where they are formed from relic stage 1 and stage 2 grains. Healed fractures and shear bands are also marked by stage 3 grains (Fig. 5.9d).

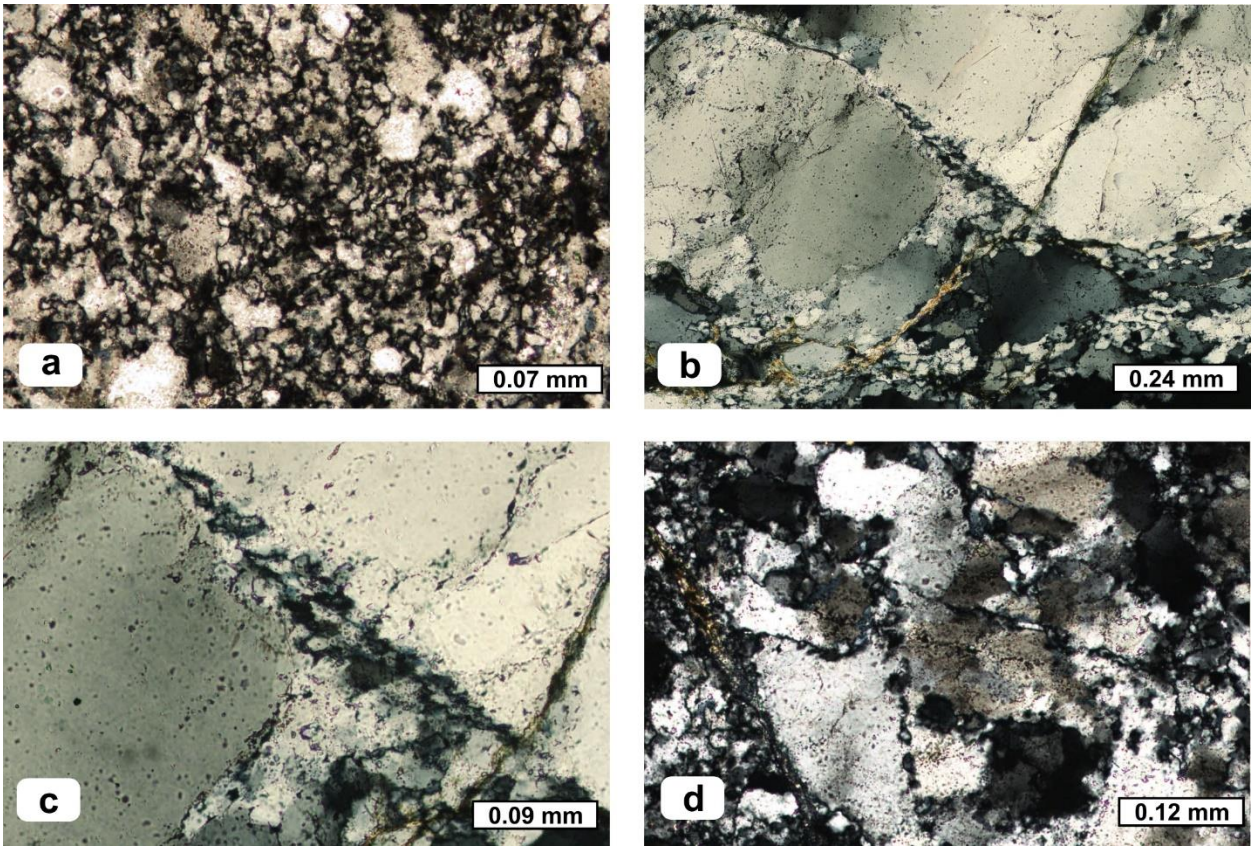

Figure 5.9 – Microphotographs of stage 3 microstructure (NX): **(a)** Widespread development of stage 3 grains close to cataclastic bands characterized by tiny serrated aggregates around larger, isolated, stage 1 and 2 grains; **(b)** Conjugate shear bands developed in coarse-grained stage 1 grains, decorated by fine-grained stage 3 grains. Note also stage 2 grains occurring on the bottom of the image; **(c)** Detail of Fig. b showing the oblique foliation defined by the shape preferred orientation of stage 3 grains, indicating local dextral sense-of-shear; **(d)** Recrystallized sets of shear fractures in the wall rock of a cataclasite marked by tiny, stage 3 grains.

5.5 Discussion

5.5.1 Deformation history of high-strain domains: insights from quartz

It is known that the deformation of quartz is controlled by a wide range of parameters, including stress, strain rate and presence of fluids (see in detail Chapter 2). A wide range of studies demonstrate the presence of three main deformation mechanisms in quartz, which, assuming constant differential stress, from high- to low-temperature conditions are: grain boundary migration (GBM), subgrain rotation (SGR) and bulging (BLG) recrystallization (Stipp et al., 2002a, b; Stipp et al., 2010).

Stage 1 microstructure (Fig. 5.7) is characterized by several microstructures indicating fast movement of grain boundaries like lobate grain boundaries, amoeboid grain shapes, dissection (Fig. 5.7d) and pinning microstructures (Fig. 5.7e), characteristics of GBM-recrystallization mechanisms. The occurrence of quartz grains clearly migrating over subparallel micas defining the foliation (Fig. 5.7e) coexisting with large areas where quartz grains share the same crystallographic orientation (Fig. 5.2a) indicate that mylonitization occurred along with GBM.

Stage 2 microstructure (Fig. 5.8) overprints relic stage 1 grains forming aggregates (Fig. 5.8b), core-and-mantle structures and recrystallized bands (Fig. 5.2b, 5.8c). The presence of subgrains in stage 1 grains with the same size and shape of stage 2 grains (Fig. 5.8b, c) is indicative of SGR-recrystallization (e.g. Stipp et al., 2002a, b). Furthermore, many features, like the localized nucleation of stage 2 grains along grain boundaries and triple junctions of stage 1 grains and the presence in type 2 aggregates of grain as fine-grained as 10 - 30 µm (e.g. Fig. 5.8b), characteristics of BLG -recrystallization, indicates that type 2 microstructure contain a range of SGR- and BLG-recrystallization microstructures. Overprinting criteria indicate that BLG- and SGR-recrystallization followed GBM-recrystallization.

Stage 3 microstructure (Fig. 5.9) reworks both stage 1 and 2 grains forming small bulges and tiny aggregates that result from dominant BLG-recrystallization, as described by Stipp et al. (2002a, b). The strict association of stage 3 grains to trails, cataclasites and shear bands, as described e.g. by van Daalen et al. (1999) and Vernooij et al. (2006a, b), indicates that other low-temperature processes may be involved, such as pressure-solution creep or low-temperature plasticity.

The comparisons of the average quartz grain size observed for the three described microstructures (stage 1, 2 and 3) is consistent with the recrystallized quartz grain size distribution compiled by

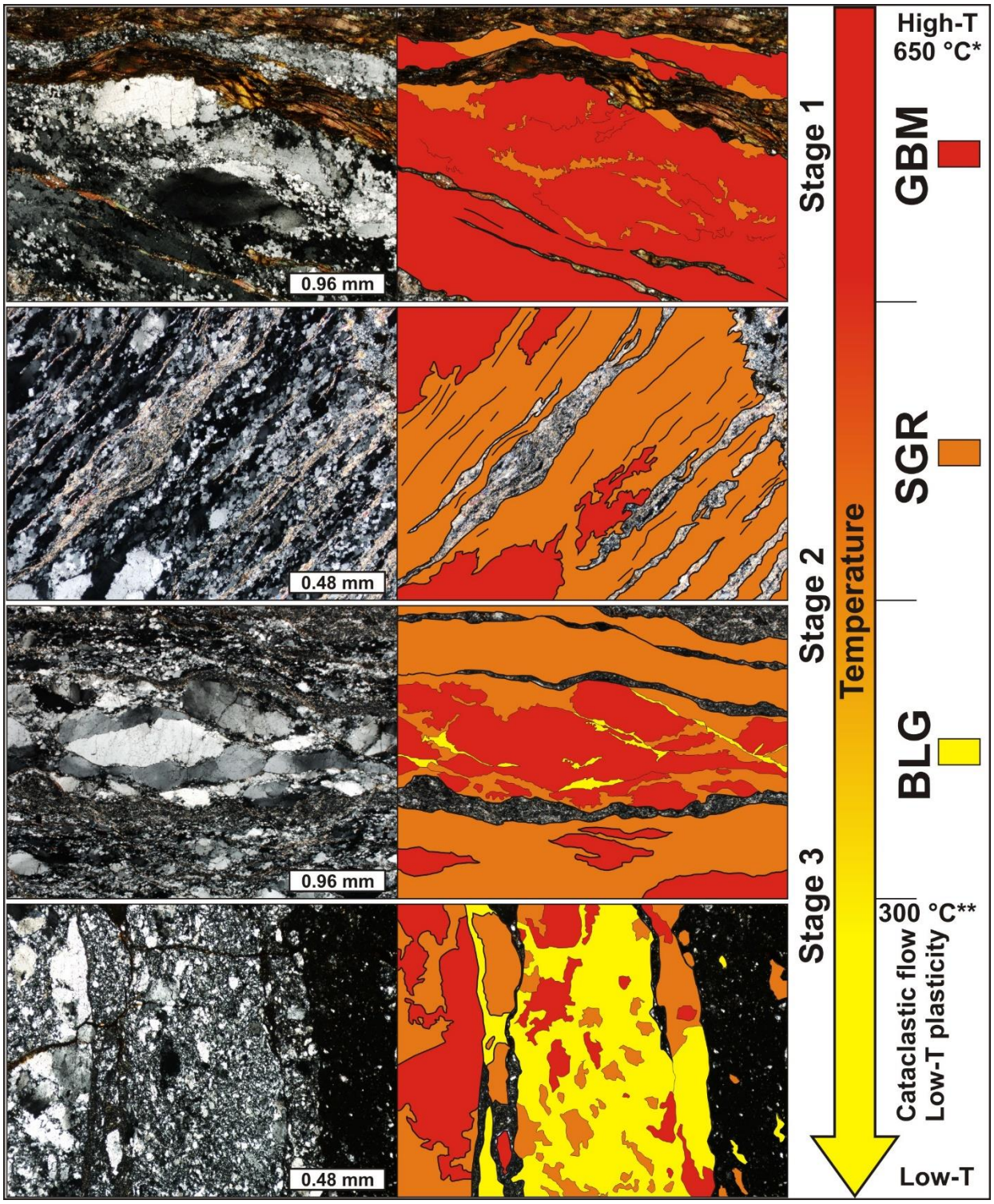

Figure 5.10 – Conceptual model explaining the development of stage 1 (Grain Boundary Migration; GBM), 2 (Subgrain Rotation; SGR and Bulging, BLG) and 3 (BLG to cataclastic flow) microstructures within high-strain domains in function of temperature decrease. *: peak temperature from Duranti et al. (1992); **: brittle-ductile transition for quartz (see text for reference).

Stipp et al. (2010) for GBM-, SGR- to BLG- and BLG-recrystallization respectively and strengthens this interpretation.

The sketch in Fig. 5.10 illustrates the relationships between GBM-, SGR- and BLG-recrystallization microstructures. GBM-dominated fabrics occur in strict association with peak metamorphic assemblages (e.g. Fig. 5.4b, d), constrained by Duranti et al. (1992) at T > 650 °C.

This temperature is consistent with the data of Stipp et al. (2002a, b), who observed GBM-recrystallization for temperatures exceeding 500 °C in the host rocks of the Adamello pluton. The GBM-fabric is overprinted by SGR- and BLG- recrystallization, the latter associated with shear fractures and brittle structures (Fig. 5.10). Bands of recrystallized grains have been observed in several studies and interpreted as evidence of low-grade deformation and alternatively interpreted as evidence for low temperature plasticity or dissolution-precipitation creep (Vernoij et al., 2006a, b; Menegon et al., 2008; Kjøll et al., 2015; Trepmann et al., 2017). Crystal-plastic deformation is, finally, overprinted by brittle structures (Fig. 5.10), indicating that deformation continued below the brittle-ductile transition for quartz (~300 °C; Voll, 1976; 250 ± 20 °C; Dunlap et al., 1997; 280 ± 30 °C; Stöckhert et al., 1999). The thermal evolution of the area suggests that changing temperature conditions was the controlling factor for the changing deformation mechanisms in the high-strain domains of the Calamita Unit. The diminishing temperature was likely associated with the vanishing thermal pulse related to the cooling Porto Azzurro Pluton, as already demonstrated by Musumeci and Vaselli (2012) and Papeschi et al. (2017, 2018). Cataclastic deformation can be viewed as the restoration of the 'normal' brittle regime at upper crustal level, once the thermal anomaly associated with the intrusion has faded away.

5.5.2 Evolution of shear zones during temperature decrease

The studied key sections in the Calamita Unit represent an example in which deformation evolves in a very short time span (~ 800 Ka; Musumeci et al., 2015; Viola et al., 2018) from metric and decametric ductile high-strain domains to narrow and localized brittle shear zones (Papeschi et al., 2017). The evolution of quartz microstructure from GBM to BLG and the retrograde metamorphism characterized by sericite + white mica + chlorite assemblages overprinting peak biotite + andalusite + cordierite bearing assemblages support an evolution from high to low temperature conditions occurred at low metamorphic pressures (< 0.18-0.20 GPa). Assuming (1) an uplift/erosion rate between 1 and 2 mm/yr and (2) an average density of 2.7 g/cm^3, a vertical exhumation of 800 - 1600 meters (0.02-0.04 GPa) can be estimated and therefore pressure can be considered nearly constant during deformation.

The reconstructed structural evolution has been summarized in Fig. 5.11. The earlier fabric, represented by a high grade metamorphic foliation, is overprinted by shear bands (Fig. 5.11a). At peak metamorphic conditions (600 - 650 °C), fast grain boundary migration, recorded within quartz porphyroclasts, allows deformation to be distributed within high strain domains. Grain boundary migration has been likely promoted by fluid circulation, which in the examined high metamorphic grade metapelites may have been generated by (1) dehydration metamorphic

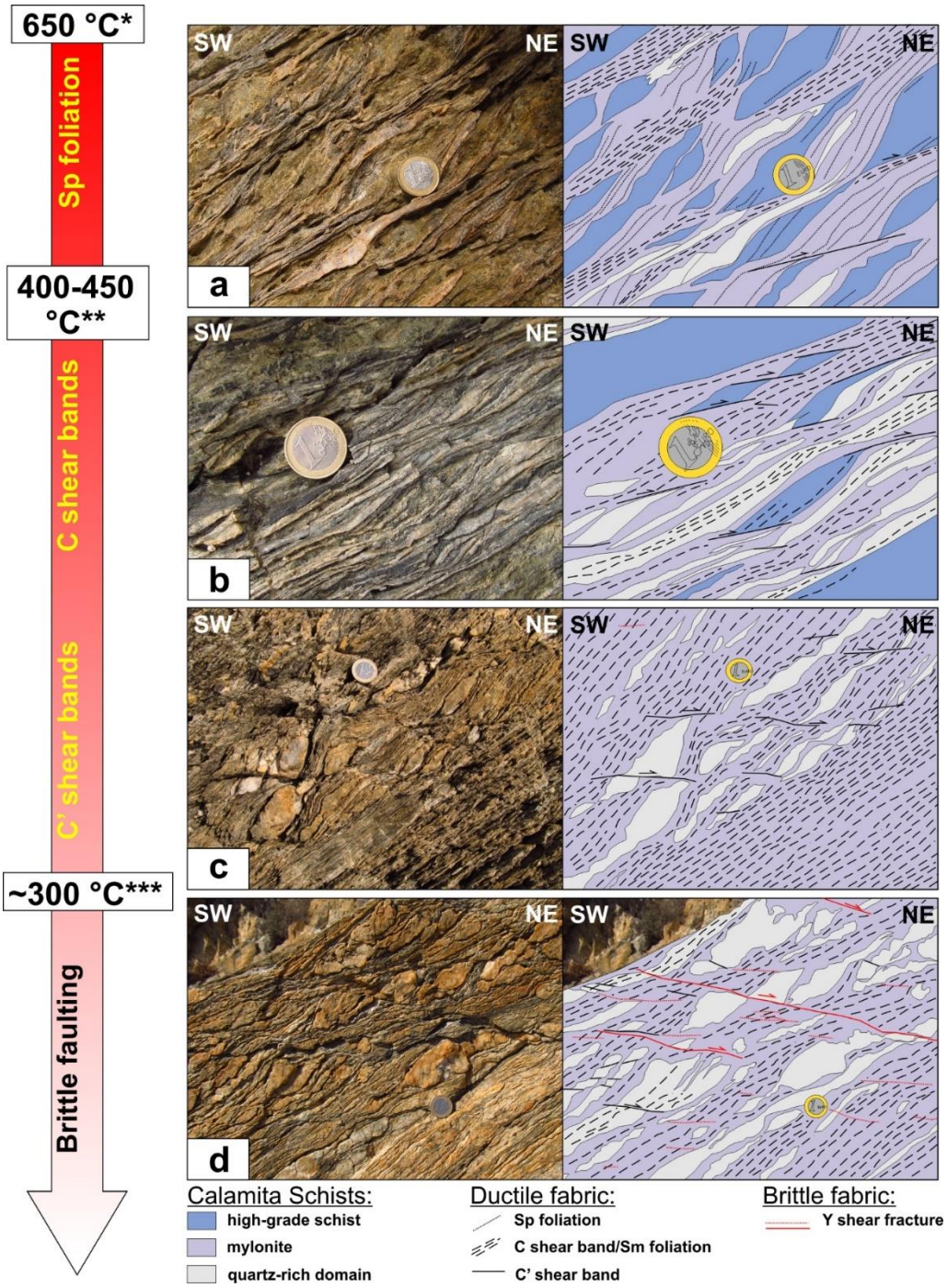

Figure 5.11 – Sketch illustrating the evolution of mylonites in high-strain domains from peak metamorphic conditions (~650 °C) to the brittle regime (< ~300 °C). Coin for scale. **(a)** Network of white mica-bearing top to the east C shear bands that surround lozenges bearing the high-grade Sp foliation. **(b)** Mylonite with a continuous Sm foliation consisting of mica-rich bands and stretched andalusite-cordierite-biotite pods, associated with top to the east C' shear bands. **(c)** White mica bearing mylonite with strong Sm foliation containing quartz-rich layers displaced by synthetic top to the east C' shear bands. **(d)** White mica bearing mylonite with quartzite boudins segmented along top to the east C' shear bands. C' shear bands have been reactivated along Y shear fractures with synthetic top to the east sense of shear. See text for discussion. (*): peak temperature for the Calamita Schists by Duranti et al., 1992. (**): temperature of chlorite bearing assemblage by Pattison and Tracy (1992). (***): brittle/ductile transition for quartz (see text for reference)

reactions (i.e. muscovite-out reaction; Pattison and Tracy, 1992) and/or by (2) hydrothermal fluids at upper crustal level emanating from igneous bodies (e.g. Dini et al., 2008). The transition from the high metamorphic grade foliation to C shear bands (Fig. 5.11a) is marked by sharp decrease in

grain size (Fig. 5.4c, e, f) and widespread growth of sericite-chlorite bearing metamorphic assemblages (Fig. 5.4c, e). These latter are retrograde over previous mineral assemblage (i.e. andalusite, cordierite, K-feldspar and plagioclase) and are indicative of low temperature conditions (T < 400-450 °C) and circulation of intragranular fluids. High-temperature quartz microstructures are overprinted by new quartz grains resulting from low- to medium- temperature bulging and subgrain rotation recrystallization (Fig. 5.4d, f; Papeschi et al. (2017). In the most deformed domains, C shear bands evolve to mylonitic shear zones (Fig. 5.11b), characterized by fine-grained quartz bands and mixed quartz-sericite layers (e.g. Fig. 5.4e). Strain hardening of the quartz-feldspathic domains (i.e. relic high grade foliation; Fig. 5.11a) favored progressive strain localization during temperature decrease in softer C shear bands, via reaction softening with fluid influx and growth of soft phyllosilicates (e.g. Stünitz and Tullis, 2001; Jessel et al., 2009; Bukovskà et al., 2016), possibly enhancing grain size sensitive creep (Kilian et al., 2011; Viegas et al., 2016). The decrease of the Sp/C angles and the near parallelism between the two foliations at the shear zone boundary (Fig. 5.5c, d) indicate passive rotation of the Sp foliation towards the orientation of C shear bands. A similar evolution has been documented by Berthé et al. (1979), who observed decrease of angles with increasing strain and the reactivation of the S foliation as C shear planes in the South Armorican Shear Zone. The data presented here suggest that shear zones (Fig. 5.11b) grew from localized shear bands (Fig. 5.11a) progressively consuming low-strain, high grade domains by (1) passive rotation and deformation of the high grade Sp foliation and (2) linkage of anastomosing shear zones, similarly to the Cap de Creus example described by Fusseis et al. (2006). This process ultimately originated wider shear zones with a well-developed mylonitic foliation (Fig. 5.11c).

The mylonitic foliation is overprinted by discontinuous C' shear bands (Fig. 5.11c). In phyllosilicate-rich domains C' shear bands are characterized by shear drag of mica and chlorite grains (Fig. 5.6a), suggesting that they formed by re-orientating pre-existing phyllosilicates parallel to the shear band itself (e.g. Jessel et al., 2009). On the other hand, in competent layers (i.e. thick and coarse-grained quartz porphyroclasts) C' shear bands form oppositely verging conjugate sets (Fig. 5.6e), marked by fine-grained phyllosilicates indicative of low temperature conditions (T < 400 °C). The incipient stage of C' shear band development is marked by trails of very fine-grained (~10 μm) new quartz grains (Fig. 5.6e), which might indicate low temperature bulging recrystallization. The development of conjugate shear bands in quartz porphyroclasts (Fig. 5.6e) might be related to the increasing effect of competency contrast at low temperature conditions (greenschist facies), driving strain hardening of 'coarse and stiff' quartz grains (e.g. Menegon et al., 2008). Patterns of fractures associated with C' shear bands indicate that brittle

mechanisms assisted shear band propagation. Thus, quartz porphyroclasts experienced a progressive embrittlement while the surrounding fine grained mylonitic foliation (recrystallized quartz grains and phyllosilicates) was still deforming in a plastic way. The growth of phyllosilicates and fine-grained quartz on C' shear bands could have been produced by low temperature recrystallization and/or precipitation from a fluid phase, as shown by Kjøll et al. (2015). These features, from a natural example, are consistent with the nucleation of C' shear bands as a consequence of rheological heterogeneities as shown by the experimental data of Holyoke III and Tullis (2006) and the numerical model of Jessel et al. (2009). Finally, microstructural data from C' shear bands, i.e. the presence of 'soft' phyllosilicates with low-friction coefficients (Niemeijer and Spiers, 2005; Zhang and He, 2016) and quartz-grains size reduction, indicate that these structures might have been easily reactivated in the brittle regime (Fig. 5.11d), as already suggested in Chapter 4.

5.6 Summary and conclusions

The microstructural observations presented in this chapter constrain the relative timing of development of structures and microstructures, providing information on the deformation mechanisms that were active in high-strain domains. Major conclusions are summarized as follows:

- Dynamic recrystallization of quartz in high-strain domains occurred by GBM at peak metamorphic conditions. GBM microstructures were progressively overprinted by new grains nucleated by SGR and BLG, in turn overprinted by brittle deformation structures. Peak metamorphic mineral assemblages, highlighted by biotite + andalusite + cordierite + K-feldspar bearing assemblages and occurring associated with quartz deformed by GBM were overprinted by synkinematic, retrograde white mica + chlorite bearing metamorphic assemblages. The evolution of quartz microstructure and mineral assemblage supports that deformation was controlled by continuous temperature decrease during deformation.
- At peak metamorphic conditions deformation was localized in relatively thick high strain domains and characterized by fast grain boundary migration. Within high strain domains deformation was relatively distributed at this stage.
- The progressive localization of strain occurred under retrograde metamorphic conditions with the development of networks of shear bands and mylonitic bands that progressively consumed the high-grade foliation. Partitioning of deformation was likely favored by strain hardening of coarse-grained domains and fluid circulation linked to retrograde metamorphic reactions that softened shear bands and assisted further localization.

5. Microtectonics

- The high-grade metamorphic fabric was overprinted by several generations of shear bands, developing a fine-grained mylonitic foliation where peak metamorphic assemblages and high grade fabrics were overprinted by low temperature recrystallization.
- At low-grade metamorphic conditions, the effect of competence contrast between the mylonitic foliation and coarse-grained, ‘stiff’ quartz domains, caused strain partitioning with the development of sets of conjugate C’ shear bands and fractures localized in quartz. Shear bands are characterized by fine-grained quartz and phyllosilicate grains that likely assisted strain localization and acted as weak phases. Shear bands may have acted as weak layers where brittle fault zones localized, in agreement with the data presented in the previous chapter.

Chapter 6

Deformation Mechanisms

This chapter focuses on the deformation mechanisms associated with the transition from mylonites to fault rocks in the Calamita Schists. The development of quartz microstructures represents the main topic of this chapter and the focus of Electron Back Scatter Diffraction (EBSD) analysis. Deformation mechanisms of phases found in association with quartz (i.e. phyllosilicates) have been inferred based on microstructural observations at the petrographic microscope and with the Scanning Electron Microscope (SEM).

6.1 Why quartz?

Quartz is one of most abundant phases in the continental crust and many authors suggested that its behavior has a deep influence upon the bulk rheology of rocks during deformation (e.g. Kohlstedt et al., 1995; Gleason and Tullis, 1995; see Chapters 1-2). Deformation of quartz has been widely explored in theoretical, experimental and natural study cases (see review in Chapter 2). Nevertheless, quartz deformation mechanisms are far to be completely understood, particularly for what concerns the complex role of fluids and the transient interaction between viscous and brittle processes in the semibrittle regime (e.g. Takeshita et al., 1998; Stöckhert et al., 1999; van Daalen et al., 1999; Vernooij et al., 2006a,b).

The Calamita Schists are characterized by quartz-rich or quartz-dominated lithologies, with K-feldspar restricted to high metamorphic grade relics, closely followed by phyllosilicates in decreasing order of abundance (e.g. biotite, white mica, chlorite). The presence of a wide range of quartz microstructures (see Chapter 5) confirms that quartz faced a transition in deformation mechanisms, likely at a varying temperature in the Calamita Schists.

The detailed mapping of quartz microstructures by precise analytical techniques such as the Electron Backscatter Diffraction (EBSD; Adams et al., 1993; Prior et al., 1999) has the potential to map the 3D orientation of the crystal lattice within a selected area. This can be used to derive strain rates, kinematics and conditions of deformation and to constrain deformation mechanisms that were active during deformation.

6. Deformation Mechanisms

6.2 EBSD analysis

6.2.1 Sample selection

The samples selected for this study come from the Praticciolo Cape section (location in Appendix C). This area has been heavily sampled since structures are well exposed and the relationships between shear zones and faults are well documented (see chapters 4-5). The main foliation there is characterized by an average dip/dip direction of 33/261 and the mean orientation of C' shear bands is 03/250, roughly parallel to sets of low-angle faults (average dip/dip direction 01/156) present at outcrop-scale. In Chapter 4, C' shear bands have been interpreted as precursory structures to brittle faults or, in other words, it has been suggested that at the brittle-ductile transition deformation localized on C' shear bands that linked up producing networks of sub-horizontal brittle structures. Therefore, the sampling strategy focused on understanding the relationships between (1) the mylonitic foliation, (2) C' shear bands and (3) brittle faults, and the deformation mechanisms involved with the development of such structures. Three samples in total were selected on a microstructural basis. Two samples (SP65 and SP78) are representative of S-C' quartz-rich mylonites and a third (SP63) has been sampled at the contact between a quartzite and a sub-horizontal cataclastic band. Sample details (GPS coordinates, assemblage, brief description…) are available in Appendix D. For the aim of this thesis, EBSD analyses have been focused on recrystallized grains rather than on relic quartz microstructures.

The main interest for this thesis is to constrain deformation mechanisms that operated at varying temperature conditions between the brittle-ductile (BDT) and the brittle-plastic transition (BPT); therefore, EBSD mapping focused on the features of recrystallized fine-grained new grains. Two areas representative of dynamically recrystallized layers parallel to the mylonitic foliation (i.e. recrystallized domains) were selected, one from sample SP65 (area SP65-01) and the other from sample SP78 (area SP78-01). Two additional areas were selected in sample SP78, representative of conjugate (area SP78-02) and synthetic C' shear bands (area SP78-03). Finally, two areas were selected within the finely recrystallized quartz at the cataclasite/wall-rock contact (SP63-01 and SP63-02). A summary of the selected areas is available in Tab. 6.1.

6.2.2 Acquisition method and processing

Electron Backscatter Diffraction (EBSD) is an automated acquisition technique that provides the full crystallographic orientation of any crystalline material within a region of interest, normally on thin sections. Grain and subgrain boundaries and twinning relationships can be detected using this technique. A general description of the method is available in Prior et al. (1999).

Table 6.1 – Summary of technical settings for selected EBSD areas. Grain size statistics available in Tab. 6.2.

Area (Map)	Brief description	Frame (pixels)	Step (µm)
SP65 - 01	Recrystallized layer (Fig. 6.2e).	684x401	1.5
SP78 - 01	Recrystallized layer (Fig. 6.6a)	414x310	2.4
SP78 - 02	Conjugate C' shear bands (Fig. 6.6b, c)	1237x927	1.1
SP78 - 03	C' shear band (Fig. 6.6d)	585x438	1.3
SP63 - 01	Recrystallized band in wall rock (Fig. 6.11b)	646x750	1
SP63 - 02	Recrystallized band in wall rock (Fig. 6.11c)	893x784	1

Thin sections for EBSD analysis were polished using an alkaloid colloidal suspension (SYTON) with a Buehler Vibromet 2 for at least 3 hours and then carbon coated to about 3.5 nm thickness. EBSD maps were acquired with a (1) JEOL 6610 LV SEM equipped with a NordLys Nano EBSD detector and a (2) JEOL 7001 FEG SEM equipped with a NordLys Max EBSD detector at the Electron Microscope Centre of Plymouth University, using the AZtec acquisition software (Oxford Instruments). The working distance was set at 20-25 mm and the accelerating voltage at 20 keV. This acquisition setting allows to map small areas (max: 1-1.5 mm^2) on a sample tilted at 70° with respect to the horizontal plane. Monoclinic sample symmetry has been used. EBSD patterns were automatically detected and indexed with the software AZTec (Oxford Instruments). Quartz was the only mineral phase indexed, using trigonal symmetry (Laue group 3/m). Analytical conditions/settings for each map are listed in Tab. 6.1.

Noise reduction, following Bestmann and Prior (2003), was performed using the HKL CHANNEL 5 software (Oxford Instruments). The critical misorientation for the definition of high angle boundaries (commonly considered as grain boundaries and shown in black in the EBSD maps) was set at 10°, allowing grain boundary completion down to 0°. Low-angle boundaries (interpreted as subgrain boundaries) were identified by setting the critical misorientation from 2 to 10° and are shown in white. Grain boundaries with 60° ± 2° of misorientation and <c> as misorientation axis were recognized as Dauphiné twin boundaries (Frondel et al., 1962) and disregarded from the grain detection procedure (shown in red in EBSD maps). The grain size was derived using the grain detection routine of Channel 5 (Tango software) that recalculates grain diameters (µm) from equivalent area circles ($µm^2$) (as in Berger and Herwegh, 2004). As a rule, grains measuring less than 3 times the step size (i.e. containing less than 4-9 pixels) were nullified. Grain diameters were hence plotted in grain diameter vs frequency and vs probability plots, to calculate the mean grain size and the mode (or geometrical mean; see stats in Tab. 6.2). The standard deviation of the mean has been calculated within 1σ (Tab. 6.2).

Table 6.2 – Grain size statistics of EBSD areas. **EX**: average, expectation; **D^2X**: variance, dispersion; **σ**: standard deviation; **σ/EX**: coefficient of variation; **Xmin**: minimum value; **Xmax**: maximum value; **N**: size of the data set.

Map	EX	D^2X	σ	σ/EX	median	mode	Xmin	Xmax	N
SP65 - 01	15.378	151.55	12.311	0.8005	11.354	6.103	4.4781	112.69	1253
SP78 - 01	20.498	347.95	18.653	0.9100	15.791	7.660	7.165	335.39	890
SP78 - 02	12.965	377.2	19.422	1.498	9.205	3.044	3.0403	612.31	1625
SP78 - 03	13.985	121.76	11.034	0.789	10.779	4.149	4.149	103.98	958
SP63 - 01	9.7316	57.661	7.593	0.7803	7.569	4.513	3.5682	117.38	3241
SP63 – 02	7.9696	25.236	5.024	0.6303	6.676	4.222	3.5682	142.84	7292

All orientation diagrams (pole figures, inverse pole figures, etc.) are plotted using Mambo (Channel 5 software). Pole figures and misorientation axis orientations in sample coordinates (MOSC) are displayed using equal angle, lower hemisphere projections oriented in the sample reference frame (X = lineation; Z = pole to the foliation). Inverse pole figures and misorientation axis orientations in crystal coordinates (MOCC) are equal area, upper hemisphere projections. Contouring was performed using a half width of 10° and cluster sizes of 0°, for inverse pole figures and MOCCs, and 10°, for pole figures and MOSCs. For pole figures, contouring is always shown for "one-point-per-grain" plots, to avoid overrepresentation of larger grains. In contoured density plots the density is shown by a scale bar as multiples of a uniform distribution (MUD). A sketch showing common <c> axis patterns in pole figures for the most common slip systems in quartz is shown in Fig. 6.1a (after Toy et al., 2008, summarizing Schmid and Casey, 1986). A scheme of the expected misorientation axis distribution clusters in crystal coordinates for the main quartz slip systems, in the case of edge dislocations, is shown in Fig. 6.1b (after Neumann, 2000 and Ceccato et al., 2017). Appendices for maps, pole figures and plots produced during processing are listed in Tab. 6.1.

6.2.3 Boundary trace analysis

Boundary trace analysis is used to infer the active slip system(s) associated with a low-angle boundary from an EBSD analysis (e.g. Prior et al., 2002). The method is based on the assumption of ideal tilt boundary associated with the activity of edge dislocations. An ideal tilt boundary must contain both the rotation axis and the 2D trace of the boundary in the EBSD map. The slip system likely associated with a tilt boundary is the one that contains the rotation axis and whose slip plane is perpendicular to the boundary (Fig. 6.1c). Twist boundaries are, by definition, perpendicular to the rotation axis (e.g. Piazolo et al., 2008; Menegon et al., 2011b; Fig. 6.1c). They are associated with at least two simultaneously operating slip systems with different Burger vectors and crystallographic modelling is required to infer the associated slip systems (see Neumann, 2000 and

Lloyd, 2004). The rotation axis can be easily identified on pole figures, where it corresponds to the direction showing little to no dispersion (e.g. Lloyd and Freeman, 1994).

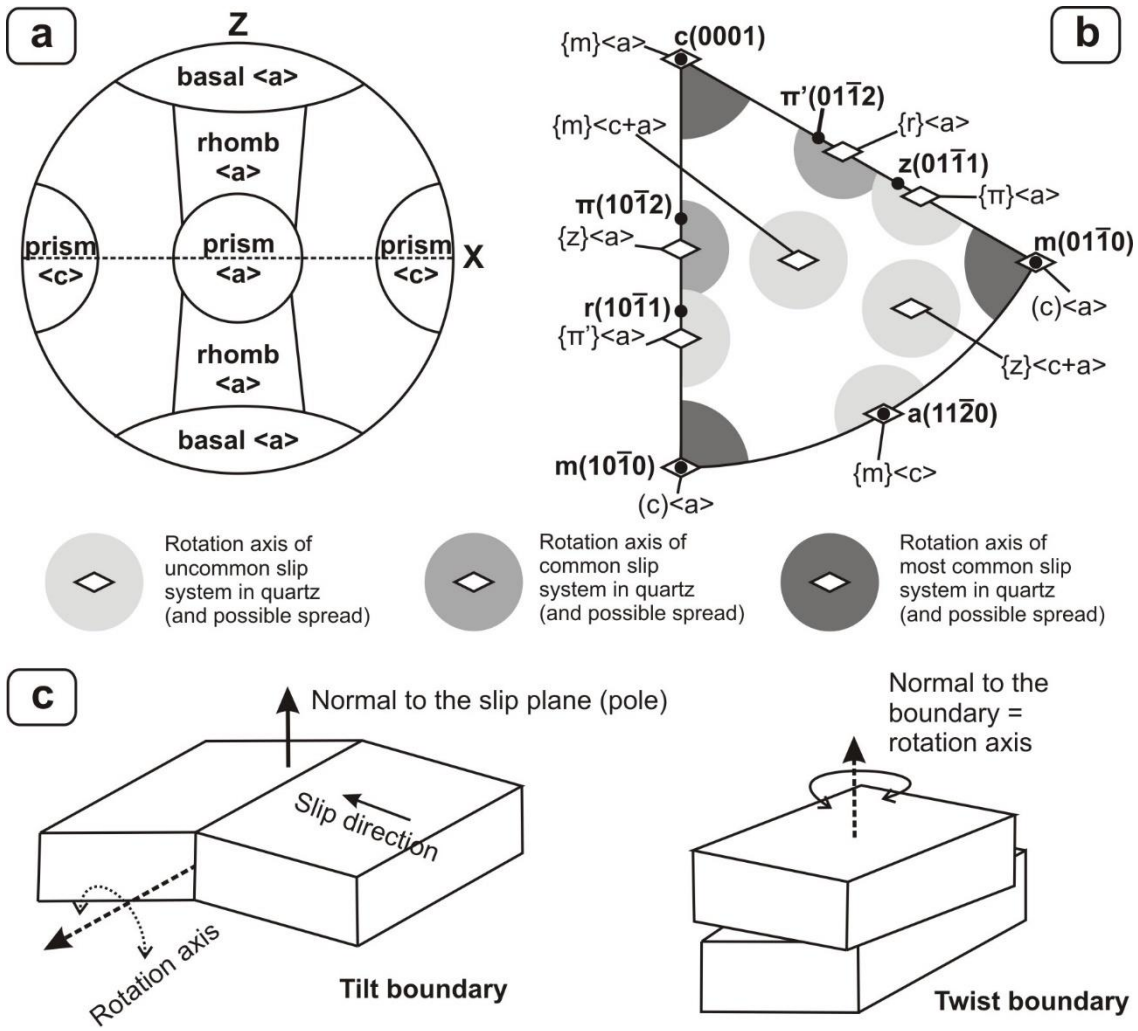

Figure 6.1 – **(a)** Schematic illustration showing the correlation between the common pole figures for quartz <c> axes and most common slip systems in quartz (after Schmid and Casey, 1986; modified after Toy et al., 2008); **(b)** Scheme illustrating the most commonly observed misorientation axes and the relative slip system (assuming edge dislocations) for quartz in misorientation axis distribution in crystal coordinates plots (modified after Neumann, 2000); **(c)** Relationships between crystal slip systems and boundary orientations assuming ideal tilt (left) and twist (right) boundaries (redrawn after Lloyd, 2004). See text for further details.

6.3 Sample SP65 microfabric

Sample SP65 is a mylonitic micaschist containing quartz + white mica + chlorite + biotite + ilmenite + andalusite + cordierite (in modal order) and accessory tourmaline, zircon, apatite and monazite. The modal proportion of quartz, estimated with the analyze particle routine of the program ImageJ (Schneider et al., 2012), is about 45-50%. The remaining proportion consists predominantly of phyllosilicates, mostly white mica. The sample displays a well-developed mylonitic foliation (dip/dip direction: 35/280), defined by subparallel quartz layers and lepidoblastic mica domains, which is cross cut and offset by several C' shear bands (Fig. 6.2a). C' shear bands show spacing between some hundreds of μm in mica domains and up to 1-1.5 cm in

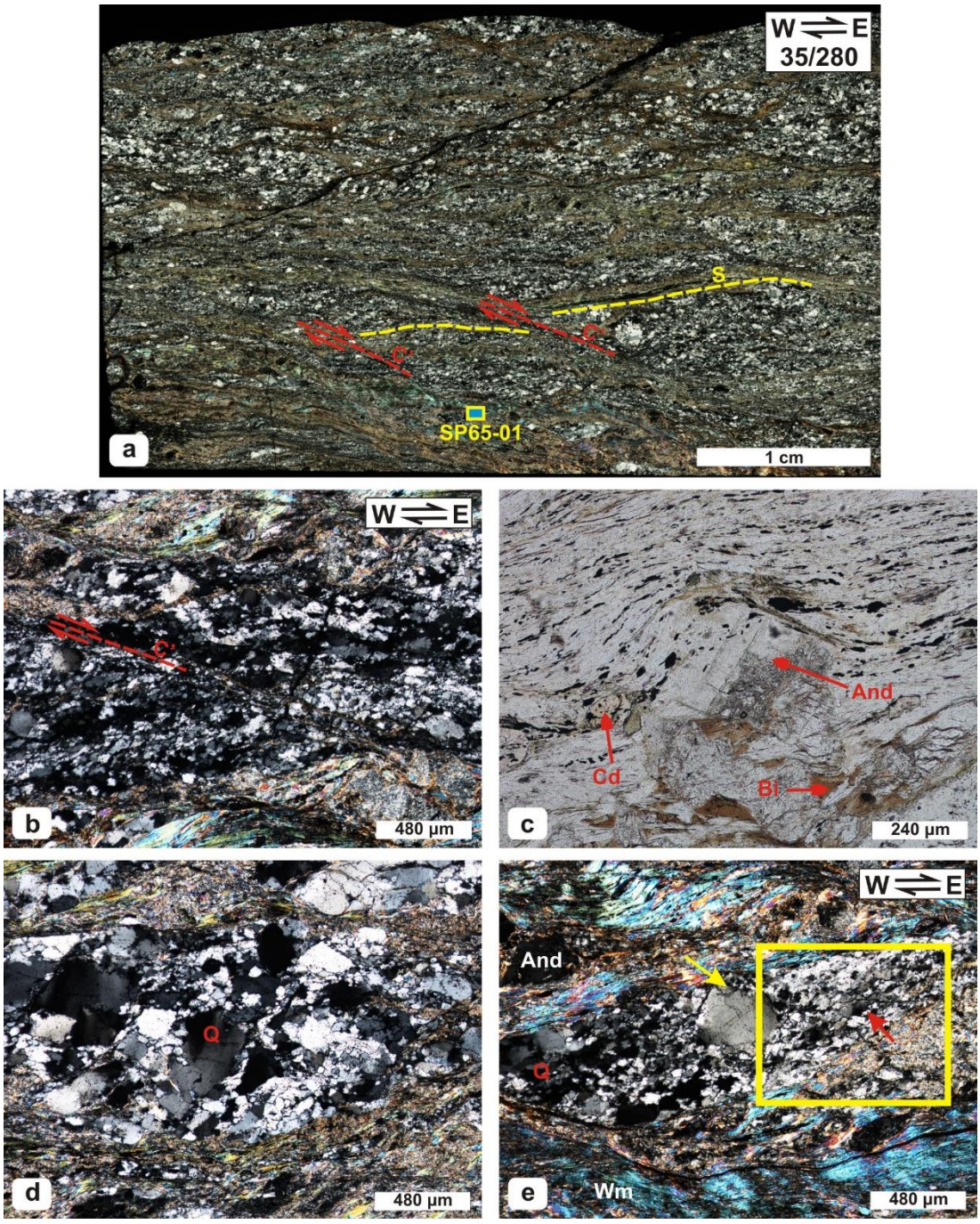

Figure 6.2 – Microstructures observed within sample SP65: **(a)** Photo stitching of the thin section showing the mylonitic foliation deflected along C' shear bands (NX). The dip/dip direction of the foliation and microscale sense of shear is provided in the box (upper-right corner). The position of the EBSD map SP65-01 is marked by a yellow-cyan box. **(b)** Detail of a C' shear band cross cutting a thick quartz layer stretched parallel to the main foliation (NX); **(c)** Euhedral andalusite porphyroclast associated with cordierite and biotite, surrounded by white mica and ilmenite with a preferred orientation parallel to the mylonitic foliation (N//); **(d)** Deformed coarse-grained quartz lens with recrystallized grains localized along grain boundaries; **(e)** Quartz layer with a central porphyroclast (yellow arrow) surrounded by elongated, recrystallized grains (red arrow) and included in fine-grained white mica defining the mylonitic foliation (NX). The yellow box highlights the position of EBSD map SP65-01.

quartz layers and contain fine-grained aggregates of white mica, chlorite and quartz (Fig. 6.2b). An average acute angle of 34.8±3.4° between C' shear bands and the foliation has been measured (see Tab. 5.1).

Mica domains (thickness: 10-200 µm) consist of very fine-grained (5-20 µm) white mica + chlorite + ilmenite surrounding larger (50-200 µm) andalusite and cordierite porphyroclasts (Fig. 6.2c). Biotite occurs as medium-grained (~50-150 µm) subhedral grains closely associated with andalusite and cordierite (Fig. 6.2c) or as biotite-rich layers, often preserved within quartz-domains. Retrograde sericite + chlorite aggregates (<5-10 µm grain size) are widespread over andalusite, cordierite and biotite, that are often reduced to sericite layers parallel to the mylonitic foliation.

Quartz layers, ranging in thickness from 50-100 µm to 1 cm, consist almost entirely of quartz with local intergranular biotite, white mica, chlorite and ilmenite grains. Large (100-500 µm) quartz grains, interpreted as porphyroclasts, are characterized by undulose extinction and amoeboid shape. These grains are variably overprinted by recrystallized grains (< 50 µm grain size) localized along grain boundaries (Fig. 6.2d) and on the edges of quartz domains. The proportion of recrystallized quartz grains is higher in thin and elongated quartz layers enveloped within mica domains (Fig. 6.2e). As shown in Fig. 6.2e, quartz layers feature elongated fine-grained grains with serrated boundaries (red arrow) that contain isolated, coarse-grained quartz relics with patchy and undulose extinction. An oblique foliation (~10-30°), marked by the preferred orientation of recrystallized quartz grains is locally present.

6.3.1 EBSD analysis (Map SP65-01)

The EBSD analysis was performed in the quartz layer shown in Fig. 6.2e, at the contact between the edge of a coarse-grained quartz porphyroclast (i.e. porphyroclast grain subset), visible on the extreme left of Fig. 6.3a, and its mantle of recrystallized grains (i.e. mantle subset). The color legend for grain boundaries shown in Fig. 6.3a is the same for all the following EBSD maps. Grains display lobate to serrated boundaries and a moderate oblique shape preferred orientation. Low-angle boundaries are discontinuously present, sometimes defining subgrains that have similar shape and grain size with respect to the neighboring mantle grains (Fig. 6.3a). Wriggly and wavy Dauphiné twin boundaries are common.

90% of the detected grains in the dataset are finer than 30 µm (Tab. 6.2). The correlated misorientation angle distribution (MAD) shows a strong maxima at low angle misorientations (< 10°) and a secondary maxima around 55-60° (Fig. 6.14a).

The porphyroclast grain presents a distorted lattice with <c> axes distributed over a ~30° girdle close to the periphery of the pole figure (Fig. 6.3b). The MOCC features strong clustering around the <c> axis for low misorientation angles (2-15°), well defined also in sample coordinates (Fig. 6.3d). <c> axes of new grains are distributed close to the periphery of the pole figure, close to X

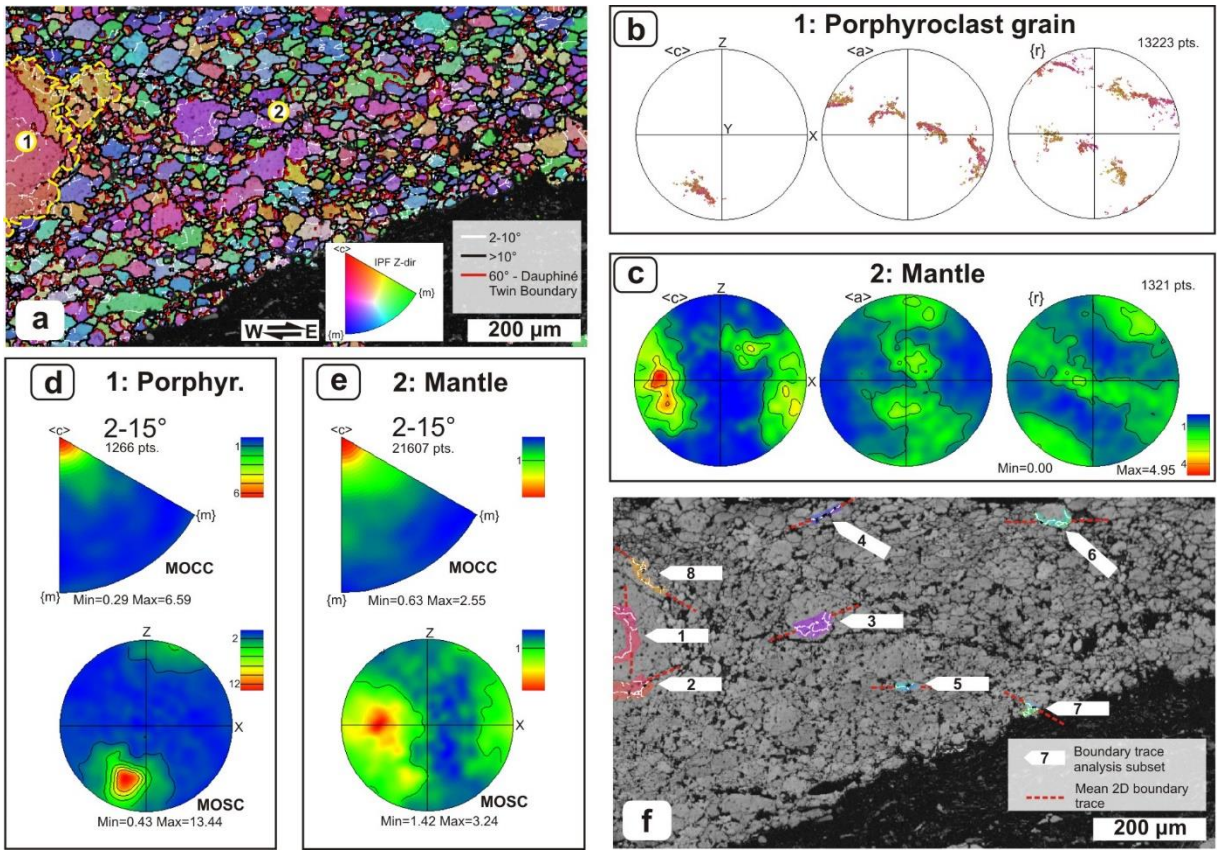

Figure 6.3 – EBSD analysis of map SP65-01: **(a)** Orientation map colored according to the inverse pole figure shown in the lower-right corner. Grain boundaries are colored according to the legend. The yellow dashed line separates 1 – porphyroclast grain subset (on the left) from 2 – mantle subset (on the right). **(b - c)** Pole figures showing the orientation of the <c> and <a> axes and the poles to the {r} plane for the **(b)** porphyroclast grain and **(c)** mantle subsets. New grains are contoured as one-point-per-grain; **(d - e)** Contoured misorientation axis distribution in crystal (above) and sample (below) coordinates for low misorientation angles (2-15°) for the porphyroclast grain **(d)** and mantle **(e)** subsets; **(f)** Band contrast map with highlighted position of the 8 subsets selected for boundary trace analysis (in Fig. 6.4).

(Fig. 6.3c). The MOCC of mantle grains for low misorientation angles (2-15°) depicts a maximum around the <c> axis with a dispersion towards the positive and negative acute rhombs (Fig. 6.3e). The MOSC is characterized by a dispersion of rotation axes spanning from the periphery of the pole figure towards Y (Fig. 6.3e).

6.3.2 Boundary trace analysis

Boundary trace analyses were performed on 8 selected areas of map SP65-01, highlighted in Fig. 6.3f, across low-angle boundaries. Many of the selected subsets contain wriggly, wavy or irregular boundaries; the mean orientation of boundaries is graphically shown in Fig. 6.3f as dashed red lines. All analyzed datasets (Fig. 6.4) are characterized by rotation axes lying between the center and the lower-left periphery of the pole figure, as in the MOSC (Fig. 6.3d, e). Identified rotation axes include <c> (datasets 1,6 and 8), {r} (datasets 3,4 and 5) and {π'} (dataset 7), all lying within the traces of their respective low-angle boundaries and, thus, fitting well with the tilt boundary model (Fig. 6.1c for reference).

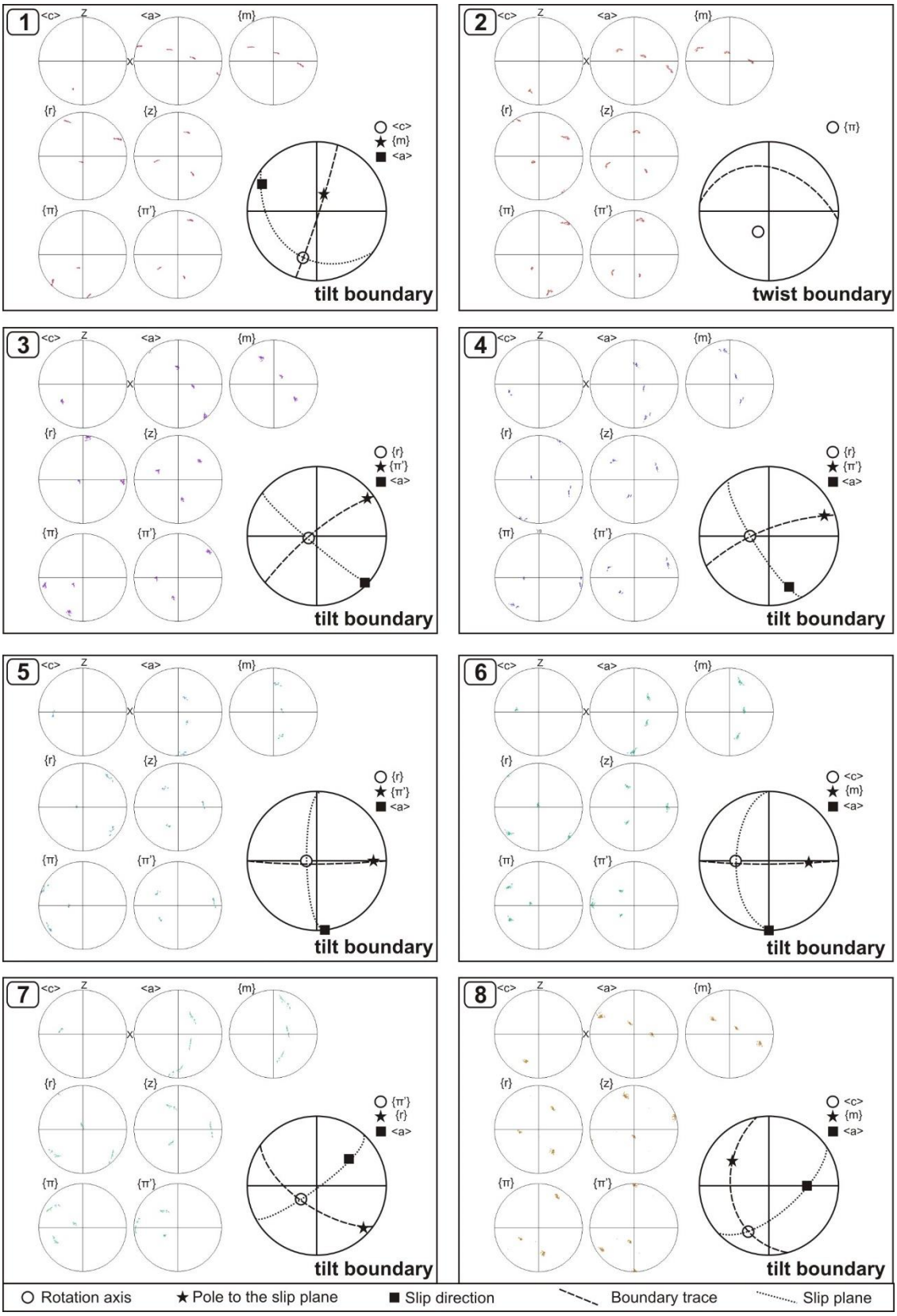

Figure 6.4 – Boundary trace analysis of 8 datasets representative of low-angle boundaries within Map SP65-01 (see Fig. 6.3). The orientation with the minimum scattering is individuated as the rotation axis (circle) and the boundary trace is sketched based on the mean orientation in Fig. 6.3. See text for further details.

Dataset 2 is characterized by a dispersion path around {π} and the boundary trace does not contain the pole which is expected in the case of a tilt boundary ({z}), therefore suggesting the presence of a twist boundary.

6.4 Sample SP78 microfabric

This sample is a mylonitic schist (Fig. 6.5a) consisting almost entirely of quartz (~80-85%, estimated with ImageJ), organized in lenses and layers (50-1000 μm thick), alternated with phyllonitic domains (50-200 μm thick), that define a strong mylonitic foliation (oriented 24/220). Phyllonitic domains contain very fine-grained (<10 μm) white mica + chlorite + quartz + biotite + ilmenite + magnetite (in modal order) and relic, fractured andalusite and cordierite porphyroclasts. Accessories are represented by small grains of tourmaline, zircon, apatite and rutile. Two nearly perpendicular sets of C' shear bands with opposite shear sense, consistent with bulk top-to-the-east sense of shear cross cut the mylonitic foliation (Fig. 6.5a): the synthetic set (C'1 in Fig. 6.5a) makes an angle of 31.2±3.1° with the foliation, while the antithetic set (C'2 in Fig. 6.5a) is oriented at 144.6±1.2° with respect to the foliation. Synthetic C' shear bands are found in both quartz and phyllonitic domains whereas conjugate shear bands are present only in thick and coarse-grained quartz lenses. The spacing of shear bands varies from 0.2-0.3 mm (mostly in phyllonitic domains) up to 1 cm, when they cross cut thick quartz lenses. Displacements range from few tens of microns up to 500 μm in some large shear bands that cross cut several layers.

Phyllonitic domains are characterized by a mixture of very fine-grained (<5-10 μm) sericite and chlorite grains mixed with very tiny quartz grains (< 5 μm), ilmenite, magnetite, and relic stacks of white mica (20 - 50 μm), partially replaced by sericite (Fig. 6.5b). Fractured to almost euhedral andalusite grains (50-200 μm) are surrounded by the finely recrystallized material (Fig. 6.5c). Other porphyroclasts (i.e. interpreted as original cordierite and K-feldspar) are reduced to elongated and fine-grained sericite layers. Larger white mica and biotite grains (20 – 100 μm) are present as small layers or single grains within quartz layers, variably overprinted by chloritization (Fig. 6.5d). Pseudomorphs composed of intergrown phyllosilicates and opaque minerals replace ellipsoidal aggregates (100-300 μm), representing original cordierite grains (Fig. 6.5d). Chlorite stacks are common within quartz, ranging in grain size from few μm up to some hundreds of μm and locally containing intergrown white mica or partially replaced biotite lamellae (Fig. 6.5e).

Coarse quartz grains, with grain size exceeding 500 μm, represent porphyroclasts that constitute the core of quartz layers and lenses (Fig. 6.5a), enclosed within layers of recrystallized quartz grains (Fig. 6.6b). These grains show neither a clear crystallographic preferred orientation nor a

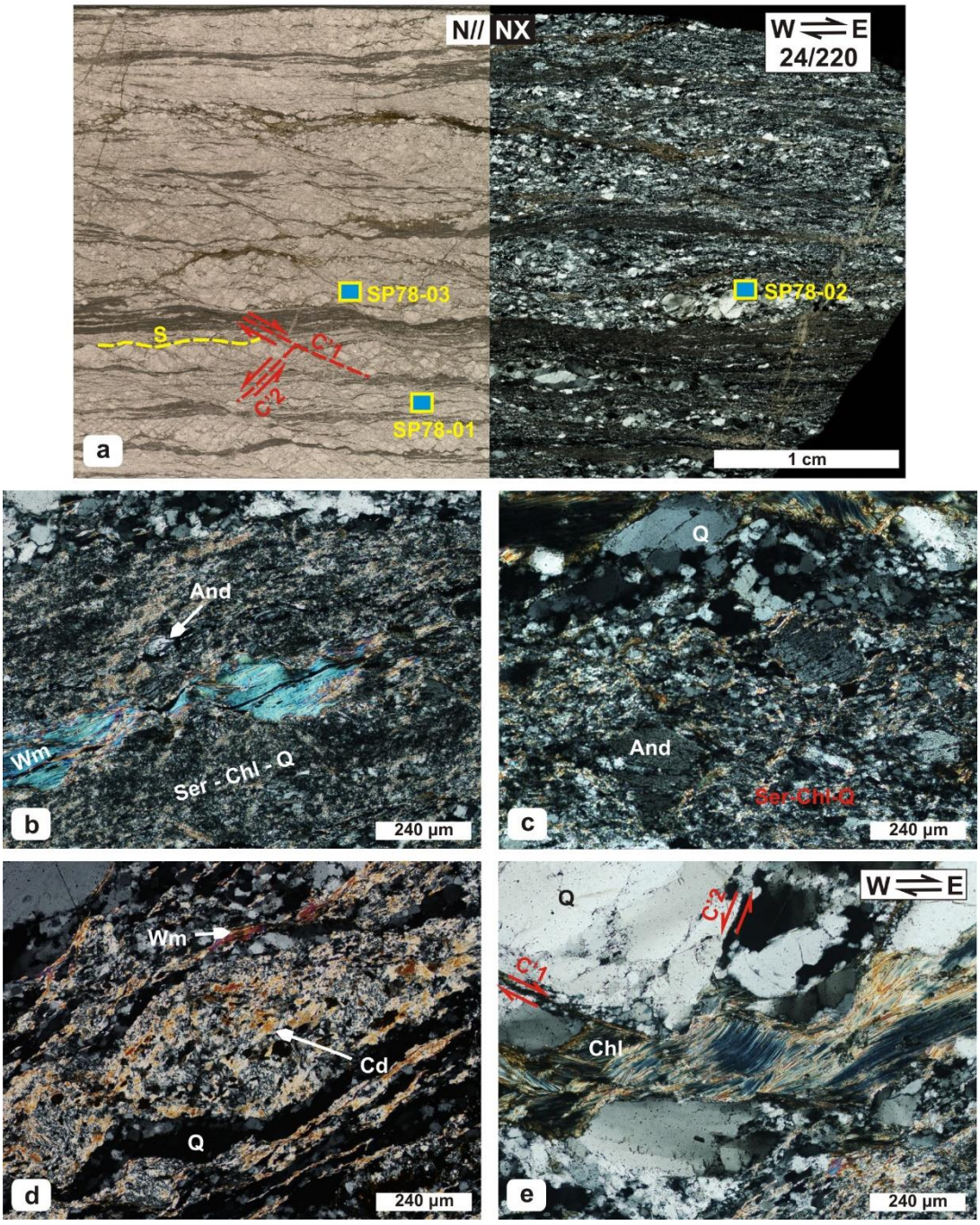

Figure 6.5 – Microstructures observed of sample SP78: **(a)** Photo stitching of the sample thin section showing the mylonitic foliation and synthetic (C'1) and antithetic (C'2) shear bands. Note the heterogeneous grain size of quartz (left: N//; right: NX). The dip/dip direction of the foliation and microscale sense of shear is provided in the box (upper-right corner). Yellow-blue boxes mark the position of EBSD maps. **(b)** Phyllonitic domains characterized by white mica flakes stretched parallel to the foliation and surrounded by a finely recrystallized quartz and phyllosilicate matrix (NX); **(c)** Detail of euhedral andalusite porphyroclasts enveloped within the phyllonitic matrix (NX); **(d)** Ellipsoidal white mica + chlorite + opaque aggregates, pseudomorph over chlorite and biotite, surrounded by dynamically recrystallized quartz layers (NX); **(e)** Large chlorite grains contained within coarse-grained quartz and associated with conjugate C' shear bands (NX).

shape-preferred orientation; they are characterized by lobate boundaries with internal patchy and undulose extinction patterns showing wide extinction bands (WEBs of Derez et al., 2015), with small recrystallized grains/bulges (< 50 µm) commonly occurring along grain boundaries.

Recrystallized quartz grains show a wide range of microstructures depending on the microstructural site of observation, each characterized by internally homogeneous microstructures.

6. Deformation Mechanisms

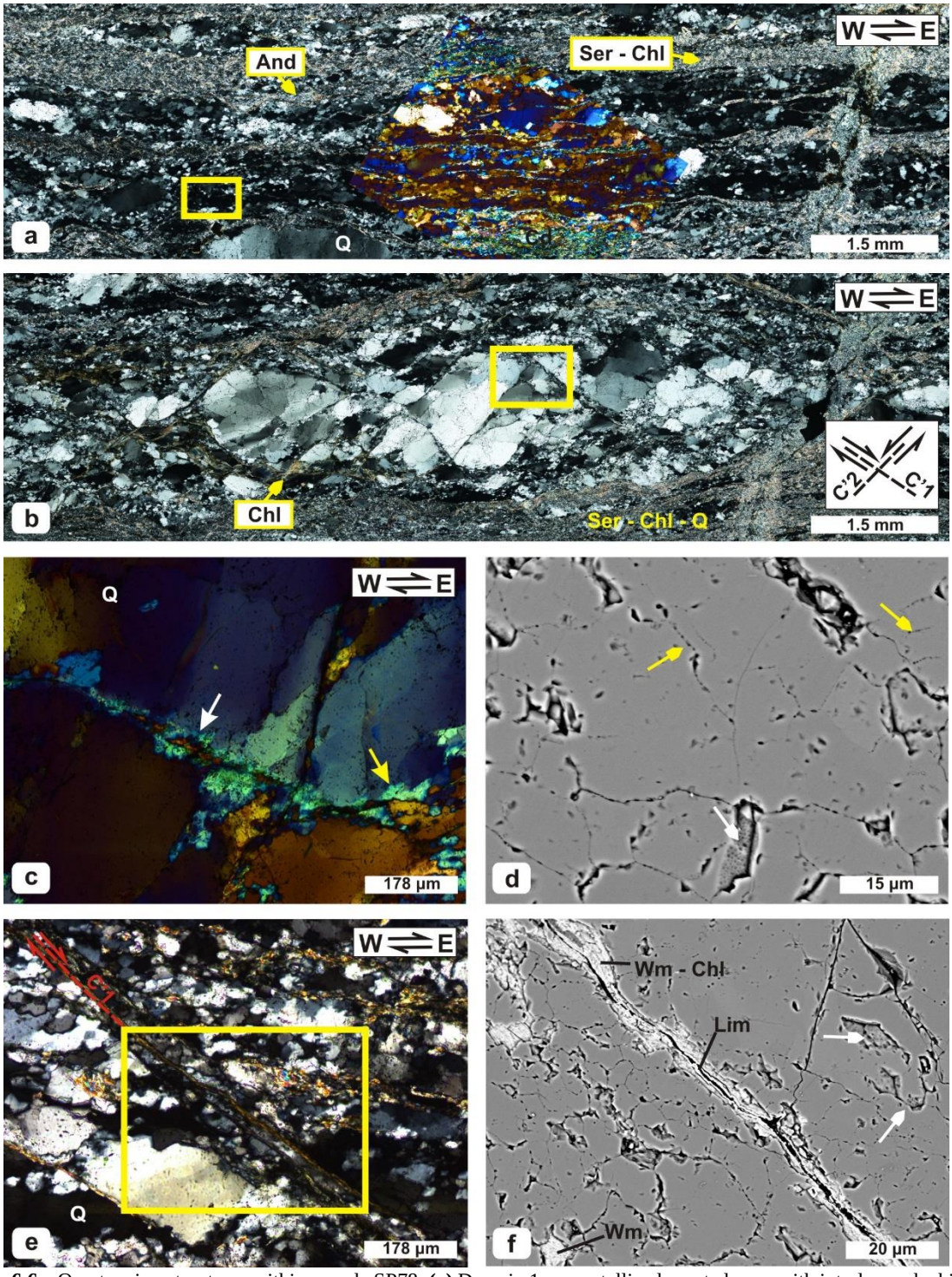

Figure 6.6 – Quartz microstructures within sample SP78: **(a)** Domain 1: recrystallized quartz layers with interlayered white mica and biotite layers. The gypsum-plate insert highlights the <c> axis orientation (NX); **(b)** Domain 2: relic quartz grains, mantled by recrystallized quartz and fractured along conjugate C' shear bands (NX); **(c)** Domain 2: detail of the tiny new grains associated with conjugate shear bands in quartz (NX; gypsum plate); **(d)** Detailed SEM-BSE image showing trails of fluid inclusions (yellow arrow) and pitted grain boundaries (white arrow); **(e)** Domain 3: synthetic C' shear bands with fine-grained quartz, chlorite and white mica grains (NX); **(f)** SEM-BSE image of a shear band showing phyllosilicate and limonite inclusions and pitted grain boundaries (white arrow) in associated quartz grains. Yellow boxes in Fig. a, b and e highlight the position of EBSD Map SP78-01, SP78-02 and SP78-03 respectively.

Three representative domains have been identified, described individually and mapped by EBSD: (1) Recrystallized quartz layers (Domain 1), (2) Conjugate C' shear bands (Domain 2) and (3)

Synthetic C' shear bands (Domain 3). In the text recrystallized grains are referred to as 'new grains' whereas the coarse-grains described above grains are interpreted as 'old grains'.

6.4.1 Domain 1 (Map SP78-01)

Recrystallized quartz layers (Domain 1) are commonly found stretched along the mylonitic foliation, enveloping sparse relic quartz grains (Fig. 6.6a). Their thickness ranges from 50 up to 500 µm and they are often interlayered with altered cordierite porphyroblasts and thin lepidoblastic biotite + white mica or fine sericite layers (visible in Fig. 6.6a). They are continuous for several centimeters, showing little evidence for necking or boudinage. C' shear bands are rare and appear mostly localized in the phyllosilicate-rich interlayers.

Quartz is dominated by old grains with lobate boundaries, amoeboid shape and undulose extinction patterns, mantled by new grains (10 - 100 µm) with serrated grain boundaries. When small inclusions of phyllosilicates are present (white mica and biotite) pinning, dragging and window microstructures are observed. Large areas of recrystallized grains appear extinct at the same polarizer orientation, indicating the presence of a CPO (see also gypsum plate insert in Fig. 6.6a).

EBSD analysis of an area representative of Domain 1 (Map SP78-01; Tab. 6.1) shows old grains (100-300 µm) surrounded by recrystallized new grains (10-50 µm; Fig. 6.7a). Old grains are characterized by amoeboid shape and relatively high aspect ratio (2-4), defining a shape preferred orientation parallel to the foliation (Fig. 6.7b). New grains display serrated grain boundaries and roughly equidimensional shape (Fig. 6.7a, b). Discontinuous low-angle boundaries with lobate shape are contained in old grains and, to a lesser extent, in some of the new grains. Dauphiné twinning is widespread in all grains and characterized by highly irregular boundaries.

The bulk c-axis distribution of both old and new grains defines a Y-max with some tails on the XY-plane, associated with <a> axes on the periphery, distributed along 6 regular maxima every 60 ° (Fig. 6.7c). The correlated distribution in the MAD shows two strong maxima, one at low angle misorientations (2-10°; Fig. 6.14b) and the other for 55-60° (Fig. 6.14b). The MOCC shows higher density towards the c-axis and, more limited, towards the acute rhombs (Fig. 6.7d). This maximum of misorientation axes in the MOSC is centered on Y, defining a strong Y-max (Fig. 6.7e).

6.4.2 Domain 2 (Map SP78-02)

Coarse-grained quartz lenses (100-1000 µm grain size; thickness: 100-200 µm up to some mm), constituted by relic grains, are present in the sample, surrounded by recrystallized quartz grains belonging to Domain 1 (Fig. 6.6b). These lenses represent 'stiff' boudins and are laterally bound

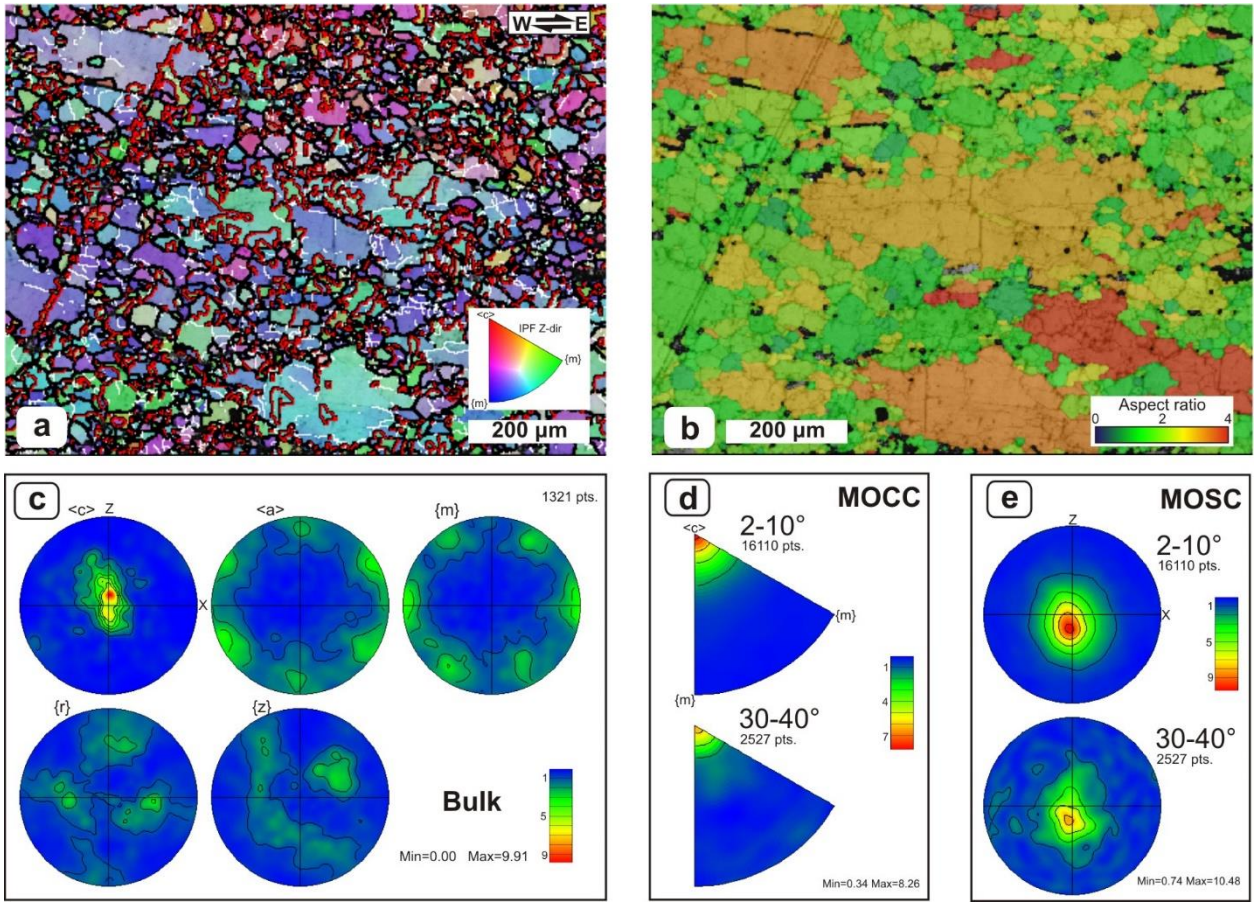

Figure 6.7 – EBSD analysis of map SP78-01: **(a)** Orientation map colored according to the inverse pole figure shown in the lower-right corner. Boundaries are colored according to Fig. 6.3a. Note that the Dauphiné twins aligned on the scratch on the left of the map are an artifact related to polishing; **(b)** Grain shape map showing the aspect ratio of the best-fit ellipse of grains, colored according to the legend in the lower-right corner. Note the strongly elongated old grains (in reds); **(c)** Contoured pole figures (one-point-per-grain) showing the poles to <c> and <a> axes and {m}, {r} and {z} planes for the complete dataset; **(d-e)** Contoured misorientation axis distribution in crystal **(d)** and sample **(e)** coordinates for 2-10° (above) and 30-40° (below) of misorientation angle for the complete dataset.

by swells where the surrounding mylonitic matrix is evidently necked (Fig. 6.6b). Old grains show extensive undulose extinction and are fragmented by conjugate sets of C'1 and C'2 shear bands associated with irregular patterns of fractures, resulting in an angular appearance of old grains. Fig. 6.6b shows clearly how shear bands are localized in old grains and do not continue in the surrounding mylonite. Domain 2 grains (shear band grains) are localized as tiny fine-grained trails (<10 µm) along conjugate C' shear bands and are shown in Fig. 6.6c with the gypsum plate inserted. Host grains are characterized by 'single-grain' orientations with angular fragments, bound by fractures, slightly misoriented with respect to the host. The contact between host grains and shear bands is marked by slightly misoriented areas (light blue in Fig. 6.6c) associated with new grains (in red) with different orientation with respect to the host and marked CPO and shape-preferred orientation (Fig. 6.6c). Fluid inclusions occur in quartz grains close to the shear band, enclosing new grains or cracks (yellow arrows in Fig. 6.6d). Pitted grain boundaries, indicative of fluid-present conditions during recrystallization (e.g. Mancktelow et al., 1998; Kjøll et al., 2015)

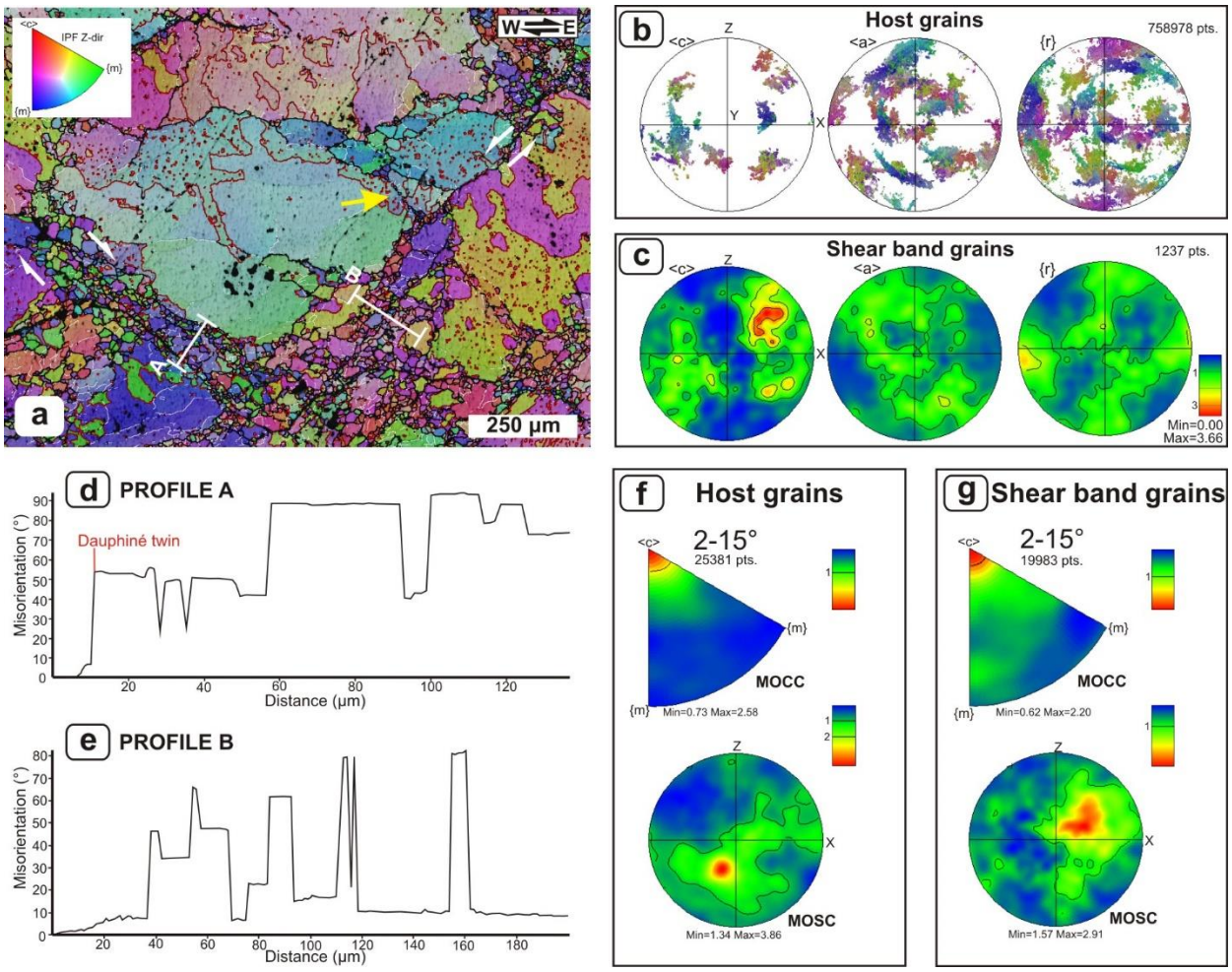

Figure 6.8 – EBSD analysis of map SP78-02: **(a)** Orientation map colored according to the inverse pole figure shown in the upper-left corner and indicated position of misorientation profiles of Fig. **(d)** and **(e).** The yellow arrow marks a small trail of recrystallized grains. White arrows mark the shear sense of conjugate shear bands. Color-coding for boundaries according to Fig. 6.3a; **(b)** Pole figures showing the poles to <c>, <a> and {r} for the host grains; **(c)** Contoured pole figures (one- point-per-grain) showing the poles to <c>, <a>, and {r} for shear band grains; (d-e) Misorientation profiles for **(d)** profile A and **(e)** profile B (location in Fig. 6.8a) with misorientation (in respect to the first point) plotted against distance (µm); **(f-g)** Contoured misorientation axis distribution in crystal (above) and sample (below) coordinates for 2-15° of misorientation angle for the **(f)** host grains and **(g)** shear band grains subsets.

are widespread (white arrows in Fig. 6.6c). Small chlorite and white mica inclusions are also locally present.

A representative area of recrystallized Domain 2 grains, located at the intersection of two conjugate C' shear bands in the host relic grains shown in Fig. 6.6b, was analyzed via EBSD (Map SP78-01; Tab. 6.1). The EBSD map shows large (>500 µm) relic grains hosting conjugate shear bands (150 – 200 µm thick) with finely recrystallized shear band grains. The MAD reveals two high values of relative frequency for the correlated distribution, one for low misorientation angles (2-15°) and the other corresponding to 55-60° of misorientation (Fig. 6.14c). Host grains display wavy grain boundaries, locally associated with tiny recrystallized grains (5-20 µm), and irregular Dauphiné twin boundaries (Fig. 6.8a). Host grains display 'single crystal' orientations, with <c> axis

randomly clustered and <a> axes and rhombs drawing small (20-40°) rotations, highlighting the internal distortion of the crystal lattice (Fig. 6.8b).

The majority of recrystallized grains is in association with the two conjugate shear bands intersecting at about 90-100° below the center of the map (Fig. 6.8a), developed at the contact to host grains with different orientation. Secondary areas of nucleation, where trails of new grains are present, correspond to small shear bands elongated parallel to the major ones, starting within host grains (yellow arrow in Fig. 6.8a). New grains range in size between 5 and 50 µm, forming heterogeneous aggregates along shear bands and enveloping larger grains (up to 100 µm) with similar orientation with respect to the neighboring host grains (Fig. 6.8a). Their crystallographic orientation mimics that of the host grains and displays a strong <c> axis maximum developed in the upper-right quadrangle of the pole figure (Fig. 6.8c). Misorientation profiles show on average very low differences in misorientations angle with respect to host grains (less than 20 - 30°; Fig. 6.8d, e) with just some small grains (<15 µm) showing sudden jumps in misorientation up to 30 - 70° with respect to the host (Fig. 6.8e). The misorientation angle distribution in both crystal and sample coordinates appear similar for host and new grains. The MOCC shows moderate maxima in correspondence of the <c> axis which spreads more for the new grains (Fig. 6.8g). MOSCs for host and new grains appear similar, showing misorientation axis weakly clustered close to Y, with a weak maxima in the lower left quadrangle for old grains (Fig. 6.8f) and in the upper right quadrangle for new grains, in the same position of the pole figure maximum (Fig. 6.8g).

Relationships between Domain 2 grains and host grains

The orientation of shear bands was compared with the orientation of the major lattice planes within 4 selected host grains, numbered from 1 to 4 in Fig. 6.9a, adjacent to the shear bands. The orientation of host grains was also compared with the orientation of new grains associated with dextral and sinistral shear bands (subsets highlighted in Fig. 6.9d). The dextral shear band separates the adjacent grains 1, 2 and 3, whereas the sinistral is found between grain 3 and 4. It should be pointed out that two grains with identical crystallographic orientation are found on the opposite sides of the sinistral shear band and interpreted to be originally part of a single grain (grain 4; Fig. 6.9a).

Host grains display c-axes oriented halfway between the periphery and the center of the pole figure (Fig. 6.9b). There is very little evidence of corresponding lattice orientation between shear bands and host grains' crystallographic planes. The orientation weakly corresponds only between the sinistral shear band and the positive and negative rhomb planes of the {r}– and {z}- Dauphiné

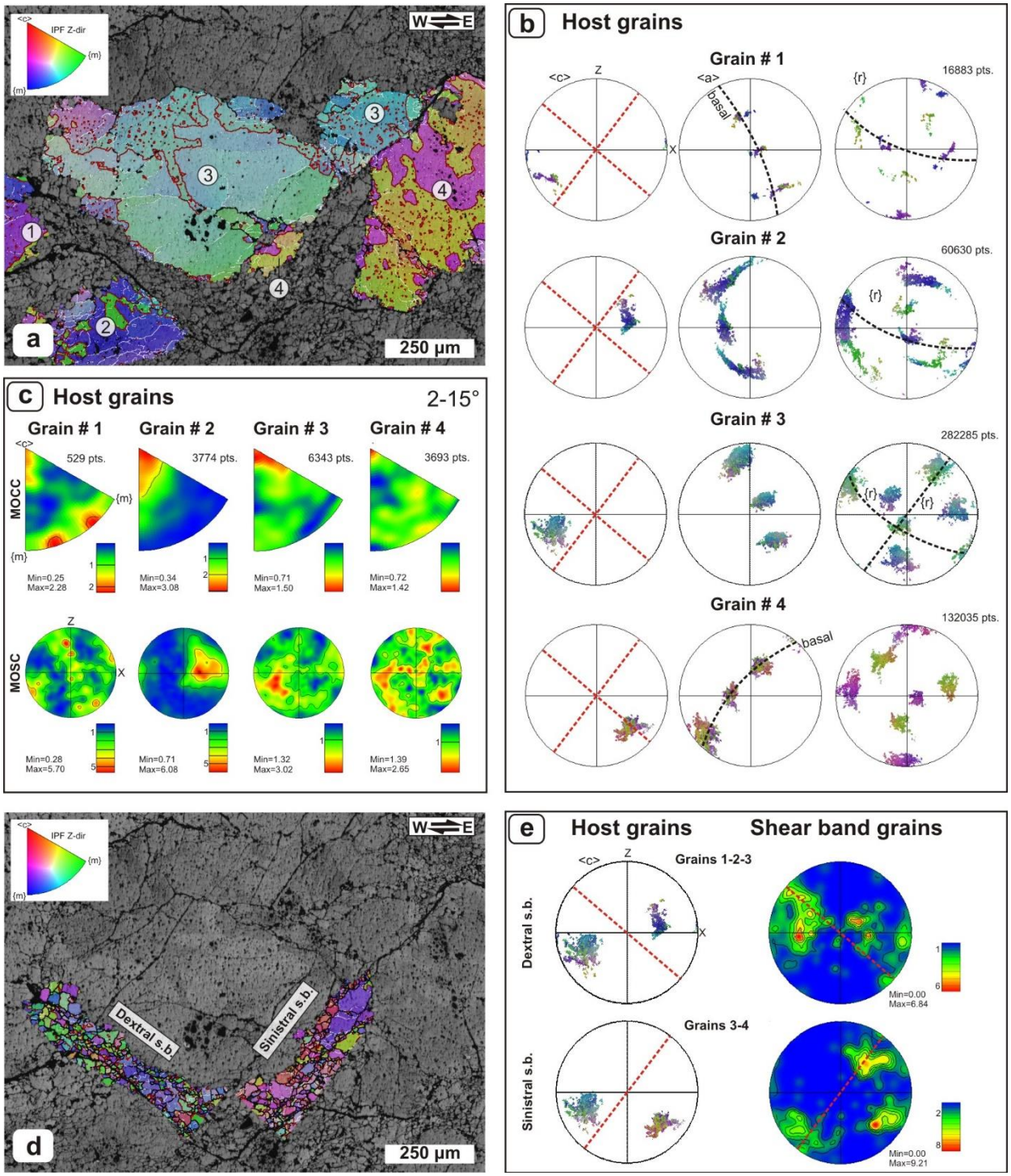

Figure 6.9 – Relationships between host grains and shear band grains in shear bands analyzed in map SP78-02: **(a)** Orientation map colored according to the inverse pole figure shown in the upper-left corner indicating 4 different host grains subsets (color-coding for boundaries according to Fig. 6.3a); **(b)** Pole figures showing the poles to <c>, <a>, {r} for the four host grains subsets. Orientation of shear bands is shown with red dotted lines. Crystallographic planes that are subparallel or closely oriented to shear bands are highlighted with black dotted lines; **(c)** Contoured misorientation axis distribution in crystal (above) and sample (below) coordinates for 2-15° of misorientation angles related to the 4 host grains subsets; **(d)** Orientation map showing the dextral and sinistral shear band subsets (color-coding according to pole figure in the upper-left corner and grain boundary coloring according to Fig. 6.3a); **(e)** Comparison between pole figures of host grains (left) and contoured one-point-per-grain pole figures for shear band grains (right) relative to the dextral (above) and sinistral shear band (below) subsets. Red dashed lines indicate the orientation of C' shear bands.

twins (twin terminology after Tullis, 1970; Tullis and Tullis, 1972; Pehl and Wenk, 2005; Menegon et al., 2011b) of grain 3 and the basal plane of grain 4 (Fig. 6.9a, b).

In other host grains, major crystallographic planes are oblique to shear bands. MOCC maxima of host grains are roughly located in correspondence of the <c> axis and the acute rhombs, associated with minor clustering also close to {m} and (c), as in grain 1 and 4 (Fig. 6.9c). In sample coordinates, host grains display clustering away from Y with faint girdles (grain 1) and secondary maxima (grains 3 and 4) (Fig. 6.9c).

<c> axes of new grains within the dextral shear band (Fig. 6.9d) cluster in the same orientations of the host grains, with secondary clusters aligned along the shear band (Fig. 6.9e). The distribution of <c> axes of new grains in respect to the host grains suggests a clockwise rotation, consistent with the, local, dextral sense of shear. The same is visible in the pole figures related to the host and new grains associated with the sinistral shear, where two major new grains <c> axis clusters coincide with the <c> axis orientation of the host grains 3 and 4 (Fig. 6.9e). The <c> axis of new grains is offset relatively to the host grains in anticlockwise direction, consistent with the sinistral sense of shear (Fig. 6.9e). A third cluster is located in the upper right quadrant of the pole figure parallel to the sinistral shear band (Fig. 6.9e). This latter do not correspond to any orientation observed in the surrounding host or new grains and is related to grains that are characterized by relative misorientation up to 70-90° with respect to the host grains that have been intercepted e.g. by misorientation profile B (Fig. 6.8).

6.4.3 Domain 3 (Map SP78-03)

Synthetic C’ shear bands, differently from conjugate bands, are not restricted to coarse quartz domains but invariably cross cut quartz layers and phyllonitic domains. In quartz domains, synthetic C’ shear bands are developed in relic and recrystallized quartz grains (Fig. 6.6e). They are characterized by very fine-grained quartz grains (i.e. shear band grains), with similar microstructure in respect to Domain 2 grains (see above) associated with bands of very fine-grained chlorite + sericite aggregates with a strong preferred orientation parallel to the shear band (Fig. 6.6e). Phyllosilicates are locally associated with oxides (i.e. limonite; Fig. 6.6f) and found also as inclusions in the surrounding quartz (Fig. 6.6f). The latter is cross cut by cracks, trails of fluid inclusions (healed cracks) and displays evident pitted grain boundaries (Fig. 6.6f).

The area to map by EBSD (SP78-03; Tab. 6.1) has been positioned within two paired, synthetic, dextral shear bands cross cutting quartz and characterized by a total offset of ~500 µm (visible in Fig. 6.6e). Since quartz is the only phase indexed, phyllosilicate-rich cores appear in black (Fig. 6.10a). Host grains and shear band grains have been separated based on a microstructural setting basis. The host grains population is characterized by grain size generally exceeding 50 µm, whereas shear band grains display grain size in the range of 5 - 30 µm (Tab. 6.2). The MAD shows

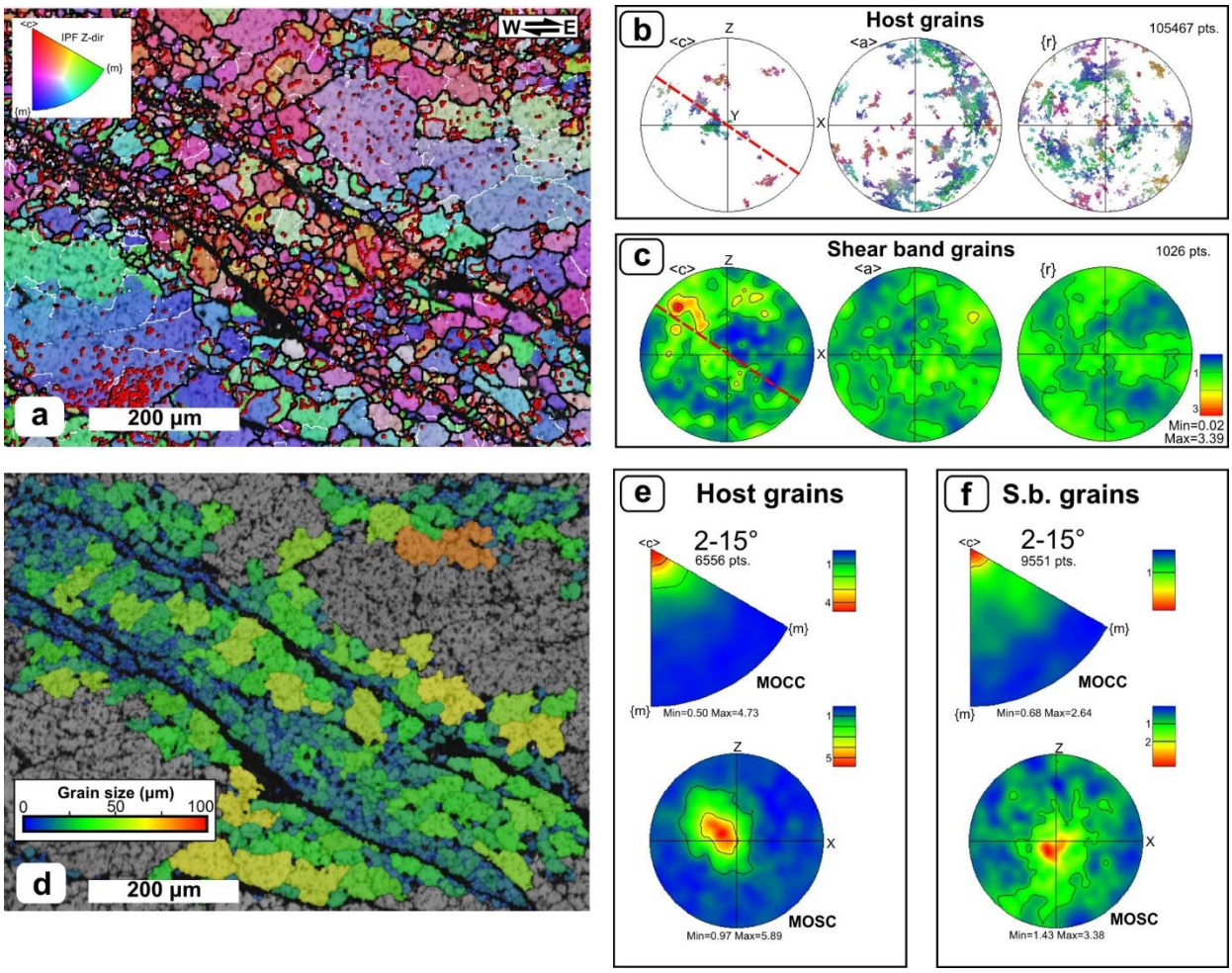

Figure 6.10 – EBSD analysis of map SP78-03: **(a)** Orientation map colored according to the inverse pole figure shown in the upper-left corner. Color-coding for boundaries according to Fig. 6.3a; **(b)** Pole figures showing the poles to <c>, <a> and {r} for the host grains. The red dashed line marks the C' shear band orientation; **(c)** Contoured pole figures (one-point-per- grain) showing the poles to <c>, <a>, and {r} for shear band grains. The red dashed line marks the C' shear band orientation; **(d)** Map showing the distribution of grains of equivalent circle diameter comprised between 0 and 100 µm, colored according to the key in the lower-left corner; **(e-f)** Contoured misorientation axis distribution in crystal (above) and sample (below) coordinates for 2-15° of misorientation angle for host grains **(e)** and shear band grains **(f)** subsets.

high correlated frequencies for low angles of misorientation (<10°) and for 55-60° of misorientation (Fig. 6.14d).

Host grains are characterized by lobate grain boundaries and relatively large grains (~200 µm) mantled by smaller equigranular grains with serrated boundaries (50 - 70 µm; Fig. 6.10a). Subgrain boundaries are present predominantly within larger grains, separating subgrains of 20-100 µm grain size. Dauphiné twinning, marked by wriggly twin boundaries, is visible in most of the grains (Fig. 6.10a). The <c> axis of host grains appears scattered on the pole figure but slightly clustered close to Y (Fig. 6.10b). In crystal coordinates, host grains are characterized by maximum on the <c> axis and the acute rhombs, which in sample coordinates coincides with the Y axis (Fig. 6.10e). Due to the strong similarities, the recrystallization features observed in the host grains were interpreted to correspond to Domain 1 grains.

Shear band grains are characterized by equigranular shape and serrated grain boundaries. The grain size is lower in correspondence of the shear bands, where the smallest grains (<< 10 μm) are localized (Fig. 6.10d). The crystallographic orientation of shear band grains is largely inherited from that of the host grains, except for a strong <c> axis maximum developed parallel to shear bands, which do not correspond to any orientation observed within host grains (Fig. 6.10c). The MOCC of shear band grains is comparable to that of the host grains, although characterized by a stronger scattering towards the rhombs (Fig. 6.10f). The MOSC is centered on Y with minor clustering randomly distributed (Fig. 6.10f).

6.5 Sample SP63 microfabric

This sample has been collected at the contact between a quartzite (main foliation: 30/280) and a cataclasite, belonging to a thrust low-angle fault oriented 22/026 (dip/dip direction). The quartzite is representative of the hanging wall block of the fault. Mesoscale kinematic indicators (Riedel shears) indicate top-to-the-E sense of shear. Two perpendicular thin sections (oriented N-S and E-W) have been obtained from this sample. The N-S oriented section is characterized by shows more clearly the relationships between the cataclastic and the wall-rock microfabric and therefore it has been selected for EBSD mapping.

The sample displays a layered microfabric, with the hanging wall quartzite visible at the top part of Fig. 6.11a, overlying a 2 cm thick foliated ultracataclasite band in the center and an unfoliated cataclasite band located at the bottom of Fig. 6.11a. The cataclastic matrix consists of very fine-grained clays/phyllosilicates (not resolvable with the SEM) and the foliated fabric in the ultracataclasite is due to subparallel trail of fragmented clasts and bands of phyllosilicates with different color. Embedded clasts consist entirely of variably fractured quartzite clasts ranging in grain size from 20 to 600-700 μm and containing a wide range of relic microstructures, affected by cataclastic overprint.

The quartzite wall-rock consists almost entirely of quartz (>95% modal proportion; estimated with ImageJ) with accessory white mica, chlorite and opaque minerals present along grain boundaries. Quartz consists of coarse grains (100-500 μm grain size) with lobate grain boundaries and amoeboid shape, showing undulose extinction and mantled by fine-grained (< 10 – 50 μm) quartz aggregates with serrated boundaries (Fig. 6.11b). A strain gradient is present within the hanging wall block away from the contact with the cataclasite. Between 5 mm to 1 mm from the contact, the hanging wall microfabric is cross cut by small conjugate bands (red dotted lines in Fig. 6.11b) decorated with tiny quartz grains trails and by discrete shear fractures, containing mixtures of fine-grained phyllosilicates (yellow arrow in Fig. 6.11b). Within 1 mm from the contact between the

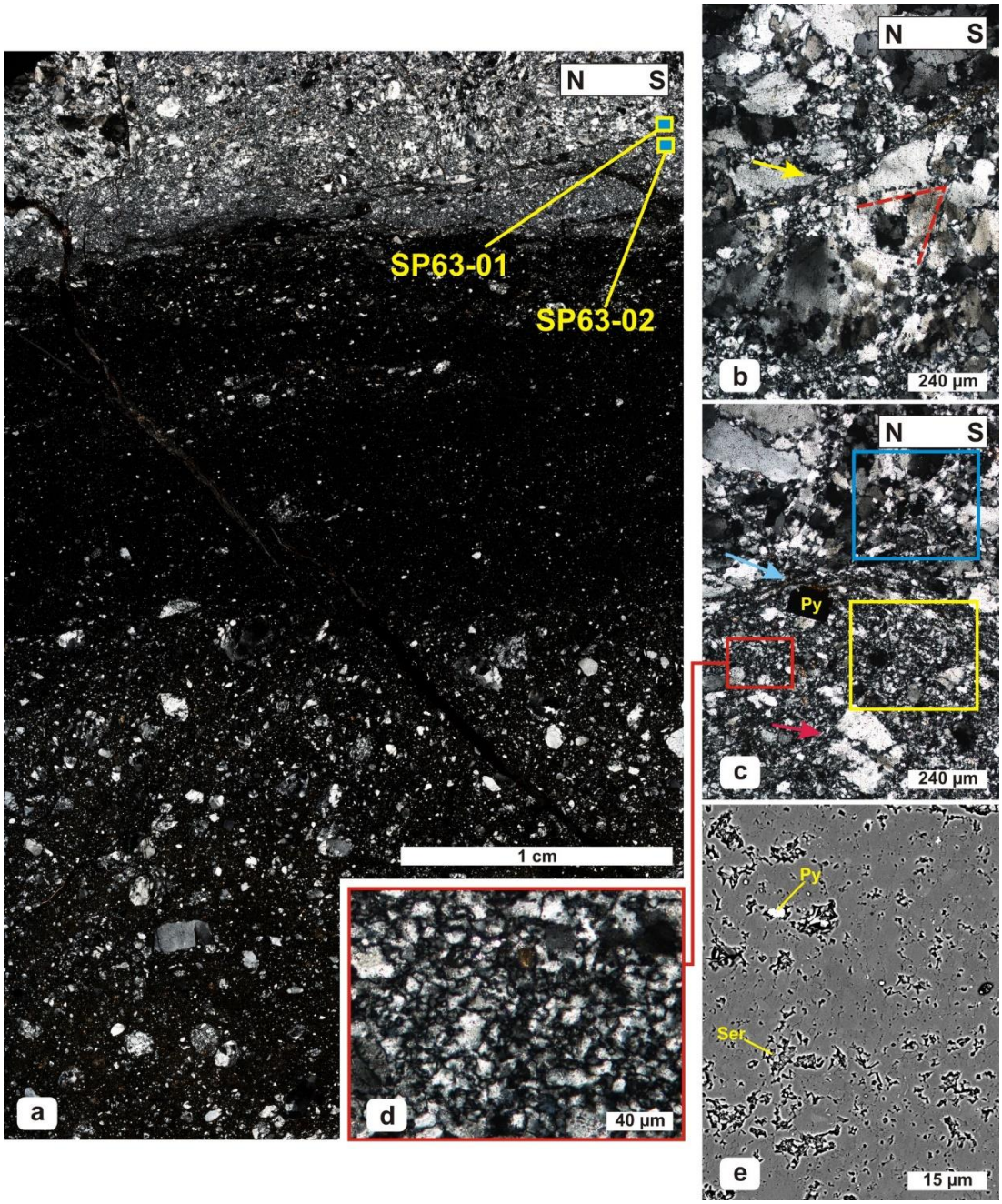

Figure 6.11 – Microstructures of sample SP63. Note that this thin section is oriented perpendicular to the cataclastic lineation: **(a)** Photo stitching of the entire thin section showing the wall rock on top, the foliated ultracataclasite band (middle) and the unfoliated cataclasite (bottom) (NX). Blue-yellow boxes highlight the position of EBSD maps. **(b)** Wall rock microfabric: quartz grains mantled by small aggregates of new grains. Red dashed lines mark trails of fine-grained quartz grains. The yellow arrow marks a sericite-filled shear fracture (NX); **(c)** Contact zone (light blue arrow) between the hanging wall and the band of very fine-grained quartz grains marking the contact with the ultracataclasite. The purple arrow indicates relic quartz grains (NX). The red frame indicate the position of Fig. d. Blue box: Map SP63-01. Yellow box: Map SP63-02. **(d)** Detail of the quartz band showing very fine-grained quartz grains with sutured grain boundaries; **(e)** SEM-BSE image of the fine-grained band of quartz grains showing the abundant phyllosilicate (Ser) and sulfide (Py) inclusions.

wall-rock and the cataclasite band, the damage zone of the quartzite is marked by a band of fine-grained quartz grains (Fig. 6.11c). The transition between this fine-grained quartz band and the coarse-grained wall rocks is sharp (light blue arrow in Fig. 6.11c) and often marked by sericite-bearing shear fractures.

Grains within the quartz band are frequently very fine-grained (< 10 μm; Fig. 6.11d) and characterized by equigranular to moderately elongate shape and serrated boundaries (Fig. 6.11c). Relic and coarser (50 – 500 μm) quartz grains are sparsely present, embedded in the very fine-grained quartz grains mass and displaying undulose extinction, microcracks and trails of quartz grains (purple arrow in Fig. 6.11c). Tiny sericite aggregates, usually smaller than 10 μm, occur mixed with quartz (Fig. 6.11d, e). Other common inclusions are characterized by sulphides (mostly pyrite; Fig. 6.11e), which locally shows euhedral habit and considerable grain size (Fig. 6.11c).

Two EBSD areas were selected in the quartzite. The first one is located in the wall rock, in a frame characterized by well-visible relic microstructures partially overprinted by smaller grains (equivalent to Fig. 6.11b). The second area has been selected in the fine-grained quartz band shown in Fig. 6.11c. Note that these EBSD maps are oriented perpendicular to the cataclastic lineation (and therefore also perpendicular to the mylonitic lineation, i.e. parallel to the YZ plane of the finite strain ellipsoid) and colored in respect to Y. Pole figures are plotted in standard orientation, except for Fig. 6.13d, which is plotted with X at the center and Y and Z close to the periphery to allow the comparison between the orientation of crystallographic planes with structural elements shown in Fig. 6.13a.

6.5.1 Wall rock (Map SP63-01)

EBSD analysis (Map SP63-01; Tab. 6.1) depicts a microstructure consisting of larger grains (i.e. host grains subset) with lobate boundaries (grain size: 50 - 140 μm) that host aggregates of smaller grains (i.e. aggregate grains subset) with grain size comprised between 5 and 50 μm (Fig. 6.12a). ~70% of the grains detected are smaller than 10 μm (Tab. 6.2 and Fig. 6.12b). The MAD shows two maxima for the correlated distribution for less than 10° of misorientation angles and between 55 - 60° of misorientation (Fig. 6.14e).

Host grains are characterized by irregular low-angle boundaries, abundant in coarser grains, and Dauphiné twin boundaries (Fig. 6.12a). They display a moderate shape preferred orientation directed obliquely to the fault zone boundary (Fig. 6.12a). Crystallographic orientations are characterized by two maxima, displaying a strong Y-max associated with a secondary X-max (Fig. 6.12c).

As shown in Fig. 6.12b, aggregate grains (highlighted by shades of blues) contain a larger generation of grains (10 – 50 μm) with serrated grain boundaries and shape similar to subgrains within old grains and a smaller generation (< 10 μm) that forms equigranular aggregates and trails cutting through old grains and that more rarely forms mantles or bulges around host grains. Quartz

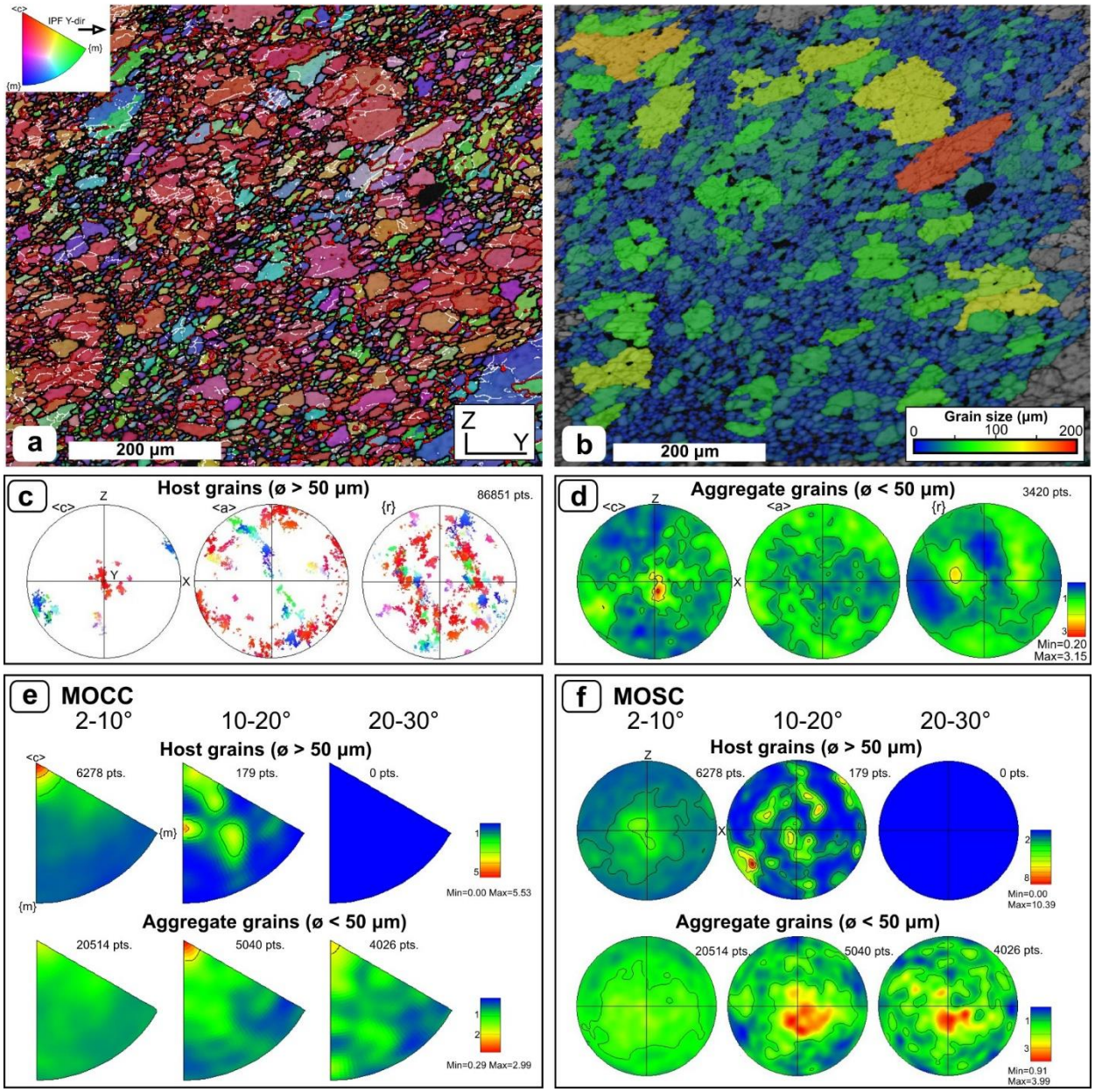

Figure 6.12 – EBSD analysis of map SP63-01: **(a)** Orientation map colored according to the inverse pole figure shown in the upper-left corner. Color-coding for boundaries according to Fig. 6.3a; **(b)** Map showing the distribution of grains of equivalent circle diameter comprised between 0 and 200 µm, colored according to the key in the lower-right corner; **(c)** Pole figures showing the poles to <c>, <a> and {r} for the host grains (Ø > 50 µm); **(d)** Contoured pole figures (one-point-per-grain) showing the poles to <c>, <a>, and {r} for the aggregate grains (Ø < 50 µm); **(e)** Contoured misorientation axis distribution in crystal coordinates for 2-30° of misorientation angle for host grains (above) and aggregate grains (below) subsets; **(f)** Contoured misorientation axis distribution in sample coordinates for 2-30° of misorientation angle for host grains (above) and aggregate grains (below) subsets.

aggregate grains broadly cluster in the same orientation with respect to host grains, with a clearly more scattered orientation relatively to the host grains (Fig. 6.12d).

In crystal coordinates, host grains are characterized by a strong <c> axis maximum for 0 – 10 ° of misorientation angle, with minor scattering towards the acute rhombs (Fig. 6.12d). In sample coordinates, such maximum corresponds to Y (Fig. 6.12e). Aggregate grains show randomly distributed misorientation axes in crystal coordinates with weak maxima around <c>, in particular for higher misorientation angles (10-30°; Fig. 6.12d). In sample coordinates, there is an evident

scattering of misorientation axes broadly clustering away from Y towards the XZ plane (Fig. 6.12f).

6.5.2 Fine-grained band (Map SP63-02)

This area (Map SP63-02; Tab. 6.1) is dominated characterized by large relic quartz grains (50 – 150 µm) surrounded by small (10 – 50 µm) and very small grains (< 10 µm), the latter dominating the dataset (Fig. 6.13a). The MAD displays two well defined maxima for the correlated distribution, in correspondence of 2 – 15° and 55 – 60° of misorientation angle (Fig. 6.14f).

The analyzed aggregate display grains with serrated grain boundaries and equigranular to elongate shape with a weak oblique shape preferred orientation, mostly defined by grains in the size range 50 – 70 µm (Fig. 6.13a). The larger grains (> 50 µm) display single-grain orientations, almost oriented on a girdle (Fig. 6.13b), whereas finer grains (< 50 µm) show a very weak c-axis CPO and only the rhombs appear slightly oriented in the same way as the larger grains (Fig. 6.13c).

A subdomain consisting of a large grain and bands/aggregates of smaller grains contained in it (labelled as 'subset 1' in Fig. 6.13a, d) was investigated in detail, in order to understand the relationships between the larger and smaller grains of the dataset. The pole figures of subset 1 are shown in Fig. 6.13d, oriented with X, Y and Z as in Fig. 6.13a to allow the comparison between the crystallographic orientation of the analyzed grains and the structures present in the EBSD area. The larger grain of subset 1 measures ~200 µm of equivalent circle diameter, contains abundant irregular low-angle boundaries defining sub-areas of 20 – 80 µm equivalent circle diameter and represents the host grain of smaller grains < 50 µm that are organized in trails and aggregates (Fig. 6.13a). Grains with 20-50 µm grain size are mostly localized in a 30 – 80 µm thick band stretching from the upper-left to lower-right portion of the host grain and display serrated boundaries (Fig. 6.13a). The smaller grains (mostly below 10 µm) form small aggregates or discontinuous trails with equigranular shape and serrated boundaries oriented almost perpendicular to the aforementioned band, stretching from the lower-left to the upper-right corner of the host grain of subset 1 (Fig. 6.13a). The trails defined by the grains with < 10 µm grain size are oriented parallel to the rhomb {r} plane of the host grain (Fig. 6.13d). Within subset 1, larger grains (~ 20 – 50 µm) show a tendency to cluster within 25° of misorientation with respect to the host, whereas smaller grains (largely below 10-15 µm) are characterized by misorientation with respect to the host often exceeding 70 – 90° and are largely responsible for the dispersion of crystallographic orientation on the pole figures (Fig. 6.13d).

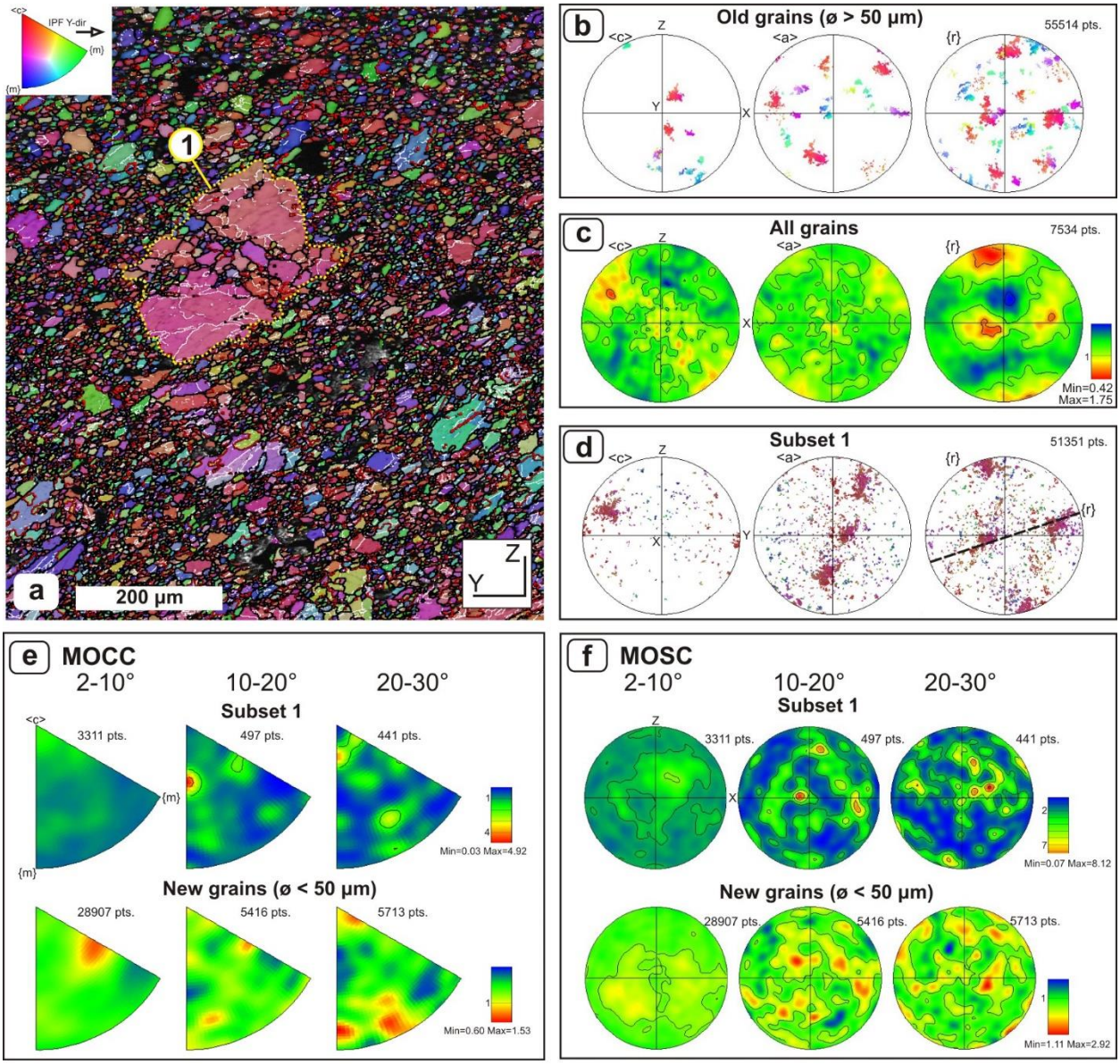

Figure 6.13 – EBSD analysis of map SP63-02: **(a)** Orientation map colored according to the inverse pole figure shown in the upper-left corner. The yellow dotted line marks the position of subset 1. The yellow lines, the orientation of quartz trails of tiny grains developed in subset 1. Color-coding for boundaries according to Fig. 6.3a; **(b)** Pole figures showing the poles to <c>, <a> and {r} for the larger grains (Ø > 50 µm); **(c)** Contoured pole figures (one-point-per-grain) showing the poles to <c>, <a>, and {r} for the bulk dataset, including subset 1; **(d)** Pole figures showing the poles to <c>, <a> and {r} for subset 1. Black dashed lines mark the orientation of the quartz trails (highlighted by yellow lines in Fig. a) in the pole figures. Note that these pole figures are oriented with X in the center and Y and Z on the periphery, to allow the comparison with Fig. a; **(e)** Contoured misorientation axis distribution in crystal coordinates for 2-30° of misorientation angle for subset 1 (above) and grains with Ø < 50 µm (below); **(f)** Contoured misorientation axis distribution in sample coordinates for 2-30° of misorientation angle for subset 1 (above) and grains with Ø < 50 µm (below).

In crystal coordinates, subset 1 is characterized by weak maxima for 2-10° of misorientation clustering close to <c> and the rhombs (Fig. 6.13e), corresponding to the orientation of the host grain <c> axis in sample coordinates (Fig. 6.13f). New grains are, on the other hand, characterized by a random distribution of misorientation axis in both crystal and sample coordinates, with a very weak Y-max (Fig. 6.13e, f).

6.6 Discussion

6.6.1 Dynamic recrystallization on the mylonitic foliation

The analyzed quartz layers (Maps SP63-01 and SP78-01; Tab. 6.1) display microstructures indicative of dynamic recrystallization. Most of the small grains display shape and aspect ratio comparable to subgrains in larger grains and are presumably formed by subgrain rotation mechanisms (i.e. Stipp et al., 2002a), as already suggested by Papeschi et al. (2017). The clusters of misorientation axis around the <c> axis and the acute rhomb observed in crystal coordinates (Fig. 6.3d, e; Fig. 6.7d) are consistent with the dominant activity of prism <a> and rhomb <a> slip systems (see Fig. 6.1b for reference). The high frequencies shown by the correlated MAD curve for low-angle misorientations is consistent with fabric development by dislocation creep (Fig. 6.14a, b). The 55-60° peak, observed in all investigated maps, is related to Dauphiné twinning (Fig. 6.14).

In Map SP78-01 (Domain 1 of sample SP78), the dominant activity of prism <a> slip led to the development of a typical Y-max microstructure (Fig. 6.1a for reference; Schmid and Casey, 1986). The misorientation axis in sample coordinates indicates that the vorticity axis of the flow and the misorientation axis are coincident (Fig. 6.7e).

Map SP65-01 is characterized by a recrystallizing old grain with a <c> axis nearly perpendicular to the foliation mantled by small grains with <c> axis clustered close to X. The dispersion of the crystallographic axes, from the crystallographic orientation of the porphyroclast grain, suggests an anticlockwise (i.e. consistent with the dextral sense of shear) rotation around Y, coinciding with the vorticity axis of the sample. Although the <c> axis CPO of the recrystallized mantle would in first order suggest prism <c> slip, the MOCC (Fig. 6.3d, e) and the slip tendency analysis (Fig. 6.4) indicate the dominant activity of prism <a> and rhomb <a> slip associated to {π} and {π'} <a> slip. This situation is similar to the XZa-type ribbon described by Ceccato et al. (2017), where the recrystallization of bands of grains hosted in a grain with <c> axis oriented perpendicular to the foliation under conditions favorably for dominant prism <a> slip was assisted by rhomb <a> slip and basal <a> slip. The activation of slip systems whose misorientation axis lies closer to the vorticity axis of the flow is well documented and described in the recent geological literature (Neumann, 2000; Lloyd, 2004; Morales et al., 2011; Muto et al., 2011; Michels et al., 2015). In Map SP65-01 it is likely that the unfavorable orientation of the porphyroclast grain hindered the development of a Y-max and that, on the other hand, the activity of rhomb <a> slip assisted the rotation around Y. The tendency of mantle grains to show MOSC clustering closer to Y relatively to the porphyroclast grain is indicative of the tendency to activate slip systems whose

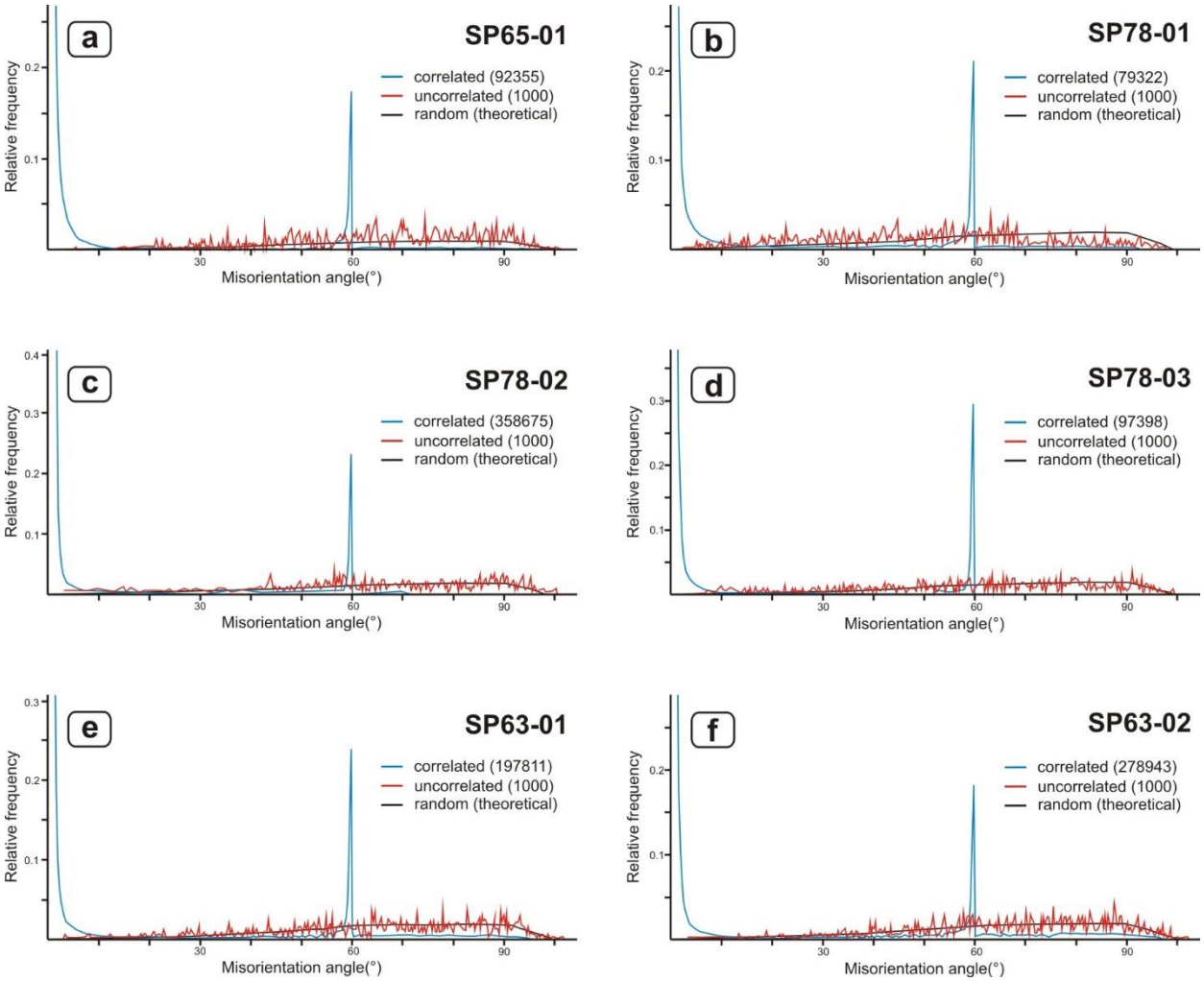

Figure 6.14 – Misorientation angle distribution (MAD) for correlated (light blue curve), uncorrelated (red curve) and for a theoretically random (black curve) distribution for EBSD maps: **(a)** SP65-01; **(b)** SP78-01; **(c)** SP78-02; **(d)** SP78-03; **(e)** SP63-01; **(f)** SP63-02. See text for further details.

misorientation axis lie closer to Y. It is also likely that many of the recrystallized grains where possibly formed from porphyroclasts that are completely recrystallized. This might help to explain the secondary <c> axis maxima present in the mantle grains subset (Fig. 6.3c).

To summarize, the EBSD analysis performed on the main foliation, indicates that under conditions favoring dominant prism <a> slip, different microstructures developed and different secondary slip systems and mechanisms were activated, controlled by the parent grain orientation. Dislocation creep was hence the dominant deformation mechanisms associated with development of mylonitic quartz layers. Dominant prism <a> slip is usually interpreted as indicative of amphibolite facies conditions (e.g. 450 – 600 °C; Schmid and Casey, 1986); however, it should be noted that layers are alternated with phyllonitic domains containing sometimes mixed quartz and phyllosilicates (e.g. Fig. 6.5b). It is likely that deformation progressively localized in such domains at low-grade conditions, as shown e.g. by Gilgannon et al. (2017) and that therefore high-grade structures were preserved in quartz lenses and recrystallized domains. Additional data about the temperature of formation of such fabrics are discussed in the following chapter (Chapter 7).

6.6.2 Shear bands: initiation and geometry

The data presented here highlights quartz and phyllosilicate microstructures developed within sets of C' shear bands. Shear bands overprint the mylonitic fabric discussed in sect. 6.6.1, cross cutting the phyllonitic domains, quartz lenses and layers. Conjugate sets of C' shear bands are preferentially developed in coarse-grained quartz, whereas synthetic C' shear bands usually affect also the surrounding mylonitic fabric. Based on the relationships between C' shear bands and host grains (Fig. 6.9, 6.10), the evidence of host control, related to planes of weakness in the host grains such as the rhombs (van Daalen et al., 1999; Vernoij et al., 2006a, b), can be demonstrated just in some cases. On the other hand, C' shear bands are mostly localized at the contact between different host grains (which itself represents a plane of weakness) in an orientation which is constant throughout the sample. Similar conjugate bands of recrystallized grains were also observed by Menegon et al. (2008), in that case just locally associated with fracturing along the rhomb planes in quartz. These authors interpreted the development of conjugate bands as a result of strain partitioning between the 'soft' phyllosilicate-rich mylonitic matrix and 'stiff' quartz. Similarly, for the Calamita Schists, the mylonitic matrix acted as the main strain-supporting framework and, within this matrix, rigid objects, like quartz lenses, localized sets of conjugate bands. Menegon et al. (2008) interpreted the origin of conjugate bands as evidence of localized coaxial deformation. In sample SP78, based on the vorticity analysis performed by Papeschi et al. (2018) and described in chapter 6, conjugate C' shear bands are indicative of non-coaxial conditions. The general lack of the steeper, C' antithetic set outside of quartz lenses may be explained as a consequence of the presence of a strong mechanical anisotropy (i.e. the mylonitic foliation), which inhibits the development of the steeper set, in agreement with Cobbold et al. (1971) and Cobbold (1976).

6.6.3 Mechanisms involved with shear band development

Bands of recrystallized grains have been largely observed in both naturally and experimentally deformed quartz grains (see Derez et al., 2015). Several mechanisms have been proposed to explain their development involving dislocation creep (Stipp and Kunze, 2008; Ceccato et al., 2017), low- temperature plasticity (Trepmann et al., 2007, 2017), a combination of cataclasis and recrystallization (can Daalen et al., 1999) or precipitation of new grains from a fluid (Takeshita and Hara, 1998; Takeshita and El-Fakharani, 2013; Kjøll et al., 2015; Goncalves et al., 2016). In the investigated sample (Domain 2 and 3), pole figures display patterns characterized by two components, showing (1) grains characterized by a general crystallographic inheritance from the orientation of the hosts coexisting with (2) grains showing a new, strong <c> axis CPO oriented

parallel to shear bands (Fig. 6.8g, 6.10f). The latter grains are strongly misoriented with respect to the host (6.9e, 6.10c). The analysis of the MOCC and the MOSC is inconsistent with prism <c> slip parallel to C' shear bands and, on the other hand, suggests the activity of the prism <a> and rhomb <a> slip systems, mostly related to the strained crystal lattice of host grains (Fig. 6.8f, 6.10e). Indication of dislocation creep is provided also by the high frequencies observed in the correlated MAD curve for low-angle misorientation (Fig. 6.14c, d). However, there is little evidence for extensive dynamic recrystallization, given the paucity of subgrain boundaries and bulges associated with the new grains (e.g. Fig. 6.8a).

Misorientation profiles show that most of the grains are just slightly misoriented with respect to the host and associated with few grains that are highly misoriented (Fig. 6.8d, e). The grain size is highly variable, with new grains enveloping fragments with the same orientation of host grains, and there is widespread evidence of fracturing within the host (Fig. 6.6a, 6.8a). These features indicate that brittle fracturing is implicated in the development of C' shear bands in quartz, as shown e.g. by van Daalen et al. (1999) and Vernoij et al. (2006a, b). Brittle fracturing is an efficient mechanism to explain the weakly misoriented new grains as fragments that slightly rotated roughly around the vorticity axis of the flow but cannot explain the development of a CPO different from the orientation of host grains. New grains precipitated from fluids may show a CPO parallel to the orientation of microcracks and shear bands, as shown by Takeshita and Hara, (1998) and Bons and den Brok (2000). Evidence for fluid-accompanied fracturing is widespread in the analyzed domains and suggested by the presence of pitted grain boundaries and trails of fluid inclusions, as well as many secondary phases trapped in quartz (Fig. 6.6d, f; Drury and Urai, 1990; Mancktelow and Pennacchioni, 2004; Kjøll et al., 2015). Therefore, the observed microstructure of C' shear bands can be explained as a combination of three mechanisms: (1) microfracturing with rigid-body rotation of fragments separated from the parent grain, (2) dynamic recrystallization assisting healing of microfractures and (3) sealing of microfractures by growth of new grains deposited from fluids with a well-developed CPO parallel to the shear bands. The CPO was likely controlled by the opening of dilatant sites that assisted the preferential growth of new grains with the <c> axis oriented parallel to shear bands. This extends the data gathered by Bons and den Brok (2000), who observed CPO development by dissolution-precipitation creep controlled by the preferential growth of grains with certain crystallographic orientation. The data presented here highlight that other mechanisms, controlled by shearing on dilatant sites, operate in nature which may cause the development of CPOs.

6.6.4 Strain localization on shear bands

The data set presented here documents an example of quartz microstructures developed in metapsammitic rocks under fluid-rich conditions and retrograde metamorphism in an upper crustal aureole (see Papeschi et al., 2017). The structural evolution, controlled by decreasing temperature during shearing, is summarized conceptually in Fig. 6.15. At relatively high grade conditions (amphibolite facies) quartz domains recrystallized producing stretched mylonitic layers (Fig. 6.15a). Recrystallization under these conditions occurred by dislocation creep dominated by prism <a> slip that led to the development of quartz layers, recrystallized by SGR and BLG. The newly formed quartz grains enveloped relic domains, where dislocation creep was recorded by intracrystalline deformation features (Fig. 6.15a). During decreasing temperature, deformation likely localized in phyllonitic domains, as suggested by the widespread growth of retrograde phyllosilicates in such domains and microstructures indicating phase mixing and intense grain size reduction (Fig. 6.15b). At the same time, in relic and coarse-grained quartz domains dislocation creep was not effective anymore to accommodate strain and such domains underwent strain hardening and fractured along conjugate and synthetic C' shear bands (Fig. 6.15b). Dynamic recrystallization affected damaged areas assisting healing of cracks on fractures (in agreement with van Daalen et al., 1999). Furthermore, the opening of cracks allowed fluids to infiltrate fractures precipitating new quartz-grains and fine-grained phyllosilicates. Fluid influx may also have aided fracture propagation by mechanisms such as stress corrosion cracking (Atkinson, 1984; Kerrich, 1986). Precipitation of very fine-grained new quartz grains and of weak and platy phyllosilicates (Fig. 6.15b) may have assisted weakening of the coarse and stiff quartz layers, enhancing strain softening by grain size reduction (e.g. White et al., 1980; Behrmann and Mainprice, 1987; Fliervoet et al., 1997) and reaction softening (e.g. White et al., 1980; Stünitz and Tullis, 2001). It is also likely that fracture propagation and fluid influx operated in a cyclical fashion with fracturing assisted by transient high-fluid pressure or strain surges, alternated with creep on shear bands, that caused the progressive propagation of C' shear bands. The development of a new chlorite + white mica foliation strictly associated with very tiny grains in synthetic C' shear bands provides additional evidence that slip was favored on synthetic C' shear bands (Fig. 6.6e, f), suggesting that these structures were able to propagate in the surrounding mylonitic matrix. As slip accumulated on synthetic C' shear bands, more fluids entered the system, activating a positive feedback mechanisms that enhanced lubrication by continuous precipitation of 'soft' phyllosilicates (Fig. 6.15c). A similar mechanism of shear band development was documented by Bukovskà et al. (2016) for the South Armorica Shear Zone where shear bands nucleated on microcracks and propagated assisted by fluid infiltration and reaction softening at very low-grade conditions.

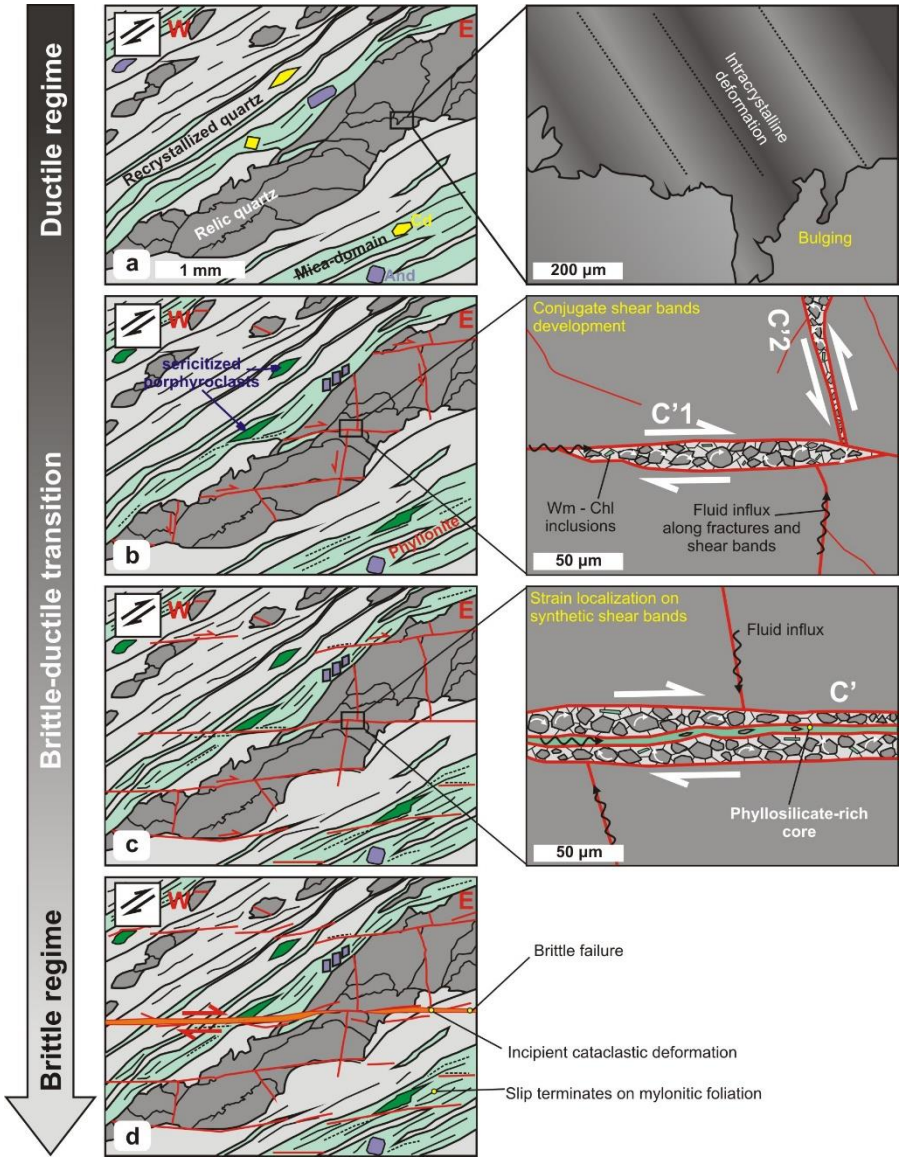

Figure 6.15 – Sketch diagram showing the evolution of mylonites in the Calamita Schists as a function of time and temperature decrease (dark grey to light grey arrow). Steps are: **(a)** recrystallization on mylonitic layers, **(b)** development of conjugate shear bands, **(c)** strain localization on synthetic C' shear bands and **(d)** reactivation of C' shear bands in the brittle regime. See text for comments.

As suggested by Papeschi et al. (2018), such C' shear bands acted as precursory structures for shear fractures and brittle fault rocks (Fig. 6.15d) in the semibrittle regime (i.e. between the BDT and BPT for quartz-rich rocks. It is likely that the process was progressive. As shown in chapter 4, phyllonitic domains, aligned on the main foliation, were misoriented during deformation in the brittle regime and therefore, strain concentrated more and more slip on C' shear bands, until finally faults propagated, linking up several C' shear bands segments.

6.6.5 Recrystallization associated with cataclastic deformation

Quartz recrystallization bands associated with cataclasites (Fig. 6.11c) form parallel to the fault and appear to be unrelated to any ductile precursor in the wall rock (i.e. foliation). Quartz microstructure in recrystallized bands records grain size reduction from original old grains (grain size> 50 µm; Fig. 6.12a) to new grains with grain size down to 5 µm (Fig. 6.11d). Old grains are characterized by a strong Y-max (Fig. 6.12c, d), which, together with the clustering around the

<c> axes in crystal coordinates (Fig. 6.12e) and around Y in sample coordinates (Fig. 6.12f), is indicative of dislocation creep by dominant prism <a> slip (Fig. 6.1b for reference; Schmid and Casey, 1986; Neumann, 2000). This appears related to the serrated grains surrounding host grains (grain size: 10 – 50 µm; Fig. 6.12a) that are also preserved as a trail in subset 1 (from upper-left to lower-right corner; Fig. 6.13a). These grains are characterized by host-controlled clustering and are likely recrystallized by SGR and BLG recrystallization (Stipp et al., 2002b).

The correlated distribution of the MAD, which shows high relative frequency values for low angles of misorientation, also supports deformation by dislocation creep. Based on the widespread evidence of dynamic recrystallization and recovery in the wall rocks (i.e. lobate grain boundaries, subgrain boundaries and undulose extinction; Fig. 6.11b), dislocation creep can be related to the plastic stage predating fault development. Furthermore, the activity of prism <a> slip is commonly associated with relatively medium- to high-grade conditions and appears unlikely for low-temperature fault rocks (Schmid and Casey, 1986; Toy et al., 2008).

The crystallographic orientation of very fine-grained new grains tends towards a random distribution, away from the Y-max observed in old grains (SP63-01; Fig. 6.12), which becomes progressively more marked in the finely recrystallized band (SP63-02; Fig. 6.13), where a high dispersion of crystallographic data with lack of clear maxima can be observed. Scattered orientations have also been observed for new grains developed parallel to the rhomb plane in subset 1 (Fig. 6.13d). Misorientation axis distribution in crystal coordinates shows, consistently, scattered maxima with a very weak maximum corresponding to the <c> axis (Fig. 6.12e, 6.13e), which is likely inherited from the host grains.

Excluding subgrain rotation, which may explain misorientations up to 20 - 40° (e.g. Hobbs, 1968) and is not compatible with the observed fabric, several mechanisms have been proposed to explain random CPOs in very fine-grained quartz aggregates, including diffusion creep and grain boundary sliding (Fliervoet et al., 1997; Halfpenny et al., 2006; Stipp and Kunze, 2008; Kilian et al., 2011), stress relaxation after low-temperature plasticity (Trepmann et al., 2007, 2017; Trepmann and Stöckert, 2013), fast annealing related to shear heating (Bestmann et al., 2012) and dissolution-precipitation creep (Kjøll et al., 2015; Goncalves et al., 2016). The high frequencies observed in the correlated MAD distribution for low angle misorientation rule out crystallographic randomization purely by diffusion creep or grain boundary sliding mechanisms. Many grains appear distributed in trails or aggregates that cut through the pre-existing fabric (Fig. 6.12a, 6.13a). In particular the parallelism of new grains trails with the rhomb plane, which is plane with the lowest surface energy for fracturing (van Daalen et al., 1999; Vernooij et al., 2006a) supports nucleation on pre-existing cracks or shear fractures. The widespread presence of fluid inclusion-

decorated planes, aggregates of sericite and even euhedral pyrite grains (Fig. 6.11c, d, e) suggest the significant presence of a fluid phase during deformation. The cataclastic band itself, consisting of very fine-grained phyllosilicates and developed within quartzites poor of phyllosilicates, is indicative of fluid-rich conditions during deformation. Therefore, this fabric is interpreted as having developed in response to a combination of cataclasis and dissolution-precipitation creep (e.g. Kjøll et al., 2015). These mechanisms may have promoted the weakening of the fault zone by (1) grain size-reduction of quartz, (2) authigenesis of very fine-grained phyllosilicates and (3) development of clay-rich ultracataclasite bands at the contact with the wall rock in association with finely recrystallized quartz.

6.6.6 Seismotectonic implications

The mylonitic and cataclastic rocks of the Calamita Schists developed in a fluid-rich system, as indicated by microstructural and EBSD data. In particular, the data presented here highlight the role played by fracturing in assisting fluid ingress (in line with Vernooij et al., 2006a and Menegon et al., 2008) and hence in promoting softening by dissolution-precipitation creep, a mechanism that assisted both mylonite and cataclasite development. Although the clay-rich ultracataclasite zone localized in the core of the fault might suggest that brittle deformation was accommodated by aseismic creep, the presence of fractures along the quartz rhomb planes and of thick cataclasites suggests episodes of transient embrittlement that might have assisted fluid ingress in the early stages of fault development. In this scenario, coseismic creep cannot be excluded although clear evidence of seismic stick-slip behaviour is not recorded in the examined cataclasites. The microstructures presented here (Fig. 6.11b, c) are, in particular, comparable to those shown by Trepmann et al. (2007, 2017), Kjøll et al. (2015) and Hirth and Beeler (2015), thus strengthening the interpretation that coseismic deformation assisted fault development. Low-temperature plasticity (i.e. nucleation of quartz grains in microcracks after earthquake-induced high-stress events) might have partially assisted the development of quartz aggregates with random crystallographic orientations, as shown experimentally by Trepmann et al. (2007) and in the Silvretta thrust by Trepmann et al., (2017). Cyclic fluid ingress assisted propagation of fractures and precipitation of quartz and phyllosilicates, hence steering deformation towards a more discrete accommodation style, characterized by aseismic slip on the ‘soft’ ultracataclasite core zone.

6.7 Conclusions

The microstructures analyzed in this chapter provide a contribution to the understanding of the switch from a well-developed mylonitic foliation to C’ shear bands and help clarify how shear

bands act as precursors for brittle structures. The data shown here supports previous studies on the subject providing additional constraints by documenting the following:

1. At relatively high grade conditions mylonitic deformation in quartz-rich rocks is accommodated by dominant dislocation creep causing the development of quartz layers aligned on the mylonitic foliation. The activity of a dominant slip system was observed (prism <a> slip) with activation of secondary slip systems controlled by the proximity of their misorientation axis with the vorticity axis of the flow, assisting recrystallization dominantly by subgrain rotation.
2. In the semibrittle regime, strain partitioning becomes important and 'stiff' relic quartz domains harden, fracturing along conjugate and synthetic shear bands. The direction exploited for fracturing is not necessarily coincident with weak crystallographic planes but may be determined by the vorticity of the flow.
3. Under fluid-rich conditions, ingress of fluids causes crystallization of new quartz grains and phyllosilicates in microfractures. The process induces strain softening and assists strain localization within synthetic shear bands. Authigenesis of new grains from fluids may have interplayed cyclically with microfracturing, enhancing further shear band propagation. A CPO may develop due to crystallization of quartz controlled by the opening of dilatant sites. The same process likely controlled the early stages of cataclasis in fault rocks with fracturing promoting fluid ingress, authigenesis of phyllosilicates a progressive grain size reduction of quartz.
4. Deformation in cataclastic rocks occurred under fluid-rich conditions with the development of recrystallized quartz bands associated with phyllosilicates and the development of random distributions.

Chapter 7

Metamorphic Constraints

The structural evolution of the Calamita Schists cannot be constrained without data on the physical conditions present during metamorphism and deformation. These parameters influence the behavior of rocks and therefore control rheology during deformation. Accurate knowledge of pressure and temperature is fundamental to link data obtained from EBSD, structural and microstructural analysis to the pressure-temperature-time path of the Calamita Schists.

In this chapter, I report pressure and temperature estimates, obtained using single mineral geothermobarometry (on white mica, chlorite and biotite) and chlorite-quartz-phengite-water multi-equilibrium calculations combined with forward thermodynamic modelling (P-T pseudosections). Results from these methods and their implications are discussed in the present chapter. With the data presented here, a temperature-stress-strain rate path of the Calamita Schists is finally reconstructed.

7.1 Previous studies on the metamorphism of the Calamita Schists

Despite the large exposure of outcrops of metasedimentary rocks and scattered metabasites (amphibolite bodies; Barberi and Innocenti, 1965), detailed investigations on the metamorphic conditions of the Calamita Schists have been largely neglected. A few studies (Duranti et al., 1992 and Caggianelli et al., 2018) have attempted to provide constraints on the metamorphic conditions experienced by the Calamita and Ortano Units as a consequence of the thermal anomaly induced by the emplacement of igneous bodies.

Duranti et al. (1992) investigated the thermal metamorphism from the Ortano Valley to Capo d'Arco (Eastern Elba), using petrogenetic grids to constrain the metamorphic assemblage recognized in different lithologies. Based on the recognition of peak cordierite + andalusite + biotite + K-feldspar bearing assemblages in the Capo d'Arco schists, they suggested peak temperatures between 600 and 650 °C at pressures below 0.18-0.20 GPa. The Capo d'Arco schists were lately assigned to the Calamita Unit (Musumeci and Vaselli, 2012; Musumeci et al., 2015) and therefore this temperature estimate was considered valid for the Calamita Peninsula, exposed in the south (Fig. 3.2).

7. Metamorphic Constraints

Caggianelli et al. (2018) represents the first geothermobarometric data of the Calamita Schists. A pressure constraint of 0.175±0.35 GPa was derived from the XFe content of biotite plotted on KFMASH grid generated using the Gibbs software by Spear and Menard (1989). Different temperature constraints were obtained using the Ti-in-biotite (Wu and Chen, 2015) and tourmaline-biotite (Colopietro and Friberg, 1987) geothermometry on the Calamita Schists and the amphibole-plagioclase geothermometer (Holland and Blundy, 1994) on amphibolite lenses. Based on their recognition of cordierite + andalusite + biotite + muscovite + K-feldspar as the peak metamorphic assemblage in the Calamita Schists, the temperatures obtained with biotite geothermometry (up to 695±44 °C) were interpreted as overestimates, while temperatures obtained using the tourmaline-biotite thermometer (between 530 and 480 °C) were interpreted as underestimates. The 560 – 630 °C temperature range obtained with the amphibole-plagioclase geothermometer was interpreted by Caggianelli et al. (2018) as the more appropriate, because it fitted well with the position of the cordierite + andalusite + biotite + muscovite + K-feldspar assemblage in the KFMASH grid. These authors estimated, hence, a peak temperature of 625 °C for the Calamita Schists.

The study of Duranti et al. (1992), though offering a first order P-T window estimate for the metamorphism of the Calamita Schists, is based on a marginal section of the aureole, away from the area investigated during this thesis. Despite this, the geothermobarometric estimates by Caggianelli et al. (2018) fit well with the data of Duranti et al. (1992), suggesting the validity of the correlation between the Capo d'Arco and Calamita Schists (Musumeci and Vaselli, 2012; Musumeci et al., 2015; Papeschi et al., 2017).

However, the conclusions drawn by Caggianelli et al. (2018) are based on a simplification of the Calamita Schists to the KFMASH system. The widespread presence of Ca- and Na-bearing phases, like plagioclase (first reported by Barberi et al., 1967a), may cause a shift of tens to hundreds of degrees of the position of reactions in the P-T field (e.g. White et al., 2007) and cannot be neglected. Moreover, Caggianelli et al. (2018) interpreted muscovite universally as a peak phase in equilibrium with biotite, cordierite, andalusite and K-feldspar, whereas detailed metamorphic investigations in this study (see Chapter 5) suggest that it often represents the result of retrograde metamorphism.

Both Duranti et al. (1992) and Caggianelli et al. (2018) focused on the peak metamorphic conditions; however, as shown in Chapter 5, the peak metamorphic assemblage was overprinted during retrograde, synkinematic metamorphism, never considered in the Calamita Schists. Therefore, the acquisition of new detailed data about the peak and retrograde metamorphism of the Calamita Schists is necessary to constrain the structural, microstructural and EBSD data.

7.2 Methodology

Sample selection

Preliminary investigations on the Calamita Schist samples (details in Appendix D) have been carried out using the optical microscope and the ZEISS-EVO Scanning Electron Microscope (SEM) equipped with an Oxford EDS detector situated at the *Instituto Nazionale di Geofisica e Vulcanologia* (INGV) in Pisa, Italy. Samples SP65 and SP78 (Praticciolo; see Chapter 6) have been selected to constraint the acquired EBSD maps and the retrograde metamorphism. In addition, one sample (CS42a; Capo Calvo), showing clearly preserved high grade mineral assemblage, has been chosen to estimate the peak metamorphic conditions experienced by the Calamita Schists.

Analytical method

Preliminary mineral chemistry and back scattered electron images have been obtained with the SEM of the INGV, Pisa. Mineral analysis and elemental X-ray maps have been performed with a Camebax SX100 Electron Micro Probe (EMPA) equipped with seven spectrometers and an EDS system at the *Institut für Mineralogie und Kristallchemie* (Stuttgart University). Analytical conditions for point analyses were 15 KeV of accelerating voltage and 15 nA of beam current with a spot size varying between 1 and 5 µm, using wollastonite (Si, Ca), Al_2O_3 (Al), Fe_2O_3 (Fe), $MnTiO_3$ (Mn, Ti), albite (Na), orthoclase (K), olivine (Mg) and barite (Ba) as standards. Monazites have also been investigated using 20 KeV of accelerating voltage and 200 nA of beam current. Structural formulae of minerals have been recalculated on 14 oxygen equivalents for chlorite, 11 for white mica, 22 for biotite, 18 for cordierite, 8 for feldspar and 5 for andalusite. Other phases analyzed include ilmenite (3 oxygen equivalents), titanite (5), rutile (4) and monazite (16). Concentration maps for major elements (Ca, Fe, Mn, Mg, Al and Na) were also produced by stepwise movements of the thin sections under the electron beam; counting times per step were 100 ms.

Whole rock chemistry of sample slabs has been determined by X-ray fluorescence spectroscopy (XRF) using the Panalytical PW2400 equipped with a PW2510 sample changer at the *Institut für Mineralogie* in Stuttgart. Whole rock analyses, expressed in wt%, were recalculated as mol% (see details in Tab. 7.1) and then modified to fit into the MnO – Na_2O – CaO – K_2O – FeO – MgO – Al_2O_3 – SiO_2 – H_2O – TiO_2 – O (MnNCKFMASHTO) system, used for pseudosection modelling: P_2O_5 was assumed to be incorporated in apatite and therefore the corresponding amount of calcium was detracted from the total amount of Ca (= P2O5 mol * 3.33). Fe_2O_3 was recalculated as FeO.

Fe^{3+} was included in pseudosection modelling (see discussion case by case) using the 'O' parameter.

Tab. 7.1 – Bulk-rock composition from XRF analyses of investigated samples, expressed in wt% and mol%. The wt% of FeO is calculated stoichiometrically as (Fe_2O_3)wt%/1.1113 and then calculated as mol%. Compositions used for pseudosection modelling are specified in the text.

Element	Studied sample					
	CS42a		SP65		SP78	
	wt%	mol%	wt%	mol%	wt%	mol%
SiO_2	72.52	79.53	73.50	81.44	86.87	92.66
TiO_2	0.67	0.55	0.66	0.55	0.23	0.18
Al_2O_3	14.44	9.33	12.45	8.13	7.16	4.50
FeO	-	3.36	-	4.29	-	1.01
Fe_2O_3	4.07	0	5.15	0	1.26	0
MnO	0.05	0.05	0.05	0.05	0.01	0.01
MgO	1.51	2.47	1.99	3.29	0.29	0.46
CaO	0.50	0.59	0.19	0.22	0.47	0.53
Na_2O	1.53	1.62	0.06	0.07	0.03	0.03
K_2O	3.47	2.43	2.72	1.92	0.82	0.56
P_2O_5	0.15	0.069	0.10	0.05	0.11	0.05

7.2.1 Geothermobarometry

In order to obtain first order geothermobarometric estimates, several classic single-mineral geothermometers were applied to the studied samples. Estimates from biotite were obtained through the Ti-in-biotite empirical geothermometers by Wu and Chen (2015) and Henry et al. (2005). Temperature estimates from chlorite were also obtained applying both empirical and semi-empirical geothermometry and geothermometry based on thermodynamic datasets. The Si content of white mica was also used to obtain first order pressure estimates based on the empirical values by Massonne and Schreyer (1987) and Massonne and Szpurka (1997). Finally, the analyzed white mica and chlorite compositions have been used to derive pressure and temperature estimates using the chlorite-quartz-water multi-equilibrium thermometer and chlorite-phengite-quartz-water multi equilibrium thermobarometry (MET; Vidal et al., 2005, 2006). Theoretical basis and analytical details regarding the above mentioned methodologies are presented in detail in Appendix E1

7.2.2 P-T pseudosection modelling

A pseudosections is a type of phase diagram that shows stability fields of different mineral assemblages for a specific bulk-rock composition (e.g. Powell and Holland, 1988; Spear and Menard, 1989; Connelly & Petrini, 2002). Pseudosection modelling allows to calculate point by point coexisting phases, their modes and composition, with the possibility to constrain petrographic and microstructural observations and to link directly the main assemblage in equilibrium observed to certain P-T conditions. Using this approach, even relic mineral assemblages may provide clues on the P-T path of a rock, before and after equilibrium has been reached (e.g. Guiraud et al., 1990; White et al., 2001; Evans, 2004; Cruciani et al., 2013; Lopez-Carmona et al., 2013). An interesting tool of pseudosection modelling is the possibility to plot compositional isopleths for one or more phases in the P-T field, which can hence be confronted with EMPA analyses and results from classical geothermobarometry. Details about the theoretical basis of this methodology and the analytical method used in this thesis are listed in Appendix E1.

7.3 Metamorphism of selected samples

This section is devoted to the metamorphism of the three selected samples - investigated using the methodologies described in detail in Appendix E1 - and includes a description of petrographic features and mineral chemistry. Appendix E2 features the location of spot analyses and X-ray maps performed, listing also the recalculated mineral formulas.

7.3.1 Sample CS42a

Petrography and mineral chemistry

Sample CS42a has been collected in high-grade Calamita Schists (Capo Calvo, location in Appendix C). It displays a high metamorphic grade mineral assemblage consisting of K-feldspar + plagioclase + cordierite + biotite + quartz + ilmenite + andalusite, which is variably overprinted by retrograde white mica + chlorite + biotite + albite + rutile. Common accessories are apatite, tourmaline, zircon, monazite and titanite. The high-grade assemblage is associated with a coarse-grained schistosity, defined by subparallel quartz- and biotite-domains (Fig. 7.1a) . Quartz is very coarse-grained (100 – 500 µm) and shows amoeboid shape, dissection and pinning microstructures around subparallel biotite inclusions, indicative of fast grain boundary migration recrystallization. Lepidoblastic biotite grains aligned on the main foliation (from now on referred to as Bi I) are characterized by a relatively large grain size (100 – 250 µm) and contain small zircon and monazite inclusions (Fig. 7.1a). Using a simple classification scheme based on the siderophyllite – eastonite

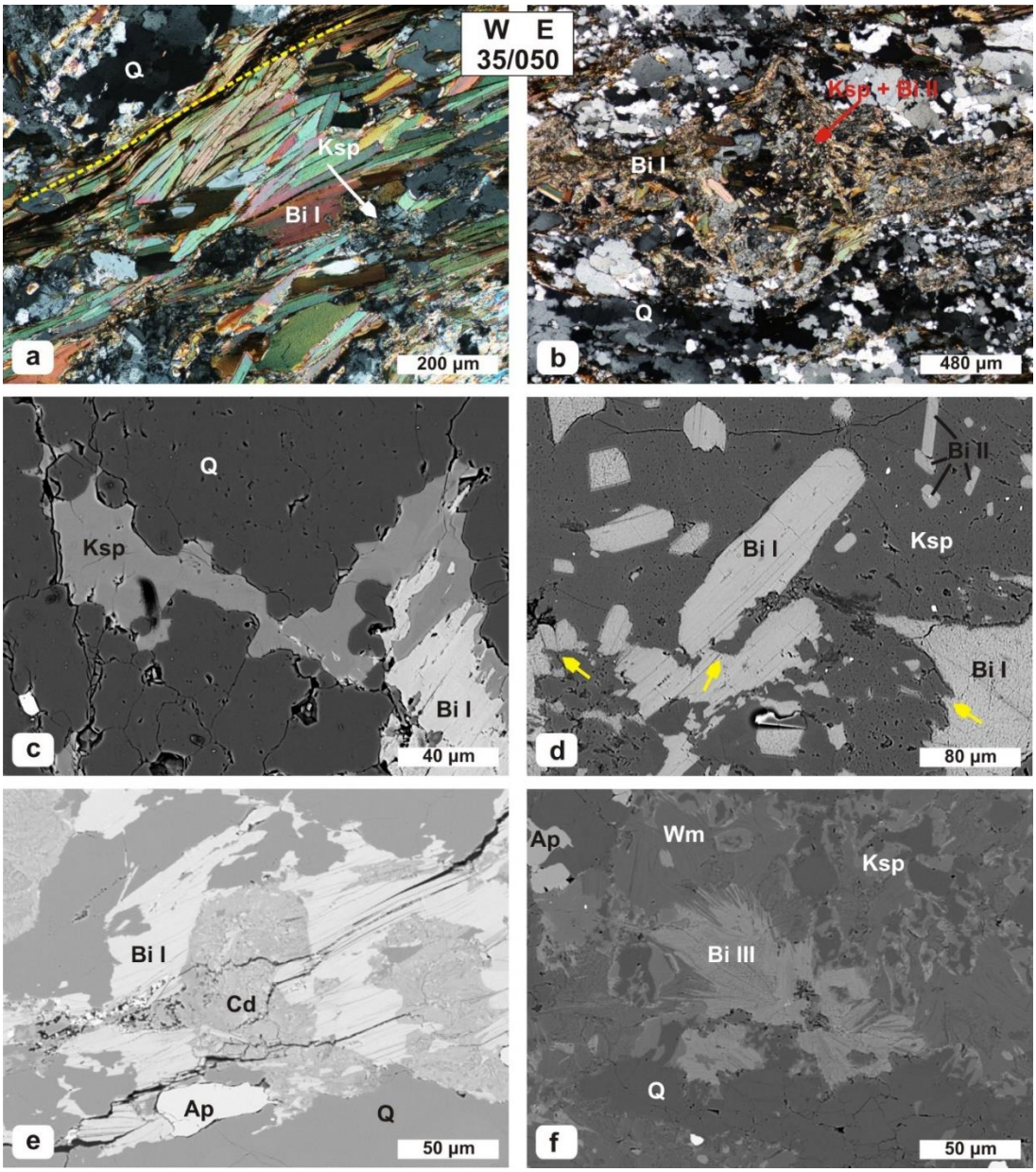

Figure 7.1 - Mineral assemblage of sample CS42a. The dip/dip direction of the foliation and microscale sense of shear is provided in the box (top, center): **(a)** Bt I grains aligned on the main foliation (yellow dashed line) associated with anhedral aggregates of plagioclase and K-feldspar (NX); **(b)** K-feldspar porphyroblast wrapped by Bt I and quartz, rich in poikiloblastic biotite inclusions (NX); **(c)** Detail of K-feldspar margin showing interstitial patches growing between quartz and biotite grain boundaries (SEM-BSE); **(d)** Biotite inclusions in K-feldspar. Note coarse Bt I grains with embayed textures (yellow arrows) coexisting with euhedral Bt II grains. The bright spots in the center are zircon cryptocrystals (SEM-BSE); **(e)** Cordierite porphyroblasts in Bt I completely replaced by pinite (SEM-BSE); **(f)** Retrograde products: diablastic white mica and biotite overgrowing Ksp (SEM-BSE).

– phlogopite – annite end-members (Fig. 7.4a; after Deer et al., 1992), Bi I show Si content is in the range 5.2 – 5.5 p.f.u. (on 22 oxygen basis) and XFe values comprised between 0.55 and 0.70. Bi I is characterized by compositional zoning -highlighted by X-Ray maps (Fig. 7.2)- with Mg rich and Fe-poor rims and Ti content that systematically increases from core (0.1 – 0.4 p.f.u.) to rim (0.3 – 0.5 p.f.u.) (Fig. 7.4b). Two feldspars are present: nearly pure K-feldspar (X_{ab} never exceeding 0.06) and plagioclase with oligoclase composition (X_{an} = 0.11 – 0.17). K-feldspar and plagioclase occur as small pockets (10 - 50 µm; Fig. 7.1a), enveloped in the Bi I foliation, and as

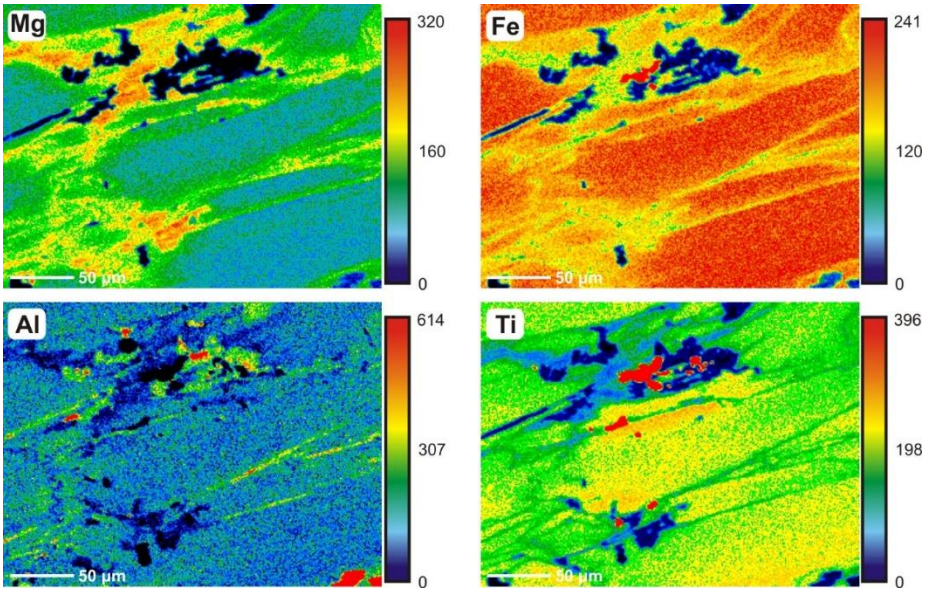

Figure 7.2 - X-Ray maps illustrating the chemical zoning of Bt I grains (area located in Fig. 7.1a) for: Mg, Fe, Al and Ti. Note the Mg and Ti enrichment from core to rim. Al-rich areas (greens in Al-map, corresponding to blues in Fe-map) is K-feldspar. Red areas in Ti-map are ilmenite aggregates.

large (up to 1-2 mm) porphyroblasts with roughly ellipsoidal shape and poikiloblastic texture due to abundant biotite inclusions (Fig. 7.1b). These large porphyroblasts are sometimes polycrystalline feldspar aggregates with K-feldspar – plagioclase often forming pavimentose textures and in which biotite is the only phase that may show a weak preferred orientation. Poikiloblastic biotite grains included in K-feldspar (from now on termed Bi II) display euhedral habit and variable grain size up to 250 µm and are largely misoriented with respect to the main foliation (Fig. 7.1d). From a compositional point of view, Bi II is similar to Bi I but it is characterized by a relatively homogeneous composition (X-Ray map: Fig. 7.3) with nearly constant XFe (0.6 – 0.65; Fig. 7.4b). The titanium content is lower and rarely exceeds 0.25 p.f.u (Fig. 7.4b). Other common inclusions in K-feldspar are represented by small cryptocrystalline zircons (Fig. 7.1d) and euhedral apatite grains (~50 µm). Microstructural evidence, mainly found around poikiloblastic K-feldspar porphyroclast, suggest that the investigated sample underwent partial melting: (1) K-feldspar is characterized by irregular and strongly cuspate/lobate bulges that penetrate between quartz and Bi II grain boundaries (Fig. 7.1c), (2) Tiny anhedral K-feldspar + plagioclase sheets are commonly found interposed between quartz and Bi I, (3) Embayed textures are visible in large Bi I grains included in K-feldspar, highlighted by the truncation of basal planes (Fig. 7.1d) and Ti-zoning patterns (Fig. 7.3). Melt pools finally crystallized as K-feldspar + Bi II + plagioclase aggregates lacking a clear preferred orientation and containing cryptocrystalline accessories (Fig. 7.1d), interpreted as crystallized from the melt.

Cordierite porphyroblasts show euhedral to subhedral habit and grain size rarely exceeding 500 µm (Fig. 7.1e). They are characterized by straight equilibrium boundaries with the surrounding biotite grains; however, they are strongly altered to mixtures of phyllosilicates with variable K (between 5 and 11 wt%) and Mg + Fe content (less than 1 wt% to more than 15 wt %) and witnessed as pseudomorphs (Fig. 7.1e). Interestingly, in spite of the alteration, the Al/Si ratio is

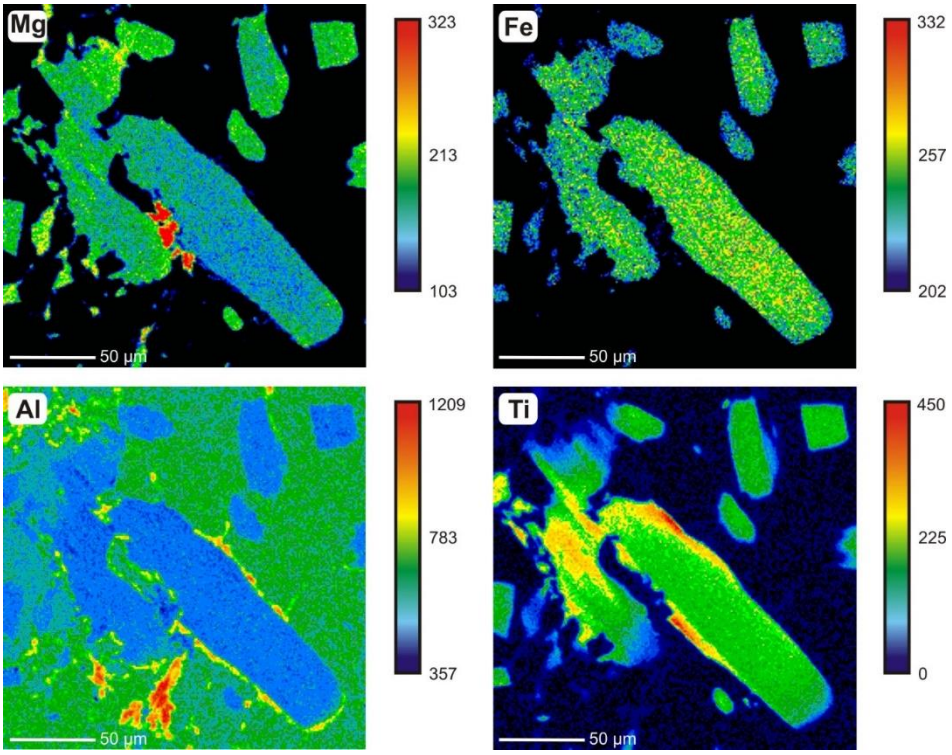

Figure 7.3 - X-Ray maps showing the chemical zoning of Bt I and Bt II grains included in K-feldspar (area located in Fig. 7.1b, d) for: Mg, Fe, Al and Ti. Note the Mg and Ti-rich biotite rim truncated by K-feldspar lobes. Red areas in the Al-map are sericite grains formed as an alteration product on grain boundaries. The small square-shaped grain in the upper-right corner is interpreted as a Bt II grain.

comprised between 0.75 and 0.8, close to that of 'fresh' cordierite. The XFe is also relatively constant, comprised between 0.47 and 0.60 with an average value of 0.53 (based on 25 analyses; Fig. 7.4d). Rare andalusite grains, strongly fractured and altered to sericite, have been found. Ilmenite (Mn between 0.05 and 0.12 p.f.u.) occur as inclusions in both biotite and K-feldspar, forming irregular aggregates up to 100 µm in size. Recalculated cation sum, using the software AX, shows that Fe is present as divalent, with Fe^{3+} < 0.01 p.f.u. Titanite is just locally present and show nearly pure composition (Al_2O_3 content around 4-5 wt%).

Retrograde/alteration products form either small aggregates of chlorite + sericite over isolated biotite grains or along grain boundaries and large domains characterized by diablastic greenish biotite (Bi III) + white mica + chlorite (Fig. 7.1f) associated with albite and rutile. Chlorite analyses show strong contaminations due to inclusions of K-bearing phyllosilicates (K contents > 0.5 wt%) and have been discarded. White mica compositions fall on the phengite series, with Si p.f.u. between 3.15 and 3.30 and XFe between 0.4 and 0.5. The proportion of paragonite is very low (Na content < 0.02 p.f.u.). Bi III composition is completely different from Bi I and Bi II, with very low Ti content (0.05 – 0.20 p.f.u.), lower XFe (0.45 – 0.50) and a composition closer to the phlogopite end-member (Fig. 7.4a, b). The plagioclase composition associated with alteration products is nearly pure albite.

Titanium in Biotite geothermometry

Temperature results from Ti-in-biotite thermometry using Wu and Chen (2015)'s relation are summarized in Fig. 7.4c, where they are plotted against the Ti p.f.u. content. For this calculation

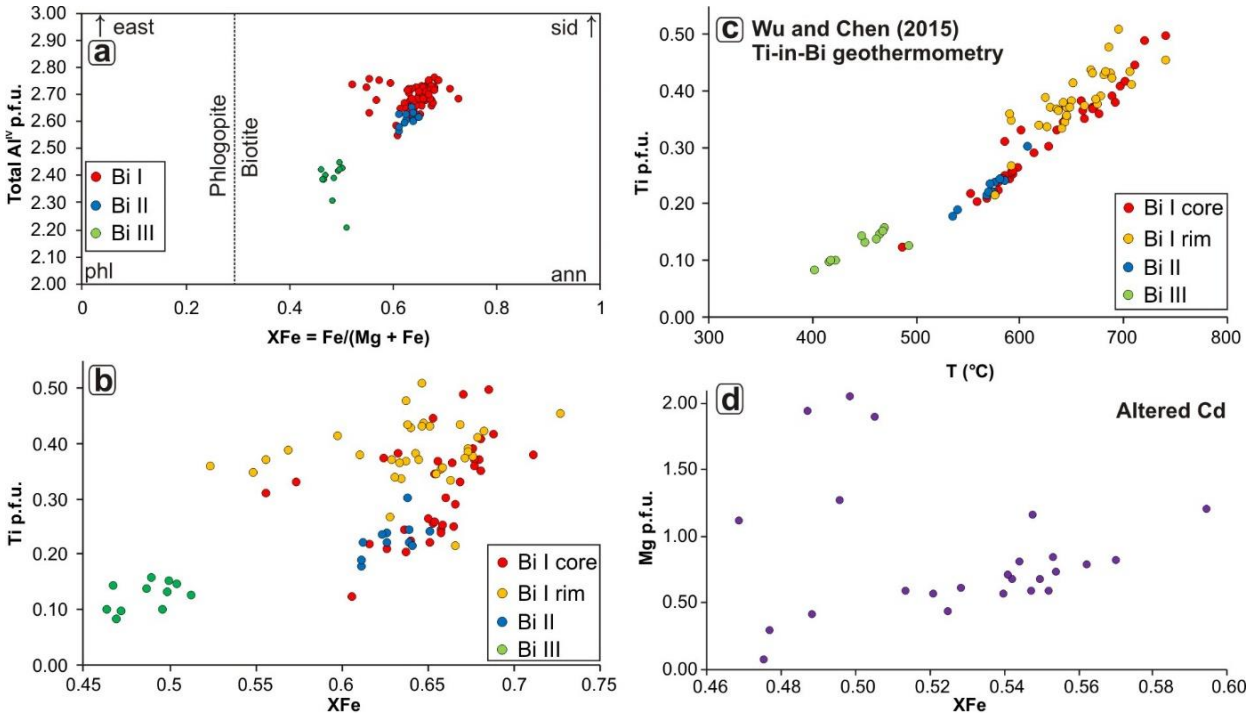

Figure 7.4 - Sample CS42a: **(a)** Biotite classification after Deer et al. (1992); **(b)** Compositional variability of biotite in the XFe – Ti p.f.u. plane; **(c)** Ti-in-biotite geothermometry after Wu and Chen (2015); **(d)** XFe – Mg p.f.u. graph for altered cordierite. See text for further details.

all iron was considered to be divalent, in agreement with the Fe^{3+} stoichiometric estimation in ilmenite, and input pressure was set at 0.2 GPa. Although Bi I cores and rims overlap compositionally, temperature estimates obtained the cores are on average lower than those obtained from the rims, respectively 630 and 650 applying Wu and Chen's geothermometer. The highest temperature estimates obtained from Bi I Ti-rich rims are in the 690 – 710 °C range. Temperature estimates obtained from Bi II grains indicate, on the other hand, lower temperatures, with an average of ~572 °C. Very low temperature were estimated for the analyzed Bi III grains (~447 °C), consistently with their interpretation as low-grade alteration products associated with chlorite and white mica.

To test the reliability of the Ti-in-biotite temperature estimates, results have been confronted with Henry et al. (2005)'s geothermometer (see estimated temperatures in Appendix E2) and tested for different XFe^{3+} (= $Fe^{3+}/[Fe^{2+} + Fe^{3+}]$) values. In spite of the different calibration pressure (restricted to 0.4 – 0.6 GPa), Henry et al. (2015)'s geothermometer exceeds Wu and Chen's estimation just by few tens of °C (10-30 °C), providing systematically higher temperatures but yet overlapping with Wu and Chen (2015)'s error range. The effect of Fe^{3+} content has been tested for an XFe^{3+} ratio of 0.5 and calculated temperatures differ by just 5-10 °C from the Fe^{3+} free case, thus suggesting that if small amounts of Fe^{3+} are present, their impact in calculated temperatures would be insignificant.

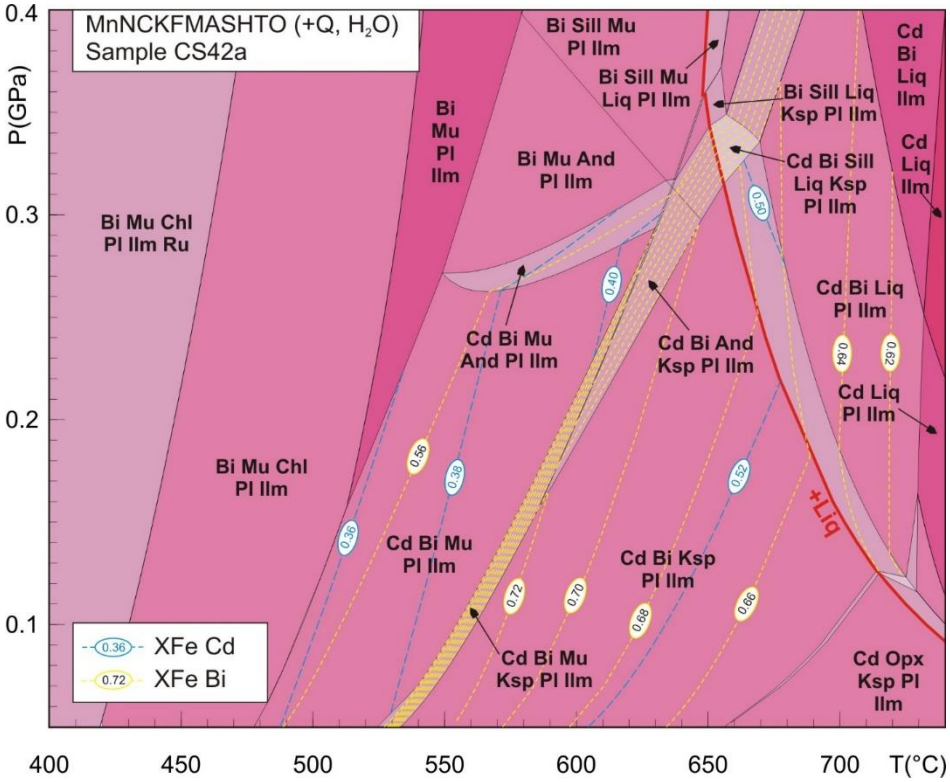

Figure 7.5 - P-T pseudosection of sample CS42a in the MnNCKFMASHTO system, with H_2O in excess, showing XFe isopleths for cordierite (light blue dashed lines) and biotite (yellow dashed lines).

Pseudosection modelling

In order to constrain the metamorphism of sample CS42a, the observed mineral assemblages and chemical compositions have been compared with the stability and composition of phases in a P-T pseudosection. One pseudosection was calculated using THERMOCALC 3.33 (Powell and Holland, 1988) and the internally consistent dataset 55 (Holland and Powell, 1998; updated 22 Nov 2003) in the system MnNCKFMASHTO, between P = 0.5 – 4.0 GPa and T = 400 – 740 °C. References for the mixing models for solid solutions of the phases considered in the calculations are: amphiboles (Diener et al., 2007), silicate melt (White et al., 2007), cordierite and staurolite (Mahar et al., 1997; Holland and Powell, 1998), chloritoid (White et al., 2000; Mahar et al., 1997) garnet, biotite, ilmenite and hematite (White et al., 2005), orthopyroxene, spinel and magnetite (White et al., 2002), muscovite and paragonite (Coggon and Holland, 2002), plagioclase and K-feldspar (Holland and Powell, 2003). The bulk composition used, listed in Tab. 7.1, was recalculated in mol%: SiO_2 = 79.53, Al_2O_3 = 9.33, CaO = 0.35, MgO = 2.47, FeO = 3.36, K_2O = 2.43, Na_2O = 1.62, TiO_2 = 0.55, MnO = 0.05 and O = 0.00. The fluid phase (pure H_2O) was set in excess, considering that fluid-saturated conditions are common in high-grade metapelites (Tajčmanová et al., 2007).

The calculated pseudosection is shown in Fig. 7.5, with fields colored in darker tones with increasing variance. Mineral abbreviations are those used by THERMOCALC and listed in Appendix B. The compositional isopleths for XFe in biotite and cordierite have been plotted in cordierite + biotite bearing fields.

7. Metamorphic Constraints

The high-grade assemblage Cd + Bi + Ksp + Pl + Ilm recognized in sample CS42a is stable in a relatively large quadrivariant field between 550 and 700 °C and pressure between 0 and 0.31 GPa. Within this field, XFe in biotite decreases with increasing temperature from 0.72 to 0.66 while XFe of cordierite remains steadily stable around 0.52. Similar XFe ratios have been observed in Bi I cores and rims; however, these values overlap with those calculated in the pseudosection (ranging between 0.6 and 0.7; Fig. 7.4b) and X-Ray maps show qualitatively an increase of the Mg and Ti contents in the rims, suggesting prograde zoning formed during re-equilibration in the Cd + Bi + Ksp + Pl + Ilm field. The XFe of altered cordierite, despite some scattering which might be partly related to alteration processes, displays an average value of 0.53 (Fig. 7.4d), which is also consistent with the values calculated in the same field. The calculated plagioclase composition (An_{11-13} compositions towards low T, reaching An_{17-20} towards high T) is also in agreement with the observed plagioclase compositional range (An_{11-17}).

Migmatite textures, highlighted by (1) embayed Bi I and Q and (2) new growth of Ksp + Pl + Bi II with magmatic fabric, suggest that the rock reached the solidus curve (in red in Fig. 7.5) during its P-T path. Since no orthopyroxene has been observed, embayed textures in biotite are interpreted to have been formed at the solidus at P higher than ~ 0.12 GPa. Ti-in-biotite geothermometric results on biotite rims (650 – 700 °C; Fig. 7.4c) are in good agreement with the observed position of the solidus between 0.12 and 0.31 GPa (~650 – 710 °C; Fig. 7.5). Beyond the solidus, K-feldspar is the phase which is selectively incorporated in the melt, disappearing completely at slightly higher temperatures. Therefore, the Ksp + Bi II + Pl aggregates can be interpreted as the product of crystallization from the first drops of K-rich melt produced at the solidus. The interpretation of Bi II as 'magmatic' biotites explains their euhedral shape, the non-oriented disposition within K-feldspar and their homogeneous composition.

Andalusite is stable just in a small field for P > 0.16 GPa (Fig. 7.5). The rare, relic andalusite grains observed may have been formed during the prograde or retrograde path. However, they are found surrounded by alteration products and therefore their relationships with other phases are not preserved. If the equilibration volume that produced andalusite grain is the same used for pseudosection modelling, then the presence of andalusite indicates pressures > 0.16 GPa, though further observations on other samples are needed to test this hypothesis.

The observed retrograde assemblage white mica + chlorite + biotite + rutile + albite is predicted to form below 400 – 450 °C. Though sericite alteration along grain boundaries (Fig. 7.3) appear to suggest a hydrothermal/metasomatic origin for these assemblages, calculated temperatures from pseudosection modelling appear in good agreement with the results of Bi III geothermometry (~447 °C; Fig. 7.4c).

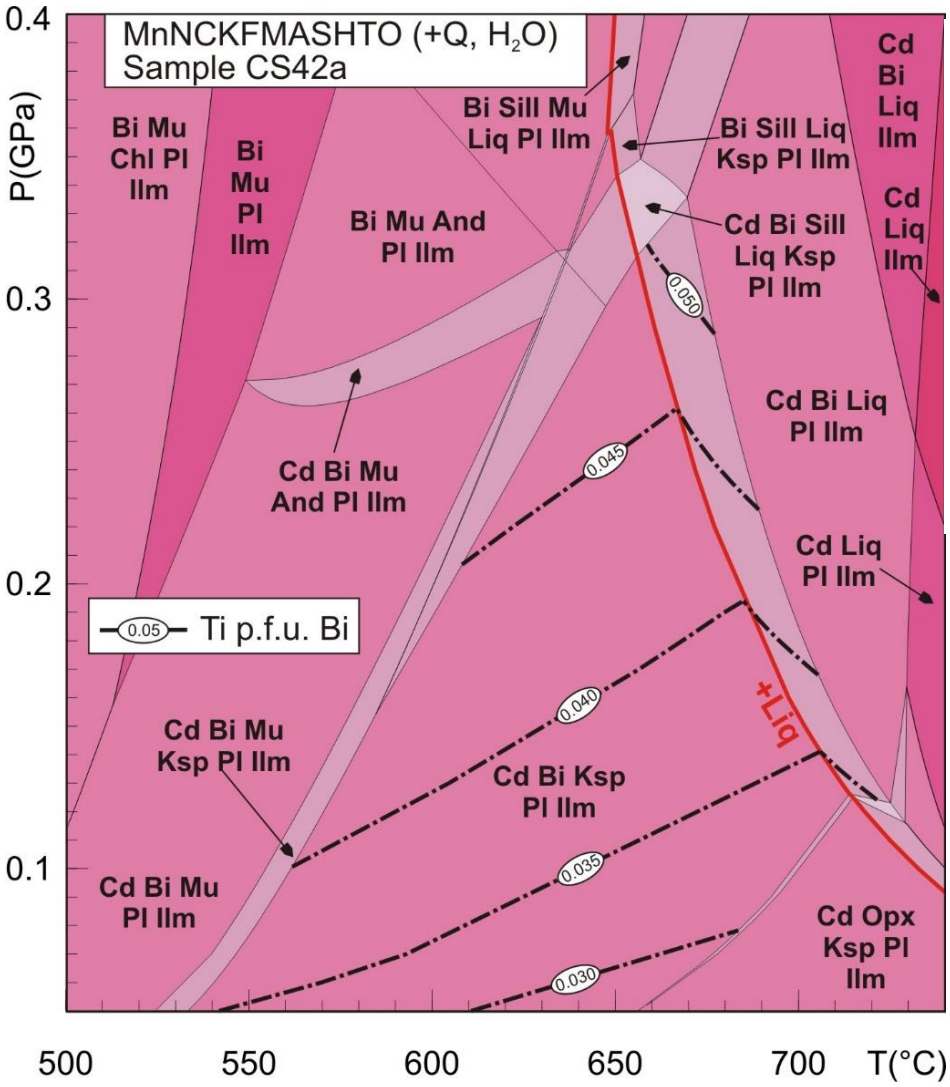

Figure 7.6 - P-T pseudosection of sample CS42a in the MnNCKFMASHTO system, with H_2O in excess, showing the Ti p.f.u. content isopleths for biotite (black dashed lines). Discussion in text.

Pseudosection modelling: Ti-in biotite

To confront the data from Ti-in-biotite geothermometry with the biotite thermodynamic model used in pseudosection modelling (i.e. White et al., 2005), Ti p.f.u. isopleths in biotite have been calculated for the Cd + Bi + Ksp + Pl + Ilm field and plotted in the P-T pseudosection (Fig. 7.6). The calculated Ti p.f.u. values are 1 order of magnitude lower than the observed Ti content in biotite (Fig. 7.4b, c). According to Tajčmanová et al., (2009), this is related to the model of White et al. (2005), which assumes Ti partitioning in the M1 site of biotite, whereas natural biotites incorporate Ti also in the M2 site. The model by Tajčmanová et al., (2009) appears to provide better estimates for Ti in biotite.

7.3.2 Sample SP65

Petrography and mineral chemistry

Sample SP65 (Fig. 6.2a) is a mylonitic schist with a psammitic composition (see tab. 7.1). This sample has been analyzed via EBSD mapping and a detailed microstructural description is

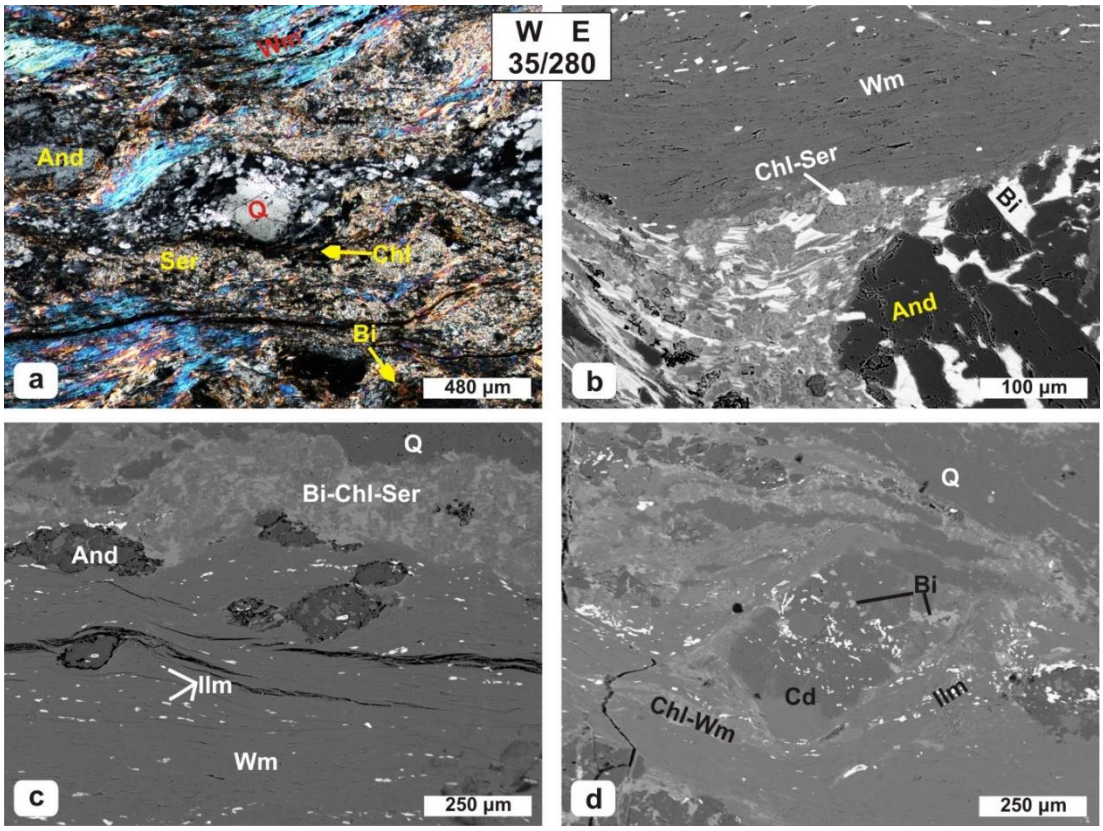

Figure 7.7 - Mineral assemblage of sample SP65. The dip/dip direction of the foliation and microscale sense of shear is provided in the box (top, center): **(a)** Recrystallized quartz layers wrapped by a chlorite – white mica mylonitic foliation with variably sericitized porphyroblasts of andalusite. Some brownish biotite grains are visible (NX); **(b)** Contact between andalusite-biotite relic aggregate and the white mica-bearing mylonitic foliation. Bright minerals associated with white mica are ilmenite grains (SEM-BSE); **(c)** Andalusite porphyroclasts wrapped by the white mica-ilmenite mylonitic foliation associated with biotite-chlorite-sericite (SEM-BSE); **(d)** Cordierite porphyroclast with rotated internal foliation, defined by ilmenite and biotite inclusions, completely pseudomorphosed by phyllosilicates (SEM-BSE).

available in Chapter 6. The sample displays a white mica + chlorite + ilmenite + quartz bearing mylonitic foliation wrapping relic biotite + cordierite + andalusite porphyroclasts and polycrystalline aggregates (Fig. 7.7a). Accessories are represented by apatite, tourmaline and zircon. The relic assemblage is preserved in biotite-rich layers (Fig. 7.7b), or as andalusite (Fig. 7.7c) and cordierite (Fig. 7.7d) porphyroclasts, wrapped by the mylonitic foliation. Andalusite represent the most abundant porphyroclast, slightly overprinted by sericitic alteration, whereas cordierite is less common and occur as deformed grains completely altered to pinite (i.e. aggregates of phyllosilicates; Fig. 7.7d) that often occur as layers of strongly pinitized/sericitized grains (Fig. 7.7a). Spot analyses on andalusite reveal almost pure composition, with Fe^{3+} content lower than 0.02 p.f.u., whereas the strong alteration of cordierite, showing 'chlorite-like' compositions with variable Na and K content, hinders the possibility to obtain indications on its original chemistry.

The contact between biotite layers and the surrounding mylonitic foliation is highlighted in Fig. 7.7b and in the X-Ray map reported in Fig. 7.8. Abundant poikiloblastic inclusions of biotite occur within the andalusite grains in biotite layers (Fig. 7.7b). Ilmenite and biotite inclusions, often

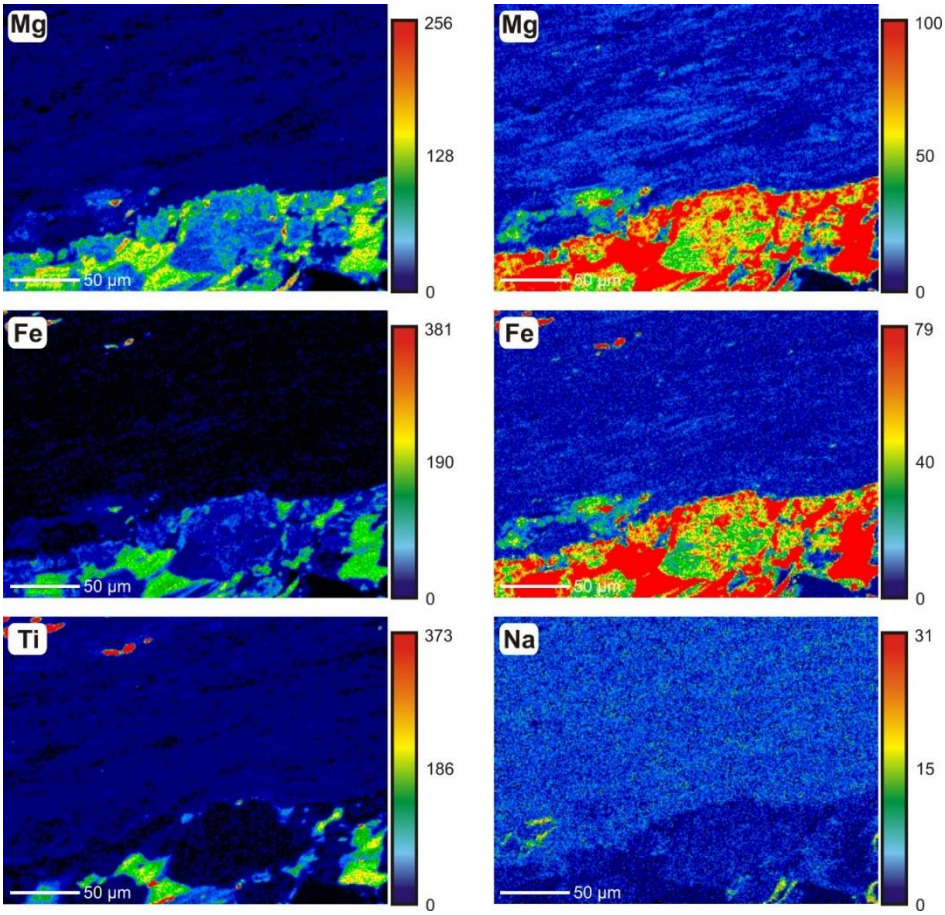

Figure 7.8 - X-Ray maps performed at the contact between relic biotite (below) and retrograde white mica (above) on the mylonitic foliation (area located in Fig. 7.7b) for: Mg, Fe, Ti and Na. The contrast of the maps on the right has been adjusted to highlight the compositional variability of white mica on the mylonitic foliation. Irregular aggregates in biotite are retrograde chlorite-sericite intergrows. Red spots in the Ti map are ilmenite (in white mica domain) and rutile (in biotite domain).

aligned on rotated internal foliations, are also found within cordierite (Fig. 7.7d). Biotite appears variably overprinted by globular aggregates of sericite-chlorite with lower Mg, Fe and Ti content with respect to biotite (Fig. 7.8). Rutile needles, interpreted as alteration products, have also been found between biotite grains (red spots in Ti map; Fig. 7.8). Biotite shows a weakly preserved zoning with subparallel lamellae characterized by different Fe, Mg and Ti intensity (Fig. 7.8). The Al^{IV} content shows a wide variability (2.5 – 2.9 p.f.u; Fig. 7.10a) while the XFe ratio is characterized by a narrow variability range (~0.60 – 0.64; Fig. 7.10b). The Ti content is also relatively constant between 0.25 and 0.35 p.f.u. (Fig. 7.10b).

The abrupt grain size drop that occurs between biotite-layers and the mylonitic foliation corresponds also to a compositional transition to a white mica-rich foliation. Chlorite is indeed uncommon in association with white mica on the mylonitic foliation, but rather forms aggregates and pseudomorphs over biotite and cordierite, with intergrowing unidentified phyllosilicates. For this reason, it was not possible to obtain uncontaminated chlorite analyses in this sample. Attempted chlorite analyses show high Na + K content (>1 wt%) and nearly constant XFe (~ 0.6).

The mylonitic foliation is constituted mainly by phengitic white micas with variable Al content that lie close to the muscovite end-member (Fig. 7.10d; classification after Bousquet et al., 2002) and are associated with ilmenite grains (Fig. 7.7c). Neighboring white mica grains are characterized by a strong variability for Mg, Fe and Ti content (Fig. 7.9) with XFe ratios ranging

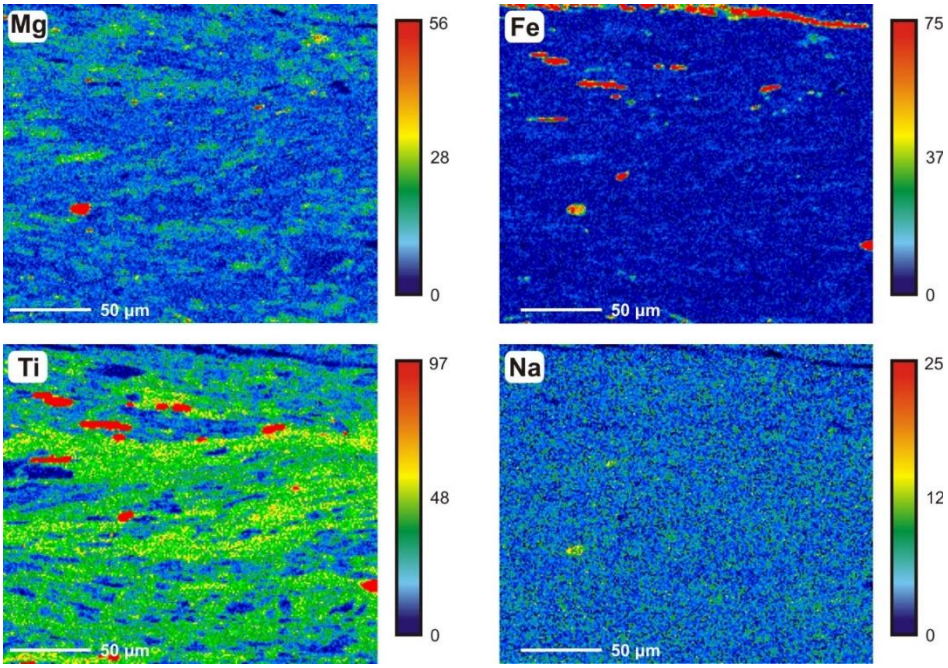

Figure 7.9 - X-Ray maps of the white mica-ilmenite mylonitic foliation (area located in Fig. 7.7c) for: Mg, Fe, Ti and Na. Note the compositional variability of white mica for Fe, Mg and Ti. Red spots in the Ti map are ilmenite grains, blue spots are tourmaline grains. The red trail on top of the Fe map is a late limonite-filled crack.

between ~0.4 and 0.6 that correlate with the variability of Si p.f.u. (Fig. 7.10e), suggesting the coeval activity of the ferromagnesian and Tschermak substitutions. Ti in white mica varies between 0 and 0.03 p.f.u (Fig. 7.10f). A similar variability range has been found for Na in white mica, which, although characterized by relatively low contents, shows higher intensity in respect to relic biotite-cordierite-andalusite domains (Fig. 7.8). Ilmenite contains ~2 wt% of Al, ~2 wt% of Si and ~4 wt% of Mn and neglectable Fe^{3+} content, based on the AX recalculation (Appendix E2).

Titanium in biotite geothermometry

Temperature results obtained from the applications of Wu and Chen (2015)'s geothermometer (Eq. 7.3) are shown in Fig. 7.10c. The average estimate yield a result of 612 ± 29 °C (method error: ±50 °C) at P = 0.2 GPa. With a lower pressure value (P = 0.1 GPa) the obtained temperature estimate is lower by just 10 °C (602 ± 29 °C). The application of Henry et al. (2005)'s geothermometer (Eq. 7.2; results in Appendix E2) yields considerably higher temperatures (637 ± 27 °C), while the Fe^{3+} effect, tested with an XFe^{3+} of 0.5, produces an increase in the estimated temperature of about 10 °C. According to the low Fe^{3+} contents reported from ilmenite and andalusite however, the assumption of $XFe^{3+} = 0$ appears more realistic.

Pseudosection modelling

A PT pseudosection was calculated in the system MnNCKFMASHTO for the analyzed bulk composition (Tab. 7.1) for P = 0.5 – 4 Kbar and T = 350 – 650 °C with H_2O considered in excess. The composition, recalculated in mol%, used was: SiO_2 = 81.44, Al_2O_3 = 8.13, CaO = 0.06, MgO

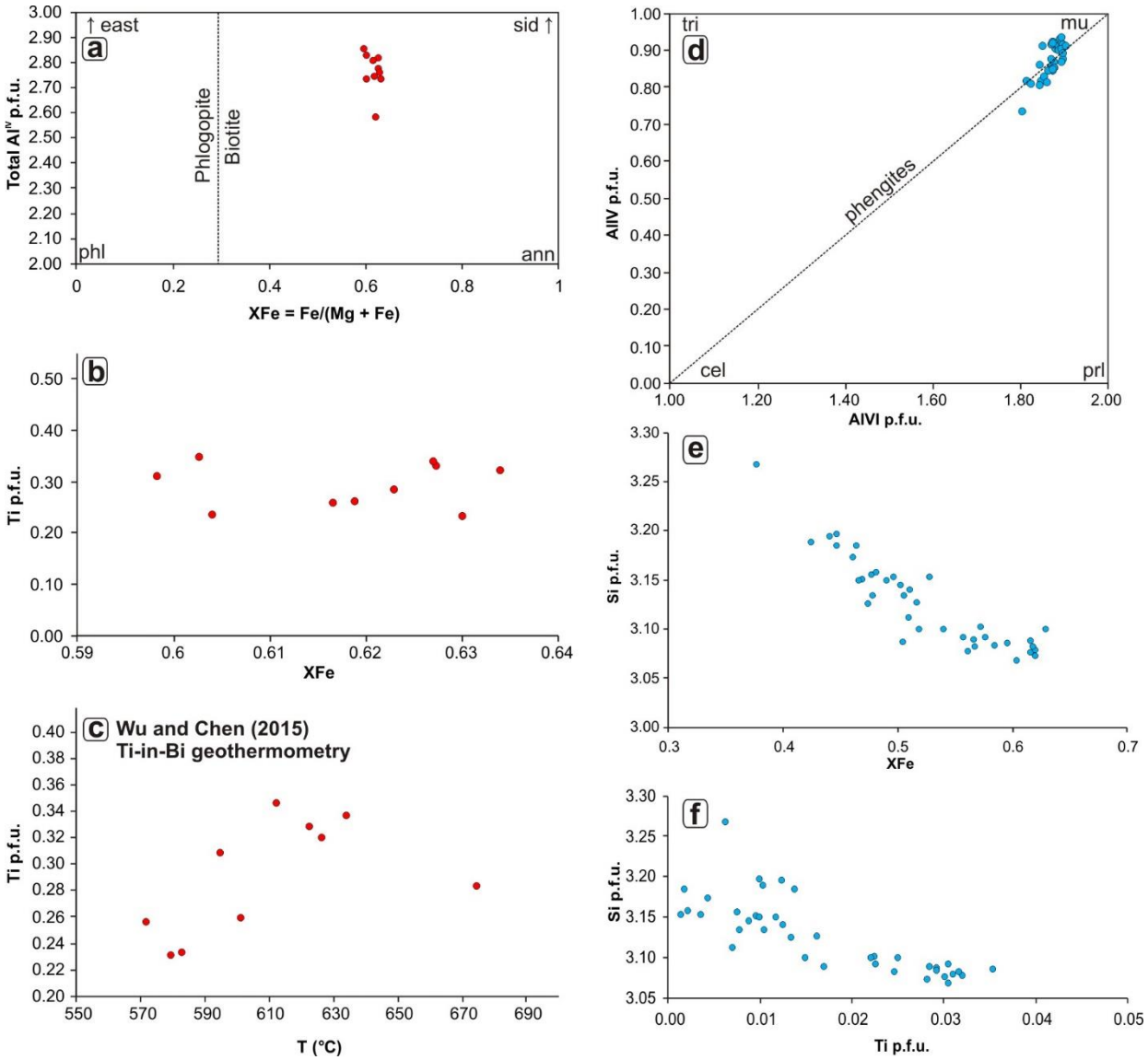

Figure 7.10 - Sample SP65: **(a)** Biotite classification after Deer et al. (1992); **(b)** Compositional variability of biotite in the XFe – Ti p.f.u. diagram; **(c)** Ti-in-biotite geothermometry after Wu and Chen (2015); **(d)** White mica (phengite) classification after Bousquet et al. (2002); **(e)** Variability of XFe of white micas plotted against the Si p.f.u. content; **(f)** Ti content plotted against Si p.f.u. content in white mica.

= 3.23, FeO = 4.29, K_2O = 1.92, Na_2O = 0.06, TiO_2 = 0.55, MnO = 0.04 and O = 0.00. Given the absence of oxides where ferric iron is present as a major constituent (e.g. hematite, magnetite) and the very low ferric iron contents recalculated from andalusite and ilmenite analyses, all iron was assumed to be divalent. The thermodynamic models and THERMOCALC version used are the same of sample CS42a. Compositional isopleths for XFe Bi and XFe Mu were plotted in all fields. The light blue line delimitates the stability field of cordierite, stable at low pressures and high temperatures in the bottom-right corner of the diagram (Fig. 7.11). Andalusite, cordierite and biotite are stable together only in the Cd + Bi + Mu + Pl + Ilm + And and in the Cd + Bi + Ksp + Pl + Ilm + And fields, respectively in the muscovite- and K-feldspar-present parts of the diagram (Fig. 7.11). Both assemblages are predicted to contain at least one feldspar (plagioclase, K-feldspar

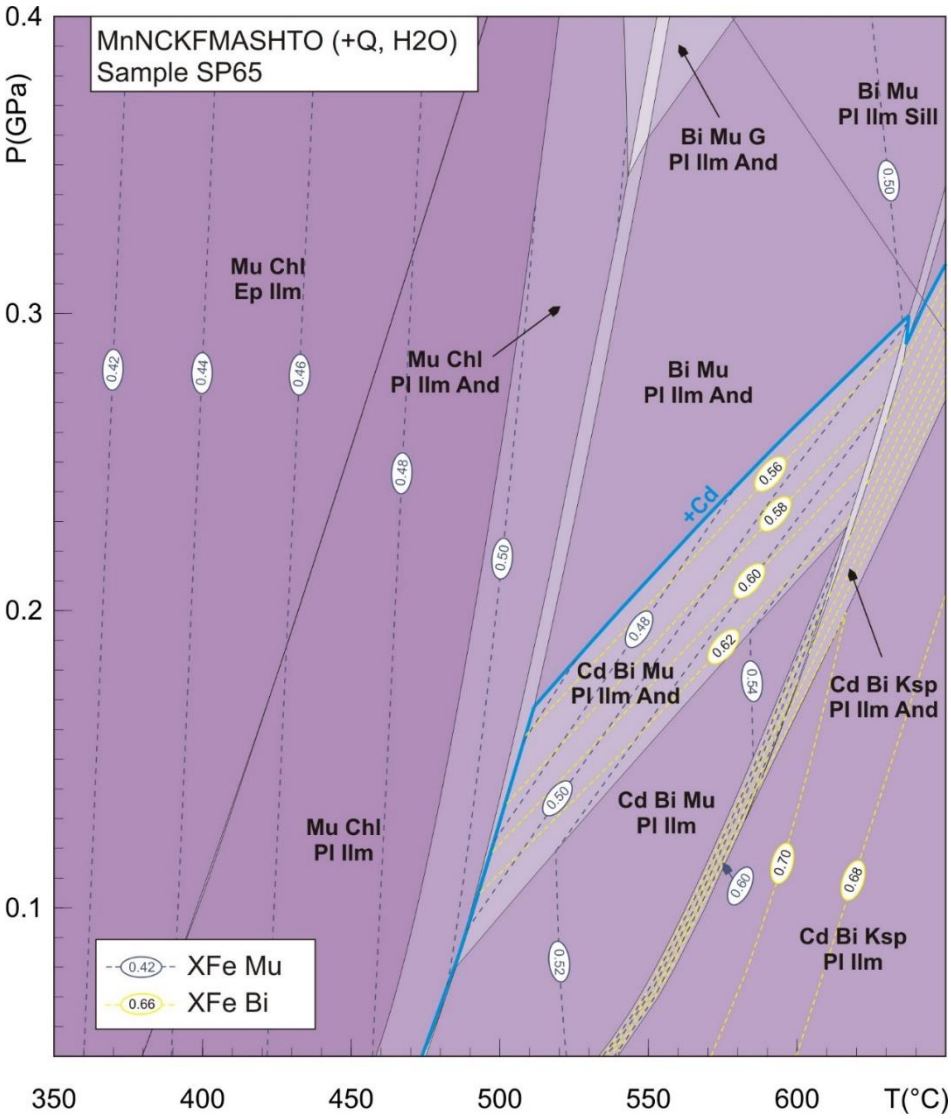

Figure 7.11 - P-T pseudosection modelled for sample SP65 in the MnNC-KFMASHTO system, with H_2O in excess, showing XFe isopleths for biotite (yellow dashed lines) and muscovite (black dashed lines).

or both), which have not been observed in the sample. It is likely that feldspars were completely overprinted by retrograde white mica during the development of the mylonitic foliation and also pseudomorphosed to form some of the observed sericite layers. The Na maps (Fig. 7.8, 7.9) show a Na-enrichment in the white mica bearing foliation, which appear to support this hypothesis. Taking into account the assumption of the original presence of plagioclase and/or K-feldspar stable together with andalusite, cordierite and biotite, the observed XFe of biotite (~0.60 – 0.64) is compatible with the high-grade part of the Cd + Bi + Mu + Pl + Ilm + And field and the high-pressure part of the Cd + Bi + Ksp + Pl + Ilm + And (Fig. 7.11). The absence of muscovite as inclusions in cordierite and andalusite, or in stable association with biotite suggests that peak metamorphism in the sample reached the muscovite-absent region of the diagram; however, it is unlikely that temperatures in excess of 600 – 620 °C were reached within this field, as small temperature increments would have caused a strong increase in the XFe content up to 0.7. Furthermore, with increasing temperature, the andalusite mode decreases very fast until it is completely removed between 620 and 640 °C. Ti-in-biotite geothermometry yield temperatures in

the range 612 ± 29 °C, suggesting low temperature of re-equilibration within this field, consistently below the disappearance of andalusite from the assemblage. This field outlines pressure during metamorphism between 0.12 and 0.29 GPa, which can be further restricted to 0.19 – 0.29 GPa considering the XFe biotite = 0.64 as marking the upper limit of metamorphism (Fig. 7.11). Furthermore, in this pressure interval during cooling of the aureole, (1) andalusite is modally higher than cordierite, as observed in the sample, and (2) cordierite becomes unstable at higher temperatures with respect to andalusite, which could possibly explain why cordierite is completely replaced during retrograde metamorphism whereas andalusite appears relatively fresh.

The assemblage observed on the mylonitic foliation and as retrograde pseudomorphs over the relic high-metamorphic grade assemblage (Mu + Chl + Ilm) is stable below ~ 450 °C in association with plagioclase and below ~ 400 °C associated with epidote. It is likely that sericite layers contain tiny epidote aggregates (saussurite), that might represent the alteration product of plagioclase and the main Ca-bearing phase of the rock. However, the very small grain size challenges the detection limit of the EMPA and only mixed analyses have been obtained from sericitic aggregates. White micas is characterized by a wide compositional range covering the entire range of XFe isopleths calculated for the PT diagram (from ~0.4 to 0.6). In particular, XFe content high as 0.6 -as observed in some white mica grains- are calculated only for T ~ 550-600 °C close to the muscovite-absent fields while low XFe contents have been calculated for low-metamorphic grade assemblages. The coexistence of such a wide compositional range suggest a strong disequilibrium during retrograde metamorphism and that recrystallized old white mica grains coexist with new white mica grains, formed at lower temperatures. It is likely that chlorites in the sample show similar compositional heterogeneities. However, due to the obvious lack of equilibrium for low-temperature assemblages, it is not possible to obtain precise P-T estimates for retrograde metamorphism in this sample. Further studies, involving multi-equilibrium calculation techniques (i.e. Vidal and Parra, 2000), are required to better constrain the retrograde path of the sample

7.3.3 Sample SP78

Petrography and mineral chemistry

Sample SP78 is a mylonitic quartzite, characterized by a silica-rich psammitic composition (Tab. 7.1). A detailed microstructural description is reported in Chapter 6. Here, the main points concerning its metamorphic assemblage are summarized. Sample SP78 feature a mylonitic fabric defined by alternations of recrystallized quartz layers (Fig. 6.5d, 7.12a) and very fine-grained phyllonitic domains (Fig. 6.5b, c). C’ shear bands cross cut this fabric, deflecting the mylonitic

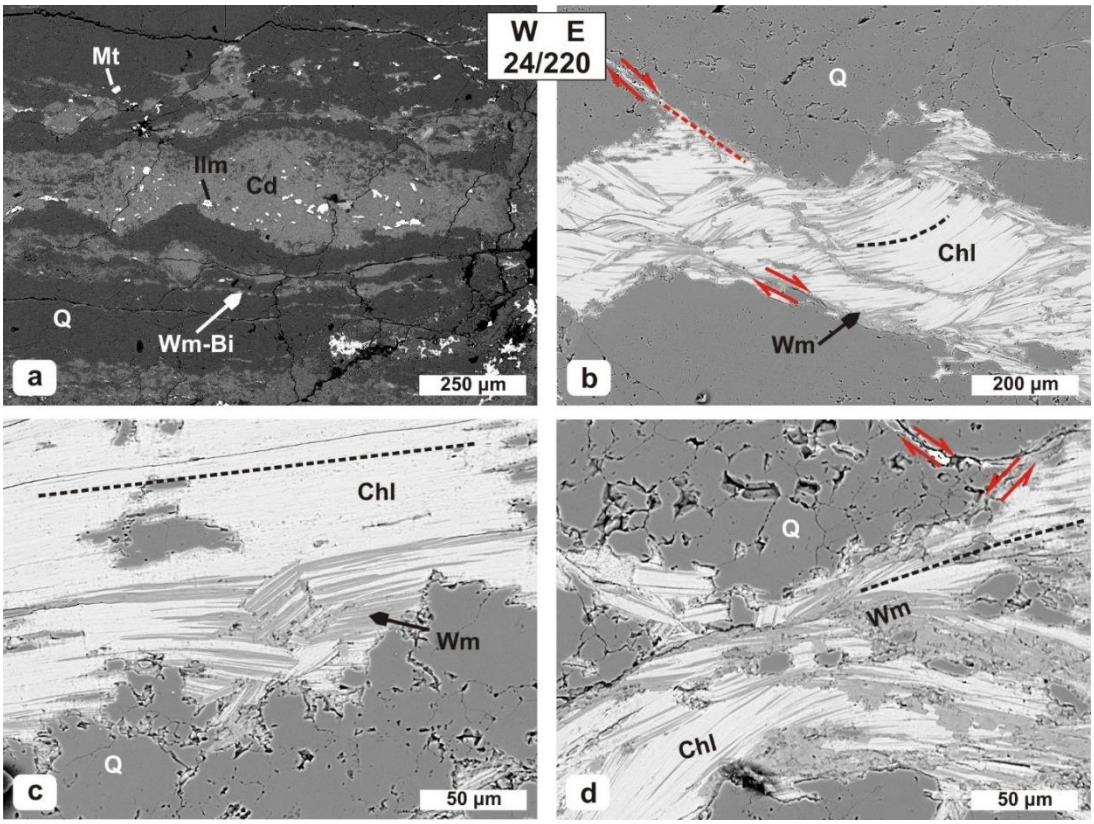

Figure 7.12 - Mineral assemblage of sample SP78. Black dotted lines mark the Sp, red dotted lines and arrows mark C' shear bands. The dip/dip direction of the foliation and microscale sense of shear is provided in the box (top, center); **(a)** Mineral assemblage associated with recrystallized quartz layers aligned on the main foliation: white mica, biotite, ilmenite, magnetite and cordierite pseudomorphs (SEM-BSE); **(b)** Chlorite aggregates within quartz domains characterized by chlorite-white mica intergrowths, aligned on the main foliation and deformed by C' shear bands (SEM-BSE); **(c)** Detail of chlorite-white mica intergrowths on the foliation (SEM-BSE); **(d)** Detail of deformed chlorite-white mica aggregates with new chlorite and white mica grains associated with C' shear bands (SEM-BSE).

foliation. The relic assemblage cordierite + andalusite + biotite is mostly preserved within recrystallized quartz layers; however, cordierite is completely replaced by pinite, showing up to 10 wt% of K_2O and 5 wt% of MgO + FeO, and biotite is mostly pseudomorphosed by chlorite. Andalusite is surprisingly fresh and found as porphyroclasts also in the phyllonitic domains (Fig. 6.5c): analyses show relatively high Fe_2O_3 content (close to 1 wt%) (Appendix E2). Analyses have been attempted on the phyllonitic domains; however, due to the very fine grain size, only mixed phyllosilicate analyses showing variable content of major elements were obtained. The presence of areas with stronger Ca, Na and K peaks and domains where Mg and Fe intensities are higher, coexisting with domains where Si was overwhelming over all other elements suggests that phyllonitic domains likely consist of a mixture of white mica, chlorite, epidote and quartz. Common accessories are represented by tourmaline, zircon, apatite and rutile. Iron oxides (goethite, limonite…) are present as alteration products over magnetite and ilmenite and in cracks/veins.

Relic quartz domains contain large chlorite grains with intergrowths of tiny, lamellar, white mica grains (Fig. 6.5e, 7.12b). Chlorite-white mica aggregates show a shape preferred orientation

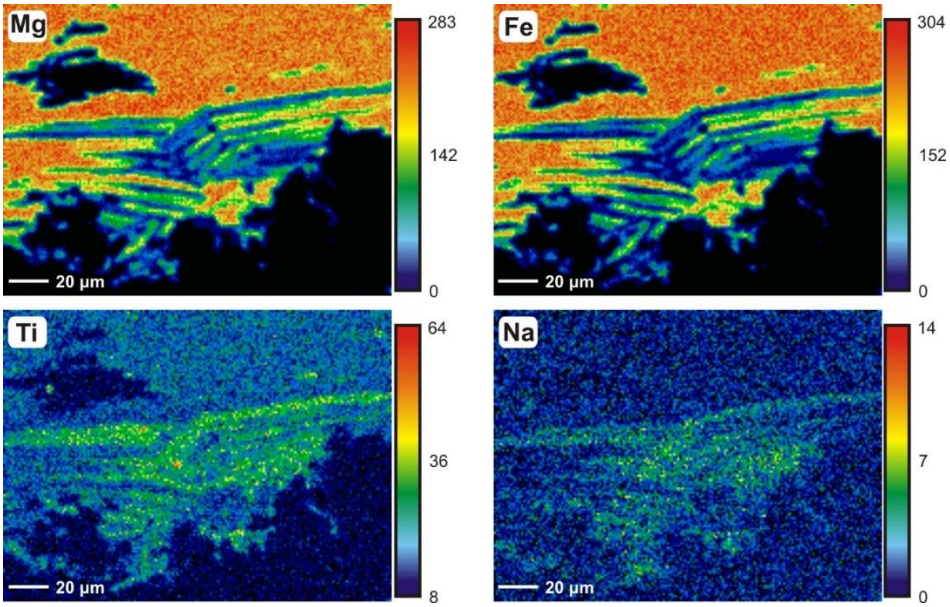

Figure 7.13 - X-Ray maps of the chlorite-white mica intergrowths aligned on the foliation (area located in Fig. 7.12c) for: Mg, Fe, Ti and Na. Fe-Mg poor areas and Ti-Na rich areas correspond to white mica grains.

parallel to the foliation (Fig. 7.12c) with sigmoidal dragging structures close to C' shear bands (Fig. 7.12d). X-Ray maps show a relatively homogeneous composition for chlorite aligned on the foliation 'far' from C' shear bands (Fig. 7.13), whereas closer to C' shear bands, zoning patterns with Fe and Mg rich cores are visible (Fig. 7.14). The observation of chemical variability within white mica in X-Ray maps is hindered by their relatively small size; however, some variability is highlighted by Ti (Fig. 7.14). Chlorite and white mica are often characterized by lamellar textures indicating equilibrium growth (Fig. 7.13). However, commonly C' shear bands are characterized by abundant anhedral white mica and quartz grains with lobate contacts with chlorite suggesting local disequilibrium (Fig. 7.15).

Spot analyses were collected in chlorite-white mica intergrowths. Due to the very fine grain size of white mica and the presence of thin lamellar inclusions in chlorite, many analyses are affected by contamination. Following Vidal and Parra (2000), all chlorite analyses characterized by more

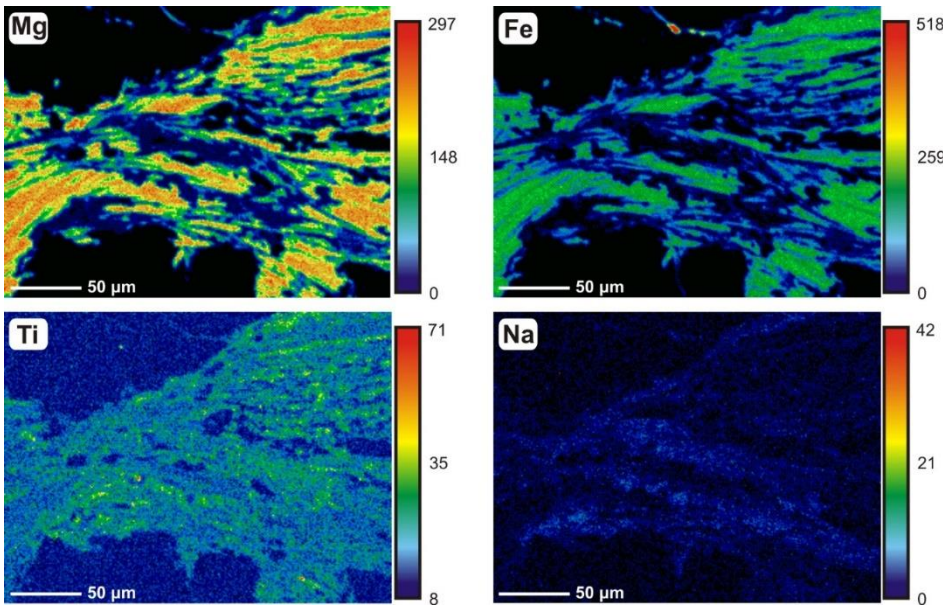

Figure 7.14 - X-Ray maps of the chlorite-white mica intergrowths at the contact between the foliation and C' shear bands (area located in Fig. 7.12d) for: Mg, Fe, Ti and Na. The blue, white mica-bearing, areas in the Mg- and Fe-maps correspond to C' shear bands. Note the Mg and Fe zoning of chlorite (shades of red in Mg-map and shades of green in Fe-map).

than 0.5 wt% K_2O + Na_2O + CaO and all white mica analyses showing more than 0.5 wt% of MnO + TiO_2 were eliminated. Recalculated analyses are shown in Appendix E2 and plotted in Fig. 7.16. White mica composition is characterized by high Al content, plotting close to the muscovite end-member (Fig. 7.16a). The trend towards the trioctahedral component suggests partial contamination by trioctahedral phyllosilicates (i.e. chlorite). The XFe varies mostly between 0.45 and 0.55 (Fig. 7.16b) and XNa is lower than 0.05 (Fig. 7.16c).

Chlorite composition, plotted in a R^{2+} - Si p.f.u. diagram (Fig. 7.16d), shows a linear trend along the $Si_{-1}\square_{-1}$[Fe, Mg] exchange vector, close to the amesite → clinochlore/daphnite mixing vector and characterized by very low proportion of sudoite in the solid solution. The distinction of chlorite analyses based on the microstructural site (C' shear bands and foliation), shows that all chlorites are characterized by variable Al content between 2.65 and 2.85 p.f.u. but that chlorites on C' shear bands are statistically higher in Si (Fig. 7.16e). The XFe is comparable, roughly between 0.56 and 0.58; however, the scattering appears higher for chlorites on C' shear bands (between 0.55 – 0.59; Fig. 7.16f).

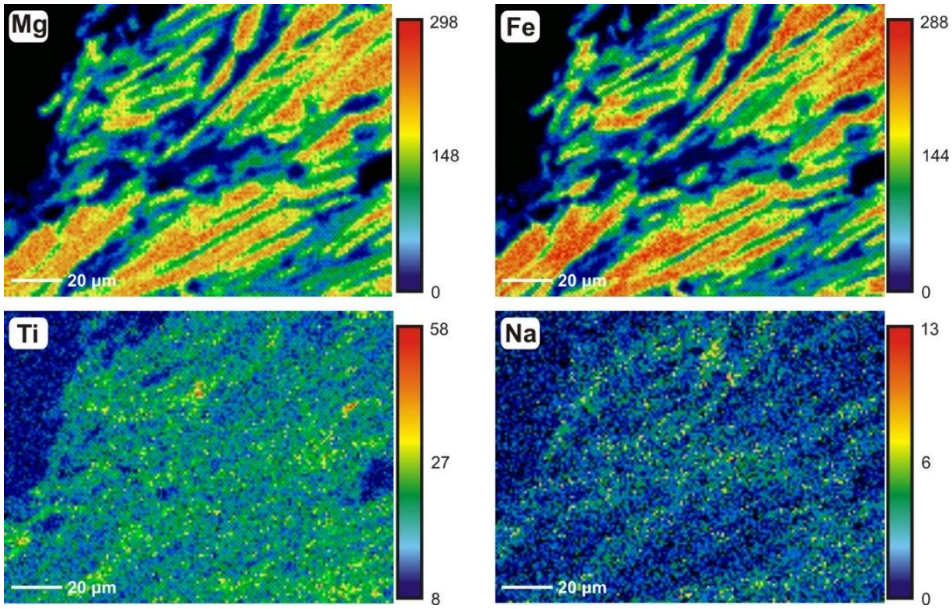

Figure 7.15 - Detail of the map shown in Fig. 7.14. Note the globular white mica aggregates and the lobate contacts between white mica and chlorite. See text for comments.

Pseudosection modelling

A PT pseudosection was computed in the system MnNCKFMASHTO for the analyzed bulk composition (Tab. 7.1), recalculated in mol%, is: SiO_2 = 92.66, Al_2O_3 = 4.50, CaO = 0.37, MgO = 0.46, FeO = 1.01, K_2O = 0.56, Na_2O = 0.03, TiO_2 = 0.18, MnO = 0.01 and O = 0.05. The recalculated O parameter considers an amount of Fe^{3+} corresponding to 10% of ΣFe in wt%, based on the observation of magnetite and the presence of higher Fe^{3+} contents in andalusite. The THERMOCALC version and thermodynamic models used for pseudosection modelling are the same listed for sample CS42a. In spite of the lack of equilibrium for the retrograde assemblage

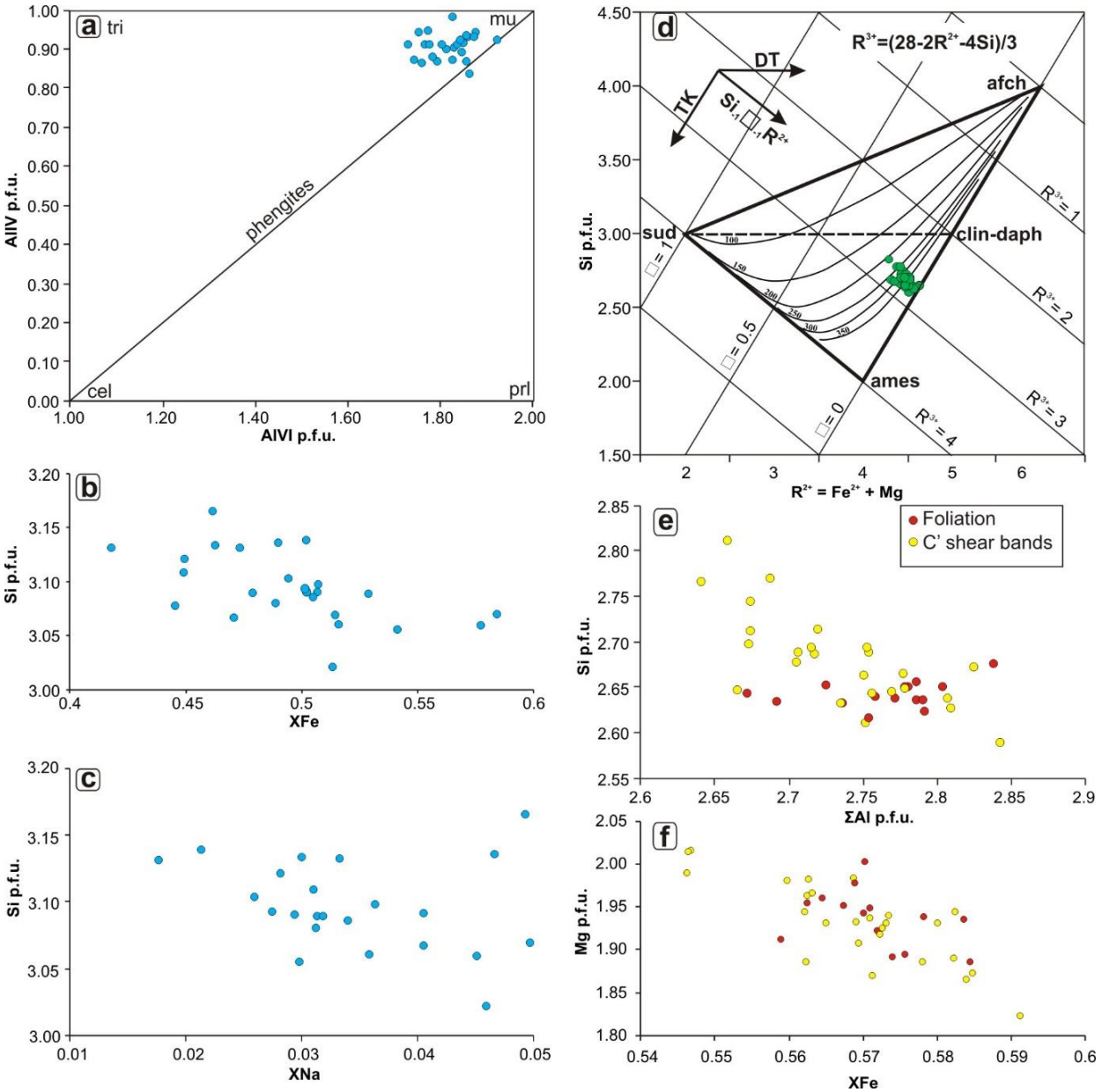

Figure 7.16 - Sample SP78: **(a)** White mica (phengite) classification after Bousquet et al. (2002); Compositional variability of phengite in the **(b)** XFe – Si p.f.u. diagram and **(c)** XNa – Si p.f.u. diagram; **(d)** Chlorite classification on a R^{2+} - Si p.f.u. diagram after Wiewìora and Weiss, 1990 with plotted chlorite isotherms after Bourdelle and Cathelineau (2015). The large black triangle shows the end-member model of Bourdelle et al. (2013) and Inoue et al. (2009), whereas the dashed line demarks the limit of the Vidal and Parra (2000)'s end-member models. See comments in text. Compositional variability of chlorite on the main foliation (red circles) and C' shear bands (yellow circles) in **(e)** ΣAl p.f.u. – Si p.f.u. diagram and **(f)** XMg – Fe p.f.u. diagram.

and the lack of analyses for the peak metamorphic assemblage, the PT pseudosection remains a useful tool to check the PT stability of the observed assemblages for P = 0.05 – 0.4 GPa and T = 350 – 650 °C (Fig. 7.17).

Cordierite, biotite and andalusite are stable together in a small region of the diagram, from 470 to 600 °C up to a maximum pressure of 0.2 GPa (Fig. 7.17). As for sample SP65 (Fig. 7.11), it is likely that plagioclase and K-feldspar have been replaced by sericite and that no obvious pseudomorphs are present; however, due to the lack of information about the high-grade assemblage, the Cd + And + Bi + Mu + Pl + Ilm ± Mt fields are assumed to be representative of

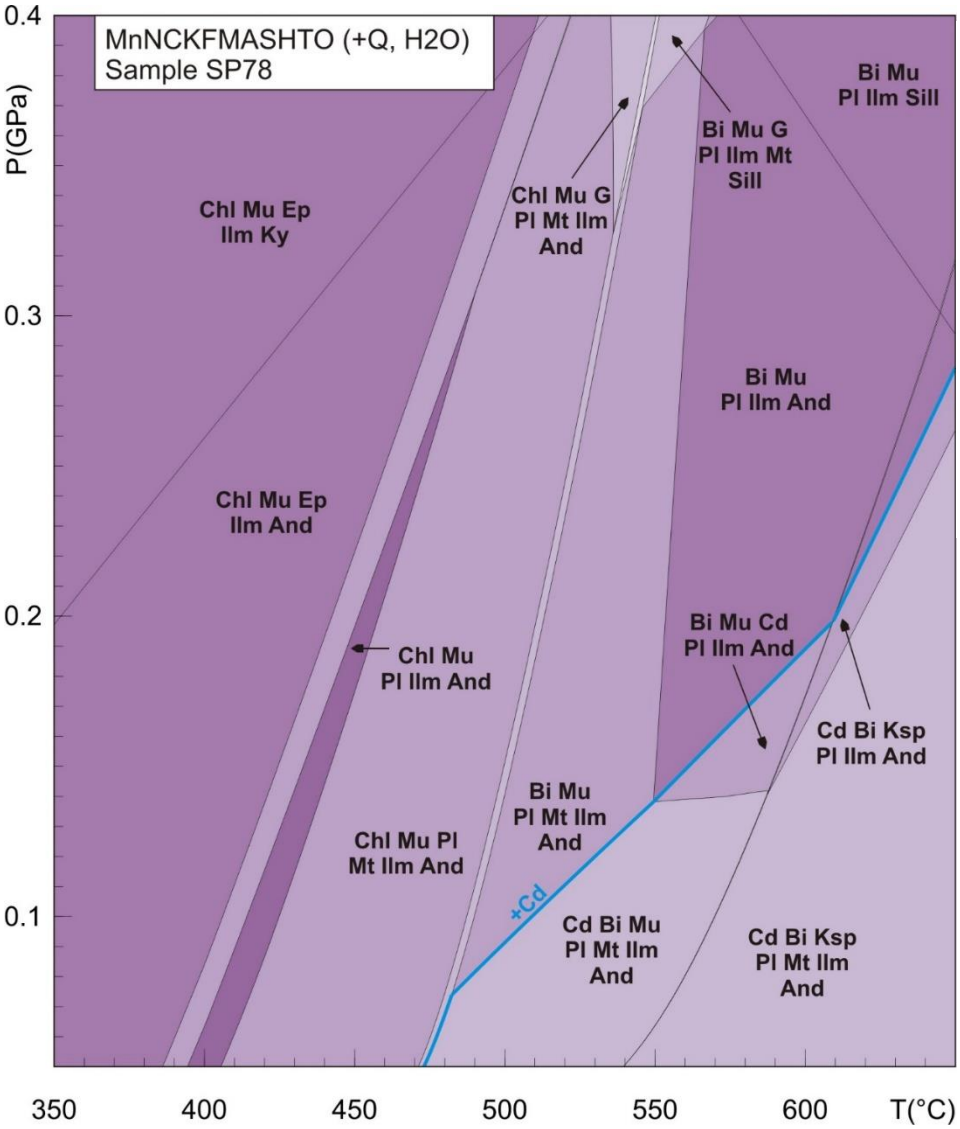

Figure 7.17 - P-T pseudosection calculated for sample SP78 in the MnNCKFMASHTO system, assuming H_2O in excess.

the peak metamorphic conditions reached. Furthermore, the ~600 °C peak temperature estimate roughly corresponds to the maximum estimate for sample SP65, from the same area.

Andalusite stability in all fields is a result of the peraluminous rock composition (Al_2O_3 mol% = 4.50 > [CaO + MgO + FeO + K_2O + Na_2O + TiO_2 + MnO + O] mol% = 2.67) and helps to explain the presence of andalusite as a relatively fresh phase even when enveloped in sericite; however, it should be noted that the 'stable' Al-bearing phase at low-grade conditions is pyrophyllite, which is not present either in the used mixing model for muscovite (i.e. Coggon and Holland, 2002) or as a separate phase in thermodynamic modelling.

Chl + Mu bearing assemblages dominate the low-T (<450 °C) half of the pseudosection. However, little can be said from pseudosection modelling because: (1) chlorite and white mica cover a wide range of compositional variability (Fig. 7.16), (2) textures suggesting local disequilibrium are present and (3) analyses have been performed only on large chlorites wrapped by quartz, due to the very low-grain size of the mylonitic foliation that hindered any possibility of analyzing the composition of phases defining it.

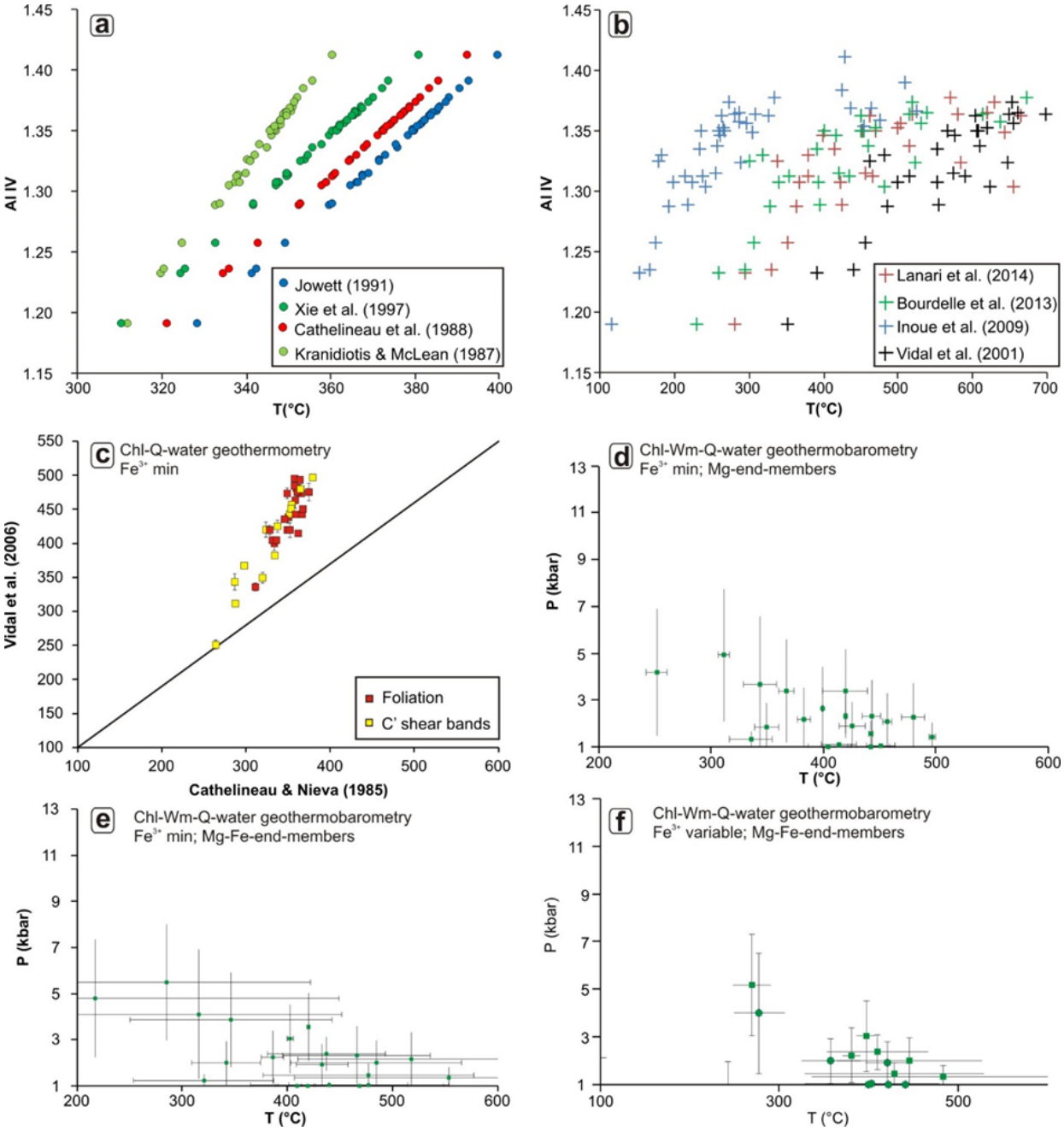

Figure 7.18 - Chlorite geothermometry of sample SP78. Results of various **(a)** empirical and **(b)** semi-empirical geothermometers plotted against the AlIV content. Results exceeding 700 °C have been discarded. **(c)** Results of the Vidal et al. (2006) chlorite geothermometer, with chlorites separated by structural location: foliation (red squares) and C' shear bands (yellow squares). Multi equilibrium calculations after Vidal et al. (2006) obtained considering **(d)** Mg-end members, and **(e)** Mg- and Fe- end members in the white mica-chlorite solid solution models with minimum Fe^{3+}. **(f)** Results of multi-equilibrium calculations using Mg- and Fe- end members and variable Fe^{3+} content.

Chlorite geothermometry: results and discussion

The temperature of equilibration of chlorite indicated by classic empirical geothermometers yielded temperatures comprised between 300 and 400 °C (Fig. 7.18a). Results based on different geothermometers appear shifted, based on the different XFe corrections, but are still characterized by a linear trend of increasing temperatures with increasing Al^{IV} content. Since they are

characterized by similar Al^{IV} content, chlorites found on the main foliation and on C' shear bands yield similar results and have not been distinguished in Fig. 7.18a. The average temperatures obtained are: 342.4 ± 10.4 °C (Kranidiotis and McLean, 1987), 355.3 ± 15.1 °C (Xie et al., 1997), 366.4 ± 15.3 °C (Cathelineau, 1988) and 373.6 ± 15.3 °C (Jowett, 1991), considering the standard deviation as error. Given the caveats of empirical chlorite geothermometers, these temperatures must not be intended as 'real' metamorphic temperatures but represents first order estimations, useful for comparisons with semi-empirical chlorite geothermometry and geothermometry based on thermodynamic datasets.

Temperatures calculated from the application of various semi-empirical geothermometers are characterized by a wide scattering from 100 to 1000 °C (results beyond 700 °C are not shown in Fig. 7.18b), well beyond the chlorite stability field calculated from pseudosection modelling (Fig. 7.17) and the maximum temperature estimate for the Praticciolo (Fig. 7.10c). The isotherms by Bourdelle and Cathelineau (2015) drawn on the R^{2+} - Si p.f.u. diagram shows that most of these chlorite compositions lie outside of the application range of Bourdelle et al. (2013)'s geothermometer (Fig. 7.16d). The same can be said for Vidal et al. (2001)'s and Lanari et al. (2014)'s geothermometers. Both geothermometers appear indeed very sensitive to the proximity of chlorite composition to the amesite → clinochlore/daphnite mixing vector: as the activity of sudoite goes to zero, the effect of Log(K)/ln(K) increases exponentially (Eq. 7.9, 7.10), yielding unreasonably high temperatures. Only some compositions (plotting below the 350 °C isotherm in Bourdelle and Cathelineau, 2015's diagram) yield reasonable results. Only Inoue et al. (2009)'s geothermometer yield lower temperatures, although they appear unrealistically low when compared the empirical geothermometers (mostly between 100 and 300 °C; Fig. 7.18b). This is related to how the Inoue's geothermometer considers $Fe^{3+;}$ indeed, for a fixed composition, the equation of Inoue et al. (2009) predicts a higher amount of vacancies and a poorer R^{2+} content in respect to other geothermometers, therefore underestimating temperatures. Furthermore, Inoue et al. (2009) indicated an upper application limit of T ~ 250 °C for their geothermometer; therefore, the SP78 chlorite compositions are well above its application limit. According to Bourdelle and Cathelineau (2015), chlorite compositions plotting close to the amesite → clinochlore/daphnite series are widespread in metamorphic rocks (e.g. Foster, 1962; Laird, 1988; Vidal and Parra, 2000); however, their temperature of formation cannot be estimated using semi-empirical geothermometers. Furthermore, the observed chlorite composition is well different from the chlorite compositions used for calibration of empirical geothermometers (e.g. Los Azufres; Cathelineau et al., 1988), therefore invalidating empirical geothermometric estimates.

Chl-Q-water geothermometry have been performed on the chlorite dataset (Fig. 7.16d) with chlorite analyses separated according to their microstructural sites (foliation or C' shear bands). Quartz and water activity were assumed as 1, as typical for metapelites (Tajčmanová et al., 2009). A minimum Fe^{3+} value has been recalculated by the macro in Vidal et al. (2006)'s spreadsheet to make chlorite compositions fully explainable with TK, DT, FM and $AlFe^{3+}$ substitutions. Recalculated XFe^{3+} values fluctuate between 0.1 and 0.16, in agreement with 'normal' chlorite compositions (max XFe^{3+} in chlorite ~ 0.3-0.4; Vidal et al., 2005, 2006; Inoue et al., 2009). The results from geothermometric calculations are shown in Fig. 7.18c, where they are confronted with empirical temperature estimates after Cathelineau and Nieva (1985). Error bars are plotted for Vidal et al. (2006)'s geothermometer.

Calculated temperature estimates lie on a single trend between 300 and 500 °C, yielding substantially higher temperature values in respect to Cathelineau and Nieva (1985). Just low temperature values (T< 350 °C; Fig. 7.18c) plot closer to the 1:1 trend, providing slightly higher results in respect to Cathelineau and Nieva (1985). Chlorites analyzed on C' shear bands and on the foliation lie on the same trend showing a partial overlap. However, temperatures estimated from chlorites located close or in correspondence of C' shear bands yield statistically lower temperature estimates (T< 400 °C; Fig. 7.18c).

Multi-equilibrium calculations: results and discussion.

Phengite analyses are characterized by very low- contents of Si (3 – 3.1 p.f.u.; Fig. 7.16b), lying close to the muscovite end-member. Given the very low-pressure values reported for the Calamita Unit (P < 0.2 GPa; Duranti et al., 1992; Caggianelli et al., 2018; this thesis), these values correlate well with the experimental data of Massonne and Schreyer (1987), who found similar Si content for very low-pressure phengites (P < 0.5 GPa).

Based on microstructural criteria suggesting equilibrium, a series of chlorite – phengite pairs were selected for multi-equilibrium calculations (couples listed in Appendix E2). Selected pairs are in strict association on the same microstructure (C' shear band or metamorphic foliation) and are devoid of textures suggesting disequilibrium (e.g. lobate contacts; Fig. 7.15). The application of MET techniques is therefore possible. However, it should be noted that, the chlorite analyses discussed above are characterized by very low vacancy content (X_{sud} = ~ 0.01 – 0.10). According to Vidal and Parra (2000), this determines a large uncertainty on the Mg-sudoite activity and minor changes in the proportion of vacancies cause large variations in the location of equilibria. Therefore, these authors suggested to use only chlorites characterized by $X_{sud} > 0.07$.

Taking into account these limitations, chlorite-phengite-water-quartz multi-equilibrium calculations were performed using Mg-end-members (Fig. 7.18d) and Mg-Fe end-members (Fig. 7.18e, f). Equilibria of Fig. 7.18d and 7.18e are calculated including a minimum amount of Fe^{3+} (Fe^{3+} is automatically increased by a macro until the chlorite composition can be fully modelled in Vidal et al., 2005's end member model). Recalculated XFe^{3+} values fluctuate between 0.1 and 0.16. For the calculation of the equilibria in Fig. 7.18f, a variable amount of Fe^{3+} is assumed: the program runs a macro recalculating equilibria for different values of XFe^{3+} increased by 0.05 steps until the XFe^{3+} value that gives the lower scattering between Eq. 7.12 to 7.15 is found; then, XFe^{3+} of phengite is adjusted to decrease the scatter between chlorite-phengite equilibria. Recalculated XFe^{3+} values are between 0.01 and 0.26. The results show that phengite-chlorite equilibria lie in the LP/HT region of the diagram, with pressure values calculated lying in large part below 0.3 GPa (Fig. 7.18d, e, f). Large uncertainties (± 0.2 GPa and ±100 °C) have been calculated for the selected equilibria. Two are the possible causes for these large uncertainties: (1) contaminated phengite compositions (which show -indeed- high proportions of the trioctahedral component; Fig. 7.16a) and (2) the low vacancy content of chlorite (i.e. sudoite end-member proportion). The comparison between Fig. 7.18e and Fig. 7.18f shows how temperature uncertainties are drastically reduced when a higher amount of XFe^{3+} is considered. This is related to the increase of vacancies in chlorites when Fe^{2+} is recalculated as Fe^{3+}, which consequently reduces the large error associated with low X_{sud} proportion in the solid solution.

Although these results are clearly preliminary, as they suffer from contamination and borderline compositions issues, they are significant because they show that chlorite-phengite compositions are in equilibrium and in good agreement with conclusions of previous authors (Duranti et al., 1992; Caggianelli et al., 2018) and P-T estimates obtained with different methods in this thesis (e.g. PT pseudosection). Therefore, future works should be aimed to the selection of new areas and samples to perform in situ chlorite-phengite calculations should be a priority.

7.4 Discussion

The Calamita Schists experienced LP/HT metamorphism at granulite/pyroxene-hornfels facies conditions. Samples from the Capo Calvo area preserve high-grade metamorphic assemblages with evidence of partial melting, whereas in the Praticciolo area, the greenschist facies retrograde overprint is documented. The prograde and retrograde metamorphic evolution was studied with classical geothermobarometry combined with pseudosection modelling. Peak metamorphic conditions reached in Capo Calvo at P = 0.1-0.3 GPa and T = 650-700 °C. Slightly lower peak temperatures were constrained for the Praticciolo area (600 – 650 °C). The retrograde path is well

recorded in the Praticciolo area where chlorites re-equilibrated between 500 and 300 °C at nearly isobaric conditions. In Capo Calvo, the retrograde path is recorded by diablastic biotite which overgrown the peak assemblage between 400 and 500 °C.

7.4.1 Constraints on the peak metamorphic conditions

Calculated phase diagrams fit reasonably well with the first order petrographic observations, mineral chemistry data and the assumption of excess H_2O during metamorphism. The observed mineral chemistry and recalculated mineral assemblage justify the assumption of $\Sigma Fe = Fe^{2+}$. In Capo Calvo, biotite geothermometry, indicating temperatures up to 710 °C, and phase diagram calculations, indicating partial melting of the observed cordierite + K-feldspar + plagioclase + biotite + ilmenite assemblage between 650 and 700 °C for P = 0.1 – 0.3 GPa, are in perfect agreement with the microstructural evidence of peak metamorphism in the presence of melt provided by: (1) prograde Ti-Mg-zoning of biotite truncated by embayed textures, (2) poikiloblastic feldspars with euhedral biotite (Bi-II) inclusions and (3) lobate patches of K-feldspar penetrating into quartz and biotite grain boundaries. It is likely that Bi II grains grew from a melt and crystallized together with K-feldspar and plagioclase, whereas textures of Bi I grains and quartz indicate disequilibrium with respect to the melt phase.

The peak assemblage in the Praticciolo area is characterized by large biotite-andalusite-cordierite aggregates, whereas poikilitic feldspars are absent. Estimates from biotite geothermometry and pseudosection modelling indicate peak temperatures around 610-630 °C, 70-90 °C lower than Capo Calvo, and similar pressures in respect to Capo Calvo (P = 0.1 – 0.3 GPa). Pseudosection modelling suggest that plagioclase (and likely also K-feldspar) were originally part of the metamorphic assemblage; however, it is likely that they were consumed by white mica producing reactions during retrograde mylonitic deformation.

Pressure estimates are in line with those from previous authors (P_{max} = 0.2 GPa; Duranti et al., 1992; Caggianelli et al., 2018) and supports the hypothesis of Duranti et al. (1992) who suggested a thermal peak reached beyond the muscovite-out reaction at 650 °C. The estimated temperatures from Ti-in-biotite geothermometry (Wu and Chen, 2015) are coherent with the maximum temperature estimates obtained by Caggianelli et al. (2018), up to 700 °C.

7.4.2 The significance of partial melting for the Calamita Schists

The data presented here highlight that peak metamorphic conditions in the Calamita Schists have been reached at T ~ 650 – 700 °C in the presence of melt. This new estimate is higher than the previous results by Duranti et al. (1992) (> 650 °C) and Caggianelli et al. (2018) (~625 °C) and

has interesting outputs for the reconstruction of the geometric and metamorphic evolution of the Calamita Schists contact aureole. Partial melting is an extremely rare process in upper crustal rocks, even around large and 'hot' intrusions, because the rapid cooling of emplaced magmas hinders effective heat transfer to the cold country rocks (Annen, 2011). Local, partially molten rocks may be present only at the contact between intrusives and host rocks (Pattison and Tracy, 1992). According to Bortolotti et al. (2001), boreholes drilled in the area reached depths of about ~100 meters below the sea level without encountering the contact with the granitic body. This may be related to the location of the borehole in correspondence of the eastern flank of the Ripalte antiform (Mazzarini et al., 2011), suggesting that the drilling was performed on a vertical or reverse limb, missing the contact with the intrusive. However, it may also be possible that the top of the intrusives is located at higher depth. In the Ballachulish Igneous Complex (Scottish Highlands), composed of granite and monzodiorite intrusions emplaced at 0.3 GPa, extensive partial melting have been reported up to 500 meters away from the contact between the country rocks and the intrusion (Pattison and Harte, 1988, 1997; Holness and Clemens, 1999). According to Pattison and Harte (1988, 1997), partial melting was controlled by the availability of fluids released from the batholith that supplied water to H_2O consuming melting reactions. In the case of the Calamita Schists, pseudosection modelling, textures and assemblages suggests that partial melting initiated from the Ksp + Pl + Cd + Bi + Q + Ilm field, below the biotite dehydration melting reaction (> 700 °C at 0.2 GPa; Le Breton and Thompson, 1988), similarly to the Ballachulish Complex. Partial melting might have been promoted by fluids released from the underlying thermal anomaly and circulating in the host rocks, as suggested by Caggianelli et al. (2018) or by metamorphic dehydration reactions (i.e. the muscovite-out reaction), which may have acted as an internal source of H_2O saturated fluids.

7.4.3 Retrograde mineral assemblage and metamorphism

Metamorphic estimates have been obtained for the retrograde path from the combined use of classic geothermobarometry and the pseudosection approach. In Capo Calvo, retrograde diablastic biotite overprinting the peak metamorphic assemblage yielded Ti-in-biotite temperatures between 400 and 500 °C. Similar results have been obtained from chlorite geothermometry in the western side (Praticciolo area), where the application of Vidal et al. (2006)'s chlorite geothermometer allowed to estimate temperatures between 300 and 500 °C, based on the assumption of a minimum Fe^{3+} content that allowed to recalculate chlorites using the Vidal et al. (2005)'s end-member model. Semi-empirical chlorite geothermometers yielded, on the other hand, unreasonable results, due to the chlorite compositional range which lies beyond the limits of the applied

geothermometers (i.e. Vidal et al., 2001; Inoue et al., 2009; Bourdelle et al., 2013; Lanari et al., 2014). Empirical geothermometers (i.e. Cathelineau and Nieva, 1985; Kranidiotis and McLean, 1987; Cathelineau, 1988; Jowett, 1991; Xie et al., 1997) yielded temperatures of 300-400 °C that are invariably lower than temperatures estimated using Vidal et al. (2006)'s thermodynamic dataset, due to the calibration range (restricted to T_{max} of 400 °C) and the different chlorite compositions of the datasets used for calibration (characterized by higher vacancy content).

In spite of the limitations of the pseudosection approach to retrograde assemblages, usually showing disequilibrium textures and a wide range of chemical variability, the muscovite XFe range calculated from peak to low temperature conditions for sample SP65 overlaps with the observed white mica compositional range. This suggests that new white mica grains formed continuously during retrograde metamorphism, a condition which is favorable for the application of multi-equilibrium calculations (e.g. Worley et al., 1997; Vidal and Parra, 2000). Furthermore, mica composition is very low in Si, as it is typical for low pressure mica (see Massonne and Schreyer, 1987 and Massonne and Szpurka, 1997). However, due to the very low grain size of chlorite-phengite aggregates, it was possible to obtain analyses of chlorite-phengite pairs only for sample SP78, where, however, phengites show contamination from a trioctahedral mica component. For this reason, the calculated phengite-chlorite equilibria are characterized by large pressure and temperature error range. Despite this, the obtained results are significative, because equilibria are located in the LP/HT part of the P/T diagram for P = 0.1 – 0.4 GPa and T = 250 – 600 °C, overlapping with previous pressure estimates (Duranti et al., 1992; Caggianelli et al., 2018) and results from this thesis (see above). Relatively high pressure results (P > 0.3 GPa) can be discarded because they are inconsistent with the observed mineral assemblage and pseudosection modelling, indicating re-equilibration within the andalusite-field. Therefore, a new sample selection and microstructural investigation aimed to localize microstructures indicative of phengite-chlorite equilibrium constituted by relatively coarse aggregates, is necessary to obtain detailed and reliable P/T estimates for the retrograde path. To summarize, the retrograde path from peak metamorphic conditions occurred at nearly isobaric conditions (P = 0.1 – 0.3 GPa) down to 250 °C – 300 °C.

7.4.4 Metamorphic constraints to EBSD data and microstructures

The P/T conditions recorded in the Calamita Schists reveals a metamorphic evolution from granulite to greenschist facies conditions that occurred during coeval shearing (Papeschi et al., 2018; Chapter 5). This is in agreement with the preliminary recognition of the evolution of quartz microstructures suggesting progressive temperature decrease during deformation, demonstrated qualitatively by Papeschi et al. (2017). As already suggested in chapter 6, EBSD analysis are also

in agreement with the development of low-temperature brittle and semi-brittle structures overprinting higher temperature quartz recrystallization microstructures. The temperature estimates obtained from geothermometry and pseudosection modelling in sample SP65 and SP78 allow to further constrain the conditions under which quartz microstructures developed.

Quartz recrystallization in the layers investigated in samples SP65 and SP78 was accommodated by dislocation creep dominated by the activity of prism <a> associated with rhomb <a> and acute rhomb <a> slip (Fig. 6.3, 6.7). According to several authors, the activity of prism <a> slip is indicative of amphibolite facies conditions (450 – 600 °C; Schmid and Casey, 1986; see also Toy et al., 2008). The recrystallized microstructures, characterized by elongated new grains and subgrains, is indicative of subgrain rotation recrystallization. Taking into account the caveat that temperature is not the only parameter controlling the mechanisms of deformation (Stipp et al., 2010; Menegon et al., 2011; Law, 2014; Viegas et al., 2016) these microstructures are indicative of 400 – 600 °C temperature range, based on a comparison with the microstructures described by Stipp et al., 2002a,b. Such first-order estimates fit well with the temperature estimates derived from pseudosection modelling. In sample SP78, recrystallized layers with Y-max pole figures wrap biotite, muscovite, andalusite and pseudomorphosed cordierite porphyroclasts (Fig. 6.5d). This association is stable between 500 and 600 °C and, close to the peak metamorphic conditions for that sample (see above). On the other hand, in sample SP65, the recrystallized layer is surrounded by a fine-grained white mica-rich mylonitic foliation, which can be bracketed between the brittle-ductile transition for quartz (280 ± 30 °C; Stöckhert et al., 1999) and the limit of the white mica + chlorite field (450 - 500 °C at 0.2 GPa; Fig. 7.11). The lack of evidence for basal <a> slip indicates that recrystallization likely occurred close to the high temperature extreme of this temperature range. In any case, dynamic recrystallization of quartz on the foliation, occurred at medium to high temperature conditions.

EBSD maps of low-temperature features (C’ shear bands) suggest, on the other hand, deformation by cataclasis assisted by infiltration of fluids and growth of new grains by dissolution and precipitation mechanisms (Fig. 6.8, 6.10). Cracks and shear bands are filled with mixtures of chlorite-phengite that are stable in the metamorphic assemblage at T < 450 °C (Fig. 7.17). Estimations on chlorite grains located on C’ shear bands indicate lower temperatures (T = ~300 – 400 °C; Fig. 7.18c) with respect to chlorite grains aligned on the main foliation (T = ~ 400 – 500 °C; Fig. 7.18c). Similar low-temperature estimates from C’ shear bands have been reported for the South Armorican Shear Zone (Berthé et al., 1979; Bukovskà et al., 2016), the Alpine Fault (Toy, 2008) and deformed granitoids (Lister and Snoke, 1984; Gapais, 1989), who suggested a diachronous origin of shear bands in respect to the main foliation. The diachronous origin is also

suggested by the data presented here, which indicates a distinct metamorphic grade associated with the development of shear bands and the mylonitic foliation. It should be stressed, however, that the mixed phyllonitic domains, aligned parallel to the mylonitic foliation, formed also at very low-grade conditions, as indicated by chlorite-sericite-quartz assemblage indicating temperatures < 400 °C. These data indicates that temperature decrease in the Calamita Schists favored strain partitioning into (1) shear bands and (2) phyllonites that progressively localized deformation during temperature decrease from high-grade conditions (Papeschi et al., 2017, 2018).

7.5 Conclusions

In this chapter, metamorphic mineral assemblages of three selected samples, representative of the Calamita Schists, have been correlated with results from classical geothermobarometry and pseudosection modelling. Results from different methodologies have been confronted and discussed. In situ thermobarometric estimates allow to constrain the results of EBSD mapping, performed in the previous chapter. The main findings are:

- The Calamita Schists experienced peak metamorphic conditions at 0.1 – 0.3 GPa and 650 - 700 °C in the eastern part and 600 – 650 °C in the western part.
- In Capo Calvo, peak metamorphism was coeval with partial melting that caused the formation of K-feldspar + biotite melt pools.
- Retrograde metamorphic overprint developed between peak metamorphic conditions down to 300 – 400 °C.
- Chlorite geothermometry indicate that C’ shear bands re-equilibrated at lower temperature conditions (250 – 400 °C) than the surrounding mylonitic foliation (400 – 500 °C), although these results are preliminary and further data are needed to constrain the temperature of re-equilibration of chlorite associated with different microsites.
- Results from chlorite-phengite multi-equilibrium calculations shows low-pressure/high-temperature of metamorphism between 300 – 500 °C and 0.1 – 0.4 GPa. These results are preliminary and further data on chlorite-phengite pairs are needed to obtain better estimates.
- Metamorphic estimates constrain the development of recrystallized quartz layers to 450 – 600 °C and the development of shear bands to the 300 – 400 °C interval. Further data are needed to constrain the development of chlorite-phengite-quartz phyllonites that likely developed at very low-grade conditions.

Chapter 8

Summary and Conclusions

The data presented in this thesis allow me to obtain new insights on the processes that are active at the brittle/ductile transition using a natural study case as a 'natural laboratory' to study and better understand processes occurring from deep to shallow crustal level in shear zones. In this chapter, I draw the major conclusions of this doctorate thesis and discuss the broader implications for deformation mechanisms, structural evolution and geometries occurring at the brittle/ductile transition.

8.1 Summary

8.1.1 Geometry, structural evolution and deformation mechanisms

The data presented here indicate that the Calamita Unit is a 'natural laboratory', where deformation occurred at constant depth (7-10 Km; P < 0.2 GPa) and was steered by the interaction between Late Miocene regional-scale tectonics and a transient (< 1 Ma) and localized thermal anomaly. The development of shear zones in the study area was controlled by temperature decrease and fluid ingress during top-to-the-E shearing. The results of this study are consistent with previous investigations in the area that recognized the coexistence of thermal anomaly and large scale structures related to regional deformation (Mazzarini et al., 2011; Musumeci and Vaselli, 2012; Musumeci et al., 2015) of late Miocene – early Pliocene age (Viola et al., 2018).

Field mapping and structural analysis of key areas (Chapter 4) have revealed a heterogeneous distribution of strain, partitioned in metric high-strain domains, marked by W-dipping foliations, E-W trending lineations and mylonitic bands. Ductile fabrics are overprinted by subhorizontal, non-Andersonian faults with E-W trending slickenlines and characterized by top-to-the-E sense of shear, indicating brittle overprint beyond the brittle/ductile transition. These new data outline that the map-scale structure of the Calamita Unit can be regarded as a large duplex, with several W-dipping high-strain domains, successively refolded by a large-scale antiform (Fig. 4.12; Papeschi et al., 2017).

The reconstructed evolution of high-strain domains, based on microstructural analysis (Chapter 5), EBSD data (Chapter 6) and geothermobarometric estimates (Chapter 7) has been summarized in Fig. 8.1. At peak metamorphic conditions the Calamita Schists were characterized by a K-

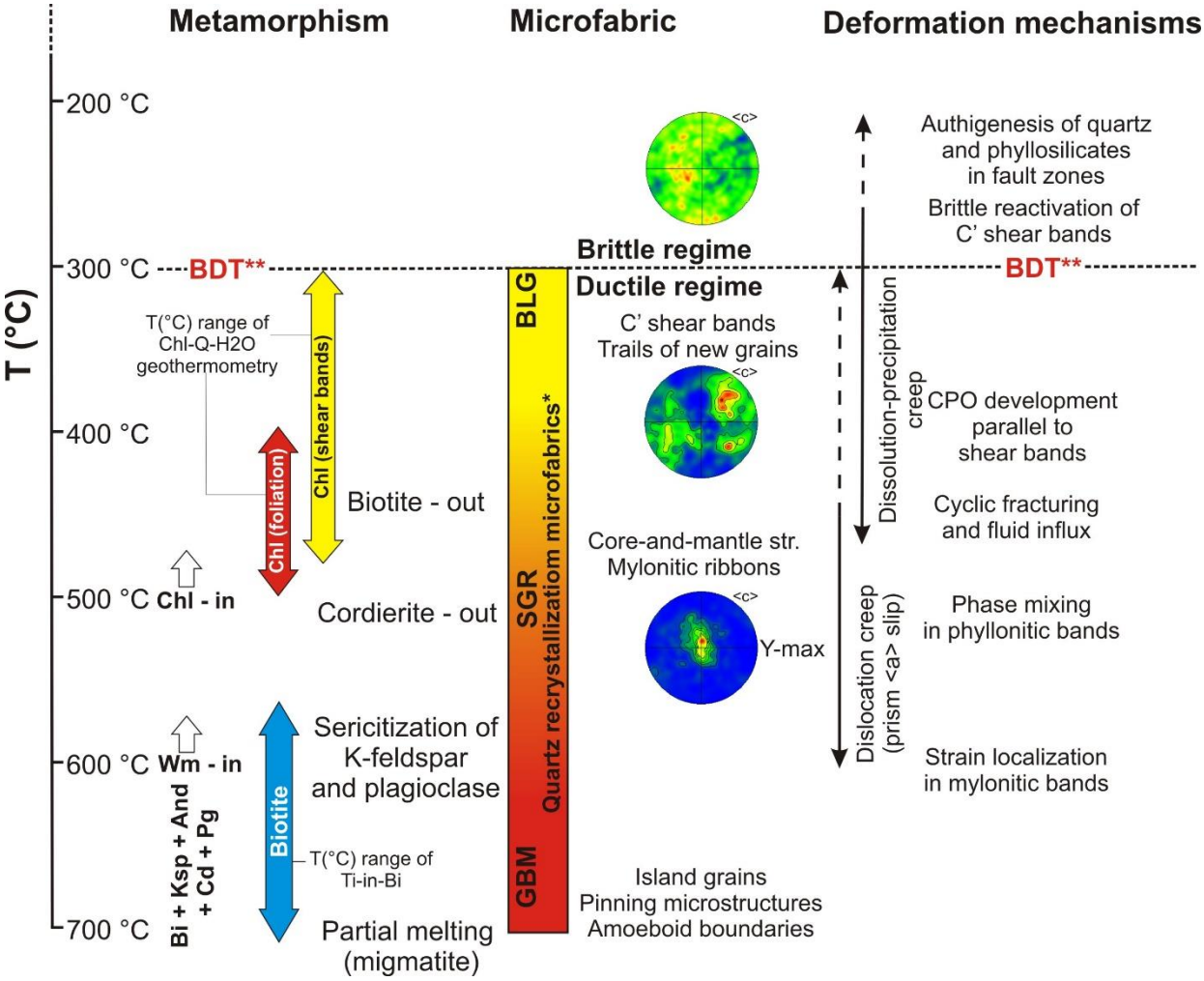

Figure 8.1 - Summary of the metamorphic and microstructural evolution reconstructed in this thesis and reconstructed deformation mechanisms for the Calamita Schists. *: after Stipp et al. (2002a); **: after Stöckhert et al. (1999). See text for comment.

feldspar + biotite + andalusite + cordierite + plagioclase assemblage defining a metamorphic schistosity. Metamorphic estimates from Ti-in-biotite geothermometry and pseudosection modelling (Chapter 7) suggest that high-strain domains experienced peak temperatures of 600 – 700 °C, with poikilitic textures indicating partial melting. Quartz microstructures, analyzed in deformed quartz lenses and mylonitic layers, records the transition from high-temperature fast grain boundary migration to medium- to low-temperature subgrain rotation and bulging recrystallization, tracking continuous deformation during decreasing temperature (Fig. 8.1; Papeschi et al., 2017). The peak, high metamorphic grade assemblage is overprinted by synkinematic biotite, white mica (i.e. sericite) and chlorite grains, indicating fluid influx during medium to low- metamorphic grade retrograde deformation. The retrograde overprint marks the transition from the high-grade schistosity, mainly preserved in lozenges, to localized shear bands and mylonites (Fig. 5.11), displaying 1) intense sericitization of relic metamorphic assemblages, 2) recrystallization of quartz layers, 3) grain size reduction and 4) synkinematic growth of fine-grained quartz and phyllosilicates (Fig. 8.1; Papeschi et al., 2018). Dislocation creep in quartz at

medium-temperature conditions occurred under dominant prism <a> slip associated with secondary rhomb and acute rhomb <a> slip, causing the recrystallization of coarse-grained quartz grains and the development of a mylonitic foliation. Prism <a> slip was likely the dominant slip system active in quartz in the 450 – 600 °C temperature interval (Fig. 8.1). At T < 450 °C, close to the brittle/plastic transition for quartz-feldspathic rocks, competency contrast between large quartz grains and the surrounding mylonitic matrix, consisting of fine-grained phyllosilicates and recrystallized quartz grains, led to the development of conjugate and synthetic C' shear bands. Chlorite geothermometry indicates systematically higher temperatures for chlorite grains aligned on the main foliation (400 – 500 °C) in respect to chlorite grains equilibrated on shear bands, indicating temperatures as low as 300 – 450 °C (Fig. 8.1). C' shear bands opened by fracturing, assisted by infiltration of fluids that deposited tiny quartz grains, with a CPO oriented parallel to shear bands, and phyllosilicate grains. Dissolution-precipitation creep interplayed, likely cyclically, with fracturing assisting propagation of shear bands between the brittle/ductile and brittle/plastic transitions. In the brittle regime, slip was unfavored on the mylonitic foliation and became concentrated on C' shear bands that propagated, developing networks of subhorizontal, non-Andersonian faults associated with Riedel shears (Fig. 8.1). The analysis of recrystallized quartz grains associated with fault zones highlights an interplay between grain size reduction by fracturing, exploiting weak crystallographic planes in quartz such as the rhomb plane, and recrystallization of fine-grained quartz grains and phyllosilicates by dissolution-precipitation creep. This suggests that fluid-assisted deformation for quartz was active during deformation in the semibrittle and brittle regime.

8.2 Implications

8.2.1 The Calamita Schists: analogue of crustal shear zones

The structural and microstructural analysis of the Calamita Unit demonstrates an evolution characterized by rheological transitions triggered by temperature decrease over time at constant depth. The recognized deformation processes are analogue to processes occurring at depth at different temperature and recorded within exhumed rocks in crustal shear zones. A comparison with the evolution of crustal shear zones is illustrated in Fig. 8.2.

It is widely accepted that rocks exhumed in crustal shear zones cross three major rheological transitions in the crust at different depth: (1) the change in deformation style from distributed to localized (i.e. localized/distributed transition, 500 – 600 °C), (2) the brittle/plastic transition and (3) the brittle/ductile transition (~ 300 °C) (see Cooper et al., 2017 and references therein). In the investigated Calamita Schist study case, these rheological transitions are well recorded and

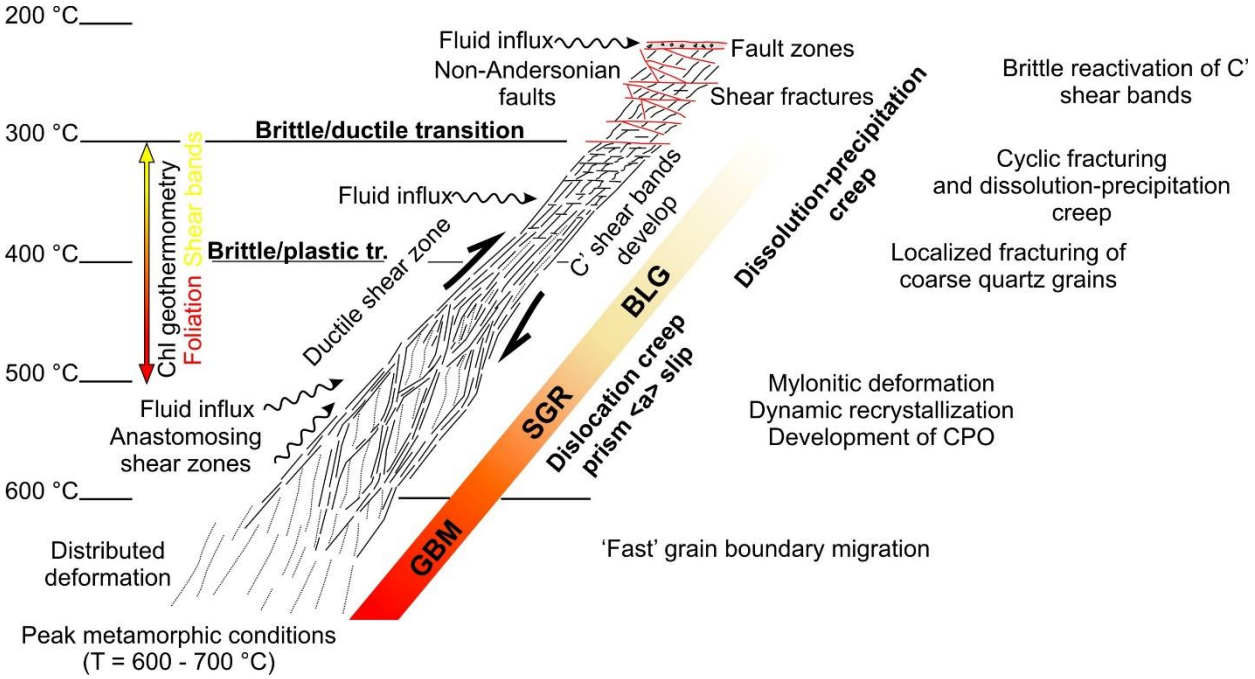

Figure 8.2 - Model of crustal shear zone extrapolated from data gathered in this thesis. Detailed comment in text.

correspond to (1) the switch from a high-grade foliation to localized shear zones, marked by the development of a mylonitic foliation with retrograde overprint between 450 and 600 °C, (2) the development of C' shear bands and localized fracturing in coarse-grained quartz layers and (3) the transition from shear zones to brittle faults with the same sense of shear (Fig. 8.2). Temperature and fluid circulation controlled (1) the switch from grain boundary migration to bulging and subgrain rotation and hence progressive grain size reduction, determining localization of strain into shear zones, (2) the onset of distributed brittle deformation and (3) the switch from semibrittle to brittle conditions at ~ 300 °C for quartz (Fig. 8.2; Stöckhert et al., 1999).

Many models predict that the brittle/ductile transition is mainly controlled by the activation of frictional mechanisms in the brittle regime and the deactivation of crystal-plastic mechanisms that were active for T > 300 °C. However, this thesis highlights the role of fluid-rock interaction assisting the transition from purely plastic to purely brittle deformation mechanisms. Indeed, the interplay between fracturing and infiltrations of fluids, between the brittle/ductile and brittle/plastic transitions (T ~ 300 – 400 °C), determined the development of C' shear bands, which became a preferred site for the nucleation of non-Andersonian fault zones in the brittle regime (Fig. 8.2). This reconstruction outlines a different modality of brittle structures development with respect the current models of shear zone evolution, predicting failure and propagation of faults subparallel to the mylonitic foliation, in detachments (e.g. Lister and Davis, 1989) and thrusts (e.g. Ebert et al., 2007). It demonstrates that under brittle conditions fault planes completely discordant with respect to the ductile fabric may nucleate in the same kinematic regime, as shown in Fig. 8.2.

8.2.2 Deformation mechanisms in the semibrittle regime

The microstructures presented in this study highlight the role played by the interplay between (1) localized fracturing and (2) fluid-rock interaction for strain partitioning in quartz-rich in the semibrittle regime, confirming observations from earlier studies (e.g. Kjøll et al., 2015; Bukovskà et al., 2016) and contributing to our refined understanding of dissolution-precipitation creep processes.

In the semibrittle regime, strain hardening may cause embrittlement and pervasive fracturing of 'stiff' quartz grains at T > 300 °C, while the surrounding mylonitic matrix is still deforming in a plastic way (Fig. 6.15). The orientation of fractures in quartz shows that the exploited direction does not necessarily correspond to a plane of weakness, such as the rhomb, as shown by van Daalen et al. (1999) and Kjøll et al. (2015) but may also correspond to C' shear bands, whose orientation is controlled by the vorticity of the system, similarly to the study case described by Menegon et al. (2008), who interpreted shear bands as related to localized pure shear. Conjugate shear bands, accommodating strain along the directions of maximum shear stress, may develop pervasively in 'stiff' quartz grains, where their propagation is not inhibited by the presence of strong anisotropies such as the foliation (Papeschi et al., 2018). Fracturing enhances fluid infiltration, assisting nucleation of arrays of new quartz grains and phyllosilicate grains by dissolution-precipitation creep. The coexistence of fractures and rigid-body rotation with growth of new grains sealing microfractures witnesses the cyclic interaction between brittle and fluid-assisted ductile deformation, probably controlled by fluctuations in pore fluid pressure and strain rate (Fig. 6.15). Dissolution-precipitation creep is an efficient mechanisms which has been demonstrated in this study to be active both in localized shear bands in the ductile regime and in fault zones under brittle conditions. Its activity causes localized grain size reduction and substitution of large quartz grains with aggregates of finely recrystallized grains and new phases, such as phyllosilicates. Moreover, the effect of dissolution-precipitation creep over CPOs is dual, causing the progressive destruction of a pre-existing CPO and the development of a new fabric which may be characterized by (1) weakly oriented new grains, in agreement with Kjøll et al. (2015) and Takeshita and Hara (1998), or a newly formed CPO, in agreement with Bons and den Brok (2000). Moreover, the results of this study offer an additional mechanism to explain the development of CPOs by dissolution-precipitation creep, related to the preferred growth of new grains in dilatant sites controlled by growing shear bands.

8.2.3 Strain softening at the brittle/ductile transition

The evidence of high differential stress values estimated from quartz paleopiezometry and relatively low differential stress values estimated from fault zones has led many authors to interpret the brittle/ductile transition as the strongest load-bearing element of the crust (e.g. Behr and Platt, 2014), where high-values of differential stress are required to accommodate deformation.

Quartz paleopiezometric estimates obtained in this study are in first order consistent with Behr and Platt (2014), showing peak differential stresses reaching 70-100 MPa and strain rate values between 10^{-12} and 10^{-13}, associated with quartz layers recrystallized by subgrain rotation at mid-crustal conditions (Fig. 8.1). Furthermore, shearing at low-metamorphic grade conditions is associated with fracturing localized in large quartz grains, indicating that differential stresses might have been, locally, high enough to trigger brittle deformation (e.g. 200 – 250 MPa; based on experiments of fracturing for single quartz crystals; Tarantola et al., 2012; Diamond and Tarantola, 2015). On the other hand, this study has shown that dislocation creep was not the primary mechanism controlling deformation at the brittle/ductile transition, as shear bands, shear fractures and faults were actively characterized by the interaction between brittle fracturing and dissolution-precipitation creep. Nucleation of new fine-grained quartz and phyllosilicate grains assisted strain softening of shear bands promoting slip within otherwise 'stiff' quartz domain. The sole influx of fluids into growing shear bands might have promoted fracture propagation by stress corrosion and/or subcritical crack growth, lowering the yield strength required for failure. As a whole, such processes might have significantly reduced the shear stress required to accommodate slip in shear bands while the total rock strength might have been reduced by the increasing number of shear bands (Fig. 8.2). Analogously, the activity of dissolution in fault zones, might have significantly lowered the strength required for failure and assisted frictional sliding.

The widespread activity of dissolution-precipitation mechanisms around in the semibrittle regime, indicate that these mechanisms control the rheology, in agreement with Niemeijer and Spiers (2005). Thus, dissolution-precipitation mechanisms effectively assist the switch from crystal-plastic to brittle deformation, reducing rock strength by (1) grain size reduction, (2) authigenesis of phyllosilicates, and frictional strength promoting (3) fracture propagation and (4) slip on growing fractures. Consequently, dissolution-precipitation creep represents a major strain softening mechanism effectively allowing deformation to occur at lower differential stress and assisting the change in deformation mode at the brittle/ductile transition (Fig. 8.2).

8.2.4 Role of precursory structures for non-Andersonian faulting

There are several mechanisms commonly invoked to explain the development of non-Andersonian faults, such as elevated pore fluid pressures or development of very weak, low-friction fault gouge (e.g. Collettini et al., 2009). This thesis highlights the role played by ductile structures as precursors for non-Andersonian faults formed in the same kinematic framework in the brittle regime (Fig. 8.2). This is in line with other case studies that observed the reactivation of metamorphic foliations and shear bands in several orogenic belts (e.g. Butler et al., 2008; Massironi et al., 2011; Bistacchi et al., 2012). However, differently from these authors, only the reactivation of shear bands, favorably oriented for slip with respect to the metamorphic foliation, as arrays of subhorizontal faults was observed (Papeschi et al., 2018). A similar situation was observed in the shear failure experiments performed by Ikari et al. (2015) on slates with foliation oriented at different angle with respect to the imposed shear stress (e.g. Fig. 4.11d). These authors observed the early nucleation of faults across the foliation, caused by the highly unfavorable orientation of the foliation, in an orientation similar to the shear bands recognized in this study. Therefore, the presence of shear bands, which may be possibly reactivated, acts as a preferred ductile precursor enhancing strain localization from the early stages of brittle deformation. The mylonitic foliation, on the other hand, is unfavorably oriented for reactivation and did not fail under brittle conditions. The data gathered in this study represents, hence, an extension of the experimental observations by Ikari et al. (2015) to a natural study case showing the importance of the orientation of ductile structures at the brittle/ductile transition, which may favor reactivation of the foliation, as in classic crustal shear zone models (e.g. Lister and Davis, 1989), shear bands (this study) or both (e.g. Bistacchi et al., 2012). The frequent presence of phyllosilicate-rich foliations with different orientation in metamorphic units is likely to influence deformation style, geometry of brittle structures and the overall strength of the brittle crust during deformation of metamorphic rocks.

8.3 Conclusions

- I have presented a case study of shear zone development in quartz-feldspathic rocks, where temperature controlled the switch of major deformation mechanisms, tracked by the transition between different quartz deformation mechanisms, and therefore localization of deformation and the development of shear zones. This led to a transition from a high-grade foliation to localized shear bands and, finally, from mylonitic shear zones to brittle, non-Andersonian faults.

8. Summary and Conclusions

- At the brittle/plastic transition, strain partitioning between domains characterized by different competence controls localized embrittlement and the development of localized shear bands in 'stiff' domains. Fluid circulation may enhance stress corrosion and assist fracture propagation, promoting further strain localization within shear bands and growth of 'soft' phyllosilicates by dissolution-precipitation creep. Dissolution-precipitation creep may interplay cyclically with fracturing responding to strain rate and fluid pressure fluctuations and hence assisting further fracturing of 'stiff' domains.
- Dissolution-precipitation creep, coupled with microfracturing, may cause the localized disruption of pre-existing CPOs. New grains may nucleate with no preferred orientation or with a new CPO controlled by the rate and direction of opening of dilatant sites, e.g. with <c> axis oriented parallel to C' shear bands.
- Dissolution-precipitation creep coupled with fracturing represents an effective mechanism acting in the semibrittle regime, which significantly reduce the strength of rocks by assisting fracturing and propagation of fractures, deposing softer fine-grained phases, and reducing friction with the crystallization of 'soft' phyllosilicates. Under fluid saturated conditions, this mechanism may control the rheology of the system, assisting the transition from crystal-plastic deformation to frictional sliding and controlling the geometries of the structures developed.
- Non-Andersonian faults may propagate at the brittle/ductile transition taking advantage of pre-existing foliations. The orientation of ductile precursors determines whether the metamorphic foliation will be reactivated or not and hence controls the geometries of faults developed in the brittle regime. Shear bands may represent a preferred site for fault nucleation with respect to the metamorphic foliation and promote the development of non-Andersonian faults, cross cutting the metamorphic foliation.

References

Labs and Facilities

Institut für Mineralogie und Kristallchemie (Universitat Stuttgart). Azenbergstraße 18, 70174 Stuttgart, Germany.

Microtectonics laboratory. *Dipartimento di Scienze della Terra* (Università di Pisa), via Santa Maria 53, 56126 Pisa (PI), Italy.

Petrology and volcanology Lab. *Istituto Nazionale di Geofisica e Vulcanologia* (INGV), via della Faggiola 32, 56126 Pisa (PI), Italy.

Plymouth Electron Microscopy Centre (PEMC). University of Plymouth, Drake Circus, Plymouth PL4 8AA, United Kingdom.

Software

AX. A program to calculate activities of mineral endmembers from chemical analyses (usually determined by electron microprobe). https://www.esc.cam.ac.uk/research/research-groups/research-projects/tim-hollands-software-pages/ax

AZtec. EBSD acquisition software. Oxford Instruments ©. https://www.oxford-instruments.com/products/microanalysis/ebsd/aztechkl-ebsd-software.

CorelDRAW X4. Vector graphics software. Corel Corporation ©, 2008. https://www.coreldraw.com/en/pages/coreldraw-x4/

HKL CHANNEL 5. EBSD post-processing software. Oxford Instruments ©. https://www.oxford-instruments.com/products/microanalysis/ebsd/ebsd-post-processing-software.

- Tango. Program for processing EBSD maps.
- Mambo. Program for plotting pole figures and inverse pole figures.
- Salsa. Program for plotting orientation distribution functions.

ImageJ 1.x. Open source image processing program. https://imagej.nih.gov/ij/download.html

MINCALC-V5. Software tool for mineral analyses data processing. Available upon request to H.J. Bernhardt.

References

OpenStereo: open source, cross-platform software for structural geology analysis. http://www.igc.usp.br/index.php?id=391

Perple_X. A collection of Fortran77 programs for calculating and displaying phase diagrams, phase equilibria, and thermodynamic data. http://www.perplex.ethz.ch/

Rick Allmendinger's stuff (Cornell University). A collection of Structural geology and education programs. http://www.geo.cornell.edu/geology/faculty/RWA/

- FaultKin. A program for analyzing fault slip data.
- Stereonet. Program for stereographic projection.

THERMOCALC. A thermodynamic calculation program that uses an internally-consistent thermodynamic dataset. http://www.metamorph.geo.uni-mainz.de/thermocalc/

Cited References

Adams, B. L., Wright, S. I., & Kunze, K. (1993). Orientation imaging: the emergence of a new microscopy. *Metallurgical Transactions A*, *24*(4), 819-831.

Agard, P., Vidal, O., & Goffé, B. (2001). Interlayer and Si content of phengite in HP–LT carpholite-bearing metapelites. *Journal of Metamorphic Geology*, *19*(5), 479-495.

Ahrendt, H. (1980). Die Bedeutung der Insubrischen Linie fur den tektonischen Bau der Alpen. *Neues Jahrbuch Geologische Paleontologische Abhandlungen*, *160*, 336-62.

Allmendinger, R. W. (2005). Stereonet. Program for stereographic projection.

Allmendinger, R.W., Marrett, R.A., Cladouhos, T. (1992) FaultKin. A program for analyzing fault slip data.

Anderson, E. M. (1951). *The dynamics of faulting and dyke formation with applications to Britain*. Hafner Pub. Co.

References

Annen, C. (2011). Implications of incremental emplacement of magma bodies for magma differentiation, thermal aureole dimensions and plutonism–volcanism relationships. *Tectonophysics*, *500* (1-4), 3-10.

Atkinson, B. K. (1984). Subcritical crack growth in geological materials. *Journal of Geophysical Research: Solid Earth*, *89*(B6), 4077-4114.

Austrheim, H. (1987). Eclogitization of lower crustal granulites by fluid migration through shear zones. *Earth and Planetary Science Letters*, *81*(2-3), 221-232.

Austrheim, H., & Boundy, T. M. (1994). Pseudotachylytes generated during seismic faulting and eclogitization of the deep crust. *Science*, *265*(5168), 82-83.

Axen, G. J., & Selverstone, J. (1994). Stress state and fluid-pressure level along the Whipple detachment fault, California. *Geology*, *22*(9), 835-838.

Bailey, J. E., & Hirsch, P. B. (1962). The recrystallization process in some polycrystalline metals. *Proc. R. Soc. Lond. A*, *267*(1328), 11-30.

Barberi, F., & Innocenti, F., (1965). Studio chimico-petrografico di un anfibolite rinvenuta negli scisti termometamorfici di Capo Calamita (isola d'Elba). *Bollettino della Società Geologica Italiana, 84*, 13-34.

Barberi F., Giglia G., Innocenti F., Marinelli G., Raggi G., Ricci C.A., Squarci P., Taffi L. & Trevisan L. (1967a) - Carta geologica dell'isola d'Elba. Scala 1:25.000. *C.N.R. Roma*.

Barberi, F., Innocenti, F., & Ricci, C. A. (1967b). Il complesso scistoso di Capo Calamita (Isola d'Elba). *Atti Soc. Tosc. Sci. Nat., Mem., Serie A 74*, 579– 617.

Barberi F., Dallan Nardi L., Franzini M., Giglia G., Innocenti F., Marinelli G., Raggi R., Ricci C.A., Squarci P., Taffi L. & Trevisan L. (1969) - Foglio 126 (Isola d'Elba). Note illustrative della Carta Geologica d'Italia alla scala 1:100.000. *Serv. Geol. d'It*., 32 pp.

References

Barboni, M., & Schoene, B. (2014). Short eruption window revealed by absolute crystal growth rates in a granitic magma. *Nature Geoscience*, *7*(7), 524.

Barboni, M., Annen, C., & Schoene, B. (2015). Evaluating the construction and evolution of upper crustal magma reservoirs with coupled U/Pb zircon geochronology and thermal modeling: A case study from the Mt. Capanne pluton (Elba, Italy). *Earth and Planetary Science Letters*, *432*, 436-448.

Beacom, L. E., Holdsworth, R. E., McCaffrey, K. J. W., & Anderson, T. B. (2001). A quantitative study of the influence of pre-existing compositional and fabric heterogeneities upon fracture-zone development during basement reactivation. *Geological Society, London, Special Publications*, *186*(1), 195-211.

Beeler, N. M., Simpson, R. W., Hickman, S. H., & Lockner, D. A. (2000). Pore fluid pressure, apparent friction, and Coulomb failure. *Journal of Geophysical Research: Solid Earth*, *105*(B11), 25533-25542.

Behr, W. M., & Platt, J. P. (2011). A naturally constrained stress profile through the middle crust in an extensional terrane. *Earth and Planetary Science Letters*, *303*(3-4), 181-192.

Behr, W. M., & Platt, J. P. (2013). Rheological evolution of a Mediterranean subduction complex. *Journal of Structural Geology*, *54*, 136-155.

Behr, W. M., & Platt, J. P. (2014). Brittle faults are weak, yet the ductile middle crust is strong: Implications for lithospheric mechanics. *Geophysical Research Letters*, *41*(22), 8067-8075.

Behrmann, J. H., & Mainprice, D. (1987). Deformation mechanisms in a high-temperature quartz-feldspar mylonite: evidence for superplastic flow in the lower continental crust. *Tectonophysics*, *140*(2-4), 297-305.

Bell, T. H., & Cuff, C. (1989). Dissolution, solution transfer, diffusion versus fluid flow and volume loss during deformation/metamorphism. *Journal of Metamorphic Geology*, *7*(4), 425-447.

References

Benn, K., Odonne, F., & de Saint Blanquat, M. (1998). Pluton emplacement during transpression in brittle crust: new views from analogue experiments. *Geology*, *26*(12), 1079-1082.

Berger, A., & Herwegh, M. (2004). Grain coarsening in contact metamorphic carbonates: Effects of second-phase particles, fluid flow and thermal perturbations. *Journal of metamorphic Geology*, *22*(5), 459-474.

Berman, R. G. (1988). Internally-consistent thermodynamic data for minerals in the system Na2O-K2O-CaO-MgO-FeO-Fe2O3-Al2O3-SiO2-TiO2-H2O-CO2. *Journal of petrology*, *29*(2), 445-522.

Berman, R. G. (1991). Thermobarometry using multi-equilibrium calculations; a new technique, with petrological applications. *The Canadian Mineralogist*, *29*(4), 833-855.

Bernhardt, H. J. (2007). MINCALC-V5, a software tool for mineral analyses data processing. *Acta Microscopica*, *16*(1-2), 43-44.

Berthé, D., & Brun, J. P. (1980). Evolution of folds during progressive shear in the South Armorican Shear Zone, France. *Journal of Structural Geology*, *2*(1-2), 127-133.

Berthé, D., Choukroune, P., & Jégouzo, P. (1979). Orthogneiss, mylonite and non coaxial deformation of granites: the example of the South Armorican Shear Zone. *Journal of Structural Geology*, *1*(1), 31-42.

Bertini, G., Casini, M., Gianelli, G., & Pandeli, E. (2006). Geological structure of a long-living geothermal system, Larderello, Italy. *Terra Nova*, *18*(3), 163-169.

Bestmann, M., & Prior, D. J. (2003). Intragranular dynamic recrystallization in naturally deformed calcite marble: diffusion accommodated grain boundary sliding as a result of subgrain rotation recrystallization. *Journal of Structural Geology*, *25*(10), 1597-1613.

Bestmann, M., Pennacchioni, G., Nielsen, S., Göken, M., & De Wall, H. (2012). Deformation and ultrafine dynamic recrystallization of quartz in pseudotachylyte-bearing brittle faults: A matter of a few seconds. *Journal of Structural Geology*, *38*, 21-38.

References

Bianco, C., Brogi, A., Caggianelli, A., Giorgetti, G., Liotta, D., & Meccheri, M. (2015). HP-LT metamorphism in Elba Island: implications for the geodynamic evolution of the inner Northern Apennines (Italy). *Journal of Geodynamics*, *91*, 13-25.

Bistacchi, A., Massironi, M., Menegon, L., Bolognesi, F., & Donghi, V. (2012). On the nucleation of non-Andersonian faults along phyllosilicate-rich mylonite belts. *Geological Society, London, Special Publications*, *367*(1), 185-199.

Blacic, J. D. (1975). Plastic deformation mechanisms in quartz: the effect of water. *Tectonophysics*, *27*(3), 271-294.

Blanpied, M. L., Lockner, D. A., & Byerlee, J. D. (1991). Fault stability inferred from granite sliding experiments at hydrothermal conditions. *Geophysical Research Letters*, *18*(4), 609-612.

Blanpied, M. L., Lockner, D. A., & Byerlee, J. D. (1995). Frictional slip of granite at hydrothermal conditions. *Journal of Geophysical Research: Solid Earth*, *100*(B7), 13045-13064.

Blenkinsop, T. G., & Treloar, P. J. (1995). Geometry, classification and kinematics of SC and SC′ fabrics in the Mushandike area, Zimbabwe. *Journal of Structural Geology*, *17*(3), 397-408.

Blumenfeld, P., Mainprice, D., & Bouchez, J. L. (1986). C-slip in quartz from subsolidus deformed granite. *Tectonophysics*, *127*(1-2), 97-115.

Boccaletti, M., & Guazzone, G. (1974). Remnant arcs and marginal basins in the Cainozoic development of the Mediterranean. *Nature*, *252*(5478), 18.

Boccaletti, M., & Sani, F. (1998). Cover thrust reactivations related to internal basement involvement during Neogene-Quaternary evolution of the northern Apennines. *Tectonics*, *17*(1), 112-130.

Boccaletti, M., Elter, P., & Guazzone, G. (1971). Plate tectonic models for the development of the Western Alps and Northern Apennines. *Nature Physical Science*, *234*(49), 108.

References

Boccaletti, M., Bonini, M., Moratti, G., & Sani, F. (1999). Compressive Neogene-Quaternary tectonics in the hinterland area of the Northern Apennines. *Journal of Petroleum Geology*, *22*(1), 37-60.

Bolognesi, F., & Bistacchi, A. (2016). Weakness and mechanical anisotropy of phyllosilicate-rich cataclasites developed after mylonites of a low-angle normal fault (Simplon Line, Western Alps). *Journal of Structural Geology*, *83*, 1-12.

Bolognesi, F., & Bistacchi, A. (2018). A km-scale "triaxial experiment" reveals the extreme mechanical weakness and anisotropy of mica-schists (Grandes Rousses Massif, France). *Journal of Structural Geology*, *107*, 53-63.

Bonini, M., & Sani, F. (2002). Extension and compression in the Northern Apennines (Italy) hinterland: Evidence from the late Miocene-Pliocene Siena-Radicofani Basin and relations with basement structures. *Tectonics*, *21*(3).

Bonini, M., Sani, F., Stucchi, E. M., Moratti, G., Benvenuti, M., Menanno, G., & Tanini, C. (2014). Late Miocene shortening of the Northern Apennines back-arc. *Journal of Geodynamics*, *74*, 1-31.

Bons, P. D. (1993). *Experimental deformation of polyphase rock analogues*. Faculteit Aardwetenschappen.

Bons, P. D., & den Brok, B. (2000). Crystallographic preferred orientation development by dissolution–precipitation creep. *Journal of Structural Geology*, *22*(11-12), 1713-1722.

Bortolotti, V., Fazzuoli, M., Pandeli, E., Principi, G., Babbini, A., & Corti, S. (2001). Geology of central and eastern Elba Island, Italy. *Ofioliti*, *26*(2a), 97-150.

Bouillin, J.P., 1983. Exemples de deformation locale liées à la mis en place de granitoides alpins dans des conditions distensives: l'ile d'Elbe (Italie) et le Cap Bougaron (Algérie). Rev. Geol. Dyn. Geogr. Phys., 24, 101–116.

References

Bourdelle, F., & Cathelineau, M. (2015). Low-temperature chlorite geothermometry: a graphical representation based on a T–R2+–Si diagram. *European Journal of Mineralogy*, *27*(5), 617-626.

Bourdelle, F., Parra, T., Chopin, C., & Beyssac, O. (2013). A new chlorite geothermometer for diagenetic to low-grade metamorphic conditions. *Contributions to Mineralogy and Petrology*, *165*(4), 723-735.

Bousquet, R., Goffé, B., Vidal, O., Oberhänsli, R., & Patriat, M. (2002). The tectono-metamorphic history of the Valaisan domain from the Western to the Central Alps: New constraints on the evolution of the Alps. *Geological Society of America Bulletin*, *114*(2), 207-225.

Brace, W. F., & Kohlstedt, D. L. (1980). Limits on lithospheric stress imposed by laboratory experiments. *Journal of Geophysical Research: Solid Earth*, *85*(B11), 6248-6252.

Brune, J. N., Henyey, T. L., & Roy, R. F. (1969). Heat flow, stress, and rate of slip along the San Andreas fault, California. *Journal of Geophysical Research*, *74*(15), 3821-3827.

Brunet, C., Monié, P., Jolivet, L., & Cadet, J. P. (2000). Migration of compression and extension in the Tyrrhenian Sea, insights from 40Ar/39Ar ages on micas along a transect from Corsica to Tuscany. *Tectonophysics*, *321*(1), 127-155.

Bucher, K., & Grapes, R. (2011). *Petrogenesis of Metamorphic Rocks*. Springer, Berlin, Heidelberg.

Bukovskà, Z., Jeřábek, P., & Morales, L. F. (2016). Major softening at brittle-ductile transition due to interplay between chemical and deformation processes: An insight from evolution of shear bands in the South Armorican Shear Zone. *Journal of Geophysical Research: Solid Earth*, *121*(2), 1158-1182.

Bürgmann, R., & Dresen, G. (2008). Rheology of the lower crust and upper mantle: Evidence from rock mechanics, geodesy, and field observations. *Annual Review of Earth and Planetary Sciences*, *36*.

References

Burnell, J. R., & Rutherford, M. J. (1984). An experimental investigation of the chlorite terminal equilibrium in pelitic rocks. *American Mineralogist, 69*, 1015-1024.

Butler, R. W. H., Bond, C. E., Shipton, Z. K., Jones, R. R., & Casey, M. (2008). Fabric anisotropy controls faulting in the continental crust. *Journal of the Geological Society, 165*(2), 449-452.

Byerlee, J. D. (1968). Brittle-ductile transition in rocks. *Journal of Geophysical Research, 73*(14), 4741-4750.

Byerlee, J. (1978). Friction of rocks. In *Rock friction and earthquake prediction* (pp. 615-626). Birkhäuser, Basel.

Caggianelli, A., Zucchi, M., Bianco, C., Brogi, A., & Liotta, D. (2018). Estimating PT metamorphic conditions on the roof of a hidden granitic pluton: an example from the Mt. Calamita promontory (Elba Island, Italy). *Italian Journal of Geosciences, 137*(2), 238-253.

Camacho, A., Vernon, R. H., & Gerald, J. F. (1995). Large volumes of anhydrous pseudotachylyte in the Woodroffe Thrust, eastern Musgrave Ranges, Australia. *Journal of Structural Geology, 17*(3), 371-383.

Carreras, J., Czeck, D. M., Druguet, E., & Hudleston, P. J. (2010). Structure and development of an anastomosing network of ductile shear zones. *Journal of Structural Geology, 32*(5), 656-666.

Carter, N. L., & Ave'Lallemant, H. G. (1970). High temperature flow of dunite and peridotite. *Geological Society of America Bulletin, 81*(8), 2181-2202.

Carter, R. T., & Norris, R. J. (1976). Cenozoic history of southern New Zealand: an accord between geological observations and plate-tectonic predictions. *Earth and planetary science letters, 31*(1), 85-94.

Cassano, E., Anelli, L., Cappelli, V., & La Torre, P. (1998). Interpretation of Northern-Apennine magnetic and gravity data in relation to the profile CROP-03. *Memorie della Societa Geologica Italiana, 52*, 413-425.

References

Cathelineau, M. (1988). Cation site occupancy in chlorites and illites as function of temperature. *Clay minerals*, *23*(4), 471-85.

Cathelineau, M., & Nieva, D. (1985). A chlorite solid solution geothermometer the Los Azufres (Mexico) geothermal system. *Contributions to Mineralogy and Petrology*, *91*(3), 235-244.

Ceccato, A., Pennacchioni, G., Menegon, L., & Bestmann, M. (2017). Crystallographic control and texture inheritance during mylonitization of coarse grained quartz veins. *Lithos*, *290*, 210-227.

Cerrina Feroni, A., Bonini, M., Martinelli, P., Moratti, G., Sani, F., Montanari, D., & Del Ventisette, V. (2006). Lithological control on thrust-related deformation in the Sassa-Guardistallo Basin (Northern Apennines hinterland, Italy). *Basin Research*, *18*(3), 301-321.

Chester, F. M., Evans, J. P., & Biegel, R. L. (1993). Internal structure and weakening mechanisms of the San Andreas fault. *Journal of Geophysical Research: Solid Earth*, *98*(B1), 771-786.

Christie, J. M. (1963). *The Moine thrust zone in the Assynt region, northwest Scotland*. University of California Press.

Clemens, J. D., & Wall, V.J. (1981). Origin and crystallization of some peraluminous (S-type) granite magmas. Canadian Mineralogist, 19, 111-131.

Cobbold, P. (1976). Mechanical effects of anisotropy during large finite deformations. *Bulletin de la Sociètè gèologique de France*, *7*(6), 1497-1510.

Cobbold, P. R., Cosgrove, J. W., & Summers, J. M. (1971). Development of internal structures in deformed anisotropic rocks. *Tectonophysics*, *12*(1), 23-53.

Coggon, R., & Holland, T. J. B. (2002). Mixing properties of phengitic micas and revised garnet-phengite thermobarometers. *Journal of Metamorphic Geology*, *20*(7), 683-696.

References

Cohen, K. M., Finney, S. C., Gibbard, P. L., & Fan, J. X. (2013). The ICS International Chronostratigraphic Chart. Episodes 36, 199-204.

Collettini, C., & Sibson, R. H. (2001). Normal faults, normal friction?. *Geology*, *29*(10), 927-930.

Collettini, C., & Holdsworth, R. E. (2004). Fault zone weakening and character of slip along low-angle normal faults: insights from the Zuccale fault, Elba, Italy. *Journal of the Geological Society*, *161*(6), 1039-1051.

Collettini, C., De Paola, N., & Goulty, N. R. (2006). Switches in the minimum compressive stress direction induced by overpressure beneath a low-permeability fault zone. *Terra Nova*, *18*(3), 224-231.

Collettini, C., Niemeijer, A., Viti, C., & Marone, C. (2009). Fault zone fabric and fault weakness. *Nature*, *462*(7275), 907.

Collins, W. J., & Sawyer, E. W. (1996). Pervasive granitoid magma transfer through the lower–middle crust during non-coaxial compressional deformation. *Journal of Metamorphic Geology*, *14*(5), 565-579.

Colopietro, M. R., & Friberg, L. M. (1987). Tourmaline-biotite as a potential geothermometer for metapelites, Black Hills, South Dakota. In *Geological Society of America, Abstract Programs* (Vol. 19, p. 624).

Compton, K. E., Kirkpatrick, J. D., & Holk, G. J. (2017). Cyclical shear fracture and viscous flow during transitional ductile-brittle deformation in the Saddlebag Lake Shear Zone, California. *Tectonophysics*, *708*, 1-14.

Connolly, J. A. D., & Kerrick, D. M. (1987). An algorithm and computer program for calculating composition phase diagrams. *Calphad*, *11*(1), 1-55.

Connolly, J. A. D., & Petrini, K. (2002). An automated strategy for calculation of phase diagram sections and retrieval of rock properties as a function of physical conditions. *Journal of Metamorphic Geology*, *20*(7), 697-708.

References

Cooper, F. J., Platt, J. P., & Behr, W. M. (2017). Rheological transitions in the middle crust: insights from Cordilleran metamorphic core complexes. *Solid Earth, 8*(1), 199.

Cox, S. F. (2010). The application of failure mode diagrams for exploring the roles of fluid pressure and stress states in controlling styles of fracture-controlled permeability enhancement in faults and shear zones. *Geofluids, 10*(1-2), 217-233.

Cross, A. J., & Skemer, P. (2017). Ultramylonite generation via phase mixing in high-strain experiments. *Journal of Geophysical Research: Solid Earth, 122*(3), 1744-1759.

Cross, A. J., Prior, D. J., Stipp, M., & Kidder, S. (2017). The recrystallized grain size piezometer for quartz: An EBSD-based calibration. *Geophysical Research Letters, 44*(13), 6667-6674.

Cruciani, G., Franceschelli, M., Groppo, C., & Spano, M. E. (2012). Metamorphic evolution of non-equilibrated granulitized eclogite from Punta de li Tulchi (Variscan Sardinia) determined through texturally controlled thermodynamic modelling. *Journal of Metamorphic Geology, 30*(7), 667-685.

de Andrade, V., Vidal, O., Lewin, E., O'brien, P., & Agard, P. (2006). Quantification of electron microprobe compositional maps of rock thin sections: an optimized method and examples. *Journal of Metamorphic Geology, 24*(7), 655-668.

de Capitani, C., & Brown, T. H. (1987). The computation of chemical equilibrium in complex systems containing non-ideal solutions. *Geochimica et Cosmochimica Acta, 51*(10), 2639-2652.

de Caritat, C. P., Hutcheon, I., & Walshe, J. L. (1993). Chlorite geothermometry: a review. *Clays and Clay Minerals, 41*.

Davis, G. A., Lister, G. S., & Reynolds, S. J. (1986). Structural evolution of the Whipple and South Mountains shear zones, southwestern United States. *Geology, 14*(1), 7-10.

References

Debenedetti, A. (1953). Osservazioni geologiche sulle zone minerarie dell'Isola d'Elba. *Boll. Serv. Geol. It*, *74*, 53-85.

Deer, W. A., Howie, R. A., & Zussman, J. (1992). *Rock-forming Minerals: 2nd edition*. Pearson Prentice Hall, Edinburgh, England.

Deino, A., Keller, J. V. A., Minelli, G., & Pialli, G. (1992). Datazioni 40Ar/39Ar del metamorfismo dell'Unità di Ortano-Rio Marina (Isola d'Elba): risultati preliminari. *Studi Geologici Camerti*, *2*, 187-192.

Derez, T., Pennock, G., Drury, M., & Sintubin, M. (2015). Low-temperature intracrystalline deformation microstructures in quartz. *Journal of Structural Geology*, *71*, 3-23.

Di Pisa, A., Franceschelli, M., Leoni, L., & Meccheri, M. (1985). Regional variation of the metamorphic temperatures across the Tuscanid I Unit and its implications on the alpine metamorphism (Apuan Alps, N Tuscany). *Neues Jahrbuch fur Mineralogie-Abhandlungen*, *151*, 197-211.

Di Rosa, M., De Giorgi, A., Marroni, M., & Vidal, O. (2017). Syn-convergence exhumation of continental crust: evidence from structural and metamorphic analysis of the Monte Cecu area, Alpine Corsica (Northern Corsica, France). *Geological Journal*, *52*(6), 919-937.

Di Toro, G., Goldsby, D. L., & Tullis, T. E. (2004). Friction falls towards zero in quartz rock as slip velocity approaches seismic rates. *Nature*, *427*(6973), 436.

Diamond, L. W., & Tarantola, A. (2015). Interpretation of fluid inclusions in quartz deformed by weak ductile shearing: Reconstruction of differential stress magnitudes and pre-deformation fluid properties. *Earth and planetary science letters*, *417*, 107-119.

Diener, J. F. A., Powell, R., White, R. W., & Holland, T. J. B. (2007). A new thermodynamic model for clino-and orthoamphiboles in the system Na2O–CaO–FeO–MgO–Al2O3–SiO2–H2O–O. *Journal of Metamorphic Geology*, *25*(6), 631-656.

References

Diener, J. F. A., & Powell, R. (2010). Influence of ferric iron on the stability of mineral assemblages. *Journal of Metamorphic Geology*, *28*(6), 599-613.

Dini, A., Innocenti, F., Rocchi, S., Tonarini, S., & Westerman, D. S. (2002). The magmatic evolution of the late Miocene laccolith–pluton–dyke granitic complex of Elba Island, Italy. *Geological Magazine*, *139*(3), 257-279.

Dini, A., Mazzarini, F., Musumeci, G., & Rocchi, S. (2008). Multiple hydro-fracturing by boron-rich fluids in the Late Miocene contact aureole of eastern Elba Island (Tuscany, Italy). *Terra Nova*, *20*(4), 318-326.

Dinter, D. A., & Royden, L. (1993). Late Cenozoic extension in northeastern Greece: Strymon Valley detachment system and Rhodope metamorphic core complex. *Geology*, *21*(1), 45-48.

Drury, M. R., & Humphreys, F. J. (1986). The development of microstructure in Al-5% Mg during high temperature deformation. *Acta Metallurgica*, *34*(11), 2259-2271.

Drury, M. R., & Urai, J. L. (1990). Deformation-related recrystallization processes. *Tectonophysics*, *172*(3-4), 235-253.

Drury, M. R., Humphreys, F. T., & White, S. H. (1985). Large strain deformation studies using polycrystalline magnesium as a rock analogue. Part II: dynamic recrystallisation mechanisms at high temperatures. *Physics of the Earth and Planetary Interiors*, *40*(3), 208-222.

Dunlap, W. J., Hirth, G., & Teyssier, C. (1997). Thermomechanical evolution of a ductile duplex. *Tectonics*, *16*(6), 983-1000.

Duranti, S., Palmeri, R., Pertusati, P. C., & Ricci, C. A. (1992). Geological evolution and metamorphic petrology of the basal sequences of eastern Elba (complex II). *Acta Vulcanologica*, *2*, 213-229.

Durney, D. W. (1972). Solution-transfer, an important geological deformation mechanism. *Nature*, *235*(5337), 315.

References

Duveau, G., Shao, J. F., & Henry, J. P. (1998). Assessment of some failure criteria for strongly anisotropic geomaterials. *Mechanics of Cohesive-frictional Materials: An International Journal on Experiments, Modelling and Computation of Materials and Structures*, *3*(1), 1-26.

Ebert, A., Herwegh, M., & Pfiffner, A. (2007). Cooling induced strain localization in carbonate mylonites within a large-scale shear zone (Glarus thrust, Switzerland). *Journal of Structural Geology*, *29*(7), 1164-1184.

Elter, P., 1975. Introduction a` la géologie de l'Apennin septentrional. Bull. Soc. Geol. Fr., 7, 956–962.

Evans, T. P. (2004). A method for calculating effective bulk composition modification due to crystal fractionation in garnet-bearing schist: implications for isopleth thermobarometry. *Journal of Metamorphic Geology*, *22*(6), 547-557.

Evans, J. P., & Chester, F. M. (1995). Fluid-rock interaction in faults of the San Andreas system: Inferences from San Gabriel fault rock geochemistry and microstructures. *Journal of Geophysical Research: Solid Earth*, *100*(B7), 13007-13020.

Evans, B., & Kohlstedt, D. L. (1995). Rheology of rocks. *Rock Physics and Phase Relations: A Handbook of Physical Constants, AGU Ref. Shelf*, *3*, 148-165.

Faccenna, C., Funiciello, F., Giardini, D., & Lucente, P. (2001). Episodic back-arc extension during restricted mantle convection in the Central Mediterranean. *Earth and Planetary Science Letters*, *187*(1-2), 105-116.

Faghih, A., & Sarkarinejad, K. (2011). Kinematics of rock flow and fabric development associated with shear deformation within the Zagros transpression zone, Iran. *Geological Magazine*, *148*(5-6), 1009-1017.

References

Fellin, M. G., Reiners, P. W., Brandon, M. T., Wüthrich, E., Balestrieri, M. L., & Molli, G. (2007). Thermochronologic evidence for the exhumational history of the Alpi Apuane metamorphic core complex, northern Apennines, Italy. *Tectonics*, *26*(6).

Ferreira, J. M., França, G. S., Vilar, C. S., do Nascimento, A. F., Bezerra, F. H. R., & Assumpção, M. (2008). Induced seismicity in the Castanhão reservoir, NE Brazil—Preliminary results. *Tectonophysics*, *456*(1-2), 103-110.

Fettes, D., & Desmons, J., (2007). Metamorphic Rocks: A Classification and Glossary of Terms. Recommendations of the International Union of Geological Sciences. Cambridge University Press, Cambridge.

Finetti, I. R., Boccaletti, M., Bonini, M., Del Ben, A., Geletti, R., Pipan, M., & Sani, F. (2001). Crustal section based on CROP seismic data across the North Tyrrhenian–Northern Apennines–Adriatic Sea. *Tectonophysics*, *343*(3-4), 135-163.

Fitz Gerald, J. D., & Stünitz, H. (1993). Deformation of granitoids at low metamorphic grade. I: Reactions and grain size reduction. *Tectonophysics*, *221*(3-4), 269-297.

Fitz Gerald, J. D., Mancktelow, N. S., Pennacchioni, G., & Kunze, K. (2006). Ultrafine-grained quartz mylonites from high-grade shear zones: Evidence for strong dry middle to lower crust. *Geology*, *34*(5), 369-372.

Fliervoet, T. F., White, S. H., & Drury, M. R. (1997). Evidence for dominant grain-boundary sliding deformation in greenschist-and amphibolite-grade polymineralic ultramylonites from the Redbank Deformed Zone, Central Australia. *Journal of Structural Geology*, *19*(12), 1495-1520.

Fliervoet, T. F., Drury, M. R., & Chopra, P. N. (1999). Crystallographic preferred orientations and misorientations in some olivine rocks deformed by diffusion or dislocation creep. *Tectonophysics*, *303*(1-4), 1-27.

Fossen, H., & Cavalcante, G. C. G. (2017). Shear zones–A review. *Earth-Science Reviews*, *171*, 434-455.

References

Fossen, H. (2016). *Structural geology*. Cambridge University Press.

Foster, M. D. (1962). Interpretation and a classification of the chlorite. *US Geological Survey Professional Paper*, *414*, 1-33.

Franceschelli, M., Leoni, L., Memmi, I., & Puxeddu, M. (1986). Regional distribution of Al-silicates and metamorphic zonation in the low-grade Verrucano metasediments from the Northern Apennines, Italy. *Journal of Metamorphic Geology*, *4*(3), 309-321.

Frassi, C. (2015). Dominant simple-shear deformation during peak metamorphism for the lower portion of the Greater Himalayan Sequence in West Nepal: New implications for hybrid channel flow-type mechanisms in the Dolpo region. *Journal of Structural Geology*, *81*, 28-44.

Frondel, C., Dana, J. D., & Dana, E. S. (1962). *The System of Mineralogy: Silica Minerals*. Wiley, New York.

Fusseis, F., & Handy, M. R. (2008). Micromechanisms of shear zone propagation at the brittle–viscous transition. *Journal of Structural Geology*, *30*(10), 1242-1253.

Fusseis, F., Handy, M. R., & Schrank, C. (2006). Networking of shear zones at the brittle-to-viscous transition (Cap de Creus, NE Spain). *Journal of Structural Geology*, *28*(7), 1228-1243.

Fusseis, F., Regenauer-Lieb, K., Liu, J., Hough, R. M., & De Carlo, F. (2009). Creep cavitation can establish a dynamic granular fluid pump in ductile shear zones. *Nature*, *459*(7249), 974.

Gansser, A. (1964). Geology of the Himalayas, Wiley Interscience, London 289.

Gapais, D. (1989). Shear structures within deformed granites: mechanical and thermal indicators. *Geology*, *17*(12), 1144-1147.

References

Garfagnoli, F., Menna, F., Pandeli, E., & Principi, G. (2005). The Porto Azzurro unit (Mt. Calamita promontory, south-eastern Elba island, Tuscany): stratigraphic, tectonic and metamorphic evolution. *Bollettino della Società Geologica Italiana*, *3*, 119-138.

Gates, A. E., & Glover III, L. (1989). Alleghanian tectono-thermal evolution of the dextral transcurrent Hylas Zone, Virginia Piedmont, USA. *Journal of Structural Geology*, *11*(4), 407-419.

Gerald, J. D. F., Mancktelow, N. S., Pennacchioni, G., & Kunze, K. (2006). Ultrafine-grained quartz mylonites from high-grade shear zones: Evidence for strong dry middle to lower crust. *Geology*, *34*(5), 369-372.

Gifkins, R. (1976). Grain-boundary sliding and its accommodation during creep and superplasticity. *Metallurgical transactions a*, *7*(8), 1225-1232.

Gilgannon, J., Fusseis, F., Menegon, L., Regenauer-Lieb, K., & Buckman, J. (2017). Hierarchical creep cavity formation in an ultramylonite and implications for phase mixing. *Solid Earth*, *8*(6), 1193-1209.

Gillam, B. G., Little, T. A., Smith, E., & Toy, V. G. (2014). Reprint of Extensional shear band development on the outer margin of the Alpine mylonite zone, Tatare Stream, Southern Alps, New Zealand. *Journal of Structural Geology*, *64*, 115-134.

Giorgetti, G., Goffe, B., Memmi, I., & Nieto, F. (1998). Metamorphic evolution of Verrucano metasediments in Northern Apennines; new petrological constraints. *European Journal of Mineralogy*, *10*(6), 1295-1308.

Gleason, G. C., & Tullis, J. (1993). Improving flow laws and piezometers for quartz and feldspar aggregates. *Geophysical Research Letters*, *20*(19), 2111-2114.

Gleason, G. C., & Tullis, J. (1995). A flow law for dislocation creep of quartz aggregates determined with the molten salt cell. *Tectonophysics*, *247*(1-4), 1-23.

References

Gleason, G. C., Tullis, J., & Heidelbach, F. (1993). The role of dynamic recrystallization in the development of lattice preferred orientations in experimentally deformed quartz aggregates. *Journal of Structural Geology*, *15*(9-10), 1145-1168.

Goncalves, P., Poilvet, J. C., Oliot, E., Trap, P., & Marquer, D. (2016). How does shear zone nucleate? An example from the Suretta nappe (Swiss Eastern Alps). *Journal of Structural Geology*, *86*, 166-180.

Grasemann, B., Stüwe, K., & Vannay, J. C. (2003). Sense and non-sense of shear in flanking structures. *Journal of Structural Geology*, *25*(1), 19-34.

Gribble, C. D., & Hall, A. J. (1992). *Optical Mineralogy: principles & practice.* CRC Press, Boca Raton, FL.

Griggs, D. T., & Blacic, J. D. (1965). Quartz: anomalous weakness of synthetic crystals. *Science*, *147*(3655), 292-295.

Grohmann, C. H., Campanha, G. A., 2010. OpenStereo: open source, cross-platform software for structural geology analysis. In: AGU Fall Meeting abstracts.

Grujic, D., Casey, M., Davidson, C., Hollister, L. S., Kündig, R., Pavlis, T., & Schmid, S. (1996). Ductile extrusion of the Higher Himalayan Crystalline in Bhutan: evidence from quartz microfabrics. *Tectonophysics*, *260*(1-3), 21-43.

Guermani, A., & Pennacchioni, G. (1998). Brittle precursors of plastic deformation in a granite: an example from the Mont Blanc massif (Helvetic, western Alps). *Journal of Structural Geology*, *20*(2-3), 135-148.

Guidotti, C. V. (1984). Micas in metamorphic rocks. *Reviews in Mineralogy and Geochemistry*, *13*(1), 357-467.

Guidotti, C. V., & Sassi, F. P. (1998). Petrogenetic significance of Na-K white mica mineralogy: Recent advances for metamorphic rocks. *European Journal of Mineralogy*, 815-854.

References

Guidotti, C. V., & Sassi, F. P. (2002). Constraints on studies of metamorphic K-Na white micas. *Reviews in Mineralogy and Geochemistry*, *46*(1), 413-448.

Guillope, M., & Poirier, J. P. (1979). Dynamic recrystallization during creep of single-crystalline halite: An experimental study. *Journal of Geophysical Research: Solid Earth*, *84*(B10), 5557-5567.

Guiraud, M., Holland, T., & Powell, R. (1990). Calculated mineral equilibria in the greenschist-blueschist-eclogite facies in Na 2 O− FeO− MgO− Al 2 O 3− SiO 2− H 2 O. *Contributions to Mineralogy and Petrology*, *104*(1), 85-98.

Guiraud, M., Powell, R., & Rebay, G. (2001). H2O in metamorphism and unexpected behaviour in the preservation of metamorphic mineral assemblages. *Journal of Metamorphic Geology*, *19*(4), 445-454.

Hacker, B. R., Yin, A., Christie, J. M., & Davis, G. A. (1992). Stress magnitude, strain rate, and rheology of extended middle continental crust inferred from quartz grain sizes in the Whipple Mountains, California. *Tectonics*, *11*(1), 36-46.

Halfpenny, A., Prior, D. J., & Wheeler, J. (2006). Analysis of dynamic recrystallization and nucleation in a quartzite mylonite. *Tectonophysics*, *427*(1-4), 3-14.

Handy, M. R. (1989). Deformation regimes and the rheological evolution of fault zones in the lithosphere: the effects of pressure, temperature, grainsize and time. *Tectonophysics*, *163*(1-2), 119-152.

Handy, M. R. (1994). Flow laws for rocks containing two non-linear viscous phases: a phenomenological approach. *Journal of Structural Geology*, *16*(3), 287-302.

Handy, M. R., Wissing, S. B., & Streit, L. E. (1999). Frictional–viscous flow in mylonite with varied bimineralic composition and its effect on lithospheric strength. *Tectonophysics*, *303*(1-4), 175-191.

References

Handy, M. R., & Brun, J. P. (2004). Seismicity, structure and strength of the continental lithosphere. *Earth and Planetary Science Letters*, *223*(3-4), 427-441.

Hannula, K. A., Lackey, J. S., Mattox, E., McGrath, G., Onasch, E., & Wertheim, J. (1999). Syn-tectonic pluton intrusion during contractional deformation: microstructural and metamorphic evidence from the aureole of the Acadian Victory Pluton, north-eastern Vermont, USA. *Journal of Metamorphic Geology*, *17*, 271-286.

Hawemann, F., Mancktelow, N. S., Wex, S., Camacho, A., & Pennacchioni, G. (2018). Pseudotachylyte as field evidence for lower-crustal earthquakes during the intracontinental Petermann Orogeny (Musgrave Block, Central Australia). *Solid Earth*, *9*(3), 629-648.

Helgelson, H. C., Delany, J., Nesbitt, H. W., & Bird, D. K. (1978). Summary and critique of the thermodynamic properties of rock forming minerals. *American Journal of Sciences, 278*, 1-229.

Henry, D. J., & Guidotti, C. V. (2002). Titanium in biotite from metapelitic rocks: Temperature effects, crystal-chemical controls, and petrologic applications. *American Mineralogist, 87*(4), 375-382.

Henry, D. J., Guidotti, C. V., & Thomson, J. A. (2005). The Ti-saturation surface for low-to-medium pressure metapelitic biotites: Implications for geothermometry and Ti-substitution mechanisms. *American Mineralogist*, *90*(2-3), 316-328.

Herwegh, M., Linckens, J., Ebert, A., Berger, A., & Brodhag, S. H. (2011). The role of second phases for controlling microstructural evolution in polymineralic rocks: A review. *Journal of Structural Geology*, *33*(12), 1728-1750.

Hillier, S., & Velde, B. (1991). Octahedral occupancy and the chemical composition of diagenetic (low-temperature) chlorites. *Clay Minerals, 26*, 149-168.

Hippertt, J., Rocha, A., Lana, C., Egydio-Silva, M., & Takeshita, T. (2001). Quartz plastic segregation and ribbon development in high-grade striped gneisses. *Journal of Structural Geology*, *23*(1), 67-80.

References

Hirth, G., & Tullis, J. (1992). Dislocation creep regimes in quartz aggregates. *Journal of Structural Geology*, *14*(2), 145-159.

Hirth, G., & Tullis, J. (1994). The brittle-plastic transition in experimentally deformed quartz aggregates. *Journal of Geophysical Research: Solid Earth*, *99*(B6), 11731-11747.

Hirth, G., Teyssier, C., & Dunlap, J. W. (2001). An evaluation of quartzite flow laws based on comparisons between experimentally and naturally deformed rocks. *International Journal of Earth Sciences*, *90*(1), 77-87.

Hobbs, B. E. (1968). Recrystallization of single crystals of quartz. *Tectonophysics*, *6*(5), 353-401.

Hobbs, B. E. (1985). The hydrolytic weakening effect in quartz. *Point defects in minerals*, *31*, 151-170.

Hobbs, B. E., Ord, A., & Teyssier, C. (1986). Earthquakes in the ductile regime?. *Pure and Applied Geophysics*, *124*(1-2), 309-336.

Hodges, K. V. (2000). Tectonics of the Himalaya and southern Tibet from two perspectives. *Geological Society of America Bulletin*, *112*(3), 324-350.

Holyoke III, C. W., & Tullis, J. (2006). Mechanisms of weak phase interconnection and the effects of phase strength contrast on fabric development. *Journal of Structural Geology*, *28*(4), 621-640..

Holland, T., & Blundy, J. (1994). Non-ideal interactions in calcic amphiboles and their bearing on amphibole-plagioclase thermometry. *Contributions to mineralogy and petrology*, *116*(4), 433-447.

Holland, T. J. B., & Powell, R. T. J. B. (1998). An internally consistent thermodynamic data set for phases of petrological interest. *Journal of metamorphic Geology*, *16*(3), 309-343.

References

Holland, T. J. B., & R. Powell (2000). "AX: A program to calculate activities of mineral end members from chemical analyses (usually determined by electron microprobe)." *Available at: http: ll\vww. esc. cam. ac. uklastafflhollandlax. html*.

Holland, T., & Powell, R. (2003). Activity–composition relations for phases in petrological calculations: an asymmetric multicomponent formulation. *Contributions to Mineralogy and Petrology*, *145*(4), 492-501.

Holness, M. B., & Clemens, J. D. (1999). Partial melting of the Appin Quartzite driven by fracture-controlled H 2 O infiltration in the aureole of the Ballachulish Igneous Complex, Scottish Highlands. *Contributions to Mineralogy and Petrology*, *136*(1-2), 154-168.

Huang, C. C. (1978). An outline of the tectonic characteristics of China. *Eclogae Geol. Helv.*, *71*(3), 611-635.

Huang, T. K. (1960). Characteristics of the structure of China: Preliminary conclusions. *Sci. Sin.*, *9*, 492-543.

Ikari, M. J., Saffer, D. M., & Marone, C. (2009). Frictional and hydrologic properties of clay-rich fault gouge. *Journal of Geophysical Research: Solid Earth*, *114*(B5).

Ikari, M. J., Niemeijer, A. R., & Marone, C. (2015). Experimental investigation of incipient shear failure in foliated rock. *Journal of Structural Geology*, *77*, 82-91.

Inoue, A., Meunier, A., Patrier-Mas, P., Rigault, C., Beaufort, D., & Vieillard, P. (2009). Application of chemical geothermometry to low-temperature trioctahedral chlorites. *Clays and Clay Minerals*, *57*(3), 371-382.

Jackson, J. A. (2002). Strength of the continental lithosphere: time to abandon the jelly sandwich?. *GSA today*, *12*, 4-10.

Jackson, J. A., Austrheim, H., McKenzie, D., & Priestley, K. (2004). Metastability, mechanical strength, and the support of mountain belts. *Geology*, *32*(7), 625-628.

References

Jaoul, O., Tullis, J., & Kronenberg, A. (1984). The effect of varying water contents on the creep behavior of Heavitree quartzite. *Journal of Geophysical Research: Solid Earth*, *89*(B6), 4298-4312.

Jégouzo, P. (1980). The south Armorican shear zone. *Journal of Structural Geology*, *2*(1-2), 39-47.

Jessell, M. W. (1987). Grain-boundary migration microstructures in a naturally deformed quartzite. *Journal of Structural Geology*, *9*(8), 1007-1014.

Jessell, M. W., Bons, P. D., Griera, A., Evans, L. A., & Wilson, C. J. (2009). A tale of two viscosities. *Journal of Structural Geology*, *31*(7), 719-736.

Ji, S., Jiang, Z., Rybacki, E., Wirth, R., Prior, D., & Xia, B. (2004). Strain softening and microstructural evolution of anorthite aggregates and quartz–anorthite layered composites deformed in torsion. *Earth and Planetary Science Letters*, *222*(2), 377-390.

John, B. E., & Blundy, J. D. (1993). Emplacement-related deformation of granitoid magmas, southern Adamello Massif, Italy. *Geological Society of America Bulletin*, *105*(12), 1517-1541.

Jolivet, L., Faccenna, C., Goffé, B., Mattei, M., Rossetti, F., Brunet, C., ... & Parra, T. (1998). Midcrustal shear zones in postorogenic extension: example from the northern Tyrrhenian Sea. *Journal of Geophysical Research: Solid Earth*, *103*(B6), 12123-12160.

Jordan, P. (1988). The rheology of polymineralic rocks—an approach. *Geologische Rundschau*, *77*(1), 285-294.

Jowett, E. C. (1991). Fitting iron and magnesium into the hydrothermal chlorite geothermometer. In *GAC/MAC/SEG Joint Annual Meeting, Toronto, May 27-29, 1991, Program with Abstracts 16*.

Jung, H., & Karato, S. I. (2001). Water-induced fabric transitions in olivine. *Science*, *293*(5534), 1460-1463.

References

Jung, H., Katayama, I., Jiang, Z., Hiraga, T., & Karato, S. I. (2006). Effect of water and stress on the lattice-preferred orientation of olivine. *Tectonophysics*, *421*(1-2), 1-22.

Kalakay, T. J., John, B. E., & Lageson, D. R. (2001). Fault-controlled pluton emplacement in the Sevier fold-and-thrust belt of southwest Montana, USA. *Journal of Structural Geology*, *23*(6-7), 1151-1165.

Karlstrom, K. E., & Williams, M. L. (1995). The case for simultaneous deformation, metamorphism and plutonism: an example from Proterozoic rocks in central Arizona. *Journal of Structural Geology*, *17*(1), 59-81.

Keller, J. V. A., & Coward, M. P. (1996). The structure and evolution of the Northern Tyrrhenian Sea. *Geological Magazine*, *133*(1), 1-16.

Kerrich, R. (1986). Fluid infiltration into fault zones: chemical, isotopic, and mechanical effects. *Pure and applied geophysics*, *124*(1-2), 225-268.

Kidder, S., Avouac, J. P., & Chan, Y. C. (2012). Constraints from rocks in the Taiwan orogen on crustal stress levels and rheology. *Journal of Geophysical Research: Solid Earth*, *117*(B9).

Kidder, S., Hirth, G., Avouac, J. P., & Behr, W. (2016). The influence of stress history on the grain size and microstructure of experimentally deformed quartzite. *Journal of Structural Geology*, *83*, 194-206.

Kilian, R., Heilbronner, R., & Stünitz, H. (2011). Quartz grain size reduction in a granitoid rock and the transition from dislocation to diffusion creep. *Journal of Structural Geology*, *33*(8), 1265-1284.

Kilian, R., Heilbronner, R., Holyoke, C. W., Kronenberg, A. K., & Stünitz, H. (2016). Dislocation creep of dry quartz. *Journal of Geophysical Research: Solid Earth*, *121*(5), 3278-3299.

References

King Hubbert, M., & Rubey, W. W. (1959). Role of fluid pressure in mechanics of overthrust faulting: I. Mechanics of fluid-filled porous solids and its application to overthrust faulting. *Geological Society of America Bulletin*, *70*(2), 115-166.

Kjøll, H. J., Viola, G., Menegon, L., & Sørensen, B. E. (2015). Brittle-viscous deformation of vein quartz under fluid-rich lower greenschist facies conditions. *Solid Earth*, *6*(2), 681.

Kligfield, R., Hunziker, J., Dallmeyer, R. D., & Schamel, S. (1986). Dating of deformation phases using K-Ar and 40Ar/39Ar techniques: results from the Northern Apennines. *Journal of Structural Geology*, *8*(7), 781-798.

Kohlstedt, D. L., & Weathers, M. S. (1980). Deformation-induced microstructures, paleopiezometers, and differential stresses in deeply eroded fault zones. *Journal of Geophysical Research: Solid Earth*, *85*(B11), 6269-6285.

Kohlstedt, D. L., Evans, B., & Mackwell, S. J. (1995). Strength of the lithosphere: Constraints imposed by laboratory experiments. *Journal of Geophysical Research: Solid Earth*, *100*(B9), 17587-17602.

Kranidiotis, P., & MacLean, W. H. (1987). Systematics of chlorite alteration at the Phelps Dodge massive sulfide deposit, Matagami, Quebec. *Economic Geology*, *82*(7), 1898-1911.

Kronenberg, A. K. (1994). Hydrogen speciation and chemical weakening of quartz. *Reviews in Mineralogy and Geochemistry*, *29*(1), 123-176.

Kronenberg, A. K., Segall, P., & Wolf, G. H. (1990). Hydrolytic weakening and penetrative deformation within a natural shear zone. *Geophysical Monograph*, *56*, 21-36.

Kruhl, J. H. (1996). Prism-and basal-plane parallel subgrain boundaries in quartz: A microstructural geothermobarometer. *Journal of metamorphic Geology*, *14*(5), 581-589.

Kruhl, J.H. (1998). Reply: prism- and basal-plane parallel subgrain boundaries in quartz: a microstructural geothermobarometer. *Journal of metamorphic Geology*, *16*, 142-146.

References

Kurz, G. A., & Northrup, C. J. (2008). Structural analysis of mylonitic rocks in the Cougar Creek Complex, Oregon–Idaho using the porphyroclast hyperbolic distribution method, and potential use of SC′-type extensional shear bands as quantitative vorticity indicators. *Journal of Structural Geology*, *30*(8), 1005-1012.

Labotka, T. C. (1983). Analysis of the compositional variations of biotite in pelitic hornfelses from northeastern Minnesota. *American Mineralogist*, *68*, 900-914.

Lachenbruch, A. H. (1980). Frictional heating, fluid pressure, and the resistance to fault motion. *Journal of Geophysical Research: Solid Earth*, *85*(B11), 6097-6112.

Laird, J. (1988). Chlorites: metamorphic petrology, in: Hydrous phyllosilicates. *Mineral. Soc. Amer. Rev. Min.*, *19*, 405-453.

Lanari, P., Guillot, S., Schwartz, S., Vidal, O., Tricart, P., Riel, N., & Beyssac, O. (2012). Diachronous evolution of the alpine continental subduction wedge: evidence from P–T estimates in the Briançonnais Zone houillère (France–Western Alps). *Journal of Geodynamics*, *56*, 39-54.

Lanari, P., Riel, N., Guillot, S., Vidal, O., Schwartz, S., Pêcher, A., & Hattori, K. H. (2013). Deciphering high-pressure metamorphism in collisional context using microprobe mapping methods: Application to the Stak eclogitic massif (northwest Himalaya). *Geology*, *41*(2), 111-114.

Lanari, P., Wagner, T., & Vidal, O. (2014). A thermodynamic model for di-trioctahedral chlorite from experimental and natural data in the system MgO–FeO–Al 2 O 3–SiO 2–H 2 O: applications to P–T sections and geothermometry. *Contributions to Mineralogy and Petrology*, *167*(2), 968.

Lanari, P., Vho, A., Bovay, T., Airaghi, L., & Centrella, S. (2018). Quantitative compositional mapping of mineral phases by electron probe micro-analyser. *Geological Society, London, Special Publications*, *478*, SP478-4.

References

Laubach, S. E., & Marshak, S. (1987). Fault patterns generated during extensional deformation of crystalline basement, NW Scotland. *Geological Society, London, Special Publications*, *28*(1), 495-499.

Law, R. D. (1987). Heterogeneous deformation and quartz crystallographic fabric transitions: natural examples from the Moine Thrust zone at the Stack of Glencoul, northern Assynt. *Journal of Structural Geology*, *9*(7), 819-833.

Law, R. D. (2014). Deformation thermometry based on quartz c-axis fabrics and recrystallization microstructures: A review. *Journal of Structural Geology*, *66*, 129-161.

Law, R. D., Knipe, R. J., & Dayan, H. (1984). Strain path partitioning within thrust sheets: microstructural and petrofabric evidence from the Moine Thrust zone at Loch Eriboll, northwest Scotland. *Journal of Structural Geology*, *6*(5), 477-497.

Law, R. D., Searle, M. P., & Simpson, R. L. (2004). Strain, deformation temperatures and vorticity of flow at the top of the Greater Himalayan Slab, Everest Massif, Tibet. *Journal of the Geological Society*, *161*(2), 305-320.

Law, R. D., Jessup, M. J., Searle, M. P., Francsis, M. K., Waters, D. J., & Cottle, J. M. (2011). Telescoping of isotherms beneath the South Tibetan detachment system, Mount Everest Massif. *Journal of Structural Geology*, *33*(11), 1569-1594.

Le Breton, N., & Thompson, A. B. (1988). Fluid-absent (dehydration) melting of biotite in metapelites in the early stages of crustal anatexis. *Contributions to Mineralogy and Petrology*, *99*(2), 226-237.

Leloup, P. H., Lacassin, R., Tapponnier, P., Schärer, U., Zhong, D., Liu, X., ... & Trinh, P. T. (1995). The Ailao Shan-Red River shear zone (Yunnan, China), Tertiary transform boundary of Indochina. *Tectonophysics*, *251*(1-4), 3-84.

Leoni, L., Sartori, F., & Tamponi, M. (1998). Composition variation in K-white micas and chlorites coexisting in Al-saturated metapelites under late diagenetic to low-grade

metamorphic conditions (Internal Liguride Units, Northern Apennines, Italy). *European Journal of Mineralogy*, *10*(6), 1321-1339.

Lev, E., & Hager, B. H. (2008). Prediction of anisotropy from flow models: A comparison of three methods. *Geochemistry, Geophysics, Geosystems*, *9*(7).

Lin, A. (1999). S–C cataclasite in granitic rock. *Tectonophysics*, *304*(3), 257-273.

Linckens, J., Bruijn, R. H., & Skemer, P. (2014). Dynamic recrystallization and phase mixing in experimentally deformed peridotite. *Earth and Planetary Science Letters*, *388*, 134-142.

Lippolt, H. J., Wernicke, R. S., & Ba, R. (1995). Paragenetic specularite and adularia (Elba, Italy): concordant (U+ Th)-He and K-Ar ages. *Earth and Planetary Science Letters*, *132*(1-4), 43-51.

Lister, G. S., & Dornsiepen, U. F. (1982). Fabric transitions in the Saxony granulite terrain. *Journal of Structural Geology*, *4*(1), 81-92.

Lister, G. S., & Snoke, A. W. (1984). SC mylonites. *Journal of Structural Geology*, *6*(6), 617-638.

Lister, G. S., & Davis, G. A. (1989). The origin of metamorphic core complexes and detachment faults formed during Tertiary continental extension in the northern Colorado River region, USA. *Journal of Structural Geology*, *11*(1-2), 65-94.

Little, T. A., Hacker, B. R., Gordon, S. M., Baldwin, S. L., Fitzgerald, P. G., Ellis, S., & Korchinski, M. (2011). Diapiric exhumation of Earth's youngest (UHP) eclogites in the gneiss domes of the D'Entrecasteaux Islands, Papua New Guinea. *Tectonophysics*, *510*(1-2), 39-68.

Lloyd, G. E. (2004). Microstructural evolution in a mylonitic quartz simple shear zone: the significant roles of dauphine twinning and misorientation. *Geological Society, London, Special Publications*, *224*(1), 39-61.

References

Lloyd, G. E., & Freeman, B. (1994). Dynamic recrystallization of quartz under greenschist conditions. *Journal of Structural Geology*, *16*(6), 867-881.

Lo Pò, D., & Braga, R. (2014). Influence of ferric iron on phase equilibria in greenschist facies assemblages: the hematite-rich metasedimentary rocks from the Monti Pisani (Northern Apennines). *Journal of Metamorphic Geology*, *32*(4), 371-387.

Lockner, D. A., Morrow, C., Moore, D., & Hickman, S. (2011). Low strength of deep San Andreas fault gouge from SAFOD core. *Nature*, *472*(7341), 82.

Logan, J. M., Dengo, C. A., Higgs, N. G., & Wang, Z. Z. (1992). Fabrics of experimental fault zones: Their development and relationship to mechanical behavior. In *International Geophysics* (Vol. 51, pp. 33-67). Academic Press.

López-Carmona, A., Pitra, P., & Abati, J. (2013). Blueschist-facies metapelites from the Malpica–Tui Unit (NW Iberian Massif): phase equilibria modelling and H2O and Fe2O3 influence in high-pressure assemblages. *Journal of Metamorphic Geology*, *31*(3), 263-280.

Luan, F. C., & Paterson, M. S. (1992). Preparation and deformation of synthetic aggregates of quartz. *Journal of Geophysical Research: Solid Earth*, *97*(B1), 301-320.

Luton, M. J., & Sellars, C. M. (1969). Dynamic recrystallization in nickel and nickel-iron alloys during high temperature deformation. *Acta Metallurgica*, *17*(8), 1033-1043.

Mahar, E. M., Baker, J. M., Powell, R., Holland, T. J. B., & Howell, N. (1997). The effect of Mn on mineral stability in metapelites. *Journal of Metamorphic Geology*, *15*(2), 223-238.

Mäder, U. K., Percival, J. A., & Berman, R. G. (1994). Thermobarometry of garnet–clinopyroxene–hornblende granulites from the Kapuskasing structural zone. *Canadian Journal of Earth sciences*, *31*(7), 1134-1145.

Maineri, C., Benvenuti, M., Costagliola, P., Dini, A., Lattanzi, P., Ruggieri, G., & Villa, I. M. (2003). Sericitic alteration at the La Crocetta deposit (Elba Island, Italy): interplay between magmatism, tectonics and hydrothermal activity. *Mineralium Deposita*, *38*(1), 67-86.

References

Mainprice, D., & Nicolas, A. (1989). Development of shape and lattice preferred orientations: application to the seismic anisotropy of the lower crust. *Journal of Structural Geology*, *11*(1-2), 175-189.

Mainprice, D., Bouchez, J. L., Blumenfeld, P., & Tubià, J. M. (1986). Dominant c slip in naturally deformed quartz: Implications for dramatic plastic softening at high temperature. *Geology*, *14*(10), 819-822.

Malinverno, A., & Ryan, W. B. (1986). Extension in the Tyrrhenian Sea and shortening in the Apennines as result of arc migration driven by sinking of the lithosphere. *Tectonics*, *5*(2), 227-245.

Mancktelow, N. S., & Pennacchioni, G. (2004). The influence of grain boundary fluids on the microstructure of quartz-feldspar mylonites. *Journal of Structural Geology*, *26*(1), 47-69.

Mancktelow, N. S., & Pennacchioni, G. (2005). The control of precursor brittle fracture and fluid–rock interaction on the development of single and paired ductile shear zones. *Journal of Structural Geology*, *27*(4), 645-661.

Mancktelow, N. S., & Pennacchioni, G. (2013). Late magmatic healed fractures in granitoids and their influence on subsequent solid-state deformation. *Journal of Structural Geology*, *57*, 81-96.

Mancktelow, N. S., Grujic, D., & Johnson, E. L. (1998). An SEM study of porosity and grain boundary microstructure in quartz mylonites, Simplon Fault Zone, Central Alps. *Contributions to Mineralogy and Petrology*, *131*(1), 71-85.

Marinelli, G. (1959). Le intrusioni terziarie dell'Isola d'Elba. *Atti Soc. Tosc. Sci. Nat., Mem., Ser. A., 66,* 50-253.

Massa, G., Musumeci, G., Mazzarini, F., & Pieruccioni, D. (2017). Coexistence of contractional and extensional tectonics during the northern Apennines orogeny: the late Miocene out-of-sequence thrust in the Elba Island nappe stack. *Geological Journal*, *52*(3), 353-368.

References

Massironi, M., Bistacchi, A., & Menegon, L. (2011). Misoriented faults in exhumed metamorphic complexes: rule or exception?. *Earth and Planetary Science Letters*, *307*(1-2), 233-239.

Massonne, H. J., & Schreyer, W. (1987). Phengite geobarometry based on the limiting assemblage with K-feldspar, phlogopite, and quartz. *Contributions to Mineralogy and Petrology*, *96*(2), 212-224.

Massonne, H. J., & Szpurka, Z. (1997). Thermodynamic properties of white micas on the basis of high-pressure experiments in the systems K2O□ MgO□ Al2O3□ SiO2□ H2O and K2□ O□ FeO□ Al3O3□ SiO2□ H3O. *Lithos*, *41*(1-3), 229-250.

Mazzarini, F., & Musumeci, G. (2008). Hydrofracturing-related sill and dyke emplacement at shallow crustal levels: The Eastern Elba Dyke Complex, Italy. *Geological Society, London, Special Publications*, *302*(1), 121-129.

Mazzarini, F., Musumeci, G., & Cruden, A. R. (2011). Vein development during folding in the upper brittle crust: The case of tourmaline-rich veins of eastern Elba Island, northern Tyrrhenian Sea, Italy. *Journal of Structural Geology*, *33*(10), 1509-1522.

McClay, K. R., & Coward, M. P. (1981). The Moine thrust zone: an overview. *Geological Society, London, Special Publications*, *9*(1), 241-260.

McNulty, B. A. (1995). Pseudotachylyte generated in the semi-brittle and brittle regimes, Bench Canyon shear zone, central Sierra Nevada. *Journal of Structural geology*, *17*(11), 1507-1521.

Means, W. D. (1983). Microstructure and micromotion in recrystallization flow of octachloropropane: a first look. *Geologische Rundschau*, *72*(2), 511-528.

Means, W. D. (1995). Shear zones and rock history. *Tectonophysics*, *247*(1-4), 157-160.

References

Menegon, L., Pennacchioni, G., Heilbronner, R., & Pittarello, L. (2008). Evolution of quartz microstructure and c-axis crystallographic preferred orientation within ductilely deformed granitoids (Arolla unit, Western Alps). *Journal of Structural Geology*, *30*(11), 1332-1347.

Menegon, L., Nasipuri, P., Stünitz, H., Behrens, H., & Ravna, E. (2011a). Dry and strong quartz during deformation of the lower crust in the presence of melt. *Journal of Geophysical Research: Solid Earth*, *116*(B10).

Menegon, L., Piazolo, S., & Pennacchioni, G. (2011b). The effect of Dauphiné twinning on plastic strain in quartz. *Contributions to Mineralogy and Petrology*, *161*(4), 635-652.

Menegon, L., Stünitz, H., Nasipuri, P., Heilbronner, R., & Svahnberg, H. (2013). Transition from fracturing to viscous flow in granulite facies perthitic feldspar (Lofoten, Norway). *Journal of Structural Geology*, *48*, 95-112.

Menegon, L., Fusseis, F., Stünitz, H., & Xiao, X. (2015). Creep cavitation bands control porosity and fluid flow in lower crustal shear zones. *Geology*, *43*(3), 227-230.

Menegon, L., Pennacchioni, G., Malaspina, N., Harris, K., & Wood, E. (2017). Earthquakes as precursors of ductile shear zones in the dry and strong lower crust. *Geochemistry, Geophysics, Geosystems*, *18*(12), 4356-4374.

Merino, E., & Ransom, B. (1982). Free energies of formation of illite solid solutions and their compositional dependence. *Clays and Clay minerals*, *30*(1), 29-39.

Michels, Z. D., Kruckenberg, S. C., Davis, J. R., & Tikoff, B. (2015). Determining vorticity axes from grain-scale dispersion of crystallographic orientations. *Geology*, *43*(9), 803-806.

Molli, G., Giorgetti, G., & Meccheri, M. (2000). Structural and petrological constraints on the tectono-metamorphic evolution of the Massa Unit (Alpi Apuane, NW Tuscany, Italy). *Geological Journal*, *35*(3-4), 251-264.

Molli, G., Menegon, L., & Malasoma, A. (2017). Switching deformation mode and mechanisms during subduction of continental crust: a case study from Alpine Corsica.

References

Morales, L. F., Mainprice, D., Lloyd, G. E., & Law, R. D. (2011). Crystal fabric development and slip systems in a quartz mylonite: an approach via transmission electron microscopy and viscoplastic self-consistent modelling. *Geological Society, London, Special Publications*, *360*(1), 151-174.

Morgan, S. S., & Law, R. D. (2004). Unusual transition in quartzite dislocation creep regimes and crystal slip systems in the aureole of the Eureka Valley–Joshua Flat–Beer Creek pluton, California: a case for anhydrous conditions created by decarbonation reactions. *Tectonophysics*, *384*(1-4), 209-231.

Morgan, S., Law, R., & de Saint Blanquat, M. (2013). Forceful emplacement of the Eureka Valley–Joshua Flat–Beer Creek composite pluton into a structural basin in eastern California; internal structure and wall rock deformation. *Tectonophysics*, *608*, 753-773.

Morgan, S. S., Nabelek, P. I., Student, J., & Sadorski, J. F. (2016). Fluid-controlled grain boundary migration and switch in slip systems in a high strain, high temperature contact aureole, California, USA. *Tectonophysics*, *676*, 42-55.

Morris, A., Ferrill, D. A., & Henderson, D. B. (1996). Slip-tendency analysis and fault reactivation. *Geology*, *24*(3), 275-278.

Morrow, C. A., Shi, L. Q., & Byerlee, J. D. (1984). Permeability of fault gouge under confining pressure and shear stress. *Journal of Geophysical Research: Solid Earth*, *89*(B5), 3193-3200.

Musumeci, G., & Vaselli, L. (2012). Neogene deformation and granite emplacement in the metamorphic units of northern Apennines (Italy): Insights from mylonitic marbles in the Porto Azzurro pluton contact aureole (Elba Island). *Geosphere*, *8*(2), 470-490.

Musumeci, G., Bocini, L., & Corsi, R. (2002). Alpine tectonothermal evolution of the Tuscan Metamorphic Complex in the Larderello geothermal field (northern Apennines, Italy). *Journal of the Geological Society*, *159*(4), 443-456.

References

Musumeci, G., Mazzarini, F., Corti, G., Barsella, M., & Montanari, D. (2005). Magma emplacement in a thrust ramp anticline: The Gavorrano Granite (northern Apennines, Italy). *Tectonics*, *24*(6).

Musumeci, G., Mazzarini, F., & Barsella, M. (2008). Pliocene crustal shortening on the Tyrrhenian side of the northern Apennines: evidence from the Gavorrano antiform (southern Tuscany, Italy). *Journal of the Geological Society*, *165*(1), 105-114.

Musumeci, G., Mazzarini, F., Tiepolo, M., & Di Vincenzo, G. (2011). U-Pb and 40Ar-39Ar geochronology of Paleozoic units in the northern Apennines: determining protolith age and alpine evolution using the Calamita Schist and Ortano Porphyroid. *Geological Journal*, *46*(4), 288-310.

Musumeci, G., Mazzarini, F., & Cruden, A. R. (2015). The Zuccale Fault, Elba Island, Italy: a new perspective from fault architecture. *Tectonics*, *34*(6), 1195-1218.

Muto, J., Hirth, G., Heilbronner, R., & Tullis, J. (2011). Plastic anisotropy and fabric evolution in sheared and recrystallized quartz single crystals. *Journal of Geophysical Research: Solid Earth*, *116*(B2).

Nabelek, P. I., & Morgan, S. S. (2012). Metamorphism and fluid flow in the contact aureole of the Eureka Valley–Joshua Flat–Beer Creek pluton, California. *Bulletin*, *124*(1-2), 228-239.

Neumann, B. (2000). Texture development of recrystallised quartz polycrystals unravelled by orientation and misorientation characteristics. *Journal of Structural Geology*, *22*(11-12), 1695-1711.

Nicolas, A., & Christensen, N. I. (1987). Formation of anisotropy in upper mantle peridotites-A review. *Composition, structure and dynamics of the lithosphere-asthenosphere system*, *16*, 111-123.

Niemeijer, A. R., & Spiers, C. J. (2005). Influence of phyllosilicates on fault strength in the brittle-ductile transition: Insights from rock analogue experiments. *Geological Society, London, Special Publications*, *245*(1), 303-327.

References

Nishikawa, O., & Takeshita, T. (1999). Dynamic analysis and two types of kink bands in quartz veins deformed under subgreenschist conditions. *Tectonophysics*, *301*(1-2), 21-34.

Nishikawa, O., & Takeshita, T. (2000). Progressive lattice misorientation and microstructural development in quartz veins deformed under subgreenschist conditions. *Journal of Structural Geology*, *22*(2), 259-276.

Pandeli, E., Corti, S., Franceschelli, M., & Pecchioni, E. (2001). The varicoloured slates of the Gràssera Unit (Central-Eastern Elba, Tuscany): petrographical-mineralogical data and comparisons with other Tuscan and Ligurian-Piedmontese units. *Ofioliti*, *26*(2a), 197-206.

Papeschi, S., Musumeci, G., & Mazzarini, F. (2017). Heterogeneous brittle-ductile deformation at shallow crustal levels under high thermal conditions: The case of a synkinematic contact aureole in the inner northern Apennines, southeastern Elba Island, Italy. *Tectonophysics*, *717*, 547-564.

Papeschi, S., Musumeci, G., & Mazzarini, F. (2018). Evolution of shear zones through the brittle-ductile transition: The Calamita Schists (Elba Island, Italy). *Journal of Structural Geology*, *113*, 100–114

Parra, T., Vidal, O., & Jolivet, L. (2002). Relation between the intensity of deformation and retrogression in blueschist metapelites of Tinos Island (Greece) evidenced by chlorite–mica local equilibria. *Lithos*, *63*(1-2), 41-66.

Passchier, C. W. (1984). The generation of ductile and brittle shear bands in a low-angle mylonite zone. *Journal of Structural Geology*, *6*(3), 273-281.

Passchier, C. W., & Trouw, R. A. (2005). *Microtectonics* (Vol. 1). Springer Science & Business Media.

Passchier, C., & Coelho, S. (2006). An outline of shear-sense analysis in high-grade rocks. *Gondwana Research*, *10*(1-2), 66-76.

References

Paterson, S. R., Vernon, R. H., & Fowler, T. K. (1991a). Aureole tectonics. *Reviews in Mineralogy and Geochemistry*, *26*(1), 673-722.

Paterson, S. R., Tobisch, O. T., & Vernon, R. H. (1991b). Emplacement and deformation of granitoids during volcanic arc construction in the Foothills terrane, central Sierra Nevada, California. *Tectonophysics*, *191*(1-2), 89-110.

Pattison, D. R. M., & Harte, B. (1988). Evolution of structurally contrasting anatectic migmatites in the 3-kbar Ballachulish aureole, Scotland. *Journal of Metamorphic Geology*, *6*(4), 475-494.

Pattison, D.R.M., & Tracy, R.J. (1992). Phase equilibria and thermobarometry of metapelites. In: Kerrick, D.M. (Ed.), Contact Metamorphism, vol. 26. pp. 105‑206 *Reviews in Mineralogy*.

Pattison, D. R., & Harte, B. (1997). The geology and evolution of the Ballachulish Igneous Complex and Aureole. *Scottish Journal of Geology*, *33*(1), 1-29.

Pehl, J., & Wenk, H. R. (2005). Evidence for regional Dauphiné twinning in quartz from the Santa Rosa mylonite zone in Southern California. A neutron diffraction study. *Journal of Structural Geology*, *27*(10), 1741-1749.

Pennacchioni, G. (2005). Control of the geometry of precursor brittle structures on the type of ductile shear zone in the Adamello tonalites, Southern Alps (Italy). *Journal of Structural Geology*, *27*(4), 627-644.

Pennacchioni, G., & Cesare, B. (1997). Ductile-brittle transition in pre-Alpine amphibolite facies mylonites during evolution from water-present to water-deficient conditions (Mont Mary nappe, Italian Western Alps). *Journal of Metamorphic Geology*, *15*(6), 777-791.

Pennacchioni, G., & Mancktelow, N. S. (2007). Nucleation and initial growth of a shear zone network within compositionally and structurally heterogeneous granitoids under amphibolite facies conditions. *Journal of Structural Geology*, *29*(11), 1757-1780.

References

Pennacchioni, G., Menegon, L., Leiss, B., Nestola, F., & Bromiley, G. (2010). Development of crystallographic preferred orientation and microstructure during plastic deformation of natural coarse-grained quartz veins. *Journal of Geophysical Research: Solid Earth*, *115*(B12).

Peretti, F., (2007). I leucograniti del promontorio del Monte Calamita, isola d'Elba. *Msc Thesys, Università di Pisa*, 155pp.

Pertusati, P. C., Raggi, G., Ricci, C. A., Duranti, S., & Palmeri, R. (1993). Evoluzione post-collisionale dell'Elba centro-orientale. *Memorie della Società Geologica Italiana*, *49*, 297-312.

Piazolo, S., Montagnat, M., & Blackford, J. R. (2008). Sub-structure characterization of experimentally and naturally deformed ice using cryo-EBSD. *Journal of Microscopy*, *230*(3), 509-519.

Pitzer, K. S., & Sterner, S. M. (1994). Equations of state valid continuously from zero to extreme pressures for H2O and CO2. *The Journal of chemical physics*, *101*(4), 3111-3116.

Platt, J. P. (2015). Influence of shear heating on microstructurally defined plate boundary shear zones. *Journal of Structural Geology*, *79*, 80-89.

Platt, J. P., & Vissers, R. L. M. (1980). Extensional structures in anisotropic rocks. *Journal of Structural Geology*, *2*(4), 397-410.

Poirier, J. P. (1985). *Creep of crystals: high-temperature deformation processes in metals, ceramics and minerals*. Cambridge University Press.

Poirier, J. P., & Nicolas, A. (1975). Deformation-induced recrystallization due to progressive misorientation of subgrains, with special reference to mantle peridotites. *The Journal of Geology*, *83*(6), 707-720.

Poirier, J.P., & Guillopé, M. (1979). Deformation-induced recrystallization of minerals. *Bulletin de Minéralogie 102*, 67-74.

References

Ponce, C., Druguet, E., & Carreras, J. (2013). Development of shear zone-related lozenges in foliated rocks. *Journal of Structural Geology*, *50*, 176-186.

Ponziani, F., De Franco, R., Minelli, G., Biella, G., Federico, C., & Pialli, G. (1995). Crustal shortening and duplication of the Moho in the Northern Apennines: a view from seismic refraction data. *Tectonophysics*, *252*(1-4), 391-418.

Post, A., & Tullis, J. (1998). The rate of water penetration in experimentally deformed quartzite: implications for hydrolytic weakening. *Tectonophysics*, *295*(1-2), 117-137.

Post, A., & Tullis, J. (1999). A recrystallized grain size piezometer for experimentally deformed feldspar aggregates. *Tectonophysics*, *303*(1-4), 159-173.

Post, A. D., Tullis, J., & Yund, R. A. (1996). Effects of chemical environment on dislocation creep of quartzite. *Journal of Geophysical Research: Solid Earth*, *101*(B10), 22143-22155.

Powell, R., & Holland, T. J. B. (1985). An internally consistent thermodynamic dataset with uncertainties and correlations: 1. Methods and a worked example. *Journal of Metamorphic Geology*, *3*(4), 327-342.

Powell, R., & Holland, T. J. B. (1988). An internally consistent dataset with uncertainties and correlations: 3. Applications to geobarometry, worked examples and a computer program. *Journal of metamorphic Geology*, *6*(2), 173-204.

Powell, R., Holland, T. J. B. H., & Worley, B. (1998). Calculating phase diagrams involving solid solutions via non-linear equations, with examples using THERMOCALC. *Journal of metamorphic Geology*, *16*(4), 577-588.

Prior, D. J., Boyle, A. P., Brenker, F., Cheadle, M. C., Day, A., Lopez, G., ... & Timms, N. E. (1999). The application of electron backscatter diffraction and orientation contrast imaging in the SEM to textural problems in rocks. *American Mineralogist*, *84*(11-12), 1741-1759.

References

Puxeddu, M., Saupé, F., Déchomets, R., Gianelli, G., & Moine, B. (1984). Geochemistry and stratigraphic correlations—Application to the investigation of geothermal and mineral resources of Tuscany, Italy: Contribution to the knowledge of the ore deposits of Tuscany, II. *Chemical Geology*, *43*(1-2), 77-113.

Ramsay, J. G. (1980). Shear zone geometry: a review. *Journal of structural geology*, *2*(1-2), 83-99.

Ramsay, J. G., & Graham, R. H. (1970). Strain variation in shear belts. *Canadian Journal of Earth Sciences*, *7*(3), 786-813.

Ranalli, G. (2000). Rheology of the crust and its role in tectonic reactivation. *Journal of geodynamics*, *30*(1-2), 3-15.

Ranalli, G., & Murphy, D. C. (1987). Rheological stratification of the lithosphere. *Tectonophysics*, *132*(4), 281-295.

Rebay, G., & Powell, R. (2002). The formation of eclogite facies metatroctolites and a general petrogenetic grid in Na2O–CaO–FeO–MgO–Al2O3–SiO2–H2O (NCFMASH). *Journal of Metamorphic Geology*, *20*(9), 813-826.

Rybacki, E., Wirth, R., & Dresen, G. (2008). High-strain creep of feldspar rocks: Implications for cavitation and ductile failure in the lower crust. *Geophysical Research Letters*, *35*(4).

Riedel, W. (1929). Zur Mechanik geologischer Brucherscheinungen ein Beitrag zum Problem der Fiederspatten. *Zentbl. Miner. Geol. Palaont. Abt.*, 354-368.

Rosenberg, C. L., & Stünitz, H. (2003). Deformation and recrystallization of plagioclase along a temperature gradient: an example from the Bergell tonalite. *Journal of Structural Geology*, *25*(3), 389-408.

Rossetti, F., Tecce, F., Billi, A., & Brilli, M. (2007). Patterns of fluid flow in the contact aureole of the Late Miocene Monte Capanne pluton (Elba Island, Italy): the role of structures and rheology. *Contributions to Mineralogy and Petrology*, *153*(6), 743-760.

References

Rutter, E. H. (1983). Pressure solution in nature, theory and experiment. *Journal of the Geological Society*, *140*(5), 725-740.

Rutter, E. H. (1986). On the nomenclature of mode of failure transitions in rocks. *Tectonophysics*, *122*(3-4), 381-387.

Rutter, E. H., Holdsworth, R. E., & Knipe, R. J. (2001). The nature and tectonic significance of fault-zone weakening: an introduction. *Geological Society, London, Special Publications*, *186*(1), 1-11.

Sawyer, E. W. (2008). *Atlas of migmatites* (Vol. 9). NRC Research Press.

Schmid, S. M. (1994). Textures of geological materials: computer model predictions versus empirical interpretations based on rock deformation experiments and field studies. In: Bunge, H. J., Siegesmund, S., Skrotzki, W., Weber, K. (Eds.) *Textures of Geological Materials. DGM Informationsgesellschaft Verlag, Oberursel*, 279-301.

Schmid, S. M., & Casey, M. (1986). Complete fabric analysis of some commonly observed quartz c-axis patterns. *Mineral and rock deformation: Laboratory studies*, *36*, 263-286.

Schmid, S. M., Aebli, H. R., Heller, F., & Zingg, A. (1989). The role of the Periadriatic Line in the tectonic evolution of the Alps. *Geological Society, London, Special Publications*, *45*(1), 153-171.

Schmid, S. M., Pfiffner, O. A., Froitzheim, N., Schonborn, G., & Kissling, E. (1996). Geophysical geological transect and tectonic evolution of the Swiss-Italian Alps, *Tectonics 15*, 1036 – 1064.

Schneider, C. A.; Rasband, W. S. & Eliceiri, K. W. (2012). NIH Image to ImageJ: 25 years of image analysis. *Nature methods* 9(7): 671-675.

Scholz, C. H. (1988). The brittle-plastic transition and the depth of seismic faulting. *Geologische Rundschau*, *77*(1), 319-328.

References

Segall, P., & Simpson, C. (1986). Nucleation of ductile shear zones on dilatant fractures. *Geology*, *14*(1), 56-59.

Seifert, F. (1976). Stability of the assemblage cordierite+ K feldspar+ quartz. *Contributions to Mineralogy and Petrology*, *57*(2), 179-185.

Selverstone, J. (2005). Preferential embrittlement of graphitic schists during extensional unroofing in the Alps: the effect of fluid composition on rheology in low-permeability rocks. *Journal of Metamorphic Geology*, *23*(6), 461-470.

Serri, G., Innocenti, F., & Manetti, P. (1993). Geochemical and petrological evidence of the subduction of delaminated Adriatic continental lithosphere in the genesis of the Neogene-Quaternary magmatism of central Italy. *Tectonophysics*, *223*(1-2), 117-147.

Shail, R. K., & Alexander, A. C. (1997). Late Carboniferous to Triassic reactivation of Variscan basement in the western English Channel: evidence from onshore exposures in south Cornwall. *Journal of the Geological Society*, *154*(1), 163-168.

Shea Jr, W. T., & Kronenberg, A. K. (1993). Strength and anisotropy of foliated rocks with varied mica contents. *Journal of Structural Geology*, *15*(9-10), 1097-1121.

Shigematsu, N. (1999). Dynamic recrystallization in deformed plagioclase during progressive shear deformation. *Tectonophysics*, *305*(4), 437-452.

Sibson, R. H. (1977). Fault rocks and fault mechanisms. *Journal of the Geological Society*, *133*(3), 191-213.

Sibson, R. H. (1980). Power dissipation and stress levels on faults in the upper crust. *Journal of Geophysical Research: Solid Earth*, *85*(B11), 6239-6247.

Sibson, R. H. (1981). Fluid flow accompanying faulting: field evidence and models. *Earthquake prediction: an international review*, *4*, 593-603.

References

Sibson, R. H. (1983). Continental fault structure and the shallow earthquake source. *Journal of the Geological Society*, *140*(5), 741-767.

Sibson, R. H. (1984). Roughness at the base of the seismogenic zone: contributing factors. *Journal of Geophysical Research: Solid Earth*, *89*(B7), 5791-5799.

Sibson, R. H. (1985). A note on fault reactivation. *Journal of Structural Geology*, *7*(6), 751-754.

Siivola, J., & Schmidt, R. (2007). List of mineral abbreviations. Recommendations by the IUGS Subcommission on the systematics of metamorphic rocks. In: *Fettes, D. Desmons, J., (Eds.) Metamorphic Rocks: A Classification and Glossary of Terms*. Cambridge University Press, Cambridge.

Simpson, C. (1985). Deformation of granitic rocks across the brittle-ductile transition. *Journal of Structural Geology*, *7*(5), 503-511.

Simpson, C., & De Paor, D. G. (1993). Strain and kinematic analysis in general shear zones. *Journal of Structural Geology*, *15*(1), 1-20.

Siniscalchi, A., Diaferia, I., Liuni, M.P., Loddo, M., Magrì, C., Moretti, P., Schiavone, D., & Tripaldi, S. (2008). Integrated geophysical approach for imaging the Porto Azzurro (Elba, Italy) pluton and the associated structures. In: *Proceedings 33rd International Geological Congress*, Oslo, 6-14 August 2008.

Sleep, N. H., & Blanpied, M. L. (1994). Ductile creep and compaction: A mechanism for transiently increasing fluid pressure in mostly sealed fault zones. *Pure and Applied Geophysics*, *143*(1-3), 9-40.

Smith, S. A. F., Holdsworth, R. E., Collettini, C., & Pearce, M. A. (2011). The microstructural character and mechanical significance of fault rocks associated with a continental low-angle normal fault: the Zuccale Fault, Elba Island, Italy. *Geological Society, London, Special Publications*, *359*(1), 97-113.

References

Spear, F. S., & Cheney, J. T. (1989). A petrogenetic grid for pelitic schists in the system SiO 2-Al 2 O 3-FeO-MgO-K 2 OH 2 O. *Contributions to Mineralogy and Petrology*, *101*(2), 149-164.

Spear, F. S., & Menard, T. (1989). Program GIBBS: A FORTRAN program for Gibbs method calculations. *Rensselaer Polytechnic Institute, Troy, NY*.

Srivastava, P., & Mitra, G. (1996). Deformation mechanisms and inverted thermal profile in the North Almora Thrust mylonite zone, Kumaon Lesser Himalaya, India. *Journal of Structural Geology*, *18*(1), 27-39.

Steffen, K., Selverstone, J., & Brearley, A. (2001). Episodic weakening and strengthening during synmetamorphic deformation in a deep-crustal shear zone in the Alps. *Geological Society, London, Special Publications*, *186*(1), 141-156.

Stipp, M., & Tullis, J. (2003). The recrystallized grain size piezometer for quartz. *Geophysical Research Letters*, *30*(21).

Stipp, M., & Kunze, K. (2008). Dynamic recrystallization near the brittle-plastic transition in naturally and experimentally deformed quartz aggregates. *Tectonophysics*, *448*(1-4), 77-97.

Stipp, M., Stünitz, H., Heilbronner, R., & Schmid, S. M. (2002a). Dynamic recrystallization of quartz: correlation between natural and experimental conditions. *Geological Society, London, Special Publications*, *200*(1), 171-190.

Stipp, M., Stünitz, H., Heilbronner, R., & Schmid, S. M. (2002b). The eastern Tonale fault zone: a 'natural laboratory'for crystal plastic deformation of quartz over a temperature range from 250 to 700 C. *Journal of Structural Geology*, *24*(12), 1861-1884.

Stipp, M., Fügenschuh, B., Gromet, L. P., Stünitz, H., & Schmid, S. M. (2004). Contemporaneous plutonism and strike-slip faulting: A case study from the Tonale fault zone north of the Adamello pluton (Italian Alps). *Tectonics*, *23*(3).

References

Stipp, M., Tullis, J., & Behrens, H. (2006). Effect of water on the dislocation creep microstructure and flow stress of quartz and implications for the recrystallized grain size piezometer. *Journal of Geophysical Research: Solid Earth*, *111*(B4).

Stipp, M., Tullis, J., Scherwath, M., & Behrmann, J. H. (2010). A new perspective on paleopiezometry: Dynamically recrystallized grain size distributions indicate mechanism changes. *Geology*, *38*(8), 759-762.

Stöckhert, B., Brix, M. R., Kleinschrodt, R., Hurford, A. J., & Wirth, R. (1999). Thermochronometry and microstructures of quartz—a comparison with experimental flow laws and predictions on the temperature of the brittle–plastic transition. *Journal of Structural Geology*, *21*(3), 351-369.

Stünitz, H., & Fitz Gerald, J. D. (1993). Deformation of granitoids at low metamorphic grade. II: Granular flow in albite-rich mylonites. *Tectonophysics*, *221*(3-4), 299-324.

Stünitz, H., & Tullis, J. (2001). Weakening and strain localization produced by syn-deformational reaction of plagioclase. *International Journal of Earth Sciences*, *90*(1), 136-148.

Suhr, G. (1993). Evaluation of upper mantle microstructures in the Table Mountain massif (Bay of Islands ophiolite). *Journal of Structural Geology*, *15*(11), 1273-1292.

Tajčmanová, L., Konopásek, J., & Connolly, J. A. (2007). Diffusion-controlled development of silica-undersaturated domains in felsic granulites of the Bohemian Massif (Variscan belt of Central Europe). *Contributions to Mineralogy and Petrology*, *153*(2), 237-250.

Takahashi, M., Mizoguchi, K., Kitamura, K., & Masuda, K. (2007). Effects of clay content on the frictional strength and fluid transport property of faults. *Journal of Geophysical Research: Solid Earth*, *112*(B8).

Takeshita, T., & Hara, I. (1998). c-Axis fabrics and microstructures in a recrystallized quartz vein deformed under fluid-rich greenschist conditions. *Journal of Structural Geology*, *20*(4), 417-431.

References

Takeshita, T., & Wenk, H. R. (1988). Plastic anisotropy and geometrical hardening in quartzites. *Tectonophysics*, *149*(3-4), 345-361.

Takeshita, T., & El-Fakharani, A. H. (2013). Coupled micro-faulting and pressure solution creep overprinted on quartz schist deformed by intracrystalline plasticity during exhumation of the Sambagawa metamorphic rocks, southwest Japan. *Journal of Structural Geology*, *46*, 142-157.

Tarantola, A., Diamond, L. W., Stünitz, H., Thust, A., & Pec, M. (2012). Modification of fluid inclusions in quartz by deviatoric stress. III: Influence of principal stresses on inclusion density and orientation. *Contributions to mineralogy and petrology*, *164*(3), 537-550.

Tchalenko, J. S. (1970). Similarities between shear zones of different magnitudes. *Geological Society of America Bulletin*, *81*(6), 1625-1640.

Theye, T., Reinhardt, J., Goffe, B., Jolivet, L., & Brunet, C. (1997). Ferro-and magnesiocarpholite from the Monte Argentario (Italy): First evidence for high-pressure metamorphism of the metasedimentary Verrucano sequence, and significance for PT path reconstruction. *European Journal of Mineralogy*, 859-874.

Thompson, A. B. (1982). Dehydration melting of pelitic rocks and the generation of H 2 O-undersaturated granitic liquids. *American Journal of Science*, *282*(10), 1567-1595.

Torgersen, E., Viola, G., Sandstad, J. S., Stein, H., Zwingmann, H., & Hannah, J. (2015). Effects of frictional–viscous oscillations and fluid flow events on the structural evolution and Re–Os pyrite–chalcopyrite systematics of Cu-rich carbonate veins in northern Norway. *Tectonophysics*, *659*, 70-90.

Toy, V. (2008). *Rheology of the Alpine Fault mylonite zone: deformation processes at and below the base of the seismogenic zone in a major plate boundary structure*(Doctoral dissertation, University of Otago).

References

Toy, V. G., Prior, D. J., & Norris, R. J. (2008). Quartz fabrics in the Alpine Fault mylonites: Influence of pre-existing preferred orientations on fabric development during progressive uplift. *Journal of Structural Geology*, *30*(5), 602-621.

Trepmann, C. A., & Seybold, L. (2018). Deformation at low and high stress-loading rates. *Geoscience Frontiers*.

Trepmann, C. A., & Stöckhert, B. (2003). Quartz microstructures developed during non-steady state plastic flow at rapidly decaying stress and strain rate. *Journal of Structural Geology*, *25*(12), 2035-2051.

Trepmann, C. A., & Stöckhert, B. (2013). Short-wavelength undulatory extinction in quartz recording coseismic deformation in the middle crust-an experimental study. *Solid Earth*, *4*(2), 263.

Trepmann, C. A., Stöckhert, B., Dorner, D., Moghadam, R. H., Küster, M., & Röller, K. (2007). Simulating coseismic deformation of quartz in the middle crust and fabric evolution during postseismic stress relaxation—an experimental study. *Tectonophysics*, *442*(1-4), 83-104.

Trepmann, C. A., Hsu, C., Hentschel, F., Döhler, K., Schneider, C., & Wichmann, V. (2017). Recrystallization of quartz after low-temperature plasticity–The record of stress relaxation below the seismogenic zone. *Journal of Structural Geology*, *95*, 77-92.

Trotet, F., Vidal, O., & Jolivet, L. (2001). Exhumation of Syros and Sifnos metamorphic rocks (Cyclades, Greece). New constraints on the PT paths. *European Journal of Mineralogy*, *13*(5), 901-902.

Tullis, J. (1970). Quartz: preferred orientation in rocks produced by Dauphiné twinning. *Science*, *168*(3937), 1342-1344.

Tullis, J., & Tullis, T. (1972). Preferred orientation of quartz produced by mechanical Dauphiné twinning: thermodynamics and axial experiments. *Flow and Fracture of Rocks*, 67-82.

References

Tullis, J., & Yund, R. A. (1977). Experimental deformation of dry Westerly granite. *Journal of Geophysical Research*, *82*(36), 5705-5718.

Tullis, J., & Yund, R. A. (1987). Transition from cataclastic flow to dislocation creep of feldspar: Mechanisms and microstructures. *Geology*, *15*(7), 606-609.

Tullis, J., & Yund, R. (1992). The brittle-ductile transition in feldspar aggregates: An experimental study. In *International Geophysics* (Vol. 51, pp. 89-117). Academic press.

Tullis, J., Christie, J. M., & Griggs, D. T. (1973). Microstructures and preferred orientations of experimentally deformed quartzites. *Geological Society of America Bulletin*, *84*(1), 297-314.

Tullis, J., Snoke, A. W., & Todd, V. R. (1982). Significance and petrogenesis of mylonitic rocks. *Geology*, *10*(5), 227-230.

Tullis, J., Dell'Angelo, L., & Yund, R. A. (1990). Ductile shear zones from brittle precursors in feldspathic rocks: the role of dynamic recrystallization. *Geophysical Monograph Series*, *56*, 67-81.

Twiss, R. J. (1977). Theory and applicability of a recrystallized grain size paleopiezometer. In *Stress in the Earth* (pp. 227-244). Birkhäuser, Basel.

Urai, J. L., Means, W. D., & Lister, G. S. (1986). Dynamic recrystallization of minerals. *Mineral and rock deformation: laboratory studies*, *36*, 161-199.

van Daalen, M., Heilbronner, R., & Kunze, K. (1999). Orientation analysis of localized shear deformation in quartz fibres at the brittle–ductile transition. *Tectonophysics*, *303*(1-4), 83-107.

Vermilye, J. M., & Scholz, C. H. (1998). The process zone: A microstructural view of fault growth. *Journal of Geophysical Research: Solid Earth*, *103*(B6), 12223-12237.

References

Vernooij, M. G., Kunze, K., & den Brok, B. (2006a). 'Brittle'shear zones in experimentally deformed quartz single crystals. *Journal of Structural Geology*, *28*(7), 1292-1306.

Vernooij, M. G., den Brok, B., & Kunze, K. (2006b). Development of crystallographic preferred orientations by nucleation and growth of new grains in experimentally deformed quartz single crystals. *Tectonophysics*, *427*(1-4), 35-53.

Vidal, O., & Parra, T. (2000). Exhumation paths of high-pressure metapelites obtained from local equilibria for chlorite–phengite assemblages. *Geological Journal*, *35*(3-4), 139-161.

Vidal, O., Goffé, B., & Theye, T. (1992). Experimental study of the stability of sudoite and magnesiocarpholite and calculation of a new petrogenetic grid for the system FeO–MgO–Al2O3–SiO2–H2O. *Journal of metamorphic Geology*, *10*(5), 603-614.

Vidal, O., Parra, T., & Trotet, F. (2001). A thermodynamic model for Fe-Mg aluminous chlorite using data from phase equilibrium experiments and natural pelitic assemblages in the 100 to 600 C, 1 to 25 kb range. *American journal of Science*, *301*(6), 557-592.

Vidal, O., Parra, T., & Vieillard, P. (2005). Thermodynamic properties of the Tschermak solid solution in Fe-chlorite: Application to natural examples and possible role of oxidation. *American Mineralogist*, *90*(2-3), 347-358.

Vidal, O., De Andrade, V., Lewin, E., Munoz, M., Parra, T., & Pascarelli, S. (2006). P–T-deformation-Fe3+/Fe2+ mapping at the thin section scale and comparison with XANES mapping: application to a garnet-bearing metapelite from the Sambagawa metamorphic belt (Japan). *Journal of Metamorphic Geology*, *24*(7), 669-683.

Viegas, G., Menegon, L., & Archanjo, C. (2016). Brittle grain-size reduction of feldspar, phase mixing and strain localization in granitoids at mid-crustal conditions (Pernambuco shear zone, NE Brazil). *Solid Earth*, *7*(2), 375-396.

Viola, G., Torgersen, E., Mazzarini, F., Musumeci, G., van der Lelij, R., Schönenberger, J., & Garofalo, P. S. (2018). New Constraints on the Evolution of the Inner Northern Apennines

by K-Ar Dating of Late Miocene-Early Pliocene Compression on the Island of Elba, Italy. *Tectonics*, *37*(9), 3229-3243.

Voll, G. (1976). Recrystallization of quartz, biotite and feldspars from Erstfeld to the Leventina Nappe, Swiss Alps, and its geological significance. *Schweizerische mineralogische und petrographische Mitteilungen 56*, p.147.

Wallis, S. (1995). Vorticity analysis and recognition of ductile extension in the Sanbagawa belt, SW Japan. *Journal of Structural Geology*, *17*(8), 1077-1093.

Walshe, J. L. (1986). A six-component chlorite solid solution model and the conditions of chlorite formation in hydrothermal and geothermal systems. *Economic Geology*, *81*(3), 681-703.

Wang, G. F., & Banno, S. (1987). Non-stoichiometry of interlayer cations in micas from low-to middle-grade metamorphic rocks in the Ryoke and the Sanbagawa belts, Japan. *Contributions to Mineralogy and Petrology*, *97*(3), 313-319.

Wei, C., & Powell, R. (2004). Calculated phase relations in high-pressure metapelites in the system NKFMASH (Na2O–K2O–FeO–MgO–Al2O3–SiO2–H2O). *Journal of Petrology*, *45*(1), 183-202.

Wellman, H. W. (1955). New Zealand quaternary tectonics. *Geologische Rundschau*, *43*(1), 248-257.

Wendel, J. (2015). Tiny mineral grains could drive plate tectonics, *Eos, 96.*

Wenk, H. R., Bennett, K., Canova, G. R., & Molinari, A. (1991). Modelling plastic deformation of peridotite with the self-consistent theory. *Journal of Geophysical Research: Solid Earth*, *96*(B5), 8337-8349.

Westerman, D. S., Dini, A., Innocenti, F., & Rocchi, S. (2004). Rise and fall of a nested Christmas-tree laccolith complex, Elba Island, Italy. *Geological Society, London, Special Publications*, *234*(1), 195-213.

References

Wheeler, J. (1992). Importance of pressure solution and Coble creep in the deformation of polymineralic rocks. *Journal of Geophysical Research: Solid Earth*, *97*(B4), 4579-4586.

White, S. (1976). A Discussion on natural strain and geological structure-The effects of strain on the microstructures, fabrics, and deformation mechanisms in quartzites. *Phil. Trans. R. Soc. Lond. A*, *283*(1312), 69-86.

White, S. (1977). Geological significance of recovery and recrystallization processes in quartz. *Tectonophysics*, *39*(1-3), 143-170.

White, S. (1979). Grain and sub-grain size variations across a mylonite zone. *Contributions to Mineralogy and Petrology*, *70*(2), 193-202.

White, S. H., Burrows, S. E., Carreras, J., Shaw, N. D., & Humphreys, F. J. (1980). On mylonites in ductile shear zones. *Journal of Structural Geology*, *2*(1-2), 175-187.

White, R. W., Powell, R., Holland, T. J. B., & Worley, B. A. (2000). The effect of TiO2 and Fe2O3 on metapelitic assemblages at greenschist and amphibolite facies conditions: mineral equilibria calculations in the system K2O-FeO-MgO-Al2O3-SiO2-H2O-TiO2-Fe2O3. *Journal of Metamorphic Geology*, *18*(5), 497-511.

White, R. W., Powell, R., & Holland, T. J. B. (2001). Calculation of partial melting equilibria in the system Na2O–CaO–K2O–FeO–MgO–Al2O3–SiO2–H2O (NCKFMASH). *Journal of metamorphic Geology*, *19*(2), 139-153.

White, R. W., Powell, R., & Clarke, G. L. (2002). The interpretation of reaction textures in Fe-rich metapelitic granulites of the Musgrave Block, central Australia: constraints from mineral equilibria calculations in the system K2O–FeO–MgO–Al2O3–SiO2–H2O–TiO2–Fe2O3. *Journal of metamorphic Geology*, *20*(1), 41-55.

White, R. W., Pomroy, N. E., & Powell, R. (2005). An in situ metatexite–diatexite transition in upper amphibolite facies rocks from Broken Hill, Australia. *Journal of Metamorphic Geology*, *23*(7), 579-602.

References

White, R. W., Powell, R., & Holland, T. J. B. (2007). Progress relating to calculation of partial melting equilibria for metapelites. *Journal of Metamorphic Geology*, *25*(5), 511-527.

Wiewióra, A., & Weiss, Z. (1990). Crystallochemical classifications of phyllosilicates based on the unified system of projection of chemical composition: II. The chlorite group. *Clay Minerals*, *25*(1), 83-92.

Wilks, K. R., & Carter, N. L. (1990). Rheology of some continental lower crustal rocks. *Tectonophysics*, *182*(1-2), 57-77.

Wintsch, R. P., Christoffersen, R., & Kronenberg, A. K. (1995). Fluid-rock reaction weakening of fault zones. *Journal of Geophysical Research: Solid Earth*, *100*(B7), 13021-13032.

Wise, D. U., Dunn, D. E., Engelder, J. T., Geiser, P. A., Hatcher, R. D., Kish, S. A., ... & Schamel, S. (1984). Fault-related rocks: Suggestions for terminology. *Geology*, *12*(7), 391-394.

Worley, B., Powell, R., & Wilson, C. J. (1997). Crenulation cleavage formation: Evolving diffusion, deformation and equilibration mechanisms with increasing metamorphic grade. *Journal of Structural Geology*, *19*(8), 1121-1135.

Wu, C. M., & Chen, H. X. (2015). Revised Ti-in-biotite geothermometer for ilmenite-or rutile-bearing crustal metapelites. *Science bulletin*, *60*(1), 116-121.

Xie, X., Byerly, G. R., & Ferrell Jr, R. E. (1997). IIb trioctahedral chlorite from the Barberton greenstone belt: crystal structure and rock composition constraints with implications to geothermometry. *Contributions to Mineralogy and Petrology*, *126*(3), 275-291.

Xypolias, P. (2010). Vorticity analysis in shear zones: a review of methods and applications. *Journal of Structural Geology*, *32*(12), 2072-2092.

Zhang, L., & He, C. (2016). Frictional properties of phyllosilicate-rich mylonite and conditions for the brittle-ductile transition. *Journal of Geophysical Research: Solid Earth*, *121*(4), 3017-3047.

References

Zhang, S., & Karato, S. I. (1995). Lattice preferred orientation of olivine aggregates deformed in simple shear. *Nature*, *375*(6534), 774.

Zang, W., & Fyfe, W. S. (1995). Chloritization of the hydrothermally altered bedrock at the Igarapé Bahia gold deposit, Carajás, Brazil. *Mineralium Deposita*, *30*(1), 30-38.

Zhu, W., & Wei, C. (2007). Thermodynamic modelling of the phengite geobarometry. *Science in China Series D: Earth Sciences*, *50*(7), 1033-1039.

Zoback, M. D., & Harjes, H. P. (1997). Injection-induced earthquakes and crustal stress at 9 km depth at the KTB deep drilling site, Germany. *Journal of Geophysical Research: Solid Earth*, *102*(B8), 18477-18491.

Appendix A

List of Abbreviations

Appendix A

This section provides a list of abbreviations of geological features, methodologies, devices or plots that have been widely used throughout the text.

ASPO: Aggregate Shape Preferred Orientation

C'1: synthetic C' shear band.

C'2: antithetic C' shear band.

Cf: cataclastic foliation.

CN-MAT: Capo Norsi – Monte Arco Thrust (following Viola et al., 2018).

CPO: Crystallographic Preferred Orientation/lattice preferred orientation.

CSZ: Calanchiole Shear Zone.

DT: Di-Trioctahedral substitution.

EBSD: Electron Back Scatter Diffraction.

EMPA: Electron Micro Probe Analysis.

FM: Ferro-Magnesian substitution

FSZ: Felciaio Shear Zone.

HSD: High-strain domain.

IPF: Inverse Pole Figure.

Lp: Main lineation.

LpH: Main lineation in high-strain domains.

LpL: Main lineation in low-strain domains.

LSD: Low-strain domain.

MAD: Misorientation Angle Distribution.

MET: Multi-Equilibrium Thermobarometry.

MUD: Multiple of a Uniform Distribution.

MOCC: Mis-Orientation angle distribution in Crystal Coordinates.

MOSC: Mis-Orientation angle distribution in Sample Coordinates.

N//: parallel polarizers or parallel Nicols.

NX: crossed polarizers or crossed Nicols.

Ø: diameter of equivalent circle (grain size parameter).

P.f.u: Per formula units.

PF: Pole Figure.

PG: Paragonitic substitution.

PY: Pyrophyllitic substitution.

R1: R1 Riedel shear, with synthetic sense of shear with respect to the Y-shear.

Appendix A

R2: R2 Riedel shear, conjugate with R1 and antithetic with respect to the Y-shear.

SEM: Scanning Electron Microscope.

Sm: Main mylonitic foliation.

Sp: Main foliation, after *Schistositè Principale* (french geologic literature).

SpH: Main foliation in high-strain domains.

SpL: Main foliation in low-strain domains.

SPO: Shape Preferred Orientation.

TK: Tschermak substitution

XFe: Ratio between Fe and Mg content expressed in p.f.u.

Y: Y-shear, master fault zone or plane parallel to the master fault (Logan et al., 1992).

ZF: Zuccale Fault.

Appendix B

List of Mineral Abbreviations

Appendix B

The abbreviations used in this thesis are largely those used by THERMOCALC (Powell et al., 1998). Some abbreviations have been changed (e.g. white mica) to avoid confusion between minerals and end-members. Abbreviations of minerals not present in the THERMOCALC dataset are from Siivola and Schmid (2007) and are listed here.

List of phase/mineral abbreviations

And	Andalusite
Ap	Apatite
Bi	Biotite
Cam	Clinoamphibole
Cc	Calcite
Cd	Cordierite
Chl	Chlorite
Di	Diopside
Dl	Dolomite
Ep	Epidote
G	Garnet
Hem	Hematite
Ilm	Ilmenite
Ksp	K-feldspar
Ky	Kyanite
Lim	Limonite***
Liq	Melt*
Mz	Monazite
Mt	Magnetite
Mu	Muscovite*
Op	Opaque mineral**
Opx	Orthopyroxene
Pl	Plagioclase
Py	Pyrite
Q	Quartz
Ru	Rutile
Ser	Sericite***
Sill	Sillimanite

Ta	Talc
Tr	Tremolite
Ttn	Titanite
Tur	Tourmaline
Ves	Vesuvianite
Wm	White Mica
Wo	Wollastonite
Zr	Zircon

*: solution model used by THERMOCALC; **: opaque mineral/phases that have been observed in thin section and not discriminated by other means (SEM/EMPA/reflected light); ***: descriptive term denoting a fine-grained variety of a mineral or a mix of different phases.

List of end-member abbreviations

ab	albite
afch	Al-free chlorite
ames	amesite
an	anorthite
ann	annite
cel	celadonite
chm	chamosite
clin	clinochlore
crdp	corundophilite
daph	daphnite
east	eastonite
fafch	Fe Al-free chlorite
fames	Fe-amesite
fsud	Fe-sudoite
mu	muscovite
olig	oligoclase
phl	phlogopite
prl	pyrophyllite
sid	siderophyllite
sud	sudoite
tri	trioctahedral mica

Appendix C

Localities and Toponyms

Appendix C

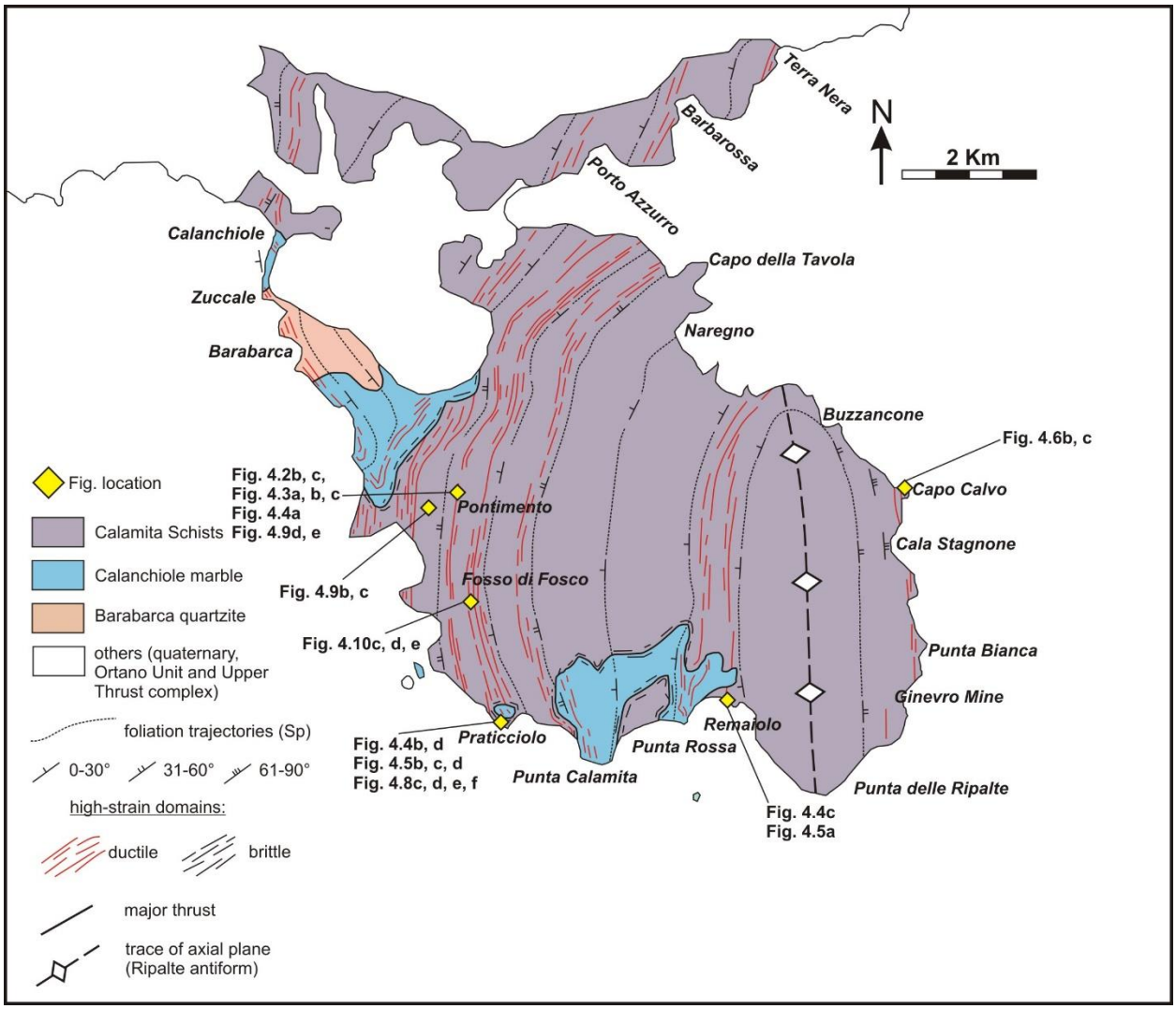

Figure C1 - Schematic geological-structural map reporting toponyms and the location of figures shown in Chapter 4.

Appendix C

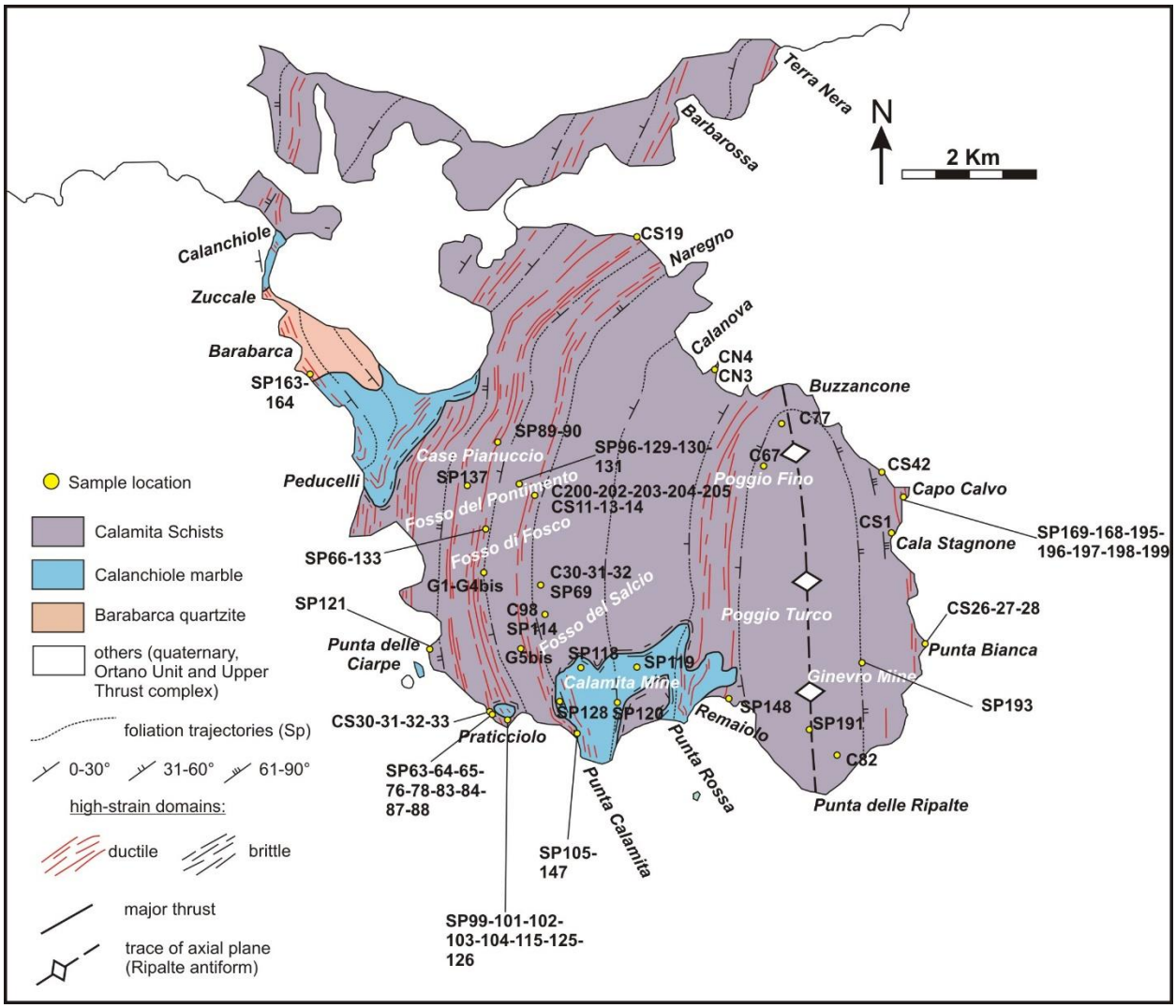

Figure C2 - Schematic geological-structural map reporting location of samples investigated in this study. GPS coordinates are available in Appendix D. Detailed location of samples in key areas in Chapter 4.

Appendix D

Sample Details

Appendix D

Table D1 – Description of samples collected in this thesis, listing: label, locality, GPS coordinates (based on WGS84 datum), mineral assemblage, lithology and fabric description. A brief description of quartz microfabric is included, when possible. Mineral abbreviations after **Appendix B**. **LSD:** Low-strain domains; **HSD:** High-strain domains. For the sake of simplicity type 1,2 and 3 quartz microfabrics (see **Chapter 4**) are directly described here as GBM-, SGR- and BLG-recrystallization features.

Label	Locality	GPS coordinates	Assemblage	Lithology	Fabric description
C30	Fosso del Salcio	42°43'25.99"N 10°23'16.96"E	**Peak:** Wm + Q + Cd + And + Bi + Op **Retrograde:** Wm (static)	Graphitic micaschist	**LSD:** decussate grains of Wm overprinting a Wm + Q + Bi foliation. Crenulated older foliation.
C31	Fosso del Salcio	42°43'25.57"N 10°23'23.18"E	**Peak:** Wm + Bi + Q + Cd + And + Op **Retrograde:** Wm + Chl + Q	Graphitic micaschist	**HSD**: well-foliated schist with quartz ribbons and synkinematic And-Cd porbhyroblasts. **Quartz:** GBM → SGR/BLG
C32	Fosso del Salcio	42°43'25.57"N 10°23'23.18"E	**Peak:** Bi + Wm + Q **Retrograde:** Ser	Foliated quartzite	**HSD:** foliated and folded quartzite with quartz bands alternating to thin lepidoblastic mica-layers. **Quartz:** GBM → SGR. Localized BLG. SGR-grains defining axial plane foliation.
C67	Poggio Fino	42°43'55.91"N 10°25'2.68"E	**Peak**: Bi + Q + Cd + And + Op **Retrograde:** Wm	Graphitic micaschist	**LSD:** Op-rich lepidoblastic Bi foliation alternated to retrograde Wm-domains and Q-ribbons. And + Cd rich in Op inclusions. **Quartz:** interlobate to granoblastic microfabric.
C77	Poggio Fino	42°44'7.86"N 10°25'7.42"E	**Peak:** Bi + Q + Op **Retrograde:** Wm	Micaschist	**HSD:** fine-grained schist with boudinated quartz layers. Local older cleavage in microlithons. Foliation boudinage **Quartz:** GBM microfabric overprinted by SGR.
C82	Punta delle Ripalte	42°42'30.42"N 10°25'20.80"E	**Peak:** Bi + Q + sericitized Cd? + And? + Ksp? + Pl? + Op **Retrograde:** Wm I (on foliation); Wm II (static)	Micaschist	**LSD:** coarse-grained micaschist with quartz boudins overprinted by diablastic Wm. **Quartz:** GBM → weakly overprinted by SGR
C98	Fosso del Salcio	42°43'19.37"N 10°23'34.26"E	**Peak:** Bi + Q + And + Op(schist) **Retrograde:** Wm (schist) **Dyke:** Qz + Ksp + Wm + Tur	foliated leucogranite / schistose host rock	**HSD:** well foliated leucogranite dyke in contact with host schistose rocks. Mylonitic foliation parallel in both domains.
C200$^{(2)}$	Fosso del Pontimento	42°44' 2.11"N 10°23'3.35"E	**Peak:** Bi + Q + And + Ksp + Pl + Cd + Op **Retrograde:** Wm + Chl + Op	Micaschist	**HSD:** Strained high-grade pods (Bi + And + Cd + Ksp) with lepidoblasytic Bi and pokiloblastic Bi + Op inclusions associated with strongly recrystallized Q-ribbons. Static retrograde Wm (Ser) + Chl **Quartz:** GBM fabric (amoeboid grain boundaries) overprinted by SGR.

Appendix D

C202[(2)]	Fosso del Pontimento	42°44' 2.11"N 10°23'3.35"E	**Peak:** Bi + Q + And + Ksp + Pl + Cd + Op **Retrograde:** Wm + Chl + Op	Micaschist	**HSD:** folded Bi-domains (lepidoblastic) and amoeboid Q-ribbons with And – Cd – Ksp porphyroclasts, overprinted by static Ser growth. **Quartz:** Island grains and reticular microstructures (GBM-recrystallization).
C203[(2)]	Fosso del Pontimento	42°44' 2.11"N 10°23'3.35"E	**Peak:** Bi + Q + And + Ksp + Pl + Cd + Op **Retrograde:** Wm + Chl + Op	Micaschist	**HSD:** Q-ribbons and lepidoblastic Bi-domains with poikiloblastic Ksp (with Bi inclusions) wrapped by well-developed schistosity. Static Ser growth. **Quartz:** GBM fabric (island grains and amoeboid grains) overprinted by subgrains (SGR).
C204	Fosso del Pontimento	42°44' 2.11"N 10°23'3.35"E	**Peak:** Bi + Q + Cd + And + Ksp + Op **Retrograde:** Wm + Chl + Op	Micaschist	**HSD:** High-grade relics (Bi + Ksp + Cd + And) largely overprinted by the development of a fine-grained Wm-rich foliation. Strong pinitization over Cd. **Quartz:** GBM microfabric preserved.
C205	Fosso del Pontimento	42°44' 2.11"N 10°23'3.35"E	**Peak:** Bi + Q + Cd + And + Op **Retrograde:** Wm + Chl + Op	Schist	**HSD:** Schistose structure characterized by alternations of Q-ribbons and fine-grained Wm-domains. Porphyroclasts largely reduced to Ser-ribbons. **Quartz:** GBM (lobate grains) overprinted by SGR/BLG.
CN3	Calanova	42°44'37.17"N 10°24'52.49"E	**Peak:** Bi + Q + sericitized Al-silicates + Op **Retrograde:** Wm + Ser	Sericite-schist	**LSD:** misoriented Wm-Bi aggregates wrapping deformed Q lenses. Strong sericitic alteration. **Quartz:** GBM overprinted by SGR.
CN4[(2)]	Punta Calanova	42°44'37.17"N 10°24'52.49"E	**Peak:** Bi + Q + And + Ksp + Op **Retrograde:** Ser + Chl	Hornfels	**LSD:** diablastic Wm-Bi aggregates intergrown with And-Cd-Ksp grains. Dynamically deformed Q. Strong sericitic alteration. **Quartz:** Strong amoeboid fabric with strong SPO (GBM).
CS1[(2)]	Cala Stagnone	42°43'47.82"N 10°25'54.57"E	**Peak:** Bi + Q + And + Cd + Ksp + Op **Retrograde:** Ser	Micaschist	**LSD:** micaschist with Q ribbons and lepidoblastic Bi-layers with And + Cd + Ksp porphyroclasts with poikilitic Bi inclusions. Static Ser overgrowth. **Quartz:** Amoeboid grain boundaries. Island grains. Pinning microstructures (GBM)
CS11	Fosso del Pontimento	42°44'2.55"N 10°23'1.11"E	**Peak:** Bi + Q + Cd + And + Wm + Op **Retrograde:** Wm + Ser + Chl	Bi-micaschist	**HSD:** Coarse grained rock with stretched quartz ribbons and boudinated Bi-CD porphyroclasts embedded in a misoriented sericitic matrix. **Quartz:** GBM + SGR. Localized BLG.
CS13	Fosso del Pontimento	42°44'2.55"N 10°23'1.11"E	**Peak:** Bi + Q + And + Op **Retrograde:** Wm + Ser + Chl	Hornfels	**LSD:** Alternations of foliated Q-lenses and mica-domains where static Wm + Ser overgrows peak Bi + And.

					Quartz: interlobate to amoeboid microfabric with island grains (GBM)
CS14	Fosso del Salcio	42°43'12.69"N 10°23'15.43"E	**Peak:** Bi + Q + Cd + And + Op **Retrograde:** Wm + Chl + Op	Micaschist	**LSD:** main foliation defined by subparallel Q-domain, Bi-ribbons and Wm-domains overprinted by diablastic micas. Sericitized Cd + And. **Quartz:** interlobate microfabric with undulose extinction and slight recrystallization (GBM → SGR)
CS19	Naregno	42°45'24.70"N 10°24'8.19"E	**Peak:** Bi + Q + Tur **Retrograde:** Chl + Wm	Foliated quartzite	**HSD:** folded quartzitewith shear planes localized on reverse limbs and new quartz grains defining the axial plane foliation. Hydrothermal Chl in veins. **Quartz:** GBM → SGR/BLG
CS26[(2)]	Punta Bianca	42°43'30.80"N 10°26'2.95"E	**Peak:** Bi + Q + Ksp + And + Pl + Op **Retrograde:** Bi + Wm + Op	Micaschist	**LSD:** Foliated Bi + Ksp + And aggregates with weak preferred orientation overprinted by late crenulations. Poikiloblastic Bi + Ksp + And intergrowths **Quartz:** Coarse-grained interlobate microfabric (GBM)
CS27	Punta Bianca	42°43'30.80"N 10°26'2.95"E	Bi + Q + Opx + Ksp + Pl + Op	Opx-quartzite	**LSD:** Fine-grained quartzite with lobate Bi grains and skeletal Opx grains in medium-grained lobate quartz. Fine-grained Ksp + Pl.
CS28	Punta Bianca	42°43'30.80"N 10°26'2.95"E	Bi + Opx + Q + And + Ksp + Pl	Micaschist	**LSD:** crenulated Bi + Ksp domains with static Ep growth. Coarse grained Q-lenses with GBM microstructures. Saussuritized Pl.
CS30	Praticciolo	42°42'52.09"N 10°23'2.07"E	**Peak:** Bi + Q + Cd + Op **Retrograde:** Wm + Chl + Op (mylonitic fol.)	Mylonitic micaschist	**HSD:** S-C' mylonitic fabric with synkinematic deformed pinitized Cd-fish (top-to-the-E) and recrystallized quartz ribbons. Relic Bi grains preserved in Q and Cd. **Quartz**: GBM overprinted by SGR (ribbons) and BLG (shear bands).
CS31	Praticciolo	42°42'52.09"N 10°23'2.07"E	**Peak:** Bi + Q + And + Cd + Op **Retrograde:** Wm + Ser + Op	And-micaschist	**HSD:** Euhedral And-Cd porphyroclasts wrapped by strain caps and lepidoblastic Bi. Recrystallized quartz ribbons and Wm aligned on the main foliation. **Quartz:** GBM → SGR
CS32	Praticciolo	42°42'52.09"N 10°23'2.07"E	**Peak:** Bi + Q + And + Cd + Op **Retrograde:** Wm + Ser + Op (mylonitic fol.)	Protomylonitic And-micaschist	**HSD:** And-Cd-Bi lenses sheared along C' shear bands (top-to-the-E) and wrapped by recrystallized quartz ribbons and lepidoblastic Wm. **Quartz:** SGR dominated.
CS33	Praticciolo	42°42'52.09"N 10°23'2.07"E	**Peak:** Bi + Q + And + Cd + Op **Retrograde:** Wm + Ser + Chl + Op (mylonitic fol.)	Mylonitic micaschist	**HSD:** And-Cd-Bi pods and quartz ribbons and lenses wrapped by Wm-rich mylonitic foliation and sheared along C' shear bands (top-to-the-E). Wm-mica fish in quartz. Synkinematic Cd. **Quartz:** GBM → SGR/BLG

Appendix D

CS42[1,2]	Capo Calvo	42°44'7.48"N 10°25'53.15"E	**Peak:** Bi + Ksp + Pl + Cd + Q + Ilm; accessory And **Retrograde:** Bi + Wm + Ser (static)	Bi-Q-Ksp micaschist (anatexite)	**HSD:** Dynamically deformed Q and lepidoblastic Bi associated to Al-silicates strongly overprinted by sericitic alteration. **Quartz:** GBM-dominated. Reticular and island grains. Pinning microstructures.
G1bis	Fosso di Fosco	42°43'28.84"N 10°22'55.93"E	**Peak:** Wm + Bi + Q + Ksp + And + Cd + Op **Retrograde:** Wm + Chl + Op	Foliated quartzite	**LSD:** quartzite interlayered with thin Bi-Wm lepidoblastic domains with porphyroblasts of Ksp + And + Cd. **Quartz:** GBM microfabric (reticular grains and island grains) with weak undulose extinction.
G4bis	Fosso di Fosco	42°43'28.84"N 10°22'55.93"E	**Pre-HT/LP:** Wm + Q + Op **Peak:** Wm + Bi + Q + And + Cd + Op **Retrograde:** Wm + Chl + Op	Micaschist	**LSD:** Micaschist with boudinated Q-lenses and relics of an older, crenulated, foliation. Bi and Wm inclusions in And. **Quartz:** GBM/SGR
G5bis	Fosso del Salcio	42°43'12.85"N 10°23'19.10"E	**Peak:** Bi + Q + Cd + And + Op **Retrograde:** Wm + Chl + Op	Micaschist	**HSD:** Foliation defined by subparallel Q-ribbons, Wm-domains and Bi-domains. Boudinated Q-lenses. Pinitized Cd **Quartz:** interlobate microfabric (GBM)
SP63[1]	Praticciolo	42°42'52.44"N 10°23'1.24"E	**Wall rock:** Q + Wm + Chl + Ilm **Cataclasite:** Q + phyllosilicates + Py + Op	Cataclasite	**HSD:** contact between cataclasite and quartzite (wall-rock). Banded microfabric with ultracataclasite localized at the contact. Top-to-the-E. **Quartz:** GBM → SGR → BLG → Brittle overprint.
SP64	Praticciolo	42°42'52.21"N 10°23'1.15"E	**Peak:** Bi + Q + And + Cd + Op **Retrograde:** Wm + Chl + Op	Mylonitic micaschist	**HSD:** Bi + And + Cd pods wrapped by a mylonitic foliation consisting of Chl + Wm and recrystallized quartz ribbons with S-C' fabric (top-to-the-E) **Quartz:** GBM → SGR/BLG
SP65[1]	Praticciolo	42°42'52.29"N 10°23'1.55"E	**Peak:** Bi + Q + And + Cd + Op **Retrograde:** Wm + Chl + Op	Mylonitic micaschist	**HSD:** Mylonitic Wm + Chl foliation eveloping Cd + And + Bi porphyroclasts and recrystallized Q-ribbons. S-C' fabric and asymmetric boudinage of Q. Top-to-the-E. **Quartz:** relic GBM-grains overprinted by dominant SGR.
SP66	Fosso Fosco	42°43'41.61"N 10°22'54.90"E	**Peak:** Bi + Q + Cd + And + Op **Retrograde:** Wm + Chl + Op	Micaschist	**LSD:** Coarse-grained Q + Bi schistosity overgrown by decussate Wm aggregates. Sericitized And + Cd porphyroclasts. **Quartz:** Slightly lobate ribbons (GBM).
SP69	Fosso del Salcio	42°43'24.07"N 10°23'28.25"E	**Pre-HT/LP:** Wm + Q + Op **Peak:** Bi + Wm + Q + And + Cd + Op	Graphitic micaschist	**LSD:** schist with asymmetric boudins and synkinematic And + Cd grains (millipede structures). Older crenulated foliation in microlithons. **Quartz:** dominant SGR

Appendix D

SP76	Praticciolo	42°42'55.35"N 10°22'56.58"E	**Peak:** Bi + Q + And + Cd + Op **Retrograde:** Wm + Chl + Ser + Op (mylonitic fol.)	Mylonitic micaschist	**HSD:** Large quartz boudin wrapped by Wm-defined mylonitic foliation and C' shear bands (top-to-the-E). Pre- to syn-kinematic And-Cd, associated with Bi. Sericite ribbons. **Quartz:** GBM → SGR. Original protolithic quartz structures locally preserved.
SP78[(1)]	Praticciolo	42°42'55.67"N 10°22'56.72"E	**Peak:** Bi + Q + And + sericitized Cd? + Op **Retrograde:** Wm + Ser + Chl + Op	Mylonitic quartzite	**HSD:** Mylonitic quartzite with ultramylonitic sericitc bands and widespread S-C' fabric anc conjugate shear bands (top-to-the-E). **Quartz:** GBM (relics) → SGR → BLG. Possible phase mixing.
SP83	Praticciolo	42°42'52.52"N 10°23'1.39"E	Q + Chl + Ser + Wm	Quartzitic schist	**HSD:** Schistose quartzite with anastomosing fine-grained Ser-bands and large Q grains with undulose extinction mantled by new grains.
SP84	Praticciolo	42°42'52.59"N 10°23'1.37"E	Cam + Q + Cc + Ep	Calcsilicate rock	**Quartz:** BLG dominated. Metasomatic rock dominated by polygonal aggregates of Cam overprinting a foliated Q + Cc matrix.
SP87	Praticciolo	42°42'52.55"N 10°23'2.18"E	Cc + Dl + Tr + Ta + Ser + Ep	Marble	**LSD:** Granoblastic marble with foliated Tr + Ta + Ser bands and tiny Ep grains.
SP88	Praticciolo	42°42'50.71"N 10°23'5.26"E	**Peak:** Bi + Q + And + Cd + Op **Retrograde:** Wm + Chl + Op	Mylonitic micaschist	**HSD:** Lepidoblastic Wm-domains and Q-ribbons with synkinematic And + Cd grains and C' shear bands (top-to-the-E) Sericitic ribbons. **Quartz:** GBM → SGR/BLG
SP89	Case Pianuccio	42°44'12.04"N 10°22'41.34"E	**Peak:** Bi + Q + And + Cd + Op **Retrograde:** Wm + Chl + Op	Micaschist	**LSD:** Thick alternations of Q-ribbons and lepidoblastic Bi-rich and Wm-rich domains with strong preferred orientation wrapping pinitized Cd and And porphyroclasts. **Quartz:** Medium to fine grained with slightly interlobate boundaries.
SP90	Case Pianuccio	42°44'12.06"N 10°22'41.48"E	Peak: Bi + Q + Cd + And + Op Retrograde: Bi + Wm + Chl + Op	Quartzitic schist	**LSD:** folded Q-rich and Bi-rich domains with And + Cd porphyroclasts. Bi + Wm + Chl aggregates parallel to the axial plane foliation. **Quartz:** equigranular to slightly lobate boundaries. Weak undulose extinction.
SP96	Fosso del Pontimento	42°44'2.93"N 10°22'58.99"E	**Leucogranite:** Q + Tur + Ksp + Wm. **Host:** Bi + Wm + Q	deformed Tur-leucogranite in micaschist	**HSD:** Fine-grained schist wrapping a deformed leucogranite dyke. **Quartz:** strong SGR to BLG.
SP99	Praticciolo	42°42'51.17"N 10°23'6.75"E	**Peak:** Bi + Q + Sericitized Al-silicates (Cd + And?) + Op	Micaschist	**HSD:** Well-developed foliation constituted by fine-grained Wm-domains, sericite ribbons, stretched Q-ribbons and boudinated Bi-rich

			Retrograde: Wm + Chl + Op		lenses. Sericite form pseudomorphs over porphyroclasts. **Quartz:** Peak interlobate fabric (GBM) overprinted by undulose extinction and core-and-mantle structures (SGR + BLG).
SP101	Praticciolo	42°42'51.15"N 10°23'7.12"E	**Peak:** Bi + Q + And + Cd + Op **Retrograde:** Wm + Chl + Op	Protomylonitic micaschist	**HSD:** High grade relics (Bi + Cd + And) wrapped by Wm + Chl mylonitic foliation. Quartz boudins wrapped by recrystallized Q-ribbons. S-C' fabric (top-to-the-E). **Quartz:** GBM → SGR + BLG
SP102	Praticciolo	42°42'52.57"N 10°23'8.41"E	Cc + Dl + Tr + Ta + Ser	Impure marble	**LSD:** Impure marble with Tr + Ta + Ser inclusions.
SP103	Praticciolo	42°42'52.70"N 10°23'8.76"E	Ep + Cam + Ves + Q + Cc	Epidosite	Metasomatic rock consisting of euhedral Ep + Cam grains and coarse accessory Q + Cc + Ves.
SP104	Praticciolo	42°42'55.53"N 10°23'13.06"E	**Pre-HT/LP:** Wm + Q + Op **Peak:** Bi + Wm + Q + Cd + And + Op	Schist	**HSD:** stretched Q-ribbons interlayered with lepidoblastic Bi-Wm domains. Strong sericitization of And + Cd. Weakly developed C' shear bands (top-to-the-E).
SP105	Calamita Mine	42°42'51.01"N 10°23'32.51"E	Wm + Q + Cd + And + Bi	Micaschist	**Quartz**: GBM + dominant SGR **LSD:** Alternations of Wm-domain and Q-domains (SGR to BLG). Pre- to synkinematic sericitized Cd – And porphyroclasts. Accessory Bi. Presence of slight crenulations.
SP114	Fosso del Salcio	42°43'19.91"N 10°23'35.09"E	Q + Wm + Ser + Bi + sericitized Al silicates (Cd + And?) + Op	Quartzitic schist	**HSD:** stretched Q ribbons elongated parallel to Wm-Bi lepidoblastic domains. Sericitized ribbons. **Quartz:** granoblastic to interlobate microfabric.
SP115	Praticciolo	42°43'10.06"N 10°23'16.35"E	**Peak:** Bi + And + Cd + Op **Retrograde:** Wm + Chl + Op	Micaschist	**HSD:** Wm-Bi lepidoblastic domains with granoblastic Q-lenses and local decussate Wm aggregates. Strongly sericitized rotated Cd + And porphyroblasts.
SP118	Calamita Mine	42°42'57.84"N 10°23'39.48"E	Cc + Dl + Tr + Phl + Ta	Impure marble	**LSD:** granoblastic Cc + Dl texture with sparse Tr + Ta + Phl aggregates.
SP119	Calamita Mine	42°42'58.79"N 10°23'50.72"E	Cc + Dl + Di + Phl + Ta + Ser	Cataclasite	**HSD:** Fragments of marble (Cc + Dl), impure marble (Tr + Ta + Phl bearing) and fractured Q embedded in a Cc + Dl + Tr + Ta rich matrix.
SP120	Calamita Mine	42°42'51.90"N 10°23'46.34"E	Cc + Dl + Tr + Ta + Phl	Impure marble	**LSD:** Fine-grained marble wrapping Tr + Ta-rich lepidoblastic domains and large Cc + Dol aggregates.
SP121	Punta delle Ciarpe	42°43'9.47"N 10°22'34.57"E	**Peak:** Bi + Q + And + Cd + Op **Retrograde:** Wm + Chl + Op	Micaschist	**LSD:** Alternations of Bi ribbons (with And + Cd) and Wm domains with interlayered coarse Q grains. Strong sericitization of And + Cd. Very weakly developed C' shear bands (top-to-the-E).

Appendix D

					Quartz: Lobate granoblastic fabric with undulose extinction.
SP125	Praticciolo	42°42'52.55"N 10°23'9.55"E	**Peak:** Bi + Q + And + Cd + Op **Retrograde:** Wm + Chl + Op	Mylonitic micaschist	**HSD:** And + Cd + Bi relics wrapped by Wm + Chl mylonitic foliation and sheared by top-to-the-E C' shear bands. **Quartz:** GBM (peak) overprinted by dominant SGR and localized BLG. Mylonitic ribbons.
SP126	Praticciolo	42°42'52.63"N 10°23'9.84"E	**Peak:** Bi + And + Cd + Q + Op **Retrograde:** Wm + Chl + Op	Micaschist	**HSD:** sheath fold refolding the And + Cd + Wm + Bi mylonitic foliation. **Quartz:** GBM/SGR
SP128	Calamita Mine	42°42'53.46"N 10°23'37.10"E	Tr + Ep + Ves + Cc + Dl	Calcsilicate rock	**LSD:** Foliated Tr-schist wrapping aggregates of Ep, Ves and Cc + Dl.
SP129	Fosso del Pontimento	42°44'2.89"N 10°22'58.63"E	**Peak:** Bi + Q + Cd + And + Op **Retrograde:** Wm + Chl + Op	Micaschist	**LSD:** Interlayered Q-ribbons, Wm-domains and Bi-ribbons with poikiloblastic And + Bi + Cd inclusions. Pinitized Cd. **Quartz:** Island grains and reticular microstructures. Amoeboid grain boundaries (GBM).
SP130	Fosso del Pontimento	42°44'2.95"N 10°22'58.38"E	**Peak:** Bi + Q + Cd + And + Ksp **Retrograde:** Wm + Chl + Op	Micaschist	**LSD:** Alternations of Bi-ribbons, Q-layers and lepidoblastic Wm-domains with sericitized And + Cd porphyroclasts. **Quartz:** GBM microfabric largely unaffected by recrystallization.
SP131	Fosso del Pontimento	42°44'3.52"N 10°22'56.69"E	**Peak:** Bi + Q + Cd + And + Ksp + Pl + Op **Retrograde:** Wm + Chl + Op	Micaschist	**LSD:** well-foliated Bi-domains and granoblastic Q-ribbons overprinted by poikiloblastic And + Cd + Ksp + Pl growth. Static sericitic overgrowth. **Quartz:** Interlobate to amoeboid microfabric (GBM)
SP133	Fosso di Fosco	42°43'41.10"N 10°22'57.71"E	**Peak:** Q + Ksp + Pl + Tur + Wm (ser) **Retrograde:** Ser	Mylonitic leucogranite	**HSD:** foliated dyke with Ksp + Q + Tur + Wm embedded in a fine grained Ser matrix. Retrograde growth of Wm in S-C' structures (top-to-the-E). Saussuritized Pl.
SP137	Fosso del Pontimento	42°43'59.19"N 10°22'45.17"E	**Peak:** Bi + Q + Cd + And + Op Retrograde: Wm + Chl + Op	Micaschist	**LSD:** folded Q- and Wm-Bi domains overprinted by decussate mica aggregates. Sericitized And + Cd.
SP147	Punta Calamita	42°42'48.35"N 10°23'35.81"E	Tr + Ta + Op (Py? Hem?) + Cc + Dl?	Tr-Ta schist	Possible metasomatic rock characterized by Tr-lenses wrapped by anastomozing Ta-rich domains and overprinted by abundant sulphides and oxides (possibly Py, Hem)
SP148	Remaiolo	42°42'58.50"N 10°24'40.56"E	**Peak:** Bi + Q + Ksp + And + Cd + Op **Retrograde:** Wm + Chl + Op	Mylonitic micaschist	**HSD:** High-grade relics (Bi + Ksp + And + Cd) overprinted by a Wm + Chl mylonitic foliation, wrapping sericitized porphyroclasts and boudinated quartz lenses and affected by C' shear bands. Pre- to synkinematic And + Cd **Quartz:** GBM relics → SGR/BLG

					recrystallization. Recrystallized Q in C' shear bands and necks of boudins.
SP163	Barabarca	42°44'41.61"N 10°21'43.72"E	Wm + Q + Cd + Bi + Op	Spotted schist	**LSD:** Schistose rock with lepidoblastic Wm + Q (mixed layers) with SPO. Inclusion-rich Cd overgrowing the foliation.
SP164	Barabarca	42°44'54.26"N 10°21'32.90"E	Q + Tur + Wm + Chl + sericitized Cd + Op	Q-metaconglomerate (Anagenite)	**HSD:** deformed quartzite-clasts wrapped in dynamically recrystallized new Q-grains. SGR → BLG
SP168	Capo Calvo	42°44'4.28"N 10°26'1.54"E	Bi + Q + Pl + Ksp + Op	Mylonitic granite	**HSD:** mylonitic foliation (Q + Bi) wrapping Q, Pl and Bi porphyroclasts. S-C fabric, sigmoidal objects and Mica-fish (top-to-the-E)
SP169	Capo Calvo	42°44'4.23"N 10°26'1.53"E	**Peak:** Bi + Q + Cd + And + Ksp + Pl + Op **Retrograde:** Wm (Ser) + Op	Sericitized micaschist	**LSD:** sericitized Bi-Cd-And-Ksp aggregates wrapped in a fine-grained retrograde Wm-rich foliation. **Quartz:** GBM with SGR overprint.
SP191	Punta delle Ripalte	42°42'33.39"N 10°25'12.83"E	**Peak:** Bi + Q + Op **Retrograde:** Wm + Op	Quartzitic schist	**LSD:** microfolded alternations of quartz-ribbons and Bi-domains. New Wm grains on axial plane foliation. **Quartz:** slightly deformed with lobate boundaries.
SP193	Ginevro Mine	42°43'10.08"N 10°25'48.79"E	**Peak:** Bi I + Q + sericitized Al-silicates (Cd? + And? + Ksp?) + Op **Retrograde:** Bi II + Wm + Op	Bi-Wm Hornfels	**LSD:** diablastic Bi aggregates and widespread sericitic alteration over -possibly- formed And, Cd and feldspars. Retrograde, diablastic Wm. **Quartz:** dominant GBM-recrystallization.
SP195	Capo Calvo	42°44'2.59"N 10°26'1.41"E	**Peak:** Bi + Q + And + Ksp + Op **Retrograde:** Wm + Bi + Ser + Op	Hornfels	**LSD:** Diablastic Bi + And + Ksp aggregates retrometamorphosed by fine-grained Ser. Quartz lenses with weakly lobate fabric.
SP196[(2)]	Capo Calvo	42°44'2.29"N 10°26'1.10"E	**Peak:** Bi + Q + And + Cd + Ksp + Pl + Op **Retrograde:** Wm + Bi + Ser + Chl + Op	Bi-micaschist wrapped by mylonitic shear zones	**HSD:** Stretched quartz ribbons and lepidoblastic Bi overprinted by mylonitic C and C' shear bands. Strong sericitization over And + Cd + Ksp. Mylonitic bands wrapping high-grade pods. Top-to-the-E. **Quartz:** GBM fabric totally overprinted by SGR. Large grains with subgrain boundaries forming core-and-mantle structures. BLG-recrystallization in mylonitic bands.
SP197	Capo Calvo	42°44'2.94"N 10°26'1.25"E	**Peak:** Bi + Q + And + sericitized grains (Cd + Ksp?) + Op **Retrograde:** Wm + Ser + Chl + Op	Mylonitic Q-Bi schist	**HSD:** Mylonitic quartz-domain with S-C fabric (top-to-the-E) and well developed Q-oblique foliation. Stretched Bi + And domains largely overprinted by Ser alteration. **Quartz:** strong SGR recrystallization.

Appendix D

SP198	Capo Calvo	42°44'2.99"N 10°26'1.40"E	**Peak:** Bi + Q + And + sericitized grains (Cd + Ksp?) + Op **Retrograde:** Wm + Ser + Chl + Op	Mylonitic micaschist	**HSD:** High-grade deformed Q + Bi + Al-silicate pods with S-C fabric and oblique foliation (top-to-the-E) overprinted by static sericitic alteration. **Quartz:** dominant SGR recrystallization over GBM structures.
SP199	Capo Calvo	42°44'2.90"N 10°26'1.38"E	**Peak:** Bi + Q + And + sericitized grains (Cd + Ksp?) + Op **Retrograde:** Wm + Ser + Chl + Op	Hornfels	**LSD:** Foliated Q + Bi pods with recrystallization microstructures wrapped by diablastic sericitic aggregates. Strong Ser alteration over Al-silicates. **Quartz:** GBM (island grains and reticular microstructures) overprinted by SGR recrystallization (core-and-mantle structures)

(1): samples described in detail in Chapters 8-9. **(2):** poikiloblastic Bi + Ksp + Pl intergrowths, possibly indicating partial melting (see Chapter 9)

Figure D1 – Photo stitching at crosser polarizers of thin section SP196 (Capo Calvo) used for the analysis of the orientations of the Sp foliation and C, C' shear bands (Figure 5.11).

Appendix D

Figure D2 – Photo scan of thin section CS30 (Praticciolo) used for the analysis of the orientations of the Sm foliation and C' shear bands (see Chapter 5).

Figure D3 – Photo scan of thin section SP65 (Praticciolo) used for the analysis of the orientations of the Sm foliation and C' shear bands (see Chapter 5).

Appendix D

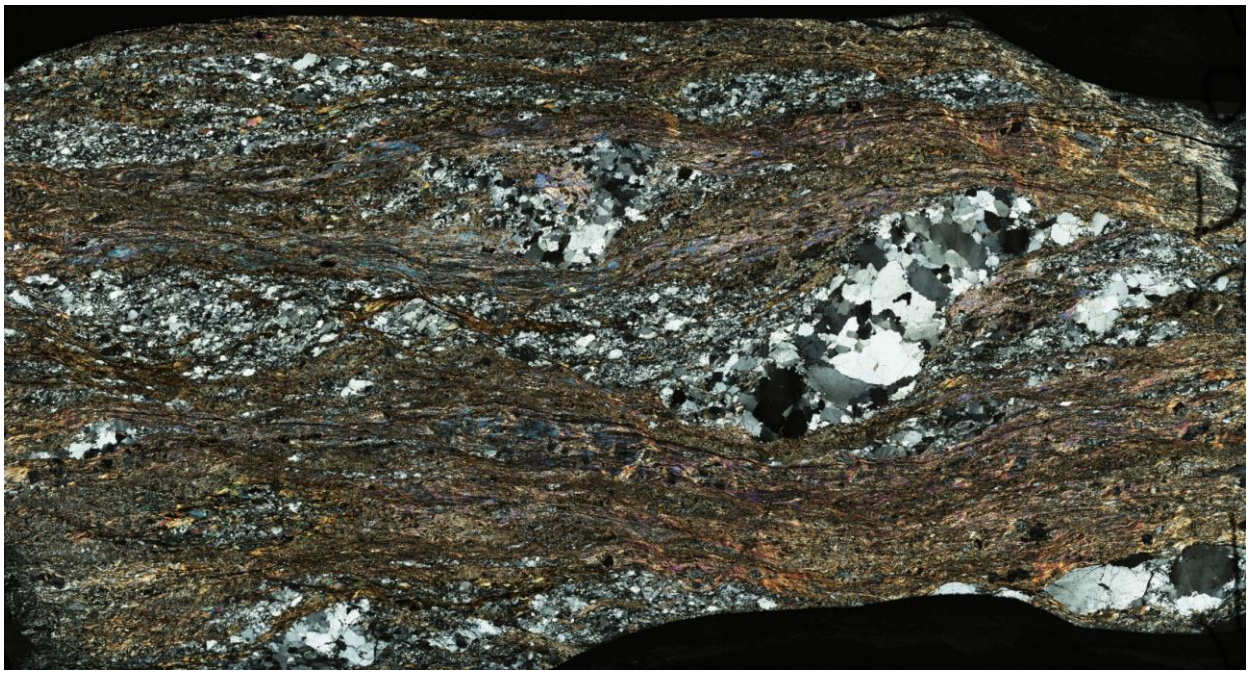

Figure D4 – Photo stitching at crossed polarizers of thin section SP76 (Praticciolo) used for the analysis of the orientations of the Sm foliation and C' shear bands (see Chapter 5).

Figure D5 – Photo scan of thin section SP78 (Praticciolo) used for the analysis of the orientations of the Sm foliation and C' shear bands (see Chapter 5).

Appendix E1

Geothermobarometry

Appendix E1

E1.1 Biotite geothermometry

For a fixed mineralogical assemblage, the solubility of TiO_2 in biotite has been shown to increase with temperature (Labotka, 1983; Guidotti, 1984; Guidotti and Sassi, 2002; Henry and Guidotti, 2002), making the titanium content of biotite a fair candidate for geothermometric estimates. However, the titanium content of biotite is also strongly influenced by the presence of coexisting Ti-bearing phases pressure (P) and the bulk-rock chemistry (i.e. by the Mg/Fe ratio).

In a couple of papers Henry and Guidotti (2002) and Henry et al. (2005) showed the variation of the titanium saturation surface for natural biotites in the T(°C) - Ti (p.f.u.) - XMg space, where XMg = Mg / [Mg + Fe]. They calibrated the following geothermometer for P ~ 0.4-0.6 GPa and T between 480-800 °C for ilmenite- or rutile-bearing, graphitic peraluminous compositions:

$$T = \left(\frac{\ln(Ti) - a - c(XMg)^3}{b}\right)^{0.333} \qquad (E1.1)$$

Where Ti(p.f.u.) is calculated on 22 oxygen equivalents, a = -2.3594 ± 0.0141, b = 4.6482 * 10^{-9} ± 5.1970 * 10^{-11} and c = -1.7283 ± 0.0584. The calculated temperatures have an associated error of ±24 °C. The geothermometer was lately recalibrated and extrapolated to a wider pressure range (P between 0.1 and 1.9 GPa) by Wu and Chen (2015), who proposed the following equation:

$$\ln[T(°C)] = a + b\ln(X_{Ti}) - c\ln(X_{Fe}) - d\ln(X_{Mg}) + e\,P \qquad (E1.2)$$

Where a = 6.313 ± 0.078, b = 0.224 ± 0.006, c = 0.288 ± 0.041, d = 0.449 ± 0.039 and e = 0.15 ± 0.01. P is the pressure expressed in GPa. The ratio X_j = (j / (Fe + Mg + Ti + Al^{VI}) corresponds to the site fraction of the j cation in the octahedral sites of biotite. The associated random error was estimated to be around ±65 °C. Wu and Chen (2015) geothermometer has the advantage that does not require graphite-bearing samples or peraluminous conditions in respect to Henry et al. (2005)'s geothermometer. Moreover, the P/T conditions experienced by the Calamita are outside the P/T range of calibration of Henry et al. (2005)'s geothermometer but fit well with the P/T range of Wu and Chen (2015)'s geothermometer. Application of Wu and Chen (2015)'s geothermometer is therefore more appropriate for the Calamita Schists; however, Henry et al. (2005)'s estimates have also been tested for comparison.

The application of biotite geothermometry is subject by an additional source of error arising from the estimation of the Fe^{3+} content of biotite, which cannot be directly assessed from EMPA analyses. An estimate of the Fe^{3+} content of biotite has been obtained from the analyses of Fe^{3+}

bearing phases associated with biotite (e.g. ilmenite, hematite...), where Fe^{3+} has been calculated stoichiometrically using the software AX (Holland and Powell, 2000). Results have been confronted with maximum and minimum temperatures estimated with Wu and Chen (2015)'s geothermometer, assuming $\Sigma Fe = Fe^{3+}$ and $\Sigma Fe = Fe^{2+}$ respectively.

E1.2 Chlorite geothermometry

Overview

Chlorites are characterized by a wide compositional variability reflecting the metamorphic conditions, rock chemistry and fluid composition associated with their formation. The main substitutions that occur in chlorites, are (1) the ferromagnesian (FM: $[Fe^{2+}, Mg_{-1}]$), (2) the Tschermak (TK: $Al^{IV}\ Al^{VI}\ Si_{-1}\ [Mg, Fe^{2+}]_{-1}$) and (3) the di/trioctahedral (DT: $[Mg, Fe^{2+}]_3\ \square_{-1}\ Al_{-2}$ where $\square$ = vacancy) substitutions (Vidal and Parra, 2000). Other common substitutions involve the replacement of Al^{3+} by Fe^{3+} in both octahedral and tetrahedral sites (Inoue et al., 2009) and the substitution $Si_{-1}\square_{-1}$ for [Fe, Mg] (Bourdelle and Cathelineau, 2015) . It has been shown that an increase in temperature causes a decrease of Si and Al^{IV}, whereas low-temperature chlorites are characterized by higher vacancy, Al^{VI} and Fe + Mg content (Cathelineau and Nieva, 1985; Hillier and Velde, 1991; De Caritat et al., 1993). Conversely, increasing pressure determines a decrease of Si and Fe + Mg and an increase of the total Al and vacancies (Leoni et al., 1998; Vidal et al., 2001). Decades of studies have shown the applicability of these wide compositional variability to obtain geothermobarometric estimates in various geological contexts (Cathelineau and Nieva, 1985; Walshe, 1986; Vidal and Parra, 2000; Inoue et al., 2009; Bourdelle et al., 2013; Lanari et al., 2014; Bourdelle and Cathelineau, 2015). Chlorite geothermometers can be distinguished in 3 main groups, based on their different approaches: (1) geothermometers based on empirical calibrations, (2) semi-empirical geothermometers and (3) geothermometers based on thermodynamic datasets.

Empirical geothermometers are linear equations that relate temperature to the tetrahedral aluminum (Al^{IV}) or the octahedral vacancy ($\square$) content of chlorite, calibrated on natural chlorite datasets with a correction based on the XFe or XMg ratio (Cathelineau and Nieva, 1985; Kranidiotis and McLean, 1987; Cathelineau et al., 1988; Hillier and Velde, 1991; Jowett, 1991; Zang and Fyfe, 1995; Xie et al., 1997). However, these methods fail to account for the three main substitutions occurring in chlorites and can be applied only in a restricted range of chlorite compositions (i.e. close to the conditions of calibration; De Caritat et al., 1993; Bourdelle and Cathelineau, 2015).

Appendix E1

Semi-empirical geothermometers rely on chlorite end-member activity models and relate the equilibrium constant of a chlorite equilibrium, which typically involves quartz and water, to temperature (Walshe, 1986; Inoue et al., 2009; Bourdelle et al., 2013; Lanari et al., 2014; Bourdelle and Cathelineau, 2015). Despite being based on a series of assumptions (water and quartz activity = 1; pressure and contributions from non-ideality not considered), they provide reasonable results and they do not require knowledge of the bulk-rock composition.

Finally, geothermometers based on thermodynamic datasets offer the most rigorous approach to chlorite geothermometry. They rely on chlorite models where mixing-properties, ideal and non-ideal contributions to the activity and the pressure effect are considered (Holland et al., 1998; Vidal and Parra, 2000; Vidal et al., 2001, 2005, 2006; Lanari et al., 2014). They require complex calculations, usually performed using a thermodynamic software (e.g. X-Map Tools; Lanari et al., 2018), and accurate knowledge of the chemistry of the phases coexisting with chlorite. Their results are also strongly dependent on the quality of the available thermodynamic datasets, solid-solution models and end-member thermodynamic data.

Empirical chlorite geothermometry

The original empirical geothermometer by Cathelineau (1988) was calibrated in geothermal wells at shallow depths between 150 and 400 °C with a systematic error of ~30 °C. Temperature is directly linked to the Al^{IV} content (calculated on a 14 oxygen equivalents basis) by the following relation:

$$T(°C) = -61.92 + 321.98(Al^{IV}) \quad (E1.3)$$

Other authors proposed new calibrations or suggested corrections for Cathelineau's geothermometer. Kranidiotis and McLean (1987) introduced a XFe correction (XFe = Fe^{2+} / [Mg + Fe^{2+}]) calculated on a 28-oxygen basis:

$$T(°C) = 106(Al^{IV} + 0.7XFe) + 18 \quad (E1.4)$$

Eq. E1.4 was subsequently modified by Jowett (1991), based on 14 oxygen equivalents and XFe < 0.6, as follows:

$$T(°C) = 319(Al^{IV} + 0.1XFe) - 69 \quad (E1.5)$$

Appendix E1

Xie et al. (1997) calibrated a different empirical geothermometer for greenschist facies conditions (T ~ 250 – 400 °C), proposing a relation between T (°C), Al^{IV} and XFe calculated on 14 oxygen equivalents:

$$T(°C) = 321.98[Al^{IV} + 0.133(0.31 - XFe)] - 61.92 \qquad (E1.6)$$

These empirical geothermometers have all been calibrated on shallow geothermal fields or hydrothermal alteration areas at shallow levels and are therefore suitable for the very low-pressure contact metamorphism of the Calamita Schists (P < 0.2 GPa). Since metamorphism in the Calamita Schists covers a wide temperature range, geothermometers calibrated for a limited temperature range (e.g. Hillier and Velde, 1991; Zang and Fyfe, 1995) have not been considered in this thesis.

Semi-empirical chlorite geothermometry

For any balanced reaction involving, j end-members, the equilibrium condition can be written as:

$$\sum_j v_j \, \Delta G_j^{P,T} - RT \ln K = 0 \qquad (E1.7)$$

Where $\Delta G_j^{P,T}$ is the apparent Gibbs free energy of formation for the reaction, v_j is the stoichiometric reaction coefficients of each end-member *j*, *T* is the temperature expressed in °K and *R* is the universal gas constant, corresponding to 8.314 J $mol^{-1}K^{-1}$. *K* is the equilibrium constant for the reaction which is directly related to the ideal activities of end-members, a_{ideal}, by the relation (after Mäder et al., 1994):

$$K = \prod_j (a_{ideal}\gamma_m)_j^{v_j} \qquad (E1.8)$$

where γ_m represent the activity coefficient, which accounts for the non-ideal contribution to the activity and that is neglected in semi-empirical geothermometers. Ideal activities of end-members are calculated from:

$$(a_{ideal})_j = \prod_s \prod_m \left(\frac{n_s X_m}{r_m}\right)^{r_m} \qquad (E1.9)$$

where n_s is the multiplicity of *s* sites, r_m and X_m are the number and the mole fraction of *m* cations in *s* sites. Temperature is directly linked to *K*, and therefore to the activities of end-members, by the following relation:

$$LogK = \frac{-\Delta G_r^0}{2.303(RT)} = \frac{A}{T} + B \qquad (E1.10)$$

Where A and B are constants that depend on the stoichiometry of the reaction and the choice of end-members performed by different authors. Inoue et al. (2009) assumes random mixing of cations in octahedral and tetrahedral sites, whereas the other models consider an ordered distribution of cations. Cation-site partitioning models after Vidal et al. (2001), Bourdelle et al. (2013) and Lanari et al. (2014) are listed in Tab. E1.1, while Tab. E1.2 lists the related activity models, calculated after Eq. E1.9. Models by Vidal et al. (2001) and Lanari et al. (2014) exclude high Si chlorites (Si p.f.u. > 3 on a 14-oxygen basis) and are therefore inappropriate for low-temperature contexts, whereas Inoue et al. (2009)'s and Bourdelle et al. (2013)'s models cover the compositional range of both low- and high- temperature chlorites. Walshe (1986)'s choice of end-members excludes a large compositional range which makes it inapplicable to both metamorphic and low-temperature environments and therefore it has not been considered. The chlorite + quartz + water equilibria considered by these authors, the equilibrium constant K, calculated after Eq. E1.8, and the semi-empirical geothermometer, after Eq. E1.10, are listed in Tab. E1.3. The equilibrium constants K are calculated assuming only ideal contribution to the activity, $a_{H2O} = 1$ and $a_Q = 1$. These geothermometers have been calibrated for pressure conditions overlapping with those of the Calamita. Lanari et al. (2014)'s geothermometers are strongly versatile as they cover a wide range of P/T conditions (100 – 500 °C and 0.1 – 2.0 GPa). Bourdelle et al. (2013) and Inoue et al. (2009) have both been calibrated for P < 0.3 – 0.4 GPa and T comprised between 50 and 350 °C; however, Inoue et al. (2009)'s relation offers a best-fit for T < 250 °C. Furthermore, Inoue et al. (2009)'s geothermometer requires accurate knowledge of the Fe^{3+} content, whereas Bourdelle et al. (2013) assumes $\Sigma Fe = Fe^{2+}$. The problem of the $Fe^{3+}/\Sigma Fe$ value is also considered by Lanari et al. (2014), who proposed two geothermometers, one based on the assumption that all iron is divalent ($\Sigma Fe = Fe^{2+}$), and the other which considers the $Fe^{3+}/\Sigma Fe$ value. According to Bourdelle et al. (2013), accounting for Fe^{3+} in the structural formulae of chlorites arithmetically increases the number of vacancies, therefore linking indirectly Fe^{3+} to temperature. Inoue et al. (2009) and Bourdelle et al. (2013)'s geothermometers have been used to calculate isotherms for chlorite compositions and plotted on a R^{2+} - Si p.f.u. diagram (after Wiewìora and Weiss, 1990; where R^{2+}

Appendix E1

Table E1.1 – Chlorite atom site distribution according to different models. Walshe (1986) and Inoue et al. (2009)'s models assume random tetrahedral and octahedral sites mixing. See text for further details.

Chlorite	$(T1)_2$	$(T2)_2$	M1	$(M2+M3)_4$	M4
		Vidal and Parra (2000); Vidal et al. (2001)			
Clinochlore	$(Si)_2$	SiAl	Mg	$(Mg)_4$	Al
Daphnite	$(Si)_2$	SiAl	Fe	$(Fe)_4$	Al
Sudoite	$(Si)_2$	SiAl	□	$(Al)_2(Mg)_2$	Al
Mg-amesite	$(Si)_2$	$(Al)_2$	Al	$(Mg)_4$	Al
Fe-amesite*	$(Si)_2$	$(Al)_2$	Al	$(Fe)_4$	Al
		Lanari et al. (2014)			
Amesite	$(Si)_2$	$(Al)_2$	Al	$(Mg)_4$	Al
Fe-amesite	$(Si)_2$	$(Al)_2$	Al	$(Fe)_4$	Al
Clinochlore	$(Si)_2$	SiAl	Mg	$(Mg)_4$	Al
Daphnite	$(Si)_2$	SiAl	Fe	$(Fe)_4$	Al
Sudoite	$(Si)_2$	SiAl	□	$(Al)_2(Mg)_2$	Al
Fe-sudoite	$(Si)_2$	SiAl	□	$(Al)_2(Fe)_2$	Al
		Bourdelle et al. (2013)			
	$(T1)_2$	$(T2)_2$	$(M1+M4)_2$	$(M2+M3)_4$	-
Al-free chlorite	$(Si)_2$	$(Si)_2$	$(Mg)_2$	$(Mg)_4$	-
Fe Al-free chlorite	$(Si)_2$	$(Si)_2$	$(Fe)_2$	$(Fe)_4$	-
Sudoite	$(Si)_2$	SiAl	Al□	$(Al)_2(Mg)_2$	-
Fe-sudoite	$(Si)_2$	SiAl	Al□	$(Al)_2(Fe)_2$	-
Amesite	$(Si)_2$	$(Al)_2$	$(Al)_2$	$(Mg)_4$	-
Fe-amesite	$(Si)_2$	$(Al)_2$	$(Al)_2$	$(Fe)_4$	-

*: since Vidal et al. (2005) and updated versions.

= Fe^{2+} + Mg) by Bourdelle and Cathelineau (2015). The comparison shows strongly different temperature estimates when pure ferrous iron is considered, with calculated temperatures which differs by more than 300 °C.

Considering these geothermometric limitations, Lanari et al. (2014)'s and Bourdelle et al. (2013)'s $\Sigma Fe = Fe^{2+}$ geothermometer have been applied for the Calamita Schists. Various Fe^{3+}/Fe^{2+} ratios have been used to test the effect of varying Fe^{3+} content on temperature, using the $\Sigma Fe = Fe^{2+}$ + Fe^{3+} geothermometers by Lanari et al. (2014) and Inoue et al. (2009).

Chlorite geothermometry based on thermodynamic datasets

Vidal et al. (2001) thermodynamically defined the mixing properties and activity-composition properties of chlorite in a four end-member model (see Tab. E1.1), which was lately expanded to include a fifth end-member, Fe-amesite, by Vidal et al. (2005, 2006). The advantage of this model, in respect to e.g. Holland et al. (1998)'s chlorite model implemented in THERMOCALC, is the inclusion of the sudoite end-member, which allows to model vacancies and is therefore optimized for low-metamorphic grade chlorites. The chlorite model by Vidal et al. (2001, 2005, 2006) was

successfully applied to greenschist and blueschist facies pelites worldwide using multi-equilibrium calculation techniques (e.g. Vidal and Parra, 2000; Trotet et al., 2001; Parra et al., 2002; Vidal et al., 2006; Lanari et al., 2012, 2014; Di Rosa et al., 2017). Vidal et al. (2005)'s five end-member model accounts for symmetric Margules parameters (W_{AlMg}, W_{AlFe}, $W_{\square Fe}$, $W_{\square Mg}$ and $W_{\square Al}$, where $\square$ = vacancy) and ideal inter-site interactions. Using these end-members, four reactions involving chlorite-quartz-water equilibria can be written (Vidal et al., 2006):

$$2clin + 3sud = 4ames + 7Q + 4H_2O \quad \text{(E1.11)}$$

$$4Clin + 5FeAm = 4daph + 5ames \quad \text{(E1.12)}$$

$$16daph + 15sud = 20fames + 6clin + 35Q + 20H_2O \quad \text{(E1.13)}$$

$$4daph + 6sud = 5fames + 3ames + 14Q + 8H_2O \quad \text{(E1.14)}$$

The equilibrium temperature of reactions E1.11 to E1.14 depends on the activity of the clinochlore, daphnite, sudoite and amesite end-members in the chlorite solid solution. These temperatures can be calculated from the condition of thermodynamic equilibrium (Eq. E1.7), while the equilibrium constant K is derived from Eq. E1.8. The a_{ideal} activity is calculated after Eq. E1.9, while the non-ideal contribution to the activity, γ_m, is calculated as follows:

$$\gamma_m = \prod_s \prod_m \gamma_m^{ns} \quad \text{(E1.15)}$$

where n_s is the multiplicity of *s* sites for *m* cations in *s* sites. Based on the assumption of symmetric interactions in Vidal et al. (2005)'s model, the activity coefficient γ_m is computed from:

$$n_s RT ln\gamma_m = \sum W_{ij} X_i X_j \left(\frac{Q_m}{X_m} - 1\right) \quad (E1.16)$$

where Q_m is the number of *i,j* subscripts that are equal to *m* (0 or 1) and W_{ij} are the Margules parameters. The thermodynamic data used in the calculation are those reported by Berman (1988), Vidal et al. (1992, 2001, 2005, 2006) and Parra et al. (2002). Calculations were performed using the Excel Spreadsheet compiled by Vidal et al. (2006).

Table E1.2 – Models for ideal activities of chlorite solid-solution end-members used in different geothermometers.

End-member (abbreviation)	Chemical formula	Ideal activity
Vidal et al. (2001) model		
Clinochlore (clin)	$[Mg_5Al][Si_3Al]O_{10}(OH)_8$	$a_{clin} = 4(X_{Mg,M1})(X_{Mg,M23})^4(X_{Si,T2})(X_{Al,T2})$
Daphnite (daph)	$[Fe^{2+}{}_5Al][Si_3Al]O_{10}(OH)_8$	$a_{daph} = 4(X_{Fe,M1})(X_{Fe,M23})^4(X_{Si,T2})(X_{Al,T2})$
Sudoite (sud)	$[Mg_2Al_3\square][Si_3Al]O_{10}(OH)_8$	$a_{sud} = 64(X_{\square,M1})(X_{Al,M23})^2(X_{Mg,M23})^2\ (X_{Si,T2})(X_{Al,T2})$
Amesite (ames)	$[Mg_4Al_2][Si_2Al_2]O_{10}(OH)_8$	$a_{ames} = (X_{Al,M1})(X_{Mg,M23})^4(X_{Al,T2})^2$
Inoue et al. (2009) model		
Al-free chlorite (afch)	$[Mg_6][Si_4]O_{10}(OH)_8$	$a_{afch} = (X_{Mg,oct})^6(X_{Si,tet})^2$
Amesite (ames)[(1)]	$[Mg_4Al_2][Si_2Al_2]O_{10}(OH)_8$	$a_{ames} = 45.563(X_{Mg,oct})^4(X_{Al,oct})^2(X_{Al,tet})^2$
Daphnite (daph)[(2)]	$[Fe^{2+}{}_5Al][Si_3Al]O_{10}(OH)_8$	$a_{daph} = 59.720(X_{Fe,oct})^5(X_{Al,oct})\ (X_{Si,tet})(X_{Al,tet})$
Sudoite (sud)	$[Mg_2Al_3\square][Si_3Al]O_{10}(OH)_8$	$a_{sud} = 1728(X_{Mg,oct})^2(X_{Al,oct})^3(X_{\square,oct})(X_{Si,tet})(X_{Al,tet})$
Bourdelle et al. (2013) model		
Al-free chlorite (afch)[(3)]	$[Mg_6][Si_4]O_{10}(OH)_8$	$a_{afch} = (X_{Si,T2})^2(X_{Mg,M23})^4(X_{Mg,M14})^2$
Fe Al-free chlorite (fafch)[(4)]	$[Fe^{2+}{}_6][Si_4]O_{10}(OH)_8$	$a_{fafch} = (X_{Si,T2})^2(X_{Fe,M23})^4(X_{Fe,M14})^2$
Amesite (ames)	$[Mg_4Al_2][Si_2Al_2]O_{10}(OH)_8$	$a_{ames} = (X_{Al,T2})^2(X_{Mg,M23})^4(X_{Al,M14})^2$
Fe-amesite (fames)	$[Fe^{2+}{}_4Al_2][Si_2Al_2]O_{10}(OH)_8$	$a_{fames} = (X_{Al,T2})^2(X_{Fe,M23})^4(X_{Al,M14})^2$
Sudoite (sud)	$[Mg_2Al_3\square][Si_3Al]O_{10}(OH)_8$	$a_{sud} = 256(X_{Si,T2})(X_{Al,T2})(X_{Al,M14})(X_{\square,M14})(X_{Mg,M23})^2(X_{Al,M23})^2$ $a_{fsud} = 256(X_{Si,T2})(X_{Al,T2})(X_{Al,M14})(X_{\square,M14})(X_{Fe,M23})^2(X_{Al,M23})^2$
Fe-sudoite (fsud)	$[Fe^{2+}{}_2Al_3\square][Si_3Al]O_{10}(OH)_8$	
Lanari et al. (2014) model		
Clinochlore (clin)	$[Mg_5Al][Si_3Al]O_{10}(OH)_8$	$a_{clin} = 4(X_{Mg,M23})^4(X_{Mg,M1})(X_{Si,T2})(X_{Al,T2})$
Daphnite (daph)	$[Fe^{2+}{}_5Al][Si_3Al]O_{10}(OH)_8$	$a_{daph} = 4(X_{Fe,M23})^4(X_{Fe,M1})(X_{Si,T2})(X_{Al,T2})$
Amesite (ames)	$[Mg_4Al_2][Si_2Al_2]O_{10}(OH)_8$	$a_{ames} = (X_{Mg,M23})^4(X_{Al,M1})(X_{Al,T2})^2$
Fe-amesite (fames)	$[Fe^{2+}{}_4Al_2][Si_2Al_2]O_{10}(OH)_8$	$a_{fames} = (X_{Fe,M23})^4(X_{Al,M1})(X_{Al,T2})^2$
Sudoite (sud)	$[Mg_2Al_3\square][Si_3Al]O_{10}(OH)_8$	$a_{sud} = 64(X_{Al,M23})^2(X_{Mg,M23})^2(X_{\square,M1})(X_{Si,T2})(X_{Al,T2})$
Fe-sudoite (fsud)	$[Fe^{2+}{}_2Al_3\square][Si_3Al]O_{10}(OH)_8$	$a_{fsud} = 64(X_{Al,M23})^2(X_{Fe,M23})^2(X_{\square,M1})(X_{Si,T2})(X_{Al,T2})$

(1) corundophilite (crdp) and (2) chamosite (chm) in the original paper by Inoue et al. (2009).

(3) Mg-chlorite S and (4) Fe-Chlorite S in the original paper by Bourdelle et al. (2013).

E1.3 White mica geobarometry

In addition to the TK, FM and DT substitutions, occurring also in chlorites (see par. E1.2), white micas are also characterized by the paragonitic (PG: $[K_{-1}Na]$), the pyrophyllitic (PY: $[KAlSi_{-1}\square_{-1}]$) and the substitution of Al by Fe^{3+} (Merino and Ransom, 1982; Wang and Banno, 1987; Leoni et al., 1998; Guidotti and Sassi, 1998; Agard et al., 2001; Bousquet et al., 2002; Vidal and Parra, 2000). At very low P-T conditions a significant proportion of the pyrophyllitic end-member is common in the solid solution leading to K- and Si- deficient compositions (Leoni et al., 1998; Vidal et al., 2001). In low to high metamorphic grade rocks, the TK substitution (also called

Appendix E1

Table E1.3 – List of reactions and K equilibrium constants calculated after the end-member ideal activities listed in Tab. E1.2, with the associated semi-empirical geothermometers. Abbreviations after Tab. E1.2.

Reaction	Equilibrium constant (K)	Geothermometer
Vidal et al. (2001) 2clin + 3sud = 4ames + 7Q + 4H$_2$O	$\log K = \log\left[\frac{a_{ames}^4}{a_{clin}^2 a_{sud}^3}\right]$	$T(°K) = \frac{1}{0.00187 + 0.000114 * logK}$
Inoue et al. (2009) 3sud + afch = 3ames + 7Q + 4H$_2$O	$\log K = \log\left[\frac{a_{ames}^3}{a_{afch} a_{sud}^3}\right]$	$T(°K) = \frac{1}{(a + b * logK + c * log^2 K)}$ a = 0.00264; b = 2.897 * 10^{-4}; c = 3.407*10^{-5}
Bourdelle et al. (2013) afch + 3sud = 3ames + 7Q + 4H$_2$O	$\log K = \log\left[\frac{a_{ames}^3}{a_{afch} a_{sud}^3}\right]$	$T(°K) = \frac{9400}{(23.40 - logK)}$
Lanari et al. (2014) 2clin + 3sud = 4ames +7Q + 4H$_2$O	$\ln K = \ln\left[\frac{a_{ames}^4}{a_{clin}^2 a_{sud}^3}\right]$	• $\Sigma Fe = Fe^{3+} + Fe^{2+}$ $T(°K) = \frac{172341}{(-RlnK - 315.149)}$ • $\Sigma Fe = Fe^{2+}$ $T(°K) = \frac{203093 + 4996.99 * P(kbar)}{(-RlnK - 455.782)}$

'phengitic' substitution in white mica) causes an increase of the celadonite end-member (with higher proportion of Si and Fe + Mg) towards high pressure conditions and an increase of the muscovite end-member for high temperature and low-pressure conditions.

Massonne and Schreyer (1987) and Massonne and Szpurka (1997) simulated the variation of phengite composition for the KMASH and KFASH systems respectively, proposing different diagrams showing phengite Si isopleths in the P-T field for various mineral assemblages. The extrapolation of these results to more complicated systems (e.g. NCKFMASH; Wei and Powell, 2004; Zhu & Wei, 2007) showed that, although Si p.f.u. content in phengites increases generally with pressure, their values are strongly dependent on the mineral assemblage coexisting with phengites i.e. the absolute position of Si isopleths is shifted on the P-T space depending on the mineral assemblage. However, the composition of phengites remain a powerful tool for pressure and temperature estimations when associated with chlorite (phengite-chlorite multi equilibrium calculations) or in pseudosection modelling.

E1.4 Phengite-chlorite multi-equilibrium thermobarometry (MET)

It is well known that at low- to medium-grade metamorphic conditions, hydrothermal environments and during retrograde metamorphism of metapelites, chlorite + phengite

assemblages are characterized by lack of equilibrium over distances of few millimeters (Worley et al., 1997; Leoni et al., 1998). This is related to the inefficiency of lattice diffusion in chlorite and phengite for T < 550 °C, that energetically favors the crystallization of new grains with different composition (Vidal et al., 2006). However, local equilibria between chlorite – phengite pairs occur at smaller scale, preserved on different microsites or locations. According to Vidal and Parra (2000), during a metamorphic evolution involving a chlorite-phengite assemblage, new chlorite-phengite pairs nucleate continuously rather than re-equilibrating the pre-existing ones. Based on this evidence Vidal and Parra (2000) and Vidal et al. (2001, 2005, 2006) developed the so-called multi-equilibrium thermobarometry (MET) for medium to high-pressure greenschist and blueschist facies metapelites.

Using the five chlorite end-members model (Tab. E1.1) defined by Vidal et al. (2005) and the five white mica end-members model (excluding phlogopite and annite; Tab. E1.4) defined by Parra et al. (2002), 64 reactions (of whom 5 are linearly independent) can be written in the system KFMAS for a chlorite – phengite – quartz – water paragenesis. Calculations were performed using the excel spreadsheet compiled by Vidal et al. (2006), which performs multi-equilibrium calculations using 11 of the 64 possible reactions. The spreadsheet runs a series of macros that calculate the minimum Fe^{3+} content, using the stoichiometric criteria reported by Vidal et al. (2005) and then calculates the more appropriate XFe^{3+} to minimize the error for the temperature estimation from reactions E1.11 to E1.14. Thermodynamic parameters used are from Berman (1988), Vidal and Parra (2000), Vidal et al. (2001, 2005, 2006) and Parra et al. (2002).

The method has been applied in a large range of tectonic settings for high to low-pressure rocks (T up to 600 °C and P from 0.1 to 2.0 GPa) and has proven to provide excellent results -in particular when combined with quantitative X-Ray mapping (e.g. De Andrade et al., 2006; Vidal et al., 2006; Lanari et al., 2012, 2013, 2018). Therefore, the method is suitable for application in the Calamita Schists.

Table E1.4 – Dioctahedral K-white mica atom site distribution after Parra et al. (2002)

K-White Mica	$(T1)_2$	$(T2)_2$	M1	$(M2+M3)_2$	A
Mg-Al-celadonite	$(Si)_2$	$(Si)_2$	□	AlMg	K
Fe-Al-celadonite	$(Si)_2$	$(Si)_2$	□	AlFe	K
Muscovite	$(Si)_2$	SiAl	□	$(Al)_2$	K
Pyrophyllite	$(Si)_2$	$(Si)_2$	□	$(Al)_2$	□
Paragonite	$(Si)_2$	SiAl	□	$(Al)_2$	Na
Phlogopite*	$(Si)_2$	SiAl	Mg	$(Mg)_2$	K
Annite*	$(Si)_2$	SiAl	Fe	$(Fe)_2$	K

*: Trioctahedral end-members not considered in multi-equilibrium calculations.

Appendix E1

E1.5 Pseudosection modelling

Fundamentals of the pseudosection approach

Phase diagrams are standard representations of the equilibrium relationships between phases in a model chemical system consisting of a certain number of components (Bucher and Grapes, 2011). They show all the possible reactions present for the model system and the phases considered. The base of phase diagram is the phase rule:

$$F = C - P + 2 \qquad (E1.17)$$

where F are the degrees of freedom, C the number of components and P the number of phases in a point of the diagram. On a univariant line (F = 1), P = C + 1; on an invariant point (F = 0), P = C + 2. Consequently, a model system cannot contain a number of phases that exceeds the number of components by more than 2. Model chemical allow to understand the thermodynamics of reactions in simplified systems in respect to nature. The addition of other components (and phases) allow to consider more equilibria, approximating progressively 'real' natural rock systems, producing petrogenetic grids that show all reactions occurring within a chemical system (e.g. Spear and Cheney, 1989; White et al., 2000, 2007; Rebay and Powell, 2002). Such petrogenetic grids are useful to understand reactions occurring in specific rock types. However, such reactions are not 'seen' by all the compositions expressed by the chemical system.

A pseudosection are a type of phase diagrams showing stability fields of phases for one specific composition. Lines and points in pseudosections are not reactions but represent the locus of the point where the mode of a phase (or two phases for points) goes to zero. Variance changes by ±1 crossing lines and by ±2 crossing points. Pseudosections are useful because allow to model a specific composition and therefore reproduce mineral assemblages observed in natural rocks.

Calculation of pseudosections requires (1) an internally consistent thermodynamic datasets, (2) an activity-composition model and (3) a software to perform the calculation.

Internally consistent thermodynamic datasets contain thermodynamic variables regressed for each phase that depend on each other for the calculation of equilibria that provide a best fit to experimental calibrations. Powell and Holland (1985 and recent updates) and Berman (1988 and recent updates) represent the most used internally consistent thermodynamic datasets. Activity-composition models describe the relationships between composition (X) and activities (a) of mineral end-members in a solid-solution using solution models. Finally, the software performs phase diagram calculations based on the thermodynamic dataset, the activity-composition model and the instructions input by the user. Several software packages have been published in the last

decades (like the milestone TWEEQU by Berman, 1991). Among them, THERMOCALC (Powell and Holland, 1988), Perple_X (Connolly and Kerrick, 1987) and Theriak-Domino (de Capitani and Brown, 1987) are the most used. In this thesis, THERMOCALC and Perple_X have been used; therefore, a summarized description of how they work is provided here.

Perple_X is a suite of programs based on the Gibbs free energy minimization principle. Given a certain number of possible assemblages, the software calculates for every node on a grid in P-T (or P-T-X) space the assemblage with the lowest Gibbs free energy (stable mineral assemblage). The input files of Perple_X are a thermodynamic datafile, a solution model and a user-defined datafile containing instructions set by the user (like the choice of the model system and various assumptions). Perple_X can autonomously generate as output phase diagrams and pseudosections without user intervention, using computing algorithms. Perple_X main advantage is the ability to generate pseudosections in relatively short time. In addition, it can perform calculations using different thermodynamic datasets and activity models. However, Perple_X's grid calculations always introduce small artifacts (line pixelization), failing to identify features that are proximal to each other. It can also fail to identify small fields, leading to diagrams that violate the phase rule; therefore, critical revision and refinement of each Perple_X diagram is necessary.

On the other hand, THERMOCALC is a non-linear equation solver that calculates specified equilibria using its own internally-consistent thermodynamic dataset (i.e. Holland and Powell's). The input files consist of the internally-consistent dataset, a datafile with the solution models for the specified model system and a script file with user-defined instructions. In contrast with Perple_X, in THERMOCALC diagram lines and points must be calculated one by one and user intervention is necessary. As a consequence, creating diagrams with THERMOCALC is quite laborious and the user is prompted to perform Schreinemaker's analysis and to understand how variance changes across field boundaries. For this reason, THERMOCALC produces smooth curves with topologically correct boundaries that respect the phase rule.

To summarize, the rapidity of calculations and the software easiness to use make Perple_X an interesting alternative to calculate phase diagrams in simple chemical systems or preliminary phase diagrams before using THERMOCALC. THERMOCALC may be preferred for calculating phase diagrams in complex chemical systems or with phases requiring complex mixing models.

In this thesis, pseudosections have been first calculated using Perple_X, to get an overview of the assemblages and field boundaries present, and then recalculated and refined using THERMOCALC. Perple_X has also been used to test the output differences using internally-consistent datasets that differ from Holland and Powell's.

Appendix E1

The problem of guessing Fe_2O_3 and H_2O

In rocks iron is found in two oxidation states, as Fe^{2+} (ferrous) or Fe^{3+} (ferric). Ferric iron enters the crystal lattice of many common rock forming minerals (e.g. epidote, amphibole, garnet, chlorite, biotite…) and accessory minerals (e.g. magnetite or ilmenite). It has been shown that the oxidation state of iron influences phase composition, equilibria and assemblage stability (Lopez-Carmona et al., 2013; Lo Po and Braga, 2014), yet its determination remains an analytical challenge. Standard techniques like XRF or EMPA cannot distinguish between Fe^{2+} and Fe^{3+}; the amount of Fe^{3+} can be determined using specific analytical techniques (e.g. titration, Mössbauer spectroscopy, synchrotron micro-XANES spectroscopy), yet the possibility remains that the measured Fe^{3+} amount was overestimated due to low-temperature alteration or even due to sample preparation (e.g. Diener and Powell, 2010; Lopez-Carmona et al., 2013). It has been shown that typical LP/HT metapelites form predominantly under reducing conditions and that the amount of Fe^{3+} has little effect on mineral equilibria (e.g. White et al., 2000, 2002, 2007). The influence of Fe^{3+} appear greater in medium- to high pressure lithologies and in mafic protoliths, where its effect cannot be neglected (Diener and Powell, 2010). It is evident that, in general, the oxidation state of iron cannot be simply assumed to be divalent. Therefore, in the absence of measurements on the amount of Fe^{3+}, it can be estimated stoichiometrically from the chemical composition, recalculating the mineral phases using the software AX (Holland and Powell, 2000). AX is an activity-composition calculation program for rock-forming minerals that calculates the amount of ferric and ferrous iron from stoichiometric constraints. It has been applied on the spot analyses performed in the Calamita Schists to estimate the Fe^{3+} content.

Water in rocks is present as $(OH)^-$ and $(H_3O)^+$ ions in minerals and as intergranular fluids. In metapelites metamorphism starts with rocks at maximum hydrated state and it is expected that water-releasing reactions contribute to maintain water high during prograde metamorphism (e.g. Bucher and Grapes, 2011). On the other hand, during retrograde metamorphism, fluids are not necessarily available to produce hydrous phases from anhydrous minerals formed at peak conditions (e.g. garnet) and rocks may become water-undersaturated (e.g. Guiraud et al., 2001).

Appendix E2

Microprobe Analyses and Spot Location

Appendix E2

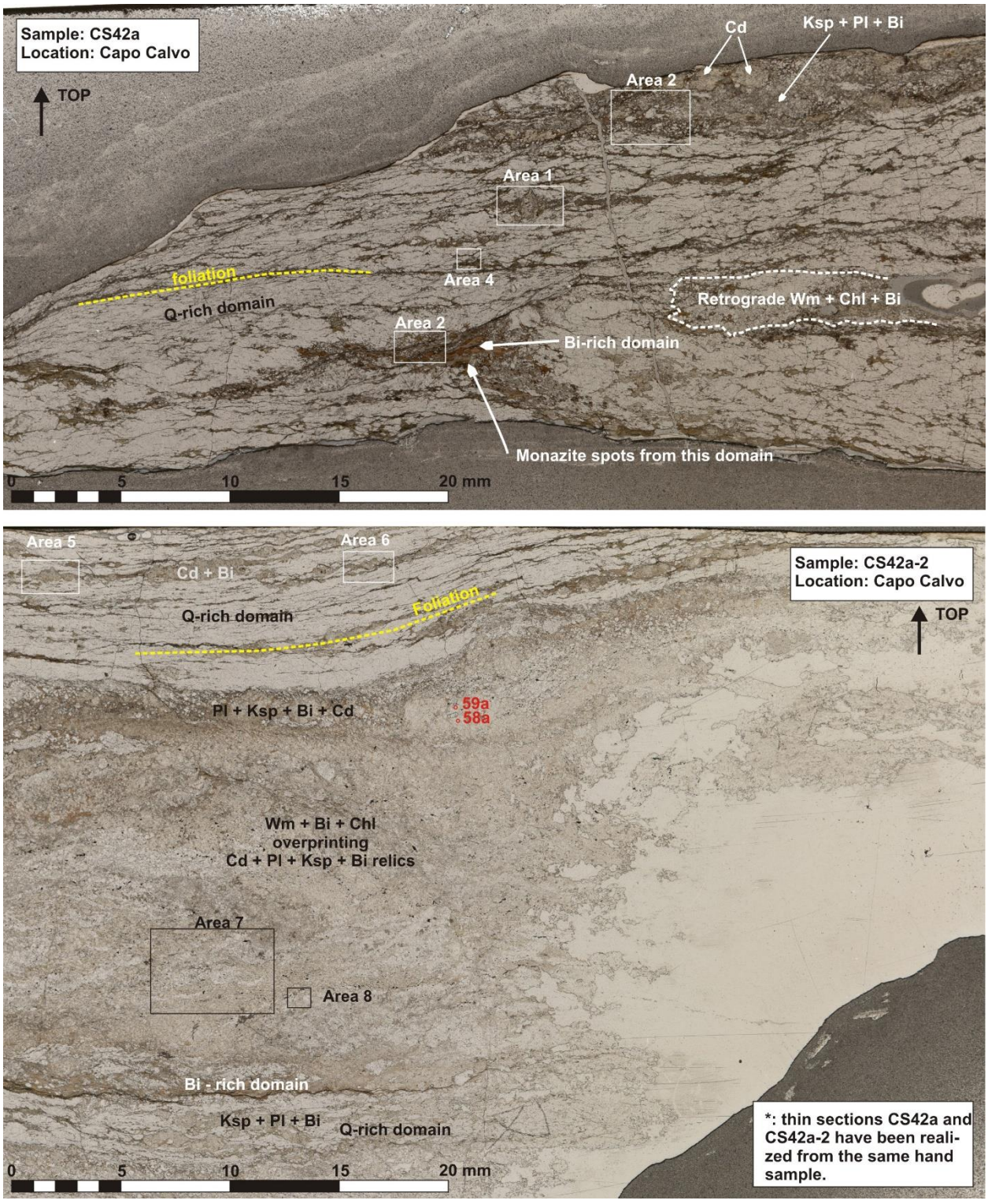

Figure E2.1 – Scans of polished thin sections derived from sample CS42a (CS42a: above; CS42a-2: below), from which EMPA spot analysis were obtained, illustrating the analyzed areas. Spots from sample CS42a-2 have been distinguished with a ‘a’ as suffix.

Appendix E2

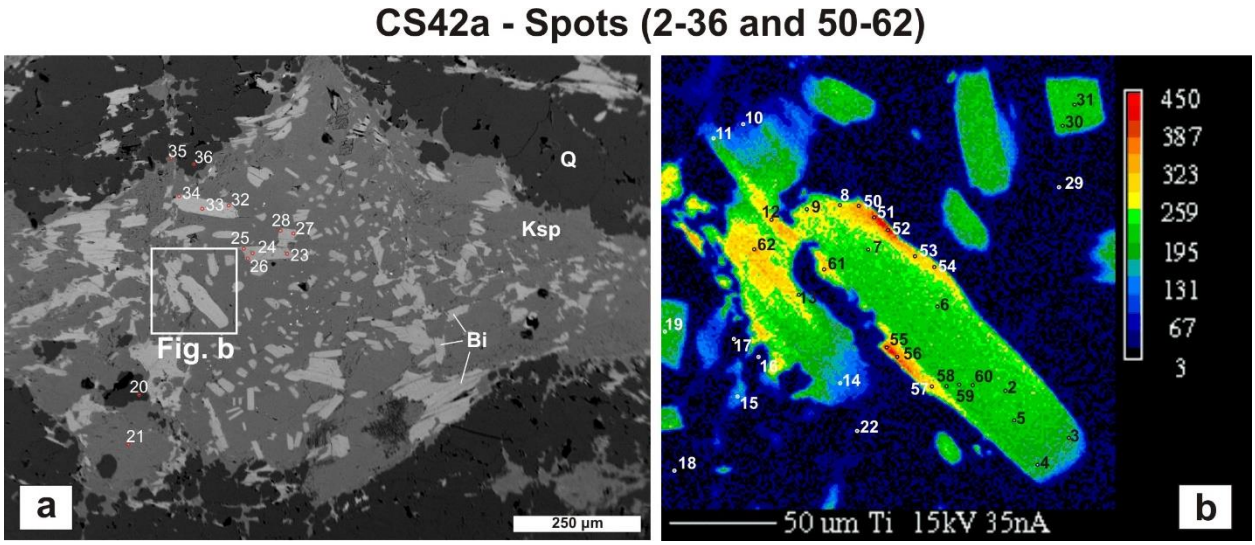

Figure E2.2 – (above) **(a)** CS42a: area 1 and **(b)** insert with X-Ray map performed on Bi included in Ksp.

Figure E2.3 – (below) CS42a – area 2 spots.

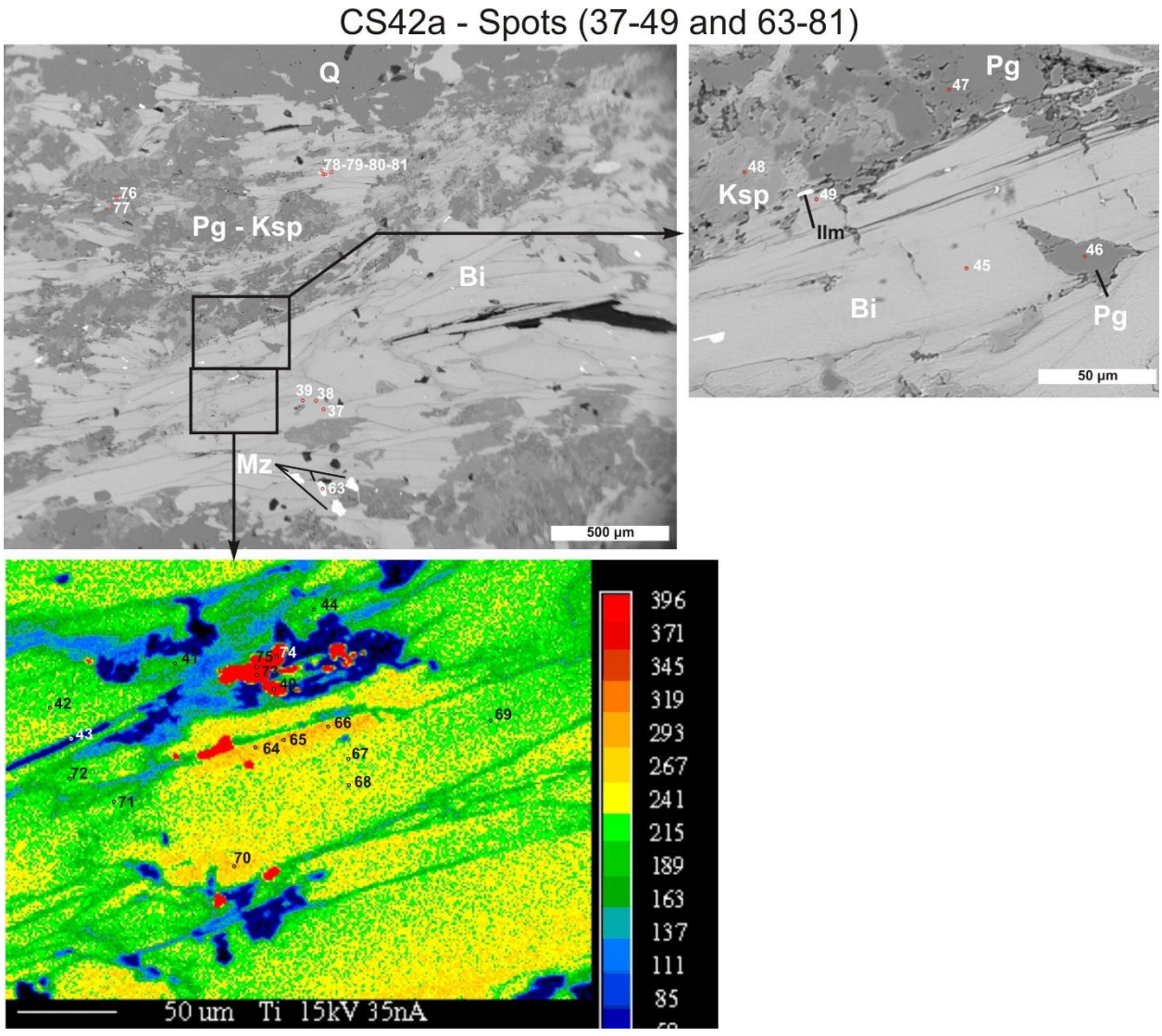

Appendix E2

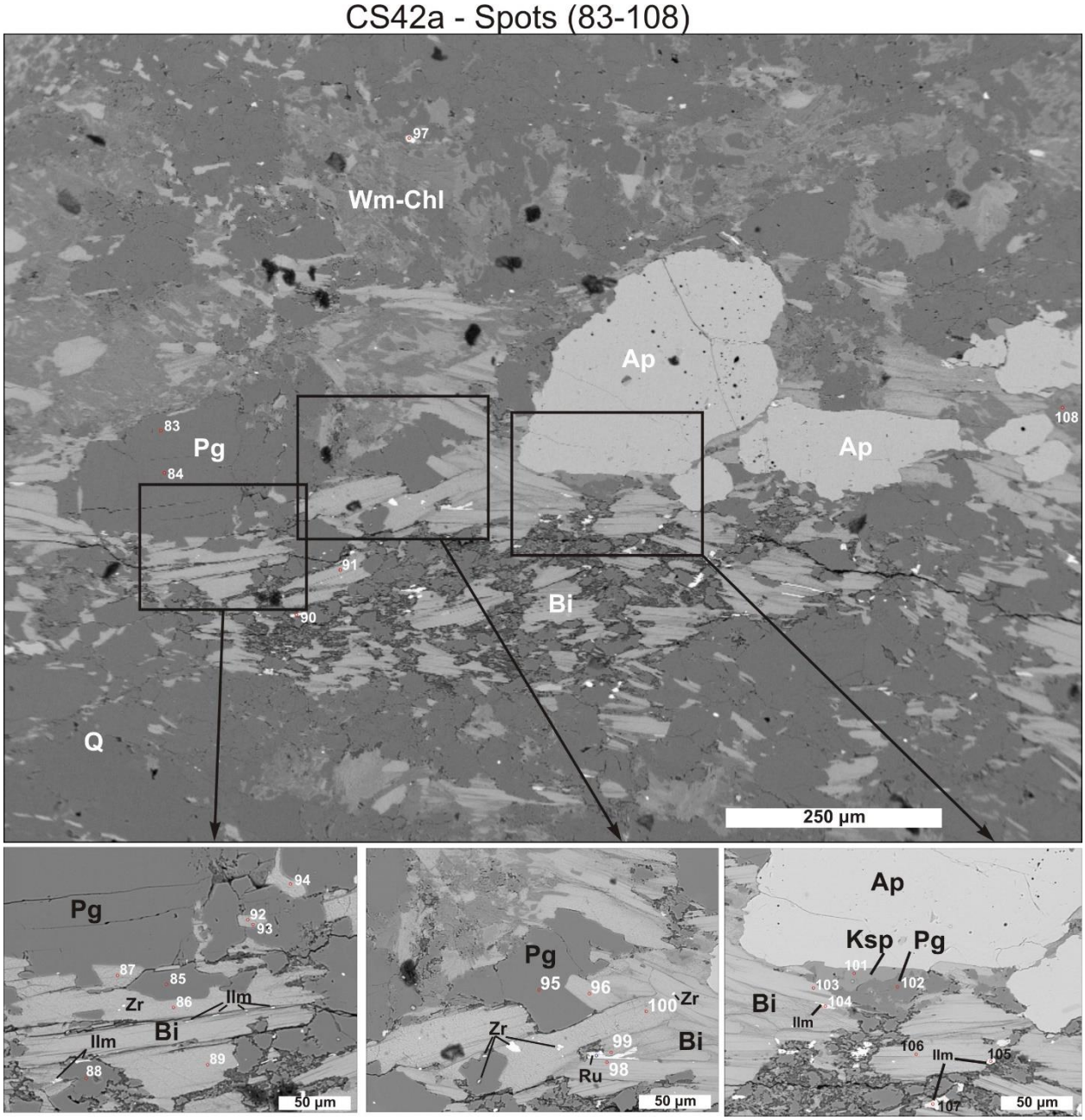

Figure E2.4 – (above) CS42a – area 3 spots.

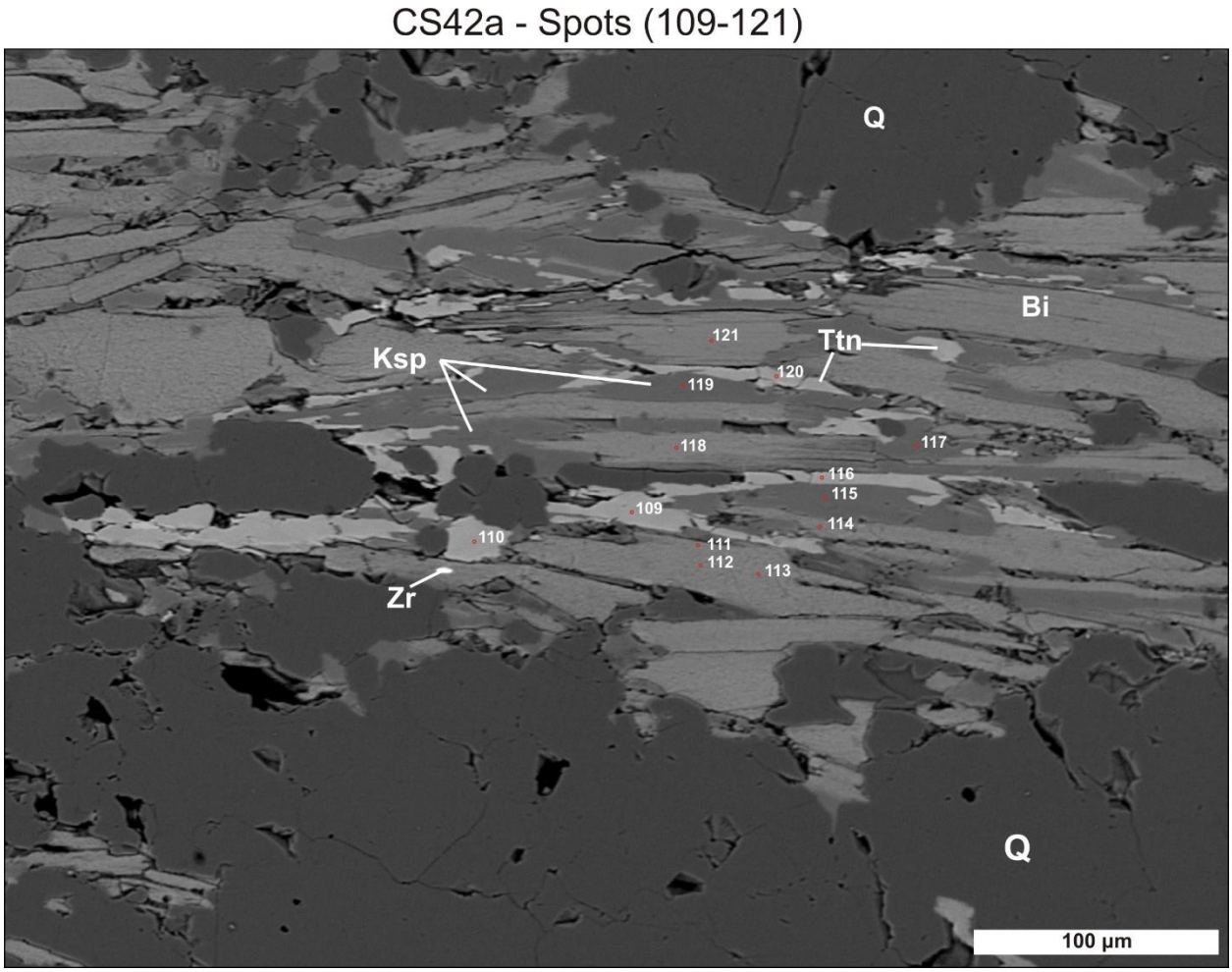

Figure E2.5 – (above) CS42a – area 4 spots.

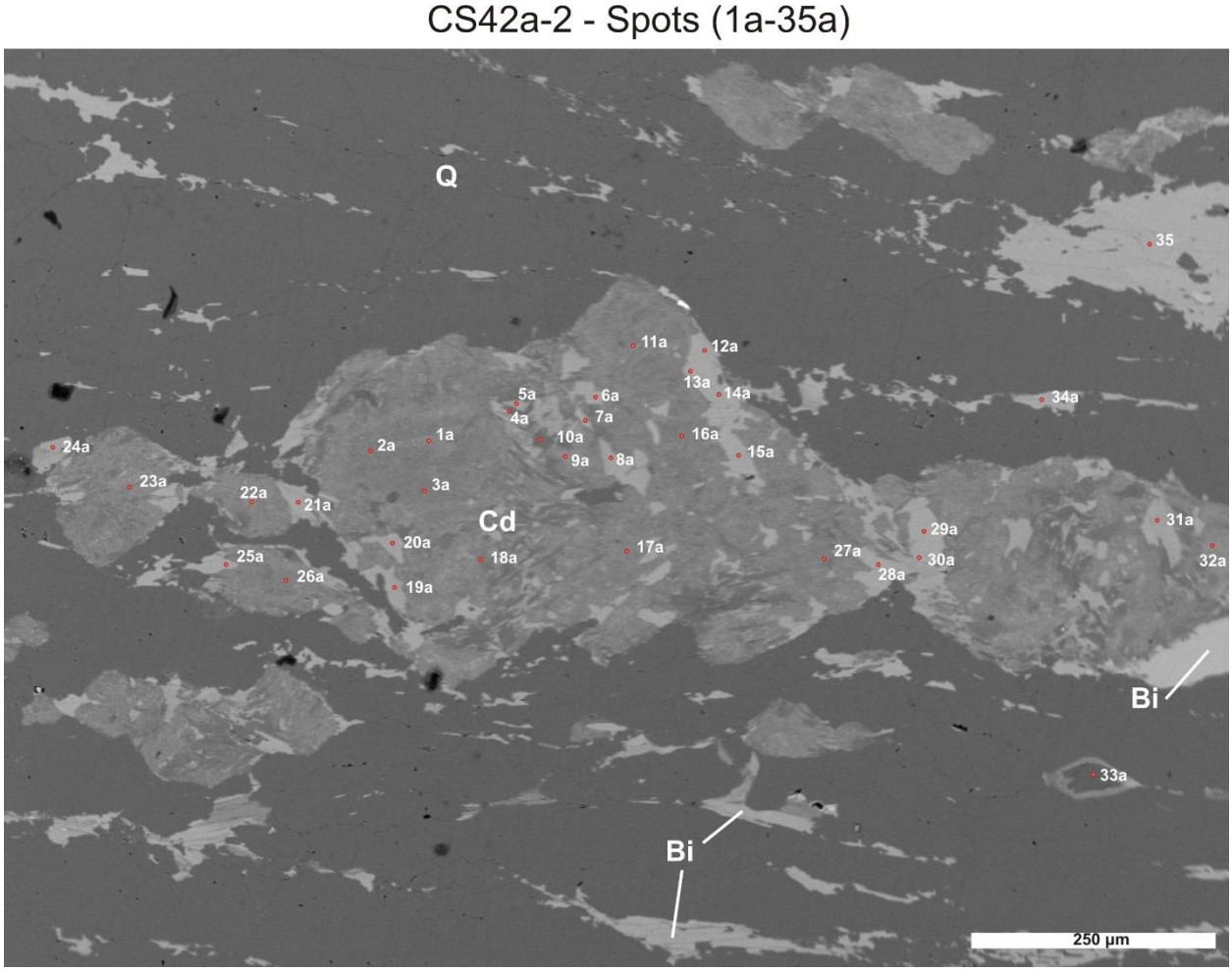

Figure E2.6 – (above) CS42a-2 – area 5 spots.

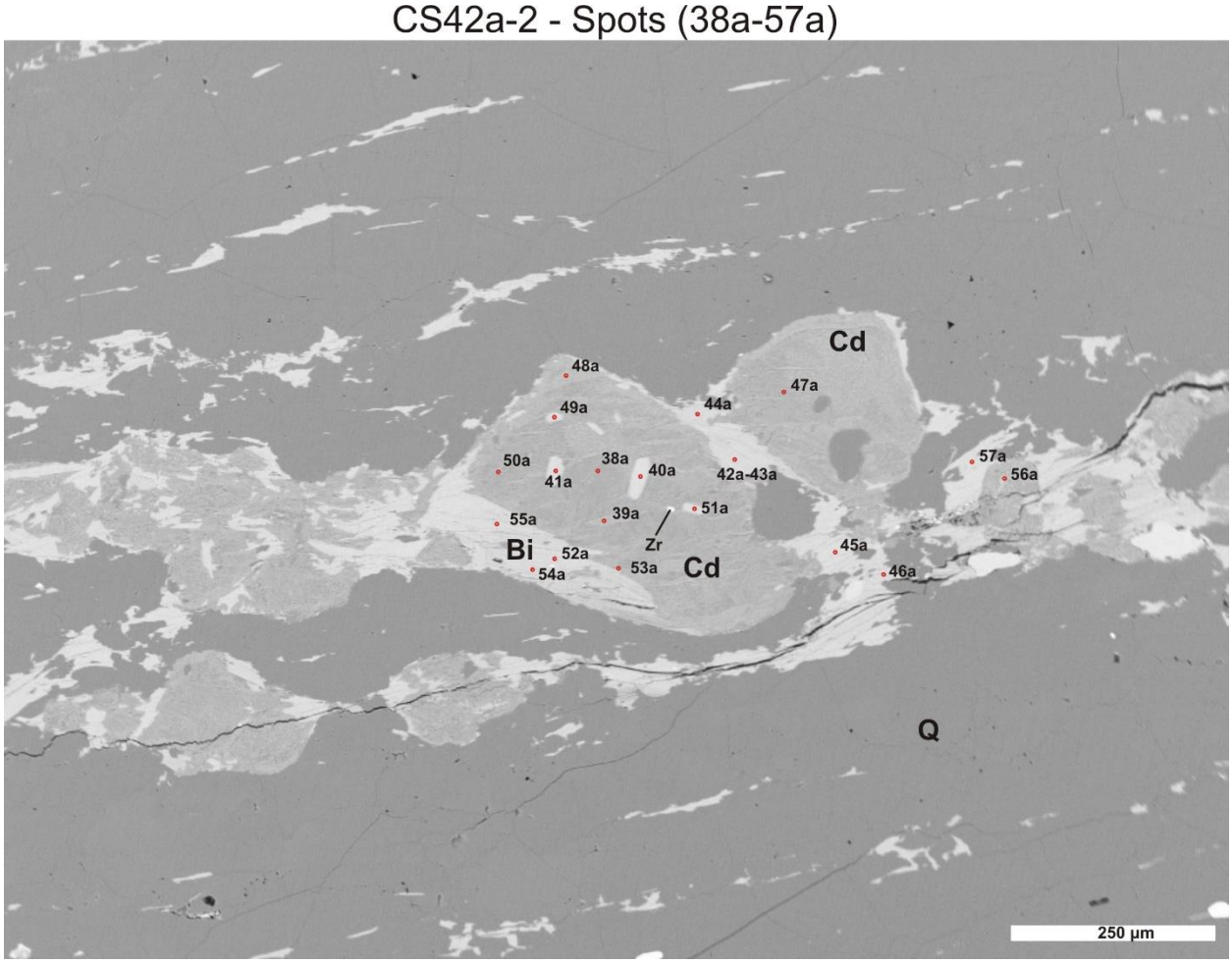

Figure E2.7 – (above) CS42a-2 – area 6 spots.

Appendix E2

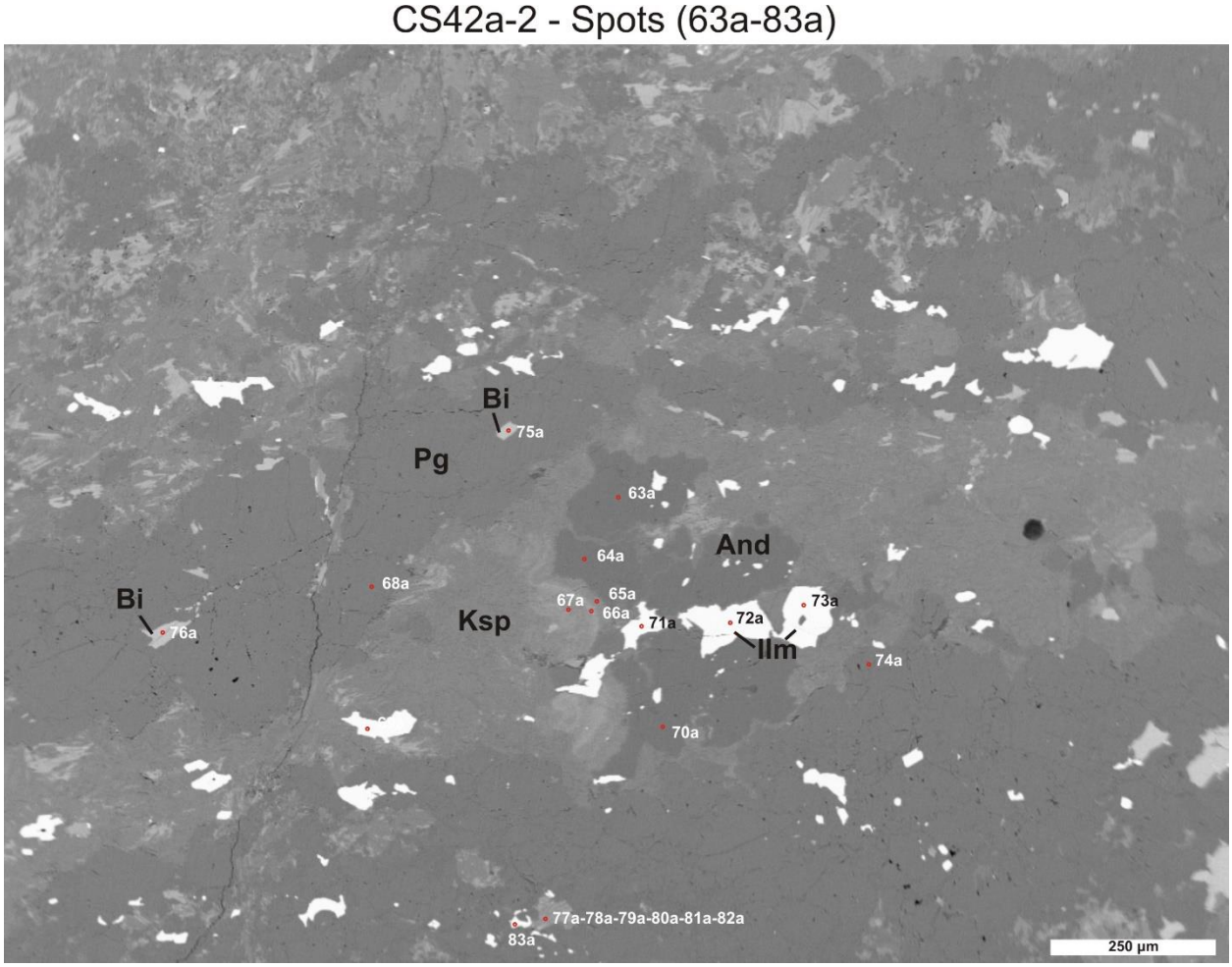

Figure E2.8 – (above) CS42a-2 – area 7 spots.

Appendix E2

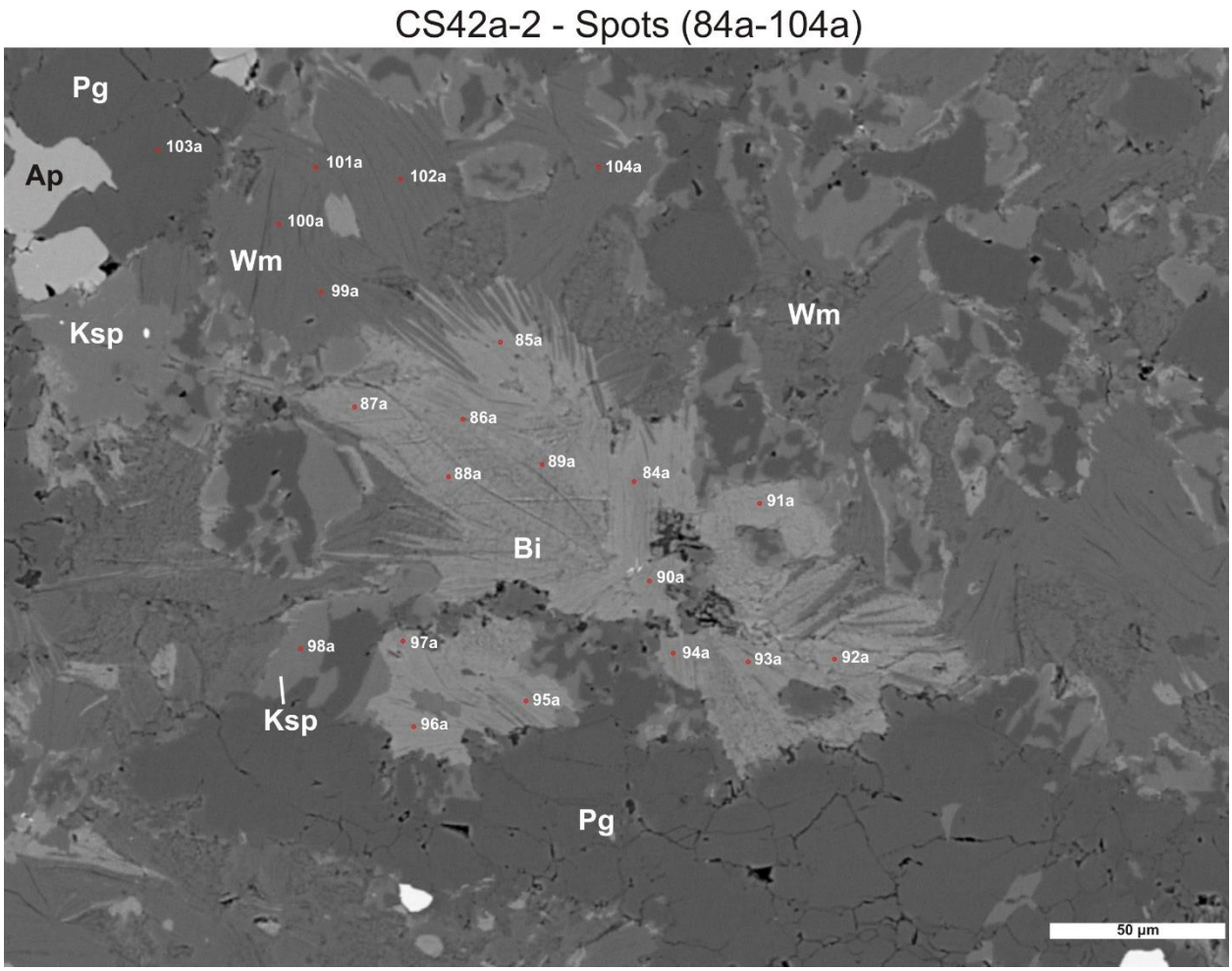

Figure E2.9 – (above) CS42a-2 – area 8 spots.

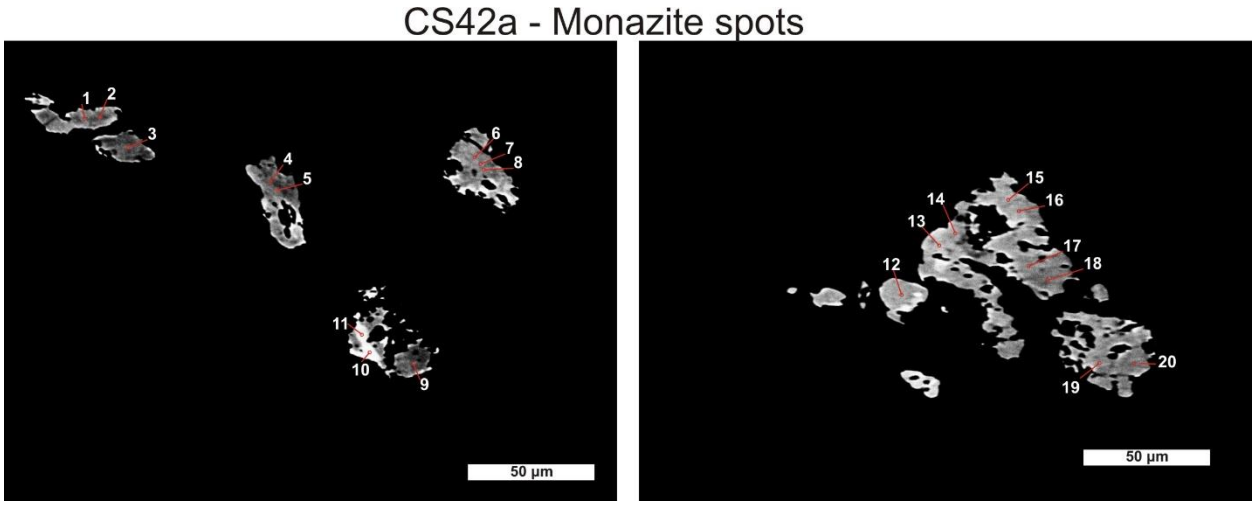

Figure E2.10 – (above) CS42a – Monazite spots.

Appendix E2

Sample CS42a

Table E2.1 – List of biotite spot analyses from **sample CS42a**. T^{H} and T^{WC} are temperatures calculated using the Henry et al. (2005) and Wu and Chen (2015) geothermometers respectively. Σ^{VI}: octahedral site sum. Σ^{A}: alkali sum.

Spot #	2	5	6	7	8	9	12	13
Comment	Bt I core	Bt I core	Bt I core	Bt I core	Bt I rim	Bt I rim	Bt I rim	Bt I rim
SiO_2	33.62	33.29	34.07	34.05	33.56	34.10	34.11	33.95
TiO_2	2.02	2.10	2.14	2.22	3.19	2.83	3.12	2.22
Al_2O_3	18.50	18.16	18.22	18.07	17.51	17.99	17.61	18.19
FeOtot	23.34	23.40	23.41	23.03	22.23	22.28	22.58	21.91
MnO	0.07	0.13	0.10	0.07	0.04	0.09	0.09	0.07
MgO	6.80	6.79	6.98	6.95	6.92	7.20	6.99	7.28
CaO	0.02	0.02	0.02	0.03	0.00	0.00	0.00	0.02
BaO	0.11	0.04	0.06	0.07	0.09	0.07	0.11	0.04
Na_2O	0.22	0.22	0.18	0.19	0.17	0.15	0.10	0.13
K_2O	8.91	9.02	8.86	9.16	9.47	9.32	9.41	9.29
Atom site distribution (22 oxygen equivalents)								
Si	5.33	5.32	5.37	5.38	5.35	5.37	5.38	5.38
Al^{IV}	2.67	2.68	2.63	2.62	2.65	2.63	2.62	2.62
Al^{VI}	0.79	0.74	0.76	0.75	0.64	0.70	0.65	0.78
Ti	0.24	0.25	0.25	0.26	0.38	0.34	0.37	0.27
Fe^{2+}	3.10	3.13	3.09	3.04	2.96	2.93	2.98	2.91
Mn	0.01	0.02	0.01	0.01	0.00	0.01	0.01	0.01
Mg	1.61	1.62	1.64	1.64	1.64	1.69	1.64	1.72
Σ^{VI}	5.75	5.76	5.75	5.71	5.63	5.67	5.65	5.69
Ca	0.00	0.00	0.00	0.00	0.00	0.00	0.00	0.00
Ba	0.01	0.00	0.00	0.00	0.01	0.00	0.01	0.00
Na	0.07	0.07	0.05	0.06	0.05	0.05	0.03	0.04
K	1.80	1.84	1.78	1.85	1.93	1.87	1.89	1.88
Σ^{A}	1.88	1.91	1.84	1.91	1.98	1.92	1.93	1.92
T^{H}(°C)	600.60	609.14	610.67	618.81	682.12	662.39	676.83	622.55
T^{WC}(°C)	591.06	593.78	593.00	598.91	650.45	627.67	645.68	593.21

Spot #	19	37	38	39	42	45	49	50
Comment	Bt I core	Bt I core	Bt I rim	Bt I core	Bt I core	Bt I core	Bt I rim	Bt I rim
SiO_2	33.73	34.11	33.99	33.67	33.90	34.19	34.82	34.12
TiO_2	1.81	3.31	3.46	3.21	3.07	3.16	3.18	3.13
Al_2O_3	18.26	18.49	18.77	18.74	18.35	18.40	19.09	17.30
FeOtot	22.06	22.86	22.43	21.39	23.00	21.80	18.97	20.54
MnO	0.07	0.11	0.10	0.13	0.07	0.07	0.05	0.13
MgO	7.72	6.14	5.94	6.95	6.53	7.34	8.50	7.34
CaO	0.05	0.01	0.00	0.00	0.00	0.03	0.02	0.00
BaO	0.06	0.12	0.07	0.10	0.10	0.09	0.12	0.11
Na_2O	0.11	0.16	0.12	0.11	0.18	0.12	0.08	0.00
K_2O	9.25	9.29	9.31	9.45	9.38	9.33	8.96	9.09
Atom site distribution (22 oxygen equivalents)								
Si	5.36	5.35	5.34	5.30	5.32	5.33	5.37	5.46
Al^{IV}	2.64	2.65	2.66	2.70	2.68	2.67	2.63	2.54
Al^{VI}	0.77	0.76	0.81	0.77	0.72	0.72	0.84	0.72
Ti	0.22	0.39	0.41	0.38	0.36	0.37	0.37	0.38
Fe^{2+}	2.93	3.00	2.94	2.81	3.02	2.84	2.45	2.75
Mn	0.01	0.01	0.01	0.02	0.01	0.01	0.01	0.02
Mg	1.83	1.43	1.39	1.63	1.53	1.71	1.95	1.75
Σ^{VI}	5.75	5.60	5.56	5.61	5.64	5.65	5.62	5.60
Ca	0.01	0.00	0.00	0.00	0.00	0.01	0.00	0.00
Ba	0.00	0.01	0.00	0.01	0.01	0.01	0.01	0.01
Na	0.03	0.05	0.04	0.03	0.05	0.04	0.02	0.00
K	1.87	1.86	1.86	1.90	1.88	1.86	1.76	1.85
Σ^{A}	1.92	1.91	1.91	1.94	1.94	1.90	1.80	1.86
T^{H}(°C)	584.13	682.35	689.07	682.52	672.10	679.61	687.93	683.47
T^{WC}(°C)	553.83	689.75	708.41	660.22	660.94	643.69	630.06	642.06

Appendix E2

Table E2.1 – (continues)

Spot #	51	52	53	54	55	56	57	58
Comment	Bt I rim	Bt I rim	Bt I rim	Bt I rim	Bt I rim	Bt I rim	Bt I rim	Bt I core
SiO_2	34.22	33.82	33.94	34.10	33.73	33.81	33.59	33.31
TiO_2	4.05	3.67	2.98	2.90	4.31	3.64	3.09	2.43
Al_2O_3	17.68	17.59	18.31	18.29	17.62	17.90	18.15	18.38
FeOtot	22.20	22.84	23.39	23.01	22.67	23.05	22.79	23.95
MnO	0.05	0.07	0.01	0.05	0.07	0.09	0.10	0.06
MgO	7.07	6.98	6.81	6.78	6.96	6.92	7.26	6.75
CaO	0.00	0.00	0.00	0.05	0.06	0.01	0.00	0.01
BaO	0.19	0.17	0.07	0.12	0.17	0.11	0.12	0.09
Na_2O	0.08	0.14	0.22	0.17	0.10	0.18	0.11	0.16
K_2O	9.32	9.26	9.08	9.19	9.37	9.16	9.32	9.31
Atom site distribution (22 oxygen equivalents)								
Si	5.34	5.32	5.31	5.34	5.27	5.29	5.28	5.27
Al^{IV}	2.66	2.68	2.69	2.66	2.73	2.71	2.72	2.73
Al^{VI}	0.59	0.58	0.69	0.72	0.52	0.60	0.64	0.70
Ti	0.48	0.43	0.35	0.34	0.51	0.43	0.37	0.29
Fe^{2+}	2.90	3.00	3.06	3.01	2.97	3.02	3.00	3.17
Mn	0.01	0.01	0.00	0.01	0.01	0.01	0.01	0.01
Mg	1.64	1.64	1.59	1.58	1.62	1.61	1.70	1.59
Σ^{VI}	5.61	5.66	5.70	5.67	5.62	5.67	5.72	5.76
Ca	0.00	0.00	0.00	0.01	0.01	0.00	0.00	0.00
Ba	0.01	0.01	0.00	0.01	0.01	0.01	0.01	0.01
Na	0.02	0.04	0.07	0.05	0.03	0.05	0.03	0.05
K	1.86	1.86	1.81	1.84	1.87	1.83	1.87	1.88
Σ^{A}	1.89	1.91	1.88	1.90	1.92	1.89	1.91	1.93
T^{H}(°C)	714.91	701.09	667.48	663.43	722.85	698.89	675.85	634.05
T^{WC}(°C)	686.19	669.82	646.04	643.86	696.27	671.50	636.77	615.08
Spot #	59	60	61	62	64	65	66	67
Comment	Bt I core	Bt I core	Bt I rim	Bt I rim	Bt I rim	Bt I rim	Bt I rim	Bt I core
SiO_2	33.31	33.63	33.82	34.08	34.99	34.71	34.67	34.16
TiO_2	1.99	2.09	2.88	3.09	3.74	3.69	3.74	3.17
Al_2O_3	18.54	18.17	18.24	18.11	18.84	18.81	18.82	18.89
FeOtot	24.07	24.47	22.89	22.44	22.36	22.07	22.04	24.24
MnO	0.14	0.16	0.08	0.11	0.10	0.06	0.10	0.12
MgO	7.03	6.92	7.51	7.28	6.86	6.96	7.00	6.40
CaO	0.00	0.04	0.03	0.03	0.03	0.03	0.04	0.00
BaO	0.09	0.07	0.14	0.11	0.12	0.12	0.15	0.11
Na_2O	0.24	0.25	0.08	0.13	0.18	0.19	0.21	0.23
K_2O	8.74	8.96	9.44	9.48	9.23	9.22	9.24	9.12
Atom site distribution (22 oxygen equivalents)								
Si	5.27	5.31	5.28	5.32	5.34	5.33	5.32	5.27
Al^{IV}	2.73	2.69	2.72	2.68	2.66	2.67	2.68	2.73
Al^{VI}	0.73	0.68	0.64	0.66	0.73	0.73	0.72	0.71
Ti	0.24	0.25	0.34	0.36	0.43	0.43	0.43	0.37
Fe^{2+}	3.19	3.23	2.99	2.93	2.86	2.83	2.83	3.13
Mn	0.02	0.02	0.01	0.01	0.01	0.01	0.01	0.02
Mg	1.66	1.63	1.75	1.69	1.56	1.59	1.60	1.47
Σ^{VI}	5.83	5.81	5.73	5.67	5.59	5.60	5.60	5.70
Ca	0.00	0.01	0.01	0.01	0.00	0.01	0.01	0.00
Ba	0.01	0.00	0.01	0.01	0.01	0.01	0.01	0.01
Na	0.07	0.08	0.02	0.04	0.05	0.06	0.06	0.07
K	1.77	1.80	1.88	1.89	1.80	1.81	1.81	1.80
Σ^{A}	1.84	1.89	1.92	1.94	1.86	1.88	1.89	1.87
T^{H}(°C)	597.32	604.83	664.33	675.49	699.49	699.14	701.15	673.07
T^{WC}(°C)	580.01	586.92	619.10	637.88	687.83	682.36	683.13	670.66

Appendix E2

Table E2.1 – (continues)

Spot #	68	69	70	71	72	86	87	89
Comment	Bt I core	Bt I core	Bt I rim	Bt I core	Bt I core	Bt I core	Bt I core	Bt I core
SiO_2	34.35	34.27	34.98	34.23	34.41	34.25	34.75	34.01
TiO_2	3.17	2.95	3.38	2.85	2.70	4.23	3.88	4.27
Al_2O_3	18.66	18.66	18.82	19.42	19.55	18.86	19.59	18.91
FeOtot	23.82	23.25	20.44	20.79	20.45	23.09	21.90	23.09
MnO	0.08	0.10	0.11	0.03	0.08	0.08	0.06	0.08
MgO	6.38	6.91	8.68	8.66	9.15	6.37	6.51	5.94
CaO	0.01	0.04	0.05	0.03	0.02	0.07	0.05	0.02
BaO	0.13	0.11	0.15	0.08	0.08	0.13	0.12	0.15
Na_2O	0.24	0.15	0.10	0.08	0.09	0.17	0.12	0.15
K_2O	9.01	9.26	9.31	9.17	9.26	9.50	9.52	9.58
Atom site distribution (22 oxygen equivalents)								
Si	5.32	5.31	5.32	5.25	5.25	5.25	5.30	5.25
Al^{IV}	2.68	2.69	2.68	2.75	2.75	2.75	2.70	2.75
Al^{VI}	0.73	0.72	0.70	0.76	0.76	0.66	0.82	0.70
Ti	0.37	0.34	0.39	0.33	0.31	0.49	0.44	0.50
Fe^{2+}	3.09	3.01	2.60	2.67	2.61	2.96	2.79	2.98
Mn	0.01	0.01	0.01	0.00	0.01	0.01	0.01	0.01
Mg	1.47	1.60	1.97	1.98	2.08	1.46	1.48	1.37
Σ^{VI}	5.67	5.69	5.67	5.74	5.77	5.58	5.54	5.55
Ca	0.00	0.01	0.01	0.01	0.00	0.01	0.01	0.00
Ba	0.01	0.01	0.01	0.00	0.00	0.01	0.01	0.01
Na	0.07	0.04	0.03	0.02	0.03	0.05	0.04	0.05
K	1.78	1.83	1.81	1.80	1.80	1.86	1.85	1.89
Σ^{A}	1.86	1.89	1.85	1.83	1.84	1.93	1.90	1.94
T^{H}(°C)	673.76	664.54	692.96	667.21	660.24	715.65	703.87	716.89
T^{WC}(°C)	672.27	643.36	625.80	602.26	586.07	721.86	711.59	742.05
Spot #	91	92	93	94	96	98	99	100
Comment	Bt I rim	Bt I core	Bt I core	Bt I rim	Bt I core	Bt I rim	Bt I rim	Bt I core
SiO_2	34.28	34.52	34.75	33.90	34.36	34.19	33.50	34.09
TiO_2	3.75	1.91	1.80	3.15	3.16	2.98	3.02	3.52
Al_2O_3	19.53	19.54	19.71	18.76	19.32	18.50	18.06	19.40
FeOtot	22.84	22.74	22.11	21.72	22.43	20.07	18.72	23.63
MnO	0.05	0.00	0.04	0.10	0.06	0.10	0.11	0.08
MgO	6.33	7.18	7.40	7.19	6.60	9.25	9.54	6.22
CaO	0.00	0.06	0.02	0.05	0.00	0.05	0.04	0.04
BaO	0.15	0.02	0.06	0.14	0.13	0.09	0.09	0.10
Na_2O	0.20	0.22	0.18	0.15	0.11	0.05	0.09	0.20
K_2O	9.63	9.51	9.41	9.54	9.40	9.72	10.01	9.46
Atom site distribution (22 oxygen equivalents)								
Si	5.25	5.33	5.35	5.29	5.31	5.28	5.26	5.24
Al^{IV}	2.75	2.67	2.65	2.71	2.69	2.72	2.74	2.76
Al^{VI}	0.77	0.88	0.93	0.74	0.82	0.64	0.61	0.75
Ti	0.43	0.22	0.21	0.37	0.37	0.35	0.36	0.41
Fe^{2+}	2.92	2.94	2.85	2.83	2.90	2.59	2.46	3.04
Mn	0.01	0.00	0.00	0.01	0.01	0.01	0.01	0.01
Mg	1.45	1.65	1.70	1.67	1.52	2.13	2.24	1.42
Σ^{VI}	5.58	5.69	5.69	5.63	5.62	5.72	5.68	5.63
Ca	0.00	0.01	0.00	0.01	0.00	0.01	0.01	0.01
Ba	0.01	0.00	0.00	0.01	0.01	0.01	0.01	0.01
Na	0.06	0.06	0.05	0.05	0.03	0.01	0.03	0.06
K	1.88	1.87	1.85	1.90	1.85	1.91	2.01	1.85
Σ^{A}	1.95	1.95	1.91	1.96	1.89	1.94	2.05	1.93
T^{H}(°C)	698.04	585.67	574.44	678.58	674.60	679.27	688.34	688.37
T^{WC}(°C)	707.24	579.52	568.92	648.25	671.05	593.21	590.63	697.90

Appendix E2

Table E2.1 – (continues)

Spot #	103	106	111	112	113	114	118	121
Comment	Bt I rim	Bt I core	*	*	*	*	*	*
SiO_2	34.33	33.82	34.13	34.17	33.84	34.50	34.63	35.06
TiO_2	3.57	3.56	1.31	1.29	1.26	1.26	1.30	1.19
Al_2O_3	19.06	18.93	20.29	20.26	20.31	20.77	20.34	20.34
FeOtot	20.89	23.88	21.15	21.24	21.26	21.14	21.04	20.15
MnO	0.06	0.05	0.12	0.08	0.10	0.09	0.02	0.04
MgO	7.89	6.07	7.70	7.25	7.28	7.11	7.77	7.40
CaO	0.03	0.03	0.12	0.05	0.05	0.11	0.05	0.05
BaO	0.11	0.14	0.00	0.04	0.06	0.00	0.05	0.02
Na_2O	0.11	0.16	0.15	0.14	0.15	0.10	0.13	0.07
K_2O	9.91	9.36	9.28	9.65	9.62	9.24	9.77	9.33
Atom site distribution (22 oxygen equivalents)								
Si	5.26	5.25	5.30	5.33	5.30	5.34	5.34	5.44
Al^{IV}	2.74	2.75	2.70	2.67	2.70	2.66	2.66	2.56
Al^{VI}	0.71	0.71	1.02	1.05	1.04	1.13	1.03	1.15
Ti	0.41	0.42	0.15	0.15	0.15	0.15	0.15	0.14
Fe^{2+}	2.68	3.10	2.75	2.77	2.78	2.74	2.71	2.61
Mn	0.01	0.01	0.02	0.01	0.01	0.01	0.00	0.00
Mg	1.80	1.40	1.78	1.69	1.70	1.64	1.78	1.71
Σ^{VI}	5.61	5.64	5.72	5.67	5.69	5.67	5.68	5.62
Ca	0.01	0.00	0.02	0.01	0.01	0.02	0.01	0.01
Ba	0.01	0.01	0.00	0.00	0.00	0.00	0.00	0.00
Na	0.03	0.05	0.05	0.04	0.05	0.03	0.04	0.02
K	1.94	1.85	1.84	1.92	1.92	1.83	1.92	1.85
Σ^{A}	1.98	1.92	1.91	1.97	1.98	1.87	1.97	1.88
T^{H}(°C)	698.66	690.88	501.08	495.02	488.42	484.20	497.35	472.72
T^{WC}(°C)	651.78	702.49	525.43	534.33	529.89	538.52	524.11	527.41
Spot #	12a	13a	14a	15a	25a	28a	29a	30a
Comment	Bt I core	Bt I core	Bt I rim	Bt I core	Bt I rim	Bt I core	Bt I rim	Bt I rim
SiO_2	34.40	34.45	34.07	33.84	34.04	33.67	34.24	34.21
TiO_2	2.21	1.74	2.84	2.56	1.82	2.78	3.34	3.02
Al_2O_3	18.61	19.25	18.35	19.01	19.11	18.25	18.45	18.25
FeOtot	23.79	23.04	23.46	23.28	24.09	23.95	23.37	23.44
MnO	0.04	0.05	0.09	0.01	0.12	0.07	0.13	0.15
MgO	7.07	7.35	6.68	6.70	6.78	6.64	6.36	6.82
CaO	0.02	0.00	0.00	0.00	0.02	0.02	0.02	0.01
BaO	0.07	0.10	0.12	0.06	0.06	0.10	0.14	0.08
Na_2O	0.16	0.10	0.09	0.04	0.12	0.11	0.09	0.10
K_2O	9.83	10.06	9.84	10.06	9.94	9.80	9.82	9.83
Atom site distribution (22 oxygen equivalents)								
Si	5.33	5.32	5.32	5.28	5.29	5.28	5.32	5.32
Al^{IV}	2.67	2.68	2.68	2.72	2.71	2.72	2.68	2.68
Al^{VI}	0.73	0.83	0.70	0.77	0.80	0.66	0.69	0.66
Ti	0.26	0.20	0.33	0.30	0.21	0.33	0.39	0.35
Fe^{2+}	3.08	2.98	3.06	3.04	3.13	3.14	3.03	3.05
Mn	0.01	0.01	0.01	0.00	0.02	0.01	0.02	0.02
Mg	1.63	1.69	1.56	1.56	1.57	1.55	1.47	1.58
Σ^{VI}	5.71	5.71	5.66	5.67	5.73	5.69	5.61	5.66
Ca	0.00	0.00	0.00	0.00	0.00	0.00	0.00	0.00
Ba	0.00	0.01	0.01	0.00	0.00	0.01	0.01	0.00
Na	0.05	0.03	0.03	0.01	0.04	0.03	0.03	0.03
K	1.94	1.98	1.96	2.00	1.97	1.96	1.94	1.95
Σ^{A}	2.00	2.02	1.99	2.02	2.01	2.01	1.99	1.98
T^{H}(°C)	613.69	566.00	658.33	640.79	573.40	655.14	682.52	668.45
T^{WC}(°C)	594.65	559.43	641.70	628.91	577.25	637.01	679.50	646.22

* Biotite coexisting with titanite, characterized by low Ti content (see text for details)

Appendix E2

Table E2.1 – (continues)

Spot #	34a	35a	44a	45a	46a	52a	54a	55a
Comment	Bt I rim	Bt I core	Bt I core	Bt I rim	Bt I core	Bt I core	Bt I core	Bt I rim
SiO_2	33.94	34.18	35.35	34.00	33.93	34.25	35.11	34.22
TiO_2	3.21	3.08	2.12	3.28	2.97	1.89	1.04	3.19
Al_2O_3	18.78	19.35	19.28	18.54	18.74	19.05	19.24	18.39
FeOtot	23.49	23.22	23.37	23.50	23.94	23.68	22.00	23.87
MnO	0.09	0.07	0.00	0.01	0.04	0.07	0.03	0.07
MgO	6.31	6.20	7.47	6.40	6.30	7.12	8.02	6.55
CaO	0.02	0.00	0.03	0.03	0.08	0.01	0.03	0.00
BaO	0.09	0.11	0.05	0.10	0.08	0.06	0.04	0.08
Na_2O	0.08	0.10	0.08	0.11	0.13	0.07	0.12	0.15
K_2O	10.08	9.91	9.84	10.03	9.80	9.95	9.81	9.80
Atom site distribution (22 oxygen equivalents)								
Si	5.27	5.28	5.36	5.29	5.28	5.31	5.42	5.30
Al^{IV}	2.73	2.72	2.64	2.71	2.72	2.69	2.58	2.70
Al^{VI}	0.71	0.80	0.81	0.68	0.72	0.79	0.92	0.66
Ti	0.37	0.36	0.24	0.38	0.35	0.22	0.12	0.37
Fe^{2+}	3.05	3.00	2.96	3.06	3.11	3.07	2.84	3.09
Mn	0.01	0.01	0.00	0.00	0.00	0.01	0.00	0.01
Mg	1.46	1.43	1.69	1.48	1.46	1.65	1.84	1.51
Σ^{VI}	5.61	5.60	5.70	5.61	5.65	5.73	5.72	5.65
Ca	0.00	0.00	0.00	0.01	0.01	0.00	0.00	0.00
Ba	0.01	0.01	0.00	0.01	0.00	0.00	0.00	0.00
Na	0.02	0.03	0.02	0.03	0.04	0.02	0.03	0.05
K	2.00	1.95	1.90	1.99	1.95	1.97	1.93	1.94
Σ^{A}	2.03	1.99	1.94	2.03	2.00	1.99	1.97	1.99
T^{H}(°C)	676.21	668.58	603.92	680.26	663.88	582.68	422.90	675.22
T^{WC}(°C)	675.39	677.86	584.13	674.66	662.67	573.90	487.33	663.55
Spot #	57a	75a	76a	23	24	25	26	27
Comment	Bt I rim	Bt I rim	Bt I rim	Bt II	Bt II	Bt II	Bt II	Bt II
SiO_2	34.11	32.69	32.90	33.83	33.92	34.43	34.06	34.45
TiO_2	3.62	3.10	3.72	1.84	1.78	1.85	1.85	1.50
Al_2O_3	18.12	17.62	17.10	18.35	18.33	18.70	18.50	18.60
FeOtot	24.22	24.17	24.16	22.13	22.47	20.83	21.89	21.51
MnO	0.09	0.03	0.10	0.06	0.03	0.05	0.12	0.09
MgO	6.33	5.51	5.09	7.02	7.06	7.38	7.31	7.66
CaO	0.01	0.00	0.03	0.01	0.02	0.08	0.04	0.02
BaO	0.12	0.15	0.18	0.06	0.07	0.10	0.07	0.07
Na_2O	0.04	0.08	0.09	0.15	0.21	0.13	0.14	0.18
K_2O	9.89	9.91	9.95	9.06	8.87	9.16	9.03	9.36
Atom site distribution (22 oxygen equivalents)								
Si	5.29	5.28	5.32	5.40	5.40	5.44	5.40	5.42
Al^{IV}	2.71	2.72	2.68	2.60	2.60	2.56	2.60	2.58
Al^{VI}	0.60	0.64	0.58	0.85	0.84	0.92	0.85	0.88
Ti	0.42	0.38	0.45	0.22	0.21	0.22	0.22	0.18
Fe^{2+}	3.14	3.27	3.27	2.95	2.99	2.75	2.90	2.83
Mn	0.01	0.00	0.01	0.01	0.00	0.01	0.02	0.01
Mg	1.46	1.33	1.23	1.67	1.68	1.74	1.73	1.80
Σ^{VI}	5.64	5.62	5.54	5.70	5.72	5.64	5.71	5.70
Ca	0.00	0.00	0.01	0.00	0.00	0.01	0.01	0.00
Ba	0.01	0.01	0.01	0.00	0.00	0.01	0.00	0.00
Na	0.01	0.03	0.03	0.05	0.07	0.04	0.04	0.05
K	1.96	2.04	2.05	1.85	1.80	1.85	1.83	1.88
Σ^{A}	1.98	2.08	2.10	1.90	1.88	1.90	1.88	1.94
T^{H}(°C)	693.82	674.50	701.10	584.62	576.86	588.32	586.39	540.27
T^{WC}(°C)	689.32	693.17	742.32	575.16	568.84	572.99	569.70	535.97

Appendix E2

Table E2.1 – (continues)

Spot #	28	30	31	32	33	34	85a	87a
Comment	Bt II	Bt II	Bt II	Bt II	Bt II	Bt II	Bt III	Bt III
SiO_2	34.12	33.67	34.18	33.66	34.18	33.90	35.83	35.50
TiO_2	1.57	1.98	1.97	2.52	2.03	2.04	0.83	0.80
Al_2O_3	18.82	18.19	18.17	17.79	18.24	18.12	16.87	16.58
FeOtot	21.63	21.82	22.06	22.63	23.31	22.69	18.98	18.18
MnO	0.08	0.06	0.07	0.05	0.04	0.10	0.06	0.10
MgO	7.71	7.31	7.46	7.19	7.00	7.19	10.81	11.39
CaO	0.00	0.05	0.09	0.03	0.04	0.01	0.00	0.03
BaO	0.04	0.05	0.08	0.09	0.07	0.10	0.00	0.02
Na_2O	0.14	0.13	0.11	0.15	0.27	0.13	0.05	0.07
K_2O	9.42	9.30	8.96	9.29	8.90	9.37	9.85	8.54
Atom site distribution (22 oxygen equivalents)								
Si	5.37	5.37	5.41	5.35	5.39	5.37	5.59	5.61
Al^{IV}	2.63	2.63	2.59	2.65	2.61	2.63	2.41	2.39
Al^{VI}	0.87	0.80	0.80	0.68	0.77	0.76	0.69	0.69
Ti	0.19	0.24	0.23	0.30	0.24	0.24	0.10	0.10
Fe^{2+}	2.85	2.91	2.92	3.01	3.07	3.01	2.48	2.40
Mn	0.01	0.01	0.01	0.01	0.01	0.01	0.01	0.01
Mg	1.81	1.74	1.76	1.70	1.64	1.70	2.51	2.68
Σ^{VI}	5.72	5.70	5.72	5.70	5.73	5.72	5.78	5.88
Ca	0.00	0.01	0.02	0.01	0.01	0.00	0.00	0.00
Ba	0.00	0.00	0.01	0.01	0.00	0.01	0.00	0.00
Na	0.04	0.04	0.03	0.05	0.08	0.04	0.02	0.02
K	1.89	1.89	1.81	1.88	1.79	1.89	1.96	1.72
Σ^{A}	1.94	1.95	1.86	1.94	1.88	1.94	1.97	1.75
T^{H}(°C)	551.91	601.98	599.03	644.10	600.45	604.20	379.46	384.67
T^{WC}(°C)	540.80	576.23	572.14	608.33	585.64	580.88	422.65	415.62
Spot #	89a	90a	91a	92a	93a	94a	95a	96a
Comment	Bt III	Bt III	Bt III	Bt III	Bt III	Bt III	Bt III	Bt III
SiO_2	35.44	35.38	35.96	35.47	35.54	37.37	35.12	35.10
TiO_2	0.82	1.22	0.69	1.13	1.32	1.06	1.08	1.26
Al_2O_3	16.76	16.60	16.68	16.06	16.22	18.36	16.43	16.50
FeOtot	17.85	18.82	17.87	17.65	18.39	16.72	18.66	18.66
MnO	0.11	0.08	0.05	0.01	0.04	0.12	0.02	0.10
MgO	11.57	10.37	11.34	10.44	10.76	8.92	10.49	10.47
CaO	0.05	0.06	0.03	0.06	0.02	0.06	0.01	0.02
BaO	0.05	0.01	0.04	0.00	0.05	0.01	0.05	0.09
Na_2O	0.08	0.07	0.09	0.09	0.05	0.04	0.07	0.05
K_2O	8.58	9.78	9.90	8.49	9.51	8.63	9.71	9.84
Atom site distribution (22 oxygen equivalents)								
Si	5.58	5.58	5.62	5.70	5.61	5.80	5.58	5.56
Al^{IV}	2.42	2.42	2.38	2.30	2.39	2.20	2.42	2.44
Al^{VI}	0.70	0.66	0.69	0.74	0.63	1.16	0.66	0.64
Ti	0.10	0.14	0.08	0.14	0.16	0.12	0.13	0.15
Fe^{2+}	2.35	2.48	2.34	2.37	2.43	2.17	2.48	2.47
Mn	0.01	0.01	0.01	0.00	0.01	0.02	0.00	0.01
Mg	2.72	2.44	2.64	2.50	2.53	2.06	2.49	2.47
Σ^{VI}	5.88	5.73	5.76	5.75	5.75	5.53	5.75	5.74
Ca	0.01	0.01	0.01	0.01	0.00	0.01	0.00	0.00
Ba	0.00	0.00	0.00	0.00	0.00	0.00	0.00	0.01
Na	0.03	0.02	0.03	0.03	0.01	0.01	0.02	0.01
K	1.73	1.97	1.97	1.74	1.92	1.71	1.97	1.99
Σ^{A}	1.76	2.00	2.01	1.78	1.94	1.73	1.99	2.01
T^{H}(°C)	400.02	514.55	277.78	506.33	541.33	465.68	485.85	527.26
T^{WC}(°C)	417.23	465.20	401.64	461.40	469.92	493.86	451.47	467.58

Appendix E2

Table E2.1 – (continues)

Spot #	97a
Comment	Bt III
SiO_2	35.61
TiO_2	1.19
Al_2O_3	15.64
FeOtot	18.07
MnO	0.03
MgO	11.53
CaO	0.06
BaO	0.07
Na_2O	0.08
K_2O	9.73
Atom site distribution (22 oxygen equivalents)	
Si	5.62
Al^{IV}	2.38
Al^{VI}	0.53
Ti	0.14
Fe^{2+}	2.39
Mn	0.00
Mg	2.71
Σ^{VI}	5.78
Ca	0.01
Ba	0.00
Na	0.02
K	1.96
Σ^{A}	2.00
T^{H}(°C)	522.72
T^{WC}(°C)	448.33

Table E2.2 – List of white mica spot analyses from **sample CS42a**.

Spot #	65a	67a	99a	100a	101a	102a	104a	22
Comment	-	-	-	-	-	-	-	-
SiO_2	46.23	48.01	47.08	46.90	46.05	46.12	46.26	45.76
TiO_2	0.06	0.03	0.14	0.14	0.09	0.16	0.16	0.03
Al_2O_3	30.23	32.73	31.63	31.54	30.94	31.40	30.62	30.43
FeOtot	4.36	1.55	2.16	1.82	2.26	2.02	2.35	2.88
MnO	0.06	0.00	0.06	0.02	0.00	0.00	0.02	0.01
MgO	2.99	1.19	1.25	1.23	1.40	1.37	1.45	2.24
CaO	0.18	0.04	0.00	0.04	0.03	0.01	0.06	0.08
BaO	0.05	0.14	0.12	0.11	0.13	0.09	0.10	0.02
Na_2O	0.18	0.23	0.26	0.21	0.35	0.32	0.21	0.24
K_2O	10.07	10.41	10.35	10.46	10.44	10.22	10.29	9.69
Atom site distribution (11 oxygen equivalents)								
Si	3.16	3.22	3.22	3.22	3.21	3.20	3.22	3.19
Al^{IV}	0.84	0.78	0.78	0.78	0.79	0.80	0.78	0.81
Al^{VI}	1.59	1.81	1.77	1.78	1.74	1.77	1.74	1.70
Ti	0.00	0.00	0.01	0.01	0.00	0.01	0.01	0.00
Fe^{2+}	0.25	0.09	0.12	0.10	0.13	0.12	0.14	0.17
Mn	0.00	0.00	0.00	0.00	0.00	0.00	0.00	0.00
Mg	0.31	0.12	0.13	0.13	0.15	0.14	0.15	0.23
Σ^{VI}	2.16	2.02	2.03	2.02	2.03	2.03	2.03	2.10
Ca	0.01	0.00	0.00	0.00	0.00	0.00	0.00	0.01
Ba	0.00	0.00	0.00	0.00	0.00	0.00	0.00	0.00
Na	0.02	0.03	0.03	0.03	0.05	0.04	0.03	0.03
K	0.88	0.89	0.90	0.92	0.93	0.90	0.91	0.86
Σ^{A}	0.92	0.93	0.94	0.95	0.98	0.95	0.95	0.90

Appendix E2

Table E2.3 – List of altered cordierite spot analyses from **sample CS42a**.

Spot #	1a	2a	3a	4a	9a	11a	16a	17a
Comment	-	-	-	-	-	-	-	-
SiO_2	44.21	43.93	43.76	47.57	39.61	43.62	45.25	44.37
TiO_2	0.04	0.01	0.02	1.35	0.04	0.00	0.00	0.01
Al_2O_3	29.57	29.38	29.72	36.22	24.52	29.04	29.98	29.53
FeOtot	6.47	7.48	6.95	0.68	14.04	8.63	7.77	7.18
MnO	0.00	0.02	0.03	0.00	0.01	0.00	0.00	0.01
MgO	3.44	3.47	3.32	0.42	6.50	3.96	3.54	3.60
CaO	0.09	0.06	0.05	0.00	0.08	0.03	0.00	0.00
BaO	0.13	0.12	0.11	0.03	0.02	0.07	0.02	0.08
Na_2O	0.20	0.18	0.23	0.95	0.10	0.19	0.20	0.20
K_2O	10.82	11.02	11.06	10.24	10.33	10.62	10.84	10.79
Atom site distribution (18 oxygen equivalents)								
Si	5.02	4.99	4.98	5.04	4.73	4.95	5.02	5.01
Al	3.96	3.93	3.98	4.52	3.45	3.88	3.92	3.93
Ti	0.00	0.00	0.00	0.11	0.00	0.00	0.00	0.00
Fe^{2+}	0.61	0.71	0.66	0.06	1.40	0.82	0.72	0.68
Mn	0.00	0.00	0.00	0.00	0.00	0.00	0.00	0.00
Mg	0.58	0.59	0.56	0.07	1.16	0.67	0.58	0.61
Ca	0.01	0.01	0.01	0.00	0.01	0.00	0.00	0.00
Ba	0.01	0.01	0.00	0.00	0.00	0.00	0.00	0.00
Na	0.04	0.04	0.05	0.19	0.02	0.04	0.04	0.04
K	1.57	1.60	1.60	1.38	1.57	1.54	1.53	1.55
XFe	0.51	0.55	0.54	0.48	0.55	0.55	0.55	0.53
Al/Si	0.79	0.79	0.80	0.90	0.73	0.78	0.78	0.78
Spot #	18a	22a	23a	26a	27a	32a	33a	36a
Comment	-	-	-	-	-	-	-	-
SiO_2	37.45	42.29	42.17	41.66	44.70	37.32	49.33	43.46
TiO_2	0.04	0.00	0.00	0.00	0.00	0.13	0.00	0.01
Al_2O_3	22.14	28.38	28.25	27.50	29.51	19.80	34.60	28.55
FeOtot	16.92	10.52	9.44	11.22	6.45	18.81	2.98	8.30
MnO	0.09	0.08	0.13	0.03	0.00	0.13	0.00	0.02
MgO	6.47	4.59	4.26	4.75	3.32	10.34	1.83	3.93
CaO	0.09	0.00	0.00	0.00	0.00	0.18	0.61	0.04
BaO	0.09	0.00	0.00	0.00	0.04	0.00	0.00	0.00
Na_2O	0.10	0.19	0.26	0.17	0.16	0.12	0.29	0.19
K_2O	9.44	10.68	10.99	10.64	10.90	7.66	5.63	11.14
Atom site distribution (18 oxygen equivalents)								
Si	4.67	4.83	4.87	4.83	5.06	4.59	5.24	4.97
Al	3.26	3.82	3.84	3.75	3.94	2.87	4.33	3.84
Ti	0.00	0.00	0.00	0.00	0.00	0.01	0.00	0.00
Fe^{2+}	1.77	1.01	0.91	1.09	0.61	1.94	0.26	0.79
Mn	0.01	0.01	0.01	0.00	0.00	0.01	0.00	0.00
Mg	1.20	0.78	0.73	0.82	0.56	1.90	0.29	0.67
Ca	0.01	0.00	0.00	0.00	0.00	0.02	0.07	0.00
Ba	0.00	0.00	0.00	0.00	0.00	0.00	0.00	0.00
Na	0.02	0.04	0.06	0.04	0.04	0.03	0.06	0.04
K	1.50	1.56	1.62	1.57	1.57	1.20	0.76	1.62
XFe	0.59	0.56	0.55	0.57	0.52	0.51	0.48	0.54
Al/Si	0.70	0.79	0.79	0.78	0.78	0.63	0.83	0.77

Table E2.3 – (continues)

Spot #	37a	38a	39a	47a	48a	50a	53a	56a
Comment	-	-	-	-	-	-	-	-
SiO_2	34.86	45.55	40.85	40.65	42.51	41.85	42.94	36.86
TiO_2	0.11	0.08	0.00	0.06	0.00	0.07	0.04	0.17
Al_2O_3	18.07	30.53	27.95	26.19	28.29	27.66	28.60	19.75
FeOtot	18.75	5.11	10.66	12.74	10.11	10.15	8.71	17.65
MnO	0.13	0.00	0.10	0.08	0.09	0.07	0.08	0.10
MgO	10.57	2.60	4.83	7.27	4.75	6.45	4.14	10.43
CaO	0.16	0.09	0.04	0.13	0.00	0.08	0.03	0.05
BaO	0.00	0.35	0.00	0.11	0.00	0.14	0.00	0.04
Na_2O	0.17	0.16	0.14	0.20	0.18	0.13	0.16	0.18
K_2O	7.20	10.35	11.18	7.33	10.54	8.16	10.74	7.28
Atom site distribution (18 oxygen equivalents)								
Si	4.54	5.11	4.76	4.74	4.86	4.82	4.92	4.60
Al	2.77	4.04	3.84	3.60	3.81	3.75	3.86	2.91
Ti	0.01	0.01	0.00	0.01	0.00	0.01	0.00	0.02
Fe^{2+}	2.04	0.48	1.04	1.24	0.97	0.98	0.83	1.84
Mn	0.01	0.00	0.01	0.01	0.01	0.01	0.01	0.01
Mg	2.05	0.43	0.84	1.26	0.81	1.11	0.71	1.94
Ca	0.02	0.01	0.01	0.02	0.00	0.01	0.00	0.01
Ba	0.00	0.02	0.00	0.01	0.00	0.01	0.00	0.00
Na	0.04	0.03	0.03	0.04	0.04	0.03	0.04	0.04
K	1.20	1.48	1.66	1.09	1.54	1.20	1.57	1.16
XFe	0.50	0.52	0.55	0.50	0.54	0.47	0.54	0.49
Al/Si	0.61	0.79	0.81	0.76	0.78	0.78	0.78	0.63

Spot #	60a
Comment	-
SiO_2	45.00
TiO_2	0.04
Al_2O_3	30.36
FeOtot	4.10
MnO	0.04
MgO	2.41
CaO	0.03
BaO	0.08
Na_2O	0.18
K_2O	10.96
Atom site distribution (18 oxygen equivalents)	
Si	5.13
Al	4.08
Ti	0.00
Fe^{2+}	0.39
Mn	0.00
Mg	0.41
Ca	0.00
Ba	0.00
Na	0.04
K	1.59
XFe	0.49
Al/Si	0.80

Appendix E2

Table E2.4 – List of feldspar spot analyses from **sample CS42a.**

Spot #	22	29	35	46	47	48	83	84
Comment	Ksp	Ksp	Ksp	Pl	Pl	Ksp	Pl	Pl
SiO_2	60.88	60.85	64.24	65.45	65.32	63.42	64.78	65.34
TiO_2	0.00	0.00	0.00	0.04	0.02	0.00	0.00	0.00
Al_2O_3	17.42	18.80	17.28	21.14	20.94	18.30	21.79	21.80
FeOtot	1.61	0.73	0.13	0.41	0.10	0.24	0.01	0.04
MnO	0.00	0.00	0.00	0.00	0.00	0.00	0.00	0.02
MgO	1.14	0.40	0.00	0.00	0.01	0.14	0.00	
CaO	0.04	0.01	0.00	2.50	2.50	0.05	2.53	2.58
BaO	0.71	0.80	0.71	0.00	0.00	0.87	0.00	0.01
Na_2O	0.51	0.58	0.54	9.99	9.76	0.64	10.04	10.24
K_2O	14.79	14.76	15.01	0.26	0.16	14.86	0.58	0.56
Atom site distribution (8 oxygen equivalents)								
Si	2.94	2.92	3.03	2.89	2.90	2.98	2.86	2.87
Al	0.99	1.06	0.96	1.10	1.10	1.01	1.14	1.13
Ti	0.00	0.00	0.00	0.00	0.00	0.00	0.00	0.00
Fe^{3+}	0.06	0.03	0.01	0.02	0.00	0.01	0.00	0.00
Mn	0.00	0.00	0.00	0.00	0.00	0.00	0.00	0.00
Mg	0.08	0.03	0.00	0.00	0.00	0.01	0.00	0.00
Ca	0.00	0.00	0.00	0.12	0.12	0.00	0.12	0.12
Ba	0.01	0.01	0.01	0.00	0.00	0.02	0.00	0.00
Na	0.05	0.05	0.05	0.85	0.84	0.06	0.86	0.87
K	0.91	0.90	0.90	0.01	0.01	0.89	0.03	0.03
Xor	0.95	0.94	0.95	0.01	0.01	0.94	0.03	0.03
Xab	0.05	0.06	0.05	0.87	0.87	0.06	0.85	0.85
Xan	0.00	0.00	0.00	0.12	0.12	0.00	0.12	0.12
Spot #	85	88	95	101	102	108	115	117
Comment	Pl	Pl	Pl	Ksp	Pl	Pl	Ksp	Ksp
SiO_2	65.84	64.85	65.13	64.14	66.14	65.59	64.11	63.66
TiO_2	0.03	0.03	0.02	0.02	0.00	0.00	0.09	0.13
Al_2O_3	22.09	22.01	22.09	18.45	22.55	21.53	18.76	18.53
FeOtot	0.11	0.20	0.10	0.14	0.04	0.07	0.17	0.17
MnO	0.00	0.00	0.00	0.01	0.01	0.00	0.00	0.00
MgO	0.00	0.00	0.00	0.01	0.00	0.00	0.00	0.00
CaO	2.65	2.73	2.59	0.09	3.31	2.43	0.07	0.07
BaO	0.00	0.00	0.00	0.69	0.00	0.01	0.91	1.09
Na_2O	10.04	10.22	10.19	0.69	8.58	10.47	0.86	0.83
K_2O	0.31	0.19	0.44	16.03	0.22	0.28	15.82	15.29
Atom site distribution (8 oxygen equivalents)								
Si	2.87	2.85	2.86	2.98	2.87	2.88	2.96	2.97
Al	1.13	1.14	1.14	1.01	1.15	1.11	1.02	1.02
Ti	0.00	0.00	0.00	0.00	0.00	0.00	0.00	0.00
Fe^{3+}	0.00	0.01	0.00	0.01	0.00	0.00	0.01	0.01
Mn	0.00	0.00	0.00	0.00	0.00	0.00	0.00	0.00
Mg	0.00	0.00	0.00	0.00	0.00	0.00	0.00	0.00
Ca	0.12	0.13	0.12	0.00	0.15	0.11	0.00	0.00
Ba	0.00	0.00	0.00	0.01	0.00	0.00	0.02	0.02
Na	0.85	0.87	0.87	0.06	0.72	0.89	0.08	0.08
K	0.02	0.01	0.02	0.95	0.01	0.02	0.93	0.91
Xor	0.02	0.01	0.02	0.94	0.01	0.02	0.92	0.92
Xab	0.86	0.86	0.86	0.06	0.81	0.87	0.08	0.08
Xan	0.13	0.13	0.12	0.00	0.17	0.11	0.00	0.00

Table E2.4 – (continues)

Spot #	119	58a	61a	68a	74a	98a	103a	105a
Comment	Ksp	Pl	Pl	Pl	Pl	Ksp	Pl	Ksp
SiO_2	64.31	62.56	61.38	63.93	63.39	62.40	63.87	63.08
TiO_2	0.11	0.00	0.00	0.02	0.01	0.00	0.00	0.00
Al_2O_3	18.68	19.67	20.35	20.62	20.99	16.64	19.76	18.05
FeOtot	0.23	0.07	0.00	0.00	0.05	0.01	0.00	0.06
MnO	0.02	0.00	0.00	0.00	0.00	0.03	0.00	0.00
MgO	0.05	0.00	0.00	0.00	0.01	0.01	0.00	0.01
CaO	0.07	2.23	2.77	2.67	2.65	0.04	1.51	0.00
BaO	0.87	0.00	0.03	0.00	0.00	0.69	0.00	0.31
Na_2O	0.69	8.76	10.32	10.19	10.27	0.72	10.73	2.06
K_2O	15.95	3.52	0.28	0.16	0.29	16.03	0.16	14.55
Atom site distribution (8 oxygen equivalents)								
Si	2.97	2.89	2.86	2.89	2.87	3.02	2.92	2.98
Al	1.02	1.07	1.12	1.10	1.12	0.95	1.07	1.00
Ti	0.00	0.00	0.00	0.00	0.00	0.00	0.00	0.00
Fe^{3+}	0.01	0.00	0.00	0.00	0.00	0.00	0.00	0.00
Mn	0.00	0.00	0.00	0.00	0.00	0.00	0.00	0.00
Mg	0.00	0.00	0.00	0.00	0.00	0.00	0.00	0.00
Ca	0.00	0.11	0.14	0.13	0.13	0.00	0.07	0.00
Ba	0.02	0.00	0.00	0.00	0.00	0.01	0.00	0.01
Na	0.06	0.78	0.93	0.89	0.90	0.07	0.95	0.19
K	0.94	0.21	0.02	0.01	0.02	0.99	0.01	0.88
Xor	0.94	0.19	0.02	0.01	0.02	0.93	0.01	0.82
Xab	0.06	0.71	0.86	0.87	0.86	0.06	0.92	0.18
Xan	0.00	0.10	0.13	0.13	0.12	0.00	0.07	0.00

Table E2.5 – Recalculated mineral formulas of ilmenite, titanite, andalusite and rutile in **sample CS42a**.

Spot #	59a	69a	71a	72a	73a	83a	40	74
Comment	Ilm	Ilm	Ilm	Ilm	Ilm	Ilm	Ilm	Ilm
SiO_2	0.00	0.00	0.00	0.00	0.00	0.04	0.19	0.46
TiO_2	49.41	51.10	51.57	50.80	50.45	50.79	56.29	52.06
Al_2O_3	0.00	0.00	0.00	0.00	0.00	0.00	0.05	0.09
FeOtot	41.12	41.53	42.25	43.55	43.34	40.31	31.21	31.31
MnO	4.13	4.37	2.38	1.74	2.25	3.89	5.91	11.39
MgO	0.07	0.06	0.14	0.16	0.11	0.03	0.05	0.07
CaO	0.00	0.00	0.00	0.00	0.00	0.06	0.05	0.01
BaO	0.00	0.00	0.00	0.00	0.00	0.00	0.00	0.00
Na_2O	0.01	0.00	0.00	0.00	0.03	0.00	0.00	0.00
K_2O	0.08	0.08	0.00	0.02	0.00	0.01	0.17	0.35
Oxygens	3	3	3	3	3	3	3	3
Si	0.00	0.00	0.00	0.00	0.00	0.00	0.01	0.01
Al	0.00	0.00	0.00	0.00	0.00	0.00	0.00	0.00
Ti	0.99	1.00	1.01	1.00	0.99	1.01	1.09	1.02
Fe^{2+}	0.89	0.89	0.92	0.95	0.94	0.89	0.67	0.68
Fe^{3+}	0.03	0.01	0.00	0.00	0.01	0.00	0.00	0.00
Mn	0.09	0.10	0.05	0.04	0.05	0.09	0.13	0.25
Mg	0.00	0.00	0.01	0.01	0.00	0.00	0.00	0.00
Ca	0.00	0.00	0.00	0.00	0.00	0.00	0.00	0.00
Ba	0.00	0.00	0.00	0.00	0.00	0.00	0.00	0.00
Na	0.00	0.00	0.00	0.00	0.00	0.00	0.00	0.00
K	0.00	0.00	0.00	0.00	0.00	0.00	0.01	0.01

Table E2.5 – (continues)

Spot #	75	77	78	80	90	105	109	110
Comment	Ilm	Ilm	Ilm	Ilm	Ilm	Ilm	Ttn	Ttn
SiO_2	0.14	0.01	0.10	0.08	0.07	0.12	30.13	30.59
TiO_2	55.13	53.78	52.71	51.54	53.34	52.91	32.65	32.46
Al_2O_3	0.00	0.00	0.00	0.00	0.00	0.00	4.67	4.71
FeOtot	33.46	34.64	35.60	36.78	36.41	34.93	0.40	0.42
MnO	6.41	7.10	7.09	7.69	7.55	8.08	0.00	0.00
MgO	0.07	0.05	0.04	0.01	0.03	0.04	0.01	0.06
CaO	0.03	0.03	0.04	0.00	0.06	0.08	27.53	27.79
BaO	0.00	0.00	0.00	0.00	0.00	0.00	1.04	1.00
Na_2O	0.01	0.03	0.00	0.00	0.01	0.01	0.00	0.02
K_2O	0.22	0.19	0.18	0.18	0.09	0.18	0.08	0.07
Oxygens	3	3	3	3	3	3	5	5
Si	0.00	0.00	0.00	0.00	0.00	0.00	1.02	1.03
Al	0.00	0.00	0.00	0.00	0.00	0.00	0.19	0.19
Ti	1.06	1.05	1.03	1.01	1.03	1.03	0.83	0.82
Fe^{2+}	0.72	0.75	0.77	0.80	0.78	0.76	0.01	0.01
Fe^{3+}	0.00	0.00	0.00	0.00	0.00	0.00	0.00	0.00
Mn	0.14	0.16	0.16	0.17	0.16	0.18	0.00	0.00
Mg	0.00	0.00	0.00	0.00	0.00	0.00	0.00	0.00
Ca	0.00	0.00	0.00	0.00	0.00	0.00	1.00	1.00
Ba	0.00	0.00	0.00	0.00	0.00	0.00	0.01	0.01
Na	0.00	0.00	0.00	0.00	0.00	0.00	0.00	0.00
K	0.01	0.01	0.01	0.01	0.00	0.01	0.00	0.00

Spot #	116	120	97	107	63	64	70
Comment	Ttn	Ttn	Ru	Ru	And	And	And
SiO_2	30.18	30.44	0.06	0.06	36.15	36.41	35.77
TiO_2	35.70	32.20	99.44	98.24	0.03	0.03	0.03
Al_2O_3	2.83	4.81	0.03	0.00	62.68	62.10	61.14
FeOtot	0.44	0.65	0.24	0.51	0.21	0.26	0.15
MnO	0.00	0.00	0.00	0.00	0.00	0.00	0.00
MgO	0.00	0.07	0.01	0.00	0.05	0.04	0.02
CaO	27.50	27.65	0.26	0.05	0.00	0.01	0.00
BaO	1.09	1.00	3.07	3.01	0.01	0.00	0.00
Na_2O	0.00	0.01	0.06	0.00	0.03	0.01	0.00
K_2O	0.18	0.23	0.03	0.16	0.00	0.00	0.01
Oxygens	5	5	4	4	5	5	5
Si	1.01	1.02	0.00	0.00	0.98	0.99	0.99
Al	0.11	0.19	0.00	0.00	2.01	2.00	2.00
Ti	0.90	0.81	1.97	1.98	0.00	0.00	0.00
Fe^{2+}	0.01	0.02	0.01	0.01	-	-	-
Fe^{3+}	0.00	0.00	0.00	0.00	0.00	0.01	0.00
Mn	0.00	0.00	0.00	0.00	0.00	0.00	0.00
Mg	0.00	0.00	0.00	0.00	0.00	0.00	0.00
Ca	0.99	1.00	0.01	0.00	0.00	0.00	0.00
Ba	0.01	0.01	0.03	0.03	0.00	0.00	0.00
Na	0.00	0.00	0.00	0.00	0.00	0.00	0.00
K	0.01	0.01	0.00	0.01	0.00	0.00	0.00

Appendix E2

Table E2.6 – Summary of monazite spot analyses in **sample CS42a**.

Spot #	Mnz-1	Mnz-2	Mnz-3	Mnz-4	Mnz-5	Mnz-6	Mnz-7	Mnz-8
SiO_2	0.29	0.23	0.27	0.32	0.25	0.32	0.33	0.34
Al_2O_3	0.00	0.00	0.00	0.00	0.00	0.00	0.00	0.00
CaO	0.39	0.42	0.60	0.28	0.30	0.42	0.76	0.96
P_2O_5	28.29	28.18	27.59	28.24	27.68	29.48	25.83	27.53
As_2O_5	0.00	0.00	0.00	0.00	0.00	0.01	0.03	0.00
SO_2	0.00	0.00	0.00	0.00	0.00	0.00	0.00	0.00
Y_2O_3	1.14	1.08	1.10	0.79	0.86	0.76	1.01	1.04
La_2O_3	15.15	15.45	15.54	15.04	15.21	13.62	12.81	12.35
Ce_2O_3	29.68	29.81	28.70	30.50	30.31	28.19	27.20	27.06
Pr_2O_3	3.11	2.93	2.90	3.12	3.13	3.34	2.84	3.13
Nd_2O_3	10.87	10.47	10.27	11.15	10.67	11.89	11.44	11.48
Sm_2O_3	1.57	1.54	1.42	1.46	1.42	1.73	1.74	1.84
Gd_2O_3	1.34	1.26	1.13	1.07	1.04	1.22	1.44	1.50
Dy_2O_3	0.63	0.64	0.57	0.50	0.52	0.51	0.61	0.64
Er_2O_3	0.10	0.10	0.10	0.07	0.08	0.07	0.11	0.10
UO_2	0.16	0.15	0.19	0.13	0.15	0.20	0.25	0.32
ThO_2	3.04	2.60	3.09	2.17	2.00	1.97	5.04	5.41
PbO	0.01	0.01	0.02	0.01	0.01	0.01	0.02	0.01
ppm(U)	1570	1480	1870	1340	1540	2000	2540	3150
ppm(Th)	30350	25980	30870	21700	19990	19670	50360	54100
ppm(Pb)	120	130	160	110	80	130	230	140
Age	9.85	36.25	38.64	32.45	1.28	56.58	45.39	1.87
1σ	10.17	11.63	9.64	14.00	14.58	14.09	6.20	5.92
Spot #	Mnz-9	Mnz-10	Mnz-12	Mnz-13	Mnz-14	Mnz-15	Mnz-16	Mnz-17
SiO_2	1.12	1.44	1.52	2.22	0.30	0.24	0.26	0.33
Al_2O_3	0.00	0.07	0.00	0.32	0.00	0.00	0.00	0.17
CaO	0.55	2.22	0.89	0.62	0.69	0.34	0.22	0.68
P_2O_5	28.51	24.58	28.84	29.94	29.12	28.75	28.86	28.63
As_2O_5	0.00	0.00	0.03	0.02	0.04	0.06	0.07	0.04
SO_2	0.00	0.01	0.00	0.01	0.00	0.01	0.01	0.01
Y_2O_3	0.64	0.48	1.31	0.64	0.78	0.74	0.77	0.83
La_2O_3	13.76	12.99	11.78	10.66	10.82	9.52	10.04	9.63
Ce_2O_3	26.29	29.40	27.58	27.01	26.88	28.39	28.77	26.83
Pr_2O_3	2.93	2.69	3.22	3.31	3.48	3.92	3.93	3.57
Nd_2O_3	10.65	10.22	13.01	12.47	14.40	16.28	16.11	14.58
Sm_2O_3	1.48	1.40	2.24	2.29	2.82	3.12	3.10	2.80
Gd_2O_3	1.11	0.94	1.55	1.41	1.73	1.85	1.79	1.63
Dy_2O_3	0.50	0.31	0.60	0.39	0.59	0.58	0.58	0.54
Er_2O_3	0.05	0.08	0.13	0.06	0.08	0.09	0.09	0.09
UO_2	0.23	0.11	0.64	0.14	0.10	0.07	0.06	0.09
ThO_2	3.49	5.36	3.54	3.36	4.19	1.55	0.99	3.50
PbO	0.02	0.03	0.02	0.02	0.01	0.01	0.01	0.01
ppm(U)	2320	1130	6430	1440	1030	730	570	890
ppm(Th)	34900	53570	35370	33620	41870	15500	9850	35020
ppm(Pb)	200	340	180	210	110	80	70	130
Age	68.36	101.63	27.12	76.96	8.23	19.57	22.41	21.83
1σ	8.74	6.56	6.61	9.91	8.11	20.33	31.21	9.92

Table E2.6 – (continues)

Spot #	Mnz-18	Mnz-19	Mnz-20
SiO_2	0.64	0.31	0.28
Al_2O_3	0.00	0.10	0.00
CaO	0.53	0.44	0.32
P_2O_5	28.25	28.32	30.63
As_2O_5	0.06	0.02	0.00
SO_2	0.01	0.00	0.01
Y_2O_3	0.91	0.84	0.60
La_2O_3	9.20	11.56	14.60
Ce_2O_3	27.91	28.68	29.96
Pr_2O_3	3.77	3.54	3.13
Nd_2O_3	15.70	14.15	10.75
Sm_2O_3	3.17	2.44	1.44
Gd_2O_3	2.02	1.53	1.06
Dy_2O_3	0.64	0.53	0.46
Er_2O_3	0.10	0.09	0.06
UO_2	0.09	0.27	0.11
ThO_2	2.71	1.82	1.95
PbO	0.01	0.01	0.02
ppm(U)	910	2730	1110
ppm(Th)	27110	18220	19470
ppm(Pb)	90	100	150
Age(Ma)	7.84	33.42	95.67
1σ	12.20	13.30	16.37

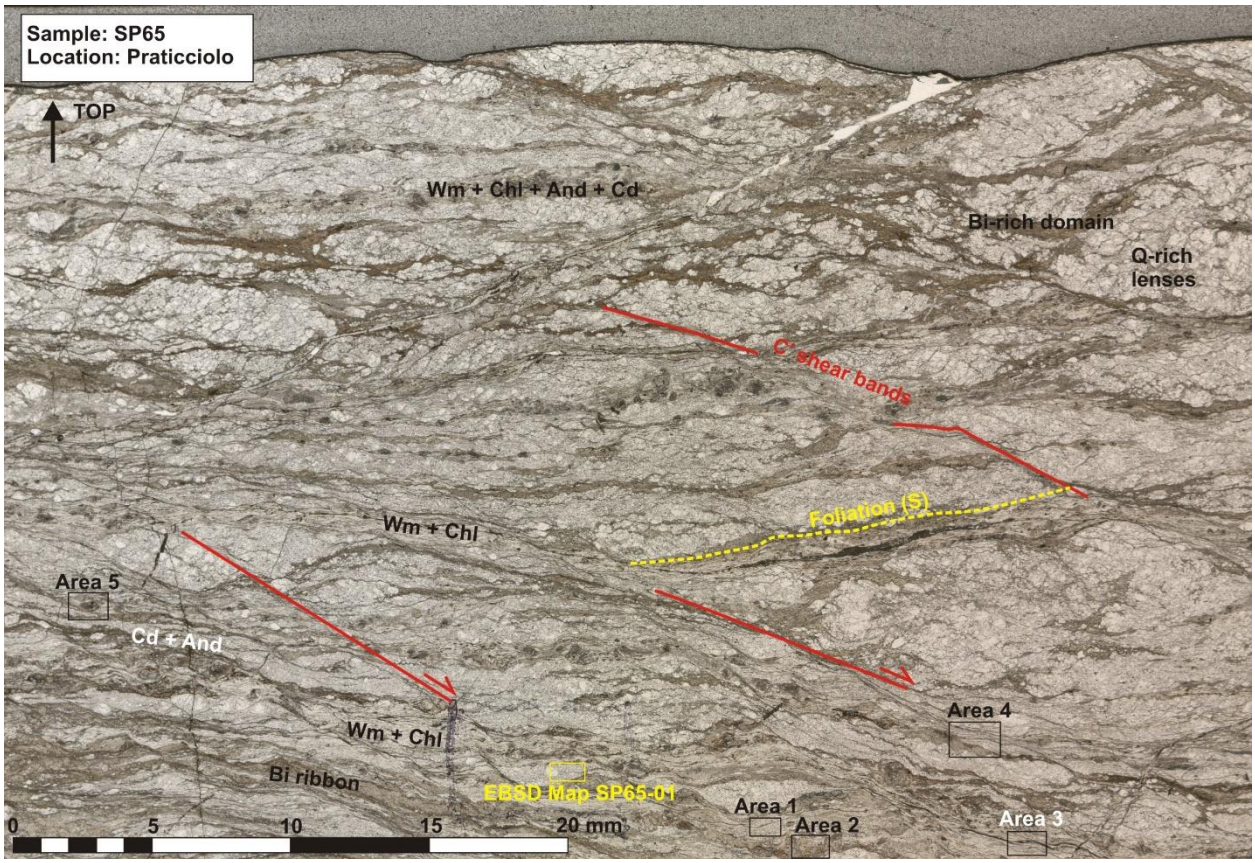

Figure E2.11 – Scan of thin section SP65 with indicated location of analyzed areas and EBSD maps.

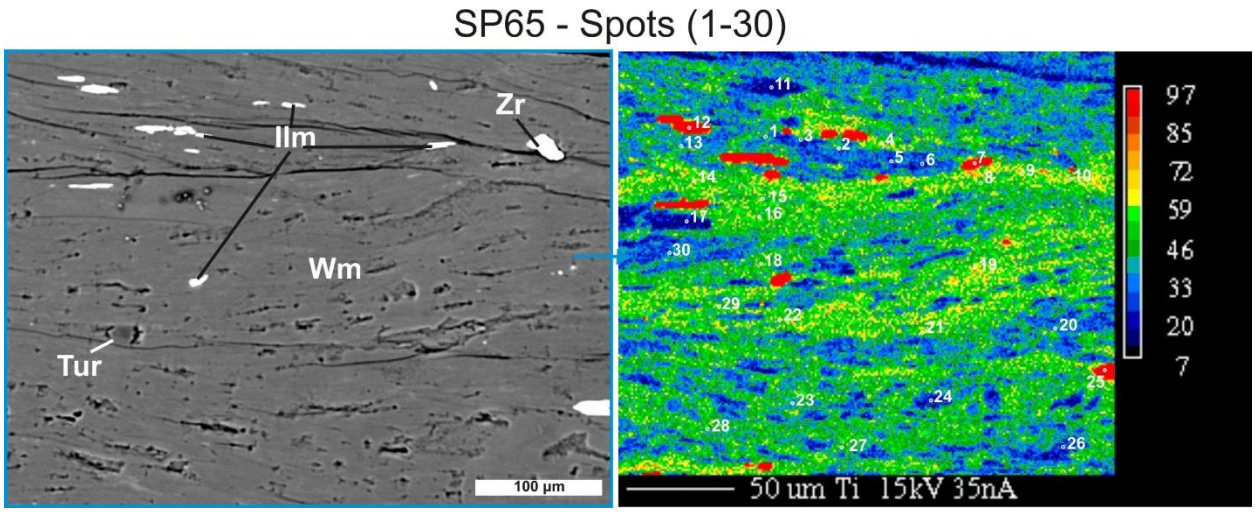

Figure E2.12 – SP65: area 1 spots.

Appendix E2

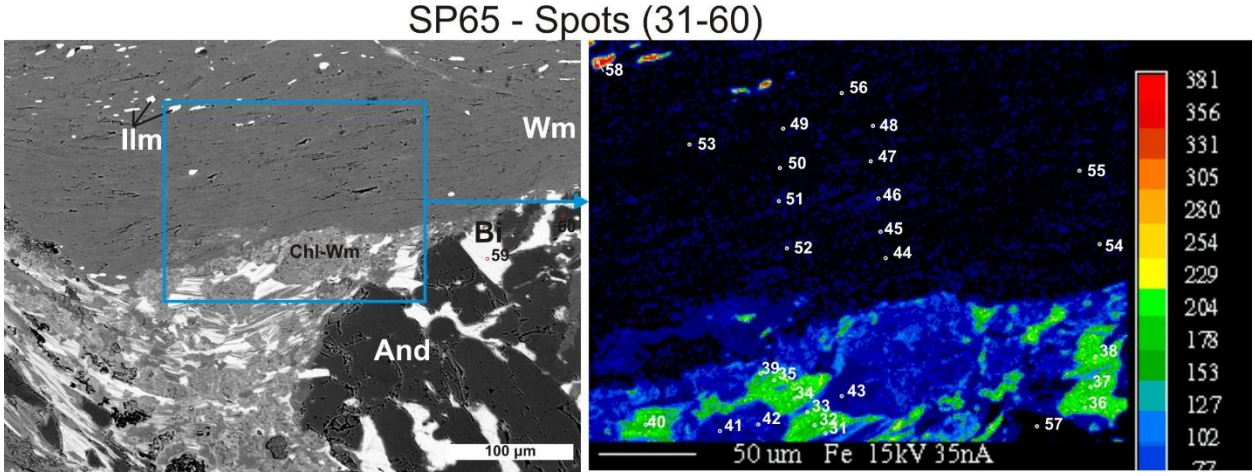

Figure E2.13 – SP65: area 2 spots.

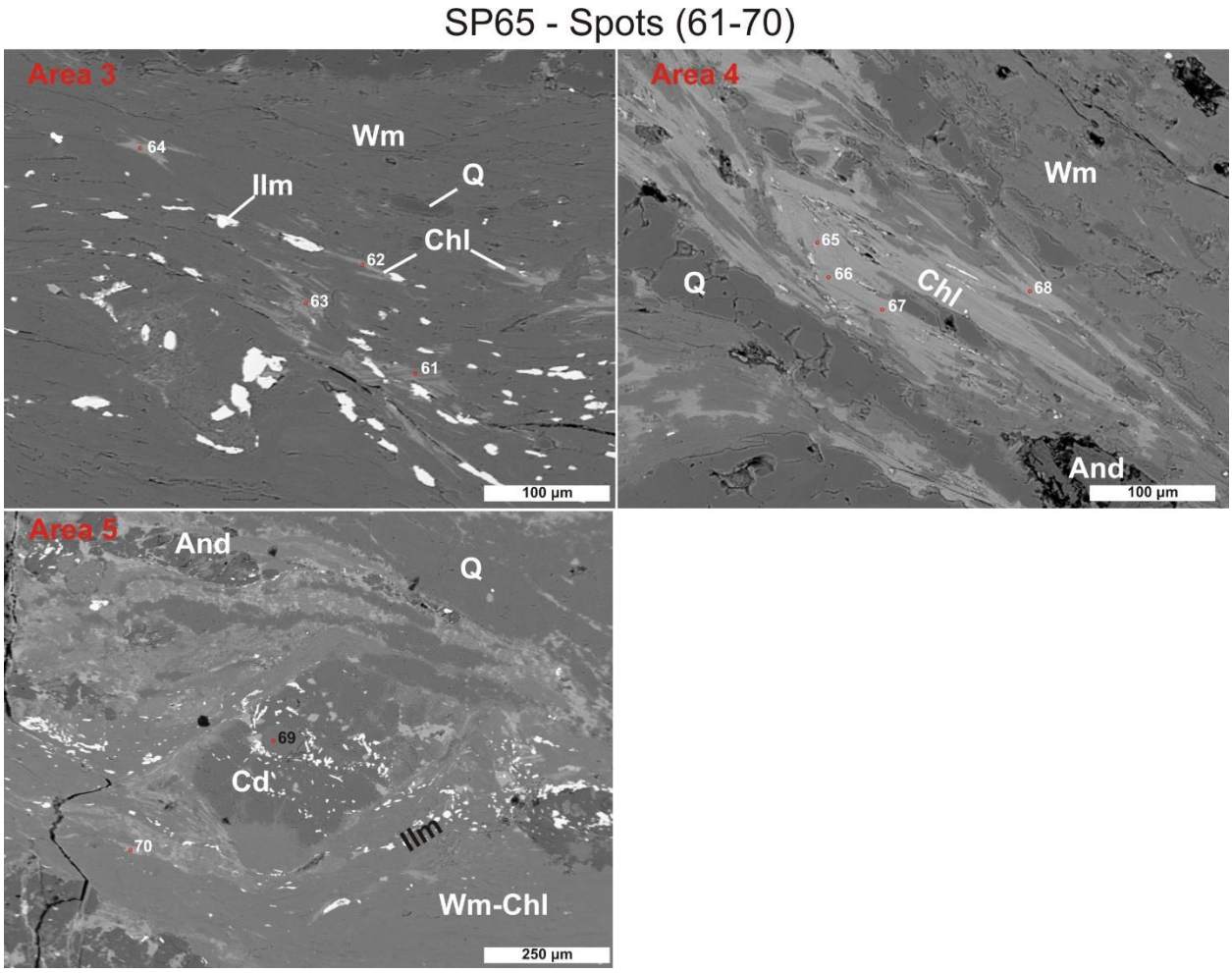

Figure E2.14 – SP65: area 3 (top left),4 (top right) and 5 (bottom left) spots.

Appendix E2

Sample SP65

Table E2.7 – List of biotite and white mica spot analyses from **sample SP65**. T^{H} and T^{WC} are temperatures calculated using the Henry et al. (2005) and Wu and Chen (2015) geothermometers respectively. Σ^{VI}: octahedral site sum. Σ^{A}: alkali sum.

Spot #	32	33	34	35	36	37	38	40
Comment	Bt	Bt	Bt	Bt	Bt	Bt	Bt	Bt
SiO_2	36.83	34.86	34.09	34.66	33.67	33.22	33.57	34.71
TiO_2	2.56	2.81	2.84	2.27	2.91	2.64	2.98	2.04
Al_2O_3	23.05	20.26	19.99	21.30	20.40	20.20	19.73	21.85
FeOtot	19.02	22.47	22.20	21.49	21.60	21.56	21.58	21.22
MnO	0.10	0.08	0.11	0.11	0.09	0.09	0.09	0.08
MgO	6.46	7.28	7.40	7.42	7.21	8.12	7.98	7.80
CaO	0.00	0.02	0.00	0.02	0.02	0.02	0.00	0.02
BaO	0.14	0.15	0.19	0.16	0.16	0.11	0.20	0.16
Na_2O	0.04	0.05	0.05	0.06	0.07	0.08	0.12	0.03
K_2O	8.70	9.51	9.29	8.61	9.67	8.69	9.51	6.89
Atom site distribution (22 oxygen equivalents)								
Si	5.42	5.26	5.23	5.25	5.18	5.15	5.17	5.26
Al^{IV}	2.58	2.74	2.77	2.75	2.82	2.85	2.83	2.74
Al^{VI}	1.42	0.87	0.84	1.06	0.88	0.83	0.75	1.17
Ti	0.28	0.32	0.33	0.26	0.34	0.31	0.35	0.23
Fe^{2+}	2.34	2.84	2.85	2.72	2.78	2.79	2.78	2.69
Mn	0.01	0.01	0.01	0.01	0.01	0.01	0.01	0.01
Mg	1.42	1.64	1.69	1.68	1.65	1.88	1.83	1.76
Σ^{VI}	5.47	5.68	5.71	5.73	5.66	5.82	5.73	5.87
Ca	0.00	0.00	0.00	0.00	0.00	0.00	0.00	0.00
Ba	0.01	0.01	0.01	0.01	0.01	0.01	0.01	0.01
Na	0.01	0.01	0.02	0.02	0.02	0.02	0.04	0.01
K	1.63	1.83	1.82	1.66	1.90	1.72	1.87	1.33
Σ^{A}	1.65	1.86	1.84	1.70	1.93	1.75	1.92	1.36
T^{H}(°C)	634.94	654.36	659.42	619.36	663.81	652.86	671.19	600.75
T^{WC}(°C)	684.90	635.91	632.07	610.42	643.56	604.04	621.80	591.72
Spot #	59	60	2	3	4	5	6	8
Comment	Bt	Bt	Wm	Wm	Wm	Wm	Wm	Wm
SiO_2	34.11	32.97	46.31	47.89	46.85	47.77	47.59	46.98
TiO_2	2.00	2.16	0.64	0.15	0.50	0.19	0.27	0.45
Al_2O_3	20.53	19.45	35.77	35.03	35.72	35.04	35.83	35.87
FeOtot	22.06	22.11	1.09	1.10	0.94	1.19	0.92	0.97
MnO	0.06	0.12	0.00	0.00	0.00	0.00	0.00	0.00
MgO	7.27	7.71	0.48	0.68	0.45	0.75	0.57	0.41
CaO	0.07	0.03	0.03	0.00	0.06	0.00	0.01	0.03
BaO	0.14	0.08	0.30	0.17	0.32	0.25	0.19	0.46
Na_2O	0.09	0.06	0.32	0.32	0.25	0.28	0.27	0.28
K_2O	9.67	9.19	10.43	10.51	10.66	10.21	10.38	10.46
Oxygens	22	22	11	11	11	11	11	11
Si	5.24	5.19	3.08	3.16	3.10	3.15	3.13	3.10
Al^{IV}	2.76	2.81	0.92	0.84	0.90	0.85	0.87	0.90
Al^{VI}	0.95	0.81	1.88	1.88	1.88	1.88	1.90	1.89
Ti	0.23	0.26	0.03	0.01	0.03	0.01	0.01	0.02
Fe^{2+}	2.83	2.91	0.06	0.06	0.05	0.07	0.05	0.05
Mn	0.01	0.02	0.00	0.00	0.00	0.00	0.00	0.00
Mg	1.66	1.81	0.05	0.07	0.04	0.07	0.06	0.04
Σ^{VI}	5.69	5.80	2.02	2.01	2.01	2.02	2.02	2.01
Ca	0.01	0.01	0.00	0.00	0.00	0.00	0.00	0.00
Ba	0.01	0.00	0.01	0.00	0.01	0.01	0.00	0.01
Na	0.03	0.02	0.04	0.04	0.03	0.04	0.03	0.04
K	1.90	1.85	0.88	0.88	0.90	0.86	0.87	0.88
Σ^{A}	1.94	1.87	0.94	0.93	0.94	0.90	0.91	0.93
T^{H}(°C)	595.36	617.29	-	-	-	-	-	-
T^{WC}(°C)	588.40	580.26	-	-	-	-	-	-

Table E2.7 – (continues)

Spot #	9	10	11	13	14	15	16	17
Comment	Wm	Wm	Wm	Wm	Wm	Wm	Wm	Wm
SiO_2	46.88	46.58	48.16	47.45	46.34	46.67	46.05	47.54
TiO_2	0.61	0.63	0.04	0.18	0.58	0.59	0.61	0.07
Al_2O_3	36.43	36.13	34.23	34.92	35.61	35.99	34.90	34.79
FeOtot	1.05	0.94	1.45	1.24	0.83	1.00	1.12	1.29
MnO	0.00	0.06	0.04	0.02	0.00	0.00	0.00	0.00
MgO	0.37	0.32	0.94	0.69	0.45	0.40	0.46	0.74
CaO	0.00	0.01	0.00	0.03	0.00	0.03	0.21	0.00
BaO	0.33	0.30	0.22	0.23	0.28	0.29	0.27	0.19
Na_2O	0.31	0.30	0.27	0.31	0.34	0.30	0.40	0.29
K_2O	10.52	10.58	10.19	10.34	10.68	10.61	10.63	10.45
Atom site distribution (11 oxygen equivalents)								
Si	3.08	3.08	3.18	3.14	3.09	3.08	3.09	3.15
Al^{IV}	0.92	0.92	0.82	0.86	0.91	0.92	0.91	0.85
Al^{VI}	1.89	1.89	1.85	1.87	1.88	1.89	1.85	1.87
Ti	0.03	0.03	0.00	0.01	0.03	0.03	0.03	0.00
Fe^{2+}	0.06	0.05	0.08	0.07	0.05	0.06	0.06	0.07
Mn	0.00	0.00	0.00	0.00	0.00	0.00	0.00	0.00
Mg	0.04	0.03	0.09	0.07	0.05	0.04	0.05	0.07
Σ^{VI}	2.02	2.01	2.03	2.02	2.00	2.01	1.99	2.02
Ca	0.00	0.00	0.00	0.00	0.00	0.00	0.02	0.00
Ba	0.01	0.01	0.01	0.01	0.01	0.01	0.01	0.01
Na	0.04	0.04	0.03	0.04	0.04	0.04	0.05	0.04
K	0.88	0.89	0.86	0.87	0.91	0.89	0.91	0.88
Σ^{A}	0.93	0.94	0.90	0.92	0.96	0.94	0.99	0.93
Spot #	18	19	20	21	22	23	24	26
Comment	Wm	Wm	Wm	Wm	Wm	Wm	Wm	Wm
SiO_2	46.87	46.73	46.82	46.95	46.38	46.23	48.23	47.63
TiO_2	0.46	0.71	0.44	0.64	0.57	0.49	0.04	0.16
Al_2O_3	36.00	35.82	35.73	36.13	36.12	35.80	35.12	35.40
FeOtot	1.01	1.04	0.94	1.13	0.97	0.93	1.28	1.11
MnO	0.05	0.00	0.00	0.00	0.00	0.02	0.03	0.00
MgO	0.45	0.39	0.49	0.39	0.33	0.40	0.77	0.61
CaO	0.01	0.00	0.00	0.04	0.00	0.00	0.00	0.00
BaO	0.30	0.31	0.27	0.34	0.33	0.33	0.19	0.21
Na_2O	0.27	0.38	0.32	0.30	0.30	0.26	0.34	0.35
K_2O	10.60	10.65	10.55	10.74	10.81	10.57	10.69	10.74
Atom site distribution (11 oxygen equivalents)								
Si	3.09	3.09	3.10	3.08	3.07	3.08	3.16	3.13
Al^{IV}	0.91	0.91	0.90	0.92	0.93	0.92	0.84	0.87
Al^{VI}	1.89	1.87	1.89	1.88	1.89	1.89	1.87	1.88
Ti	0.02	0.04	0.02	0.03	0.03	0.02	0.00	0.01
Fe^{2+}	0.06	0.06	0.05	0.06	0.05	0.05	0.07	0.06
Mn	0.00	0.00	0.00	0.00	0.00	0.00	0.00	0.00
Mg	0.04	0.04	0.05	0.04	0.03	0.04	0.08	0.06
Σ^{VI}	2.02	2.00	2.01	2.01	2.01	2.01	2.01	2.01
Ca	0.00	0.00	0.00	0.00	0.00	0.00	0.00	0.00
Ba	0.01	0.01	0.01	0.01	0.01	0.01	0.00	0.01
Na	0.03	0.05	0.04	0.04	0.04	0.03	0.04	0.04
K	0.89	0.90	0.89	0.90	0.91	0.90	0.89	0.90
Σ^{A}	0.93	0.95	0.94	0.95	0.96	0.94	0.94	0.95

Table E2.7 – (continues)

Spot #	27	28	29	30	44	45	46	47
Comment	Wm	Wm	Wm	Wm	Wm	Wm	Wm	Wm
SiO_2	46.42	46.94	47.45	48.01	48.34	46.84	48.90	48.82
TiO_2	0.61	0.58	0.33	0.24	0.09	0.30	0.28	0.20
Al_2O_3	36.32	36.25	35.37	35.31	34.70	35.87	34.29	34.32
FeOtot	0.83	0.88	1.07	0.98	1.27	1.17	1.64	1.21
MnO	0.02	0.04	0.04	0.01	0.02	0.02	0.01	0.00
MgO	0.31	0.31	0.56	0.63	0.83	0.39	1.14	0.84
CaO	0.00	0.01	0.01	0.03	0.06	0.01	0.04	0.00
BaO	0.27	0.35	0.31	0.21	0.17	0.35	0.20	0.23
Na_2O	0.33	0.32	0.31	0.26	0.28	0.32	0.26	0.31
K_2O	10.79	10.49	10.72	10.62	10.49	10.48	10.37	10.58
Atom site distribution (11 oxygen equivalents)								
Si	3.07	3.09	3.13	3.15	3.17	3.10	3.18	3.20
Al^{IV}	0.93	0.91	0.87	0.85	0.83	0.90	0.82	0.80
Al^{VI}	1.90	1.90	1.87	1.88	1.86	1.90	1.82	1.84
Ti	0.03	0.03	0.02	0.01	0.00	0.01	0.01	0.01
Fe^{2+}	0.05	0.05	0.06	0.05	0.07	0.06	0.09	0.07
Mn	0.00	0.00	0.00	0.00	0.00	0.00	0.00	0.00
Mg	0.03	0.03	0.06	0.06	0.08	0.04	0.11	0.08
Σ^{VI}	2.00	2.01	2.01	2.01	2.01	2.01	2.03	2.00
Ca	0.00	0.00	0.00	0.00	0.00	0.00	0.00	0.00
Ba	0.01	0.01	0.01	0.01	0.00	0.01	0.01	0.01
Na	0.04	0.04	0.04	0.03	0.04	0.04	0.03	0.04
K	0.91	0.88	0.90	0.89	0.88	0.88	0.86	0.88
Σ^{A}	0.96	0.93	0.95	0.93	0.92	0.94	0.90	0.93
Spot #	48	49	50	51	52	53	54	55
Comment	Wm	Wm	Wm	Wm	Wm	Wm	Wm	Wm
SiO_2	50.57	47.06	47.76	48.39	47.85	48.19	49.07	47.99
TiO_2	0.13	0.34	0.21	0.25	0.25	0.20	0.21	0.03
Al_2O_3	33.33	36.44	35.72	33.85	34.99	35.47	34.95	35.16
FeOtot	1.35	0.93	0.90	1.35	1.52	1.22	1.05	1.37
MnO	0.02	0.02	0.01	0.00	0.00	0.00	0.00	0.00
MgO	1.25	0.40	0.55	0.96	0.82	0.71	0.80	0.69
CaO	0.01	0.03	0.01	0.00	0.04	0.01	0.02	0.00
BaO	0.17	0.31	0.20	0.21	0.19	0.16	0.25	0.08
Na_2O	0.29	0.33	0.23	0.30	0.28	0.25	0.27	0.27
K_2O	10.39	10.47	10.64	10.53	10.69	10.32	10.36	10.66
Atom site distribution (11 oxygen equivalents)								
Si	3.27	3.09	3.13	3.19	3.14	3.15	3.19	3.15
Al^{IV}	0.73	0.91	0.87	0.81	0.86	0.85	0.81	0.85
Al^{VI}	1.81	1.91	1.90	1.83	1.85	1.88	1.86	1.87
Ti	0.01	0.02	0.01	0.01	0.01	0.01	0.01	0.00
Fe^{2+}	0.07	0.05	0.05	0.07	0.08	0.07	0.06	0.08
Mn	0.00	0.00	0.00	0.00	0.00	0.00	0.00	0.00
Mg	0.12	0.04	0.05	0.09	0.08	0.07	0.08	0.07
Σ^{VI}	2.01	2.02	2.01	2.01	2.02	2.03	2.01	2.02
Ca	0.00	0.00	0.00	0.00	0.00	0.00	0.00	0.00
Ba	0.00	0.01	0.01	0.01	0.00	0.00	0.01	0.00
Na	0.04	0.04	0.03	0.04	0.04	0.03	0.03	0.03
K	0.86	0.88	0.89	0.89	0.89	0.86	0.86	0.89
Σ^{A}	0.90	0.93	0.92	0.93	0.94	0.90	0.90	0.93

Table E2.7 – (continues)

Spot #	56
Comment	Wm
SiO_2	47.40
TiO_2	0.14
Al_2O_3	36.04
FeOtot	1.07
MnO	0.00
MgO	0.58
CaO	0.00
BaO	0.25
Na_2O	0.26
K_2O	10.58
Atom site distribution (11 oxygen equivalents)	
Si	3.11
Al^{IV}	0.89
Al^{VI}	1.90
Ti	0.01
Fe^{2+}	0.06
Mn	0.00
Mg	0.06
Σ^{VI}	2.02
Ca	0.00
Ba	0.01
Na	0.03
K	0.89
Σ^{A}	0.93

Table E2.8 – Recalculated mineral formulas of ilmenite and andalusite in **sample SP65**.

Spot #	7	12	25	58	57
Comment	Ilm	Ilm	Ilm	Ilm	And
SiO_2	2.25	2.04	0.10	0.15	36.487
TiO_2	50.79	49.59	53.16	51.73	0.003
Al_2O_3	2.05	1.98	0.03	0.04	62.702
FeOtot	36.09	37.71	38.42	40.93	0.538
MnO	3.50	4.46	4.27	4.40	0.5979
MgO	0.04	0.04	0.00	0.01	0.00
CaO	0.02	0.04	0.00	0.02	0.045
BaO	0.00	0.00	0.00	0.00	0.00
Na_2O	0.00	0.00	0.01	0.04	0.00
K_2O	0.77	0.64	0.22	0.26	0.00
Oxygens	3	3	3	3	5
Si	0.06	0.05	0.00	0.00	0.988
Al	0.06	0.06	0.00	0.00	2.002
Ti	0.97	0.95	1.03	1.00	0.000
Fe^{2+}	0.76	0.80	0.83	0.88	-
Fe^{3+}	0.00	0.00	0.00	0.00	0.012
Mn	0.08	0.10	0.09	0.10	0.000
Mg	0.00	0.00	0.00	0.00	0.002
Ca	0.00	0.00	0.01	0.00	0.000
Ba	0.00	0.00	0.00	0.00	0.000
Na	0.04	0.03	0.03	0.00	0.000
K	0.00	0.00	0.00	0.01	0.001

Appendix E2

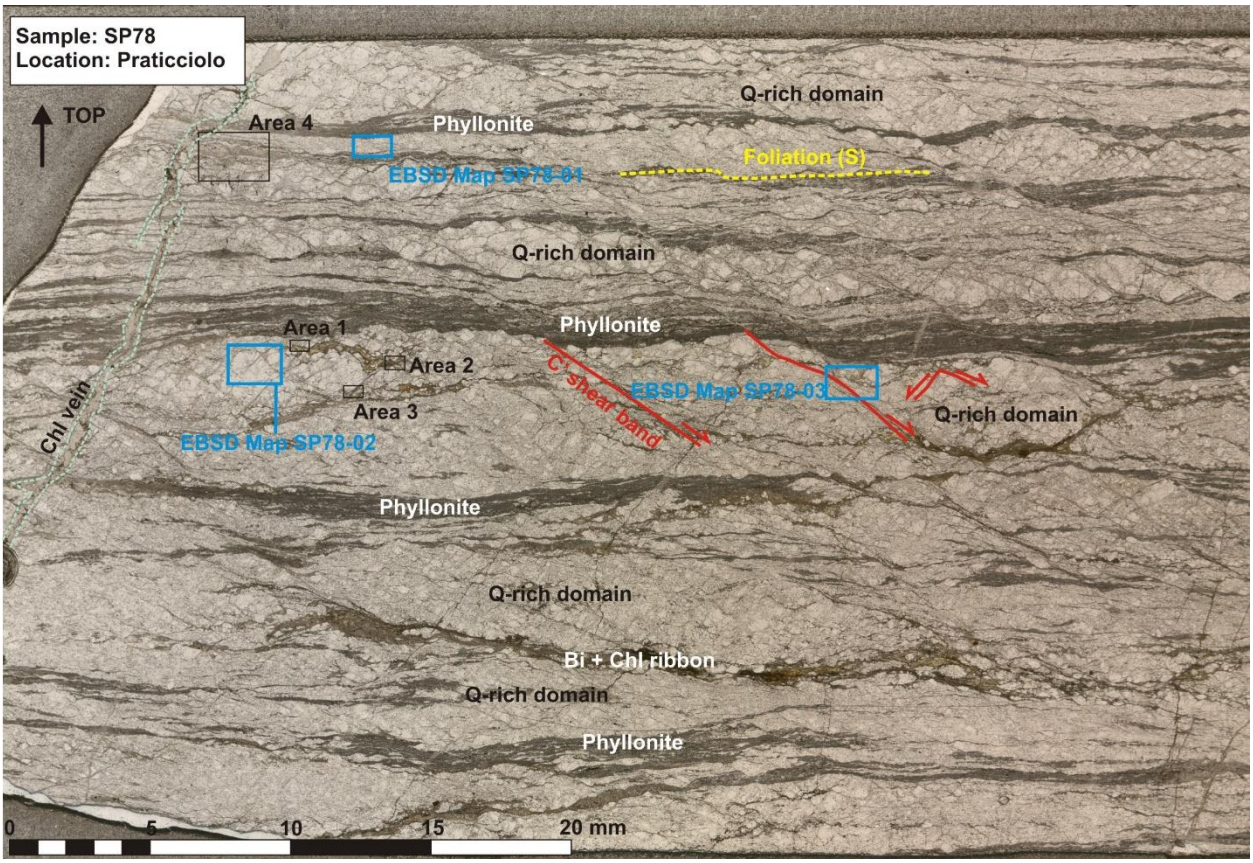

Figure E2.15 – Thin section scan of sample SP78 illustrating major features and location of analyzed areas and EBSD maps.

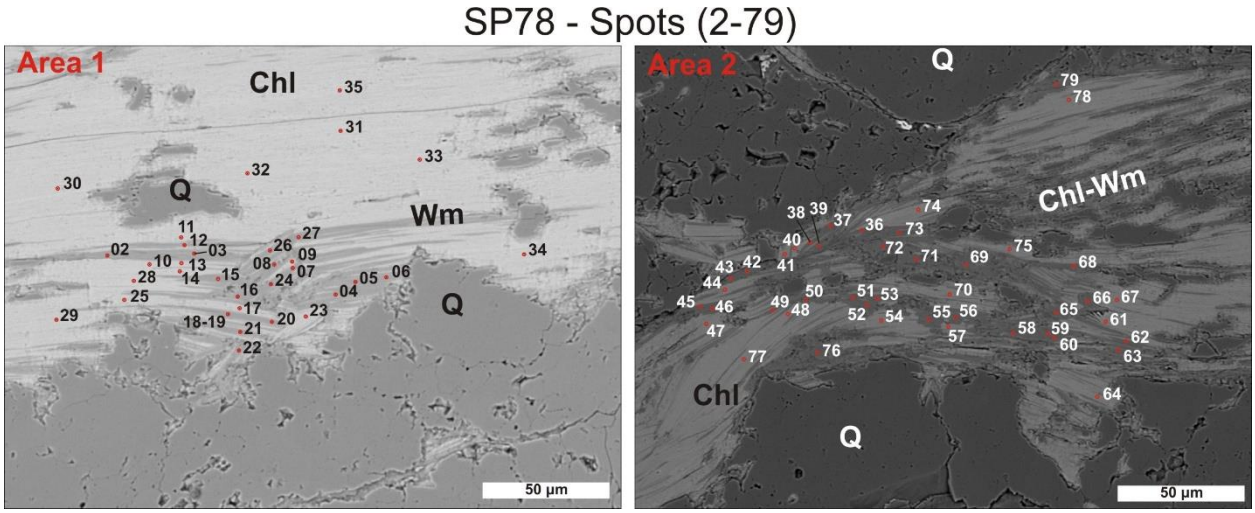

Figure E2.16 – SP78: area 1 (left) and 2 (right) spots.

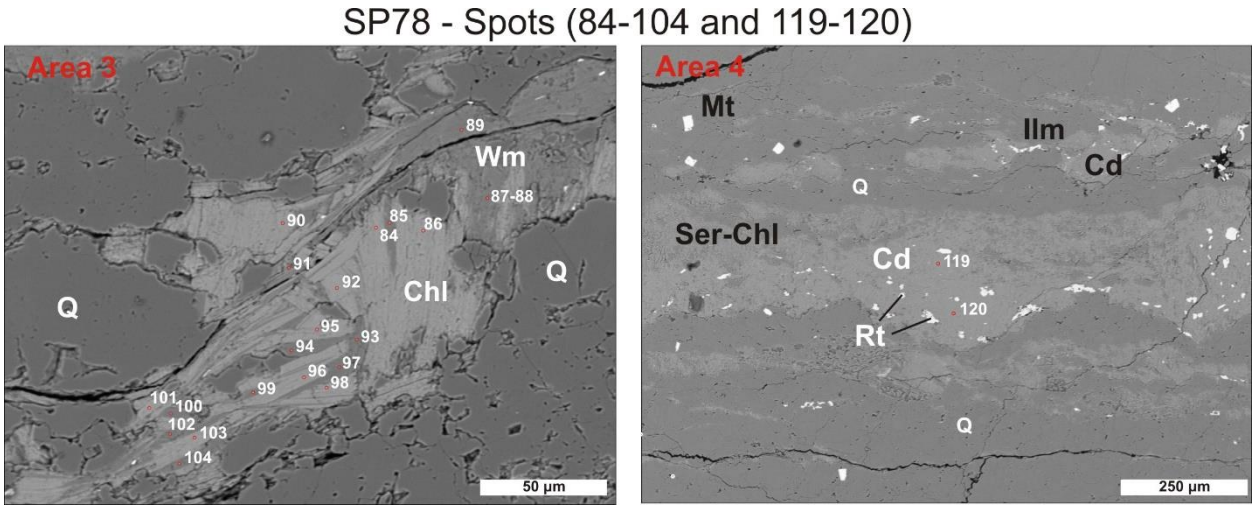

Figure E2.17 – SP78: area 3 (left) and 4 (right) spots.

Appendix E2

Sample SP78

Table E2.9 – List of white mica spot analyses from **sample SP78**. Σ^{VI}: octahedral site sum. Σ^{A}: alkali sum.

Spot #	15	16	24	51	53	55	56	58
Comment								
SiO_2	47.52	45.86	45.65	46.67	45.16	47.93	46.48	46.26
TiO_2	0.30	0.31	0.25	0.19	0.10	0.03	0.10	0.07
Al_2O_3	34.75	33.77	33.73	34.96	35.63	35.36	35.40	34.89
FeOtot	1.56	2.86	2.56	2.05	2.52	1.57	1.73	1.93
MnO	0.02	0.01	0.06	0.00	0.00	0.01	0.01	0.00
MgO	1.22	1.56	1.56	1.12	1.34	0.92	0.95	1.08
CaO	0.02	0.03	0.02	0.04	0.03	0.02	0.02	0.00
BaO	0.11	0.08	0.16	0.41	0.43	0.30	0.41	0.46
Na_2O	0.23	0.20	0.22	0.25	0.32	0.33	0.25	0.29
K_2O	10.32	10.05	10.11	10.19	10.00	10.36	10.56	10.43
Atom site distribution (11 oxygen equivalents)								
Si	3.13	3.09	3.09	3.10	3.02	3.14	3.09	3.09
Al^{IV}	0.87	0.91	0.91	0.90	0.98	0.86	0.91	0.91
Al^{VI}	1.83	1.77	1.78	1.83	1.83	1.86	1.85	1.84
Ti	0.02	0.02	0.01	0.01	0.00	0.00	0.00	0.00
Fe^{2+}	0.09	0.16	0.14	0.11	0.14	0.09	0.10	0.11
Mn	0.00	0.00	0.00	0.00	0.00	0.00	0.00	0.00
Mg	0.12	0.16	0.16	0.11	0.13	0.09	0.09	0.11
Σ^{VI}	2.05	2.11	2.10	2.06	2.11	2.04	2.05	2.06
Ca	0.00	0.00	0.00	0.00	0.00	0.00	0.00	0.00
Ba	0.00	0.00	0.00	0.01	0.01	0.01	0.01	0.01
Na	0.03	0.03	0.03	0.03	0.04	0.04	0.03	0.04
K	0.87	0.86	0.87	0.86	0.85	0.86	0.89	0.89
Σ^{A}	0.90	0.89	0.91	0.91	0.91	0.92	0.94	0.94
Spot #	59	60	65	66	69	71	72	76
Comment								
SiO_2	46.20	46.05	48.23	47.08	45.97	46.33	45.70	46.70
TiO_2	0.12	0.05	0.06	0.21	0.13	0.07	0.15	0.05
Al_2O_3	35.22	35.59	34.95	35.23	35.96	35.96	35.33	36.70
FeOtot	1.89	1.64	1.26	1.39	1.68	1.61	1.38	0.73
MnO	0.00	0.00	0.01	0.00	0.00	0.01	0.00	0.00
MgO	1.11	0.87	0.82	0.96	0.69	0.64	0.87	0.51
CaO	0.00	0.03	0.01	0.00	0.01	0.01	0.00	0.02
BaO	0.55	0.47	0.34	0.20	0.38	0.49	0.50	0.42
Na_2O	0.22	0.37	0.35	0.23	0.33	0.43	0.30	0.44
K_2O	10.23	10.61	10.28	10.92	10.47	10.58	10.85	10.33
Atom site distribution (11 oxygen equivalents)								
Si	3.08	3.07	3.16	3.11	3.06	3.07	3.07	3.08
Al^{IV}	0.92	0.93	0.84	0.89	0.94	0.93	0.93	0.92
Al^{VI}	1.85	1.86	1.87	1.85	1.88	1.88	1.86	1.93
Ti	0.01	0.00	0.00	0.01	0.01	0.00	0.01	0.00
Fe^{2+}	0.11	0.09	0.07	0.08	0.09	0.09	0.08	0.04
Mn	0.00	0.00	0.00	0.00	0.00	0.00	0.00	0.00
Mg	0.11	0.09	0.08	0.09	0.07	0.06	0.09	0.05
Σ^{VI}	2.07	2.04	2.02	2.03	2.05	2.03	2.03	2.02
Ca	0.00	0.00	0.00	0.00	0.00	0.00	0.00	0.00
Ba	0.01	0.01	0.01	0.01	0.01	0.01	0.01	0.01
Na	0.03	0.05	0.04	0.03	0.04	0.06	0.04	0.06
K	0.87	0.90	0.86	0.92	0.89	0.89	0.93	0.87
Σ^{A}	0.91	0.96	0.91	0.95	0.94	0.96	0.98	0.94

Table E2.9 – (continues)

Spot #	82	85	87	89	94	97	100	102
Comment								
SiO_2	45.28	46.77	47.37	46.56	45.85	46.49	47.46	45.46
TiO_2	0.25	0.32	0.30	0.44	0.31	0.32	0.32	0.43
Al_2O_3	32.79	34.70	33.62	32.99	34.65	34.72	34.24	33.98
FeOtot	3.30	2.14	2.85	2.70	3.06	2.19	1.92	2.88
MnO	0.02	0.01	0.00	0.01	0.00	0.00	0.00	0.02
MgO	1.84	1.23	1.58	1.69	1.45	1.10	1.25	1.52
CaO	0.01	0.00	0.03	0.03	0.01	0.01	0.00	0.00
BaO	0.04	0.10	0.05	0.14	0.11	0.22	0.11	0.29
Na_2O	0.19	0.18	0.15	0.12	0.21	0.24	0.22	0.26
K_2O	10.12	10.38	10.19	10.20	10.51	10.93	10.94	10.51
Atom site distribution (11 oxygen equivalents)								
Si	3.09	3.10	3.14	3.13	3.05	3.09	3.13	3.06
Al^{IV}	0.91	0.90	0.86	0.87	0.95	0.91	0.87	0.94
Al^{VI}	1.73	1.81	1.76	1.74	1.78	1.81	1.80	1.76
Ti	0.01	0.02	0.01	0.02	0.02	0.02	0.02	0.02
Fe^{2+}	0.19	0.12	0.16	0.15	0.17	0.12	0.11	0.16
Mn	0.00	0.00	0.00	0.00	0.00	0.00	0.00	0.00
Mg	0.19	0.12	0.16	0.17	0.14	0.11	0.12	0.15
Σ^{VI}	2.12	2.07	2.09	2.09	2.11	2.05	2.04	2.09
Ca	0.00	0.00	0.00	0.00	0.00	0.00	0.00	0.00
Ba	0.00	0.00	0.00	0.00	0.00	0.01	0.00	0.01
Na	0.02	0.02	0.02	0.02	0.03	0.03	0.03	0.03
K	0.88	0.88	0.86	0.87	0.89	0.93	0.92	0.90
Σ^{A}	0.91	0.90	0.88	0.90	0.92	0.96	0.95	0.94

Spot #	104
Comment	
SiO_2	46.21
TiO_2	0.31
Al_2O_3	33.49
FeOtot	1.95
MnO	0.00
MgO	1.34
CaO	0.02
BaO	0.02
Na_2O	0.21
K_2O	10.86
Atom site distribution (11 oxygen equivalents)	
Si	3.12
Al^{IV}	0.88
Al^{VI}	1.79
Ti	0.02
Fe^{2+}	0.11
Mn	0.00
Mg	0.14
Σ^{VI}	2.05
Ca	0.00
Ba	0.00
Na	0.03
K	0.94
Σ^{A}	0.96

Appendix E2

Table E2.10 – List of chlorite spot analyses from **sample SP78**. Σ^{VI}: octahedral site sum. *: chlorites with Σalkali > 0.5 wt%

Spot #	11	23	29	30	31	32	33	34
Comment								
SiO_2	25.04	24.67	24.57	24.76	24.60	24.64	24.65	24.90
TiO_2	0.10	0.06	0.09	0.12	0.11	0.11	0.12	0.10
Al_2O_3	22.30	22.14	21.80	22.36	21.32	21.74	21.16	22.20
FeOtot	28.98	28.43	28.86	29.07	30.28	29.75	29.66	28.91
MnO	0.30	0.24	0.21	0.26	0.18	0.18	0.17	0.31
MgO	11.98	12.30	12.17	12.29	12.11	12.17	12.53	12.36
CaO	0.01	0.03	0.04	0.01	0.06	0.00	0.06	0.03
BaO	0.00	0.00	0.00	0.00	0.00	0.01	0.00	0.02
Na_2O	0.00	0.07	0.02	0.02	0.03	0.00	0.03	0.02
K_2O	0.07	0.09	0.09	0.05	0.05	0.04	0.06	0.10
ΣAlkali	0.07	0.20	0.15	0.08	0.14	0.04	0.14	0.17
Atom site distribution (14 oxygen equivalents)								
Si	2.65	2.64	2.64	2.62	2.63	2.63	2.64	2.64
Al^{IV}	1.35	1.36	1.36	1.38	1.37	1.37	1.36	1.36
Al^{VI}	1.44	1.42	1.40	1.42	1.33	1.37	1.31	1.41
Ti	0.01	0.00	0.01	0.01	0.01	0.01	0.01	0.01
Fe^{2+}	2.57	2.54	2.59	2.58	2.71	2.66	2.66	2.56
Mn	0.03	0.02	0.02	0.02	0.02	0.02	0.02	0.03
Mg	1.89	1.96	1.95	1.94	1.93	1.94	2.00	1.95
Σ^{VI}	5.94	5.95	5.96	5.96	6.00	5.99	6.00	5.96
Ca	0.00	0.00	0.01	0.00	0.01	0.00	0.01	0.00
Ba	0.00	0.00	0.00	0.00	0.00	0.00	0.00	0.00
Na	0.00	0.02	0.00	0.00	0.01	0.00	0.01	0.00
K	0.01	0.01	0.01	0.01	0.01	0.00	0.01	0.01

Spot #	35	64	78	80	86	92	106	10
Comment								
SiO_2	24.99	24.05	25.05	24.55	24.76	24.38	25.24	24.86
TiO_2	0.16	0.06	0.09	0.08	0.08	0.07	0.03	0.12
Al_2O_3	21.79	21.52	22.27	20.98	21.84	22.71	22.32	22.14
FeOtot	29.90	29.40	29.21	30.07	29.44	29.65	29.86	28.17
MnO	0.29	0.29	0.18	0.18	0.12	0.27	0.19	0.34
MgO	11.92	11.94	12.31	12.09	12.52	11.93	11.58	12.29
CaO	0.07	0.04	0.03	0.13	0.05	0.00	0.11	0.02
BaO	0.00	0.00	0.00	0.00	0.00	0.00	0.00	0.00
Na_2O	0.04	0.04	0.00	0.06	0.00	0.00	0.04	0.02
K_2O	0.09	0.09	0.09	0.10	0.05	0.00	0.07	0.13
ΣAlkali	0.20	0.17	0.13	0.28	0.10	0.00	0.22	0.17
Atom site distribution (14 oxygen equivalents)								
Si	2.65	2.61	2.64	2.65	2.63	2.59	2.66	2.65
Al^{IV}	1.35	1.39	1.36	1.35	1.37	1.41	1.34	1.35
Al^{VI}	1.38	1.36	1.41	1.31	1.37	1.43	1.44	1.43
Ti	0.01	0.00	0.01	0.01	0.01	0.01	0.00	0.01
Fe^{2+}	2.65	2.67	2.58	2.71	2.62	2.63	2.64	2.51
Mn	0.03	0.03	0.02	0.02	0.01	0.02	0.02	0.03
Mg	1.89	1.93	1.94	1.94	1.98	1.89	1.82	1.95
Σ^{VI}	5.96	5.99	5.95	5.99	5.99	5.98	5.92	5.94
Ca	0.01	0.00	0.00	0.01	0.01	0.00	0.01	0.00
Ba	0.00	0.00	0.00	0.00	0.00	0.00	0.00	0.00
Na	0.01	0.01	0.00	0.01	0.00	0.00	0.01	0.00
K	0.01	0.01	0.01	0.01	0.01	0.00	0.01	0.02

Appendix E2

Table E2.10 – (continues)

Spot #	14	17	25	28	41	44	47	48
Comment								
SiO_2	25.04	24.90	24.92	24.51	26.70	25.61	26.18	25.12
TiO_2	0.08	0.08	0.09	0.10	0.08	0.06	0.12	0.07
Al_2O_3	22.55	22.35	22.39	21.89	22.00	22.27	21.65	22.34
FeOtot	27.11	28.64	29.03	29.22	27.60	28.44	27.73	28.60
MnO	0.29	0.24	0.24	0.22	0.16	0.26	0.09	0.23
MgO	12.00	11.92	12.19	12.42	12.86	12.42	12.90	12.47
CaO	0.01	0.01	0.04	0.03	0.00	0.07	0.04	0.04
BaO	0.00	0.00	0.01	0.00	0.00	0.00	0.00	0.00
Na_2O	0.01	0.03	0.03	0.02	0.02	0.00	0.05	0.02
K_2O	0.26	0.21	0.10	0.15	0.34	0.19	0.33	0.11
ΣAlkali	0.28	0.25	0.18	0.20	0.37	0.26	0.41	0.17
Atom site distribution (14 oxygen equivalents)								
Si	2.67	2.65	2.64	2.62	2.77	2.69	2.74	2.65
Al^{IV}	1.33	1.35	1.36	1.38	1.23	1.31	1.26	1.35
Al^{VI}	1.51	1.45	1.43	1.37	1.46	1.44	1.42	1.43
Ti	0.01	0.01	0.01	0.01	0.01	0.00	0.01	0.01
Fe^{2+}	2.42	2.55	2.57	2.61	2.39	2.50	2.43	2.52
Mn	0.03	0.02	0.02	0.02	0.01	0.02	0.01	0.02
Mg	1.91	1.89	1.92	1.98	1.99	1.94	2.01	1.96
Σ^{VI}	5.88	5.92	5.95	5.98	5.86	5.91	5.88	5.94
Ca	0.00	0.00	0.00	0.00	0.00	0.01	0.00	0.00
Ba	0.00	0.00	0.00	0.00	0.00	0.00	0.00	0.00
Na	0.00	0.01	0.01	0.00	0.00	0.00	0.01	0.00
K	0.04	0.03	0.01	0.02	0.05	0.02	0.04	0.01

Spot #	54	61	67	70	74	75	77	81
Comment								*
SiO_2	26.96	24.69	25.99	25.45	24.99	25.84	25.93	26.02
TiO_2	0.13	0.06	0.10	0.04	0.06	0.10	0.14	0.15
Al_2O_3	21.64	22.41	22.11	22.84	22.25	22.42	21.02	21.71
FeOtot	27.78	28.83	28.73	28.38	28.79	28.92	27.21	29.40
MnO	0.17	0.23	0.19	0.22	0.27	0.17	0.16	0.14
MgO	12.13	12.09	12.40	11.95	12.23	12.27	12.67	10.97
CaO	0.04	0.05	0.05	0.08	0.06	0.06	0.05	0.10
BaO	0.00	0.00	0.00	0.00	0.00	0.01	0.00	0.00
Na_2O	0.03	0.04	0.05	0.04	0.02	0.04	0.05	0.03
K_2O	0.62	0.18	0.22	0.30	0.13	0.19	0.33	0.38
ΣAlkali	0.70	0.26	0.32	0.41	0.21	0.31	0.42	0.51
Atom site distribution (14 oxygen equivalents)								
Si	2.81	2.63	2.71	2.67	2.65	2.69	2.76	2.76
Al^{IV}	1.19	1.37	1.29	1.33	1.35	1.31	1.24	1.24
Al^{VI}	1.47	1.44	1.43	1.50	1.43	1.45	1.41	1.47
Ti	0.01	0.00	0.01	0.00	0.00	0.01	0.01	0.01
Fe^{2+}	2.42	2.56	2.51	2.49	2.55	2.52	2.43	2.61
Mn	0.01	0.02	0.02	0.02	0.02	0.01	0.01	0.01
Mg	1.88	1.92	1.93	1.87	1.93	1.91	2.01	1.73
Σ^{VI}	5.80	5.94	5.89	5.88	5.94	5.90	5.87	5.83
Ca	0.00	0.01	0.01	0.01	0.01	0.01	0.01	0.01
Ba	0.00	0.00	0.00	0.00	0.00	0.00	0.00	0.00
Na	0.01	0.01	0.01	0.01	0.00	0.01	0.01	0.01
K	0.08	0.02	0.03	0.04	0.02	0.03	0.04	0.05

Table E2.10 – (continues)

Spot #	83	84	90	95	96	98	101	103
Comment								
SiO_2	25.71	25.20	25.42	24.87	24.77	24.88	25.88	25.33
TiO_2	0.12	0.09	0.13	0.09	0.08	0.06	0.12	0.12
Al_2O_3	21.52	22.09	21.72	22.01	22.37	21.36	21.62	21.31
FeOtot	29.24	28.51	28.67	29.19	29.00	29.23	28.50	28.65
MnO	0.17	0.19	0.22	0.19	0.21	0.19	0.21	0.17
MgO	12.24	12.57	12.47	12.19	11.87	11.63	12.15	12.49
CaO	0.11	0.01	0.06	0.03	0.04	0.02	0.03	0.03
BaO	0.00	0.00	0.01	0.03	0.00	0.00	0.00	0.00
Na_2O	0.02	0.05	0.02	0.06	0.00	0.01	0.06	0.04
K_2O	0.23	0.18	0.22	0.19	0.14	0.17	0.47	0.33
ΣAlkali	0.35	0.24	0.31	0.31	0.18	0.20	0.56	0.41
Atom site distribution (14 oxygen equivalents)								
Si	2.71	2.66	2.69	2.64	2.64	2.69	2.73	2.70
Al^{IV}	1.29	1.34	1.31	1.36	1.36	1.31	1.27	1.30
Al^{VI}	1.39	1.41	1.39	1.40	1.45	1.40	1.42	1.37
Ti	0.01	0.01	0.01	0.01	0.01	0.00	0.01	0.01
Fe^{2+}	2.58	2.52	2.54	2.59	2.58	2.64	2.52	2.55
Mn	0.01	0.02	0.02	0.02	0.02	0.02	0.02	0.02
Mg	1.92	1.98	1.97	1.93	1.89	1.87	1.91	1.98
Σ^{VI}	5.91	5.94	5.92	5.95	5.94	5.94	5.87	5.93
Ca	0.01	0.00	0.01	0.00	0.00	0.00	0.00	0.00
Ba	0.00	0.00	0.00	0.00	0.00	0.00	0.00	0.00
Na	0.00	0.01	0.00	0.01	0.00	0.00	0.01	0.01
K	0.03	0.02	0.03	0.03	0.02	0.02	0.06	0.04

Spot #	105	107
Comment		
SiO_2	25.01	25.31
TiO_2	0.05	0.06
Al_2O_3	21.45	21.66
FeOtot	29.13	29.43
MnO	0.21	0.22
MgO	12.15	11.76
CaO	0.03	0.12
BaO	0.00	0.01
Na_2O	0.02	0.01
K_2O	0.16	0.18
ΣAlkali	0.21	0.32
Atom site distribution (14 oxygen equivalents)		
Si	2.68	2.69
Al^{IV}	1.32	1.31
Al^{VI}	1.38	1.41
Ti	0.00	0.01
Fe^{2+}	2.61	2.62
Mn	0.02	0.02
Mg	1.94	1.86
Σ^{VI}	5.95	5.92
Ca	0.00	0.01
Ba	0.00	0.00
Na	0.00	0.00
K	0.02	0.02

Appendix E2

Table E2.11 – Recalculated mineral formulas of andalusite and altered cordierite in **sample SP78**. * = altered

Spot #	1	114	115	118	119	120
Comment	And	And	And	And	Cd*	Cd*
SiO_2	36.32	36.79	36.78	36.30	47.02	46.87
TiO_2	0.04	0.05	0.02	0.00	0.10	0.10
Al_2O_3	62.79	63.18	62.86	61.66	32.12	32.35
FeOtot	0.84	0.86	0.94	0.32	3.28	3.45
MnO	0.00	0.00	0.02	0.00	0.00	0.00
MgO	0.01	0.00	0.05	0.01	2.02	1.98
CaO	0.01	0.00	0.01	0.70	0.08	0.11
BaO	0.00	0.00	0.00	0.00	0.20	0.17
Na_2O	0.01	0.02	0.01	0.09	0.14	0.14
K_2O	0.00	0.03	0.00	0.22	10.35	10.51
Oxygens	5	5	5	5	18	18
Si	0.98	0.99	0.99	0.99	5.17	5.15
Al	2.00	2.00	1.99	1.99	4.16	4.19
Ti	0.00	0.00	0.00	0.00	0.01	0.01
Fe^{2+}	-	-	-	-	0.30	0.32
Fe^{3+}	0.00	0.00	0.00	0.00	-	-
Mn	0.00	0.00	0.00	0.00	0.00	0.00
Mg	0.00	0.00	0.00	0.02	0.33	0.32
Ca	0.00	0.00	0.00	0.00	0.01	0.01
Ba	0.00	0.00	0.00	0.00	0.01	0.01
Na	0.00	0.00	0.00	0.01	0.03	0.03
K	0.00	0.00	0.00	0.00	1.45	1.47

Table E2.12 – Chlorite – phengite couples used for multi-equilibrium calculations in **sample SP78**.

Chlorite	Phengite
11	15
23	16
29	24
64	51
78	53
41	55
44	56
47	58
48	59
54	60
61	65
67	66
70	69
74	71
75	72
77	76
95	94
96	97
98	100
101	102
103	104

Appendix F

Published Articles

Appendix F

F1. Article I

Title: Heterogeneous brittle-ductile deformation at shallow crustal levels under high thermal conditions: The case of a synkinematic contact aureole in the inner northern Apennines, southeastern Elba Island, Italy.

Authors: Papeschi, S., Musumeci, G. and Mazzarini, F.

Published on Tectonophysics 717, 547-564.

Abstract: We present an example of interaction between magmatism and tectonics at shallow crustal levels. In the Late Miocene the metamorphic units of the eastern Elba Island (northern Apennines) were intruded at very shallow crustal levels by a large pluton (>60 km^2) with the development of an hectometre-sized contact aureole defined by growth of low-pressure/high-temperature mineral assemblages (P_{max}<0.2 GPa, T_{max}~ 650°C). Structural data show that the contact aureole is associated with a km-sized antiform of the foliation and by several metre- to decametre-thick high-strain domains consisting of strongly foliated rocks containing synkinematic HT/LP mineral assemblages and ductile shear zones of variable thickness. These shear zones are characterized by a mylonitic foliation variably overprinted by cataclasis. Quartz microfabrics indicate that the dynamic crystallization processes progressively changed from grain boundary migration, associated with the thermal peak of contact metamorphism, to subgrain rotation and bulging recrystallization, the latter mostly associated with the cataclastic overprint. These transitions of recrystallization mechanisms in quartz are related to a progressive decrease of temperature during deformation. Deformation accompanied the development and cooling of the contact aureole, which recorded the switch from high temperature ductile to low temperature brittle conditions. The geometry of the studied deformation structures is consistent with the constraints of the regional tectonic evolution and its local interaction with the localized and transient thermal anomaly related to the coeval emplacement of igneous rocks.

Appendix F

F2. Article II

Title: Evolution of shear zones through the brittle-ductile transition: The Calamita Schists (Elba Island, Italy).

Authors: Papeschi, S., Musumeci, G. and Mazzarini, F.

Published on the Journal of Structural Geology 113, 100-114.

Abstract: A network of shear zones that evolved through the brittle-ductile transition is exposed in the Calamita Schists, Elba Island, Italy. The shear zones formed during Late Miocene contractional deformation coeval with high grade contact metamorphism (~650 °C) related to the emplacement of plutonic rocks at shallow crustal levels (~7-10 Km). An early stage high metamorphic grade foliation was overprinted by mylonitic deformation that progressively localized on low-metamorphic grade shear bands producing S-C mylonites during cooling of contact aureole. Localization of deformation on shear bands was driven by temperature decrease that triggered strain partitioning between 'hard' high grade relics and 'soft' shear bands. Softening of shear bands occurred likely due to fluid influx and retrograde growth of fine-grained phyllosilicates. The interconnection of anastomosing shear bands and passive rotation of the relic high grade foliation caused widening of the shear bands producing mylonites with a composite mylonitic foliation and C' shear bands. An estimate of the vorticity number Wk of the flow of ~0.3 – 0.5 was obtained from the orientation of C' shear bands measured at the meso- and thin section-scale. Close to the brittle-ductile transition, the growth of soft phyllosilicates allowed C' shear bands to act as precursory structures to brittle deformation localized into an array of low-angle faults and shear fractures.